Genetic and optogenetic analysis of cell cleavage plane positioning

Ruben Schmidt

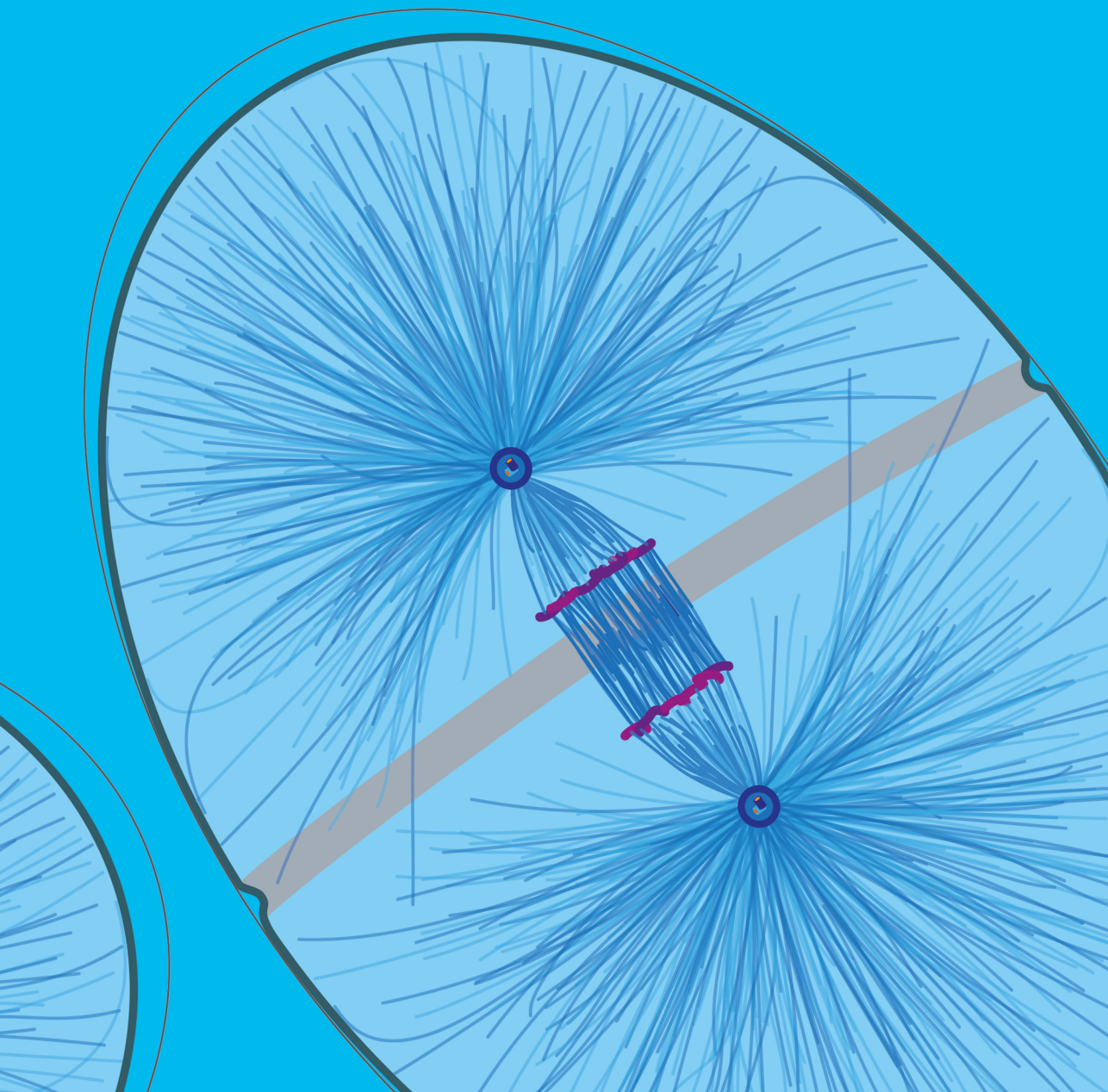

Genetic and optogenetic analysis of cell cleavage plane positioning

Ruben Schmidt

ISBN: 978-90-393-7238-8

Printed by Gildeprint, Enschede
Cover, design and layout by Ruben Schmidt and Peter Schmidt

Genetic and optogenetic analysis of cell cleavage plane positioning

Genetische en optogenetische analyse van de regulatie van asymmetrische celdeling

(met een samenvatting in het Nederlands)

Proefschrift

ter verkrijging van de graad van doctor aan de Universiteit Utrecht op gezag van de rector magnificus, prof.dr. H.R.B.M. Kummeling, ingevolge het besluit van het college voor promoties in het openbaar te verdedigen op woensdag 29 januari 2020 des middags te 2.30 uur

door

Ruben Schmidt

geboren op 24 juni 1989 te Rotterdam

Promotoren: Prof.dr. S.J.L. van den Heuvel
Prof.dr. A.S. Akhmanova

Table of contents

Chapter 1

General introduction

Ruben Schmidt and Sander van den Heuvel

Cells form the basis of all known life on Earth. Being the smallest structural and functional unit of life, the cell has continuously adapted and diversified through heritable genetic variation ever since its appearance around 3.5 billion years ago. The human body is made up of these essential building blocks, as are all other organisms that have evolved from the ancestral eukaryote. Cells cooperate to form functional tissues and organs through communication, migration, and the production and consumption of complex molecules (Alberts et al., 2008). Intriguingly, every animal starts its life as a single cell, yet through repeated rounds of tightly regulated divisions all cells of the body are generated. Thus, proper development requires a zygote to initiate the generation of not only adequate numbers, but also functionally diverse types of cells (Wolpert et al., 2007). How does a single fertilized egg cell manage to give rise to the highly organized and specialized tissues that together constitute a living organism? With constant technological advances and scientific inquiry, the intricate workings of animal development are gradually coming into focus. In this introductory chapter, we will briefly discuss the basic aspects of developmental cell division and the mechanisms that regulate this fundamental process. Continuing from there, we will zoom in further and focus on the mechanisms that determine spindle positioning and cleavage plane positioning in animal cells.

Proper development requires a balance of symmetric and asymmetric cell divisions

During each round of cell division, the genetic content of the mother cell is replicated and segregated over two daughter cells. DNA replication takes place in S (synthesis) phase, which is separated from division by the preceding G1 and succeeding G2 gap phases. Together these phases constitute the cell cycle, with a temporary or permanent phase of quiescence (G0) marking exit from the cell cycle (**Figure 1a**). The actual division of the nucleus and cytoplasm occurs during M phase, or mitosis, a term coined by Walther Flemming in 1882. Mitosis stems from the Greek word *mitos*, for ‘warp thread’, which refers to the thread-like chromosomes he observed during cellular division. These structures consist of DNA that is tightly packaged by a dense mass of associated proteins. After duplication, the two copies of each chromosome (sister chromatids) are evenly distributed to the future daughters before physical division occurs. However, not all contents of the mother cell are necessarily equally distributed, which means that the outcome of cell division can demonstrate asymmetry in multiple ways. Daughter cells may attain different sizes, inherit divergent sets of proteins, lipids, mRNA molecules and organelles (Ouellet and Barral, 2012; Jongsma and Neefjes, 2015), or end up in different cellular environments after division (**Figure 1b**) (Knoblich, 2008). Asymmetric divisions can be orchestrated extrinsically by the surrounding milieu of the cell. For example, communication with other cells, the extracellular matrix, or secreted molecules can instruct division asymmetry. Alternatively, intrinsic asymmetric divisions result from a single cell unequally segregating cellular components to its daughter cells, which commonly results

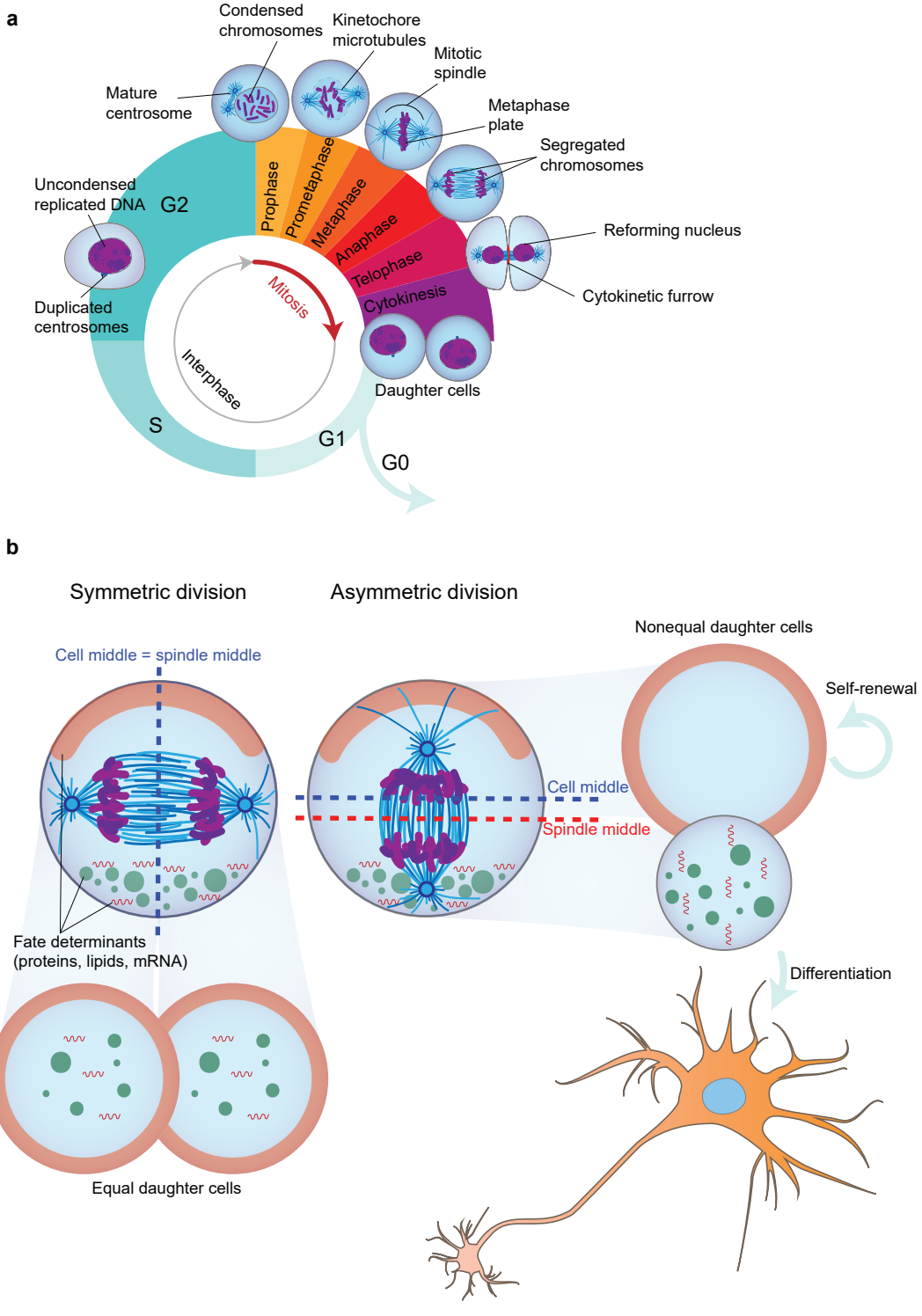
a
Condensed chromosomes
Kinetochore microtubules
Mitotic spindle
Mature centrosome
Metaphase plate
Segregated chromosomes
Uncondensed replicated DNA
G2
Prophase
Prometaphase
Metaphase
Anaphase
Telophase
Cytokinesis
Reforming nucleus
Cytokinetic furrow
Duplicated centrosomes
Mitosis
Interphase
Daughter cells
S
G1
G0
b
Symmetric division
Asymmetric division
Nonequal daughter cells
Cell middle = spindle middle
Self-renewal
Cell middle
Spindle middle
Fate determinants (proteins, lipids, mRNA)
Differentiation
Equal daughter cells

Figure 1. **Cell division**.
(**a**) Overview of the cell cycle. DNA replication occurs in S phase, and the cell divides in M phase. The gap phases G1 and G2 separate S from M phase. Cells that no longer progress through the cell cycle enter quiescence (G0 phase). Following their condensation in prophase, the chromosomes are released from the nucleus and captured by kinetochore MTs in prometaphase. After metaphase plate formation, the chromosomes are segregated by the spindle during anaphase. In telophase a cytokinetic ring contracts with the cell membrane, and nuclei reform around the genetic material. During cytokinesis the cytoplasm of the two daughter cells is physically separated. (**b**) Overview of the geometries that occur during cell divisions. Symmetric divisions (left) yield daughter cells that are equal in size and molecular fate determinants. In asymmetric cell divisions (right), spindle rotation or displacement from the cell center combined with the unequal segregation of fate determinants yields different daughter cells. This process enables stem cells to self-renew and generate differentiating daughter cells simultaneously.

in daughter cells with diverging developmental fates. This intrinsic asymmetric division process is especially important during early embryonic development, where specific cell fates and contacts are yet to be defined. The balance between symmetric and asymmetric divisions is tightly controlled during both embryonic development and adult tissue homeostasis. Thus, it might not come as a surprise that failure to maintain this balance leads to dysregulation of daughter cell differentiation and proliferative behavior, which contributes to tumorigenesis or developmental abnormalities (Knoblich, 2010). Importantly, the mitotic spindle, which coordinates DNA segregation with cell cleavage, plays an essential role in determining whether cells divide symmetrically or asymmetrically. In this chapter, we will initially focus on how the spindle apparatus is positioned, after which we will elaborate on how spindle position is eventually translated into determination of the cell cleavage plane.

Part 1 Positioning the mitotic spindle

The mitotic spindle guides the geometry of cell division

The mitotic spindle consists of a bipolar array of hollow cable-like protein polymers known as microtubules (MTs). Spindle construction starts early in M phase concurrent with the breakdown of the nuclear envelope during prometaphase, which occurs after the condensation of chromosomes and separation of centrosomes in prophase (**Figure 1a**). The sister chromatids are captured by kinetochore MTs and gathered in the metaphase plate before being segregated during anaphase. Subsequently, a cleavage furrow is formed that constricts during telophase. M phase is concluded by cytokinesis, during which abscission of the plasma membrane physically separates the cytoplasm of the two daughter cells. Importantly, the mitotic spindle provides positional information to the cell during the division process. The region of the cell cortex where the cleavage furrow forms is instructed by the position of the spindle. Thus, asymmetric positioning of the mitotic spindle results in asymmetric division and daughter cells with different sizes (Siller and Doe, 2009; Morin and Bellaïche, 2011; di Pietro et al., 2016). Tight regulation of spindle positioning is vital for controlling daughter cell fate and orientation, and its dysregulation results in divergent pathologies, including but not limited to microcephaly and cancer (Caussinus et al., 2005; Quyn et al., 2010; Noatynska et al., 2012; Hehnly et al., 2015; Fededa et al., 2016).

To correctly position the spindle, segregate cellular components and exert diverse functions, a cell must contain some initial asymmetry. This can be defined by asymmetry in structure, molecular composition and function, a set of properties that we collectively refer to as cell polarity. Striking examples of this are found in neurons, where axons and dendrites are the functionally and morphologically distinct features that are essential for proper communication between cells that make up the nervous system. Another example is found in epithelial cells, where the continuous apical side of adjacent neighbors is exposed to a common lumen. In combination with tight junctions that form a diffusion barrier, these cells perform selective transport and nutrient uptake. Importantly, cell polarity drives asymmetric divisions by controlling the position of the spindle during mitosis. Loss of cell polarity is thus directly associated with failure of cell fate determination and thereby proper development. A classic model organism in which the translation of cell polarity to spindle positioning has been studied extensively is the nematode *Caenorhabditis elegans*, and this will be the main model organism discussed in this thesis.

Asymmetric cell divisions in the early *C. elegans* embryo

Some 50 years ago, Sidney Brenner selected *C. elegans* as a model system to study how genes control the complex features of higher organisms. He shared the 2002 Nobel Prize in Physiology or Medicine with John Sulston and Robert Horvitz for their discoveries

regarding the genetics of organ development and programmed cell death. Over the past decades, *C. elegans* has become a leading model system in developmental biology and genetics, amongst many other fields. This broad use is mainly due to practical advantages such as a largely invariant and completely mapped cell lineage, relatively simple genetics, and ease of maintenance. Most importantly in the context of this thesis, however, is its large (~30x50 µm) oval embryo, which provides an excellent model for studying how the mitotic spindle is positioned.

The one-cell *C. elegans* embryo starts out as an unpolarized cell, which rapidly polarizes after fertilization. An asymmetric first division ensues, which results in the formation of two unequally sized daughter cells with diverg ent developmental fates. This initial division, as well as those performed by succeeding daughter blastomeres, relies on robust spindle positioning to ensure the emergence of different cell fates, appropriate cell sizes and cell-cell contacts that drive further development. Through asymmetric fate segregation and a highly stereotyped pattern of oriented cell divisions, the embryo eventually generates all the different cell types that constitute the tissues found in the adult worm. Similar developmental processes are found in mammals, albeit in more complex form, as the adult *C. elegans* hermaphrodite consists of only around a thousand cells as opposed to the ~37 trillion cells found in the human body (Brenner, 1974; Sulston and Horvitz, 1977; Kimble and Hirsh, 1979; Sulston et al., 1983). Early *C. elegans* development starts with a series of successive asymmetric divisions in which rapid S and M phases with no or very short gap phases interlay. Genetic screens, which are a hallmark of *C. elegans* research, have identified ~600 genes that are essential for these early divisions (Sönnichsen et al., 2005). These screens made use of efficient large-scale inactivation of genes by RNA interference (RNAi) (Fire et al., 1998; Montgomery et al., 1998; Timmons and Fire, 1998; Fraser et al., 2000; Rual et al., 2004) combined with time-lapse differential interference contrast (DIC) microscopy. Such combined methods make a valuable tool for identifying genes involved in the coordination of embryonic cell divisions.

The very first mitotic cycle is initiated after completion of meiosis II, which occurs after fertilization of the egg. Sperm entry delivers the centrosomes and paternal DNA, and determines the future posterior pole of the egg. A combination of centrosome maturation and cortical cytoskeletal flows results in symmetry breaking and polarity establishment (O'Connell et al., 2000; Wallenfang et al., 2000; Cowan and Hyman, 2004; Motegi et al., 2006). At the basis of cell polarity lie the PAR proteins (for partitioning defective), which were identified in *C. elegans* using a clever screening method. Survival of an egg-laying defective mutant was used to search for genes required for correct cleavage patterning. This allowed Kemphues et al. to identify *par* gene mutant one-cell embryos that divided symmetrically. Such *par* mutants eventually form amorphous differentiated cell masses after consecutive divisions (Kemphues et al., 1988; Kemphues, 2000). Later studies characterized the highly conserved PAR proteins and showed that they form two mutually exclusive cortical domains in the embryo, which we refer to as the anterior and posterior

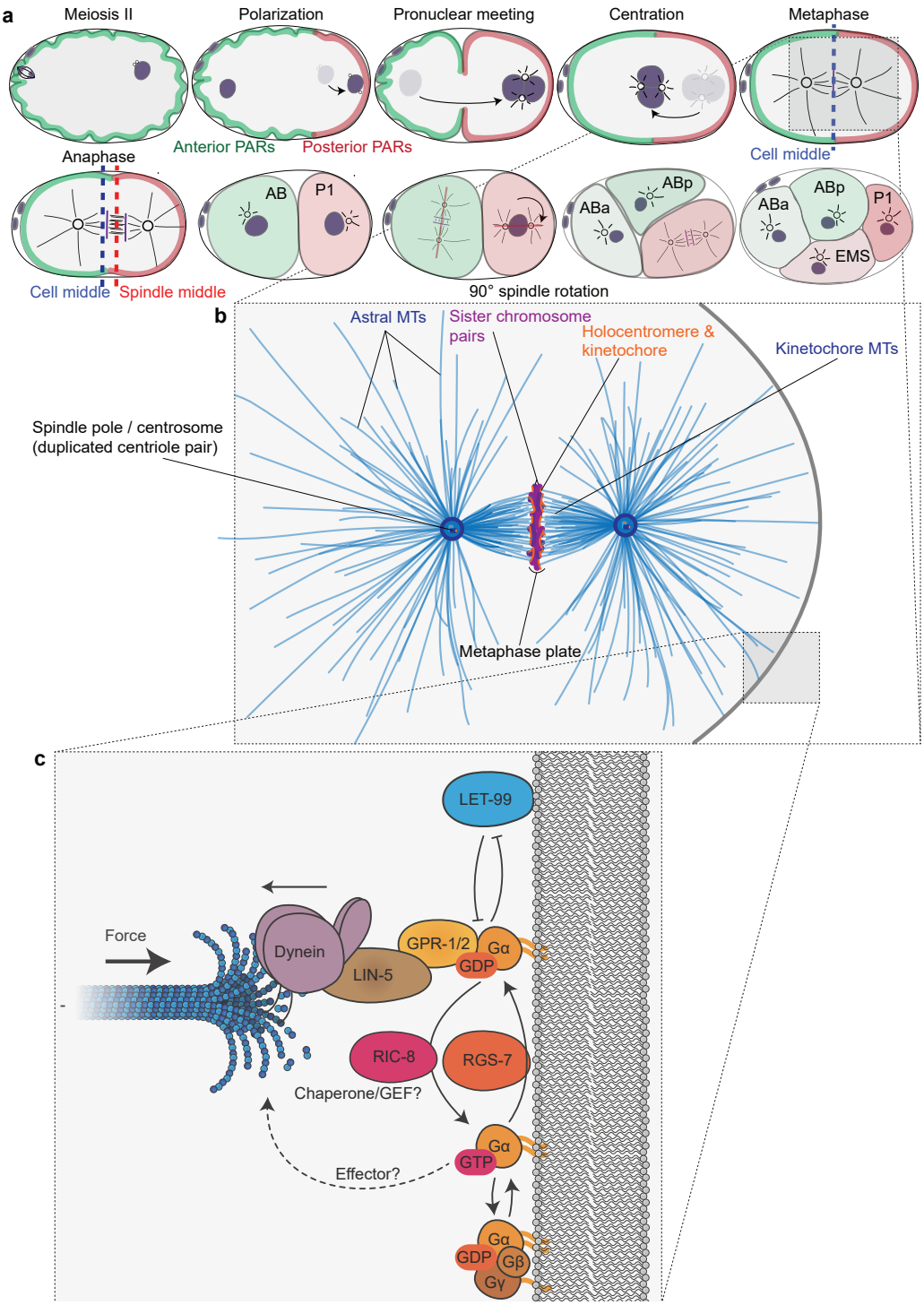
a
Meiosis II
Polarization
Pronuclear meeting
Centration
Metaphase
Anterior PARs
Posterior PARs
Cell middle
Anaphase
AB
P1
ABp
ABa
EMS
Cell middle
Spindle middle
90° spindle rotation
b
Astral MTs
Sister chromosome pairs
Holocentromere & kinetochore
Kinetochore MTs
Spindle pole / centrosome (duplicated centriole pair)
Metaphase plate
c
LET-99
Force
Dynein
LIN-5
GPR-1/2
Gα
GDP
RIC-8
RGS-7
Chaperone/GEF?
Effector?
GTP
Gβ
Gγ

Figure 2. **Mitosis in the one-cell *C. elegans* embryo**.
(**a**) Schematic representation of early divisions in the *C. elegans* embryo. Meiosis II completes following fertilization of the egg. The point of sperm entry determines the future posterior pole. Posterior PAR proteins locally exclude the anterior PAR complex, which initiates formation of the anterior-posterior polarity axis. The male and female pronucleus meet in the posterior and migrate to the center of the cell. Nuclear envelope breakdown ensues, the mitotic spindle is assembled and the condensed chromosomes are gathered at the metaphase plate. The chromosomes segregate as the spindle migrates towards the posterior. Asymmetric division results in formation of a smaller posterior P1 (red) and larger anterior AB blastomere (green). In the second round of mitosis, the P1 spindle rotates by 90˚. This rotation results in a division axis perpendicular to that of AB. This division pattern determines the cell-cell contacts required for further fate specification and development. (**b**) Detailed schematic view of the *C. elegans* metaphase mitotic spindle. Different types of spindle MTs are indicated, as are the holocentromeric chromosomes in the metaphase plate and the two centrosomes that nucleate MTs. (**c**) Schematic representation of the *C. elegans* force generator complex and its regulators as discussed in the text. Membrane-associated Gα·GDP binds to GPR-1/2–LIN-5. LIN-5 tethers dynein to the cortex either directly or via a yet undescribed adaptor protein. Dynein associates with the plus ends of dynamic astral MTs. Cortex-directed pulling forces (large arrow) are likely exerted through a combination of MT depolymerization and dynein processivity (small arrow). LET-99 locally counteracts Gα·GDP–GPR-1/2, which spatially restricts force generation. The exact role for Gα regulators RIC-8^{GEF} and RGS-7^{GAP} is under debate and might involve a cycle of GEF/GAP activity and/or Gα chaperone activity by RIC-8.

PAR domains (Goldstein and Macara, 2007; Motegi et al., 2013). These domains are set up by remodeling of the cortical actomyosin cytoskeleton, which contracts heavily over the whole surface of the embryo cortex before symmetry is broken. After completion of meiosis II, the first signs of polarity become apparent (**Figure 2a**). Contractions gradually disappear from the posterior cortex, starting at the cortical region closest to the site of fertilization. The result is a smooth posterior and a ruffled anterior cortex, each of which occupies roughly half of the embryo cortex (Munro et al., 2004). In between these domains a pseudocleavage furrow appears, which does not fully ingress and disappears before spindle assembly occurs. Symmetry breaking appears to be triggered by local inhibition of cortical contractility, which in turn depends on the presence of centrosomes and their maturation. Whether this process also requires actual microtubule polymerization remains under debate (Cowan and Hyman, 2004; Motegi et al., 2007; Tsai and Ahringer, 2007; Klinkert et al., 2019; Zhao et al., 2019). Clearly, multiple redundant pathways act to polarize the embryo. The anterior PAR complex, which consists of the proteins PAR-3, PAR-6 and PKC-3^{aPKC}, is initially distributed uniformly over the cortex. Concurrent with retraction of the cortical cytoskeleton this PAR complex localizes to the anterior. Displacement of the anterior PAR complex allows PAR-1 and PAR-2 to move from the cytoplasm to the posterior cortex, where they establish the posterior domain. In this fashion, two opposing cortical domains are set up. This anterior-posterior polarity axis will be maintained throughout the first division. Disruption of either anterior or posterior PAR complexes results in the opposite complex spreading over the whole cortex, which indicates that these protein complexes form mutually exclusive domains that counteract one another's localization (Etemad-Moghadam et al., 1995; Boyd et al., 1996).

The events leading to polarization and division of the one-cell embryo occur in a highly reproducible manner (**Figure 2a**), which makes this model very accessible for quantitative analyses. First, the maternal pronucleus migrates from the anterior to meet with the paternal pronucleus in the posterior. The pseudocleavage furrow retracts while the pronuclei move toward the cell center and the chromosomes condense. Centration is coordinated with rotation of the nucleocentrosomal complex, which aligns the then separated centrosomes with the long axis of the cell (de Simone et al., 2016). Subsequently, the nuclear envelopes start breaking down and at the same time the mitotic spindle becomes assembled (Lee et al., 2000) (**Figure 2b**). While other MT-nucleating centers such as chromatids and existing MTs have been described, the one-cell *C. elegans* embryo spindle is heavily reliant on centrosomal MT nucleation for constructing the spindle (Hamill et al., 2002; Kemp et al., 2004; Pelletier et al., 2004; Conduit et al., 2015; Prosser and Pelletier 2017; David et al., 2019). Upon correct attachment of kinetochore microtubules to the chromosomes and formation of the metaphase plate, the spindle is properly set up for anaphase chromosome segregation (Musacchio et al., 2017). At this moment, the spindle consists of an incredibly dense network of around 20,000 MTs, of which an estimated 6-50 kinetochore MTs connect to each of the 12 chromatids (Redemann et al., 2017). In *C. elegans* embryos, anaphase chromosome segregation predominantly involves spindle pole separation (anaphase B), as opposed to the shortening of kinetochore MTs or poleward flux (anaphase A) that precedes this phase in other systems (Oegema et al., 2001). Importantly, shortly before the transition of metaphase to anaphase, the spindle moves from the cell center towards the posterior. Asymmetric spindle positioning continues during anaphase, and eventually results in a 3-4 µm shift of the spindle midzone from the cell center (Valfort et al., 2018). This displacement is dictated by cortical polarity and has to occur in order for an asymmetric division to ensue, as the cell eventually cleaves through the middle of the spindle (Reviewed in Galli and van den Heuvel, 2008; Pintard and Bowerman, 2019).

Control of spindle positioning through cell polarity

How do two opposing cortical polarity domains control physical displacement of the mitotic spindle? Classical experiments have shown that this process is governed by cortical pulling forces that act on the astral MTs that emanate from the spindle to the cell cortex. In a famous study, Grill et al. sought to distinguish between models of 1) internal spindle pushing forces (Leslie and Pickett-Heaps, 1996; Pavin and Tolic, 2016), and 2) cortical pulling forces acting on astral MTs (Aist and Bayles, 1991). Both of these mechanisms had previously been shown to control spindle pole positioning in other systems. The authors employed a combined approach of time-lapse DIC microscopy and severing of the mitotic spindle midzone with a focused UV laser (Grill et al., 2001). When bisection is executed during spindle displacement in early anaphase, independent movement of both spindle poles towards their respective cortical poles follows. Importantly, the dynamics of these

movements can be quantified. The posterior pole moves further, oscillates transversely, and migrates with greater peak velocity compared to the anterior pole. The difference in peak velocities between the anterior and posterior pole is reproducible and approximately 1.4-fold. Similar pole movements were observed when Grill et al. bisected the spindle using genetic depletion of the *C. elegans* MCAK homolog KLP-7, which is a kinesin that limits centrosomal MT outgrowth (Desai et al., 1999; Srayko et al., 2005). Two conclusions can be drawn from these experiments: 1) forces that position the poles act external to the spindle as opposed to depending on pushing forces acting from within, and 2) higher net forces act on the posterior pole, which explains the posterior displacement of the spindle and eventual asymmetric division. Interestingly, depletion of either anterior or posterior PAR complex components by RNAi results in opposite effects on spindle pole velocities; disruption of PAR-2 leads to an anteriorized cortex, which causes the velocities of both poles after spindle bisection to become equal and comparable to the speed of a normal anterior pole. Conversely, disruption of PAR-3 results in a posteriorized cortex. In such embryos pole velocities become equal and resemble the behavior of the posterior pole in a control situation. Collectively, these experiments show that cortical polarity domains control asymmetric positioning of the spindle via pulling forces acting on astral MTs (Grill et al., 2001; Labbé et al., 2004). This naturally leads to the question: how are these cortical forces generated?

Identification of a cortical force generator complex

A body of follow-up studies have revealed multiple genes involved in that translation of polarity cues to asymmetric spindle positioning. The first gene identified in this context is *lin-5* (lineage abnormal), which was found in a screen for disruption of postembryonic mitoses (Albertson et al., 1978; Horvitz and Sulston, 1980; Sulston and Horvitz, 1981) using the mutagenic compound ethyl methane sulfonate (EMS, not to be confused with the *C. elegans* four-cell blastomere with the same abbreviation). Further characterization of *lin-5* revealed its contribution to spindle positioning in the one-cell embryo (Lorson et al., 2000). Other genes with spindle positioning functions in the early embryo were identified in RNAi screens for embryonic cell division mutants (Gönczy et al., 2000), and an EMS screen for the regulation of neurotransmitter secretion (Miller et al., 1996; Miller et al., 2000). Further analyses of these genes and their encoded proteins revealed an evolutionarily conserved force generator complex consisting of Gα, GPR-1/2, LIN-5 and the motor protein dynein, which is required for spindle positioning (Lorson et al., 2000; Miller and Rand, 2000; Gotta and Ahringer, 2001; Grill et al., 2001; Colombo et al., 2003; Gotta et al., 2003; Srinivasan et al., 2003; Nguyen-Ngoc et al., 2007). In this section, we will focus on how these proteins cooperate to create pulling forces on astral MTs in the early *C. elegans* embryo. We will describe many components involved in spindle positioning that are conserved from nematodes to fruit flies and all the way to man, and the diverse tools that are available to study this process. Ultimately, the study of conserved

mechanisms in *C. elegans* embryos allows us to uncover the basic principles by which spindles are positioned in the animal kingdom (Bergstralh et al., 2017; Kotak, 2019; Pintard and Bowerman, 2019).

While the *lin-5* gene was first identified by its postembryonic requirement for cell division, it is not essential for the earliest rounds of cell division in the embryo (Albertson et al., 1978). Homozygous *lin-5* null mutant larvae complete embryonic development, after which cells still enter and exit M phase but fail to segregate their DNA or perform cytokinesis. This eventually results in sterility due to failed germline formation, so homozygous mutants for *lin-5* cannot be maintained. Successful progression through embryonic development is a result of LIN-5 function being provided through the germline of heterozygous mother animals, which is known as maternal contribution. Conversely, embryos depleted of *lin-5* function by RNAi of the parent or by use of a temperature-sensitive allele, stop cell division after 2-4 rounds of mitoses. Despite the failure to undergo cytokinesis, blastomeres continue to progress through the cell cycle. Centrosomes and DNA continue to replicate, and *lin-5* null embryos mutant embryos eventually arrest with a few polyploid cells containing multiple centrosomes each. One-cell embryos without LIN-5 function successfully assemble a spindle and metaphase plate and segregate chromosomes in anaphase, yet show no posterior displacement of the spindle, and as a result divide symmetrically (Lorson et al., 2000). In addition, meiotic defects arise in such embryos due to perturbed rotation of the meiotic spindle (van der Voet et al., 2009). Some stereotypical mitotic events are also disrupted, such as posterior spindle displacement, spindle rocking, posterior centrosome flattening and rotation of the P1 spindle, which is required for the correct specification of cell fate in daughter blastomeres (**Figure 2a**). Immunolocalization experiments showed the presence of LIN-5 at meiotic and mitotic spindles and at the cell cortex, which is in agreement with LIN-5 performing a role in generating spindle pulling forces. Functional homologs of LIN-5 include *Drosophila melanogaster* Mud (mushroom body defect) and vertebrate NuMA (nuclear mitotic apparatus protein), which are also involved in spindle orientation and will be discussed in detail below (Schaefer et al., 2000; Du and Macara, 2004).

The effects of *lin-5* disruption on spindle movements in the one-cell embryo are similar to those following loss of *gpr-1* and *gpr-2*. These genes show more than 97% similarity to each other at the nucleotide level, and code for nearly identical proteins. For this reason, we collectively refer to them as *gpr-1/2* (G protein regulator-1/2). Both were identified in an RNAi screen for embryonic cell division mutants located on chromosome III (Gönczy et al., 2000). While performing strongly redundant functions, these genes could regardless be picked up in the screen because RNAi for one will also target the other due to their strong sequence conservation. One-cell embryos subject to *gpr-1/2(RNAi)*, like those with disrupted *lin-5* function, set up a metaphase spindle and enter anaphase. However, the spindle does not become displaced from the cell center and a symmetric division ensues. In addition, posterior pole rocking or flattening and P1 spindle rotation fail to occur, and

occasional chromosome segregation defects have been observed. Importantly, pull-down and western blot analyses revealed that GPR-1/2 and LIN-5 interact both in vitro and in vivo (Srinivasan et al., 2003), and the proteins are interdependent for their cortical localization (Gotta et al., 2003; Srinivasan et al., 2003; Park and Rose, 2008). Anterior and posterior PAR complex distributions are not affected by loss of either *gpr-1/2* or *lin-5* function, which indicates that the proteins act downstream of anterior-posterior polarity to position the spindle (Colombo et al., 2003; Gotta et al., 2003; Srinivasan et al., 2003).

In addition to *gpr-1/2* and *lin-5*, multiple components of G protein signaling are essential for positioning the spindle in the early embryo. The well-known G protein signaling pathways relay diverse extracellular stimuli to the cell interior. In short, a transmembrane receptor performs guanine exchange factor (GEF) activity towards its intracellularly associated Gα subunit when ligands bind its extracellular domain. This exchange of guanosine diphosphate (GDP) for guanosine triphosphate (GTP) on the Gα overcomes its interaction with subunits Gβɣ and in doing so initiates downstream signaling (Reviewed in Hilger and Kobilka, 2018). In contrast to this well-known G protein signaling pathway, receptor-independent G protein signaling was found to contribute to spindle positioning. First, the *C. elegans* Gβ gene, *gpb-1* (G protein subunit beta 1), was found to be essential for proper embryonic development, as proper spindle orientation was disrupted in a loss-of-function mutant (Zwaal et al., 1996). Later analysis of diverse *C. elegans* Gα isoforms revealed that *goa-1* (G protein, o, alpha subunit 1) mutants exhibit partially penetrant spindle positioning phenotypes in the early embryo (Miller and Rand, 2000). Co-depletion of $G\alpha_o$ (GOA-1) and $G\alpha_{i/o}$ (GPA-16; G protein alpha subunit i16) isoforms led to fully penetrant spindle positioning defects and embryonic lethality (Gotta and Ahringer, 2001; Afshar et al., 2004). Because of their redundant critical functions, we will from now on focus on GOA-1 and GPA-16 and refer to them collectively as 'Gα' for simplicity. RNAi of one of the *C. elegans* Gɣ-encoding genes, *gpc-2* (ortholog of human G protein gamma subunit 13), but not *gpc-1* (ortholog of human G protein gamma subunit 7), also resulted in embryonic spindle positioning defects and embryonic lethality comparable to loss of *gpb-1* (Zwaal et al., 1996). Further phenotypic analyses started pointing towards a role of Gαβɣ signaling in properly orienting the spindle during embryonic divisions (Gotta and Ahringer, 2001). However, depletion of *G*β nor *G*ɣ resembled the phenotype of Gα loss-of-function, and their combination did not result in additional phenotypes on top of those observed for Gα. Therefore, Gβ and Gɣ RNAi were concluded to lead to Gα activation.

GPR-1/2 and their homologs in *D. melanogaster* (Pins; partner of inscuteable) and vertebrates (LGN; leucine(L)-glycine(G)-asparagine(N) repeat-enriched protein and AGS3; activator of G-protein signaling 3) contain conserved GoLoco domains which regulate the activity of $G\alpha_o$ and $G\alpha_i$ proteins (de Vries et al., 2000; Kimple et al., 2001; Natochin et al., 2001; Reviewed in Mccudden et al., 2005). Contrary to Gβɣ, inactivation of Gα resembles depletion of GPR-1/2, and GPR-1/2 and Gβɣ were shown to compete for binding of Gα·GDP (Srinivasan et al., 2003; Tsou et al., 2003b; Afshar et al., 2005). These results

indicate that instead of acting via release of and signaling by Gβɣ (and Gα·GTP), Gα·GDP interacts with GPR-1/2 to control spindle positioning. *Gα, gpr-1/2* and *lin-5* depletion all lead to strongly overlapping and non-additive phenotypes in the early embryo. The subcellular colocalization of their encoded proteins (at centrosomes, spindle MTs and the cell cortex), as judged by immunostainings and in vitro and in vivo co-purification, strongly suggest that they form a functional complex. As their inactivation does not alter the localization of PAR proteins, but still leads to symmetric divisions, Gα–GPR-1/2–LIN-5 were proposed to control spindle orientation downstream of cell polarity. While GPR-1/2 and LIN-5 depend on both Gα and one another for their cortical localization, cortical Gα does not require either. In conjunction with the direct membrane association of Gα proteins through lipidation (commonly N-myristoylation and palmitoylation (Reviewed in Chen et al., 2018)), the currently favored model is one in which Gα recruits GPR-1/2–LIN-5 to the cortex to control spindle positioning (**Figure 2c**) (Lorson et al., 2000; Gotta and Ahringer, 2001; Colombo et al., 2003; Gotta et al., 2003; Srinivasan et al., 2003).

Importantly, homologs of Gα–GPR-1/2–LIN-5 also coordinate cell divisions in other organisms. *Drosophila* $Pins^{GPR\text{-}1/2}$ was initially shown to control the division of neuroblasts and sensory organ precursor (SOP) cells (Schaefer et al., 2000; 2001). Neuroblasts divide asymmetrically along their apical-basal axis, and in doing so generate both a larger stem cell-like neuroblast and a smaller ganglion, which produces neurons based on asymmetric fate determinant inheritance. In SOP cells, Gα controls the anterior-posterior orientation of division downstream of planar cell polarity (Reviewed in Knoblich, 2008). $Mud^{LIN\text{-}5}$, Pins and Gα control spindle orientation downstream of the *D. melanogaster* homolog of PAR-3, Bazooka. The same complex controls the orientation of symmetric divisions relative to the apical-basal axis in epithelial cells (Schaefer et al., 2000; Bowman et al., 2006; Izumi et al., 2004; 2006; Siller et al., 2006). In mammalian cells, $LGN^{GPR\text{-}1/2}$ interacts with Gα and $NuMA^{LIN\text{-}5}$ to orient the spindle. FRET (Förster resonance energy transfer (Zadran et al., 2012)) experiments showed that LGN acts as a conformational switch. The protein's N- and C-termini interact in its closed state, which is released by association with Gα and NuMA. Simultaneous interaction of LGN with both proteins was proposed to lead to the formation of a complete cortical complex (Du and Macara, 2004; Lechler and Fuchs, 2005). By coupling these complexes to the apical cortex via interaction with integrins and cadherins, epidermal cells achieve asymmetric division and delamination, which lie at the basis of skin stratification (Lechler and Fuchs, 2005). To summarize, we have discussed that the evolutionarily conserved force generator complex controls spindle orientation in diverse contexts, depending on its subcellular distribution. But how exactly does this complex manage to pull on spindle asters? To find the answer, we shall discuss the dynamic behavior of MTs and their interactors.

Microtubules and the molecular motor dynein

The MTs that are assembled from polymers of tubulin protein control many aspects of cellular processes. These include but are not limited to cell migration, intracellular transport, and cell polarity. Depending on the species, cell type, and phase of the cell cycle, the MT network is greatly reorganized to enable proper cellular function. MTs can be nucleated from several non-centrosomal cellular structures, including the Golgi apparatus (Yang et al., 2017), the apical membrane in epithelial cells (Toya and Takeichi, 2016), the vicinity of mitotic chromosomes (Carazo-Salas et al., 1999; 2001; Wilde et al., 2001), and the MT lattice itself by branch formation (Petry et al., 2013). However, the centrosome is classically regarded as the dominant MT organizing center (MTOC) of the cell. During mitosis, the spindle is assembled by two opposing centrosomes, and as we have discussed previously, the MT-dense asters are in contact with the cortex to mediate spindle positioning.

MTs dynamically cycle through alternate phases of growth and shrinkage, which are connected by catastrophe and rescue events (**Figure 3a**). Addition of soluble GTP-bound α- and β-tubulin dimers results in MT growth from the dynamic plus end. β-tubulin-bound GTP gradually hydrolyses following its incorporation into the MT lattice. Loss of the GTP cap at the growing plus end leads to catastrophes, during which the MT shrinks rapidly and protofilaments curl outwards (**Figure 3a**). Catastrophes can be reverted by rescue events, which are promoted by different MT-associated proteins (MAPs). Recent work revealed that islands of GTP-bound tubulin along the MT lattice can be formed after local removal of tubulin from the lattice by severing enzymes, which ultimately improves MT stability (Akhmanova and Steinmetz, 2015; Schaedel et al., 2015; Aumeier et al., 2016; Vemu et al., 2018). Furthermore, MT dynamics at both the minus and plus end are strictly regulated by an extensive number of MAPs and dynamics strongly depend on cell-cycle regulation (Akhmanova and Steinmetz, 2015; 2019; Bendris et al., 2015).

The outer surface of MTs offers binding sites for a diverse group of molecular motors; large protein complexes that hydrolyze ATP to move along MTs in a stepwise manner. These MT motors can be classified into two main groups, kinesins and dyneins. Together, these protein complexes drive diverse cellular processes including transport of intracellular cargo, MT organization and chromos ome segregation (**Figure 3b**). Kinesins consist of a highly diverse superfamily which harbors 21 members in *C. elegans* and almost 50 in humans (Siddiqui, 2002). The position of the motor domain within the molecule is indicative of its function, as it grossly determines whether a kinesin walks to the plus or minus end, or even depolymerizes MTs (reviewed in Hirokawa et al., 2009). Dynein, on the other hand, strictly moves toward the MT minus end (Reck-Peterson et al., 2006), and is based on a single type of heavy chain in animals. This motor protein performs a diverse set of functions in animal cells, including chromosome segregation, MT organization and organelle transport (reviewed in Reck-Peterson et al., 2018). The dynein heavy chain interacts with a wide variety of subunits and activators that determine its subcellular

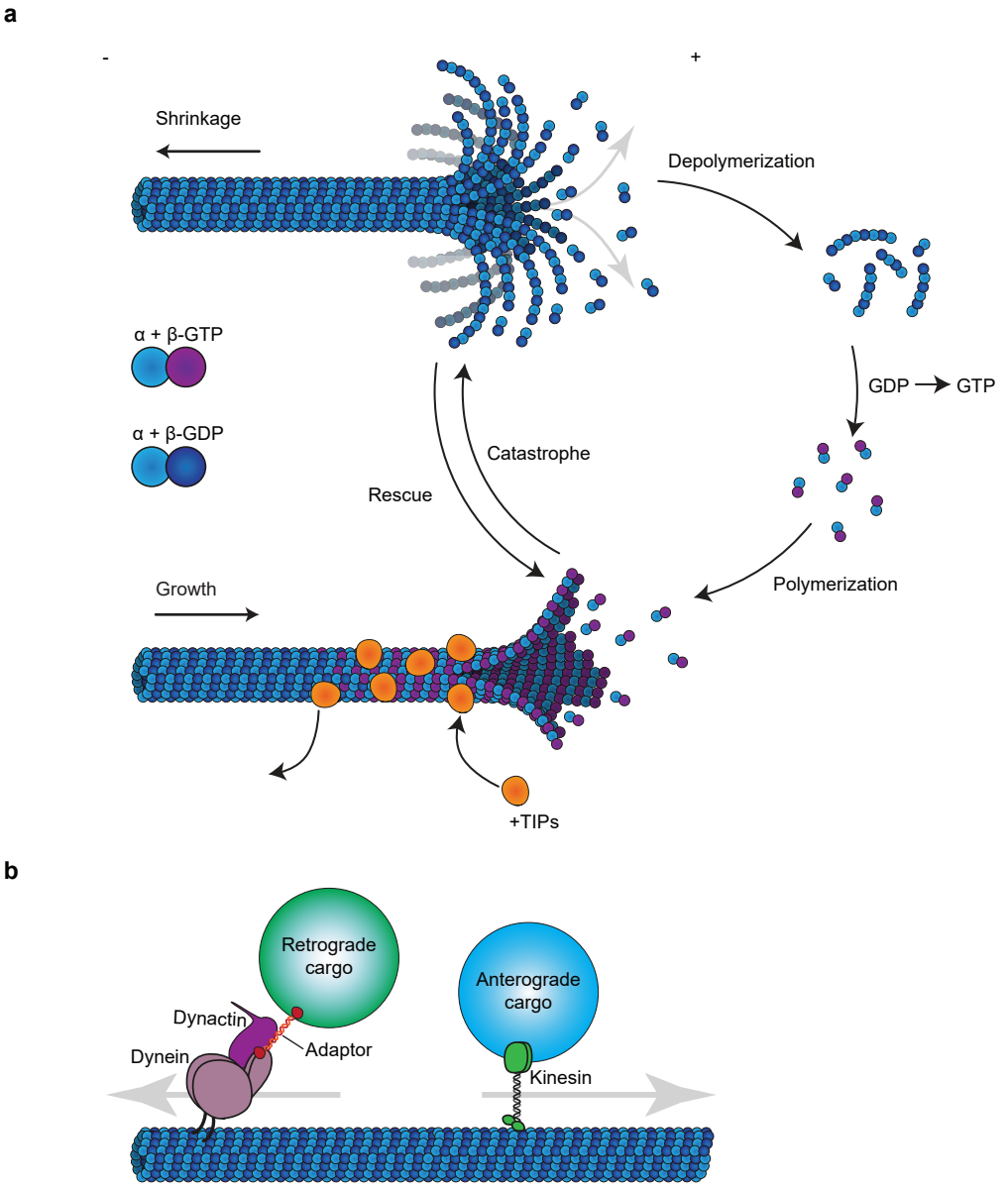

Figure 3. **MTs and molecular motors**.
(**a**) Schematic representation of MT growth and shrinkage. The dynamic instability of MTs involves alternate phases of growth by polymerization and shrinkage by depolymerization. Free GTP-bound tubulin dimers are built into the growing plus end of the MT. GTP hydrolysis ensues with a delay, creating a transient GTP cap to which autonomous +TIPs such as EB proteins can bind. Catastrophe occurs when the GTP cap is lost and growth reverts to shrinkage, which can be reverted through rescue events. (**b**) Schematic representation of molecular motor proteins that migrate over MTs. Dynein is the main minus-end directed motor protein complex that transports cargo in association with its activator dynactin and molecular adaptors (e.g. BICD1 in mammals), among many other cellular functions. Kinesins consist of a more diverse group and generally migrate towards the plus end of the MT.

localization, specificity, and activity (Redwine et al., 2017). In addition to the cytoplasmic dynein 1 that we discuss here, cytoplasmic dynein 2 is specifically involved in intraflagellar transport. Also, an independent class of axonemal dyneins mediates the beating of motile cilia and flagella (Ishikawa, 2016; Roberts, 2018). The ~1.2 MDa cytoplasmic dynein 1 complex will be referred to as 'dynein' from now on. At its core, dynein consists of the large homodimerized heavy chains (~500 kDa). Dimers of the non-catalytic intermediate and light intermediate chains assemble directly on the heavy chains. The light chain 8, light chain 7 (roadblock) and T-complex testis-specific protein 1 (TCTEX1) subunits in turn assemble on the intermediate chains. The C-terminal dynein motor domain consists of a ring of six AAA domains that bind and hydrolyze ATP. This leads to a cycle of conformational changes in which MT association and release by the globular MT binding domain allows dynein to take steps along its track. Its composition determines the specificity of the dynein complex to cargo and other molecular interactors. These bind with the N-terminal tail of the heavy chain and in doing so modulate motor and MT binding activity (Reviewed in Kardon and Vale, 2009). Further regulation of dynein will be discussed later, as we will first visit its central role in positioning the mitotic spindle.

As in other animal cells, dynein is required for a diverse set of processes in the one-cell *C. elegans* embryo. RNAi-mediated disruption of *dhc-1*, the gene encoding the dynein heavy chain, abolishes migration of the maternal pronucleus and separation of the centrosomes around the paternal pronucleus. Similar defects result from disruption of *dnc-1* and *dnc-2*, the genes that encode the regulatory subunits $p50^{dynamitin}$ and $p150^{glued}$ of the dynactin complex (Gönczy et al., 1999). Based on studies in other organisms, these subunits are known to be required for most of dyneins cellular functions (Schroer, 2004). Weak RNAi of *dhc-1* allows for centrosome separation and spindle assembly and revealed that dynein contributes to spindle positioning. However, as RNAi-mediated depletion of *dhc-1* or other essential subunits disrupts diverse meiotic and mitotic events prior to mitotic spindle assembly and positioning, a different strategy is required for accurately studying the role of dynein in spindle positioning. Conveniently, various fast-acting conditional temperature-sensitive alleles have been isolated for *dhc-1* (Schmidt et al., 2005). These alleles allow for disruption of dynein function after assembly of the spindle, by shifting embryos to a higher temperature at the appropriate time. When grown at the non-permissive temperature, one-cell embryos show defects in centrosome separation, pronuclear migration and rotation, spindle assembly, chromosome segregation, and cytokinesis. Furthermore, timed temperature shift experiments confirmed that dynein is also specifically required for nucleocentrosomal complex rotation, metaphase plate formation and anaphase initiation, which collectively are comparable phenotypes to *dhc-1(RNAi)*. However, no evidence was found for the requirement of dynein for spindle pole separation (Schmidt et al., 2005). A follow-up study analyzed spindle movements and pole velocities upon spindle bisection and reported reductions for both upon inactivation of dynein. However, the observed defects were not as severe as observed after *lin-5(RNAi)*,

which resulted in the conclusion that dynein is required, at least in part, for generating spindle pulling forces (Nguyen-Ngoc et al., 2007). The partial overlap in phenotypes observed here could be due to incomplete protein inactivation on short timescales, or the fact that the two *dhc-1* temperature-sensitive alleles used are hypomorphs and might not fully inactivate dynein function.

LIS-1 (lissencephaly-1) is one of the dynein complex components that is involved in regulating spindle positioning. This protein was shown to co-immunoprecipitate with Gα, GPR-1/2 and LIN-5 (Nguyen-Ngoc et al., 2007). Dynein was absent in GPR-1/2 pulldowns combined with *lin-5(RNAi)*, and present in GPR-1/2 and LIN-5 pulldowns combined with *Gα(RNAi)*. These observations would be consistent with dynein binding to the Gα–GPR-1/2–LIN-5 complex through LIN-5. While cortical dynein is not readily detectable in one-cell embryos, dynein is visible at the cell cortex of two-cell embryos and this localization depends on Gα–GPR-1/2–LIN-5 (Cockell et al., 2004; Nguyen-Ngoc et al., 2007). Further investigation using nonpolarized cultured mammalian cells revealed that the dynein complex controls spindle alignment to a patterned fibronectin substrate via its recruitment to the cortex by an N-terminal extension of NuMA (Théry et al., 2005; Toyoshima and Nishida, 2007). Overexpression of Gα or LGN in these cells, or GPR-1/2 in *C. elegans* embryos, led to excess cortical dynein localization and defective spindle positioning. Thus, the level of cortical Gα–GPR-1/2–LIN-5–dynein is critical for proper spindle movements. In addition, LIN-5–dynein is also required for positioning the spindle during meiosis (van der Voet et al., 2009). Direct tethering of full-length NuMA or solely its N-terminal domain to the cortex of human cells is sufficient to co-recruit the dynein complex and induce spindle movements. This could indicate that recruitment to the cortex through NuMA is the main way in which dynein controls spindle positioning, although these experiments were performed in the presence of wild type Gα and LGN (Kotak et al., 2012). Thus, whether the complex functions simply as a cortical anchor for dynein, or whether it also regulates dynein activity remains to be explored. Nevertheless, other studies have revealed a requirement for the NuMA complex in recruiting dynein to the cell cortex, which firmly establishes Gα–GPR-1/2–LIN-5–dynein as the major effector of spindle positioning in different species and cell types (Woodard et al., 2010; Kiyomitsu and Cheeseman, 2012). But how does this complex physically achieve spindle positioning?

Generating the forces that position the spindle

Different mechanisms are thought to generate the forces that position the spindle, and these involve the dynamic behavior of astral MTs and their interaction with the cell cortex. In vitro reconstitution experiments, which use minimal protein and buffer components, have provided much insight in these processes. Conveniently, purified or artificially generated centrosomes can be induced to nucleate MTs in vitro in the presence of only GTP, free tubulin and proper buffer compositions (Holy et al., 1997). Such asters can position themselves in the center of microfabricated square chambers as a result of MT

pushing and buckling against the outer chamber walls; a process which required solely MT growth. The resulting forces were estimated at ~5 pN, which increases when asters are in closer vicinity to the barrier. This is a result of the length-dependency of pushing forces, because longer MTs have a stronger tendency to buckle when pushing against a barrier (Dogterom et al., 2005; Howard, 2006). In this fashion, a simple model of MT pushing could be sufficient for balancing a MTOC in the center of a cell, depending on its geometry (Tran et al., 2001; Laan et al., 2012a). However, in symmetrically shaped cells this mechanism alone could not account for asymmetric spindle positioning (Grill and Hyman, 2005).

In addition to pushing through MT growth, cortical dynein can dictate MTOC centering in a variety of model systems and computational simulations (Carminati and Stearns, 1997; Koonce et al., 1999; Burakov et al., 2003; Zhu et al., 2010). One such system makes use of purified dynein from yeast, which is constitutively active (Reck-Peterson et al., 2006; Gennerich et al., 2007). When yeast dynein is attached to the walls of microfabricated chambers, astral MTs are efficiently tethered depending on the density of dynein molecules. This capture leads to the inhibition of MT growth due to simultaneous catastrophe induction and prevention of MT shrinkage. As such, dynein generates pulling forces of up to ~5 pN by remaining in contact with MTs that are in a depolymerizing state (Laan et al., 2012b). It is important to note that dynein can 'switch gears', meaning that it can take smaller steps while producing higher force when bearing a load (e.g., membrane vesicles) (Mallik et al., 2004). Constitutively active yeast dynein shows a stall force of ~7-8 pN (Gennerich et al., 2007; Cho et al., 2008), which is comparable to purified porcine brain dynein (Toba et al., 2006) and recombinant mammalian dynein (Nicholas et al., 2015). However, earlier in vitro work showed that depolymerizing MTs by themselves (i.e., without associated motors) can generate a pulling force on laser-trapped beads of up to 30-65 pN. Such behavior could result from the outwards curling of protofilaments that transiently capture an object in their vicinity. This force production was observed both in the presence and absence of enzymes such as kinesins that capture the depolymerizing MT plus end (Lombillo et al., 1995; Grishchuck et al., 2005; McIntosh et al., 2010). Possibly, the cooperation of multiple dynein molecules could be required to harness the force exerted by a single depolymerizing MT (Okumura et al., 2018). By attaching the growing MT end to a barrier (e.g., the cell cortex), its growth is inhibited and depolymerization ensues. In vitro, ATP hydrolysis is required for this pulling to occur, which indicates that dynein either needs to be motile in order to generate pulling forces, and/or that cycles of MT association and release are required to efficiently capture the depolymerizing MT tip. Moreover, cortical dynein has been proposed to prevent the outwards curl of disassembling protofilaments, which could stall MT shrinkage (Laan et al., 2012b). Such a model for end-on MT interaction has also been proposed to apply to *S. cerevisiae* Dam1, which is a load-bearing protein complex that connects MTs to the kinetochore and maintains their interaction even under tension when depolymerization

follows (Franck et al., 2007). It is also of importance to note that capture of MTs by cortical dynein proved to be a more reliable way of centering an artificial aster compared to MT pushing alone (Laan et al., 2012b). Thus, cells might also control the position of MTOCs through multiple mechanisms. But how do these observations translate to in vivo models?

In *S. cerevisiae* (budding yeast) cortical dynein is required for the proper positioning of a mitotic spindle-like structure. In this case, dynein interacts with the MT lattice and walks towards the minus end. As a result, the MTOC is pulled along as the MT slides along the cortex (Carminati and Stearns, 1997). Force generation by this means is clearly distinct from the end-on interaction that is observed in the above discussed in vitro experiments. In *C. elegans* embryos, such lateral MT–dynein sliding appears to be more prominent during centration of the nucleocentrosomal complex prior to spindle assembly, while this mode of force generation is probably insufficient for positioning the spindle during anaphase (Gusnowski and Srayko, 2011). In addition, coupling of dynein to organelles in the cytoplasm via the dynein light chain DYRB-1^{roadblock} was shown to enable their minus end-directed transport, which generates a drag force that aids centration of the nucleocentrosomal complex. Interestingly, this mechanism could provide an explanation for the observation that pulling force is proportional to MT length. Not due to the effect on MT buckling, but by reasoning that longer MTs would capture more dynein-organelle couples on average (Hamaguchi and Hiramoto, 1986; Kimura and Kimura, 2011). Stokes' law states that the drag force created by a round object in a viscous fluid is proportional to its speed and radius. Assuming that this applies in the one-cell embryo, Kimura and Kimura reasoned that the drag force created by a single ~0,5 µm endosome at 1 µm s^{-1} is sufficient to move the ~5 µm diameter nucleocentrosomal complex at 0,1 µm s^{-1} during centration. Together, both the end-on and lateral interaction of MTs with cortical dynein are thought to play a role in spindle positioning in the one-cell embryo (Labbé et al., 2003; Kozlowski et al., 2007; Gusnowski and Srayko, 2011; Kimura and Kimura, 2011). The combination of substrates that is used to anchor dynein during its interaction with MTs to position the mitotic spindle remains unclear. Possibly, a combination of approaches results in robust spindle positioning. The use of different adaptor complexes to tether dynein to diverse subcellular substrates could underlie the different modes of pulling force generation. Consistent with this idea, LIN-5–dynein is required for proper nucleocentrosomal complex centration, while Gα–GPR-1/2 is not. However, Gα–GPR-1/2 probably plays some role in this process, as their depletion results in more rapid centration and regulators of Gα–GPR-1/2 are required for centration to complete (Gotta et al., 2001; Tsou et al., 2002; 2003b; Goulding et al., 2007; Kimura and Onami, 2007).

A study by Kozlowski et al. focused on the number of MTs and their dynamics during mitosis in the one-cell *C. elegans* embryo. These factors should be expected to play a strong role in cortical force generation as they determine how many MT tips reach the cortex at any given time. The authors analyzed the localization of both fluorescently labeled tubulin and the MT end binding protein EBP-2^{EB1}, which marks growing MT tips

and acts as a core component and binding hub for the growing plus end (Reviewed in Akhmanova and Steinmetz, 2015). Quantifications indicated that MT plus ends interact with the cortex for ~1 s before depolymerizing (Kozlowski et al., 2007). This would indicate that a 'touch-and-pull' mechanism applies to puling force generation, in which dynein mainly translates MT depolymerization into pulling force. At the same time, this observation does not exclude that motor processivity plays a role in the generation of pulling forces. This idea is supported by the observation that cortical NuMA–dynein can pull on taxol-stabilized astral MTs in cultured mammalian cells (Arnal and Wade, 1995; Okumura et al., 2018). Conversely, a study in *C. elegans* embryos showed that spindle pole movements were almost completely abolished following the local stabilization of MTs by taxol. In this case, the authors proposed that force generation requires dynamic MTs because cortical dynein has to be continually brought in contact with MT tips, which it pulls on by attempting to walk towards their minus end while staying anchored to the cortex. In this manner, frequent MT depolymerization would also prevent continuous MT growth against the cortex, which might inhibit dynein activity (Nguyen-Ngoc et al., 2007). Whether MT pulling relies mainly on depolymerization, dynein minus end-directed motility or a combination of both mechanisms remains a topic of discussion. Interestingly, modeling of posterior spindle displacement and spindle rocking dynamics indicate that both processes are sensitive to modulation of MT growth dynamics, while posterior displacement is less prone to be affected by subtle parameter variation (Kozlowski et al., 2007). Oscillations of the spindle during anaphase were proposed to require a threshold number of active cortical force generators, which could theoretically arise due to an increase in motor activity from metaphase through anaphase. This model also reproduces the temporal delay between the start of posterior spindle displacement and the pole oscillations that follow (Pecreaux et al., 2006). Exactly how such a global increase in motor activity would be achieved remains to be elucidated. Possibilities include the modulation of dynein processivity through regulation of its interaction with dynactin (King and Schroer, 2000) or a gradual increase in the number of active cortical force generators (Grill et al., 2003). In addition, the cortical residence time of MT tips is regulated through EFA-6, which is a non-essential cortical protein that limits MT growth specifically in early embryos. EFA-6 could indirectly affect the rate at which cortical catastrophes occur by promoting end-on contacts through dynein, for which it acts as a genetic suppressor (O'Rourke et al., 2010; Gusnowski and Srayko, 2011). The rate of MT catastrophe that is observed at the *C. elegans* embryo cortex cannot be explained solely by MTs pushing against the cortex. In that regard, the active induction of MT catastrophe through the collective effort of EFA-6 and dynein might offer an explanation. Such a model would also correspond to predictions made based on in vitro studies (Janson et al., 2003; Kozlowski et al., 2007).

To conclude, a complex of Gα–GPR-1/2–LIN-5 recruits the motor protein dynein to the cortex to control spindle positioning. How exactly dynein generates pulling forces in vivo remains unclear, but multiple redundant mechanisms could underlie its role in robust

spindle positioning. In the following section, we will focus on the question of how cortical pulling forces are regulated to result in asymmetric spindle positioning and cell division.

Creating asymmetry in cortical pulling forces

In 1884 the German zoologist Oscar Hertwig stated that cell shape is a major determinant in orienting cell divisions. His physical manipulation experiments using frog eggs revealed that forcing the cells from their original round shape to a more elongated form leads to non-random divisions perpendicular to the long axis of the cell. Thus, Hertwig's long axis rule was born: by default, cells orient their spindle to the long axis of the cell. Even in recent studies this rule is often verified, while some exceptions have been described throughout the years. For example, cells that were artificially deformed to take on square or rectangular shapes often divide at different angles (Minc et al., 2011). While the one-cell *C. elegans* embryo follows Hertwig's rule by dividing perpendicular to its long axis, the geometry of this cell does not explain how its first division could be asymmetric. The previously discussed complex of Gα–GPR-1/2–LIN-5–dynein is essential for this asymmetry. How is this complex regulated to achieve an asymmetric division?

When the spindle is positioned asymmetrically during late metaphase and early anaphase, it is likely that the centering mechanisms that balance it in the cell center during earlier phases remain active. For example, the number of cortical MT tips does not vary significantly between the anterior and posterior cortex during spindle displacement (Kozlowski et al., 2007). A mechanism that promotes decentering would have to counteract existing forces, either by applying extra forces to destabilize the system, or by inhibiting or somehow modulating the existing forces that center the spindle (Grill and Hyman, 2005). A recent study by Garzon-Coral et al. assessed the mechanic properties of the *C. elegans* mitotic spindle by exerting pushing forces on the apparatus during metaphase in one-cell embryos. A pushing force of up to 200 pN can be projected on the spindle with the help of magnetic beads that are controlled by a combination of a locally applied magnetic field and optical tweezers. Applying 20-60 pN is sufficient to displace either of the two spindle poles during metaphase in one-cell embryos. Centrosomes subjected to a constant force initially move with a constant rate, but this speed decreases after a few seconds. After the pushing force is released, subjected spindle poles return almost completely to their original position. Based on these data, the authors concluded that the metaphase spindle is centered by a spring-like (viscoelastic) counterforce. The average force required to move a spindle pole 1 µm in a direction transverse to the length axis of the cell was measured at 16 pN. This force could be delivered by an estimated ~200 astral MTs pushing against the cortex at any given time. This is equal to around 10% of the total number of astral MTs present in the metaphase spindle (Redemann et al., 2017). Interestingly, the centering force increases to 100 pN μm^{-1} when the cell transitions into anaphase. This correlates with increased anaphase MT nucleation and cortical residence time. Increasing the number of astral MTs by depletion of KLP-7 also increases

the centering force. Furthermore, two-cell embryos show a higher centering force, which correlates with their twofold higher density of cortex-astral MT contacts (Garzon-Coral et al., 2016).

While it has previously been suggested that pulling forces mediated by cortical dynein could increase the robustness of MTOC centering (Laan et al., 2012b), Garzon-Coral et al. state that these pulling forces in fact counteract the centering force. Inactivation of *gpr-1/2* by RNAi increases the spindle stiffness twofold, which does not change upon anaphase onset. This indicates that cortical Gα–GPR-1/2–LIN-5 destabilizes the centering force mediated by pushing astral MTs to displace the spindle towards the posterior. A displacement of 3 μm was estimated to require ~50 pN, translating to only about 10-20 active force generator complexes (Garzon-Coral et al., 2016). Similarly, a study that used large symmetrically dividing sea urchin embryos showed that cortical dynein counteracts the centering pushing forces that control spindle localization. By clustering magnetic beads with spontaneous dynein-activating properties, a cortical domain that concentrated pulling forces can be established. This results in off-center spindle positioning and artificial asymmetric divisions. Interestingly, off-center positioning of the spindle only occurs after it has first reached the center of the cell as a result of centering forces. The authors concluded that centering forces diminish with progression through the cell cycle, and after a centering phase become diminished to a level that allows for asymmetric positioning of the spindle (Sallé et al., 2018).

As a follow-up to their earlier work describing pulling forces that position the spindle downstream of cell polarity, Grill et al. used centrosome fragmentation assays to probe for the distribution of cortical force generators. They reasoned that asymmetry in the system can be based on a difference in the number, strength, or the distribution of force generating MT-cortex interactions. Based on the speed and direction of centrosome fragment trajectories, a difference of approximately 50% more active cortical force generators was estimated to account for the displacement of the spindle in one-cell *C. elegans* embryos. Interestingly, the force exerted by each active cortical complex was proposed to be equal (Grill et al., 2003). Other studies proposed that, in addition to asymmetry in the number of active force generators, differential stiffness of the cortex could account for asymmetrically distributed pulling forces. Compared to the posterior cortex, the anterior cortex is relatively stiff, and thus less readily deformed. This increased stiffness is the result of the presence of a pronounced actomyosin network, which was shown to modulate the efficiency of force generation (Kozlowski et al., 2007; Redemann et al., 2010). One way in which cortical stiffness could modulate pulling is by affecting how long cortical force generators can remain in contact with shrinking MTs; a more deformable and elastic cortex would allow for more prolonged dynein-MT interaction. However, while disruption of the anterior actomyosin cap by chemical or genetic means increases anterior-directed pulling forces, it could not result in symmetric spindle positioning. This indicates that differences in stiffness between the anterior and posterior cortex could not be the only

means to generating asymmetric pulling (Redemann et al., 2010; Berends et al., 2013). These results are in line with the observation that actin microfilaments are not required for asymmetric spindle positioning, while they are essential for the early phase of polarity establishment (Hill and Strome, 1988).

Asymmetric positioning of the spindle is a conserved feature of the one-cell stage in nematode embryos. While subtle differences in cell size and geometry exist between 42 examined *C. elegans*-related species, and the closely related *C. briggsae* portrays marked differences in the dynamics of nucleocentrosomal complex centration and spindle movements, an asymmetric initial division always ensues in unperturbed embryos (Riche et al., 2013; Valfort et al., 2018). Another conserved mechanism is the existence of a positional switch in spindle oscillations. Posterior spindle oscillations during anaphase initiate only when a certain level of posterior spindle displacement has been reached, and this position correlates with the posterior enrichment of cortical GPR-1/2 (Riche et al., 2013). Earlier studies connected the asymmetric localization of GPR-1/2 between late prophase and early anaphase with PAR asymmetry and asymmetric spindle positioning. The extent of GPR-1/2 enrichment was proportional to the assumed difference in active cortical force generators between the anterior and posterior cortex. Thus, the authors concluded that the asymmetric effect of GPR-1/2 on Gα signaling is required for asymmetric spindle positioning (Colombo et al., 2003; Gotta et al., 2003; Grill et al., 2003; Tsou et al., 2003b; Park and Rose, 2008). However, the correlation of cortical LIN-5 distribution to asymmetric positioning of the spindle has long been under debate. One might expect posterior enrichment of GPR-1/2 to directly translate into asymmetric enrichment of its binding partner LIN-5. While some studies report asymmetric localization of LIN-5 (Colombo et al., 2003; Gotta et al., 2003; Park and Rose, 2008), others did not find a significant enrichment in the posterior during posterior spindle displacement (Srinivasan et al., 2003; Galli et al., 2011a; b; Berends et al., 2013). In addition, the distribution of dynein at the cortex has only been quantitatively assayed at the adjacent cortices of two-cell embryos (Nguyen-Ngoc et al., 2007), and was either not measured to be enriched on the cortex or globally enriched in one-cell embryos overexpressing GPR-1. Global enrichment of GPR-1 artificially enhances both levels of global cortical dynein and spindle pulling forces (Kotak et al., 2012). Conversely, GPR-1/2 and LIN-5 are enriched in the anterior during nucleocentrosomal complex centration (Tsou et al., 2003b; Park and Rose, 2008). In late anaphase, both GPR-1/2 and LIN-5 show increased and posteriorly enriched cortical localization, but whether this is causative or secondary to asymmetric spindle positioning remains unclear. Thus, whether asymmetric enrichment of Gα–GPR-1/2–LIN-5-dynein lies at the basis of asymmetric pulling forces, or whether other means of regulation function in its place or redundantly remains to be determined.

Relaying polarity through LET-99

One factor that controls the distribution of cortical force generation is the DEP (Dishevelled, EGL-10 and Pleckstrin) domain protein LET-99. This protein was identified in a screen for *let* (maternal effect lethal) alleles that affect cell cleavage patterns in the early embryo (Rose and Kemphues, 1998). One-cell embryos carrying a mutant *let-99* allele start showing defects after pronuclear meeting. The maternal and paternal pronuclei meet, but subsequently fail to rotate and incompletely migrate towards the center of the cell. Elongation of the spindle in anaphase often corrects this misorientation, and spindles eventually align properly along the A-P axis. Surprisingly, embryos still manage to divide asymmetrically and even portray a relatively smaller P1 cell compared to control embryos (Rose and Kemphues, 1998). For this reason, LET-99 was initially thought not to be involved in asymmetric force generation (Colombo et al., 2003). In two-cell *let-99* embryos, both AB and P1 blastomeres show spindle orientations defects. These are independent of their altered cell sizes, and later developmental stages show improper cellular arrangements as a result. Additionally, the nucleocentrosomal complex and metaphase spindle perform excessive rocking motions in one-cell embryos, which indicates that cortical force generation is dysregulated. Loss of LET-99 function does not appear to affect the cortical distribution of anterior and posterior PAR complexes, so the protein is not likely to control cell polarity (Rose and Kemphues, 1998). Follow-up studies identified a role for LET-99 in asymmetric spindle pole movements through the modulation of cortical dynein-dependent pulling forces. Interestingly, immunolocalization experiments revealed that LET-99 concentrates in a mid-posterior cortical band from prophase onwards, and that this localization pattern depends on PAR polarity. Thus, LET-99 was proposed to inhibit pulling forces at the lateral cortex, whereby it could deliver asymmetry to forces downstream of cell polarity, enable rotational force during centration, and posterior-directed force during spindle positioning (Tsou et al., 2002). DEP domain proteins are generally involved in the regulation of G protein signaling, phospholipid binding and recruitment of proteins to the cell cortex (Consonni et al., 2014). Considering these roles, LET-99 was proposed to locally regulate the function of Gα, which itself is uniformly distributed over the cortex and shows no obvious asymmetries. The asymmetric distribution of GPR-1/2 depends on its antagonistic interaction with LET-99, downstream of PAR-3. In addition, this mechanism is important during asymmetric division of the EMS cell as a response to MES-1/SRC-1 signaling (Srinivasan et al., 2003; Tsou et al., 2003a). Spindle severing and centrosome fragmentation experiments showed that LET-99 inhibits lateral forces in the posterior. This establishes the LET-99 band as a third cortical domain that controls force generation, in addition to the previously defined anterior and posterior regions (Krueger et al., 2010). Astral MTs that contact the cortex in this region are more dynamic, which fits into a model where the lateral region shows a relatively lower astral MT association rate. The interaction of astral MTs with force generators results in lower detachment rates (Pecreaux et al., 2006), which could lead to higher pulling forces being generated outside of the

lateral band region. While there appear to be no obvious homologues of LET-99 that mediate spindle positioning in *Drosophila*, a wide range of other organisms including mammals harbors a LET-99-related DEPDC1 protein family (Bringmann et al., 2007; Sendoel et al., 2014). Whether these proteins perform similar functions in spindle positioning remains to be determined.

The regulation of Gα function

In addition to LET-99, other modulators of Gα function at the cortex have been described. Double inactivation of *let-99* and *Gα* rescues the excessive centrosome movements observed after loss of *let-99*, which indicates that loss of *let-99* function results in hyperactive Gα. Similarly, double inactivation of *let-99* and *ric-8* (resistant to inhibitors of cholinesterase) rescues these hyperactive centrosome movements (Couwenbergs et al., 2004). *ric-8* was identified in a screen for genes involved in synaptic transmission, which is the chemical communication between neurons at the synapse (Miller et al., 1996). *ric-8* mutants exhibit 15-29% embryonic lethality, which increases to 100% when combined with a heterozygous *goa-1* mutant. RIC-8 is required for proper spindle positioning together with Gα during early embryonic divisions (Miller et al., 2000; Afshar et al., 2004). In mammalian cells, the isoforms RIC-8A and RIC-8B both interact with Gα, and biochemical analyses showed that RIC-8A is a potent GEF that targets multiple Gα isoforms. RIC-8A has been proposed to perform this function by binding to Gα·GDP, promoting the release of GDP and subsequently forming a stable nucleotide-free state that is dissolved upon Gα·GTP formation (Tall et al., 2003). Despite these clear effects, the exact role of RIC-8 in spindle positioning remains elusive. In *Drosophila* and mammalian cells, RIC-8 is required for the cortical localization of Gα, which would hint at a role as a protein chaperone (David et al., 2005; Hampoelz et al., 2005; Wang et al., 2005; Gabay et al., 2011). In contrast, mammalian RIC-8A catalyzes the dissociation of Gα·GDP–LGN–NuMA complexes by stimulating Gα·GTP formation, thus freeing LGN from NuMA (Tall and Gilman, 2005). In *C. elegans*, RIC-8 binds to both GOA-1 and GPA-16, shows GEF activity towards GOA-1·GDP, and was proposed to act before GPR-1/2 in the activation of Gα (Afshar et al., 2004). Conversely, RIC-8 appears to exert a more chaperone-like function towards GPA-16 by promoting its protein levels and cortical localization (Afshar et al., 2005).

In addition to RIC-8, another regulator of Gα function was identified in a screen for *C. elegans* genes that encode GAP domain-containing proteins. RGS-7 (regulator of G-protein signaling 7) was the only putative GAP to be identified that is fully required for embryonic viability. *rgs-7* inactivation leads to hyperactive rocking of the posterior spindle pole during anaphase in one-cell embryos. Surprisingly, spindle severing experiments showed that this effect results from a reduction of cortical pulling forces that act on the anterior pole. Further analysis showed that RGS-7 acts as a GAP for GOA-1, which would explain its positive effect on spindle positioning. RGS-7 could act by generating Gα·GDP, which is a binding target for GPR-1/2. While both RIC-8 and RGS-7 show weak cortical

localization in the one-cell embryo, no obvious asymmetries have been described (Hess et al., 2004). Thus, how RGS-7 asymmetrically affects spindle positioning remains unclear. The above data might indicate that a cycle of GTP hydrolysis is important for the control of spindle positioning by Gα. However, whether this cycle is required for release of Gα·GDP–GPR-1/2–LIN-5, as was observed in mammalian cells, remains unclear. Such a model is further complicated by the differential preferences of RIC-8 and RGS-7 for the two spindle-positioning Gα isoforms acting in *C. elegans* embryos. In addition, while RIC-8 does not appear to target Gαβɣ complexes, depletion of the Gβ subunit GPB-1 rescues the effect of depleting RIC-8 (Afshar et al., 2004). Thus, it is likely that Gα activation depends on multiple levels of regulation, possibly involving both GAP/GEF activity and chaperone function.

On a similar note, GPR-1/2 was found to act as a guanine dissociation inhibitor (GDI) for both of the *C. elegans* Gα isoforms, and to serve as a competitor for Gα binding with Gβɣ (Afshar et al., 2005). Regulation of GPR-1/2 binding to Gα is possibly modulated by LET-99, which counteracts the localization of GPR-1/2 at the cortex (Bringmann et al., 2007). Furthermore, the cortical levels of GPR-1/2 are essential for the proper regulation of pulling forces, as overexpression of GPR-1 leads to excess spindle movements in one-cell embryos (Redemann et al., 2011). This further indicates that protein levels of GPR-1/2 might be rate-limiting for force generation. Overexpression of GPR-1 resultes in its increased cortical localization, which either indicates that there are excess binding sites available for GPR-1/2 in a wild-type situation, or, although less likely, that Gα expression is upregulated by overexpression of GPR-1. This model is further supported by the observation that knockout of either *gpr-1* or *gpr-2* reduces the amplitude of spindle pole oscillations during anaphase (Redemann et al., 2011).

Phosphoregulation of LIN-5 and the cortical recruitment of dynein

To uncover how cell polarity regulates Gα–GPR-1/2–LIN-5 function, Galli et al. compared the effects of kinase knockdowns in early embryos by quantitative mass spectrometry (Galli et al., 2011a). These experiments revealed that four serine residues in LIN-5 are phosphorylated by PKC-3, which is a component of the anterior PAR complex. Phosphorylation of LIN-5 by PKC-3 requires activity of CDK1, an essential cyclin-dependent kinase that controls G1/S and G2/M transitions. Immunolocalization experiments showed that phospho-LIN-5 colocalizes with PKC-3 at the anterior cortex and cytoplasm. Interestingly, this enrichment of phospho-LIN-5 occurs specifically during the transition of anterior- to posterior-directed MTOC migration between prometaphase and early anaphase. Preventing this phosphorylation by mutation of the four residues targeted by PKC-3, or by *pkc-3* RNAi, results in an overshoot of the nucleocentrosomal complex towards the anterior during centration. In addition, anterior-directed pole movements are enhanced in early anaphase. However, most embryos expressing an unphosphorylatable LIN-5 mutant manage to displace their spindle towards the posterior in late mitosis and

divide asymmetrically. In contrast, this process is disrupted in both *pkc-3(RNAi)* and *lin-5(RNAi)* embryos. Thus, additional levels of regulation through PKC-3 and LIN-5 are likely to determine asymmetric spindle positioning. On the contrary, mimicking phosphorylation of LIN-5 by PKC-3 leads to a partial *lin-5* loss of function phenotype, which could be a result of lowered protein levels or a requirement for dynamic instead of constitutive phosphorylation. Either mimicking or disrupting phosphorylation of LIN-5 by PKC-3 does not significantly alter GPR-1/2–LIN-5 localization. Thus, it is likely that phosphorylation instead regulates other aspects of LIN-5 functionality, for example by altering its dynamics or possibly the recruitment of dynein. Interestingly, 19 other phosphorylated residues were identified within LIN-5, which indicates that phosphorylation by additional protein regulators could play a role in controlling LIN-5 function (Galli et al., 2011a). A similar type of force generator complex regulation was identified in Madin-Darby canine kidney (MDCK) cells, which form an epithelial layer with a central lumen and show apical-basal polarity in 3D in vitro cultures (Montesano et al., 1991). In these cells, spindle orientation was found to be controlled by Par3-aPKC through phosphorylation of LGN. This modification excludes the force generator complex from the apical cortex through inhibition of the interaction between LGN and Gα (Hao et al., 2010; Zheng et al., 2010). Furthermore, in *D. melanogaster* epithelia the apical exclusion of Pins by aPKC-mediated phosphorylation was also shown to control planar spindle orientation (Guilgur et al., 2012). Collectively, these studies clearly show that pulling forces are modulated by phosphoregulation of cortical force generators throughout the animal kingdom.

In cultured mammalian cells, NuMA, LGN and Gα are required for the proper cortical localization of dynein during cell division. In an elegant series of experiments, Kiyomitsu et al. showed that the cortical distribution of dynein is dynamic and responds to the proximity of spindle poles in cultured human cells. As a consequence, metaphase spindles show oscillating movements, which the authors proposed could be important for probing of the cell center. Spindle pole proximity affects the cortical localization of dynein, but not LGN, through the release of polo-like kinase (Plk1). This kinase in turn regulates the cortical localization of the dynein-dynactin motor complex by inhibiting its interaction with LGN–NuMA. Interestingly, Plk1 phosphorylates NuMA and the dynactin components $p150^{glued}$ and $p50^{dynamitin}$, but not LGN. Thus, Plk1 could determine the cortical localization of dynein and possibly its activity through multiple levels of regulation. In addition, Kiyomitsu et al. identified a signal from the chromosomes that regulates cortical force generation. A gradient of RanGTP restricts the localization of LGN–NuMA to the polar cortex, which is important for the maintenance of proper spindle orientation. RanGTP possibly acts by regulating the binding of importin-β to the NuMA nuclear localization sequence, which affects the ability of LGN–NuMA to associate with the cortex while not disrupting their complex formation (Kiyomitsu et al., 2012; Tame et al., 2016).

Interestingly, Gα–LGN is not the only anchor used by NuMA–dynein to associate with the cortex. A study by Kiyomitsu et al. revealed that in addition to the Gα–LGN–NuMA

pathway, dynein can also be tethered to the cortex via Gα–LGN-independent 4.1G/R–NuMA. Surprisingly, this pathway appeared to be anaphase-specific (Kiyomitsu et al., 2013). The 4.1 superfamily consists of multifunctional cortical proteins that contain a highly conserved N-terminal FERM domain, and are known to regulate mechanical properties of the cell membrane (Diakowski et al., 2006; Reviewed in Baines et al., 2014). However, a follow-up study by Kotak et al. determined that 4.1 proteins affect the cortical levels of NuMA and $p150^{Glued}$ indirectly through their effect on the cortical actin network. An intact actin cytoskeleton is required for the cortical localization of NuMA during mitosis (Kotak et al., 2014). The same study showed that NuMA interacts with the phosphoinositides PIP and PIP_2 specifically during anaphase, independently of their effect on cortical actin (Kotak et al., 2014). The PIP/PIP_2–NuMA interaction requires a C-terminal motif in NuMA and is inhibited by CDK1 phosphorylation (Zheng et al., 2014). These observations constitute a clear difference with the situation in *C. elegans* one-cell embryos during anaphase, where Gα–GPR-1/2 is fully required for the cortical localization of LIN-5 (Srinivasan et al., 2003; Park and Rose, 2008). However, the *C. elegans* gamma isoform of casein kinase 1 (CSNK-1) was shown to regulate the cortical levels of GPR-1/2–LIN-5. Loss of CSNK-1 function results in uniformly high levels of cortical GPR-1/2–LIN-5, increased spindle pulling forces and elevated levels of cortical PPK-1, a type I PIP kinase that stimulates PIP_2 synthesis. In unperturbed embryos, CSNK-1 is enriched on the anterior cortex downstream of PAR polarity, while PPK1 localizes more strongly to the posterior. Thus, cell polarity could be translated to asymmetric spindle positioning by local action of PPK-1 on GPR-1/2–LIN-5 directly, or indirectly via the generation of PIP_2 (Panbianco et al., 2008). In addition, the phosphatase PPH-6–SAPS-1 complex contributes to cortical GPR-1/2–LIN-5 localization and proper pulling force generation. PPH-6–SAPS-1 is also required for proper contractility via the organization of cortical NMY-2, but this role is independent of its effect on GPR-1/2–LIN-5. It is of interest to note that the regulation of GPR-1/2–LIN-5 by CSNK-1 described above requires PPH-6–SAPS-1 function (Afshar et al., 2010). Thus, while there are clear differences in the regulation of the anaphase LIN-5^{NuMA} complex, a role for phosphoinositides in regulating its cortical localization could be conserved from *C. elegans* to man.

Experiments in cultured mammalian cells have shown that rising cortical levels of NuMA during anaphase lead to a concomitant gradual increase in cortical dynein levels. During metaphase, NuMA is phosphorylated at residue T2055 by CDK1, and this modification is counteracted by the phosphatase PPP2CA. Loss of this phosphorylation during anaphase as a result of CDK1 inactivation leads to increased cortical NuMA–dynein localization, which is required for proper spindle elongation (Kotak et al., 2013; Seldin et al., 2013). Such dynamic phosphorylation patterns could be important for spindle positioning in the *C. elegans* embryo as well. This might offer one explanation for why PKC-3-mimicking constitutively phosphorylated LIN-5 does not rescue its function (Galli et al., 2011a).

Interestingly, NuMA also interacts with MTs directly via its MT binding domain (MTBD),

which allows the protein to localize to dynamic MT plus ends during M phase (Seldin et al., 2016). This direct interaction with MTs can occur concomitantly with the interaction of NuMA with LGN (Gallini et al., 2016). The cortical localization of dynein is insufficient for proper spindle orientation in mouse keratinocytes. This process also requires the intact MTBD of NuMA. Likewise, the direct interaction of NuMA with MTs is required for proper spindle orientation and morphogenesis in mouse hair follicles (Seldin et al., 2016). Dynein plus end tracking has also been implicated in its cortical localization and spindle positioning in yeast (Markus and Lee, 2011). The role of dynein plus end-tracking in the context of mitotic spindle positioning will be further explored in one of the experimental chapters of this thesis.

Besides the regulation of cortical dynein recruitment by its anchor Gα–GPR-1/2–LIN-5, the differential regulation of dynein motor activity could contribute to proper spindle positioning. As mentioned previously, the temporal coordination of posterior spindle displacement with anaphase spindle oscillations can be explained by a gradual increase in dynein processivity from metaphase through anaphase (Pecreaux et al., 2006). This suggests that dynein processivity is tightly regulated during mitosis to ensure proper spindle positioning. A variety of dynein-dynactin complex components perform essential functions during mitosis, and dynein generally requires dynactin for most of its cellular functions (Raaijmakers et al., 2013). The assembly of active dynein-dynactin complexes is achieved by different adapters depending on their subcellular localization and the phase of the cell cycle (McKenney et al., 2014; Schlager et al., 2014a; b). In one-cell *C. elegans* embryos, the dynactin components DNC-1^{p150Glued}, DNC-2$^{p50/dynamitin}$ and DNC-3$^{p24/p22}$ are essential for proper spindle positioning (Skop and White, 1998; Severson et al., 2003; Terasawa et al., 2010). Whether an adaptor is required to connect dynactin to dynein as in other species, and whether such an adaptor is important for the translation of cell polarity to asymmetric spindle positioning remains to be explored. Many proteins potentially contribute to this process. For example, LIS-1, an essential component of the dynein complex (Faulkner et al., 2000), was shown to be essential for proper spindle positioning (Nguyen-Ngoc et al., 2007), and a diverse set of genetic suppressors have been identified for the embryonic lethality caused by conditional *dhc-1* alleles (Schmidt et al., 2005; O'Rourke et al., 2007). Collectively, these studies indicate that a great variety of proteins could be involved in regulating dynein function during spindle positioning.

It is probably evident from working through this part of the introduction that the exact mechanisms controlling asymmetric cell division are numerous, complex and to a large extent still unknown. Clearly, robust spindle positioning plays a central role in guiding asymmetry and cell diversification. While the core machinery that drives spindle positioning is conserved, its regulation varies depending on the model organism and cell type. Accordingly, not all factors that have been implicated in spindle positioning could be discussed in this introduction, nor will they be in the whole extent of this thesis. Continuing from here onwards, we will focus instead on the question of how spindle position is

translated into determination of the cleavage plane. As for spindle positioning, many of the mechanisms that function in cleavage plane specification have been uncovered using the *C. elegans* one-cell embryo as a model, as they are strongly conserved throughout the animal kingdom.

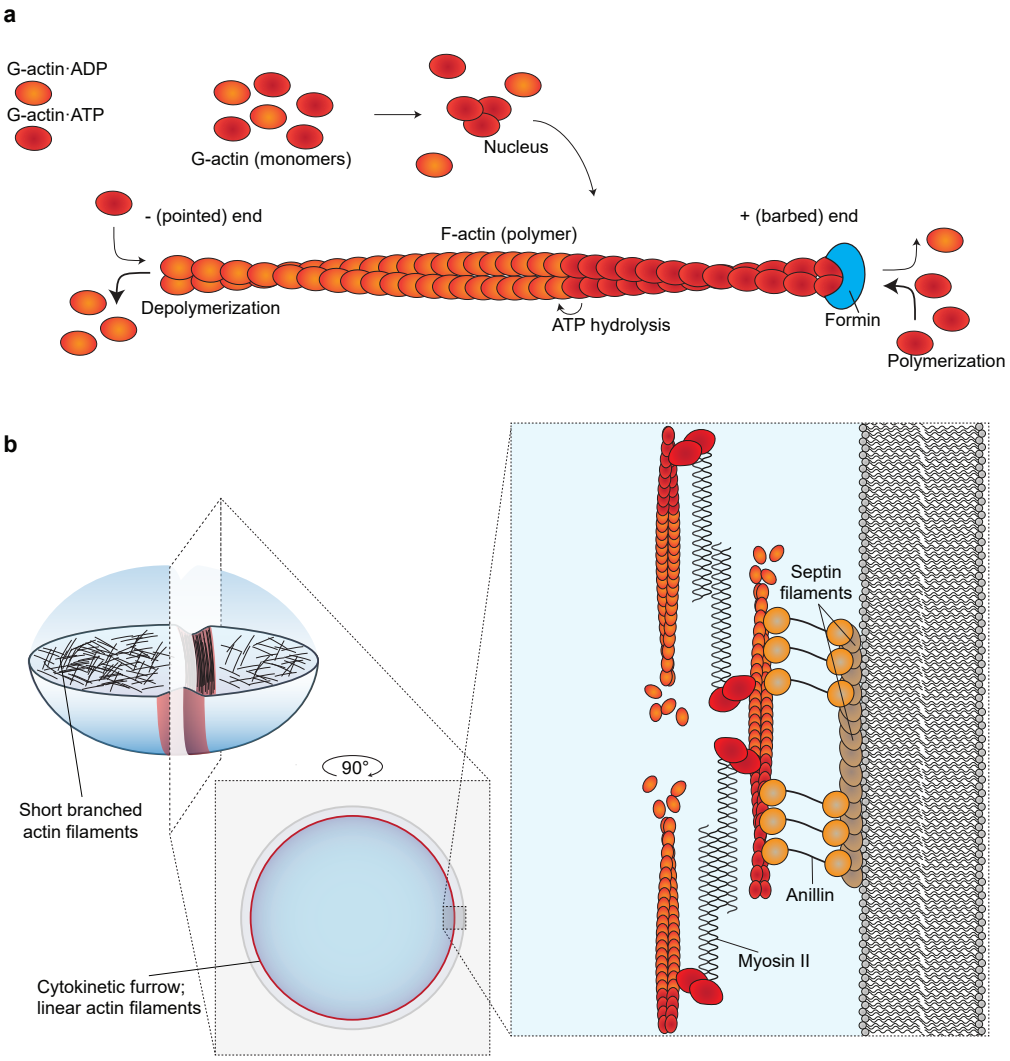

Figure 4. **An actomyosin-based cytokinetic furrow drives bisection of the mitotic cell**. (**a**) Schematic representation of actin polymerization. Globular (monomeric) G-actin bound to ATP spontaneously nucleates. Actin nuclei initiate the formation of polymeric F-actin filaments. Depolymerization occurs at the minus (pointed) end, and polymerization at the plus (barbed) end. Spontaneous ATP hydrolysis increases the stability of actin filaments. Growth at the plus end is promoted by factors that include the formin proteins. (**b**) Lateral view of schematically represented dividing one-cell *C. elegans* embryo. Branched actin filaments decorate the cortex of the embryo. During cytokinesis the equatorial cortex is remodeled to include preferentially linear actin filaments. The mechanism by which actin is tethered to the cortex involves septin filaments and anillin, but is yet to be fully established. Cytokinetic ring constriction is driven by the actin molecular motor non-muscle myosin II.

Part 2 Positioning the cytokinetic furrow

Translating spindle position to local formation of the cytokinetic ring

In part I of this introduction we discussed what is known about the mechanisms that position the spindle during mitosis. But even when the spindle is positioned correctly, the cell still needs to translate this information to proper formation of a cleavage furrow. To achieve this, the spindle has to communicate with the cell cortex to drive its dramatic remodeling into a ring that constricts and physically divides the cell. How this communication is achieved, and which factors play a role in building an ingressing furrow will be discussed next.

In animals, cell cleavage is achieved through the constriction of an actomyosin ring that is constructed during anaphase and ingresses during telophase. While plants and single-celled organisms apply the fusion of membrane vesicles to achieve daughter cell separation, animals have evolved a mechanism that uses non-muscle myosin to deliver the forces that contract the cytokinetic furrow (Odronitz and Kollmar, 2007). While the components involved in furrowing appear to be strongly conserved throughout the animal kingdom, variations based on cell type, size, shape and developmental context deliver a wide range of variations on a central theme. Currently, many questions which were posed some decades ago remain unanswered or are answered incompletely (Pollard, 2017). Such questions include: what proteins participate in cytokinesis? What specifies the site of furrow formation? How does the contractile ring assemble? As for other important biological processes, the regulation of cytokinesis shows strong redundancy; multiple pathways can lead to the construction of a furrow and we will discuss these further onwards. Clearly, the combination of experiments in different model systems and their integration with computational analyses will be required to understand this process (Cortes et al., 2018).

The contractile ring is a complex assembly of higher-order structures consisting of the core components filamentous actin (F-actin) (**Figure 4a**), the actin motor non-muscle myosin II, septin filaments, regulators of actin dynamics and scaffolding proteins such as anillin that connect these components (**Figure 4b**) (D'Avino et al., 2008; Piekny and Maddox, 2010, reviewed in Green et al., 2012). Assembly of the cytokinetic furrow starts with activation of the GTPase RhoA, which is modulated by specific GEFs and GAPs (Reviewed in Tcherkezian and Lamarche-Vane 2007; Basant and Glotzer, 2018). Artificial activation of RhoA, even in interphase cultured cells, is sufficient to instruct actin remodeling and formation of a cleavage furrow (Wagner and Glotzer, 2016). RhoA·GTP stimulates downstream mDia2^{formin}, which drives the assembly of F-actin (Goode et al., 2007). RhoA·GTP also activates its downstream effectors Rho kinase (ROCK) and citron kinase, which lead to the phosphorylation of regulatory myosin light chain, and with that the activation of myosin II (Reviewed in Matsumura et al., 2011).

The mitotic spindle modulates contractility through local RhoA activation

The mitotic spindle has long been known to orchestrate cleavage furrow positioning. Raymond Rappaport famously performed micromanipulation experiments in which he physically displaced the mitotic spindle during anaphase. This often results in repositioning of the cleavage plane, even when a furrow has already formed. While unknown at the time, such experiments show that activated furrowing components such as RhoA can either shift along the cortex, or that they can be inactivated and sequentially reactivated at the new cortical site that overlays the center of the spindle. Using the Rho GTPase-binding domain of the scaffold rhotekin fused to GFP as a probe (Benink and Bement, 2005), the cortical distribution of activated RhoA has been studied in fertilized sea urchin (genus *Strongylocentrotus*) and African clawed frog (*X. laevis*) embryos. Bement et al. observed low levels of global RhoA activation prior to anaphase, and a local patch of active RhoA that forms during anaphase at the equatorial cortex. Disruption of either MT or actin polymerization through nocodazole or cytochalasin D drug treatment, respectively, suggested that formation of the active RhoA zone depends on an intact MT network, but not on actin polymerization. Thus, F-actin assembly is probably stimulated downstream of MT-mediated RhoA activation. Treatment of embryos with high doses of nocodazole prior to furrowing fully disrupts spindle and RhoA zone formation. Conversely, addition of nocodazole following the onset of furrowing does not prevent RhoA zone maintenance nor furrow ingression. Lower doses of nocodazole lead to a broadening of the RhoA zone and cause furrowing failure in a subset of cells. Collectively, these experiments indicate that MTs control focusing of the RhoA activation zone prior to furrow ingression. This is further illustrated by micromanipulation of the mitotic spindle, which results in repositioning of the cleavage furrow as observed in earlier studies (Rappaport, 1996; Alsop and Zhang, 2003). Such a shift is preceded by a gradual migration of the active RhoA zone, which suggests that RhoA is locally activated and deactivated in response to the position of the spindle (Bement and von Dassow, 2005; Reviewed in Bement and von Dassow, 2006). Similar to other small GTPases, the intrinsic GTPase activity of RhoA is extremely low (Zhang et al., 2000), which suggests that constant modulation of RhoA activity, as opposed to a single activation event, could be important for proper cytokinesis.

Figure 5. **The *C. elegans* anaphase mitotic spindle.**
(**a**) In between the segregated chromosomes the spindle midzone is assembled. (**b**) Overlapping antiparallel MTs are condensed into stable bundles by cell cycle-regulated MT bundling proteins. SPD-1^{PRC1} associates with the centralspindlin complex (ZEN-4 and CYK-4) to specifically bind to and bundle MTs in an antiparallel orientation. (**c**) Centralspindlin associates with ECT-2 at the cortex in a cell cycle-regulated manner. ECT^{GEF} stimulates exchange of RhoA-bound GDP for GTP, leading to its activation and the initiation of furrow construction.

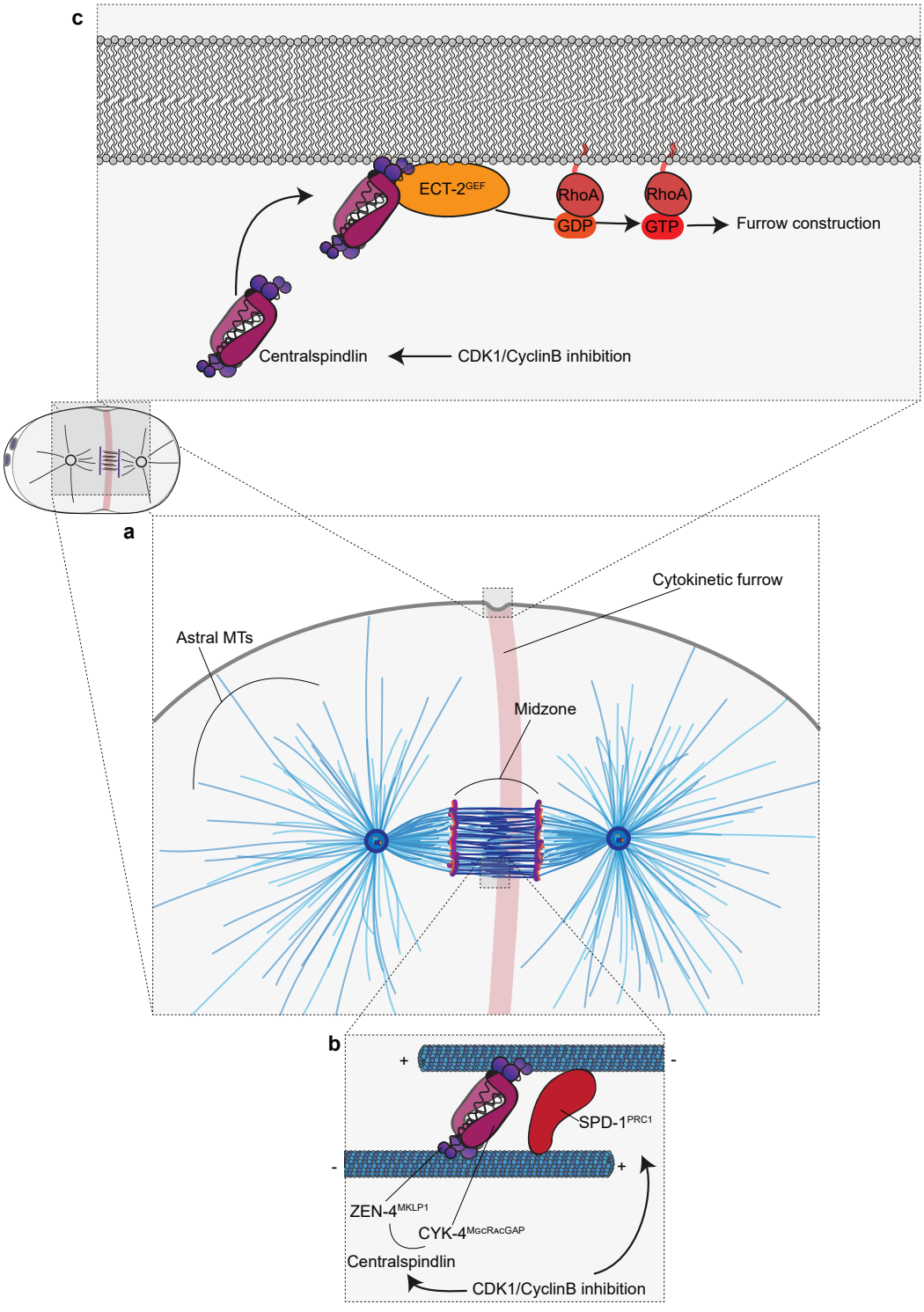
c
ECT-2GEF
RhoA
GDP
RhoA
GTP
Furrow construction
Centralspindlin
CDK1/CyclinB inhibition
a
Cytokinetic furrow
Astral MTs
Midzone
b
+
-
SPD-1PRC1
-
+
ZEN-4MKLP1
CYK-4MgcRacGAP
Centralspindlin
CDK1/CyclinB inhibition

The spindle midzone stimulates cortical furrowing

How do spindle MTs determine where RhoA is activated? To answer this question, it is important to consider the structure of the anaphase spindle (**Figure 5a**). After the onset of anaphase chromosome segregation, an interpolar array of tightly bundled MTs emerges, which is known as the central spindle. This structure is part of the spindle midzone, or the region in between the segregated chromosomes. The terms 'midzone' and 'central spindle' are often used interchangeably in the literature, so we will adhere to the use of 'midzone' to avoid confusion. The midzone consists of antiparallel bundles of MTs and their zone of overlap condenses as anaphase progresses (Euteneuer and McIntosh, 1980; Mastronarde et al., 1993). The construction of the midzone, like anaphase induction, depends on the inactivation of CDK1 at the end of metaphase, through degradation of cyclin B by the anaphase promoting complex/cyclosome (APC/C) and 26S proteasome (**Figure 5b**) (Niiya et al., 2005; Potapova et al., 2006; Reviewed in Pines, 2011). Successive steps in the progression of mitosis following metaphase result from progressive decrease in CDK1 activity, which coordinates spindle elongation with DNA segregation, furrow induction and finally exit from mitosis (Wolf et al., 2007).

The spindle midzone is formed by tightly bundled antiparallel MTs

A key player in the organization of the midzone is PRC1 (protein regulating cytokinesis 1), which was identified as one of the 54 candidates in a screen for CDKs substrates in HeLa cells. PRC1 is phosphorylated by CDK1 in vitro and its protein levels are high specifically during mitosis. Disruption of PRC1 function blocks cytokinesis in HeLa cells (Jiang et al., 1998). Cells in different model systems are capable of initiating a cytokinetic furrow but fail to complete abscission in the absence of PRC1 function (Vernì et al., 2004; Mollinari et al., 2005). On a molecular level, PRC1 and its homologs were specifically shown to be involved in the antiparallel bundling of MTs, while these proteins display no affinity towards MTs oriented in parallel (**Figure 5b**) (Loïodice et al., 2005; Janson et al., 2007; Gaillard et al., 2008; Lee et al., 2015). Not every homolog of PRC1 is essential for division; *C. elegans* SPD-1$^{Feo/PRC1}$ (spindle defective) is required for midzone stability in the one-cell embryo but its depletion by RNAi does not block division (Verbrugghe and White, 2004). Abscission defects appear only from the four-cell stage onwards. Interestingly, the outward push generated by the *C. elegans* midzone is sufficient to segregate chromosomes in the absence of spindle poles, and SPD-1 is involved in regulating such forces (Nahaboo et al. 2015). PRC1 localizes to the midzone and is essential for its proper organization together with its binding partner KIF4 (Kurasawa et al., 2004; Zhu et al., 2008). This kinesin-4 family member is recruited to the midzone through its interaction with PRC1, after which it actively migrates to MT plus ends. There PRC1 acts as a negative regulator of MT dynamics, it and controls the length of antiparallel MT overlap in the midzone during anaphase (Zhu and Jiang, 2005; Hu et al., 2011). In vitro experiments showed that the minimal interaction of MTs with PRC1 and KIF4 can reconstitute

antiparallel MT overlaps with geometries similar to midzones found in living cells, which suggests that these proteins can regulate overlap length intrinsically (Bieling et al., 2010; Hannabuss et al., 2019). Importantly, SPD-1 is not required for the initial phase of midzone assembly. Instead, this step is regulated by the kinetochore components KNL-1, BUB-1, HCP-1/2 and CLS-2^{CLASP} (cytoplasmic linker-associated protein), which concentrate on the mitotic chromosomes before migrating to the future midzone at anaphase initiation (Maton et al., 2015). The MT bundling activity of SPD-1 is required to confer mechanical resilience to cortical pulling forces acting on the neighboring spindle poles during anaphase elongation of the midzone (Lee et al., 2015). Interestingly, even when SPD-1 is depleted and the midzone is torn apart by the forces acting on spindle poles, the cytokinetic furrow shows normal ingression kinetics (Verbrugghe and White 2004; Lewellyn et al., 2010). Midzone organization by PRC1/KIF4 is regulated through Plk1, which is essential for both spindle elongation and cytokinesis in human cells (Brennan et al., 2007; Burkard et al., 2007; Reviewed by Petronczki, 2008). Mammalian Plk1$^{Polo/PLK1}$ phosphorylates PRC1 after anaphase onset, which enables its own midzone localization (Neef et al., 2007). This possibly leads to the inhibition of the MT bundling activity of PRC1 and its binding partner KIF4, whereby it controls the structure of the midzone (Hu et al., 2011; Adriaans et al., 2019).

Activation of RhoA through centralspindlin and the RhoGEF ECT-2

Classically, the midzone has been implicated in stimulating furrow formation at the equatorial cortex through a diffusible signal that is active from early anaphase onwards. This was initially shown by insertion of a barrier in between the midzone and equatorial cortex at different points in mitosis, which prevents furrowing on one side of the cell when performed during metaphase or early anaphase (Cao and Wang, 1996). Two central players in the midzone-derived signal are ECT-2$^{Pebble/ECT2}$ (epithelial cell transforming 2), a RhoGEF that is essential for the activation of RhoA during division (Prokopenko et al., 1999; Tatsumoto et al., 1999; Motegi and Sugimoto, 2006), and the centralspindlin complex. Centralspindlin consists of the kinesin-6 family member ZEN-4$^{Pavarotti/MKLP1}$ and the RacGAP CYK-4$^{RacGAP50C/MgcRacGAP}$ (**Figure 5b**) (reviewed by White and Glotzer, 2012). The centralspindlin complex is strongly conserved and essential for all animal cells that have been studied to complete cytokinesis (Mishima et al., 2002). MKLP1 was identified as a kinesin-6 family member that is required for the progression of cytokinesis (Nislow et al., 1990; Nislow et al., 1992; Julian et al., 1993; Adams et al., 1998). In *C. elegans*, its homolog ZEN-4 is similarly important for midzone stability and cytokinesis completion (Powers et al., 1998; Raich et al., 1998). The motor activity of ZEN-4, and with that its midzone localization, is inhibited by CDK-1-mediated phosphorylation until anaphase onset (Mishima et al., 2004). CYK-4 was identified in a screen for chromosome III maternal effect lethal mutations (Gönczy et al., 1999). Subsequent analysis revealed that, like ZEN-4, it manages midzone stability and cytokinesis (Jantsch-Pluner et al., 2000).

CYK-4 is a RacGAP that forms the heterotetrameric centralspindlin complex with ZEN-4. This complex performs MT bundling in vitro, contrary to the ZEN-4 and CYK-4 proteins individually (Mishima et al., 2002; Pavicic-Kaltenbrunner et al. 2007; Davies et al., 2015). Furthermore, clustering of centralspindlin through oligomerization is required for its proper localization and function in cells (Hutterer et al., 2009). This oligomerization is inhibited by PAR-5$^{14\text{-}3\text{-}3}$ in the early *C. elegans* embryo, which is in turn inhibited by the CPC (chromosomal passenger complex; Kaitna et al. 2000; Severson et al. 2000; Douglas et al., 2010; Basant et al., 2015) and the RNA-binding protein ATX-2$^{ataxin\text{-}2}$ (Gnazzo et al., 2016). CYK-4 binds to ECT-2, which functionally links midzone MTs to the cortical activation of RhoA (**Figure 5c**) (Mishima et al., 2002; Somers and Saint, 2003; Yuce et al., 2005; Zavortink et al., 2005; Nishimura and Yonemura, 2006).

In mammalian cells, ECT2 is autoinhibited through interaction of its BRCT-containing N-terminus and Rho-GEF containing C-terminal domain (Kim et al., 2005). The latter also contains a pleckstrin homology (PH) domain and polybasic cluster, which are required for ECT2 membrane association through phosphoinositide binding (Su et al., 2011). Autoinhibition of ECT2 is relieved by its association with MgcRacGAP, which occurs when the latter has been phosphorylated by Plk1 (Burkard et al., 2009; Wolfe et al., 2009). In addition, midzone localization of ECT2 is holstered prior to anaphase through inhibiting phosphorylation by CDK-1 on two of its residues. Subsequent interaction with MgcRacGAP allows ECT2 to associate with both the midzone and cortex (Yüce et al., 2005; Leung and Glover, 2011; Su et al., 2011). In cultured human cells, the association of ECT2 with the midzone is not essential for cytokinesis (Chalamalasetty et al., 2006). However, ECT2 membrane localization is essential for the activation of RhoA and successful cytokinesis (Su et al., 2011; Kotynkova et al.,2016).

Centralspindlin has not been observed at the equatorial cortex in wild type *C. elegans* one-cell embryos prior to ring formation, but ZEN-4 and CYK-4 can be observed at the tip of the ingressing furrow both in control and midzone-defective embryos (Verbrugghe and White, 2004). These observations suggest that at least part of centralspindlin function is performed at the cortex. Interestingly, CYK-4 and SPD-1 interact in vivo, and this interaction is important for the maintenance of midzone stability during anaphase in one-cell embryos (Ban et al., 2004; Lee et al., 2015). Counterintuitively, CYK-4 is a RacGAP but intact centralspindlin is required to activate RhoA and complete cytokinesis. Other known RhoGAPs such as RGA-3/4, have been shown to counteract RhoA activity (Schmutz, 2007; Schonegg et al., 2007). The exact role of CYK-4 GAP activity has been under dispute and appears to diverge depending on the species (White and Glotzer, 2012). In some systems, homologs of CYK-4 promote RhoA activity (D'avino et al., 2004; Zavortink et al., 2005; Loria et al., 2012), while in others it is dispensable for RhoA activity (Goldstein et al., 2005; Yamada et al., 2006). Yet in others, the GAP activity of CYK-4 homologs appears important to inhibit the formation of branched F-actin at the equatorial cortex through its target Rho-family GTPase CED-10^{Rac1} (D'avino et al., 2004; Canman et

al., 2008; Bastos et al., 2012; Loria et al., 2012). In more recent studies, CYK-4 was instead shown to be required for the activation of RhoA. This function requires CYK-4 cortical localization via its C1 domain, which is dispensable for midzone formation. In addition, RhoA activation was shown to require the interaction of CYK-4 with ECT-2 via the catalytic sites of both proteins. This offers an explanation for how the CYK-4 GAP domain can promote RhoA activity (Lekomtsev et al., 2012; Zhang and Glotzer, 2015; Reviewed in Basant and Glotzer, 2017). Furthermore, centralspindlin requires CPC function for its localization to the midzone. Cytokinesis is likely to involve multiple CPC functions, considering that double depletion of ZEN-4 and AIR-2 leads to additive furrowing defects (Lewellyn et al., 2011). The CPC performs a multitude of functions during mitosis and consists of AIR-2$^{\text{Aurora B}}$, ICP-1$^{\text{INCENP}}$, BIR-2$^{\text{Survivin}}$ and CSC-1$^{\text{Borealin}}$ (Reviewed in Ruchaud, 2007). Depletion of the CPC by disruption of any one component prevents chromosome segregation, blocks midzone formation, reduces furrow ingression speed, and results in a late failure of cytokinesis (Kaitna et al. 2000; Hauf et al., 2003; Giet and Glover, 2001; Hutterer et al. 2009; Lewellyn et al. 2011; Basant et al. 2015). A link between the CPC and the centralspindlin complex is found in the direct interaction between and phosphorylation of ZEN-4 by AIR-2, which is essential for ZEN-4 midzone localization and cytokinesis (Severson et al., 2000; Guse et al., 2005; Davies et al., 2014). Furthermore, negative regulation of centralspindlin oligomerization by PAR-5 binding of ZEN-4 is counteracted through its phosphorylation by AIR-2. Finally, oligomerization of centralspindlin enables the activation of RhoA through ECT-2, which initiates furrow formation (Douglas et al., 2010. Basant et al., 2015).

The regulation of cortical contractility by astral MTs

As we discussed in the previous section, the midzone plays a major role in the regulation of cytokinesis in different cell types. However, experiments with sand dollar eggs that were performed more than 50 years ago revealed that this structure is not the only part of the mitotic spindle with furrow-inducing capacity. Raymond Rappaport elegantly used pushing with a glass bead in the middle of a one-cell egg to manipulate cell shape and spindle position, as shown in **figure 6a**. In the second round of mitosis, two spindles originate in a common cytoplasm as a result. Both of these spindles progress to anaphase and induce formation of a cleavage furrow overlying their midzones. However, in between the two asters, another furrow forms and ingresses to completion. This so-called Rappaport furrow does not rely on an underlying set of separated chromosomes and midzone. Thus, not only the midzone, but also opposite pairs of asters harbor furrow-inducing capacity (Rappaport, 1961). This effect is not specific to sand dollar eggs, as later experiments have shown that aster-induced furrowing also occurs in sea urchin eggs and cultured mammalian cells (Rieder et al., 1997; Reviewed in Oegema and Mitchison, 1997) as well as early *C. elegans* embryos (Baruni et al., 2008).

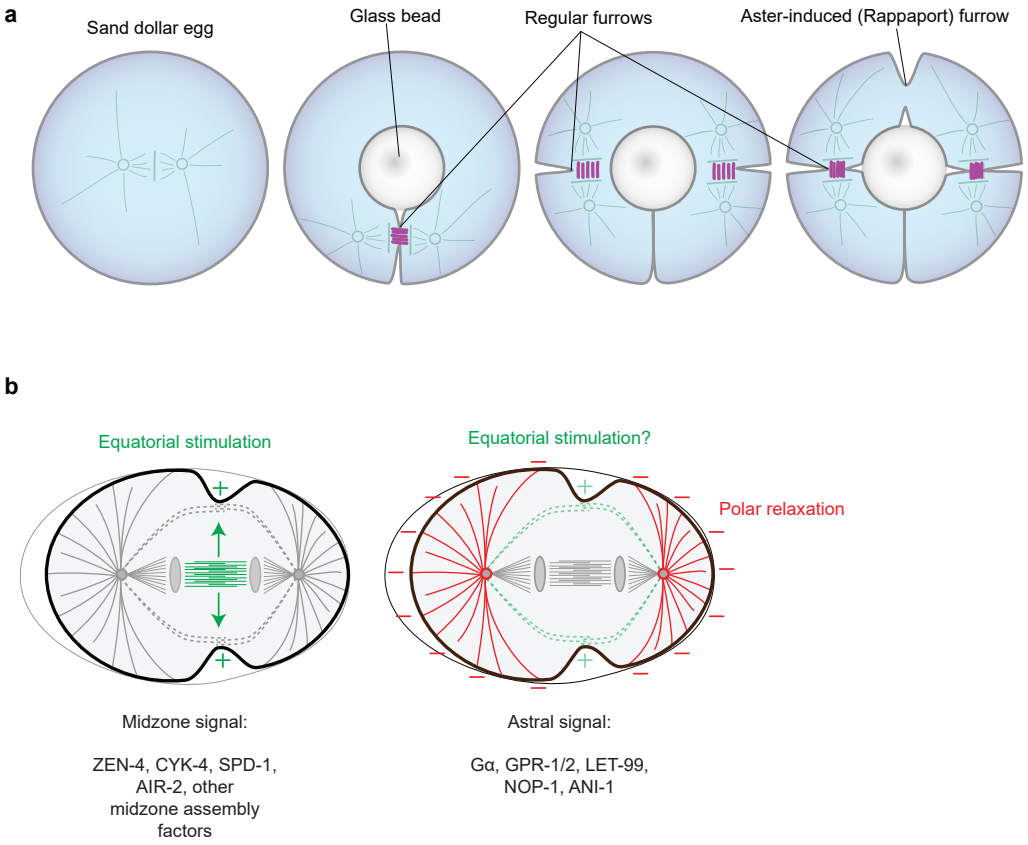

Figure 6. **Redundant signals from the spindle midzone and asters control cytokinetic furrowing.** (**a**) Schematic representation of classic micromanipulation experiments in sand dollar eggs. A glass bead is pushed into the cell during mitosis to displace the spindle. The ensuing cell division results in a single hoof-shaped cell. In the subsequent round of cell division three furrows form and complete cytokinesis. One overlies each of the two spindles as would occur in a normal situation. An additional 'Rappaport' furrow forms in between the adjacent asters of the two spindles that have no segregated DNA nor a spindle midzone. (**b**) Models for the different furrowing signals originating from the spindle midzone and asters. Equatorial stimulation (left) by the spindle midzone promotes furrowing at the equatorial cortex. Asters could deliver either polar relaxation by inhibiting contractility outside of the equatorial cortex, and/or stimulate furrowing at the equator through the formation of midzone-like antiparallel MTs close to the cortex.

Polar relaxation and equatorial stimulation

How do astral MTs regulate cytokinetic furrowing? Different models have been proposed throughout the years (**Figure 6b**), one of which was termed polar relaxation (Wolpert, 1960; White and Borisy, 1983). If asters locally inhibit instead of stimulate contractility, then a furrow could form where inhibition is lowest, i.e. the midway point between the two opposing asters. Alternatively, a second model referred to as equatorial stimulation states

that signals from the asters instead stimulate signaling, and that such signals would be strongest midway between their origin (Rappaport, 1986; Devore et al., 1989). Even though both models find experimental support, no decisive single mechanism has been identified. Equatorial stimulation by asters could occur via the formation of midzone-like structures close to the cortex, which has been observed in *D. melanogaster* spermatocytes (Inoue et al., 2004). If MTs emanating from opposite spindle poles form antiparallel bundles near the equatorial cortex, then these could be expected to recruit factors such as centralspindlin to signal to the cortex and locally activate RhoA. As a consequence of declining levels of active CDK/cyclin complexes in anaphase, MTs start to progressively elongate and stabilize, which possibly promotes the formation of such antiparallel bundles (Verde et al., 1992). Conversely, experiments in PtK (*Potorous tridactylis* kidney) cells suggested that antiparallel bundles of MTs are not required for the initiation of aster-directed furrows. However, the presence of centralspindlin, part of the CPC and MT bundles were associated with furrows that ingress completely (Savoian et al., 1999).

Polar relaxation might act independently or in concert with an equatorial stimulation mechanism. Interestingly, global contractility is induced independently of MT polymerization in mitotic cells that artificially bypass the spindle assembly checkpoint (SAC) through injection of Mad2 antibodies (Canman et al., 2000). Thus, astral MTs might direct cytokinesis by locally inhibiting an otherwise globally contractile cortex. In both grasshopper spermatocytes and the *C. elegans* one-cell embryo, experimental manipulations that lead to severe asymmetric placement of the spindle on one side of the cell result in repositioning of the actomyosin cytoskeleton away from the cortex adjacent to the spindle poles (Werner et al., 2007; Chen et al., 2008). This indicates that astral MTs that do not form antiparallel bundles with those from opposing asters can locally inhibit contractility of the cortex. Such relaxation of the cortex depends on MT dynamics but not on the activity of RhoA. However, in the same cells, antiparallel astral MTs can locally stimulate furrowing instead, and this is largely independent of MT dynamics but instead relies on RhoA activity (Chen et al., 2008).

The above observations would suggest that antiparallel bundles of MTs, which originate from the midzone region or from the asters, promote RhoA activation and, with that, local contractility. Conversely, dynamic astral MTs inhibit contractility without inactivating RhoA, which hints at a role in transporting active contracting factors such as actin or myosin II from the cortex, or otherwise locally inactivating them. Contradictory results were found in cultured mammalian cells. Here, RhoA can be locally activated in interphase or mitosis using an ectopically expressed and locally controlled RhoGEF (Wagner and Glotzer, 2016). The resulting zone of active RhoA was not modulated by the presence of astral MTs. These experiments might indicate that astral MTs modulate contractility upstream of RhoA activation instead of downstream, as was proposed for grasshopper spermatocytes. Possibly, differences between experimental systems or the phases of mitosis that were tested could account for such contradictory results.

The molecular components that mediate cortical contractility through astral MTs

How do astral MTs modulate cortical contractility at a molecular level? TIRF (total internal reflection fluorescence) microscopy of fluorescently tagged myosin and actin revealed that myosin II is assembled on the equatorial cortex in a de novo manner in cultured rat kidney cells. In these cells, myosin II disassembly is locally inhibited during early cytokinesis, and no flow from the polar regions towards the equator was observed. Possibly, polar disassembly of myosin II could focus furrowing in the equatorial region and thus provide a connection between astral MTs and the inhibition of contractility. Actin, on the other hand, shows a strong myosin II-dependent equatorial-directed flux during early cytokinesis. However, the concentration of actin in this region does not depend on flux, which indicates that an independent mechanism assembles actin filaments in the equator in a de novo manner (Zhou and Wang, 2008). It is important to note that such independency between cortical actin and NMY-2 flows might not be strongly conserved, considering that both show pronounced flows during cortical ingression in the *C. elegans* one-cell embryo (Reymann et al., 2016).

Experiments in sea urchin embryos provided further insights into the role of astral MTs in regulating contractility. In these cells, centrosome ablation, or the application of nocodazole at doses low enough to specifically inhibit the polymerization of astral MTs, results in a significant broadening of the cortical RhoA zone during anaphase. In addition, cortical imaging of a RhoA biosensor in frog and echinoderm embryos showed that RhoA activation is lowest in the regions that display the highest MT density. Dynamic waves of RhoA activity and F-actin assembly were observed, which depend on Ect2 and establish an excitable cortex that could dynamically respond to changes in spindle position (Benink et al., 2005; Bement et al., 2015). Further experiments using sea urchin and sand dollar embryos revealed that a global depletion of cortical phosphorylated myosin regulatory light chain (RLC) occurs prior to anaphase. Subsequently, in the large zygote, but not in smaller blastomeres, a pool of stable astral MTs forms that contacts the equatorial cortex, which correlates with the local appearance of phosphorylated myosin RLC. These stable astral MTs could play a role in the induction of contractility. Similarly, in mammalian cultured cells with monopolar spindles, a stable array of astral MTs extends past the chromosomes and contacts the cell cortex. These stable MTs reproducibly induce cytokinesis at a site distal to the single aster and chromosomes (Canman et al., 2003). Concomitantly to stable astral MTs reaching the equatorial cortex in sea urchin embryos, a separate dynamic population of astral MTs was found to suppress activation of myosin outside the equatorial region. This activation depends on the activity of RhoA, but not on F-actin, and similar observations were made in cultured mammalian cells (Foe and von Dassow, 2008; Murthy and Wadsworth, 2008; von Dassow et al., 2009). Furthermore, cells without astral MTs perform cytokinesis, as will anucleate cells that harbor no midzone but manage to properly separate their asters. Ablation of one centrosome displaces the region where furrowing

occurs away from the leftover spindle pole, while ablation of two centrosomes causes furrows to become excessively broad (von Dassow et al., 2009). Interestingly, the total amount of active cortical RhoA remains constant in this situation, and the concentration of active RhoA in the equator depends on astral MTs.

Collectively, the experiments mentioned above suggest that global cortical contractility is initiated early in mitosis, and that this contractility is then spatially restricted to the equatorial cortex by astral MTs. The current data support that, at least in sea urchin and frog embryos, the midzone provides a positive signal to activate RhoA in a broad pattern, while astral MTs spatially confine this signal (von Dassow et al., 2009). Regardless of its nature, the question of how a signal from the spindle midzone could reach the cortex in time and in a focused enough manner remains, especially in the context of large embryos such as those of sea urchins, frogs, and nematodes. Different scenarios for the focusing of such a signal have been proposed by von Dassow et al., which include 1) sequestration of the signal by centrosomes/astral MTs that grow in the vicinity of the midzone, 2) increased mobility of the diffusible signal in the low-density astral MT region between the midzone and equatorial cortex, and 3) sharpening of the signal at or close to the cortex either by MT-dependent or independent means. One such focusing mechanism could function through the association of centralspindlin with the plus ends of dynamic astral MTs that grow towards the equatorial cortex, or transport of these complexes along the MT lattice. Plus end-tracking of centralspindlin has been observed in *X. laevis* embryos, *D. melanogaster* S2 cells and cultured mammalian cells. In these systems, centralspindlin contributes to localized ECT2 concentration and RhoA activation via an EB interaction motif in Tumbleweed/RacGAP50C^{CYK-4} (Nishimura and Yonemura, 2006; Breznau et al., 2017; Verma and Maresca, 2019). Plus end-tracking of centralspindlin could provide a local furrow-stimulating signal, which suggests that midzone and astral MTs cooperate to restrict an ECT-2 activating signaling complex to the equatorial cortex. Whether this is a common molecular mechanism by which astral MTs regulate furrowing remains to be investigated.

A cell-free system reconstitutes diverse aspects of cytokinesis

It is important to note that the extent to which either the midzone or asters contribute to cytokinesis seems to depend on the cell type and size (Basant and Glotzer, 2018). Conceivably, a diffusing midzone-derived signal might take longer to reach the cortex and be less precise compared to an aster-derived signal. This would offer an explanation for why larger blastomeres rely strongly on aster-derived signaling (Wang, 2001). In a landmark study, Nguyen et al. reconstituted the conditions that lead to cytokinetic furrow formation in vitro. Growth of dense MT asters was initiated in *X. laevis* egg cytoplasm extracts by the addition of Aurora A-coated beads and Ca^{2+} influx, which induces a fertilization-like reaction (Groen et al., 2014). When these artificial asters grow sufficiently close to one another, a zone of overlapping antiparallel MTs forms in between (Nguyen et

al., 2014). As in intact eggs, CPC and centralspindlin components are recruited to this MT overlap zone. Interestingly, when a lipid bilayer was included in the system, local activation of RhoA could be observed at the membrane overlying the zone of antiparallel MT overlap. Proper organization of this activated RhoA zone requires CPC function, but not Kif23^{ZEN-4}. However, this is consistent with a previous report stating that this component of centralspindlin is not required for cytokinesis in *X. laevis* embryos (Miller and Bement, 2009). Furthermore, the local activation of RhoA leads to a reorganization of the initially branched actin network into long actin cables, which resembles the organization of actin in normal cells that undergo cytokinesis. These longitudinal actin structures also localized anillin and the septin complex (Nguyen et al., 2014). Clearly, this cell-free system could prove to be a valuable tool for further exploring the mechanisms that drive cytokinesis. However, considering that the midzone and membrane are in close contact to each other in this system, other experimental contexts will be required to study how a RhoA-activating signal from the midzone acts at a distance from the cell cortex.

The role of astral MTs in the *C. elegans* embryo

Studies using the early *C. elegans* embryo as a model have been vital for our understanding of how the mitotic spindle controls furrow positioning. While the midzone is not required for successful cytokinesis in the *C. elegans* zygote, it becomes essential when the extent of anaphase spindle elongation is reduced. By combining midzone disruption through *zen-4* depletion with decreased spindle elongation through *Gα* RNAi, the Glotzer lab showed that furrow initiation could be blocked completely (Dechant et al., 2003). Their quantifications of astral MT density indicated that furrowing is induced where a local MT minimum occurs in the vicinity of the equatorial cortex. This lower MT density is required for cytokinesis only in midzone-defective embryos, which suggests that the two pathways function redundantly (Dechant et al., 2003). It should be noted that *zen-4(RNAi)* embryos are capable of initiating a cytokinetic furrow, but complete ingression and cytokinesis do not occur. In addition, *zen-4* depletion does not perturb the actual formation of the midzone, but rather perturbs its mechanical stability. This is probably due to a requirement for ZEN-4 MT crosslinking activity together with SPD-1 and CYK-4 (Maton et al., 2015; Mishima et al., 2004). Aster separation and cytokinesis have also been proposed to be linked in other systems (Rappaport, 1969; Lewellyn et al., 2010), and even in some very early studies (Teichmann, 1903; Wilson, 1928). Yet, a correlation between the two was not observed in other reports (Verbrugge and White, 2007; Price and Rose, 2017). As an alternative model, astral MTs have been proposed to play two distinct roles in furrow initiation in the one-cell *C. elegans* embryo. Early anaphase astral MTs could locally stimulate furrowing, while separated astral MT arrays in late anaphase inhibit contractility outside of the equatorial region. These two temporally separated populations of astral MTs were shown to differentially depend on the function of γ-tubulin and AIR-1, respectively (Motegi et al., 2006). However, it remains unclear how physical separation of the asters

regulates furrowing on a molecular level. Possibly, aster separation functions by promoting a local minimum of cortex-MT interactions, by correctly distributing a diffusible signal from the asters, or by an indirect mechanism that is yet to be described.

The asters and midzone deliver redundant cytokinetic signals

Two landmark studies by Bringmann et al. further explored the nature of the astral signal through physical and genetic disruption of the midzone in one-cell *C. elegans* embryos. Bisection of the spindle with a focused UV laser, which we previously discussed in the context of studying cortical force generation (Grill et al., 2001), allowed the authors to uncover that the cytokinetic furrow is positioned by two consecutive signals. First, the spindle was severed asymmetrically by targeting the kinetochore MTs attached to one of the two spindle poles. This leads to a displacement of the spindle midzone from the center point between the adjacent asters. Intriguingly, such asymmetric spindle severing results in the induction of two cytokinetic furrows. An initial furrow is directed by the opposing asters and forms in their midplane. This is followed by a second furrow that forms at the cortex overlying the new position of the midzone. Either of these furrows can completely ingress and carry the one-cell embryo through cytokinesis, which suggests that they may be based on separate molecular pathways (Bringmann et al., 2005). Diverse key players that signal through the midzone to stimulate cortical contractility had previously been identified, as discussed above. To describe genetic requirements specifically for the astral signal, Bringmann et al. combined disruption of the midzone using the conditional *spd-1(oj5)* allele with a candidate RNAi screen. Multiple genes were identified, the disruption of which led to the formation of multinucleated cells (indicative of cytokinesis failure) only when the midzone was simultaneously disrupted. Thus, it is likely that these genes are specifically required for aster-mediated cytokinesis. These include some interesting candidates, most notably *cls-2*, *gpr-1/2* and *let-99*. As we discussed previously, GPR-1/2 and LET-99 are involved in the correct positioning of the spindle. Interestingly, CLS-2 is a TOG (tumor overexpressed gene) domain protein of the CLASP family, which is implicated in kinetochore function, chromosome segregation, midzone assembly, spindle assembly and positioning through regulation of the number of MT-cortex contacts (Maiato et al., 2003; Cheeseman et al., 2005; Espiritu et al., 2012; Maton et al., 2015). These known roles suggest that the contribution of CLS-2 to cytokinesis could be indirect through its function as a general regulator of MT dynamics. Both *let-99(RNAi)*; *spd-1(oj5)* and *gpr-1/2(RNAi)*; *spd-1(oj5)* one-cell embryos form furrows, but these do not complete cytokinesis. Thus, Bringmann et al. concluded that LET-99 and GPR-1/2 are specifically required for aster-mediated cytokinesis. Surpassing the effect of the *spd-1* mutation, combination of midzone ablation with *Gα(RNAi)*, *gpr-1/2(RNAi), let-99(RNAi)* or a *let-99* null allele results in a full failure of embryos to initiate cytokinetic furrowing. These results indicate that *spd-1(oj5)* does not result in a full loss of midzone function, or that its effect is partially rescued by depleting other components. Global cortical contractility was still

induced when formation of a proper furrow failed, as judged by the appearance of small ingressions along the entire cortex (Bringmann et al., 2007). Thus, the astral signal could modulate midzone-independent cortical contractility during anaphase to produce a focused furrow. Consistent with this idea, Gα and cortical localization of the centralspindlin component ZEN-4 were found to act in parallel pathways to control furrow initiation in the *C. elegans* embryo (Verbrugghe and White, 2007).

let-99 mutant embryos show delays in furrow induction, possibly as a result of their dependency on a midzone signal that could take longer to travel to the cortex. Studying the localization of LET-99 revealed that, in addition to the mid-posterior cortical band pattern described earlier during metaphase, the peak of LET-99 intensity shifts to the posterior during anaphase. This localization pattern depends on the position of the mitotic spindle, and allows cortical LET-99 to eventually match the site of furrow formation (Bringmann et al., 2007). GPR-1/2, on the other hand, shows an inverse cortical localization pattern; it localizes to regions surrounding the site of furrow formation. Interestingly, these cortical localization patterns for LET-99 and GPR-1/2 are interdependent. Thus, a model emerged in which the balance between Gα–GPR-1/2 at the polar cortex and LET-99 at the equatorial cortex conveys the astral cytokinesis signal that regulates furrowing redundantly with the midzone (Bringmann et al., 2007; Galli and van den Heuvel, 2008). However, whether this astral signal involves equatorial stimulation through LET-99, or polar relaxation through Gα–GPR-1/2, or possibly both, remains unexplored. LET-99 could directly organize cortical contractility by stimulating the proper distribution of cortical actomyosin distribution (Rose and Kemphues, 1998). Such a role was described for LET-99 during nucleocentrosomal complex centration in conjunction with Gα (Goulding et al., 2007), in embryos with severely posteriorly displaced spindles (Werner et al., 2007), and more recently independently of Gα and spindle positioning during cytokinesis in both symmetrically and asymmetrically dividing blastomeres (Price and Rose, 2017). Alternatively, LET-99 might determine the angle at which astral MTs interact with the cortex, which could generate unequal tension across the cortex and direct furrowing towards the equator (Bringmann et al., 2007). Conversely, Gα–GPR-1/2 might inhibit contractility outside of the equatorial cortex through maintaining MT-cortex interactions that facilitate transport of contractility factors off the cortex. Whether the full cortical force generator complex of Gα–GPR-1/2–LIN-5–dynein is involved in astral cytokinesis, and whether this effect is independent of its role in spindle positioning, is yet to be explored.

In addition to Gα, GPR-1/2 and LET-99, additional components of the *C. elegans* aster-dependent cytokinesis pathway have been identified in recent years. Follow-up studies have shown that both NOP-1 and ANI-1^{anillin} are required for cytokinesis in the one-cell embryo in absence of a functional midzone (Tse et al., 2011; Tse et al., 2012). NOP-1 is a *C. elegans*-specific, nonessential protein with no clearly predictable domain structure. It plays a role in embryo polarization, pseudocleavage furrowing (which is dispensable for

development (Rose et al., 1995)) and aster-induced cytokinetic furrowing. In parallel to CYK-4, NOP-1 contributes to the activation of RhoA via ECT-2 (Zonies et al., 2010; Tse et al., 2012). ANI-1 also contributes to cell polarization, and to the proper distribution of cortical NMY-2 during cytokinesis. Its ability to simultaneously associate with both the cortex and MTs could indicate that ANI-1 stimulates cytokinesis by mediating MT-cortex contacts. This was suggested in studies using both cultured human cells and the early *C. elegans* embryo (Tse et al., 2011; Van Oostende Triplet et al., 2014). In the absence of centralspindlin and NOP-1 function, the cortical levels of ANI-1 are dramatically reduced in one-cell embryos (Tse et al., 2012). However, single or double depletion of *nop-1* and *ani-1* function does not result in full cytokinesis failure, which indicates that these factors are redundant with other signals. Interestingly, ANI-1 and LET-99 were recently described to act in parallel aster-directed pathways (Price and Rose, 2017). ANI-1 functions as a molecular scaffold that associates with NMY-2, RhoA and actin, and recruits septin to the cytokinetic furrow (Maddox et al., 2005; 2007). Depletion of *ani-1* alone results in only low levels of cytokinesis failure, and the septins are only required for cytokinesis after the completion of embryogenesis (Nguyen et al., 2000; John et al., 2007). In *D. melanogaster* larval brain and cultured S2 cells, anillin and RacGAP50C$^{CYK\text{-}4}$ are interdependent for their equatorial cortex localization during cytokinesis (D'Avino et al., 2008; Gregory et al., 2008). However, these cells fail to undergo cytokinesis in the absence of anillin, which constitutes a clear difference with the *C. elegans* embryo (Somma et al., 2002; Straight et al., 2004). Moreover, the interaction between anillin and Ect2 is important for the stabilization of cortical MTs in cultured human cells. This interaction might serve a similar role as the anillin–RacGAP50C interaction found in *D. melanogaster* (Frenette et al., 2012). Finally, a more recent study revealed that anillin promotes contractility in cultured breast cancer MCF-7 (Michigan Cancer Foundation-7) cells. Here, anillin was proposed to function by simultaneously inhibiting the dissociation of RhoA·GTP from the cortex while also locally concentrating PIP_2, which retains RhoA at the cortex when it disengages from anillin (Budnar et al., 2019). Collectively, the exact role of anillin in regulating contractility could depend on different interactors, and is likely to diverge depending on the cell type and model organism.

While different cytokinesis pathways have been identified throughout the years, a direct mechanism for the regulation of cortical contractility through astral MTs is yet to be uncovered. In a recent study, a role was described for the mitotic kinase AIR-1 in regulating cortical contractility in the one-cell *C. elegans* embryo. TPXL-1^{TPX2} (targeting protein for Xklp2) was shown to activate AIR-1, and this interaction is required for the cortical clearance of F-actin and ANI-1 from the polar regions of the cell during anaphase (Mangal et al., 2018). However, the mechanism at work remains unclear, and Aurora A–TPX2 has previously been implicated in centrosome maturation, MT dynamics and mitotic spindle assembly (Hannak et al., 2001; Srayko et al., 2005). Interestingly, phosphorylation by Aurora A facilitates the cortical localization of NuMA and its role in

spindle positioning in cultured human cells. Also, AIR-1 is required for proper spindle movements in *C. elegans* embryos (Schumacher et al., 1998; Gallini et al., 2016). Whether Aurora A and TPX2 perform active roles in astral cytokinesis independently of their roles in spindle assembly and orientation remains to be experimentally tested. Finally, another possible connection between astral MTs and the regulation of cortical contractility was recently identified using *C. elegans*. The oligomerization and cortical localization of centralspindlin complexes is inhibited by PAR-5 in the one-cell embryo. Depletion of *par-5* function allows embryos to form a cytokinetic furrow, but with decreased precision (Basant et al., 2015). Interestingly, when the mitotic spindle is set up in the extreme posterior of the embryo as a result of nocodazole treatment, cortical centralspindlin induces ectopic furrowing only at cortical regions of low astral MT density. Thus, astral MTs could either modulate the activity or the cortical distribution of centralspindlin. Alternatively, astral MTs might regulate a factor downstream of centralspindlin function, such as ECT-2 or RhoA. The observed effect is NOP-1-independent, which indicates that aster-mediated regulation of cortical contractility through centralspindlin does not rely on the same mechanisms that have been proposed for astral cytokinesis in previous studies.

Concluding remarks

As the constriction of the cytokinetic furrow completes, midzone MTs bundles and their associated proteins become increasingly condensed until they eventually form the midbody. This structure of high protein density emerges at the intercellular bridge, which is the last connection between the soon-to-be daughter cells. The midbody anchors the fully constricted cytokinetic furrow and drives abscission, after which the two daughter cells no longer share a plasma membrane nor a continuous cytoplasm. Abscission is driven by distinct machineries compared to the earlier stages of cytokinesis. It involves vesicle traffic by motor proteins that include dynein, their sorting via the ESCRT (endosomal sorting complexes required for transport) machinery and SNARE (Snap receptor)-mediated membrane fusion as opposed to the constriction of the actomyosin network (Reviewed in Mierzwa and Gerlich, 2014; Freemont and Echard, 2018). We will revisit the abscission process later, as we further explore cytokinesis in the one-cell *C. elegans* embryo.

To conclude this introductory chapter, we have discussed how asymmetric cell divisions are driven by robust spindle and cytokinetic furrow positioning mechanisms. Both rely on strongly conserved core machineries in animal cells. It is evident that some of the factors involved are redundant and play a role in both aspects of cell division, which complicates their study. Importantly, many of the proteins discussed here have been identified and studied extensively in the early *C. elegans* embryo, which will be the main model discussed in the experimental chapters of this thesis. Even though strong advances have been made in the past decades, the intricate workings of cell division remain elusive, and we are still faced with diverse questions, including (but by no means limited to): how do polarity proteins regulate the cortical force generator complex at a molecular level? What

are the exact contributions of MT dynamics and dynein processivity to pulling force generation? Is there a direct role for the force generator complex in mediating both spindle positioning and the translation of MT contact into cortical contractility? Do multiple pathways drive furrowing, or do astral and midzone MTs modulate the function of the same core signaling machinery? These are the questions that will be addressed in the following experimental chapters.

Scope of this thesis

In this introductory chapter we have discussed the mechanisms that drive mitotic spindle positioning and local cleavage furrow formation. To summarize: by positioning the spindle based on cell polarity and extracellular signaling, cells steer the further development of their daughter cells. Correct spindle positioning determines the relative size, molecular composition and position of daughter cells in the larger context of an embryo or tissue. We discussed how a cortical complex of Gα–GPR-1/2–LIN-5 controls the pulling forces that position the mitotic spindle. This conserved complex is regulated by both cell cycle and polarity cues. Gα–GPR-1/2–LIN-5 recruits dynein to the cell cortex, which likely coordinates minus end-directed motility with the utilization of MT dynamics to generate pulling forces. In the one-cell *C. elegans* embryo, higher net forces in the posterior result in off-center spindle positioning and an asymmetric initial division (Lorson et al., 2000; Miller and Rand, 2000; Grill et al., 2001; Gotta and Ahringer, 2001; Colombo et al., 2003; Gotta et al., 2003; Srinivasan et al., 2003; Nguyen-Ngoc et al., 2007). The Gα–GPR-1/2–LIN-5–dynein complex also controls spindle positioning in subsequent embryonic cell divisions, and depending on varying cellular contexts and species, orients divisions to orchestrate tissue formation. Last but not least, this force generator complex is involved in regulating the astral cytokinesis pathway through yet unknown mechanisms. Needless to say, this core machinery has to communicate with a vast array of interactors to perform its diverse set of functions. The spatiotemporal regulation of proteins often involves protein-protein interactions, posttranslational modifications such as phosphorylation, and molecular switches such as GTPases. In the following chapters, we will explore diverse aspects of regulation that control the activity and distribution of Gα–GPR-1/2–LIN-5–dynein in the early *C. elegans* embryo.

One of the most important practical implications incorporated in all chapters of this thesis is the use of CRISPR/Cas9-mediated genome engineering. This technique has revolutionized in vivo studies and will no doubt continue to do so for years to come. Initial applications of the system were elaborated using mammalian cell culture (Cong et al., 2013; Mali et al., 2013). The adaptation of the system for use in *C. elegans* followed rapidly, to which our lab has delivered important contributions (Waaijers et al., 2013). In recent years, the efficiency of CRISPR/Cas9 techniques continues to be optimized through the development of diverse genetic targeting and selection strategies (Dickinson et al., 2013; Arribere et al., 2014; Kim et al., 2014; Dickinson et al., 2015; Reviewed in Dickinson et al., 2016). In all of the following experimental chapters CRISPR/Cas9 technology takes a central position as we apply this system to generate point mutants, to insert genetic sequences coding for fluorophores, protein-protein interaction domains and lox sites, or to create complete gene knockouts.

In **chapter 2**, we followed up on experiments previously conducted in our lab. These concern the role of LIN-5 phosphorylation in translating cell cycle and polarity cues to

proper spindle positioning. In short, 25 phosphorylated residues in LIN-5 have been identified through immunopurification followed by quantitative mass spectrometry analysis (Galli et al., 2011a). Further analysis revealed that the anterior PAR complex component PKC-3 phosphorylates a cluster of 4 residues in the LIN-5 C-terminus, and thereby inhibits pulling forces in the anterior during the switch of anterior- to posterior-directed spindle movements. In this follow-up work, we further explored how asymmetric spindle positioning is mediated through phosphorylation of LIN-5. We show that an additional four in vitro and in vivo phosphorylated residues are critical for proper spindle positioning in the early *C. elegans* embryo. Two of these residues form a recognition site for the CDK1–Cyclin B complex, and they affect the cortical recruitment of dynein. The remaining two residues are located in a region of the LIN-5 protein that mediates the interaction with GPR-1/2 and proper cortical pulling force generation. We show that this interaction is primed by consecutive phosphorylation by the serine/threonine kinase GSK3 (glycogen synthase kinase 3) and CK-1 (casein kinase 1). This study was one of the first to show the broad application of CRISPR/Cas9 technology for in vivo experiments. Through the substitution of endogenous residues of interest with either unphosphorylatable or phosphomimicking alternatives, and by applying a novel balancing strategy to study functionally compromised alleles, we were able to analyze the effects of specific protein phosphorylations at endogenous expression levels. As such, this study not only provided more insight into how LIN-5 is modulated in a posttranslational manner to regulate spindle positioning, it also introduced powerful new approaches to study the role of essential protein residues in vivo.

Dynein has long been known to function at the heart of diverse cellular functions, one of which is spindle positioning. While its role in this process was firmly established by previous studies, no description of the dynamics of the dynein motor was available for the early *C. elegans* embryo. In **chapter 3**, we endogenously labeled the dynein heavy chain, which allowed us to study the distribution of cytoplasmic dynein complexes during asymmetric spindle positioning. In addition to previously described subcellular locations, we identified an astral MT plus end-tracking population of dynein. Association with the MT plus end depends on EBP-2, homologs of which are described as master regulators of the MT plus end. Interestingly, we discovered that loss of dynein from the MT plus end does not result in obvious defects in spindle positioning. Furthermore, we used CRISPR/Cas9 to generate genetic knockouts for all EB homologs in *C. elegans*, and found that that EBP-1/2/3 are not required for proper spindle positioning or viability. While triple EB knockout does not significantly affect cortical pulling forces, as assayed by spindle severing assays, partial disruption of dynein function combined with loss of EBP-2 results in diminished pole movements. These results indicate that the plus end population of dynein could serve as a supplementary mechanism to ensure robust pulling force generation. In addition, we identified a second population of dynein at the cell cortex that depends on LIN-5, but not on EBP-2. Thus, the localization of dynein at MTs tips is not

required for the motor protein to associate with the cortex. As we quantified the dynamics of this cortical pool by FRAP analysis, we found that the LIN-5 dependent cortical dynein fraction exhibits altered dynamics in the anterior and posterior cortex that depend on PAR polarity. Thus, using a combination of CRISPR/Cas9-mediated tagging of proteins and quantitative microscopy techniques, we revealed two different populations of dynein, and their contributions to spindle positioning. This chapter highlights the strength of combined endogenous labeling and high-resolution microscopy approaches.

The Gα–GPR-1/2–LIN-5 complex has been described in diverse species as a complex that recruits dynein to the cortex to control spindle positioning. However, little is known about the requirements for assembling an active cortical force generator. Previous reports suggested that the force generator complex could simply function as an anchor for dynein, while such studies were carried out in the presence of endogenous complex components. Thus, the individual contributions of Gα, GPR-1/2 and LIN-5 to cortical pulling force generation remained unexplored. A major roadblock for studying these individual functions is that the depletion of any component of the force generator complex results in a loss of cortical pulling forces. To study these individual contributions, we aimed to reconstitute cortical complexes lacking specific components in vivo. Multiple light-inducible protein heterodimerization systems have been described in recent years, and have already proven to be valuable experimental tools (Strickland et al., 2012; Guntas et al., 2015). Our close colleagues applied such systems in both cultured mammalian cells and the *C. elegans* soma to control organelle movement through the recruitment of kinesins and dyneins to specific cargoes (van Bergeijk et al., 2015; Harterink et al., 2016). In **chapter 4**, we further optimized the TULIP (tunable light-controlled interacting protein tags) system for use in the *C. elegans* embryo. We show that the TULIP system can be used to assume rapid, reversible and local control of protein localization in the early embryo. Surprisingly, we found that Gα·GDP and Gα·GTP are not required to generate spindle pulling forces by directly recruiting GPR-1 to the cortex combined with *Gα(RNAi)*. However, pole movements become symmetrical in such embryos. Thus, Gα–GPR-1/2 is clearly essential for distributing the forces that mediate asymmetric spindle positioning in unperturbed embryos. Furthermore, we observed that direct recruitment of dynein to the cortex does not rescue spindle pulling forces in the absence of *gpr-1/2* function. Instead, we identified LIN-5 as a potent activator of dynein-dependent cortical pulling forces. The proper cortical spatiotemporal distribution of LIN-5 is critical to ensure that dynein is both recruited to the cortex and activated at the right moment. Excitingly, we managed to experimentally control both the position of the spindle and orientation of the cleavage plane in early embryos by locally recruiting LIN-5 to the cortex. This system should prove to be an invaluable tool for further research into spindle and cleavage plane positioning. Last but not least, we used the CRISPR/Cas9-mediated integration of *lox* sites and their germline-specific recombination to overcome the roadblock of incomplete RNAi-mediated gene inactivation. As such, we efficiently depleted the Gα regulators RGS-7 and RIC-8 in early embryos, and

show for the first time that their concerted effort is required for Gα function during spindle positioning.

In **chapters 2** to **4**, we explored diverse aspects of how the mitotic spindle is positioned in the early *C. elegans* embryo. A long-standing related question is how this cue is transferred to the cortex to define the site of cell cleavage. Previous studies have shown that the induction of cytokinesis is a robust process that relies on redundant signals from the spindle midzone and asters (Bringmann et al., 2005). Surprisingly, Gα, GPR-1/2 and LET-99 have been implicated in the astral cytokinesis pathway in addition to their role in spindle positioning (Bringmann et al., 2007). In **chapter 5**, we used genetic and optogenetic approaches to further explore the contributions of different factors to cytokinesis in the one-cell *C. elegans* embryo. We inactivated the midzone using diverse methods, and simultaneously controlled the cortical localization of endogenous proteins of interest as described in **chapter 4**. We created a new LOV membrane anchor to optimize spatiotemporal control over ePDZ-tagged proteins. In doing so, we found that the bipolar cortical distribution of LIN-5 is important for proper cytokinesis in embryos without a functional midzone. Furthermore, we expanded on previous reports by showing that LET-99 promotes cytokinetic furrowing, possibly through stimulating cortical centralspindlin localization. This function of LET-99 is at least partially independent of LIN-5, which inhibits cortical contractility outside of the equatorial cortex. Finally, we show that the cortical localization of CYK-4$^{RacGAP/MgcRacGAP}$ promotes contractility, which is likely to occur through ECT-2^{RhoGEF}.

Finally, in **chapter 6** we will close off with a summary and general discussion of the work presented in this thesis, as well as its practical and theoretical implications and the questions that remain to be explored in future studies.

Chapter 2

Multisite phosphorylation of NuMA-related LIN-5 controls mitotic spindle positioning in *C. elegans*

Vincent Portegijs[1], Lars-Eric Fielmich[1,◊], Matilde Galli[1,a,◊], **Ruben Schmidt[1,2]**, Javier Muñoz[3,b], Tim van Mourik[1], Anna Akhmanova[2], Albert J. R. Heck[3], Mike Boxem[1] and Sander van den Heuvel[1,*]

◊ These authors contributed equally to this publication

1 Developmental Biology, Department of Biology, Faculty of Science, Utrecht University, Padualaan 8, 3584 CH Utrecht, The Netherlands.

2 Cell Biology, Department of Biology, Faculty of Science, Utrecht University, Padualaan 8, 3584 CH Utrecht, The Netherlands.

3 Biomolecular Mass Spectrometry and Proteomics, Bijvoet Center for Biomolecular Research and Utrecht Institute for Pharmaceutical Sciences, Utrecht University, Padualaan 8, 3584 CH Utrecht, The Netherlands.

a Present address: Hubrecht Institute, Uppsalalaan 8, 3584 CT Utrecht, The Netherlands.

b Present address: Spanish National Cancer Research Centre (CNIO), ProteoRed-ISCIII, Melchor Férnandez Almagro, 3, 28029 Madrid, Spain.

* s.j.l.vandenHeuvel@uu.nl

The manuscript in this chapter was adapted from:
Portegijs, V., Fielmich, L-E., Galli, M., **Schmidt, R.**, Muñoz, J., van Mourik, T., Akhmanova, A., Heck, A.J.R., Boxem, M. and van den Heuvel, S. (2016). Multisite phosphorylation of NuMA-related LIN-5 controls mitotic spindle positioning in *C. elegans*. PLoS Genet. 12, 1-32.

Abstract

During cell division, the mitotic spindle segregates replicated chromosomes to opposite poles of the cell, while the position of the spindle determines the plane of cleavage. Spindle positioning and chromosome segregation depend on pulling forces on microtubules extending from the centrosomes to the cell cortex. Critical in pulling force generation is the cortical anchoring of cytoplasmic dynein by a conserved ternary complex of Gα, GPR-1/2, and LIN-5 proteins in *C. elegans* (Gα–LGN–NuMA in mammals). Previously, we showed that the polarity kinase PKC-3 phosphorylates LIN-5 to control spindle positioning in early *C. elegans* embryos. Here, we investigate whether additional LIN-5 phosphorylations regulate cortical pulling forces, making use of targeted alteration of in vivo phosphorylated residues by CRISPR/Cas9-mediated genetic engineering. Four distinct in vivo phosphorylated LIN-5 residues were found to have critical functions in spindle positioning. Two of these residues form part of a 30 amino acid binding site for GPR-1, which we identified by reverse two-hybrid screening. We provide evidence for a dual-kinase mechanism, involving GSK3 phosphorylation of S659 followed by phosphorylation of S662 by casein kinase 1. These LIN-5 phosphorylations promote LIN-5–GPR-1/2 interaction and contribute to cortical pulling forces. The other two critical residues, T168 and T181, form part of a cyclin-dependent kinase consensus site and are phosphorylated by CDK1-cyclin B in vitro. We applied a novel strategy to characterize early embryonic defects in lethal T168,T181 knockin substitution mutants, and provide evidence for sequential LIN-5 N-terminal phosphorylation and dephosphorylation in dynein recruitment. Our data support that phosphorylation of multiple LIN-5 domains by different kinases contributes to a mechanism for spatiotemporal control of spindle positioning and chromosome segregation.

Introduction

Animal development and tissue homeostasis depend critically on cell divisions that create cells with specific shapes and functions, in the right numbers and at the proper positions. The spindle apparatus plays a central role in the cell division process, as it segregates the chromosomes in mitosis and determines the plane of cell cleavage during cytokinesis (Galli and van den Heuvel, 2008; McNally, 2013; Morin and Bellaïche, 2011). Placement of the spindle in the cell center during division results in the formation of daughter cells of equal size, whereas off-center migration and spindle rotation allows the creation of differently sized daughter cells at specific locations. Moreover, the plane of cell cleavage determines whether polarized cells undergo symmetric or asymmetric cell division. Asymmetric cell divisions create cell diversity and allow maintenance of tissue-specific stem cells, by combining self-renewal with the generation of differentiating daughter cells

(Reviews: (Gönczy, 2008; Knoblich, 2010). Thus, tight control of the spindle function and position is needed to coordinate chromosome segregation with cleavage plane determination, which is essential for genetic stability, tissue integrity and stem cell maintenance in a wide variety of evolutionary contexts.

Pioneering studies in *Caenorhabditis elegans* and *Drosophila melanogaster* revealed that the position of the spindle responds to polarity cues during asymmetric cell division (Galli and van den Heuvel, 2008; Gönczy, 2008; Knoblich, 2010; Morin and Bellaïche, 2011). In *C. elegans,* anterior-posterior (A-P) polarity is established after fertilization of the oocyte. This involves re-distribution of specific partitioning-defective (PAR) proteins into two opposing domains of the cell cortex. The PDZ-domain proteins PAR-3 and PAR-6 form a complex with the PKC-3 aPKC polarity kinase and become restricted to the anterior half of the zygote, while the PAR-2 ring-finger protein and PAR-1 kinase occupy the posterior domain (Rose and Gönczy, 2014). This A-P polarity guides the asymmetric localization of cytoplasmic determinants as well as the position of the mitotic spindle. During the first mitotic division, the spindle is positioned off-center, to instruct an asymmetric cell division that creates a larger anterior blastomere (AB) and smaller germline precursor cell (P1). Next, the spindle rotates by 90 degrees in P1, to instruct another asymmetric division with a cleavage plane perpendicular to the one of AB. These early divisions of the *C. elegans* embryo have served as an important model for studies of the coordinated regulation of cell polarity, fate determinant localization, and spindle positioning during asymmetric cell division.

In addition, studies in *C. elegans* and *Drosophila* uncovered an evolutionarily conserved protein complex that mediates spindle positioning. This complex consists of the alpha subunit of a heterotrimeric G protein in association with the TPR/GoLoco protein GPR-1/2 and coiled-coil protein LIN-5 in *C. elegans* (Gα–Pins–Mud in *Drosophila*, Gα–LGN–NuMA in mammals) (Reviews: (Galli and van den Heuvel, 2008; Gönczy, 2008; Knoblich, 2010; McNally, 2013; Morin and Bellaïche, 2011; Rose and Gönczy, 2014)). The GPR-1/2 GoLoco motifs interact with Gα·GDP (Kimple et al., 2002), while the tetratricopeptide repeats (TPR) associate with the C-terminus of LIN-5 (**Figure 1a**). The ternary protein complex acts at the cell cortex in conjunction with cytoplasmic dynein and microtubule plus ends to generate microtubule pulling forces that promote chromosome segregation and position the spindle (Couwenbergs et al., 2007; Kotak et al., 2012; Kozlowski et al., 2007; Laan et al., 2012; Nguyen-Ngoc et al., 2007). Based on results obtained for NuMA, an extended N-terminal domain of LIN-5 likely mediates interaction with the dynein motor complex (Kotak et al., 2012). It remains unclear how Gα–GPR-1/2–LIN-5 engages dynein and microtubule depolymerization in the generation of cortical pulling forces, and how pulling forces are temporally and spatially restricted.

Asymmetric positioning and rotation of the spindle result from imbalance in the pulling forces. It has long been known that the cortical polarity of the *C. elegans* zygote is fundamental for the spatial organization of pulling forces, creating a higher net force in the

posterior than the anterior, which causes the spindle to move off center (Grill et al., 2003, 2001). This is in part achieved through PKC-3 mediated phosphorylation of LIN-5, which inhibits anteriorly directed pulling forces (Galli et al., 2011). Phosphorylation also appears to regulate cortical pulling forces in other systems. For example, phosphorylation by aPKC inhibits Pins/LGN localization to the apical cell membrane and promotes planar cell division of MDCK canine kidney cells during cyst formation (Du and Macara, 2004). Moreover, phosphorylation of NuMA by PLK1 and CDK1 has been implicated in the timing of chromosome segregation and positioning of the mitotic spindle in human cells (Kiyomitsu and Cheeseman, 2012; Kotak et al., 2013). In addition to spindle positioning, the Gα–GPR-1/2–LIN-5 complex is essential for chromosome segregation, in all cell divisions except for the first few embryonic divisions in *C. elegans* (Albertson et al., 1978; Lorson et al., 2000; Srinivasan et al., 2003). Phosphorylation is likely to play a key role in coordinating chromosome segregation and spindle positioning through spatiotemporal regulation of Gα–GPR-1/2–LIN-5 function.

Our previous studies identified extensive in vivo phosphorylation of LIN-5 in *C. elegans* embryos (Galli et al., 2011). The function of the majority of these phosphorylations remained unknown. Here we apply a combination of techniques to determine which phosphorylations are critical for LIN-5 function. CRISPR/Cas9-mediated genetic engineering allowed us to introduce single codon alterations in the *C. elegans* genome, and to compare non-phosphorylatable and potentially phosphomimetic LIN-5 mutants. In addition to PKC-3, we found that the PAR-1 polarity kinase likely phosphorylates LIN-5 in vivo, but physiological consequences of this phosphorylation were not detected. Alanine substitution mutagenesis of *lin-5* transgenes pointed to four phosphorylated residues with critical functional contributions. Two of these residues form part of a 30 amino-acid domain of LIN-5 required for binding GPR-1/2. Phosphorylation of these residues promotes cortical pulling forces and GPR-1/2 localization in vivo, and appears to occur sequentially by GSK3 and casein kinase 1 (CK1). Moreover, we identified essential residues in the LIN-5 N-terminus that are phosphorylated by CDK1. Our data from extensive knockin replacement mutants are consistent with a mechanism involving sequential phosphorylation and dephosphorylation of the LIN-5 N-terminus in dynein recruitment to the meiotic spindle and cell cortex. Thus, a combination of phosphorylations by cell-cycle and polarity associated kinases likely underlies the spatiotemporal control of pulling forces in chromosome segregation and asymmetric cell division.

Results

Multiple in vivo phosphorylated residues are critical for LIN-5 function

Previously, we described that at least 25 residues of LIN-5 are phosphorylated in vivo (**Figure 1a**) (Galli et al., 2011). To acquire insight in which phosphorylations are functionally relevant, we replaced each phosphorylated serine or threonine with an alanine residue that cannot be phosphorylated. The relevant codon alterations were introduced in a cloned genomic *lin-5* DNA fragment and subsequently tested for functionally complementing the *lin-5*(*e1348*) null mutation in vivo (Lorson et al., 2000). In the presence of maternal product, *lin-5*(*e1348*) mutants fail to undergo chromosome segregation during postembryonic divisions and continue abortive mitoses (Albertson et al., 1978; Lorson et al., 2000; Srinivasan et al., 2003). Transgenes containing wild type *lin-5* or *gfp*::*lin-5* coding sequences restored post-embryonic cell divisions in *lin-5*(*e1348*) null mutants (**Figure 1b**). However, these *lin-5* transgenes appeared susceptible to germline and somatic silencing, as reliable rescue and GFP-LIN-5 expression was observed only in the F1 generation. Hence, we examined transgenic F1 animals, focusing on vulval development and nuclear divisions in the intestine as a quantitative measure for LIN-5 function (**Figure 1b**).

Alanine substitutions of threonine 168, serine 659, and serine 662 were the only single amino acid changes that significantly compromised LIN-5 function in vivo. The T168A mutation had the strongest effect and almost completely eliminated the ability to restore intestinal divisions in *lin-5*(*e1348*) null mutants (**Figure 1b**). Interestingly, this strong effect was specific for the intestine: LIN-5^{T168A} expression allowed *lin-5* mutants to develop a normal vulva (**Figure S1**). T168 forms part of an ideal consensus phosphorylation site (S/T*-P-x-K/R) for the mitotic cyclin-dependent kinase 1 (CDK-1) (Errico et al., 2010). CDK-1 is likely to regulate LIN-5, as multiple CDK-1 consensus sites are present in the LIN-5 N- and C-terminus, and CDK1 phosphoregulation of the NuMA C-terminus has been reported (Kotak et al., 2013; Seldin et al., 2013). We generated double alanine substitutions of T168 in combination with T181 or S199, two nearby candidate residues for CDK-1 phosphorylation. Strikingly, the transgene encoding LIN-5[T168A,T181A], but not LIN-5[T168A,S199A], completely failed to rescue intestinal mitoses and vulva formation in *lin-5*(*e1348*) mutants (**Figure 1b** and **S1**). Because phosphorylation of T181 by itself was not essential for post-embryonic divisions, T168 and T181 phosphorylations likely cooperate to control LIN-5 function.

The individual and combined S659A and S662A substitutions (LIN-5[S659A,S662A]) also reduced *lin-5*(*e1348*) complementation. By contrast, simultaneous alanine substitutions of serines 729, 734, 737, and 739 did not prevent LIN-5 function (**Figure 1b** and **S1**). In agreement with the latter result, PKC-3 (aPKC) phosphorylation of these residues inhibits LIN-5 function and is not required for cell division (Galli et al., 2011). Our alanine-substitution experiments indicate that in addition to spatiotemporal regulation of

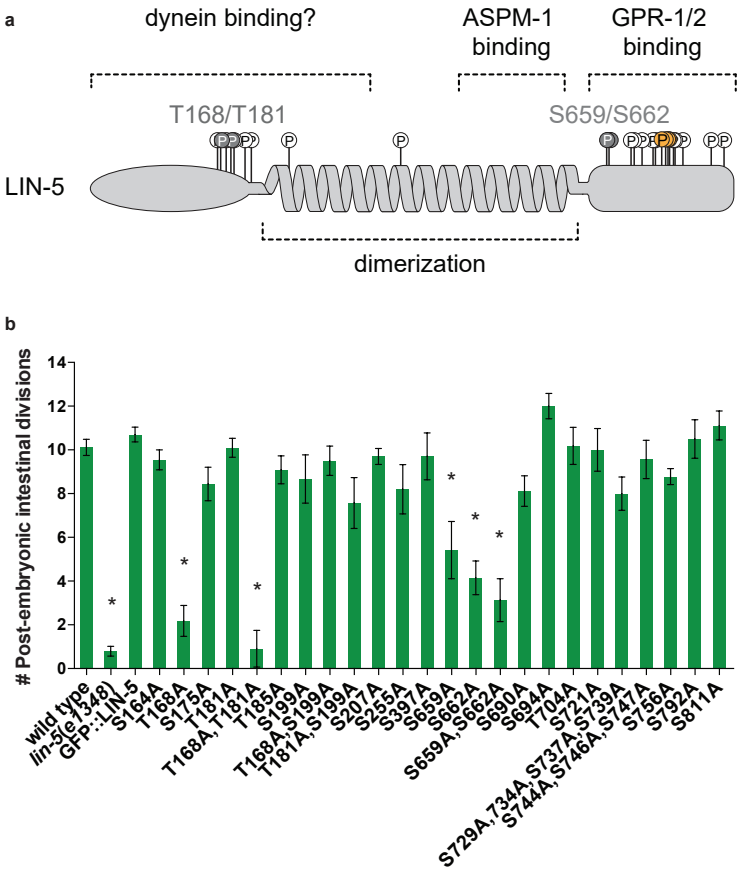

Figure 1. **Phosphorylation of LIN-5 controls post-embryonic divisions in the intestine.** (**a**) Overview of LIN-5 structure and binding domains. In vivo phosphorylated residues are indicated by open circles. Grey circles and numbers represent the phosphorylated amino acids essential for LIN-5 function. Yellow circles indicate previously identified residues phosphorylated by PKC-3. (**b**) Quantification of post-embryonic intestinal divisions in heterozygous *lin-5(e1348) / mIn1* (wild type), homozygous *lin-5(e1348)* animals and homozygous *lin-5(e1348)* animals expressing GFP-LIN-5 transgenes with alterations of the indicated phosphosite(s). n=7-22 (average: 15). Error bars, s.e.m. * P < 0.01 compared to wild type, Unpaired Students T-test.

LIN-5 by PKC-3, phosphorylation of LIN-5 residues in the dynein-interacting N-terminus and GPR-1/2 binding C-terminus may contribute to LIN-5 regulation in vivo.

In vitro kinase assays reveal candidate LIN-5 kinases

To determine whether CDK1 is indeed able to phosphorylate T168 and T181 of LIN-5, we performed in vitro kinase assays with recombinant GST-LIN-5 expressed in *E. coli* as a substrate. Indeed, immunopurified human CDK1/cyclin B phosphorylated GST-LIN-5, but not GST alone (**Figure S2a** and **S2b**). Analysis of in vitro phosphorylated GST-LIN-5 by mass spectrometry revealed extensive phosphorylation of T168, T181, and S744 of LIN-5

(**Figure S2b**). Additionally, peptides containing phosphorylated T704 and S756 were also found, and some other phosphopeptides less frequently. Taken together, CDK1/cyclin B phosphorylates LIN-5 in vitro at multiple sites including T168 and T181, and phosphorylation of T168 and T181 in vivo appears to be required for LIN-5 function.

In contrast to T168 and T181, residues S659 and S662 are not part of apparent consensus phosphorylation sites. In our previous in vivo mass-spectrometry data, the S659,S662 double phosphorylated peptides were abundant, while the corresponding unphosphorylated peptides were not detected (Galli et al., 2011). This may indicate that S659 and S662 are constitutively phosphorylated in early embryos. To gain insight in which kinases may be involved, we examined LIN-5 phosphorylation in vitro with a series of polarity and cell cycle kinases, followed by mass spectrometry analyses. This revealed several residues that were phosphorylated by multiple kinases in vitro (**Figure 2a**). In striking contrast, S659 was only phosphorylated by GSK3, and none of the tested kinases phosphorylated S662 (**Figure 2a**). We considered several potential explanations for this lack of phosphorylation: the responsible kinase(s) may not have been included in the assays, residue S662 may not be accessible in the recombinant protein, or S662 phosphorylation may require a priming event. To test the latter possibility, we performed in vitro kinase assays with synthetic peptides that contain the S659 and S662 residues, either unphosphorylated or phosphorylated at one of the positions. Testing several kinases, we found that casein kinase 1 (CK1) efficiently phosphorylates S662, but only when the peptide contained a phosphorylated S659 residue (**Figure 2b**). As for the full length protein, only GSK3 phosphorylated S659 in the unphosphorylated peptide. Based on the combined in vitro data, we propose that GSK3 phosphorylation of residue S659 is a priming reaction for CK1 phosphorylation of S662. Highly similar phosphorylation has been reported for the Wnt/Frizzled co-receptor LRP6, with GSK3 priming for CK1 phosphorylation at similar sites (Niehrs and Shen, 2010; Zeng et al., 2005).

In addition to CDK1, GSK3 and CK1 phosphorylation, our analyses revealed phosphorylation of LIN-5 by the polarity kinase PAR-1. While several phosphopeptides were detected, some were rare and the quantitative software program MaxQuant only recognized the S397 and S739 LIN-5 residues as in vitro phosphorylated by PAR-1 (**Figure 2a**). S397 is located in the LIN-5 coiled coil region and its phosphorylation was previously observed in embryos (**Figure 2a**) (Galli et al., 2011). However, our previous in vivo analysis failed to identify LIN-5 phosphorylations that were diminished after *par-1* RNAi (Galli et al., 2011). Re-evaluation of the quantitative mass spectrometry data revealed that, although masked by an abundant unrelated peptide, the ratio between the phosphorylated and unphosphorylated S397 peptide was severely reduced in *par-1(RNAi)* embryos compared to control RNAi embryos (**Figure S3**). In contrast, S739 phosphorylation was not significantly affected by *par-1* knockdown in vivo (Galli et al., 2011). Taken together, we identified multiple phosphorylated LIN-5 residues as well as candidate kinases that could be important in the regulation of LIN-5 function. In addition to

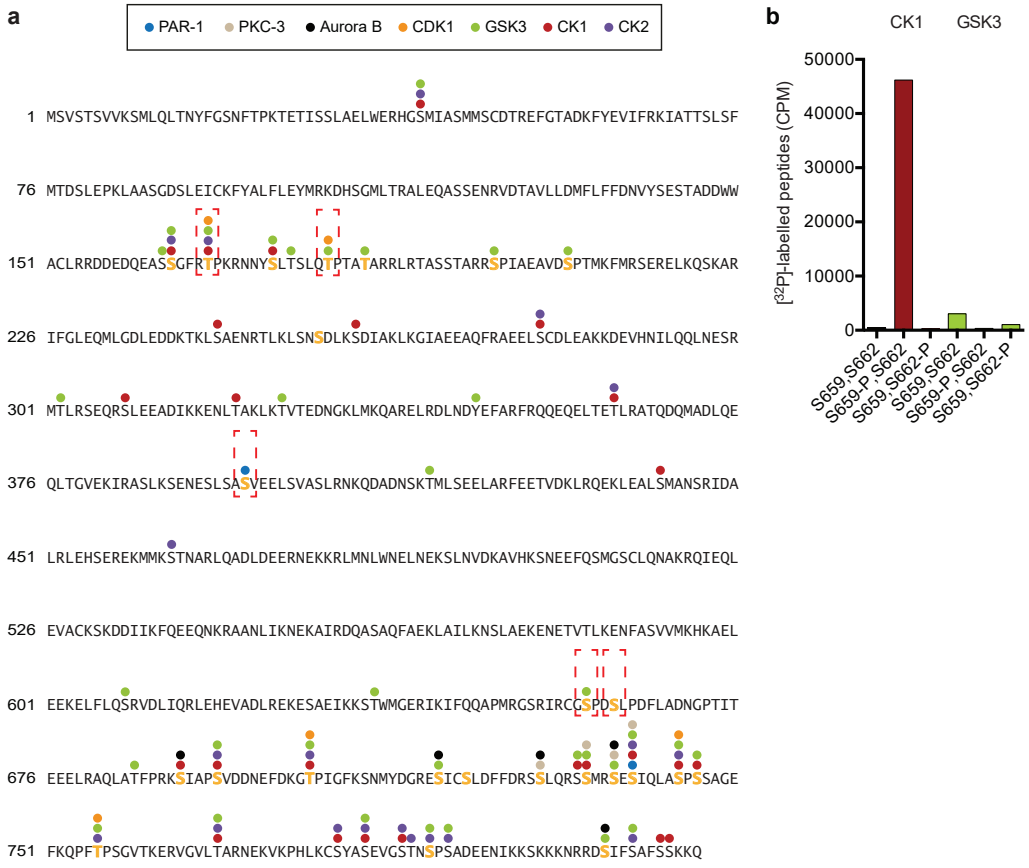

Figure 2. **LIN-5 phosphorylation by cell cycle and polarity kinases in vitro.** (**a**) Graphic overview of mass spectrometry analysis of in vitro kinase assays, revealing multiple target residues in LIN-5 phosphorylated by PAR-1, PKC-3, CK1, CK2, GSK3, CDK1 and Aurora B kinase. Yellow residues indicate in vivo phosphorylated residues, brackets indicate essential residues identified in complementation assay. (**b**) Radioactive counts (CPM) of in vitro kinase assays with CK1 and GSK3 on a synthetic LIN-5 peptide 654-670 with or without synthetic incorporation of phosphorylated amino acids S659 or S662.

four adjoining residues phosphorylated by PKC-3 in the C-terminus, T168 and T181 may be phosphorylated by CDK-1, S397 by PAR-1, and S659 by GSK-3, to prime phosphorylation of S662 by CK1.

A 30 amino acid LIN-5 domain that includes S659,S662 mediates GPR-1/2 interaction

Both S659,S662 and the four residues phosphorylated by PKC-3 are located in the LIN-5 C-terminus which mediates GPR-1/2 binding (Fisk Green et al., 2004; Galli et al., 2011). As phosphorylation could affect GPR-1/2 association, we wanted to define which LIN-5 residues are critical for GPR-1/2 binding. Testing deletion constructs in yeast two-hybrid assays confirmed that the LIN-5 C-terminal region is sufficient for GPR-1 association.

GPR-1 interaction was observed for all truncated LIN-5 proteins except for those with deletions in the 609-671 amino acid region (**Figure 3a**). At the same time, including only the 609-671 LIN-5 fragment did not allow growth in this assay, possibly due to an inability of this short fragment to fold properly in yeast (**Figure 3a**). The essential 609-671 region does not contain serine 729, 734, 737, and 739 phosphorylated by PKC-3 in vivo, in agreement with our previous conclusion that PKC-3 phosphorylation of LIN-5 does not prevent interaction with GPR-1/2 (Galli et al., 2011).

To identify specific LIN-5 amino acids required for GPR-1/2 interaction, we performed "reverse yeast two-hybrid screening". This method selects mutations that disrupt bait-prey protein interactions, making use of *URA3*-mediated conversion of 5-fluoroorotic acid (5-FOA) to a toxic product (Vidal et al., 1996a). The normal interaction between LIN-5 and GPR-1 leads to GAL4-controlled *URA3* expression in yeast two-hybrid assays, and causes cell death in the presence of 5-FOA. Thus, following mutagenesis of one of the binding partners, interaction-deficient alleles can be recovered from 5-FOA-resistant colonies (Vidal et al., 1996b). We used PCR-based random mutagenesis of LIN-5 prey fragments (amino acids 609-821), and isolated 163 5-FOA resistant yeast colonies in a reverse yeast two-hybrid screen (for details see Materials and Methods, **Figure S4a**). 89 colonies contained a single missense mutation in the LIN-5 coding sequences, together changing 15 different amino acids. Substitutions of 12 of these 15 individual amino acids caused loss of GPR-1 interaction again in the re-test (**Figure 3b** and **3c**). The 12 affected residues were all located between amino acids 638-667 of LIN-5. Importantly, the interaction-defective alleles included missense mutations of the phosphorylated residues S659 and S662. In fact, S662 was found altered to glycine, cysteine and asparagine (**Figure S4b**). These data indicate that a 30 amino acid stretch in the LIN-5 C-terminal region, which includes the in vivo phosphorylated S659 and S662 residues, mediates the interaction with GPR-1.

Following up on the interaction defective alleles, we noticed that the effect of missense mutations was substantially reduced when tested in the context of full length LIN-5, compared to the C-terminus only. Western blot analysis did not reveal substantial differences in protein levels compared to wild type (**Figure S5a**). The LIN-5 coiled-coil region promotes dimerization and is thereby expected to increase GPR-1 binding avidity. Only one of the four most frequently identified mutations, L663S, also interfered with full length LIN-5 binding to GPR-1 (**Figure 3d**, left panel). However, at a reduced temperature (20°C), this leucine 663 to serine (LIN-5[L663S]) mutation still allowed growth on selective media, indicating that GPR-1 interaction is not completely abolished. We also tested S659 and S662 phosphorylation-site mutants in the context of full length LIN-5. While the single mutations had little effect on GPR-1 binding, replacement of both serine 659 and 662 by alanine reduced GPR-1 interaction in yeast, as detected by lack of growth on -His plates at 30°C (**Figure 3d**, right panel). Phosphomimetic substitutions (S to D or E) of S659, S662, or both, did not reduce interaction (**Figure 3d**, right panel). These results are

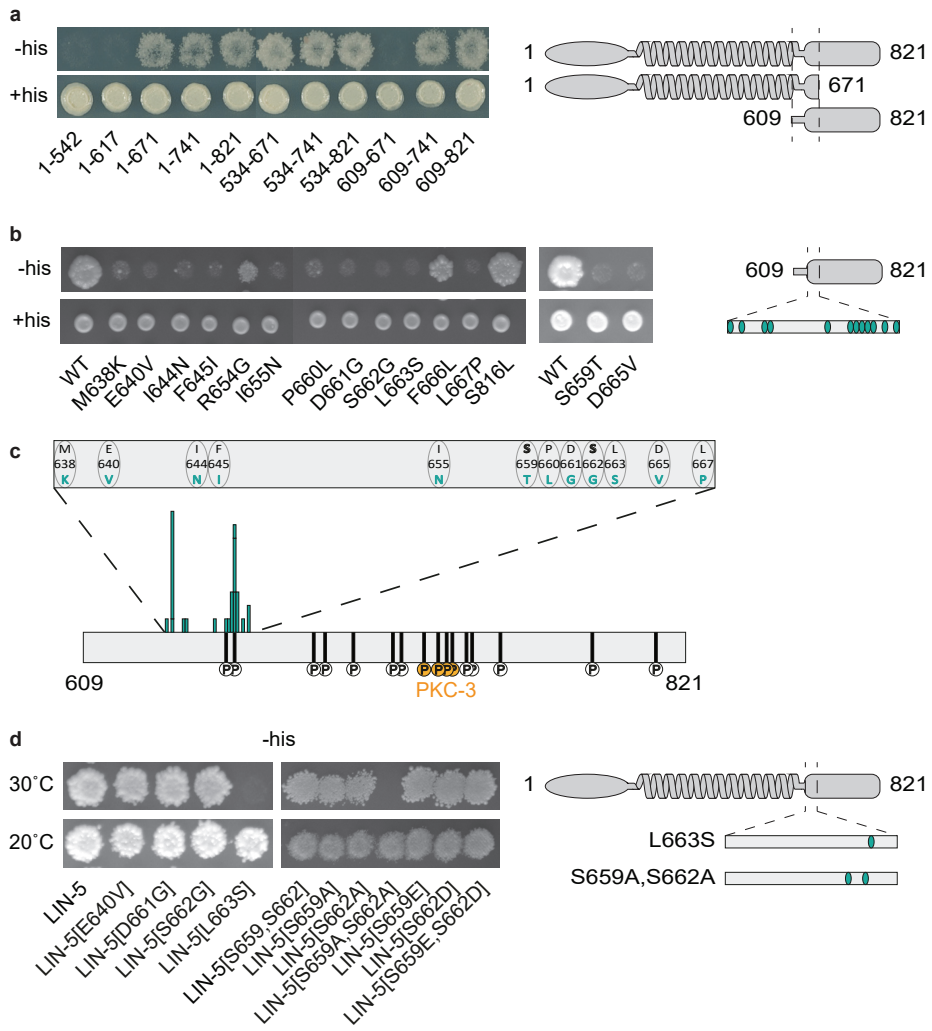

Figure 3. **Yeast two-hybrid assays identify critical residues in LIN-5 for GPR-1 interaction.** (**a**) Yeast two-hybrid analysis of DB::GPR-1 (bait) interaction with AD::LIN-5 (prey) fragments of varying sizes on Sc (synthetic complete) -Leu-Trp (+His, control) and Sc -Leu-Trp-His + 3-AT (-His, selection) plates. (**b**) Yeast two-hybrid analysis of DB::GPR-1 (bait) interaction with AD::LIN-5 (prey) fragments containing single amino acid changes on Sc -Leu-Trp and Sc -Leu-Trp-His + 3-AT plates. (**c**) Graphical representation of LIN-5 residues required for GPR-1 binding. Size of bars indicates frequency of found mutations, with every bar representing a different amino acid change. (**d**) Yeast two-hybrid analysis of DB::GPR-1 (bait) interaction with AD::LIN-5 (prey) full length containing single amino acid changes on Sc -Leu-Trp-His + 3-AT plates at 20˚C and 30˚C.

consistent with phosphorylation of S659 and S662 contributing to GPR-1/2 binding, and taking place in yeast as well as *C. elegans*. Taken together, our forward and reverse yeast two-hybrid assays identified LIN-5 residues that appear to mediate interaction with

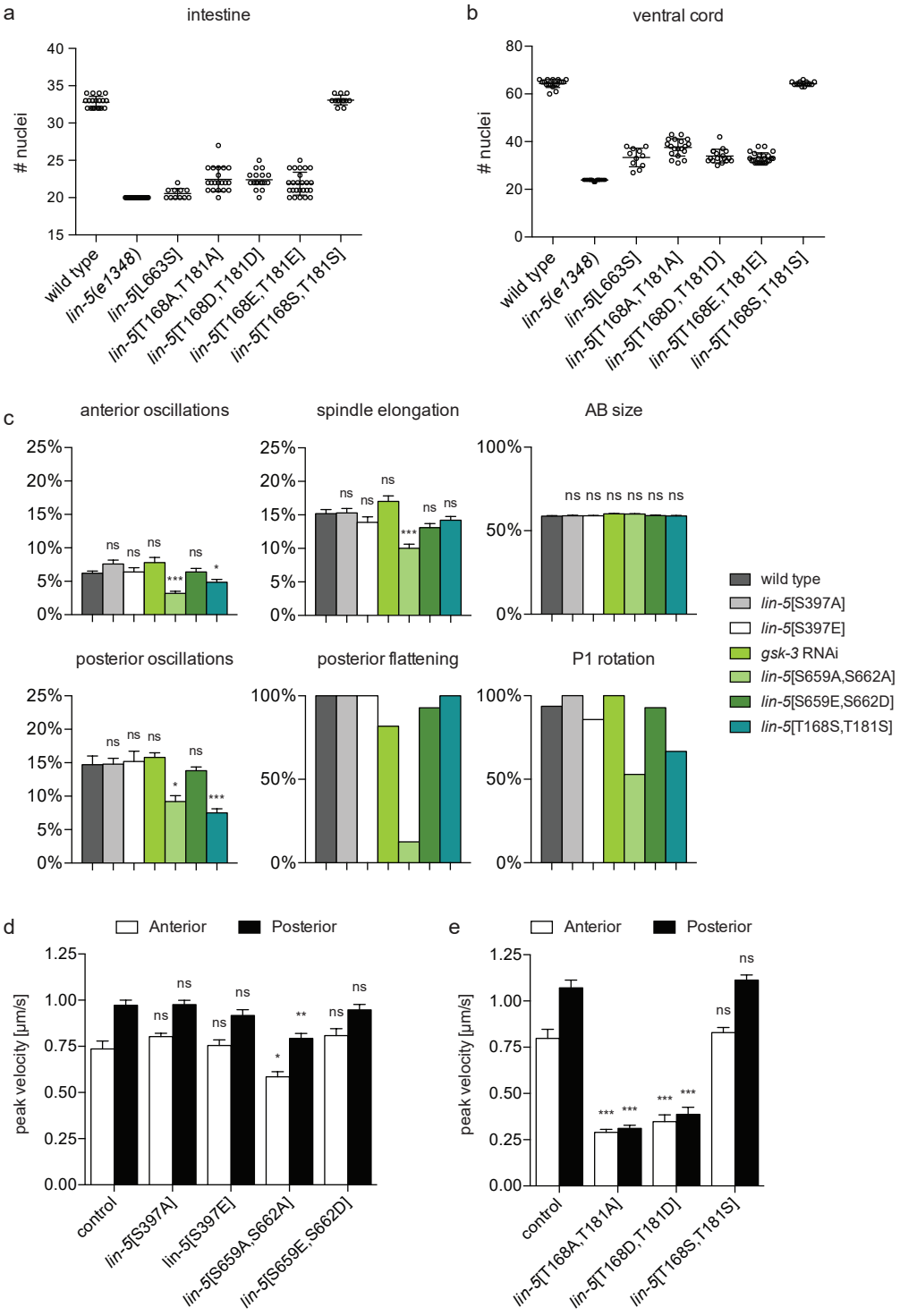
a
intestine
nuclei
wild type
lin-5(e1348)
lin-5[L663S]
lin-5[T168A,T181A]
lin-5[T168D,T181D]
lin-5[T168E,T181E]
lin-5[T168S,T181S]
b
ventral cord
nuclei
c
anterior oscillations
spindle elongation
AB size
posterior oscillations
posterior flattening
P1 rotation
wild type
lin-5[S397A]
lin-5[S397E]
gsk-3 RNAi
lin-5[S659A,S662A]
lin-5[S659E,S662D]
lin-5[T168S,T181S]
d
Anterior
Posterior
peak velocity [µm/s]
control
lin-5[S397A]
lin-5[S397E]
lin-5[S659A,S662A]
lin-5[S659E,S662D]
e
Anterior
Posterior
peak velocity [µm/s]
control
lin-5[T168A,T181A]
lin-5[T168D,T181D]
lin-5[T168S,T181S]

Figure 4. **In vivo phenotypical analysis shows developmental defects in LIN-5 phosphomutants.** (**a**) Quantification of intestinal nuclei following propidium iodide staining in homozygous LIN-5 phosphorylation mutants compared to wild type and *lin-5*(*e1348*) null animals. Null mutants are expected to contain 20 nuclei, wild type animals 32-34 nuclei. Individual values are plotted, n>11. (**b**) Quantification of P-cells and juvenile motor neurons in the ventral cord region P2-P10 in propidium iodide stained homozygous LIN-5 phosphorylation mutants compared to wild type and *lin-5*(*e1348*) null animals. Nuclei were counted in late larval stages of asynchronous populations of worms, with null mutants expected to have 24 nuclei (9 P cells and 15 juvenile motor neurons) and wild type animals 65 nuclei. Individual values are plotted, n>11. (**c**) Analysis of hallmarks of the first 2 embryonic divisions in LIN-5 phosphorylation mutant, based on time-lapse DIC microscopy. Oscillations are plotted as percentage of embryo height, elongation and AB size as a percentage of embryo width, flattening and rotation as a total fraction of analyzed embryos. (**d**, **e**) Mean peak velocities (μm s^{-1}) of anterior and posterior spindle poles measured in a 12.5 s time frame after spindle severing in one-cell embryos of the indicated genotypes, cultured at 25°C (**d**) or 20°C (**e**). Error bars: s.e.m. Statistical analyses: Unpaired Welch Students T-test, *P < 0.01 compared to wild type, ** P < 0.001 compared to wild type, *** P < 0.0001 compared to wild type, ns not significant.

GPR-1/2, which are located within a 30 amino acid C-terminal domain. This includes S659 and S662, of which the phosphorylation in vivo likely contributes to GPR-1/2 binding.

Examining LIN-5 phosphoregulation in vivo by CRISPR/Cas9-mediated genome engineering

We used CRISPR/Cas9-mediated gene targeting to engineer *lin-5* alleles and examine the effects of amino acid substitutions in vivo (Chen et al., 2013; Dickinson et al., 2013; Kim et al., 2014; Waaijers et al., 2013). First, we created the *lin-5*[L663S] mutation by introducing a single nucleotide alteration in the endogenous *lin-5* locus. This resulted in a typical *lin-5* loss-of-function phenotype, with homozygous sterile, thin and uncoordinated larvae that fail to undergo chromosome segregation but continue abortive mitoses (Albertson et al., 1978; Lorson et al., 2000). We determined the number of nuclei in the intestine and ventral cord, following fixation and staining of DNA. In *lin-5*[L663S] mutants, both tissues contained severely reduced numbers of nuclei compared to the wild type, consistent with a failure to undergo chromosome segregation in most post-embryonic divisions (**Figure 4a**, **b**, and **S6a**). Thus, a single change of amino acid L663 in the GPR-1-binding motif of LIN-5 results in strong loss-of-*lin-5* function. This result confirms the power of reverse yeast two-hybrid screening in identifying amino acids that affect protein-protein interactions in vivo (Vidal et al., 1996a).

Next, we used genome engineering to alter the in vivo phosphorylated residues T168, T181, S397, S659 and S662. For each residue, we created a non-phosphorylatable alanine substitution allele, as well as one or more potentially phosphomimetic alleles that contain aspartic acid or glutamic acid at the relevant positions. Alteration of the PAR-1 phosphorylated S397 residue had no apparent effect. Homozygous S397A and S397E animals were viable and showed normal development. Even close examination of LIN-5-mediated processes did not reveal abnormalities (See below; **Figure 4c**, **d**, and **S6a**, **b**). Thus, although this phosphorylation occurs in vivo, it is by itself not a major determinant of LIN-5 function.

Compared to our transgene rescue experiments (**Figure 1b** and **S1**), the effect of S659 and S662 alanine substitution mutations in endogenous *lin-5* was quite mild. The *lin-5*[S659A,S662A] double mutant animals were viable, with only a slight reduction in intestinal nuclei number (**Figure S6a**), but displayed a significant increase in embryonic lethality (3.6±1.0% at 25°C, wild type 0.9±0.4%). The phosphomimetic *lin-5*[S659E,S662D] mutation did not cause embryonic lethality or larval defects, consistent with constitutive phosphorylation of these residues in early embryos (**Figure S6a**).

In stark contrast, alteration of the candidate CDK-1 phosphorylated residues in the N-terminus, threonine 168 and 181 to alanine (*lin-5*[T168A,T181A]), aspartic acid (*lin-5*[T168D,T181D]) or glutamic acid (*lin-5*[T168E,T181E]), all resulted in typical *lin-5* mutant offspring. Regardless of the mutant combination, homozygous animals derived from heterozygous parents developed into sterile, thin and uncoordinated larvae, and showed severely impaired cell division during larval development (**Figure 4a**, **b**). Importantly, substitution of threonine 168 and 181 with serine residues (*lin-5*[T168S, T181S]) did not lead to any detectable phenotype or defects in cell division (**Figure 4a**, **b**). These observations and the in vivo phosphorylation of T168 and T181 indicates that phosphoregulation of T168 and T181 is critical for LIN-5 function, in agreement with the results of the transgene rescue experiments (**Figure 1b** and **S1**). Together, our targeted genome alterations identified several individual amino acids that are required for the in vivo function of LIN-5, including phosphorylated residues in the N-terminus and residues in the GPR-1 binding domain.

LIN-5 S659S662 phosphorylation contributes to cortical pulling forces

Additional characterizations of the non-phosphorylatable and phosphomimetic mutants revealed insight in the functional contribution of LIN-5 phosphorylation. As the contribution of S659 and S662 phosphorylation appeared quite subtle, we examined the spindle in early embryos with substitutions of these residues in detail. In the wild type, meiosis completes after fertilization and results in the formation of a haploid maternal pronucleus, which migrates to meet the paternal pronucleus in the posterior, after which the adjoined pronuclei and centrosomes migrate to the center, rotate and form a spindle along the long axis of the zygote (Galli and van den Heuvel, 2008; Rose and Gönczy, 2014) (**Video S1**). Observations with differential interference contrast (DIC) microscopy showed that these events all occur normally in *lin-5*[S659A,S662A] and *lin-5*[S659E,S662D] mutants. Subsequently, in wild type embryos, the chromosomes become aligned at the metaphase plate and are segregated to opposite poles during anaphase. During spindle elongation, the posterior spindle pole oscillates extensively, while the anterior pole remains relatively steady. This coincides with spindle movement towards the posterior, and is followed by flattening of the posterior pole (**Video S1**). Starting in anaphase, mutant embryos with non-phosphorylatable *lin-5*[S659A,S662A] deviated from the wild type, while *lin-5*[S659E,S662D] mutants showed no phenotype. Specifically, *lin-5*[S659A,S662A]

mutants showed significantly dampened oscillation of both the anterior and posterior pole, reduced spindle elongation, and nearly absent flattening of the posterior spindle pole (**Figure 4c** and **S6b**). Nevertheless, both non-phosphorylatable and phosphomimetic S659,S662 mutants underwent asymmetric division of the zygote as normal, which resulted in the formation of a larger anterior blastomere (AB) and smaller germline precursor cell (P1). The spindle normally rotates by 90 degrees prior to division of the P1 blastomere (**Video S1**). This failed to occur or was incomplete in 47.1% of the *lin-5*[S659A,S662A] two-cell embryos, compared to 6.3% and 7.3% incomplete rotation scored in wild type and *lin-5*[S659E,S662D] mutant embryos, respectively (**Figure 4c** and **6b**). As protein levels were comparable to wild type (**Figure S5b**), these results suggest that cortical pulling forces are reduced in *lin-5*[S659A,S662A] mutants. Interestingly, this does not disrupt the asymmetry of the first division and has only a small effect on viability.

To determine cortical pulling forces more directly, we performed spindle severing assays with a UV laser beam (Grill et al., 2001). Confirming our DIC analyses, the peak velocities of spindle pole movements were significantly reduced in *lin-5*[S659A,S662A] embryos (anterior pole 20.5%, posterior pole 18.4% reduced compared to wild type) (**Figure 4d**). Similar experiments performed with *lin-5*[S659E,S662D] mutant embryos and PAR-1 phosphorylation site mutants (S397A and S397E) did not reveal significant divergence from the wild type (**Figure 4d**). These data support the conclusion that phosphorylation of S659 and S662 contributes to cortical pulling forces, both in the anterior and posterior, and thereby to spindle pole oscillation, spindle elongation, posterior pole flattening and spindle rotation in P1. Moreover, the finding that pulling forces, albeit reduced, remained asymmetric in *lin-5*[S659A, S662A] mutants explains why these mutants show normal asymmetry of the first division, and normal sizes of the AB and P1 blastomeres.

We wondered whether Wnt-signaling could locally control GSK-3 kinase activity to affect LIN-5 S659, S662 phosphorylation and asymmetric cell division. In the EMS blastomere of the 4-cell embryo, the spindle rotates from a left/right to anterior/posterior position to correctly specify and position the E and MS daughter cells (Sulston et al., 1983). This rotation is redundantly controlled by MES-1/SRC-1 and MOM-2/MOM-5 Wnt/Frizzled signaling pathways (Bei et al., 2002). We examined whether the Wnt pathway contributes to EMS spindle rotation through phosphorylation of LIN-5[S659,S662]. Making use of a *mes-1*(*bn74*ts) mutant strain expressing GFP-β-tubulin, we observed normal spindle rotation in *lin-5*[S659A,S662A] mutant embryos, with only one of 13 embryos showing a tilted spindle angle in the EMS blastomere (**Figure S6c**). *mes-1*(*bn74*ts); *lin-5*[S659E,S662D] mutant embryos showed an occasional failed rotation or tilted spindle angle. In control *mes-1*(*bn74*ts); *gsk-3(RNAi)* mutants, the EMS spindle failed to rotate in 9/11 embryos (**Figure S6c**). This clear difference in phenotype shows that LIN-5 S659 phosphorylation is not the major contribution of GSK-3 in EMS spindle rotation. Asymmetric divisions of epithelial seam cells in the *C. elegans* epidermis also depend on a Wnt-β- catenin asymmetry pathway (Takeshita and Sawa, 2005; Wildwater et

al., 2011), and remained normal in *lin-5*[S659A,S662A] and *lin-5*[S659E,S662D] mutants. Thus, evidence for developmental regulation of LIN-5–GPR-1/2 interaction through Wnt-signaling was not obtained. Instead, absence of unphosphorylated S659,S662 peptides in our mass spectrometry analyses, and the wild type appearance of phosphomimetic mutants point to constitutive phosphorylation of the S659,S662 residues.

GPR-1 fails to localize to the centrosome in LIN-5[S659A,S662A] mutants

Our yeast two-hybrid data showed reduced interaction between LIN-5[S659A,S662A] and GPR-1 compared to wild type, which likely explains the reduced pulling forces observed in vivo. We examined whether the colocalization between LIN-5 and GPR-1 in vivo depends on LIN-5 phosphorylation. Hereto, we generated strains with *lin-5*[S659,S662] double phosphorylation-site alterations in combination with *egfp::gpr-1*, a CRISPR/Cas9-mediated knockin allele of the endogenous *gpr-1* locus. Immunohistochemical detection of eGFP

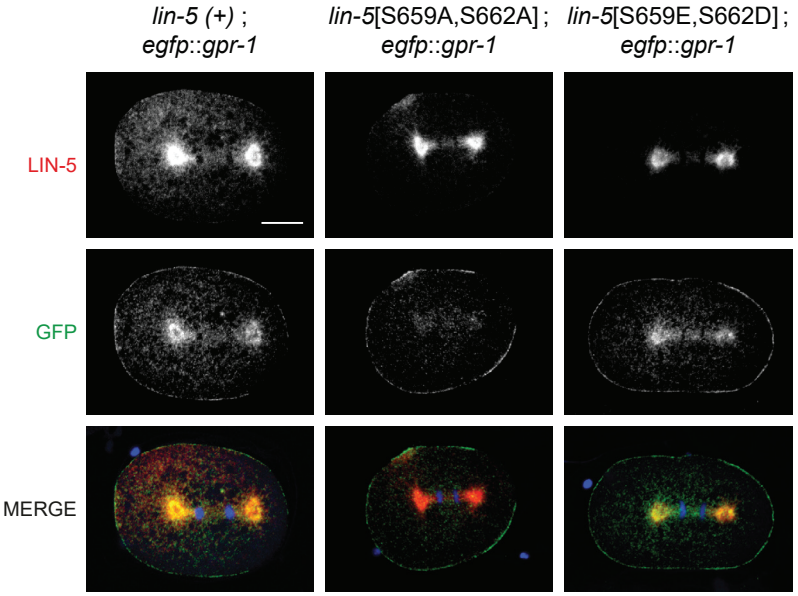

Figure 5. **Localization of LIN-5 and GPR-1 in phosphorylation mutants.** Immunohistochemical staining of embryos expressing wild type or phosphomutant *lin-5* and endogenously tagged *egfp*::*gpr-1*. Representative images of one-cell embryos in anaphase, stained with anti-LIN-5 (red) and anti-eGFP (green) antibodies, and DAPI to visualize DNA. All images taken with same exposure time, objective and magnification. Anterior to the left, scale bars 10 µm.

and LIN-5 showed normal colocalization of LIN-5 and GPR-1 in phosphomimetic *lin-5*[S659E,S662D] mutants at the centrosomes and cell cortex (**Figure 5** and **S6c**; note that LIN-5 becomes clearly visible at the cortex only after the one-cell stage). In contrast, in *lin-5*[S659A,S662A] mutant embryos, GPR-1 localized to the cortex but no longer accumulated at the centrosomes (**Figure 5**). Notably, GPR-1/2 localization at the cortex primarily depends on association with the GOA-1 and GPA-16 Gα proteins and is required for pulling forces, whereas ASPM-1–LIN-5 anchors GPR-1/2 at the centrosome without early embryonic requirement (Srinivasan et al., 2003; van der Voet et al., 2009). Thus, while the loss of centrosomal GPR-1 appears to confirm a reduced binding affinity for LIN-5[S659A,S662A] compared to wild type LIN-5, the reduced pulling forces likely result from a similarly reduced affinity between these proteins at the cortex. Nevertheless, LIN-5 still localized to the cortex in *lin-5*[S659A,S662A] mutants (**Figure S7**). This likely reflects different dynamics of the two complexes; with rapid exchange of LIN-5 at the cortex while centrosomal GPR-1/2 accumulation likely depends on prolonged LIN-5 association. The combined observations in yeast two-hybrid assays, phenotypic analyses, and protein localization studies strongly indicate that phosphorylation of LIN-5 residues S659 and S662 contributes to the affinity of the LIN-5/GPR-1/2 interaction in vivo.

A potential LIN-5 phosphorylation-dephosphorylation cycle in dynein recruitment

Characterization of the CDK-1 phosphorylation site mutants required a different strategy, as homozygous *lin-5*[T168A,T181A] and *lin-5*[T168D,T181D] mutants are fully sterile. To be able to examine the effects of these mutations in early embryos, we created trans-heterozygotes carrying these mutations and *egfp*::*lin-5*, a functional CRISPR/Cas9-generated knockin allele of endogenous *lin-5*. The *egfp*::*lin-5* allele served both as a visible balancer for the *lin-5* phosphorylation site mutations, and allowed selective knockdown of functional *lin-5* by RNAi against *egfp*. This strategy allowed us to obtain and characterize early embryos with CDK1-phosphorylation site alterations in LIN-5.

Control immunohistochemical staining experiments confirmed that *egfp* RNAi treatment of homozygous *egfp*::*lin-5* adults completely removed LIN-5 and eGFP from the offspring (**Figure S8**). Following *egfp* RNAi treatment of heterozygous animals with wild type *lin-5 (lin-5(+) / egfp::lin-5),* LIN-5 localized normally, but the eGFP staining was lost (**Figure 6**). These results demonstrate that the RNAi effect remains specific for *egfp::lin-5* and does not carry over to the untagged *lin-5* allele. Testing balanced *lin-5*[T168A,T181A] and *lin-5*[T168D,T181D] animals the same way, we observed that the mutant LIN-5 proteins are expressed and localize as normal to the cortex and centrosomes, while the early embryonic divisions were clearly defective (**Figure 6** and **5c**). Interestingly, *lin-5*[T168A,T181A] and *lin-5*[T168D,T181D] showed similar abnormalities, emphasizing the critical role for the in vivo phosphorylated threonine residues at these positions.

Using the above-described method, we also performed live imaging by time-lapse DIC microscopy and spindle severing experiments with *lin-5*[T168A,T181A] and *lin-5*[T168D,T181D] mutant embryos. Again, the defects observed in both mutants resembled *lin-5* strong loss-of-function (Fisk Green et al., 2004; Lorson et al., 2000), and cortical pulling forces were greatly reduced in both mutants (**Figure 4e**). In contrast, homozygous *lin-5*[T168S,T181S] mutants showed normal spindle pulling forces (**Figure 4e**). This indicates that the two threonine residues are not essential per se, but phosphorylation and de-phosphorylation at these sites is likely critical. The *lin-5*[T168S,T181S] mutants did show dampened spindle oscillation, which might result from somewhat different kinetics of threonine versus serine phosphorylation and dephosphorylation in CDK1 substrates (Suzuki et al., 2015).

Because the N-terminus of LIN-5 is implicated in the recruitment of dynein (Kotak et al., 2012), we crossed both mutants with an *mcherry*::*dhc-1* strain, in which the mCherry tag was introduced into the endogenous dynein heavy chain gene by CRISPR/Cas9-mediated knockin. This homozygous *mcherry*::*dhc-1* strain is viable and develops as normal. mCherry::DHC-1 was diffusely detected in the cytoplasm, and distinctly localized at the nuclear envelope, kinetochores, astral microtubules, spindle poles and cell cortex.

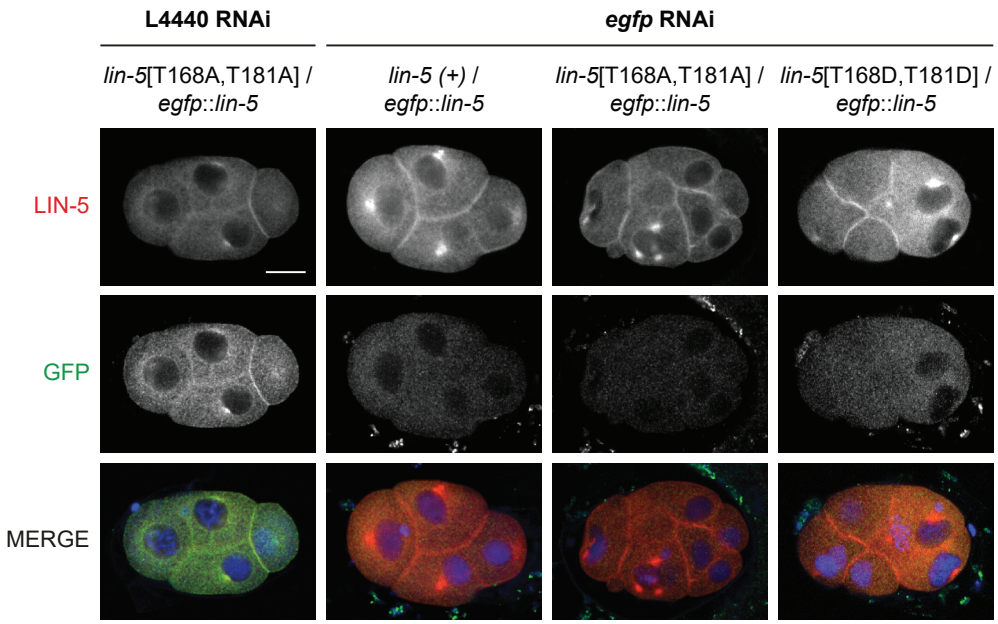

Figure 6. **T168 and T181 mutants show normal subcellular LIN-5 localization.** Immunohistochemical staining of embryos heterozygous for *egfp::lin-5* and wild type or phosphomutant *lin-5* as indicated. L4 animals were treated with feeding RNAi against control or *egfp* RNAi to specifically remove *egfp::lin-5* function, 48 hours before fixation of their embryos. Representative fluorescence microscopy images of embryos stained with anti-LIN-5 (red) and anti-GFP (green) antibodies, and DAPI to visualize DNA. All images taken with same exposure time, objective and magnification. Anterior to the left, scale bars 10 μm.

a

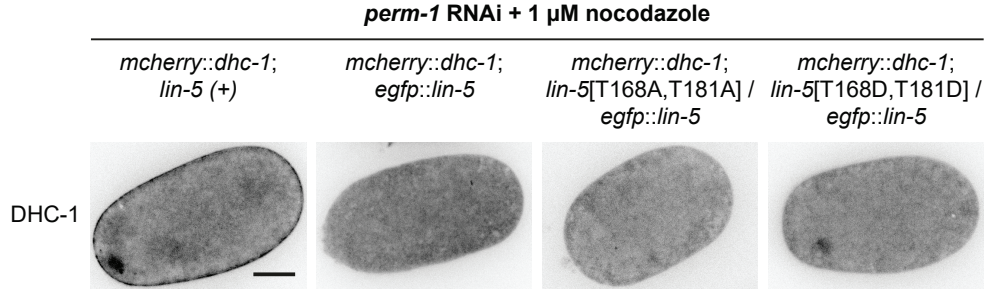

Cortical DHC-1	8/10 embryos	0/15 embryos	0/14 embryos	0/15 embryos
Parents	N/A	N/A	6	6

b

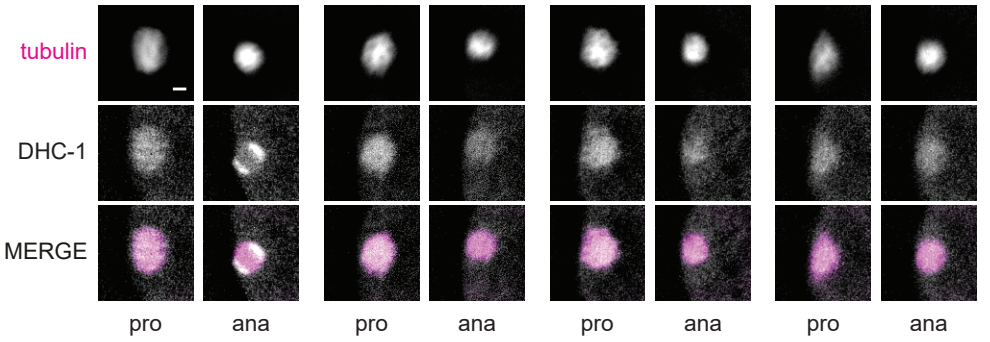

Focus DHC-1	10/11 embryos	0/10 embryos	0/17 embryos	0/16 embryos

Figure 7. **DHC-1 fails to accumulate at meiotic spindle poles in LIN-5 T168, T181 phosphosite mutants.** (**a**) Representative still images of *mcherry::dhc-1; lin-5*[T168,T181] one-cell embryos treated with *perm-1* RNAi, *egfp* RNAi and 1 µM nocodazole, and imaged by spinning disk confocal microscopy. The number of embryos with cortical mCherry::DHC-1 is indicated, with "parents" indicating the number of animals from which embryos were analyzed. All images were taken with the same objective, magnification, and exposure time. Anterior to the left, scale bars 10 µm. (**b**) Representative snapshots of live imaging of *mcherry::dhc-1; tubulin::gfp; lin-5*[T168,T181] meiotic embryos treated with *egfp* RNAi, and imaged by wide field microscopy. Time interval between prophase and anaphase is 100 s. All images were taken with same exposure time, objective and magnification. Anterior to the left, scale bars 2 µm.

Localization of dynein was dynamic during all stages of mitosis, but cortical dynein was barely detectable at the one-cell stage. However, following treatment of permeabilized embryos with nocodazole to depolymerize microtubules, mCherry::DHC-1 accumulated on the cell cortex of one-cell embryos in metaphase and anaphase (**Figure 7a** and **S9**). Strikingly, this cortical dynein localization was abolished by *lin-5* RNAi, and did not occur in *lin-5*[T168A,T181A] and *lin-5*[T168D,T181D] mutant embryos (**Figure 7a**). Since these mutant LIN-5 forms localize to the cell cortex, T168 and T181 are critical for the function of LIN-5 as a cortical dynein anchor.

In addition to cortical localization of dynein in mitosis, LIN-5 is also required for dynein recruitment to the poles of the meiotic spindle (van der Voet et al., 2009). Accumulation of dynein at the spindle poles, as well as the cell cortex, occurs coincident with anaphase onset of meiosis I and II, and is needed for spindle rotation and expulsion of chromosomes into a polar body (Crowder et al., 2015; Ellefson and McNally, 2011; van der Voet et al., 2009). While homozygous *lin-5*[T168S,T181S] mutants showed normal meiosis, we observed polar body absence and abnormally large polar bodies in eGFP::LIN-5-depleted *lin-5*[T168A,T181A] and *lin-5*[T168D,T181D] embryos, consistent with *lin-5* loss of function. To examine meiotic spindle rotation and dynein localization in such embryos, we combined the *lin-5* mutations, balanced by *egfp::lin-5*, with homozygous *gfp::tbb-2* β-tubulin and mCherry::DHC-1 dynein reporters (**Figure 7b**). In a control strain with wild type LIN-5, spindle rotation and dynein accumulation occurred in 10 of 11 embryos (the one exception showed rotation but only weak mCherry::DHC-1 accumulation) (**Figure 7b** left). Examination of *egfp* RNAi treated *egfp::lin-5* embryos with combined DIC and fluorescence microscopy revealed normal diffuse association of DHC-1 with the meiotic spindle in meiotic prophase, followed by gradual loss of mCherry::DHC-1 from the anaphase spindle, rather than accumulation of dynein at the poles. The failure in dynein localization coincided with failure to rotate the meiotic spindle (**Figure 7b**). These results agree with our previously reported meiotic *lin-5* RNAi phenotype (Srinivasan et al., 2003; van der Voet et al., 2009), although this time we also observed abnormally elongated meiotic spindles in meiosis II in a subset of the embryos, as has been reported for dynein complex subunits (Crowder et al., 2015). eGFP::LIN-5-depleted *lin-5*[T168A,T181A] and *lin-5*[T168D,T181D] embryos were indistinguishable from *lin-5* knockdown mutants (**Figure 7b**).

In conclusion, substitution of LIN-5 T168 and T181 with non-phosphorylatable alanine or phosphomimetic aspartic acid residues creates a severe defect in LIN-5-mediated dynein recruitment. In contrast, replacement of the same residues with phosphorylatable serine residues did not compromise LIN-5 function (**Figure 4a**, **b**, and **e**). Combined with the available literature (Ellefson and McNally, 2011; McCarthy Campbell et al., 2009; van der Voet et al., 2009), these data point to CDK-1-mediated phosphorylation and subsequent dephosphorylation of the LIN-5 N-terminus as a critical step in dynein recruitment to the meiotic spindle and cell cortex (see below).

Discussion

In this study, we investigated whether the extensive in vivo phosphorylation of the LIN-5^{NuMA} protein is important for chromosome segregation and cell cleavage plane determination. We combined in vivo and in vitro phosphorylation analysis, identified critical phosphorylated LIN-5 residues by complementation, and defined the LIN-5–GPR-1 interaction domain by reverse yeast two-hybrid screening. Using this information, we created phosphosite mutants and tagged alleles by genetic engineering, and determined the in vivo contribution of individual phosphorylated residues by protein localization studies, time-lapse microscopy and spindle severing experiments. The combined data indicate that a variety of cell cycle and polarity kinases phosphorylate LIN-5, with specific phosphorylations promoting pulling force generation while others inhibit LIN-5 function. The combined phosphorylations of the LIN-5 N-terminus and C-terminus are critical in the spatiotemporal control of cortical pulling forces, and thereby for correct chromosome segregation and spindle positioning (**Figure 8**).

CRISPR/Cas9-mediated genomic engineering has added an important tool to a powerful genetic system, and more efficient procedures are continuously developed (Arribere et al., 2014; Dickinson et al., 2015; Kim et al., 2014; Paix et al., 2015; Waaijers and Boxem, 2014; Ward, 2015). The use of CRISPR/Cas9 allowed us to precisely alter one or two codons of specific serine/threonine residues within the normal genetic background. Using knockin alleles eliminates unwanted effects of transgene overexpression or silencing. In particular transgene silencing has long hampered *lin-5* studies and was also observed in our complementation studies. Transgene expression levels that are close to a threshold level may explain why the *lin-5*[S659A,S662A] mutation showed a strong loss-of-function phenotype, while the effect of the same mutations introduced in the endogenous locus was less severe. In addition to phosphosite mutations, we also created tagged endogenous alleles of *lin-5*, *gpr-1* and *dhc-1* for fluorescent fusion protein expression. This allowed the development of a novel method for analysis of early lethal mutations. This method makes use of a functional eGFP-tagged allele, which acts as a visible balancer and allows the specific removal of wild type function by *egfp* RNAi.

In a previous study, we revealed in vivo kinase activity through differential labeling of *C. elegans* cultures with stable nitrogen isotopes, followed by kinase knockdown and quantitative analysis of phosphopeptides by mass spectrometry (Galli et al., 2011). This strategy worked well for PKC-3, but various limitations can prevent detection of kinase-substrate relations in vivo. The phosphorylation of LIN-5 by PAR-1 was missed in our previous analysis, because of overlap between the relevant LIN-5 phosphopeptides and unrelated peptides. Identification of mitotic substrates of CDK-1 is difficult in vivo, because CDK-1 knockdown results in complete sterility and arrest of fertilized oocytes before completion of meiosis (Boxem et al., 1999). Casein kinase I, in turn, is represented by 87 family members in *C. elegans* (Plowman et al., 1999), making it less likely that knockdown

experiments will reveal a quantitative difference in substrate phosphorylation. The in vitro kinase assays in the current study revealed candidate kinases that were otherwise difficult to detect. The PAR-1 in vitro kinase assays pointed to a specific LIN-5 phosphorylation that was subsequently confirmed by our in vivo data. The in vitro phosphorylation of peptides with single phosphorylated residues was instrumental in detecting a probable two-step mechanism for S662 phosphorylation by CKI, following a priming phosphorylation by GSK3. Thus, while detecting direct phosphorylation in vivo remains the ultimate goal, in vitro assays continue to provide meaningful insight.

The combined in vitro and in vivo kinase analyses strongly suggest that PAR-1 phosphorylates LIN-5 at serine 397. Replacing this serine with non-phosphorylatable alanine or phosphomimetic glutamic acid apparently did not affect viability, development, cell division, chromosome segregation or spindle pulling forces. In fact, many phosphorylations that occur in vivo may be bystander rather than regulatory events, and determining which phosphorylations are critical in vivo has received great attention in the current study. The first selection came from alanine substitution mutagenesis combined with complementation of a *lin-5* null mutation. This revealed that 4 of the 25 phosphorylated residues are critical for LIN-5 function. As we could only score larval divisions in this assay, we cannot exclude that additional phosphorylations may be critical

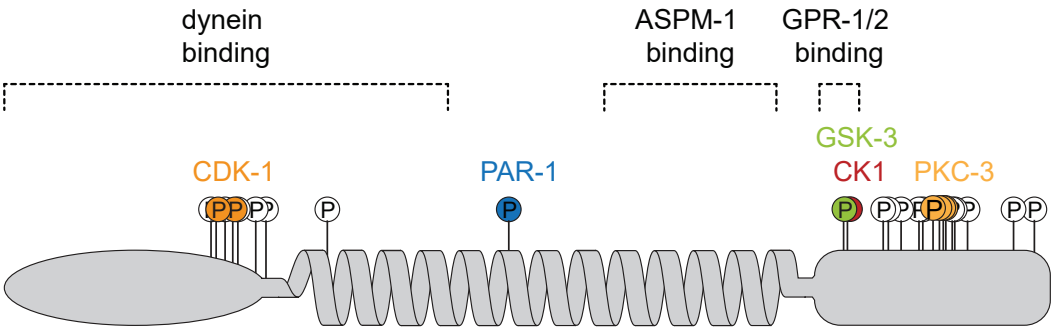

phosphorylated sites	kinase	phenotype
T168, T181	CDK-1	loss of cortical dynein and strong loss of pulling forces
S397	PAR-1	none observed
S659, S662	GSK-3, CK1	reduced GPR-1 binding and reduced pulling forces
S729, S734, S737, S739	PKC-3	increased anterior pulling forces

Figure 8. **Summary of the proposed critical phosphorylations of LIN-5 by CDK-1, PAR-1, GSK3, CK1 and PKC-3.** Overview of how phosphorylation-site mutations affect LIN-5 function in vivo in regulating cortical pulling forces that position the mitotic spindle and contribute to chromosome segregation.

during embryogenesis. Remarkably, 2 of the 4 critical residues form part of a probable GPR-1/2 binding domain, while the other 2 appear to mediate contact with dynein at the cortex.

We defined the GPR-1/2 binding domain through screening for LIN-5 residues that are essential for GPR-1 interaction in yeast two-hybrid assays. The strong clustering of missense mutations in this screen combined with results from deletion analyses suggests a short linear GPR-interaction epitope. This is in full agreement with results from crystal structure studies of the related NuMA-LGN complex. The TPR repeats in the N-terminal half of LGN form helix-turn-helix repeats that together organize into a superhelical bundle (Culurgioni et al., 2011; Zhu et al., 2011). The inner surface of this bundle forms a binding channel for an extended NuMA peptide of 28 amino acids (Zhu et al., 2011). Many electrostatic and hydrogen interactions between side chains of the NuMA peptide and TPR motifs together provide a high affinity binding site.

The TPR-repeat interaction site in LIN-5 resembles that of NuMA in size, position, and overall amino-acid composition. The exact residues are not well-conserved, however, probably because the many amino acids that contribute weak interactions provide a limited biological constraint for the conservation of individual amino acids. Notably, the core of the binding site contains EPEQLDDW in human NuMA and SPDSLPDF in LIN-5, sharing three identical and two similar residues as well as negative charge. The NuMA peptide contains four acidic residues (D, E), while two D residues and two phosphorylated serines are negatively charged in the LIN-5 peptide.

Phosphorylation offers the opportunity to regulate LIN-5–GPR-1/2 binding. In fact, dual GSK3 and CK1 phosphorylation of the LRP6 Wnt-co-receptor regulates the interaction of LRP6 with axin (Wu et al., 2009; Zeng et al., 2005). We did not obtain evidence to support developmentally regulated LIN-5–GPR-1 binding. Alanine substitution of S659 and S662 significantly reduced spindle pulling forces, but division of the zygote, EMS blastomere and seam cells continued to be asymmetric. The latter types of divisions depend on the Wnt-b-catenin asymmetry pathway, which in EMS positions the spindle redundantly with *mes-1/src-1* signaling (Bei et al., 2002). Even the combined *lin-5*[S659A,S662A] mutation and *mes-1* knockdown did not interfere with A-P positioning of the spindle in EMS. Moreover, we could functionally replace serine 659 and 662 with glutamic and aspartic acid, suggesting that charge, rather than phosphoregulation, is critical for GPR-1/2 interaction.

A contribution of CDK-1 phosphorylation in LIN-5 regulation was expected. CDK1/cyclin B kinases are the master regulators of mitosis that phosphorylate hundreds of substrate proteins (Errico et al., 2010; Holt et al., 2009; Olsen et al., 2010). The LIN-5 N- and C-terminus and corresponding domains in NuMA contain multiple CDK1 consensus sites. CDK1/cyclin B has been shown to regulate *Xenopus* and human NuMA through phosphorylation of the C-terminus (Gehmlich et al., 2004; Kotak et al., 2013). Specifically, phosphorylation at T2055 interferes with the cortical localization of NuMA, thereby

inhibiting dynein recruitment until CDK1/cyclin B is inactivated at the metaphase/anaphase transition (Kotak et al., 2013). Our results indicate that this temporal regulation may also involve critical phosphorylation of the dynein-interacting N-terminus of NuMA by CDK1/cyclin B.

In *C. elegans,* dynein recruitment to the meiotic spindle and cell cortex, as well as mitotic pulling forces, depend on activation of the anaphase promoting complex/cyclosome (APC/C), and inactivation of CDK-1/cyclin B (Ellefson and McNally, 2011; McCarthy Campbell et al., 2009; van der Voet et al., 2009). Thus, phosphorylation of specific mitotic substrates by CDK-1/cyclin B is likely to inhibit dynein recruitment and pulling force generation. A recent study identified the p150 dynactin subunit as a likely candidate for inhibition by CDK-1/cyclin B phosphorylation (Crowder et al., 2015). Our results point to the LIN-5 N-terminus as another critical target for CDK-1 regulation. Supporting this conclusion, T168, T181 are part of CDK consensus sites, are phosphorylated in vivo, and are efficiently phosphorylated by CDK1/cyclin B in vitro. Substitution of LIN-5 T168 and T181 with phosphomimetic glutamic acid or aspartic acid residues resulted in strong loss of LIN-5 function, supporting that CDK-1 phosphorylation normally inhibits LIN-5. More surprising, an indistinguishable phenotype was observed following T168 and T181 replacement with non-phosphorylatable alanine. This could indicate that the threonine residues are critical for LIN-5 folding, or that phosphorylation of these threonines in the N-terminus also contributes to dynein recruitment. In stark contrast to alanine substitution, replacement of the same residues with phosphorylatable serine had no detectable effect on pulling forces, meiotic and mitotic cell divisions, viability and fertility. While other explanations are possible, these data are consistent with a required sequential CDK-1 phosphorylation and dephosphorylation of LIN-5 T168 and T181. Therefore, we propose a two-step model, in which CDK-1/cyclin B induces the assembly of a LIN-5 pre-force generating complex in prometaphase. Subsequent removal of the phosphates, which follows CDK inactivation by the APC/C at anaphase onset, promotes interaction of this complex with dynein.

Many of the lessons learned from studies in worms and flies have subsequently been found to apply broadly to the animal kingdom. The initial discovery of LIN-5 requirement in spindle positioning in *C. elegans* (Lorson et al., 2000) has contributed to identifying similar functions for NuMA in mammalian systems (Lechler and Fuchs, 2005). It will be intriguing to find out to what extent the phosphoregulation of pulling forces translates from *C. elegans* to mammalian systems, and specifically whether reversible CDK1 phosphorylation of the NuMA N-terminus controls dynein interaction and spindle positioning.

Materials and Methods

C. elegans strains

Strains were cultured on nematode growth medium plates, seeded with Escherichia coli OP50 as previously described (Brenner, 1974). Animals were maintained at 20°C, unless stated otherwise. All strains used in this study are found in **table S1**. Genome modifications in strains SV1568, SV1569, SV1586, SV1588, SV1589, SV1590, SV1600, SV1619, SV1621, SV1622, SV1695 and SV1901 were introduced by making use of CRISPR/Cas9 genome editing as described below.

Post-embryonic analysis of LIN-5 phosphomutants

For functional analysis of wild type and phosphomutant LIN-5, 5 ng/µl *Plin-5::gfp::lin-5* DNA, together with 5 ng/µl *Psur-5::dsRed* and 25 ng/µl Lambda DNA (Fermentas), was injected into the gonad of SV918 young adults. *Psur-5::dsRed* positive F1 progeny were selected making use of a fluorescence stereo microscope (Leica, MZ16F). After this, *lin-5(e1348)* homozygous animals were selected based on absence of pharyngeal *Pmyo-2::gfp*, expressed from the mIn1 balancer chromosome. Rescue analysis of *lin-5* null animals was performed by Differential Interference Contrast and fluorescence microscopy, using a Zeiss Axioplan microscope. Intestinal nuclei were counted only in animals expressing *Psur-5::dsRed* in all intestinal nuclei. Vulval development was assayed for all animals L4 and older.

For quantification of cell numbers in CRISPR/Cas9 knockin mutants, asynchronous populations of animals were fixed, DNA stained with propidium iodide and intestinal and ventral cord nuclei were counted using a Zeiss Axioplan fluorescence microscope. Cells were counted at late larval stages. For the ventral cord, all nuclei of the P2-to-P10 daughter cells and juvenile motor neurons in the region between these cells were counted.

In vitro and in vivo kinase assays

For in vitro CDK1 kinase assays, immunoprecipitations were performed from mitotic lysates of HeLa cells using mouse monoclonal anti cyclin B1 (GNS1) or beads alone as negative control. Immunoprecipitations were incubated for 30 min at 30°C with either Histone H1, bacterially produced GST or GST-LIN-5 in kinase buffer containing 50 mM HEPES at pH 7.5, 5 mM $MgCl_2$, 2.5 mM $MnCl_2$, 1 mM dithiothreitol, 50 µM ATP and 2.5 µCi [γ-^{32}P] ATP. Reactions were terminated by the addition of SDS (5x sample buffer). For mass spectrometry analysis, no [γ-^{32}P] ATP was added to the kinase assays and incubation time was prolonged to 2 hours at 30°C.

For in vitro GSK3 and CK1 kinase assays, peptides (RRRIRCGSPDSLPDFLADN) containing either unphosphorylated, phosphorylated S659 or phosphorylated S662 were used. Kinases were incubated for 30 min at 25 °C with synthetic peptide in kinase buffer containing 200 µM ATP, 50 mM HEPES at pH 7.5, 10 mM $MgCl_2$, 1 mM EGTA, 2 mM

dithiothreitol, supplemented with 20 µCi [γ-^{32}P] ATP for radioactive kinase assays. Reactions were terminated by the addition of SDS (4x sample buffer).

All other in vitro kinase assays were performed as previously described (Galli et al., 2011). In short, kinases were incubated for 30 min at 25 °C with bacterially produced GST or GST-LIN-5 in kinase buffer containing 200 µM ATP, 50 mM HEPES at pH 7.5, 10 mM $MgCl_2$, 1 mM EGTA, 2 mM dithiothreitol, supplemented with 20 µCi [γ-^{32}P] ATP for radioactive kinase assays. Reactions were terminated by the addition of SDS (4x sample buffer). For mass spectrometry analysis, no [γ-^{32}P] ATP was added to the kinase assays and incubation time was prolonged to 2 hours at 25°C. Kinases used in this study were: recombinant *C. elegans* PAR-1 (a kind gift from Erik Griffin and Geraldine Seydoux), and mammalian Aurora B (a kind gift from Susanne Lens), CK1 (New England Biolabs), CK2 (New England Biolabs), and GSK3 (New England Biolabs).

In-gel digestion and phosphopeptide enrichment

Gel bands were cut and processed for protein in-gel digestion as described elsewhere (Galli et al., 2011). Briefly, proteins were reduced with dithiothreitol and then alkylated with iodoacetamide. Trypsin was added at a concentration of 10 ng/µl and the mixture was digested overnight at 37°C. Subsequently, peptides were collected from the supernatants and a second extraction using 10% formic acid was performed. Phosphopeptides from LIN-5 were enriched using TiO_2 chromatography (Pinkse et al., 2008). Basically, home-made GELoader tips (Eppendorf, Hamburg, Germany) were packed with TiO_2 beads (5 µm, INERTSIL). Peptides were loaded in 10% formic acid and subsequently washed with 20 µl of 80% acetonitrile, 0.1% trifluoroacetic acid (Fluka, Sigma-Aldrich). Phosphopeptides were then eluted twice with 20 µl of 1.25% ammonia solution (Merck, Germany), pH 10.5, and 3 µl of 100% formic acid was finally added to acidify the samples.

Mass-spectrometry analysis

Nanoflow LC-MS/MS was carried out by coupling an Agilent 1100 HPLC system (Agilent Technologies, Waldbronn, Germany) to an LTQ-Orbitrap XL mass spectrometer (Thermo Electron, Bremen, Germany). Peptide samples were delivered to a trap column (AquaTM C18, 5 µm (Phenomenex, Torrance, CA); 20 mm x 100-µm inner diameter, packed in house) at 5 µl/min in 100% solvent A (0.1 M acetic acid in water). Next, peptides eluted from the trap column onto an analytical column (ReproSil-Pur C18-AQ, 3µm (Dr. Maisch GmbH, Ammerbuch, Germany); 40 cm x 50-µm inner diameter, packed in house) at ~100 nl/min in a 90 min or 3 h gradient from 0 to 40% solvent B (0.1 M acetic acid in 8:2 (v/v) acetonitrile/water). The eluent was sprayed via distal coated emitter tips butt-connected to the analytical column. The mass-spectrometer was operated in data-dependent mode, automatically switching between MS and MS/MS. Full-scan MS spectra (from m/z 300 to 1500) were acquired in the Orbitrap with a resolution of 60,000 at m/z 400 after accumulation to target value of 500,000 in the linear ion trap. The five most intense ions at

a threshold above 5000 were selected for collision-induced fragmentation in the linear ion trap at a normalized collision energy of 35% after accumulation to a target value of 10,000. Peak lists were created from raw files with MaxQuant (Waaijers et al., 2013). Peptide identification was carried out with Mascot (Matrix Science) against a *Caenorhabditis elegans* protein database (http://www.wormbase.org) supplemented with all the frequently observed contaminants in MS (23,502 protein sequences in total). The following parameters were used: 10 ppm precursor mass tolerance, 0.6 Da fragment ion tolerance, up to 3 missed cleavages, carbamidomethyl cysteine as fixed modification, oxidized methionine, phosphorylated serine, threonine and tyrosine as variable modifications. Alternatively, MaxQuant and its search engine Andromeda was also employed for peptide identification and quantification.

Yeast two-hybrid fragment analysis

Full length *gpr-1* was PCR amplified from the ORFeome library (kind gift from Marc Vidal) using KOD polymerase (Novagen) and cloned into bait vector pPC97. Fragments of *lin-5* were PCR amplified from the ORFeome library with KOD polymerase (Novagen) and cloned into prey vector pPC86-AN (Boxem et al., 2008). DB::GPR-1- and AD::LIN-5-encoding plasmids were transformed sequentially into yeast strain Y8930 (Boxem et al., 2008). Positive interactions were identified on the basis of the activation of the HIS3 and ADE2 reporter genes, indicated by growth on synthetic complete -leucine -tryptophan -histidine + 2 mM 3-Amino-1,2,4-triazole (Sc -leu-trp-his + 3-AT) and synthetic complete -leucine -tryptophan -adenine (Sc -leu-trp-ade) plates.

Generation and verification of yeast two-hybrid *lin-5* mutants

To generate mutant clones, PCR was performed on pVP054 (pPC86-AN containing nucleotides 1821-2466 encoding amino acid 609-821 of *lin-5*) with increased $MgCl_2$ concentration of 7 mM. PCR products were cloned into pPC86-AN and transformed to DH5α competent cells. Bacterial colonies were collected and the DNA was isolated using a Nucleobond Xtra DNA purification kit (Macherey-Nagel). Bacterial clones were transformed into MB004 (Y8930 in which ADE2 is replaced by URA3 by homologous recombination) containing DB::GPR-1 and plated on synthetic complete -leucine -tryptophan + 2 g/l 5-fluoroacetic acid (Sc -leu-trp + FOA). Colonies were picked and spotted to synthetic complete -leucine -tryptophan (Sc -leu-trp) plates for validation, PCR and sequencing. Clones with single amino acid changes were re-tested by PCR amplification of the fragment and re-cloning into pPC86-AN. Interaction deficient alleles were identified on the basis of no activation of the HIS3 or URA3 reporter gene, indicated by absence of growth on Sc -leu-trp-his + 3-AT plates and synthetic complete -leucine -tryptophan -uracil (Sc -leu-trp-ura) plates.

Validation of yeast two-hybrid full length mutants

For generation of full length mutant clones, plasmids containing fragment clones with selected point mutations were digested and cloned into pVP055 (pPC86-AN containing nucleotides 1-2466 encoding amino acid 1-821 *of lin-5*). Phosphomutants were generated by either site-directed mutagenesis of pVP055 or Gibson assembly into pVP055 of short regions of *lin-5* with point mutations carried in the overlapping region. DB::GPR-1 and AD::LIN-5-encoding plasmids were transformed sequentially into yeast strain MB004. Interaction deficient alleles were identified on the basis of no activation of the HIS3 or URA3 reporter gene, indicated by absence of growth on Sc -leu-trp-his + 3-AT plates and Sc -leu-trp-ura plates.

Generation of CRISPR/Cas9 repair templates

CRISPR repair constructs were inserted into the pBSK vector using Gibson Assembly (New England Biolabs). Homologous arms of at least 1500 bp upstream and downstream of the CRISPR/Cas9 cleavage site were amplified from either cosmid C03G3 (for *lin-5* constructs) or *C. elegans* genomic DNA using KOD Polymerase (Novagen). Linkers containing the altered cleavage sites and point mutations were synthesized (Integrated DNA technologies). For *fkbp::egfp::gpr-1*, codon-optimized fkbp was synthesized (Integrated DNA technologies) and codon-optimized egfp was amplified from pMA-*egfp* (a kind gift from Anthony Hyman). For *egfp::lin-5*, codon-optimized *egfp* was amplified from pMA-*egfp*. For *mcherry::dhc-1*, codon-optimized mcherry was amplified from TH0563-PAZ-mCherry (a kind gift from Anthony Hyman). Mismatches were introduced in the sgRNA target site to prevent cleavage of knockin alleles. All plasmids and primers used for cloning are available upon request.

CRISPR/Cas9 genome editing

Young adults were injected with a solution containing the following injection mix: 30-50 ng/µl *Peft-3::Cas9* (Addgene 46168; (Friedland et al., 2013), 30-100 ng/µl u6::sgRNA with appropriate target for *dhc-1*, *gpr-1* and *lin-5*, 30-50 ng/µl repair template and 2.5 ng/µl *Pmyo-2::tdtomato*. Progeny of animals that express tdTomato were picked to new plates 3-4 days post injection. PCRs with primers diagnostic for homologous recombination at the endogenous locus were performed on F2-F3 populations, where one primer targeted the altered basepairs in the sgRNA site, point mutation or fluorescent tag and the other targeted a region just outside the homology arm. All primers used for genome editing are available upon request.

Preparation of protein lysates for Western blot analysis

For yeast protein lysates, cultures were grown overnight at 30°C. Yeast cells corresponding to 4 OD of culture were harvested, treated with Sodium hydroxide and resuspended in 100µl 2X sample buffer containing β-mercaptoethanol (Kushnirov, 2000).

For *C. elegans* protein lysates, strains SV1569, SV1663 and SV1664 were grown at 20°C one generation on NGM plates seeded with HB101, followed by a second generation in S-Medium with HB101 bacteria. Gravid adults were harvested and embryos were isolated by hypochlorite treatment. Embryo pellets were snap frozen in liquid nitrogen, grinded using mortar and pestle and resuspended in 5 ml fresh lysis buffer (containing 20 mM Tris-HCl pH 7.8, 250 mM NaCl, 15% glycerol, 0.5% IGEPAL, 0.5 mM EDTA, 50 mM Sodium fluoride, 1 mM β-mercaptoethanol and protease inhibitors (Roche complete, Mini, EDTA-free)). The suspension was passed through a French press 3 times, and the lysate was cleared at 13,000 rpm for 15 min at 4°C.

Western blot Analysis

Protein samples were separated on gradient acrylamide gels and subjected to western blotting on polyvinylidene difluoride membrane (Immobilon-P, Millipore). Membranes were blocked with 5% skim milk in PBST for 1 hour at room temperature, or overnight at 4°C for stripped blots. For protein detection, primary antibodies used in this study were: mouse anti-LIN-5 (1:1000) (Lorson et al., 2000) and rabbit anti-Tubulin (1:1000, Abcam) for stripped blots. Secondary antibodies used were: donkey anti-mouse HRP (1:5000, Abcam) and goat anti-rabbit HRP (1:5000, Jackson Immunoresearch). Proteins were dectected with Signalfire Plus chemiluminescent detection (Cell Signaling Technologies) and a Chemidoc MP Imager (Bio-Rad).

Time-lapse imaging and live-cell imaging

DIC time-lapse imaging was performed on strains N2, SV1568, SV1588, SV1590 and SV1600. Animals were grown overnight at 25°C. RNAi feeding of N2 against *gsk-3* was performed with the bacterial clone from the Orfeome-based RNAi Library (Rual et al., 2004; Timmons and Fire, 1998). L4 animals were grown for approximately 32 hours at 15°C before shifting overnight to 25°C for imaging, except SV1901 which was kept at 20°C. Embryos were dissected from adults in a solution of 0.8x egg salt (containing 94 mM NaCl, 32 mM KCl, 2.7 mM $CaCl_2$, 2.7 mM $MgCl_2$, 4 mM HEPES, pH 7.5; (Tagawa et al., 2001)) on coverslips and mounted on slides with 3% agarose prepared with egg salt. Embryos were imaged with 5s time intervals with a 100x/1.4 NA lens on a Zeiss microscope at 20°C. Relative positions of the spindle and furrow were analyzed manually using ImageJ.

Live-cell imaging of EMS rotation was performed on strains SV1783, SV1784 and SV1785. L4 animals were grown overnight at 20°C. Embryos were dissected from young adults as above and imaged with a 100x/1.4 NA lens on a Zeiss microscope at 20°C. Spindle rotation in EMS was followed over time with images taken at several time points.

Live-cell imaging of microtubule depolymerization upon nocodazole treatment was performed on strain AZ244. Young adult animals were injected with dsRNA (Fire et al., 1998) against *perm-1* and grown for 20 hours at 15°C. Embryos were dissected from

young adults in a solution of 0.8x egg salt containing 1 µM nocodazole on coverslips and mounted on concave slides. Embryos were imaged with a 60x/1.4 NA lens on a Nikon Eclipse Ti microscope with Perfect Focus System and Yokogawa CSU-X1-A1 spinning disk confocal head at room temperature.

Live-cell imaging of mitotic DHC-1 localization was performed on strains SV1619, SV1635, SV1638 and SV1639. Young adult animals were injected with dsRNA (Fire et al., 1998) against *perm-1* and *egfp* and grown for 20 hours at 15°C. Embryos were dissected from young adults in a solution of 0.8x egg salt containing 1 µM nocodazole on coverslips and mounted on concave slides. Still images of mitotic embryos in metaphase were taken within minutes after nocodazole addition. Eliminating nonspecific toxic effects, embryos on the same slide at the same time continued nuclear envelope degradation, and *perm-1(RNAi)* embryos continued embryonic development in the absence of nocodazole.

Embryos were imaged with a 60x/1.4 NA lens on a Nikon Eclipse Ti microscope with Perfect Focus System and Yokogawa CSU-X1-A1 spinning disk confocal head at room temperature. mCherry::DHC-1 localization was analyzed in mitotic one-cell embryos after nuclear envelope breakdown. Mitotic embryos were also identified based on presence of a polar body, enlarged centrosomes and remnant of the mitotic spindle.

Live-cell imaging of meiotic DHC-1 localization was performed on strains SV1702, SV1898, SV1899 and SV1902. For RNAi treated animals, young adult animals were injected with dsRNA (Fire et al., 1998) against *egfp* and grown for 24 hours at 15°C. Embryos were dissected from young adults as above and imaged with 10s time intervals with a 100x/1.4 NA lens on a Zeiss microscope at 20°C. For images presented in **figure 7b**, images were processed by subtracting a Gaussian-blur filtered image (Sigma(Radius): 20) using ImageJ.

UV laser spindle ablation

Spindle severing with a UV laser microbeam was performed on strains SV1585, SV1594, SV1596, SV1618, SV1700 and SV1701 essentially as previously described (Grill et al., 2001). RNAi feeding of SV1700 and SV1701 against *egfp* was performed with a bacterial clone containing full length egfp in the L4440 double T7 plasmid (Timmons and Fire, 1998). L4 animals were grown on RNAi for approximately 48 hours. For analysis of spindle pulling forces, animals were kept at 25°C for 24 h before ablations. Spindle ablations were carried out at 25°C (**Figure 4d**) or 20°C (**Figure 4e**) on a spinning disk confocal microscope. The spindle midzones were severed at anaphase onset and images of GFP-β-tubulin were taken at 0.5 s intervals. For analysis, the position of the spindle poles was automatically tracked using the MTrack2 plugin in ImageJ. Peak velocities of the anterior and posterior spindle poles were determined within a 12.5 s time frame after ablation.

Microscope setup: Nikon Eclipse Ti microscope with Perfect Focus System, Yokogawa CSU-X1-A1 spinning disk confocal head, S Fluor 100x N.A. 0.5-1.3 objective (at 1.3),

Photometrics Evolve 512 EMCCD camera, Cobolt Calypso 491 nm (100 mW) and Teem Photonics 355 nm Q-switched pulsed lasers, ILas system (Roper Scientific France/PICT-IBiSA, Institut Curie) to control the UV laser, ET-GFP (49002) filter, ASI motorized stage MS-2000-XYZ with Piezo top plate with Tokai hit INUBG2E-ZILCS stage top incubator (controlled at 25°C), controlled by MetaMorph 7.7 software.

Antibodies and immunohistochemistry

For immunostaining, embryos were dissected from adults in 8 µl of water on poly-L-lysine-coated slides. Embryos were freeze-cracked and fixed for 5 min in methanol at -20°C and then for 20 min in acetone at -20°C. After fixation, embryos were rehydrated in phosphate-buffered saline (PBS) containing 0.05% Tween-20 (PBST) and blocked with blocking solution (PBST containing 1% bovine serum albumin and 1% goat serum [Sigma-Aldrich]) for 1 h. Embryos were stained with primary and secondary antibodies for 1 h and washed after each incubation with PBST four times, 15 min each time. Finally, the embryos were embedded in ProLong Gold Antifade containing 4′,6-diamidino-2-phenylindole (DAPI). Primary antibodies used in this study were: mouse anti-LIN-5 (1:10; (Lorson et al., 2000) and rabbit anti-GFP (1:500, Life Technologies). Secondary antibodies were used at a concentration of 1:500. Secondary antibodies used were: goat anti-rabbit Alexa Fluor 488, and goat anti-mouse Alexa Fluor 568 (Invitrogen). Images were taken with a 63x/1.4 NA lens on a Zeiss confocal microscope.

Immunohistochemistry quantification of LIN-5 levels

Embryos were dissected and stained with antibodies as described above. Images were taken with a 63x/1.4 NA lens on a Zeiss confocal microscope using identical microscope setting for all images taken for every secondary antibody. Mean intensity of LIN-5 was measured using ImageJ by selecting fixed size regions that depended on the developmental stage. For every embryo 2 centrosomes and cytoplasmic regions were quantified.

Acknowledgements

We thank Erik Griffin and Geraldine Seydoux for recombinant PAR-1 kinase, Susanne Lens for Aurora B kinase, Anthony Hyman for plasmids, Marvin Tanenbaum for help with the CDK1 kinase assays, Adri Thomas for critically reading the manuscript, and all members of the van den Heuvel and Boxem groups for helpful discussions. We acknowledge Wormbase, and the Biology Imaging Center Faculty of Sciences, Department of Biology, Utrecht University. Some strains were provided by the CGC, which is funded by NIH Office of Research Infrastructure Programs (P40 OD010440).

Author Contributions

Conceptualization:VP, MG, SvdH
Formal analysis: VP, LEF, MG, JM
Funding acquisition: AA, AJRH, SvdH
Investigation: VP, LEF, MG, RS, JM, TvM
Methodology:VP, MG, MB, SvdH
Resources: VP, LEF, MG, RS, JM, SvdH
Visualization: VP, SvdH
Writing - original draft: VP, SvdH
Writing - review& editing: VP, SvdH

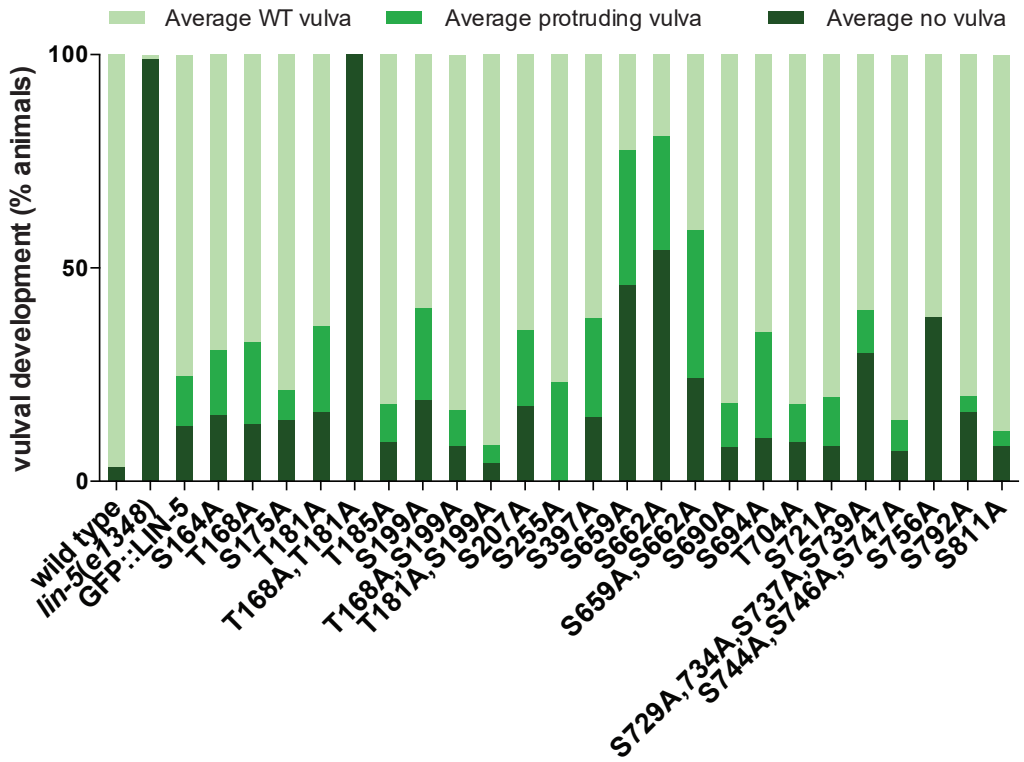

Supplementary figure S1. **Phosphorylation of LIN-5 controls post-embryonic divisions in the vulva.** Quantification of vulval development in heterozygous *lin-5*(*e1348*) / *mIn1* (Wild type), homozygous *lin-5*(*e1348*) animals, and homozygous *lin-5*(*e1348*) animals expressing *gfp::lin-5* transgenes.

a

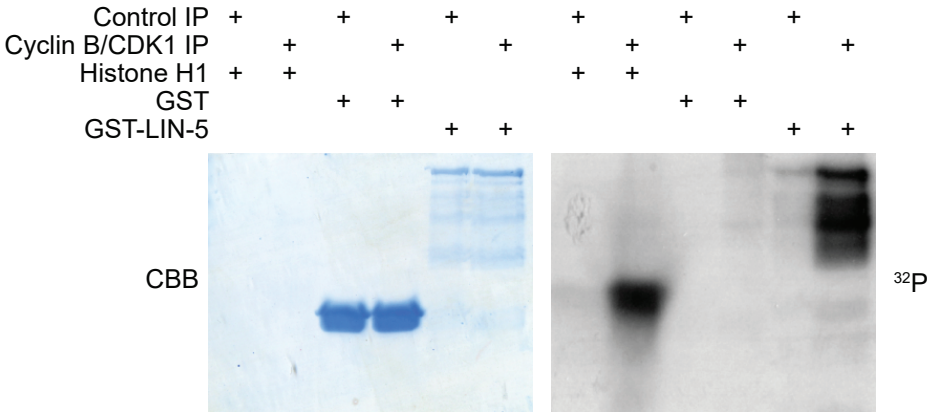

b

		peptide mascot scores						
residue	peptide sequence	CDK1 kinase assay						
T168	RDDEDQEASSGFRTPK	47.4	47.2	32.6	41.8	27.2		
	DDEDQEASSGFRTPK	24.8						
T181	RNNYSLTSLQTPTATAR	42.4						
	NNYSLTSLQTPTATAR	82.0	81.9	26.0	40.3			
T704	KSIAPSVDDNEFDKGTPIGFK	46.6	32.4					
S744	SESIQLASPSSAGEFK	53.3	40.3	84.3	32.4	95.0	26.5	37.3
S756	QPFTPSGVTK	21.0						

Supplementary figure S2. **CDK1 phosphorylates LIN-5 in vitro.** (**a**) In vitro CDK1 kinase assay with recombinant GST-LIN-5, GST alone, or Histone H1. Left; coomassie brilliant blue (CBB)-stained gel. Right; autoradiogram. (**b**) List of LIN-5 phosphopeptides identified by mass spectrometry analysis of CDK1 in vitro kinase assay with GST-LIN-5. Phosphopeptides are shown with individual Mascot Scores. Only Mascot Scores above 20 were accepted as reliable peptide identifications.

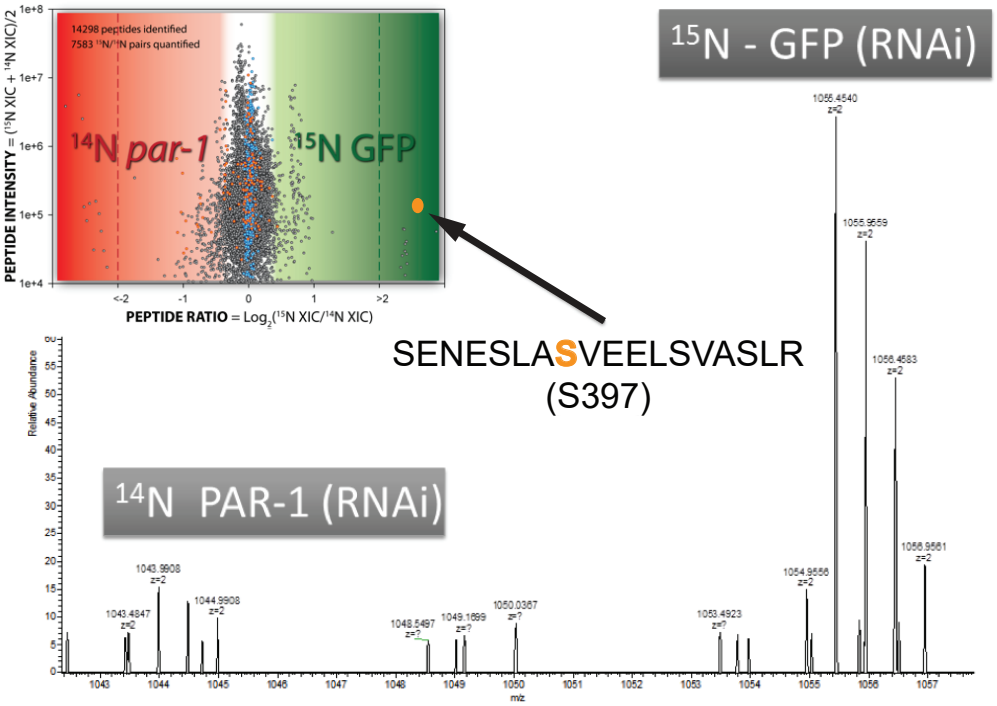

Supplementary figure S3. **PAR-1 phosphorylates LIN-5 in vivo.** Log_2 ratios for all of the quantified $^{15}N/^{14}N$ peptide pairs as a function of their mass-spectrometry intensities in the three LIN-5 immunoprecipitates. LIN-5 phosphopeptides are represented in red, and LIN-5 regular peptides are represented in blue. Peptides belonging to other proteins are shown in grey. Peptide intensities were calculated using the average of the ^{14}N and ^{15}N extracted ion chromatograms.

a

summary	mutations identified	possible total
unique nucleotides mutated	184	642 nucleotides
unique amino acids changed	111	213 amino acids
single amino acid changes (not stop)	15	213 amino acids
amino acids changed to early stops	31	213 amino acids
DNA changes	clones identified	possible total
clones without nucleotide changes	2	163 clones
clones with 1 nucleotide changed	89	163 clones
clones with 2 nucleotides changed	31	163 clones
clones with 3 nucleotides changed	25	163 clones
clones with >3 nucleotides changed	16	163 clones
clones with nucleotide deletion	38	163 clones
clones with nucleotide insertion	1	163 clones
amino acid changes	clones identified	possible total
clones without amino acid changes	4	163 clones
clones with 1 amino acid change (excluding frame shift)	77	163 clones
clones with 1 amino change leading to an early stop	49	163 clones
clones with 2 amino acid changes (excluding frame shift)	31	163 clones
clones with 2 amino changes leading to an early stop	7	163 clones
clones with 3 amino acid changes (excluding frame shift)	12	163 clones
clones with 3 amino changes leading to an early stop	4	163 clones
clones with >3 amino acid changes	3	163 clones
clones containing frame shifts	36	163 clones

b

residue	changed to	times found	validated mutation	interaction deficient
M638	K	2	YES	YES
	T	1	NO	n/a
E640	K	1	NO	n/a
	V	8	YES	YES
I644	N	1	YES	YES
F645	I	1	YES	YES
R654	G	2	YES	NO
I655	N	1	YES	YES
S659	T	1	YES	YES
P660	L	1	YES	YES
D661	G	1	YES	YES
S662	C	3	NO	n/a
	G	4	YES	YES
	N	1	NO	n/a
L663	S	3	YES	YES
D665	V	3	YES	YES
F666	L	2	YES	NO
L667	P	2	YES	YES
S816	L	1	YES	NO

Supplementary figure S4. **Summary of GPR-1 interaction-deficient LIN-5 alleles.** (**a**) Summary of sequencing results of all interaction-deficient alleles of LIN-5 identified in the reverse yeast two-hybrid assay before further validation. (**b**) Overview of all interaction deficient alleles of LIN-5 containing a single amino acid change identified in the reverse yeast two-hybrid assay before further validation. Validation is shown in **figure 3b**.

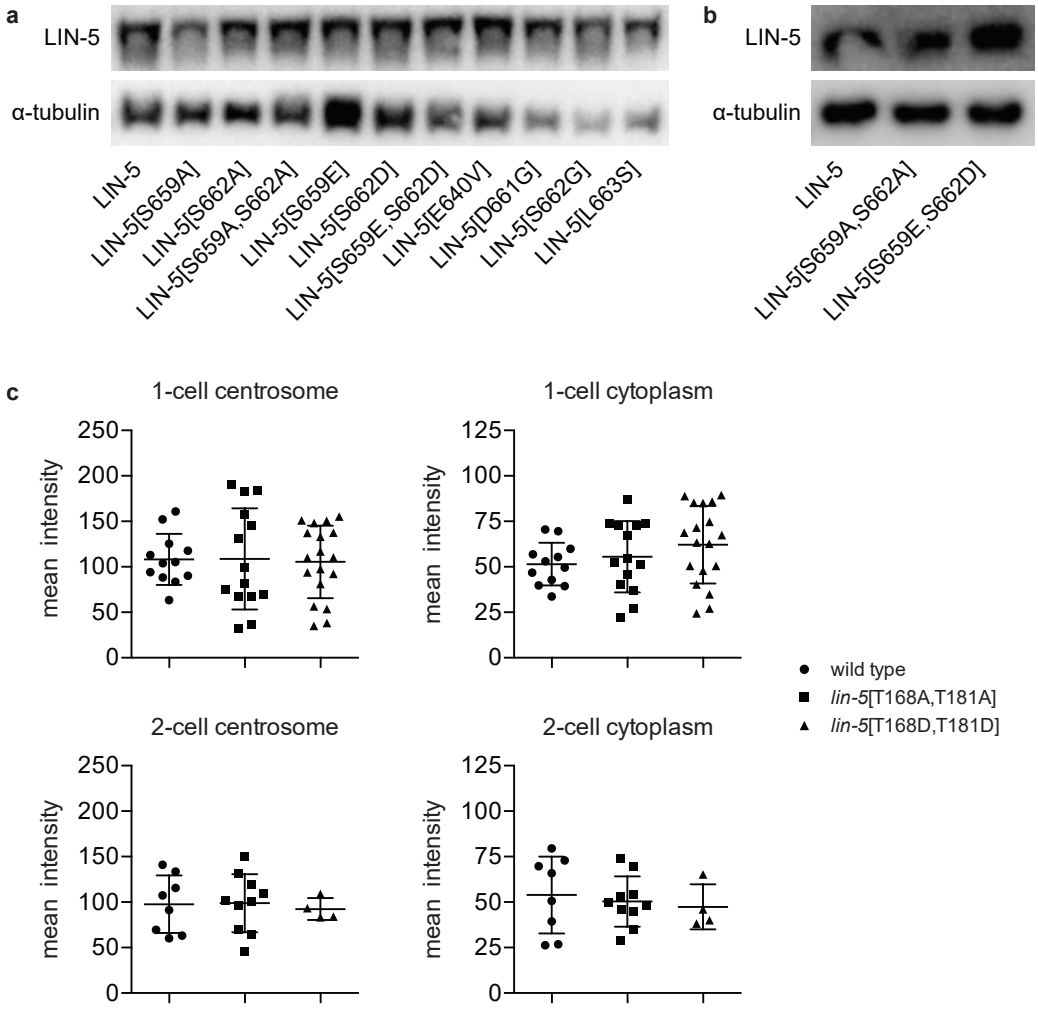

Supplementary figure S5. **Detection of protein levels in LIN-5 mutants.** (**a**) Western blots of lysates of yeast clones containing the indicated LIN-5 expression constructs, probed for LIN-5 and tubulin (loading control) levels. (**b**) Western blots of *C. elegans* lysates with detection of LIN-5 and tubulin (loading control). (**c**) Quantification of mean intensity of immunostainings of *lin-5*[mutant T168,T181] / *egfp*::*lin-5* embryos treated with *egfp* RNAi and stained with LIN-5 antibodies. Graphs indicate single values for centrosomes and cytoplasm in one- and two-cell embryos.

a

mutation	intestinal nuclei	ventral cord nuclei	n
wild type	32.8±0.2	64.4±0.4	18
lin-5(*e1348*)	20.0±0.0	23.9±0.1	20
lin-5[L663S]	20.6±0.2	33.4±1.2	11
lin-5[T168A,T181A]	22.5±0.4	37.6±0.8	19
lin-5[T168D,T181D]	22.4±0.3	33.9±0.7	17
lin-5[T168E,T181E]	21.9±0.3	33.1±0.4	24
lin-5[T168S,T181S]	33.1±0.2	64.3±0.2	13
lin-5[S397A]	32.5±0.3	64.0±0.3	13
lin-5[S397E]	32.3±0.3	63.4±0.4	13
lin-5[S659A,S662A]	32.0±0.3	64.0±0.3	10
lin-5[S659E,S662D]	32.9±0.3	63.9±0.5	11

b

	anterior oscillations	posterior oscillations	spindle elongation	posterior flattening	AB size	P1 rotation
wild type	6.2±1.0% (n=10)	14.7±4.1% (n=10)	15.2±1.8% (n=9)	100.0% (n=13)	58.7±1.7% (n=24)	93.7% (n=16)
lin-5[S397A]	7.6±1.8% (n=10)	14.8±2.7% (n=10)	15.3±2.1% (n=10)	100.0% (n=12)	59.0±1.1% (n=17)	100.0% (n=12)
lin-5[S397E]	6.4±1.9% (n=9)	15.2±4.6% (n=9)	13.9±2.4% (n=9)	100.0% (n=13)	58.9±1.3% (n=17)	85.7% (n=14)
gsk-3 RNAi	7.8±2.4% (n=10)	15.8±2.2% (n=10)	17.0±2.4% (n=9)	81.8% (n=11)	60.1±0.9% (n=12)	100.0% (n=10)
lin-5 [S659A,S662A]	3.2±1.1% (n=13)	9.2±3.2% (n=13)	10.0±2.3% (n=15)	12.5% (n=8)	60.0±1.4% (n=27)	52.9% (n=17)
lin-5 [S659E,S662D]	6.4±1.8% (n=12)	13.8±2.0% (n=12)	13.1±2.0% (n=11)	92.9% (n=14)	59.1±1.2% (n=20)	92.9% (n=14)
lin-5 [T168S,T181S]	4.9±1.5% (n=12)	7.5±2.2% (n=12)	14.2±1.9% (n=12)	100.0% (n=12)	58.8±1.1% (n=13)	66.7% (n=12)

c

	wt	A-P	L-R	n	defective A-P	defective L-R
mes-1(*bn74 ts*) ; *lin-5*[S659A,S662A]	12	1	0	13	7,7%	0%
mes-1(*bn74 ts*) ; *lin-5*[S659E,S662D]	14	3	1	18	16,7%	5,6%
mes-1(*bn74 ts*) ; *gsk-3 (RNAi)*	1	1	9	11	9,1%	81,8%

Supplementary figure S6. **Phenotypical analysis shows developmental defects in LIN-5 phosphomutants.** (**a**) Averages of quantification of intestinal nuclei and P-cells plus juvenile motor neurons (P2-P10 region) by propidium iodide staining in wild type, homozygous LIN-5 phosphorylation mutants, and homozygous *lin-5*(*e1348*) null animals. Statistical analysis in s.e.m., analyzed by Graphpad PRISM. (**b**) Statistical averages of DIC microscopy imaging of hallmarks of the first 2 embryonic divisions in LIN-5 phosphorylation mutants. Oscillations are plotted in percentage of embryo height, elongation and AB size as a percentage of embryo width, flattening and rotation as a total fraction of analyzed embryos. Statistical analysis in s.e.m., analyzed by Graphpad PRISM. (**c**) Quantification of EMS spindle rotation in *mes-1*(*bn74ts*); *lin-5[S659,S662]* phosphorylation mutant and *mes-1*(*bn74ts*); *gsk-3(RNAi)* embryos. Spindle rotation was quantified by live-imaging of the *gfp*::*tubulin* marker. Wt indicates number of embryos with wild type rotation, defective A-P indicates number of embryos with a failure to fully align in the anterior-posterior direction, defective L-R indicates number of embryos with a failure to rotate in the left-right direction.

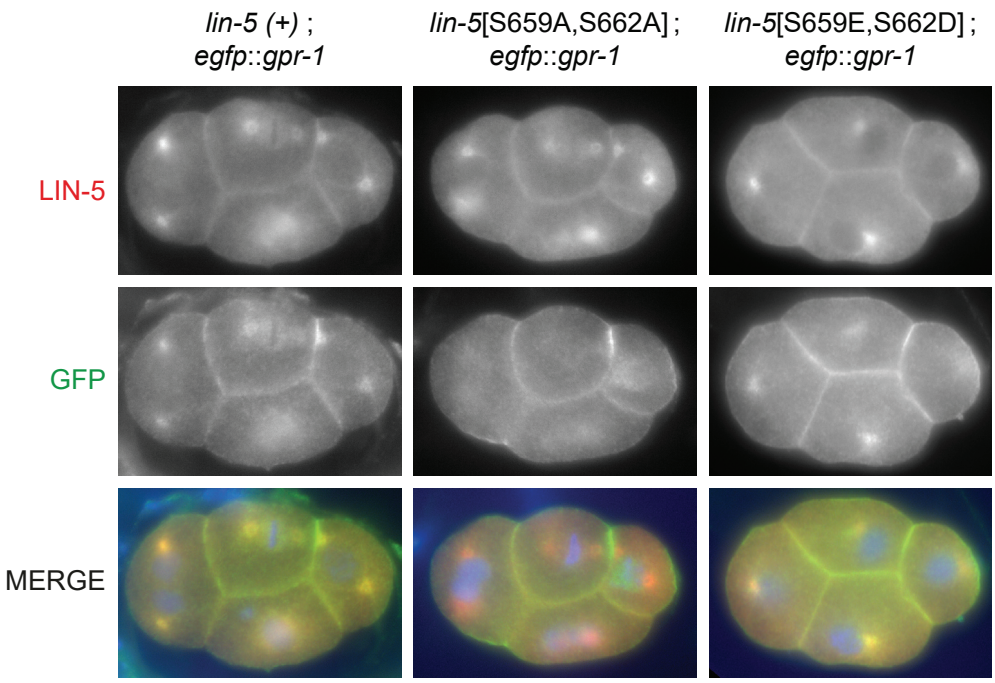

Supplementary figure S7. **Localization of LIN-5 and GPR-1 in phosphorylation mutants.** Immunohistochemical staining of embryos expressing wild type or phosphomutant *lin-5* and endogenously tagged *egfp*::*gpr-1*. Representative images of four-cell embryos, stained with anti-LIN-5 (red) and anti-eGFP (green) antibodies, and DAPI to visualize DNA. All images taken with same exposure time, objective and magnification. Anterior to the left, ventral up.

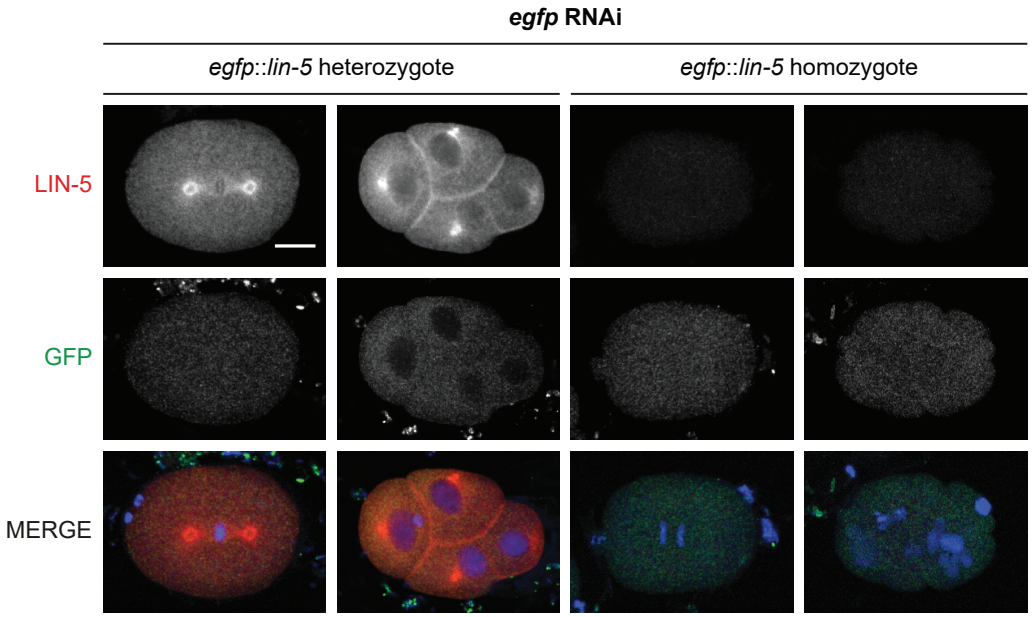

Supplementary figure S8. **Specific knockdown of eGFP::LIN-5 upon *egfp* RNAi.** Immunohistochemical staining of heterozygous and homozygous *egfp*::*lin-5 C. elegans* embryos with anti-LIN-5 (red) and anti-GFP (green) antibodies, DNA stained with DAPI. Two representative embryos are shown for every condition. All images same objective and magnification, anterior to the left, scale bars 10 µm.

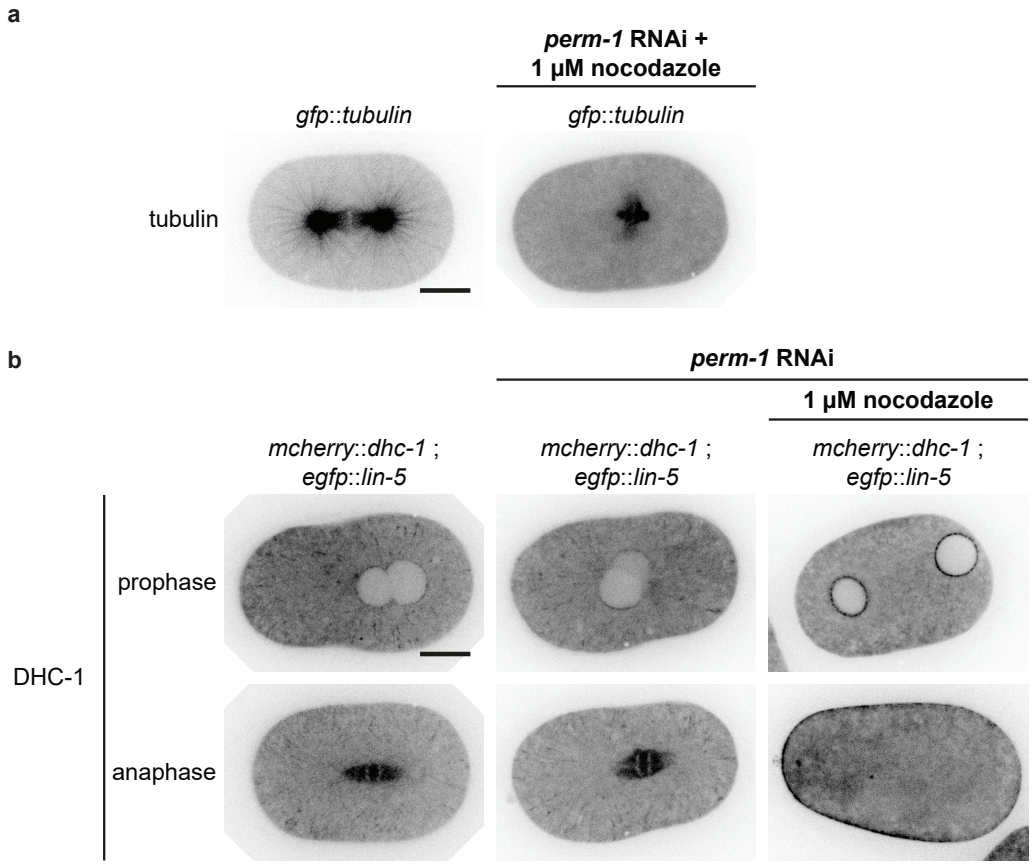

Supplementary figure S9. **Cortical localization of mCherry::DHC-1 after nocodazole treatment.** (**a**) Representative snapshots of live imaging of GFP::tubulin in *gfp::tubulin* one-cell embryos treated with or without *perm-1* RNAi + 1 µM nocodazole, and imaged by spinning disk confocal microscopy. Scale bars, 10 µm, all images with same objective and magnification. (**b**) Representative snapshots of live imaging of mCherry::DHC-1 in *mcherry::dhc-1; egfp::lin-5* one-cell embryos in prophase and anaphase treated with or without *perm-1* RNAi in the presence or absence of 1 µM nocodazole, and imaged by spinning disk confocal microscopy. All images taken with same objective and magnification, anterior to the left, scale bars 10 µm.

Strain	Genotype	Comment
N2	wild type	Fig. 4a-c, S6a-b
SV13	*lin-5*(*e1348*) / *mnC1 dpy-10*(*e128*) *unc-52*(*e444*)	Fig. 4a-b, S6a
SV918	*lin-5*(*e1348*) / *mln1*	Fig. 1, S1
SV1568	*lin-5(he237*[S659A,S662A])	Fig. 4a, S6a-b, CRISPR allele
SV1569	*gpr-1(he238[fkbp:: egfp::gpr-1]*)	Fig. 5, CRISPR allele
SV1585	*lin-5(he237*[S659A,S662A]); *ruIs57* [*unc-119(+*); *Ppie-1*::*gfp*::β-*tubulin*]	Fig. 4d
SV1586	*lin-5(he240*[L663S])	Fig. 4a, S6a, CRISPR allele
SV1587	*lin-5(he241*[T168A,T181A]) / +	CRISPR allele
SV1588	*lin-5(he242*[S397E])	Fig. 4a, S6a-b, CRISPR allele
SV1589	*lin-5(he244[egfp::lin-5])*	Fig. S7, CRISPR allele
SV1590	*lin-5(he243*[S397A])	Fig. 4a, S6a-b, CRISPR allele
SV1594	*lin-5(he242*[S397E]); *ruIs57[unc-119(+); Ppie-1*::*gfp*::β-*tubulin]*	Fig. 4d
SV1596	*lin-5(he243*[S397A]); *ruIs57[unc-119(+); Ppie-1*::*gfp*::β-*tubulin]*	Fig. 4d
SV1600	*lin-5(he249*[S659E,S662D])	Fig. 4a, S6a-b, CRISPR allele
SV1618	*lin-5(he249*[S659E,S662D]); *ruIs57[unc-119(+); Ppie-1*::*gfp*::β-*tubulin]*	Fig. 4d
SV1619	*dhc-1(he250[mcherry::dhc-1])*	Fig. 7a, S8b, CRISPR allele
SV1620	*lin-5(he251*[T168D,T181D]) / +	CRISPR allele
SV1621	*lin-5(he251*[T168D,T181D]) / *lin-5(he244[egfp::lin-5])*	Fig. 4a, 6, S6a
SV1622	*lin-5(he241*[T168A,T181A]) / *lin-5(he244[egfp::lin-5])*	Fig. 4a, 6,S6a
SV1635	*dhc-1(he250[mcherry::dhc-1])*; *lin-5(he244[egfp::lin-5])*	Fig. 7a
SV1638	*dhc-1(he250[mcherry::dhc-1])*; *lin-5(he251*[T168D,T181D]) / *lin-5(he244[egfp::lin-5])*	Fig. 7a
SV1639	*dhc-1(he250[mcherry::dhc-1])*; *lin-5(he241*[T168A,T181A]) / *lin-5(he244[egfp::lin-5])*	Fig. 7a
SV1663	*lin-5(he237*[S659A,S662A]); *gpr-1(he238[fkbp::egfp::gpr-1])*	Fig. 5
SV1664	*lin-5(he249*[S659E,S662D]); *gpr-1(he238[fkbp:: egfp::gpr-1])*	Fig. 5

Strain	Genotype	Comment
SV1695	*lin-5(he261*[T168E,T181E]) / +	Fig. 4a, S6a, CRISPR allele
SV1700	*lin-5(he241*[T168A,T181A]) / *lin-5(he244[egfp::lin-5]); ruIs57[unc-119(+); Ppie-1*::*gfp*::β-*tubulin]*	Fig. 4e
SV1701	*lin-5(he251*[T168D,T181D]) / *lin-5(he244[egfp::lin-5]); ruIs57[unc-119(+); Ppie-1*::*gfp*::β-*tubulin]*	Fig. 4e
SV1702	*dhc-1(he250[mcherry::dhc-1])*; *ruIs57[unc-119(+)Ppie-1*::*gfp*::β-*tubulin]*	Fig. 7b
SV1783	*lin-5(he237*[S659A,S662A]); *ruIs57[unc-119(+); Ppie-1*::*gfp*::β-*tubulin]*; *mes-1(bn74*)	Fig. S6c, grown at 15°C
SV1784	*lin-5(he249*[S659E,S662D]); *ruIs57[unc-119(+); Ppie-1*::*gfp*::β-*tubulin]; mes*-1(*bn74*)	Fig. S6c, grown at 15°C
SV1785	*ruIs57[unc-119(+); Ppie-1*::β-*tubulin::GFP]; mes-1(bn74*)	Fig. S6c, grown at 15°C
SV1898	*dhc-1(he250[mcherry::dhc-1])*; *lin-5(he241*[T168A,T181A]) / *lin-5(he244[egfp::lin-5])*; *ruIs57[unc-119(+); Ppie-1*::*gfp*::β-*tubulin]*	Fig. 7b
SV1899	*dhc-1(he250[mcherry::dhc-1])*; *lin-5(he251*[T168D,T181D]) / *lin-5(he244[egfp::lin-5]); ruIs57[unc-119(+); Ppie-1*::*gfp*::β-*tubulin]*	Fig. 7b
SV1901	*lin-5* (*he281*[T168S,T18S])	Fig. 4a, S6a
SV1902	*dhc-1(he250[mcherry::dhc-1])*; *lin-5(he244[egfp::lin-5]); ruIs57[unc-119(+); Ppie-1*::*gfp*::β-*tubulin]*	Fig. 7b, CRISPR allele
SV1911	*lin-5* (*he281*[T168S,T18S]); *ruIs57[unc-119(+); Ppie-1*::*gfp*::β-*tubulin]*	Fig. 4e
AZ244	*unc-119 (ed3); ruIs57[unc-119(+); Ppie-1*::*gfp*::β-*tubulin]*	Fig. 4d-e, S8a
SS392	*mes-1(bn74*)	grown at 15°C

Table S1. **Overview of *C. elegans* strains used in this study.** Overview of all strains used in this study, including the corresponding figure. CRISPR/Cas9 genome engineered strains are indicated in the comment section.

Chapter 3

Two populations of cytoplasmic dynein contribute to spindle positioning in *C. elegans* embryos

Ruben Schmidt[1,2], Lars-Eric Fielmich[1], Ilya Grigoriev[2], Eugene A. Katrukha[2], Anna Akhmanova[2] and Sander van den Heuvel[1]

[1] Developmental Biology, Department of Biology, Faculty of Sciences, Utrecht University, Utrecht, Netherlands

[2] Cell Biology, Department of Biology, Faculty of Sciences, Utrecht University, Utrecht, Netherlands
Correspondence to Sander van den Heuvel: s.j.l.vandenHeuvel@uu.nl;
Anna Akhmanova: a.akhmanova@uu.nl

The manuscript in this chapter was adapted from:
Schmidt, R., Fielmich, L-E., Grigoriev, I., Katrukha, E.A., Akhmanova, A. and van den Heuvel, S. (2017). Two populations of cytoplasmic dynein contribute to spindle positioning in *C. elegans* embryos. J. Cell Biol. 216, 2777-2793.

Abstract

The position of the mitotic spindle is tightly controlled in animal cells as it determines the plane and orientation of cell division. Contacts between cytoplasmic dynein and astral microtubules (MTs) at the cell cortex generate pulling forces that position the spindle. An evolutionarily conserved Gα–GPR-1/2$^{Pins/LGN}$–LIN-5$^{Mud/NuMA}$ cortical complex interacts with dynein and is required for pulling force generation, but the dynamics of this process remain unclear. In this study, by fluorescently labeling endogenous proteins in *Caenorhabditis elegans* embryos, we show that dynein exists in two distinct cortical populations. One population directly depends on LIN-5, whereas the other is concentrated at MT plus ends and depends on end-binding (EB) proteins. Knockout mutants lacking all EBs are viable and fertile and display normal pulling forces and spindle positioning. However, EB protein-dependent dynein plus end tracking was found to contribute to force generation in embryos with a partially perturbed dynein function, indicating the existence of two mechanisms that together create a highly robust force-generating system.

Introduction

The mitotic spindle dictates the plane of cell cleavage through its position and interactions with the cell cortex (Galli and van den Heuvel, 2008; Morin and Bellaïche, 2011). Therefore, the position of the spindle determines the relative size and location of daughter cells and controls whether polarized cells divide symmetrically or asymmetrically. Thus, accurate positioning of the spindle is critical for a wide range of processes that include maintenance of tissue integrity, creation of different cell types, and coordination of stem cell proliferation and differentiation.

The *Caenorhabditis elegans* early embryo provides an important in vivo model for studies of spindle position regulation. The one-cell embryo divides asymmetrically based on an anterior-posterior (A-P) polarity axis established after fertilization (Rose and Gönczy, 2014). Spindle severing experiments revealed that pulling forces acting from the cell cortex on astral microtubules (MTs) position the spindle and are higher in the posterior than in the anterior (Grill et al., 2001). This pulling force asymmetry leads to posterior displacement of the spindle and allows cell cleavage to create two blastomeres of unequal size and developmental fate.

Genetic screens and biochemical experiments have revealed a variety of factors that control cortical pulling forces. Among these are the evolutionarily conserved proteins Gα, GPR-1/2$^{Pins/LGN}$, and LIN-5$^{Mud/NuMA}$ (Lorson et al., 2000; Gotta and Ahringer, 2001; Colombo et al., 2003; Gotta et al., 2003; Srinivasan et al., 2003). These proteins are needed to form the force generator complex (FGC), which also includes cytoplasmic dynein (Nguyen-Ngoc et al., 2007). This large multisubunit protein complex is the major minus end-directed motor in cells and is essential for a large variety of cellular processes

(Kardon and Vale, 2009). In the current model, dynein is recruited to the cell cortex either directly or indirectly via an extended N-terminal region of LIN-5 (Kotak et al., 2012). Dynein then associates with astral MTs in an end-on configuration, inducing pulling forces via both MT depolymerization and minus end-directed movement. Both in vivo and in vitro studies support this model (Nguyen-Ngoc et al., 2007; Gusnowski and Srayko, 2011; Hendricks et al., 2012; Laan et al., 2012).

It remains unclear, however, how dynein is recruited to the cortex and how MT dynamics are coupled to force generation and mitotic spindle positioning. MT growth and shrinkage are spatiotemporally modulated by a large variety of MT-associated proteins, a subset of which concentrates at the growing MT plus end (Akhmanova and Steinmetz, 2015). These MT plus end-tracking proteins (+TIPs) form a highly interconnected and dynamic network, which is regulated in a cell cycle- and position-dependent manner to fine-tune MT dynamics (Honnappa et al., 2006; Zimniak et al., 2009; Ferreira et al., 2013; Tamura et al., 2015). Members of the end-binding (EB) protein family are seen as master regulators of the +TIP network, as they bind autonomously to the growing MT end and recruit multiple other +TIPs (Honnappa et al., 2006; Bieling et al., 2007; Maurer et al., 2012; Akhmanova and Steinmetz, 2015; Zhang et al., 2015b).

Dynein is known to behave as a +TIP in a variety of cellular contexts (Vaughan et al., 1999; Han et al., 2001; Lenz et al., 2006; Kobayashi and Murayama, 2009). In mammals, this is classically regarded as part of a “search and capture” mechanism, by which the complex finds cargo molecules via the MT plus end before initiating transport (Kirschner and Mitchison, 1986; Vaughan et al., 2002). Interactions between EB1, CLIP-170, and the dynactin protein p150Glued recruit the human dynein complex to the MT plus end (Berrueta et al., 1999; Lansbergen et al., 2004; Duellberg et al., 2014). In the budding yeast *Saccharomyces cerevisiae*, dynein plus end tracking is coupled to offloading at the cortex and association of dynein with its cortical anchor Num1 (Lee et al., 2003; Sheeman et al., 2003; Markus and Lee, 2011). Disruption of dynein plus end recruitment is thus associated with spindle positioning defects in yeast, but whether this applies to animals remains to be determined.

In this study, we explore the localization of dynein during mitotic pulling force generation in the one-cell *C. elegans* embryo. Fluorescent protein (FP) tagging of endogenous dynein helped reveal two cortical populations, one enriched at MT plus ends depending on EB protein 2 (EBP-2) along with an MT-independent population recruited by LIN-5. The LIN-5-dependent dynein population exhibited significant asymmetry in cortical retention, governed by PAR polarity. This indicates that a subpopulation of LIN-5 is dynein associated and differentially regulated. We created single-, double-, and triple-deletion mutants of EB family genes and found that spindle positioning and embryonic development can proceed as normal in the absence of dynein plus end tracking. However, plus end tracking appeared to provide a backup mechanism to ensure robust force generation when dynein function was partially perturbed.

Results

Visualization of the endogenous dynein complex

We applied a CRISPR/Cas9-assisted knock-in strategy to visualize the dynamics of cytoplasmic dynein in the early *C. elegans* embryo. To label all possible compositions of the dynein complex, we added an FP to the dynein heavy chain, encoded by *dhc-1* in *C. elegans* (**Figure 1a**). To allow for functional comparison, we inserted *mcherry* directly upstream of the *dhc-1* stop codon, and we also inserted *mcherry* or *egfp* directly upstream of the *dhc-1* start codon. A glycine linker was inserted between FPs and *dhc-1* to preserve independent protein folding (**Figure 1a**).

Multiple homozygous viable knock-in strains were obtained with N- or C-terminal DHC-1 protein fusions. However, C-terminal tagging of *dhc-1* caused severe embryonic lethality and a reduced brood size (**Figure 1b**). Differential interference contrast (DIC) microscopy revealed spindle positioning and cell division defects from the one-cell stage onward in two independent strains. These defects are in accordance with perturbed dynein function (Schmidt et al., 2005). We concluded that C-terminal tagging of endogenous DHC-1 causes partial loss of function and did not further study dynein in these strains. Homozygous larvae with N-terminally tagged DHC-1 were fully viable, produced a normal brood size (**Figure 1b**), and appeared healthy during all stages of development. Thus, N-terminal tagging of DHC-1 with mCherry or eGFP does not perturb dynein function.

Epifluorescence microscopy revealed that mCherry::DHC-1 and eGFP::DHC-1 are expressed in all somatic tissues and in the germline (**Figure 1c**, zoomed image). After imaging early embryos by spinning-disk confocal fluorescence microscopy (SDCM), DHC-1 was detected in the cytoplasm during all stages of the cell cycle and localized specifically to the nuclear envelope, centrosomes, kinetochores, kinetochore MTs, central spindle, astral MTs, and the cell cortex during mitosis (**Figure 1d**). This localization pattern is in accordance with previous immunohistochemistry and overexpression studies (Schmidt et al., 2005; Nguyen-Ngoc et al., 2007; Gassmann et al., 2008; Kimura and Kimura, 2011). In addition, we noticed cometlike accumulations of dynein radiating from the centrosomes to the cell periphery in a pattern that appeared to follow the mitotic astral MT network.

Dynein tracks MT plus ends during mitosis

To further explore the dynein localization pattern, *Ppie-1*::*gfp::tbb-2*$^{\beta\text{-tubulin}}$ (Praitis et al., 2001) was coexpressed with *mcherry::dhc-1* and imaged in embryos. Dynein comets were clearly MT associated (**Figure 2a**, arrow, and **video 1**). Because dynein is a minus end-directed motor protein, cortex-directed dynein comets may represent a plus end tracking population. To examine this possibility, we coexpressed *mcherry::dhc-1* with *Ppie-1::ebp-2::gfp* (Srayko et al., 2005; Kozlowski et al., 2007). This revealed a strong overlap between dynein and EBP-2::GFP comets (**Figure 2b**, **c**, and **video 2**). Moreover,

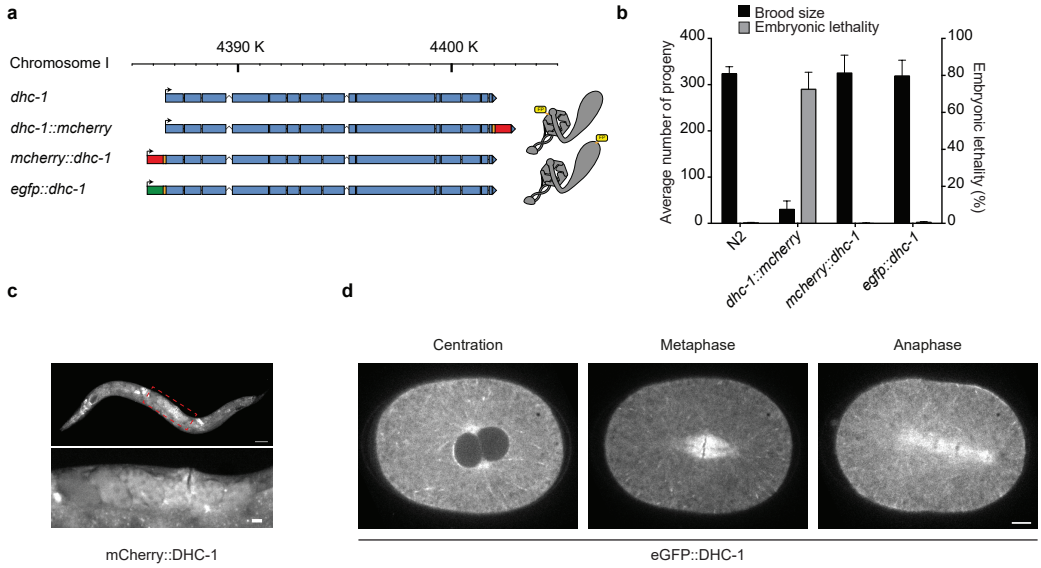

Figure 1. **Endogenous tagging of *dhc-1*.** (**a**) Dynein tagging strategies. Colors indicate *dhc-1* exons (blue), *mcherry* (red), *egfp* (green), and linkers (orange). Cartoons illustrate dynein heavy chain with FP fused to the C (top) or N terminus (bottom). (**b**) Brood size and embryonic lethality of *dhc-1* knock-in strains shown as means ± SD. *n*=4 animals each. (**c**) Widefield image showing mCherry::DHC-1 expression in an adult with a zoom of the germline (red dashed box) below. Bars: (top) 50 µm; (bottom) 10 µm. (**d**) SDCM images of eGFP::DHC-1 localization in the one-cell embryo. Bar, 5 µm.

the velocities of mCherry::DHC-1 and EBP-2::GFP comets were almost identical (**Figure 2d**) and agree with previous measurements of MT growth speeds during metaphase (0.72 ± 0.02 µm/s; Srayko et al., 2005). Dynein accumulation at MT plus ends appears to be a general feature of mitotic animal cells, as we also observed this in HeLa cells stably expressing labeled dynein intermediate chain 2 (DIC2-GFP; Poser et al., 2008; Splinter et al., 2012). Moreover, we observed MT plus end tracking of dynein in later stages of *C. elegans* embryos (**Figure S1a**, **b**) as well as overlap between dynactin components GFP::DNC-1^{p150Glued} and GFP::DNC-2$^{p50/dynamitin}$ and mCherry::DHC-1 comets (**Figure S2a**). Collectively, our data show that the endogenous dynein complex tracks MT plus ends.

Next, we addressed whether MT plus end tracking of the dynein complex relates to pulling force generation. Using dual-color total internal reflection fluorescence (TIRF) microscopy, we observed simultaneous appearance and strong colocalization of dynein comets with end-on MT plus end-cortex contacts in mitosis (**Figure 2e-g**, and **videos 3**, **4**). Interestingly, the concentrated mCherry::DHC-1 signal dissipated when MTs stopped growing, as judged by the loss of EBP-2::GFP signal, suggesting that the majority of dynein molecules are released.

To image dynein comets during cortical force generation, we focused on invaginations of the plasma membrane, which appear to visualize individual force generation events

(Redemann et al., 2010). To readily detect such invaginations, we created a reporter strain with single copy-integrated PH::eGFP expressed from the general *eft-3* promoter. Dual-color imaging of PH::eGFP and mCherry::DHC-1 revealed frequent co-occurrence of dynein comets reaching the cortex and emergence of membrane invaginations (13/25 events; **Figure 2h** and **video 5**). However, there was no enrichment of dynein after the initiation of invaginations. This confirms that a significant part of the dynein population present at the MT plus end dissipates upon membrane contact and likely does not contribute to pulling forces.

EBs and dynein plus end tracking are not required for development and spindle positioning

To examine its contribution in cortical pulling forces, we decided to disrupt dynein plus end accumulation by removing EBs. Two homologues of mammalian EBs, EBP-1 and EBP-2, exhibit plus end tracking activity when overexpressed in the *C. elegans* embryo (Srayko et al., 2005). An annotated third homologue, *ebp-3*, has likely arisen by duplication of the genomic region containing the *ebp-1* gene, and their nearly identical DNA sequences suggest that this was a recent event. However, the predicted EBP-3 protein lacks the calponin homology domain, which is required for recognition of the MT plus end (Slep and Vale, 2007; Maurer et al., 2012). Although we suspect that *ebp-3* is a pseudogene, we will refer to the *ebp-1* and *ebp-3* genes collectively as *ebp-1/3*.

Knockdown of *ebp-1/3* by RNAi did not appear to affect eGFP::DHC-1 plus end tracking. In contrast, loss of *ebp-2* expression abolished the appearance of dynein comets (**Figure 3a**). Interestingly, this did not result in obvious spindle positioning or cell division defects. As RNAi knockdown probably is incomplete, we used CRISPR/Cas9 to create knockout alleles for both *ebp-2* and *ebp-1/3* (**Figure 3b**). The *ebp-1* and *ebp-3* genes were removed together by excision of a ~17-kb region. For *ebp-2,* the coding region and ~1 kb upstream of the start codon was deleted. Both the *Δebp-1/3* and *Δebp-2* strains could be stably maintained as homozygotes, indicating that neither *ebp-1/3* nor *ebp-2* is required for normal development and reproduction.

The *ebp* deletion mutants closely resembled the RNAi embryos in dynein localization. In Δ*ebp-1/3* embryos, dynein still localized to the MT plus ends, whereas this localization was completely absent in *Δebp-2* embryos (**Figure 3c** and **video 6**). In contrast, dynein localization to the nuclear envelope, spindle midzone, and poles did not appear to be affected in either case, which indicates that dynein depends on EBP-2 specifically for recruitment to MT plus ends (**Figure S2c-e**).

Although general development was normal, *Δebp-1/3* caused a slight reduction in brood size and a slight increase in embryonic lethality (**Figure 3d**). Surprisingly, *Δebp-1/2/3* animals were viable and could be maintained as triple-homozygous mutants, showing that development and reproduction can proceed in the absence of EBs. Triple mutants showed a stronger reduction in brood size than *Δebp-1/3* animals, which indicated

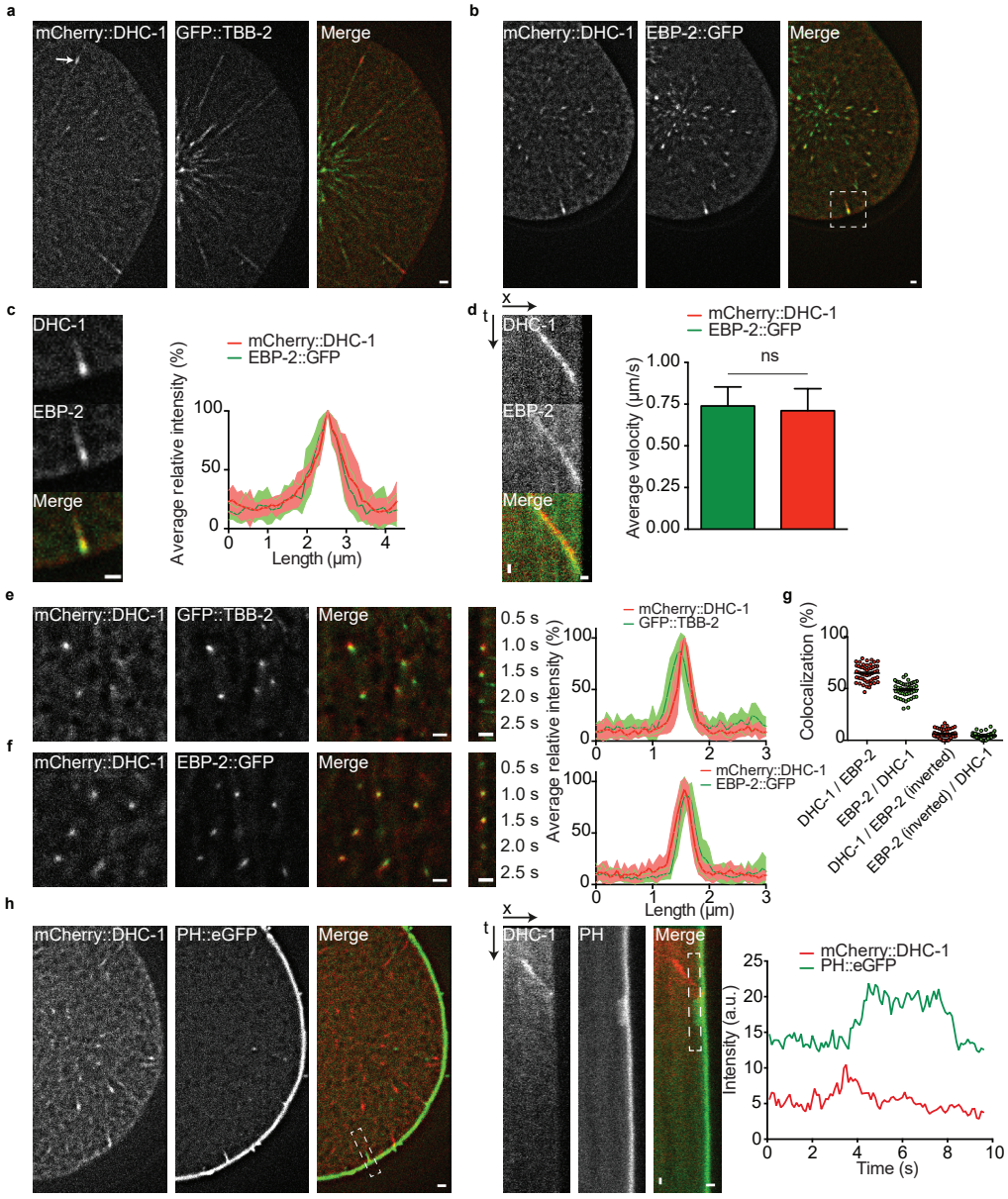

Figure 2. **Dynein tracks MT plus ends during mitosis.** (**a** and **b**) SDCM images of embryos expressing mCherry::DHC-1 and GFP::TBB-2 (**a**) or EBP-2::GFP (**b**). The arrow indicates dynein at the plus end. The white box indicates the zoomed image in c. (**c**) Intensity profiles of mCherry::DHC-1 and EBP-2::GFP comets shown as percentages of maximum. Means ± SD are shown. *n*=10. (**d**) Kymographs (left) and mean velocities (right) of metaphase comets; mCherry::DHC-1 (*n*=57) and EBP-2::GFP (*n*=116) means ± SD. Unpaired Welch's Student's *t* test; not significant. (**e** and **f**) TIRF images of early anaphase mCherry::DHC-1 and GFP::TBB-2 (**e**) or EBP-2::GFP (**f**) localization. Graphs show intensity profiles as mean (*n*=10) percentage of maximum ± SD. (**g**) Quantification of EBP-2::GFP and mCherry::DHC-1 colocalization

as in (**f**), shown as means ± SEM of per frame percentage colocalization of 2,351 mCherry::DHC-1 and 3, 178 EBP-2::GFP particles from three embryos. (**h**) SDCM images of anaphase mCherry::DHC-1 and PH::eGFP localization. The leftmost three panels are kymographs of the invagination indicated in the third panel from the right (white dashed box). Graph shows intensity profiles as measured along the box in the rightmost panel, representative of *n*=25 events. Bars: (horizontal) 1 µm; (vertical) 1 s.

some redundancy among the EBs. Embryonic lethality remained low, which is remarkable given the expected profound disruption of the +TIP network. Although *Δebp-1/2/3* larvae generally did not show developmental defects, we observed a low penetrant pleiotropic phenotype among adults. This included a low frequency of dumpy, sterile, and/or uncoordinated animals as well as nonviable larvae that exploded through the vulva. In addition, some triple mutant adults developed irregularities that seemed epidermal bulges. Because of the very low penetrance, we did not further examine these abnormalities.

Next, we assessed whether spindle positioning was affected in *ebp*-deletion mutants. Importantly, asymmetric positioning of the spindle and subsequent asymmetric division of the one-cell embryo was not affected in any of the mutants (**Figure S3a**). *Δebp-1/2/3* embryos exhibited a slightly rounder shape compared with WT embryos (**Figure S3b**). The position of pronuclear meeting did not change significantly (**Figure S3c**), whereas centration of the nucleocentrosomal complex occurred slightly more posterior in each mutant (**Figure S3d**). Spindles formed along the long axis as normal (**Figure S3e**), whereas their elongation during anaphase was slightly increased in *Δebp-1/2/3* embryos (**Figure S3f**). Regardless of these small deviations, the outcome of mitosis was not affected. However, all *Δebp* strains showed accelerated progression through mitosis (**Figure 3e**, **figure S3g**, and **video 7**). This was observed in *Δebp-1/3* and *Δebp-2* embryos but was most dramatic in *Δebp-1/2/3* mutants. Both the progression from pronuclear meeting to nuclear envelope breakdown and the time between the start of chromosome segregation and cytokinesis were significantly faster than normal (**Figure S3g-j**). However, there was no significant reduction in the time between nuclear envelop breakdown and anaphase onset (**Figure S3i**), indicating that the accelerated mitosis does not result from bypassing or premature satisfaction of the spindle assembly checkpoint.

EBs and dynein plus end tracking are not required for cortical pulling forces

We quantified the amplitudes of spindle pole movements during anaphase as a first readout for cortical force generation (Pecreaux et al., 2006). Interestingly, spindle rocking was generally not affected by the removal of EBs. The posterior pole showed a slight but significant increase in maximum amplitude in the *Δebp-1/3* background, but this was not observed in *Δebp-1/2/3* mutants (**Figure 4a**).

To more directly quantify cortical pulling forces during spindle displacement, we performed spindle severing assays with a focused UV laser beam (Grill et al., 2001). Upon severing the spindle during anaphase onset, the centrosomes separated with a velocity

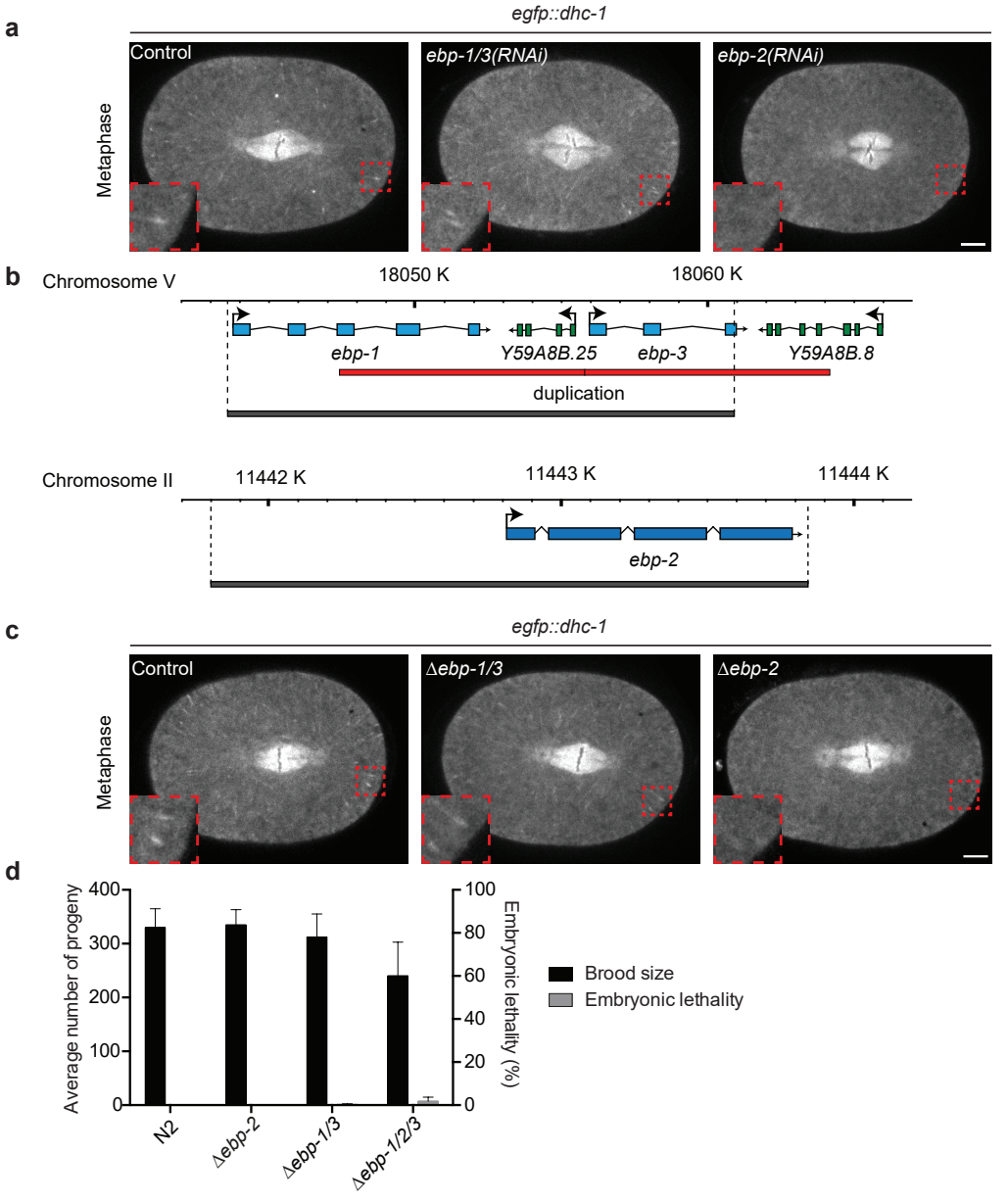

Figure 3. **Analysis of dynein plus end tracking and development of *Δebp* mutants.** (**a**) SDCM images illustrating eGFP::DHC-1 localization in WT, *ebp-1/3(RNAi)*, and *ebp-2(RNAi)* embryos. Insets highlight the presence or absence of dynein comets. (**b**) *ebp-1/3* and *ebp-2* knockout strategies. Relevant genes are shown in blue and green, genetic duplication is in red, and genetic deletions are in gray. (**c**) SDCM images illustrating eGFP::DHC-1 localization in WT, *Δebp-2*, and *Δebp-1/3* embryos. Insets highlight the presence or absence of dynein comets. (**d**) Embryonic lethality and brood size of *Δebp* mutants shown as means ± SD. *n*=4 animals each. (**e**) DIC images of N2, *Δebp-2*, *Δebp-1/3*, and Δ*ebp-1/2/3* one-cell embryos. Time past pronuclear meeting (*t*=0) is indicated in seconds. Bar, 5 µm.

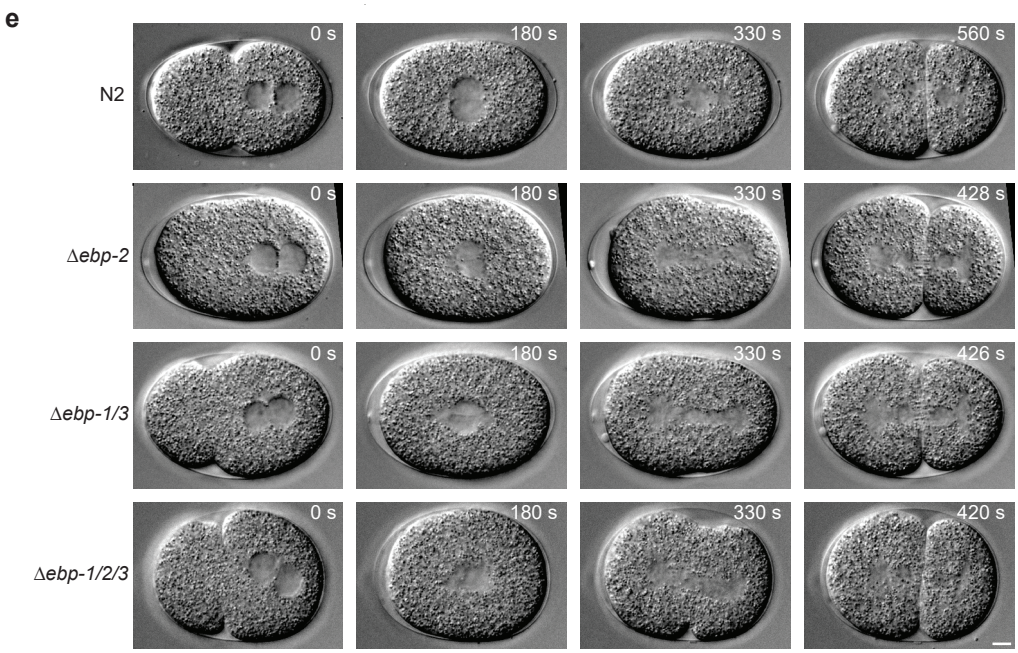

proportional to the net forces acting on their astral MTs (**Figure 4b** and **video 9**; Grill et al., 2001). Remarkably, all *Δebp* mutants assembled apparently normal mitotic spindles and showed normal spindle pole peak velocities (**Figure 4c**). Thus, cortical pulling force generation during spindle positioning is largely unaltered in the absence of EB proteins.

In addition to recruiting proteins to the MT plus end, EB proteins affect MT dynamics (Komarova et al., 2009; Zanic et al., 2013; Maurer et al., 2014; Zhang et al., 2015b). However, the effect of complete loss of EB family members on MT dynamics has not been reported in vivo. A hurdle for studying MT dynamics in the one-cell worm embryo is the extremely dense MT network (Kozlowski et al., 2007). Therefore, we imaged labeled MTs at the cortex by TIRF microscopy and quantified the duration of end-on MT-cortex contacts during spindle displacement (**Figure 4d**). This revealed a slight increase in mean residence time in all *Δebp* mutants, of which only *Δebp-2* was significantly different from WT, whereas the mean density of cortical MT contacts remained constant (**Figure 4e** and **video 10**). This indicates that loss of EBP-2 either reduces MT growth rate, catastrophe frequency, or both, thereby allowing prolonged contact with the cell cortex. Interestingly, *Δebp-2* and *Δebp-1/2/3* embryos also exhibited reduced midzone MT densities (**Figure S4a-c**), which led to full or partial bisection of spindles during anaphase and could be caused by altered MT dynamics. This phenotype is reminiscent of *spd-1*^{PRC1} loss of function, which diminishes the mechanical strength of the midzone by loss of MT bundling (Verbrugghe and White, 2004). In addition, the intensity profile of the metaphase astral MT network was slightly steeper in *Δebp-2* and *Δebp-1/2/3* mutants compared with controls

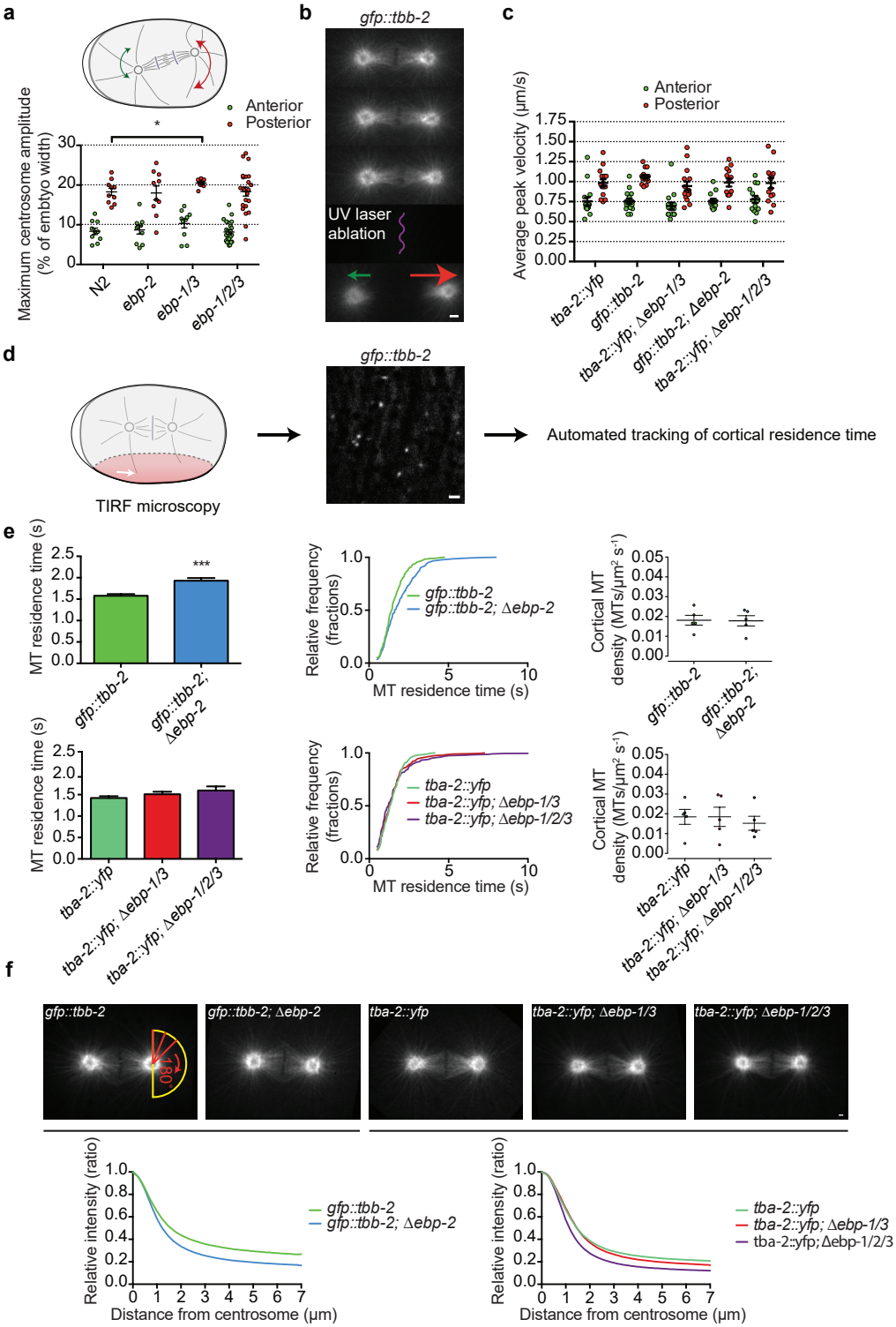
a
Anterior
Posterior
Maximum centrosome amplitude (% of embtyo width)
N2
ebp-2
ebp-1/3
ebp-1/2/3
b
gfp::tbb-2
UV laser ablation
c
Anterior
Posterior
Average peak velocity (µm/s)
tba-2::yfp
gfp::tbb-2
tba-2::yfp; Δebp-1/3
gfp::tbb-2; Δebp-2
tba-2::yfp; Δebp-1/2/3
d
TIRF microscopy
gfp::tbb-2
Automated tracking of cortical residence time
e
MT residence time (s)
gfp::tbb-2
gfp::tbb-2; Δebp-2
Relative frequency (fractions)
MT residence time (s)
Cortical MT density (MTs/µm² s⁻¹)
tba-2::yfp
tba-2::yfp; Δebp-1/3
tba-2::yfp; Δebp-1/2/3
f
gfp::tbb-2
gfp::tbb-2; Δebp-2
tba-2::yfp
tba-2::yfp; Δebp-1/3
tba-2::yfp; Δebp-1/2/3
180
Relative intensity (ratio)
Distance from centrosome (µm)

Figure 4. **Loss of EBP-1/2/3 mildly affects MT dynamics and does not perturb normal mitotic pulling force generation.** (**a**) Quantification of anaphase centrosome rocking in WT and *Δebp* embryos. Maximum amplitudes are shown as means ± SEM. Unpaired Welch's Student's *t* test; *, P < 0.05. *n*=10–23. (**b**) Example of spindle severing with a UV laser (purple) in a GFP::TBB-2 embryo. Arrows indicate the direction and relative speed of centrosome displacement upon bisection. (**c**) Quantification of centrosome velocities upon spindle severing in WT and *Δebp* embryos shown as means ± SEM. Unpaired Welch's Student's *t* test. *n*=13–15. (**d**) Method for quantification of cortical MT residence time by TIRF microscopy of embryos expressing fluorescent tubulin. (**e**) Quantifications as illustrated in D for control and *Δebp* embryos. Bars represent means ± SEM. Mann–Whitney *U* test; ***, P < 0.001. 233 ≤ *n* ≤ 343 events from five embryos for each condition. Graphs show cumulative relative fractions of residence time distributions. Right graphs show density of cortical MT contacts as mean MTs/μm^2 s^{-1} per embryo, and bars are means ± SEM. (**f**) Example images and quantifications of astral MT densities in control and *Δebp* mutant embryos, illustrated as radial intensity plots of fluorescent tubulin in metaphase (indicated in leftmost image). Plots were aligned and normalized to maximum values at the centrosome. *n*=20 asters from 10 embryos per condition. Bars, 1 µm.

(**Figure 4f**), indicating that the distribution of MT length was mildly altered. Collectively, these results indicate that complete loss of EBs has a mild effect on MT organization and dynamics in vivo, but does not significantly change spindle assembly and positioning.

LIN-5 recruits dynein to the cell cortex independent of MT plus end tracking

If dynein plus end tracking is not required for spindle positioning, then how does dynein reach the cortex? Previous studies have visualized cortical dynein localization by immunohistochemistry (Nguyen-Ngoc et al., 2007; Kotak et al., 2012). Although cortical dynein could be observed in two-cell embryos, staining of one-cell embryos did not show clear cortical localization. Time-lapse SDCM of eGFP::DHC-1 zygotes revealed no measurable enrichment of dynein at the cortex over cytoplasmic values during metaphase spindle displacement, similar to *lin-5(RNAi)* embryos (**Figure 5a**). However, we observed transient regions of DHC-1 enrichment in cortical patches during late anaphase (**Figure 5b**). These patches were most pronounced at the posterior cortex during spindle rocking and often followed the oscillatory behavior of the spindle poles (**Figure S4d**, **e**). This indicates that spindle pole proximity and cortical dynein recruitment could be coupled like they are in mammalian cells (Kiyomitsu and Cheeseman, 2012). The cortical enrichment of dynein was not perturbed in *Δebp-1/3* or *Δebp-2* mutant embryos. In contrast, *lin-5(RNAi)* abolished cortical dynein localization but did not affect its plus end tracking (**Figure 5b**). Thus, EBP-2 and EBP-1/3 are not required for the cortical localization of dynein during anaphase, which fully depends on LIN-5.

To explore the relative cortical localization patterns of LIN-5 and dynein, *egfp::lin-5; mcherry::dhc-1* embryos were imaged by SDCM (**Figure 5c**). In late metaphase, eGFP::LIN-5 became modestly enriched at the cortex as compared with the adjacent cytoplasm, both in the anterior and posterior. Although this was not observed for dynein (**Figure 5a**, **c**), both LIN-5 and dynein showed higher cytoplasmic levels in the anterior compared with the posterior during all mitotic stages (**Figure S5a**). This gradient

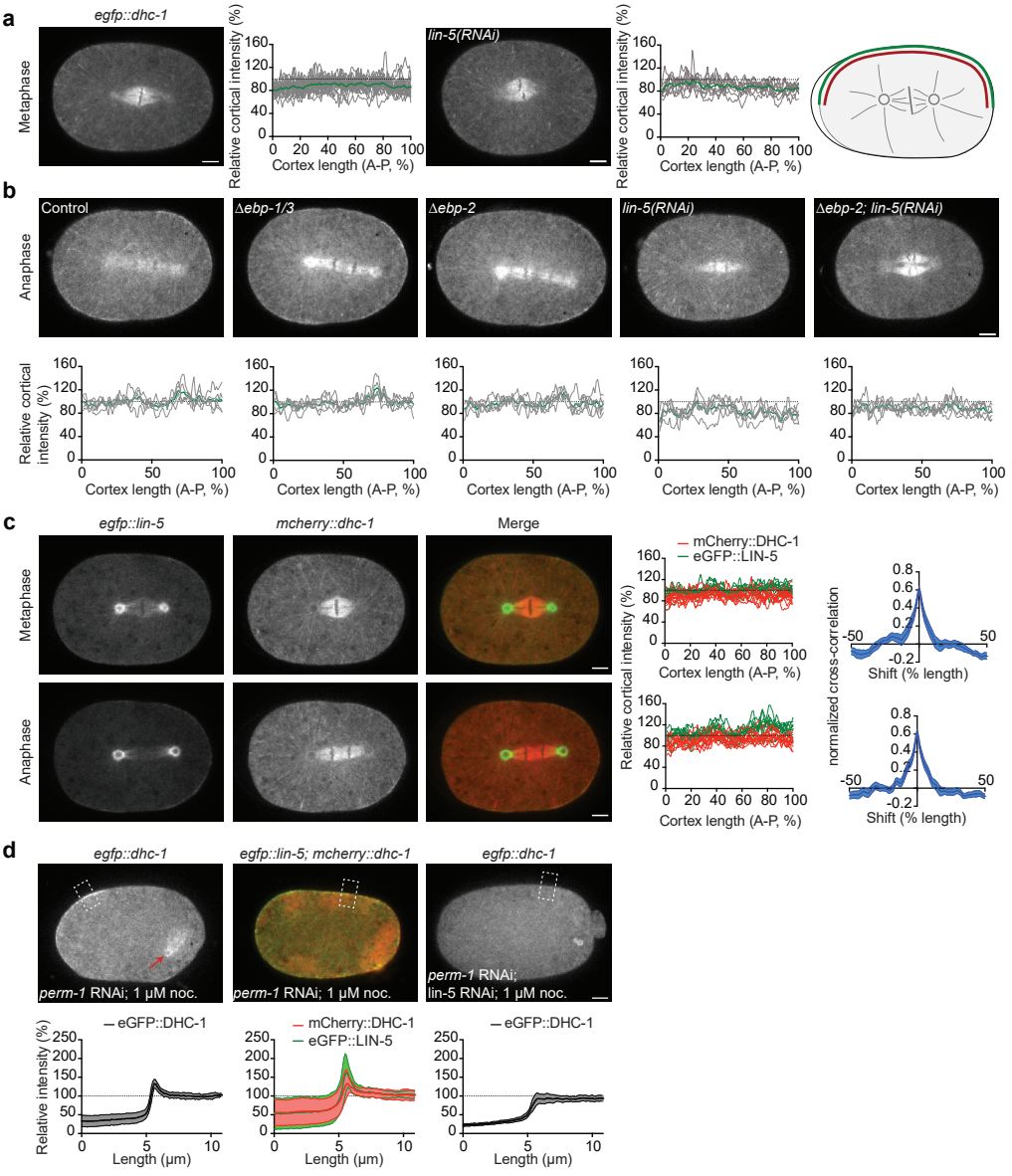

Figure 5. **Cortical dynein depends on recruitment from the cytoplasm by LIN-5 but not on EBP-2–mediated plus end tracking.** (**a**) SDCM images showing eGFP::DHC-1 localization in control and *lin-5(RNAi)* metaphase embryos. Graphs show relative cortical over cytoplasmic eGFP::DHC-1 intensities as measured along the cortex (far right, green line) and normalized to a cytoplasmic line (red). Dotted lines at y=100% indicate a 1:1 cortex/cytoplasm ratio. Mean (green) and individual (gray) traces are shown. *n*=12 embryos and 24 cortexes for control, and *n*=5 embryos and 10 cortexes for *lin-5(RNAi)*. (**b**) SDCM images of anaphase embryos of indicated genotypes. Graphs show relative cortical over cytoplasmic eGFP::DHC-1 intensities, quantified and shown as described in A. *n*=6 embryos per condition. (C) SDCM images show mCherry::DHC-1 and eGFP::LIN-5 localization. Mean (thick lines) and individual

(thin lines) intensity plots are shown in left graphs. Right graphs show cross-correlation between cortical LIN-5 and DHC-1 plots expressed as means ± SEM. *n*=10 embryos and 20 cortexes. (**d**) SDCM images showing dynein or LIN-5 localization in *perm-1(RNAi)* or *perm-1(RNAi); lin-5(RNAi)* embryos treated with 1 µM nocodazole (noc.). Graphs indicate fluorescence intensity profiles as measured in dashed boxes shown in superimposed panels. The red arrow points to mitotic spindle remnant. Plots are mean (*n*=10) intensities relative to cytoplasmic values ± SD. Bars, 5 µm.

affected the relative cortex/cytoplasm ratios calculated for the anterior and posterior and caused the increase of cortical levels observed in the posterior, which was not observed when a mean cytoplasmic value was used for normalization of all points instead (**Figure S5a**).

During anaphase, cortical enrichment of eGFP::LIN-5 increased substantially, most noticeably in the posterior. When averaging fluorescence intensities from multiple embryos, mCherry::DHC-1 did not show clear enrichment at the cortex above local cytoplasmic levels during anaphase. This reflects the patchy appearance of cortical dynein enrichment along the A-P axis (**Figure 5c**; also see **figure 5b**). Importantly, side-by-side comparison of nonnormalized cortical line scans revealed a strong cross-correlation between cortical eGFP::LIN-5 and mCherry::DHC-1 (**Figure 5c**; examples in **figure S5b**). This indicates that both proteins follow a similar cortical distribution, in agreement with LIN-5-dependent dynein localization. These protein localization patterns can account for force asymmetries in anaphase, but not during metaphase spindle displacement.

In a previous study, we observed cortical dynein localization in the absence of astral MTs (Portegijs et al., 2016). We repeated this experiment for *egfp::dhc-1* and *mcherry::dhc-1; egfp::lin-5* embryos permeabilized by *perm-1* RNAi treatment and exposed to 1 µM nocodazole (Carvalho et al., 2011; Berends et al., 2013). The use of tubulin and EBP-2 markers confirmed the absence of astral MTs, whereas the presence of a spindle remnant revealed cells in mitosis (**Figure 5d**, arrow). Dynein still localized to the cortex during mitosis in these embryos, and this localization strongly overlapped with and depended on LIN-5 (**Figure 5d**). Thus, LIN-5 recruits dynein to the cell cortex during mitosis, which can occur directly from the cytoplasm and in the absence of astral MTs.

As SDCM did not reliably detect dynein at the cortex during metaphase, we visualized cortical eGFP::DHC-1 more selectively at this stage by TIRF microscopy. Notably, this revealed two cortical populations of dynein that could be genetically separated. One population was detected as bright fluorescent spots that were absent in the *Δebp-2* background and thus represented dynein comets at the cell cortex (**Figure 6a**, arrow). A second population consisted of relatively dim spots that were absent in *lin-5(RNAi)* embryos (**Figure 6a**, arrowhead). Most notably, *Δebp-2; lin-5(RNAi)* embryos showed almost complete loss of detectable cortical dynein (**Figure 6a** and **video 8**). Furthermore, the increase in dynein levels associated with MT plus ends at the cortex in *lin-5(RNAi)* embryos may indicate that the cortex and MT plus ends compete for dynein binding or that LIN-5 suppresses dynein plus end accumulation (relative cumulative

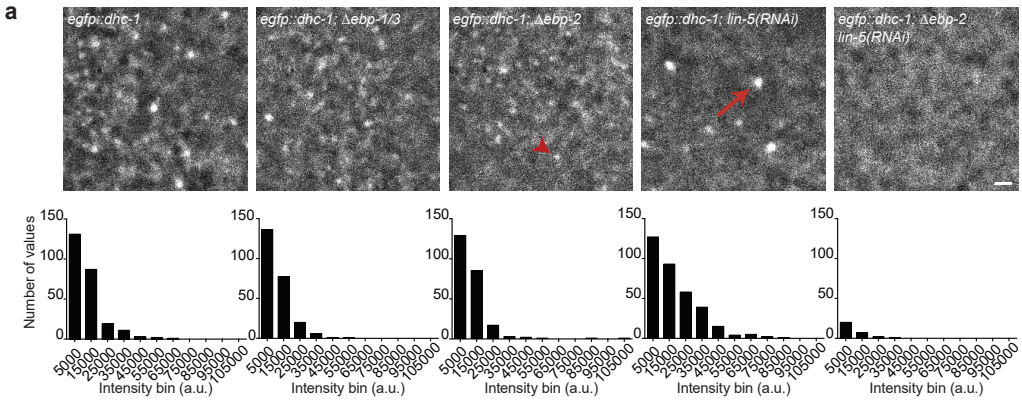
a
egfp::dhc-1
egfp::dhc-1; Δebp-1/3
egfp::dhc-1; Δebp-2
egfp::dhc-1; lin-5(RNAi)
egfp::dhc-1; Δebp-2 lin-5(RNAi)
Number of values
Intensity bin (a.u.)

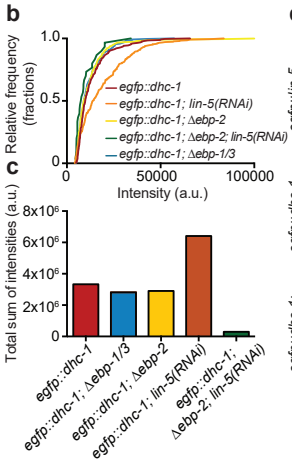
b
Relative frequency (fractions)
Intensity (a.u.)
egfp::dhc-1
egfp::dhc-1; lin-5(RNAi)
egfp::dhc-1; Δebp-2
egfp::dhc-1; Δebp-2; lin-5(RNAi)
egfp::dhc-1; Δebp-1/3
c
Total sum of intensities (a.u.)
egfp::dhc-1
egfp::dhc-1; Δebp-1/3
egfp::dhc-1; Δebp-2
egfp::dhc-1; lin-5(RNAi)
egfp::dhc-1; Δebp-2; lin-5(RNAi)

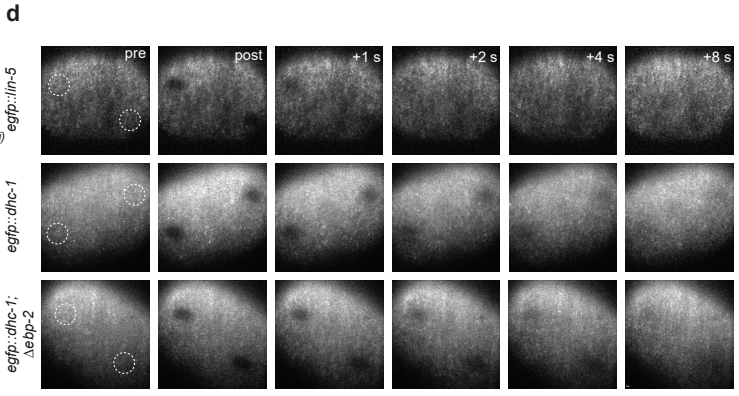
d
pre
post
+1 s
+2 s
+4 s
+8 s
egfp::lin-5
egfp::dhc-1
egfp::dhc-1; Δebp-2

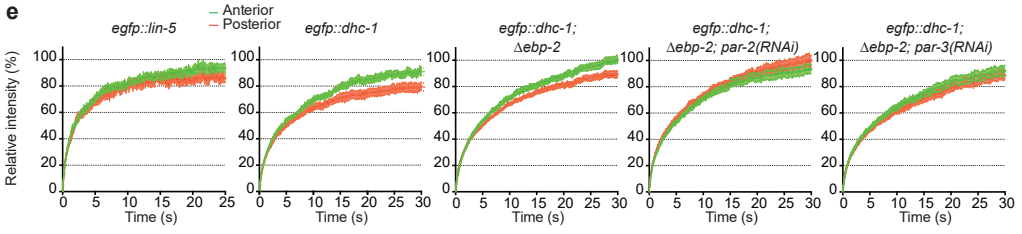
e
Anterior
Posterior
egfp::lin-5
egfp::dhc-1
egfp::dhc-1; Δebp-2
egfp::dhc-1; Δebp-2; par-2(RNAi)
egfp::dhc-1; Δebp-2; par-3(RNAi)
Relative intensity (%)
Time (s)

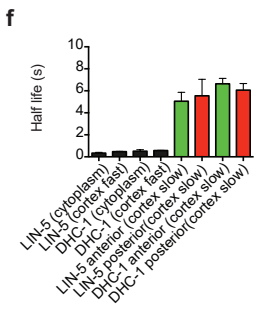
f
Half life (s)
LIN-5 (cytoplasm)
LIN-5 (cortex fast)
DHC-1 (cytoplasm)
DHC-1 (cortex fast)
LIN-5 anterior (cortex slow)
LIN-5 posterior(cortex slow)
DHC-1 anterior (cortex slow)
DHC-1 posterior(cortex slow)

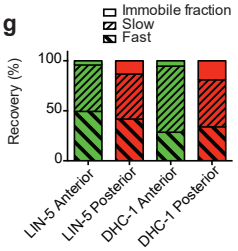
g
Immobile fraction
Slow
Fast
Recovery (%)
LIN-5 Anterior
LIN-5 Posterior
DHC-1 Anterior
DHC-1 Posterior

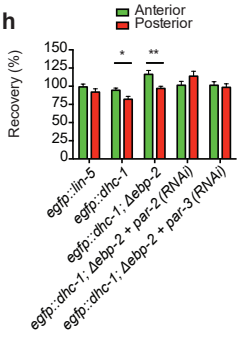
h
Anterior
Posterior
Recovery (%)
egfp::lin-5
egfp::dhc-1
egfp::dhc-1; Δebp-2
egfp::dhc-1; Δebp-2 + par-2(RNAi)
egfp::dhc-1; Δebp-2 + par-3(RNAi)

Figure 6. **Cortical dynein shows PAR polarity-dependent asymmetric dynamics in metaphase.** (**a**) TIRF images of early anaphase cortical eGFP::DHC-1 in different genetic backgrounds, showing plus end-associated (arrow) and cortical dynein dots (arrowhead). Bar graphs show frequency distributions of particle intensities from *n*=6 embryos per condition during 10 s starting at posterior spindle displacement. Bar, 1 µm. (**b**) Cumulative frequency distribution of the data shown in a. (**c**) Comparison of total particle intensity sums (*n*=30-344 particles) for each condition shown in a. (**d**) TIRF microscopy and FRAP of cortical eGFP::LIN-5 and eGFP::DHC-1 in anterior and posterior regions (indicated with dashed circles) during metaphase. (**e**) Quantification of FRAP as shown in d. Curves show means ± SEM. *egfp::lin-5*, *n*=28 anterior and 22 posterior; *egfp::dhc-1* control, *n*=19;, *Δebp-2*, *n*=35; *Δebp-2*; *par-2(RNAi)*, *n*=24; *Δebp-2*; *par-3(RNAi)*, *n*=21. (**f**) Half-lives for cytoplasmic (one phase) and cortical (two phases: fast and slow) recovery curves. Bars represent means ± SEM. *egfp::lin-5* (cytoplasm), *n*=7; *egfp::dhc-1* (cytoplasm), *n*=30. *n* values for cortical FRAP curves are as in e. Unpaired Welch's Student's *t* test. (**g**) Quantification of the contribution of fast and slow phases of eGFP::LIN-5 and eGFP::DHC-1 to FRAP. *n* values are as in e. (**h**) Recovery of curves shown in (**e**). *egfp::lin-5*, *egfp::dhc-1*; Δ*ebp-2, egfp::dhc-1*; Δ*ebp-2*; *par-2(RNAi)* anterior versus posterior. Wilcoxon matched-pairs signed rank test. *egfp::dhc-1*; *egfp::dhc-1*; Δ*ebp-2*; *par-3(RNAi)* anterior versus posterior. Paired Student's *t* test; *, P < 0.05; **, P < 0.01. *n* values are as in (**e**).

distribution in **figure 6b** and sum of intensities in **figure 6c**). Thus, two populations of dynein are present at the cortex in metaphase: an EBP-2-dependent plus end tracking population and a LIN-5-dependent cortical population. As shown in **figure 5d**, LIN-5 can most likely recruit dynein directly from the cytoplasm to the cortex, which would explain why plus end tracking of dynein is not required for its cortical localization during mitosis.

To investigate whether the cortical populations of dynein and LIN-5 show asymmetries that relate to asymmetric spindle positioning, we examined their dynamics by time-lapse TIRF microscopy combined with FRAP analysis. To this end, eGFP::DHC-1 and eGFP::LIN-5 embryos were photobleached in regions in the anterior and posterior, after which recovery of fluorescence was recorded during a 30-s timespan relevant for spindle positioning (**Figure 6d**). Overall, LIN-5 recovered more quickly than dynein in WT as well as in Δ*ebp-2* embryos (**Figure 6f**, **g** and **supplementary table 2**). As dissociation of LIN-5 also removes dynein, more stable cortical retention of dynein compared with LIN-5 would not be expected. However, statistical analyses indicated that the averaged eGFP::LIN-5 and eGFP::DHC-1 fluorescence recovery curves are most reliably fit by two-phase nonlinear regression analysis (extra sum-of-squares F test one- vs. two-phase fit; ****, P < 0.0001). The half-lives of the fast phases of cortical eGFP::LIN-5 and eGFP::DHC-1 recovery were similar to the recovery half-life of the corresponding proteins in the cytoplasm (**Figure 6f** and **S5d**). This probably reflects that our FRAP measurements include a cytoplasmic protein fraction or alternatively that part of the cortical population exchanges at a speed similar to cytoplasmic diffusion. The contribution of the fast phase was larger for LIN-5 recovery compared with DHC-1, which contributed to the faster overall recovery of LIN-5 (**Figure 6g**).

Importantly, the half-lives for the slow phase of recovery were similar for LIN-5 and dynein (**Figure 6f**, colored bars). Thus, this phase likely reflects the dynamics of a LIN-5-bound dynein population at the cortex. In addition to a fast and slow recovering phase, a

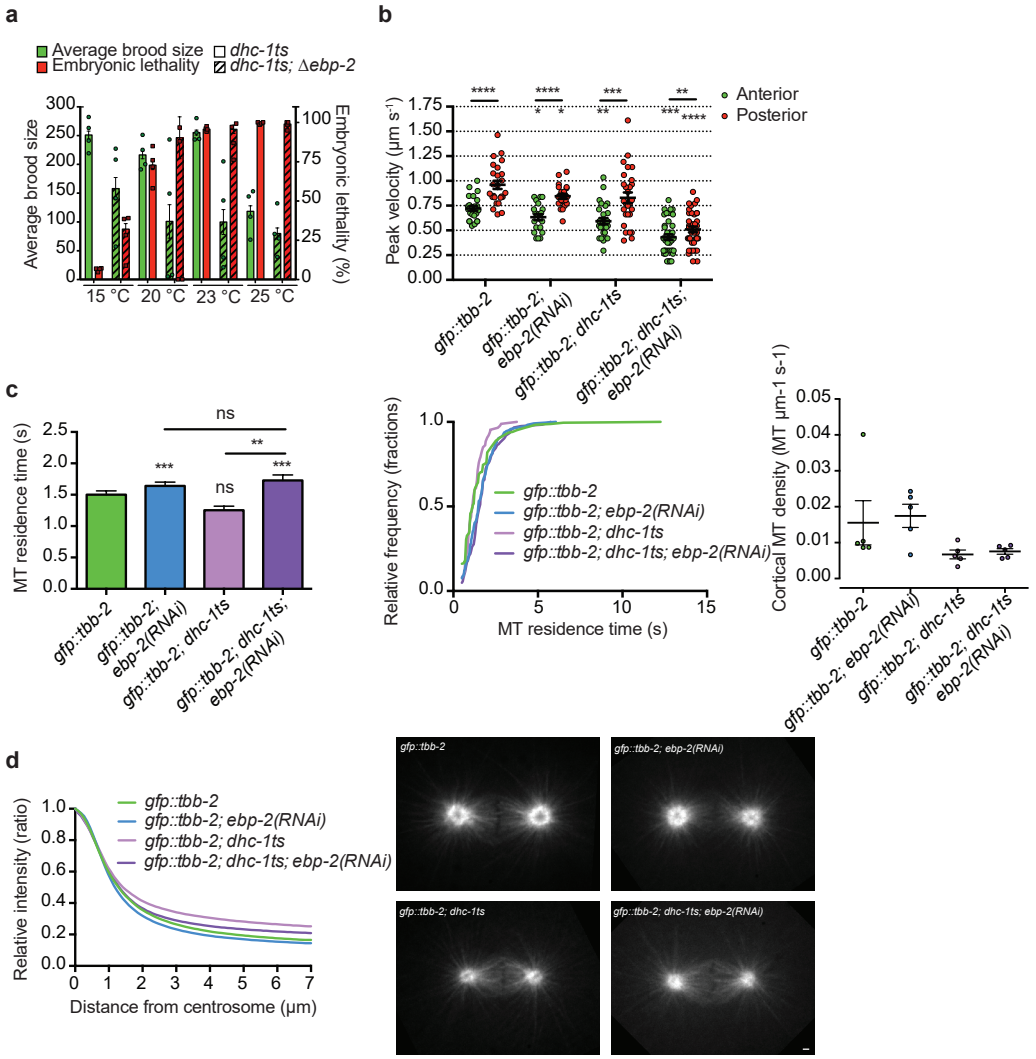

Figure 7. **EBP-2 is required for efficient force generation when dynein function is partially perturbed.** (**a**) Embryonic lethality and brood size of *dhc-1(or195*ts*)* and *dhc-1(or195*ts*); Δebp-2* strains at different temperatures shown as means ± SD. *n*=4 animals each. (**b**) Quantification of centrosome velocities upon spindle severing. Bars show means ± SEM. Unpaired (between genotypes) and paired (within embryos) Student's *t* tests; **, P < 0.01; ***, P < 0.001; ****, P < 0.0001. *gfp::tbb-2* control, *n*=25; *ebp-2(RNAi)*, *n*=21; *dhc-1*ts, *n*=28; *dhc-1*ts; *ebp-2(RNAi)*, *n*=38. (**c**) Quantification of cortical MT residence time as described in **figure 4d**. Bars are means ± SEM. Mann-Whitney *U* test; **, P < 0.01; ***, P < 0.001. *n*=87-410 events from five embryos for each condition. Graphs show cumulative fractions of residence time distributions. Right graphs show density of cortical MT contacts as mean MTs/µm^2 s^{-1} per embryo, and bars are means ± SEM. (**d**) Quantification of astral MT densities in metaphase embryos measured as shown in **figure 4f**. Plots were aligned and normalized to maximum values at the centrosome. *n*=20 asters from 10 embryos per condition. Bar, 1 µm.

small protein fraction remained immobile within the 30-s interval. Interestingly, individual fits revealed a statistically larger immobile fraction of eGFP::DHC-1 in the posterior compared with the anterior (**Figure 6g**, **h**). This difference also appeared detectable for eGFP::LIN-5 but was not significant (**Figure 6g**, **h**). FRAP analysis of eGPF::DHC-1 in *Δebp-2* embryos also showed asymmetry in dynein dynamics, indicating that the asymmetry resides in the LIN-5-dependent cortical dynein population, as detected in **figure 6a-c**. Notably, the FRAP curves of *Δebp-2* embryos showed higher recovery than WT (**Figure 6e**), even extending beyond 100% (**Figure 6h**). This may be attributed to the faster progression through mitosis in *Δebp-2* embryos (**Figure S3g-j**) in combination with an increase in cortical dynein during mitosis from metaphase onwards. Nevertheless, extrapolation of the curves confirmed a higher percentage recovery in the anterior compared with posterior of *Δebp-2* embryos, similar to WT eGFP::DHC-1 embryos (**Figure 6h**). Disruption of polarity by knockdown of *par-2* or *par-3* abolished the observed asymmetry in cortical eGFP::DHC-1 recovery (**Figure 6e**, **h**).

In summary, the obtained FRAP curves probably result from combined measurements of dynein in the cytoplasm and LIN-5-associated dynein at the cortex. The LIN-5-associated cortical dynein includes a relatively stable population, which, depending on PAR polarity, is enriched in the posterior, and thus may be critical for pulling forces.

Partial dynein perturbation reveals a contribution of dynein plus end tracking

Although dynein plus end tracking is not required for force generation and spindle positioning in WT conditions, it might function as a backup mechanism to ensure robust force generation. If so, a contribution of dynein plus end tracking may become detectable in certain stress conditions such as, for example, when dynein function is partially compromised. To examine this possibility, we used the temperature-sensitive (ts) allele *dhc-1(or195)*, which causes severe perturbation of DHC-1 function and 100% embryonic lethality at nonpermissive temperatures (Schmidt et al., 2005). We aimed to partially interfere with DHC-1 function at semipermissive temperatures to be able to examine whether *ebp-2* loss causes an enhanced or synthetic phenotype. Exposure of *dhc-1(or195)* mutants to temperatures ranging from 15 to 25°C revealed progressively more severe defects at higher temperatures (**Figure 7a**). The reduction in brood size and increase in embryonic lethality were strongly enhanced by the simultaneous presence of the *Δebp-2* allele at temperatures <25°C (**Figure 7a**). To assess whether this synergistic effect is related to spindle positioning, we performed spindle severing experiments with *dhc-1(or195)* and *dhc-1(or195); ebp-2(RNAi)* embryos, as homozygous *gfp::tbb-2; dhc-1(or195);* Δ*ebp-2* mutants were not viable. Most *dhc-1(or195); ebp-2(RNAi)* embryos could assemble functional mitotic spindles (100% for *gfp::tbb-2* and *gfp::tbb-2; ebp-2(RNAi)*, 87.5% for *gfp::tbb-2; dhc-1(or195)*, and 73.3% for *gfp::tbb-2; dhc-1(or195); ebp-2(RNAi)* at 20°C). Interestingly, *ebp-2* RNAi strongly reduced pulling forces at the semipermissive temperature of 20°C (**Figure 7b**). This reduction did

not result from an indirect effect on MT dynamics, as the *dhc-1(or195)* mutation itself did not significantly affect cortical MT residence time at 20°C or perturb the prolonged cortical contact caused by *ebp-2* RNAi (**Figure 7c**). Furthermore, although the density of astral MTs was reduced in the metaphase spindles of *dhc-1(or195)* embryos compared with WT, this mild effect was not further exacerbated by the knockdown of *ebp-2* (**Figure 7c**, **d**). Based on these results, we conclude that EBP-2-dependent plus end tracking of dynein contributes to robust spindle positioning and can serve as a backup mechanism that ensures efficient force generation when dynein function is partially perturbed.

Discussion

In this study, we investigated the localization and dynamics of the dynein complex during asymmetric spindle positioning in a well-established in vivo model, the *C. elegans* one-cell embryo. By tagging endogenous dynein and live imaging, we revealed two populations of dynein that together ensure robust cortical pulling force generation. To critically examine the importance of the MT plus end-bound dynein population, we generated a complete knockout of all *ebp* family members and demonstrated that these genes are not essential but contribute to the control of MT dynamics and spindle formation. Finally, we provide a detailed analysis of the asymmetries and dynamics of the major FGC components dynein and LIN-5 at the cortex of one-cell embryos.

Although C-terminal tagging of the *dhc-1* dynein heavy chain was recently used (Zhang et al., 2015a), we observed that this creates partial loss of function. It is currently unclear whether this translates to dynein in other organisms. N- and C-terminally tagged yeast Dyn1 appear functional (Reck-Peterson et al., 2006). However, Dyn1 lacks the C-terminal regulatory extension present in the cytoplasmic dynein heavy chain of *C. elegans* and other organisms (Nicholas et al., 2015). A BAC transgene with a C-terminally GFP-tagged mouse dynein heavy chain is commonly used in mammalian studies (for example, see Poser et al., 2008). However, cells in culture with normal endogenous DHC do not depend on the tagged protein. Therefore, tagging the N-terminal DHC tail region instead of the C-terminal motor domain seems the best option for future in vivo studies.

Dynein plus end tracking was previously described for other organisms (Vaughan et al., 1999; Han et al., 2001; Lenz et al., 2006; Kobayashi and Murayama, 2009). In budding yeast, dynein is actively delivered to the cortex by a plus end tracking complex that also contains a kinesin (Lee et al., 2003; Sheeman et al., 2003; Markus and Lee, 2011). In animal cells, MT plus end-bound dynein is not transported by kinesins but is merely concentrated by binding to +TIPs, which are organized by EB proteins (Akhmanova and Steinmetz, 2015). Indeed, we found that loss of EBs completely abolished dynein plus end tracking. Strikingly, this mechanism, and in fact the whole EB protein family, turned out to be dispensable for *C. elegans* development and viability.

It is surprising that EBs are not essential in worms, because significant defects in MT dynamics and spindle formation or positioning have been reported in mammalian cells (Green et al., 2005; Draviam et al., 2006; Toyoshima and Nishida, 2007; Ban et al., 2009; Komarova et al., 2009; Xia et al., 2012; Ferreira et al., 2013). These studies did not report a block of cell division upon EB loss, and in fact, the phenotypes associated with EB knockouts in yeast and plants are relatively mild (Berlin et al., 1990; Bisgrove et al., 2008). Several considerations may explain the weak phenotypes. First, EB-dependent plus end tracking does not mediate transport and delivery of +TIPs but just promotes their transient concentration from the surrounding cytoplasm. This probably provides a limited gain over diffusion. Moreover, EB loss removes plus end recruitment of both positive and negative

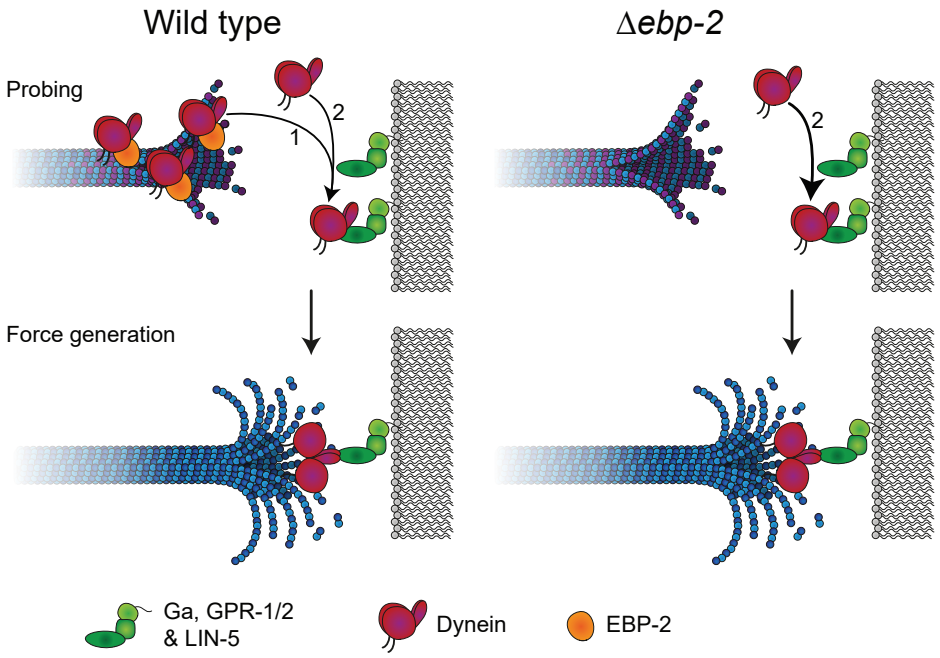

Figure 8. **Model.** Model of force generation in WT (left) and Δ*ebp-2* (right) situations as explained in the discussion.

MT regulators. In addition, the phenotypes of constitutive knockouts might be milder than acute protein depletions because of compensatory mechanisms.

In contrast to EB-dependent plus end tracking, LIN-5 is essential for asymmetric spindle positioning. Using endogenously tagged LIN-5 and dynein, we observed that both proteins display a shallow cytoplasmic gradient throughout mitosis, reminiscent of the pattern described for GPR-1/2 and LIN-5 in fixed embryos (Park and Rose, 2008). Although the biological cause and function of this cytoplasmic asymmetry remains unknown, it indicates that cortical enrichment as judged by eye or cytoplasm-normalized plots can lead to its over- or underestimation. Thus, we compared nonnormalized cortical traces instead and found a strong correlation between LIN-5 and dynein cortical intensity patterns. Interestingly, our analysis did not reveal a clear A-P asymmetry in cortical localization for either protein at the time of initial spindle displacement in late metaphase. However, FRAP analysis combined with TIRF microscopy revealed an asymmetric and PAR-dependent stable population of dynein in the posterior. This subpopulation of LIN-5-bound dynein may be critical in force generation, as the number of active force generators has been reported to be higher in the posterior (Grill et al., 2003). LIN-5 showed only a small stable fraction at the cortex, which was nonsignificantly enriched in the posterior. We assume that not all cortical LIN-5 is dynein associated. Hence, the relevant population might be somewhat

obscured in the total pool of cortical LIN-5. Collectively, our observations indicate that asymmetries in dynein behavior during initial spindle displacement probably do not result from asymmetric enrichment of LIN-5. Instead, other levels of control, such as protein phosphorylation and the Gα GTPase cycle, may determine LIN-5-dynein retention and pulling force asymmetry (Galli et al., 2011; Portegijs et al., 2016).

Dynein still localized to the cortex in embryos that lacked EBs or were treated with nocodazole. This strongly suggests that LIN-5 can recruit dynein directly from the cytoplasm as opposed to an MT-mediated delivery mechanism. MT-independent dynein recruitment has also been observed in nocodazole-treated mammalian cells; however, the correct cortical distribution of human dynein appears to depend on a dynamic astral MT network (Tame et al., 2014). Similarly, the localization of cortical dynein seemed randomized after nocodazole treatment of *C. elegans* embryos. Thus, in *C. elegans* and mammalian cells, MT-mediated delivery does not appear necessary for dynein localization to the cortex, but dynamic MTs appear to be required for the proper levels and distribution of dynein at the cortex.

We propose that dynein plus end tracking functions as a local enrichment mechanism (**Figure 8**). By concentrating dynein at the plus end, MTs could promote local interaction of dynein with Gα–GPR-1/2–LIN-5 complexes at the cortex (**Figure 8**, arrow 1). This hypothesis is supported by our finding that knockdown of EBP-2 enhances the reduction in forces caused by partial loss of DHC-1 function. In this context, enrichment of dynein at the plus end appears to be needed for efficient force generation. In the absence of EBs and thus dynein plus end tracking, FGCs would need to form through contacts between astral MTs and dynein-containing cortical complexes (**Figure 8**, arrow 2). Although this single mechanism was thought to be less efficient (Ananthanarayanan et al., 2013), the prolonged cortical residence of MTs in the absence of EBP-2 might allow for successful probing of the cortex, which could explain why Δ*ebp-2* does not solely lead to reduced force generation. In WT cells, +TIPs form a protein-dense network, and the number of available binding sites in the vicinity of an MT plus end is limited (Duellberg et al., 2014). In EB-depleted cells, MT plus ends are probably less crowded, and cortical FGCs may associate with MTs more efficiently. Collectively, our work illustrates the complexity and robustness of the molecular mechanisms controlling the critical process of spindle positioning.

Materials and methods

C. elegans strains

A summary of the strains used in this study is included in **supplementary table 1**. All strains were maintained at 20°C as described previously (Brenner, 1974) unless stated otherwise. Animals were grown on plates containing nematode growth medium seeded with OP50 *Escherichia coli* bacteria.

Generation of CRISPR/Cas9 repair templates and gRNAs

Homology arms of at least 1,500 bp flanking the CRISPR/Cas9 cleavage site were generated by PCR amplification from purified *C. elegans* genomic DNA using the KOD polymerase (Novagen). PCR products were inserted into the pBSK backbone by Gibson assembly (New England Biolabs, Inc.). For the generation of *ph::egfp::lov* and *egfp::dhc-1*, *egfp* was amplified from pMA-*egfp*, *ph* from P*wrt-2::gfp::ph* (Wildwater et al., 2011), and *lov* from *gfp::lovpep::unc-54UTR* (Harterink et al., 2016).
For *mcherry::dhc-1* and *dhc-1::mcherry*, codon-optimized *mcherry* was amplified from TH0563-PAZ-*mcherry* (a gift from A. Hyman, Max Planck Institute of Molecular Cell Biology and Genetics, Dresden, Germany). Primers containing overlaps between PCR fragments, linker sequences encoding four glycine residues, and mutated gRNA sites were synthesized (Integrated DNA Technologies) and are listed in **supplementary table 3**. For the generation of gRNA vectors, oligonucleotides were annealed and inserted into pJJR50 using T4 ligation (New England Biolabs, Inc.). Vectors were used to transform and were purified from DH5α-competent cells (QIAGEN).

CRISPR/Cas9-mediated genome editing

Injection of *C. elegans* adults in the germline was performed using an inverted microscope microinjection setup. Injection mixes contained a combination of 30-50 ng/µl *Peft-3::cas9* (46168; Addgene; Friedland et al., 2013), 50-100 ng/µl u6::sgRNA with sequences targeted against either *cxTi10816*, *dhc-1*, *ebp-1*, *ebp-2*, or *ebp-3*, 30-50 ng/µl of the repair template, 50 ng/µl PAGE-purified *pha-1* repair oligonucleotide (Integrated DNA technologies), 60 ng/µl pJW1285 (61252; Addgene; Ward, 2015), and 2.5 ng/µl P*myo-2::tdtomato* as a coinjection marker. Animals were grown for 3-5 d at either 20 or 25°C after injection, and transgenic progeny was selected based on either expression of tdTomato in the pharynx or survival at the nonpermissive temperature (25°C). Subsequent assessment of genome editing events was performed by either visual inspection using a widefield fluorescence microscope and/or PCR amplification using primers targeting the inserted FP and a genomic region situated outside of the range of homology arms, in case of *dhc-1*, or sequences flanking the predicted cut sites as well as an internal control, in case of the Δ*ebp-1/2/3* knockout mutants. The contexts of PCR-confirmed edited genomic loci were further inspected by sequencing (Macrogen Europe).

Quantification of embryonic lethality and total brood size

In three separate experiments, N2, SV1598, SV1619, and SV1803; N2, SV1868, SV1872, SV1877, and SV1882; or EU828 and SV1956 single L4-stage hermaphrodites were placed on OP50 feeding plates and kept at 15, 20, 23, and/or 25°C depending on the experiment. Animals were transferred to a new plate every day. On each plate, embryonic lethality was scored after 24 h, and brood size was scored 48 h after removal of the parent. Experiments were executed in quadruplicate.

Microscopy

For time-lapse imaging, embryos were dissected from *C. elegans* adults on coverslips in 0.8× egg salts buffer (94 mM NaCl, 32 mM KCl, 2.7 mM $CaCl_2$, 2.7 mM $MgCl_2$, and 4 mM Hepes, pH 7.5; Tagawa et al., 2001) and subsequently mounted on 4% agarose pads. Live-cell SDCM imaging of one-cell embryos and HeLa cells was performed on an Eclipse T*i* with Perfect Focus System (Nikon), a CSU-X1-A1 spinning-disk confocal head (Yokogawa Electric Corporation), Plan Apochromat VC 60× 1.40 NA oil and S Fluor 100× 0.5-1.3 NA (at 1.3, for photoablation) objectives, an Evolve 512 electron-multiplying charge-coupled device camera (Photometrics), a DV2 two-channel beam-splitter for simultaneous dual-color imaging, Cobolt Calypso 491 nm (100 mW), Cobolt Jive 561 nm (100 mW), and Teem Photonics 355 nm Q-switched pulsed lasers controlled with the ILas system (Roper Scientific France/PICT-IBiSA, Institut Curie, used for photoablation), ET-GFP (49002), ET-mCherry (49008), and ET-GFPmCherry (49022) filters, ASI motorized stage MS-2000-XYZ with Piezo Top Plate, and an LB10-3 filter wheel (Sutter Instrument). The microscope was controlled with MetaMorph 7.7 software and situated in a temperature-controlled room at 20°C.

HeLa cells were cultured as described previously (Splinter et al., 2012). For imaging of the dynein complex during mitosis, HeLa cells stably expressing DIC2-GFP were used. This cell line was generated and described previously in a BAC TransgeneOmics project (Poser et al., 2008). Imaging of mitotic cells was performed using the spinning-disk setup described in the previous paragraph, where the temperature was controlled at 37°C with a Tokai Hit INUBG2E-ZILCS Stage Top Incubator during experiments.

For regular single- and dual-color channel imaging experiments, images were acquired in either streaming mode with 50, 100, 250, 500, or 1,000 ms exposure or time-lapse mode with 500 ms exposure and 5-s intervals. Laser power was kept constant within experiments. For spindle bisection assays, spindles were imaged after photoablation in streaming mode with 500 ms exposure time.

Simultaneous dual-color TIRF imaging of embryos was performed on an Eclipse Ti with Perfect Focus System, an Apochromat TIRF 100× 1.49 NA oil objective (Nikon), an Evolve 512 electron-multiplying charge-coupled device camera, an Optosplit III beam-splitter (Andor Technology) for simultaneous dual-color imaging, 488-nm (150 mW) and Cobolt Jive 561-nm (100 mW) lasers, ET-GFP (49002), ET-mCherry (49008), and

ET-GFPmCherry (49022) filters, an ASI motorized stage MS-2000-XY System for Inverted Microscope Te/Ti 2000 (Nikon), and an LB10-3 filter wheel. Acquisition was controlled with MetaMorph 7.7 software (Molecular Devices), and the setup was situated in a temperature-controlled room at 20°C.

Single-color TIRF imaging of embryos was performed on either the above-mentioned TIRF setup or on an identical TIRF setup in which lasers were controlled by the Ilas-2 system (Roper Scientific), and image acquisition was controlled with MetaMorph 7.8 software (Molecular Devices).

Live-cell widefield time-lapse DIC microscopy imaging of embryos was performed on an Axioplan upright microscope with a 100× 1.4 NA Plan Apochromat objective controlled by AxioVision Rel 4.7 software (ZEISS) at an acquisition rate of one image per 2 s with constant exposure time and light intensity. Embryos were followed from pronuclear meeting until completion of the first cell division.

Images acquired by SDCM and TIRF microscopy were prepared for publication in ImageJ (National Institutes of Health) by linear adjustment of brightness and contrast, subtraction of background intensity as measured in images outside cells, and frame averaging. For images in **figures 2**, **4d**, **6a**, and **S2a**, **b**, a Gaussian blur filter was applied for background subtraction using ImageJ. Fluorophores used in this study to visualize proteins of interest include eGFP, mCherry, and YFP.

RNA-mediated interference

For feeding RNAi experiments (Timmons and Fire, 1998), L4 animals were grown on seeded RNAi plates for 24 h at 20°C or 48 h at 15°C before imaging sessions (*lin-5*, *ebp-1/3*, *ebp-2*, and *gpr-1*). Alternatively, the gonads of young adults were injected with double-stranded RNA targeting RNA molecules of interest (*perm-1* and *perm-1* + *lin-5*) and grown for 20 h at 15°C (Fire et al., 1998). For these experiments, the products of T7 PCRs on RNAi clones were used as templates for in vitro double-stranded RNA synthesis using the MEGAscript T7 transcription kit (Thermo Fisher Scientific). Clones from both the Vidal and Ahringer RNAi libraries were used (Kamath et al., 2003; Rual et al., 2004).

UV laser spindle midzone severing

Severing of the mitotic spindle was performed in essence as described previously (Grill et al., 2001; Portegijs et al., 2016). AZ224, TH65, SV893, SV1874, SV1879, and SV1900 one-cell embryos were imaged during mitosis at 20°C using a spinning-disk confocal microscope equipped with a Teem Photonics 355-nm Q-switched pulsed laser controlled with the ILas system. At anaphase onset, as judged by spindle morphology visualized with GFP::TBB-2 or TBA-2::YFP, embryos were subjected to spindle bisection as shown in **figure 4b** and **video 9**. Subsequent displacement of centrosomes was followed by stream acquisition with 500-ms exposure time. Centrosome peak velocities after spindle severing were subsequently tracked automatically using the FIJI TrackMate plugin (ImageJ).

FRAP

Local photobleaching of eGFP::LIN-5 and eGFP::DHC-1 fluorescence signal was performed during metaphase in a circular region with a diameter of 45 px (~2.8 µm) in both the anterior and posterior cortex (except for cytoplasmic LIN-5 FRAP experiments, which were performed only in the anterior), and recovery was followed for up to 30 s afterward. Intensities within the photobleached regions and a background area outside the signal of the embryo cortex were measured using a circular region with a diameter of 54 px (~3.38 µm), and a bleaching control was taken between but not overlapping the anterior and posterior photobleached regions. Recovery of the fluorescent signals was set to 100% based on the mean intensity from 20 frames (1 s) before bleaching in the same region and was set to 0% directly after. All values were normalized to account for camera background and acquisition photobleaching as described previously (Phair et al., 2003). Recovery curves of cortical FRAP experiments were aligned at their minimum value and fitted using one- and two-phase nonlinear regression analysis in Prism 6 (GraphPad Software). For unpaired statistical comparison with initial phase parameters of cortical FRAP fits, individual cytoplasmic recovery parameters were approached by one-phase nonlinear regression analysis and subsequently averaged and tested for significance. For paired statistical testing of plateau values from cortical FRAP curves, individual curves were fit by one-phase nonlinear regression analysis, and anterior and posterior parameters were subsequently compared within samples.

Drug treatment of early embryos

To allow for small molecule drugs to enter the early *C. elegans* embryo, L4 animals were treated with *perm-1* RNAi for 20 h before experiments (Carvalho et al., 2011). Egg-laying SV1803 or SV1635 adults were then splayed onto coverslips in 0.8× egg salts buffer with 1 µM nocodazole and mounted on slides with a concave indentation, which prevents compression of the embryos. Metaphase one-cell embryos were identified by the presence of polar bodies, enlarged centrosomes, a spindle remnant, and absence of a nuclear envelope, and then they were imaged by SDCM (Portegijs et al., 2016).

Data analysis

All intensity profile measurements of SDCM and TIRF microscopy data were generated using ImageJ and FIJI. For cortical intensity profiles of strains SV1589, SV1619, SV1635, and SV1803, both halves of each embryo were traced with a 5-px-wide freehand line from the anterior to the posterior pole with five replicates, and five matching traces were generated below each cortex in the cytoplasm. Intensity profiles were background corrected, and each group of five traces was then averaged and subsequently divided into 100 bins to correct for varying lengths of the plots. Cortical plots were then plotted either with or without normalization over corresponding cytoplasmic measurements or the mean thereof.

Analysis of the timing of key mitotic events and position of the nucleocentrosomal complex and centrosomes from DIC videos of N2, SV1868, SV1872, SV1877, and SV1882 strains was performed by hand using ImageJ.

Quantifications of cortical MT residence time were performed automatically by use of the FIJI plugin TrackMate v3.4.2 at 6 px estimated blob diameter and a threshold value of 1,500. TIRF microscopy videos from strains AZ244, SV1874, TH65, SV1879, SV1900, and SV893 starting at posterior spindle displacement with 20 s total duration were background corrected by application of a Gaussian blur filter before analysis. Detected spots were then filtered to contain only those with <10 px displacement, which excludes any laterally growing MTs from the analysis.

Speeds of EBP-2::GFP and mCherry::DHC-1 comets in strain SV1857 as imaged by SDCM during metaphase were calculated based on angles made by tracks in kymograph images generated in ImageJ with the KymoResliceWide plugin. Kymograph locations were manually selected between the centrosome and cell cortex.

Quantification of the colocalization between EBP-2::GFP and mCherry::DHC-1 comets in strain SV1857 as imaged by simultaneous dual-color TIRF microscopy was executed using the ComDet plugin v0.3.6, and the same dual-color images with one channel inverted horizontally were used as an internal control. Particles were detected in both green and red channels independently at approximated particle sizes of 4 (red) and 4.5 (green) px with sensitivities of signal/noise ratio equaling 4 and 5, respectively. Colocalization was determined based on a maximum distance of 8.00 px.

Automatic tracking of particle intensities in TIRF videos of SV1803, SV1874, and SV1879 was executed using the ImageJ Analyze Particles plugin with parameter size=10-∞ px, circularity=0.10-1.00, and with exclusion of particles on edges after background-subtraction and manual image thresholding.

Radial intensity profiles of astral MT networks were generated using the Radial Profile Angle plugin for ImageJ, set to measure intensities in a 180° angle around each of two centrosomes with a radius of 150 px in metaphase embryos. Intensity profiles were then aligned at their maximum values corresponding with the outer rim of the centrosome and normalized to their maximum values.

Cross-correlation analysis was performed on averaged nonnormalized cortical intensity profiles of strain SV1635 using a custom MATLAB (MathWorks) script and the following equation, which calculates the normalized cross-correlation for each Δx shift of one channel with respect to another:

$$\gamma(\Delta x) = \frac{\sum_x \left[I_1(x) - \langle I_1 \rangle \right] \left[I_2(x - \Delta x) - \langle I_2 \rangle \right]}{\sqrt{\sum_x \left[I_1(x) - \langle I_1 \rangle \right]^2 \sum_x \left[I_2(x - \Delta x) - \langle I_2 \rangle \right]^2}}.$$

All numerical data processing and graph generation was performed using Excel 2011 (Microsoft) and Prism 6.

Statistical analysis

All data are expressed as means with either SD or SEM as indicated in the legends of each figure. Statistical differences were determined using two-tailed paired and unpaired Student's *t* tests, Mann-Whitney *U* tests, and the Wilcoxon matched-pairs signed rank test. Before selection of appropriate statistical analyses, datasets were tested for a Gaussian distribution using the D'Agostino-Pearson omnibus K2 normality test. A p-value of <0.05 was considered to be significant. *, $P < 0.05$; **, $P < 0.01$; ***, $P < 0.001$; ****, $P < 0.0001$. All statistical analyses were performed using Prism 6.

Online supplemental material

Figure S1 shows dynein plus end tracking in cell types other than the one-cell *C. elegans* embryo. **Figure S2** shows the localization of dynein at the mitotic spindle and its colocalization with dynactin at the MT plus end. **Figure S3** contains quantifications of various mitotic events and their timing as visualized by DIC microscopy as in **figure 3e**. **Figure S4** shows that EBP-2 is required for assembly of the spindle midzone and that cortical dynein patches follow the oscillatory behavior of the anaphase spindle. **Figure S5** contains extended analyses of the subcellular localization patterns of LIN-5 and DHC-1 shown in **figure 5c** as well as recovery curves for the cytoplasmic FRAP experiments quantified in **figure 6f**, **h**. **Supplementary table 1** contains a list of the *C. elegans* strains used in this study. **Supplementary table 2** contains parameters from nonlinear regression curve fits of eGFP::LIN-5 and eGFP::DHC-1 FRAP experiments. **Supplementary table 3** contains a list of the primers used in this study for CRISPR/Cas9-assisted genome engineering. **Video 1** shows overlap of mCherry::DHC-1 with GFP::TBB-2 as in **figure 2a**. **Video 2** shows colocalization of mCherry::DHC-1 with EBP-2::GFP as in **figure 2b**. **Video 3** shows cortical overlap of mCherry::DHC-1 with GFP::TBB-2 as in **figure 2e**. **Video 4** shows cortical overlap of mCherry::DHC-1 with EBP-2::GFP as in **figure 2f**. **Video 5** shows co-occurrence of dynein comets reaching the cortex and the formation of membrane invaginations as in **figure 2h**. **Video 6** shows the localization of eGFP::DHC-1 in Δ*ebp* mutants as in **figure 3c**. **Video 7** shows DIC videos of mitotic WT and Δ*ebp* one-cell embryos as in **figure 3e**. **Video 8** shows the genetic dissection of two cortical dynein populations as in **figure 6a**. **Video 9** shows an example of UV laser-mediated spindle severing as in **figure 4b**. **Video 10** shows end-on MT-cortex contacts as visualized by TIRF microscopy as shown in **figure 4d**.

Acknowledgements

We thank all members of the van den Heuvel, Akhmanova, and Boxem groups for helpful discussions and support. We acknowledge Wormbase and the Biology Imaging Center at the Faculty of Sciences, Department of Biology, Utrecht University. Some strains were provided by the Caenorhabditis Genetics Center funded by National Institutes of Health Office of Research Infrastructure Programs (P40 OD010440).

This work was supported by a European Research Council Synergy grant 609822 to A. Akhmanova and is part of the Netherlands Organization for Scientific Research program CW711.011.01 (to S. van den Heuvel).

The authors declare no competing financial interests.

Author contributions

A. Akhmanova, R. Schmidt, and S. van den Heuvel designed the study, analyzed the data, and wrote the paper. R. Schmidt carried out most experiments, L.-E. Fielmich performed the LIN-5 knock in and FRAP studies, I. Grigoriev was responsible for the analysis of HeLa cells and, with E.A. Katrukha, provided technical support of microscopy, and E.A. Katrukha supported data analysis.

Footnotes

Abbreviations used:

+TIP	plus end-tracking protein
A-P	anterior-posterior
DIC	differential interference contrast
EB	end-binding
FGC	force generator complex
FP	fluorescent protein
MT	microtubule
SDCM	spinning-disk confocal fluorescence microscopy
TIRF	total internal reflection fluorescence
ts	temperature-sensitive

Online supplemental material

Video 1. **Co-localization of mCherry::DHC-1 comets with astral MTs.**
Simultaneous dual-color SDCLM movie of mCherry::DHC-1 (red) and GFP::TBB-2 (MTs, green) localization at the posterior pole during mitosis in a one-cell *C. elegans* embryo. Images were streamed with 100 ms exposure time, averaged for each 2 consecutive frames, and displayed at 15 frames per second. Movie corresponds to **figure 2a**.

Video 2. **Co-localization of mCherry::DHC-1 comets with EBP-2::GFP.**
Simultaneous dual-color SDCLM movie of mCherry::DHC-1 (red) and EBP-2::GFP (MT plus-end, green) localization at the posterior pole during mitosis in a one-cell *C. elegans* embryo. Images were streamed with 100 ms exposure time, averaged for each 2 consecutive frames, and displayed at 15 frames per second. Movie corresponds to **figure 2b**.

Video 3. **Cortical co-localization of mCherry::DHC-1 comets with astral MTs.**
Simultaneous dual-color TIRF movie of mCherry::DHC-1 (red) and GFP::TBB-2 (MTs, green) cortical localization during mitosis in a one-cell *C. elegans* embryo. Images were streamed with 100 ms exposure time, averaged for each 5 consecutive frames after background subtraction by a gaussian blur filter, and displayed at 10 frames per second with the posterior to the right. Movie corresponds to **figure 2e**.

Video 4. **Cortical co-localization of mCherry::DHC-1 comets with EBP-2::GFP.**
Simultaneous dual-color TIRF movie of mCherry::DHC-1 (red) and EBP-2::GFP (MT plus-end, green) cortical localization during mitosis in a one-cell *C. elegans* embryo. Images were streamed with 100 ms exposure time, averaged for each 5 consecutive frames after background subtraction by a gaussian blur filter, and displayed at 10 frames per second with the posterior to the right. Movie corresponds to **figure 2f**.

Video 5. **Co-localization of mCherry::DHC-1 comets with PH::eGFP membrane invaginations.**
Simultaneous dual-color SDCLM movie of mCherry::DHC-1 (red) and PH::eGFP (plasma membrane, green) localization at the posterior pole during mitosis in a one-cell *C. elegans* embryo. Images were streamed with 100 ms exposure time, averaged for each 2 consecutive frames, and displayed at 10 frames per second. Movie corresponds to **figure 2h**.

Video 6. **Localization of eGFP::DHC-1 in Δ*ebp* mutant backgrounds.**
Single-color SDCLM movies of eGFP::DHC-1 localization during mitosis in one-cell *C. elegans* embryos of otherwise wt (left), Δ*ebp-1/3* (middle) and Δ*ebp-2* (right) genetic

backgrounds. Images were acquired every 5 seconds with 1000 ms exposure time and equal laser power, background corrected and displayed at 5 frames per second with the posterior to the right. Movies correspond to **figure 3c**.

Video 7. **Time-lapse DIC movies of wt and Δ*ebp* embryos.**
Wide-field DIC movies of (from left to right) N2, Δ*ebp-2,* Δ*ebp-1/3* and Δ*ebp-1/2/3* one-cell *C. elegans* embryos during mitosis. Images were acquired every 2 seconds with 15 ms exposure time, equal transmitted light intensities and displayed at 20 frames per second with the posterior to the right. Movies correspond to **figure 3e**.

Video 8. **Two distinct cortical populations of eGFP::DHC-1.**
Single-color TIRF movies of eGFP::DHC-1 cortical localization in (from left to right) otherwise wt, Δ*ebp-1/3,* Δ*ebp-2, lin-5* RNAi and Δ*ebp-2* + *lin-5* RNAi-treated one-cell *C. elegans* embryos. Images were streamed with 50 ms exposure time, averaged for each 10 consecutive frames after background subtraction by a gaussian blur filter, and displayed at 10 frames per second. Movies correspond to **figure 6a**.

Video 9. **UV-laser mediated spindle midzone severing.**
Single-color SDCLM movie of GFP::TBB-2 (MTs) UV-laser-mediated spindle bisection at anaphase onset in a one-cell *C. elegans* embryo. Images were streamed with 500 ms exposure time and displayed at 15 frames per second with the posterior to the right. Movie corresponds to **figure 4b**.

Video 10. **Residence time of end-on MT-cortex contacts.**
Single-color TIRF movie of GFP::TBB-2 (MTs) cortical localization in a one-cell *C. elegans* embryo. Images were streamed with 500 ms exposure time and displayed at 10 frames per second with the posterior to the right. Movie corresponds to **figure 4d**.

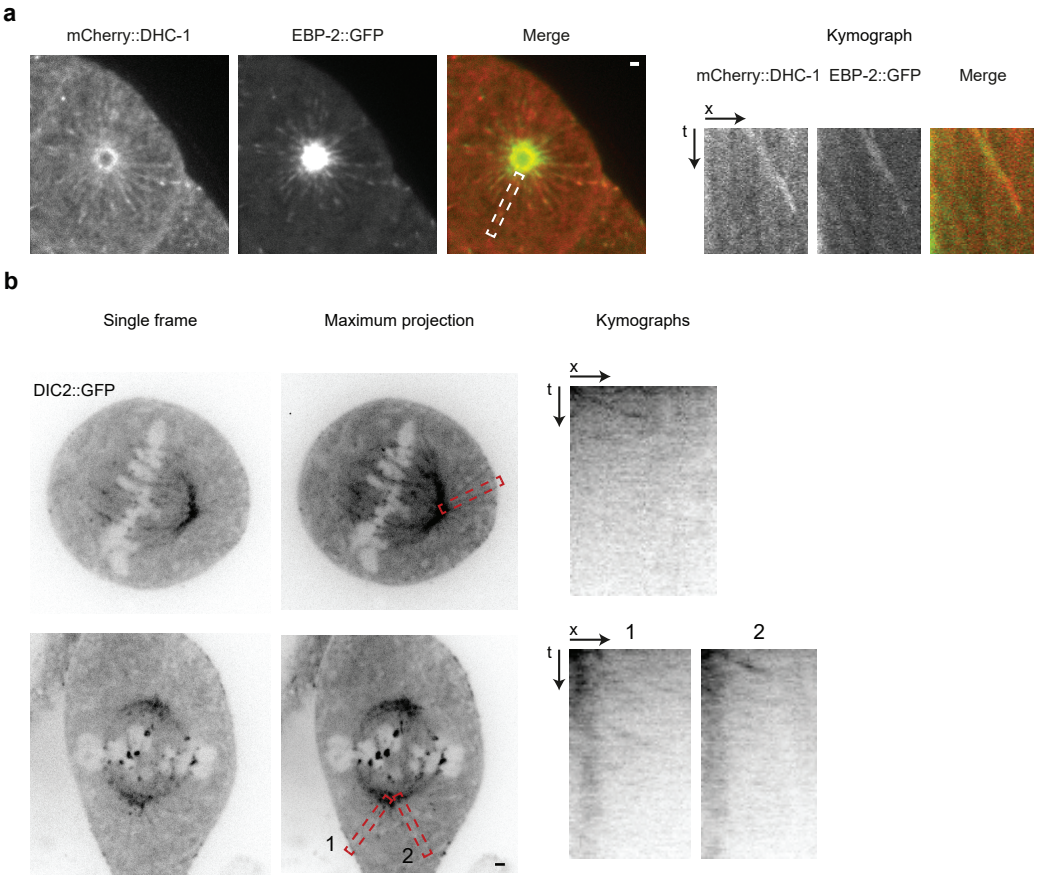

Figure S1. **Dynein tracks plus-ends of astral MTs in cell types other than the *C. elegans* zygote.** (**a**) Representative images of mCherry::DHC-1 (red) and EBP-2::GFP (green) localization in a 4-cell embryo. Images are averages of 10 consecutive frames taken from 100 ms stream-lapse movies. Kymograph position is indicated with the dashed line box. Scale bar, 1 µm. (**b**) Representative single frames (left), maximum projections (middle) and kymographs (right) of DIC2-GFP localization in metaphase HeLa cells. Images taken from 500 ms ms stream-lapse movies. Kymograph positions are indicated with dashed line boxes. Scale bar, 1 µm.

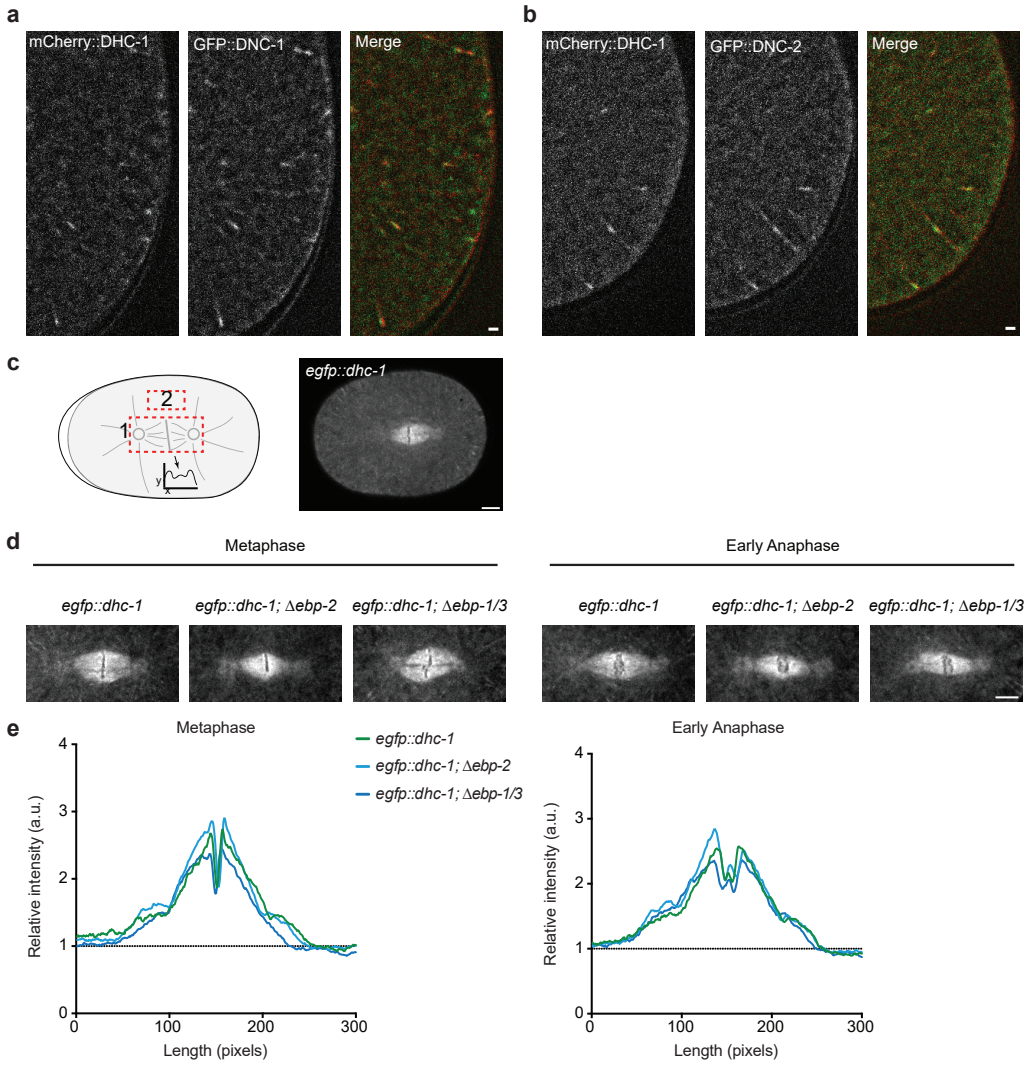

Figure S2. **Dynactin components track MT plus-ends together with DHC-1, and dynein localization to the spindle midzone, kinetochores, kinetochore MTs and poles is not altered upon loss of EBP-1/2/3.** (**a**, **b**) Representative simultaneous dual-color SDCLM images of mCherry::DHC-1 (red) and either GFP::DNC-1(A) or GFP::DNC-2 (**b**) localization during mitosis. Images are averages of 5 consecutive frames taken from 100 ms stream-lapse movies, after background subtraction by a gaussian blur filter. Scale bars, 1 µm. (**c**) Schematic representation (left) of approach to measure eGFP::DHC-1 (right) intensity along the mitotic spindle. Scale bar, 5 µm. (**d**) Representative SDCLM images of eGFP::DHC-1 localization in different wt or Δ*ebp* mutant backgrounds as indicated in each image, both during metaphase and early anaphase. Scale bar, 5 µm. (**e**) Quantification of dynein distribution along the horizontal axis of the spindle in different genetic backgrounds as indicated in the graph, represented as average (N=4) intensity normalized to average cytoplasmic values (measured in box in (**a**)). Spindle length in pixels.

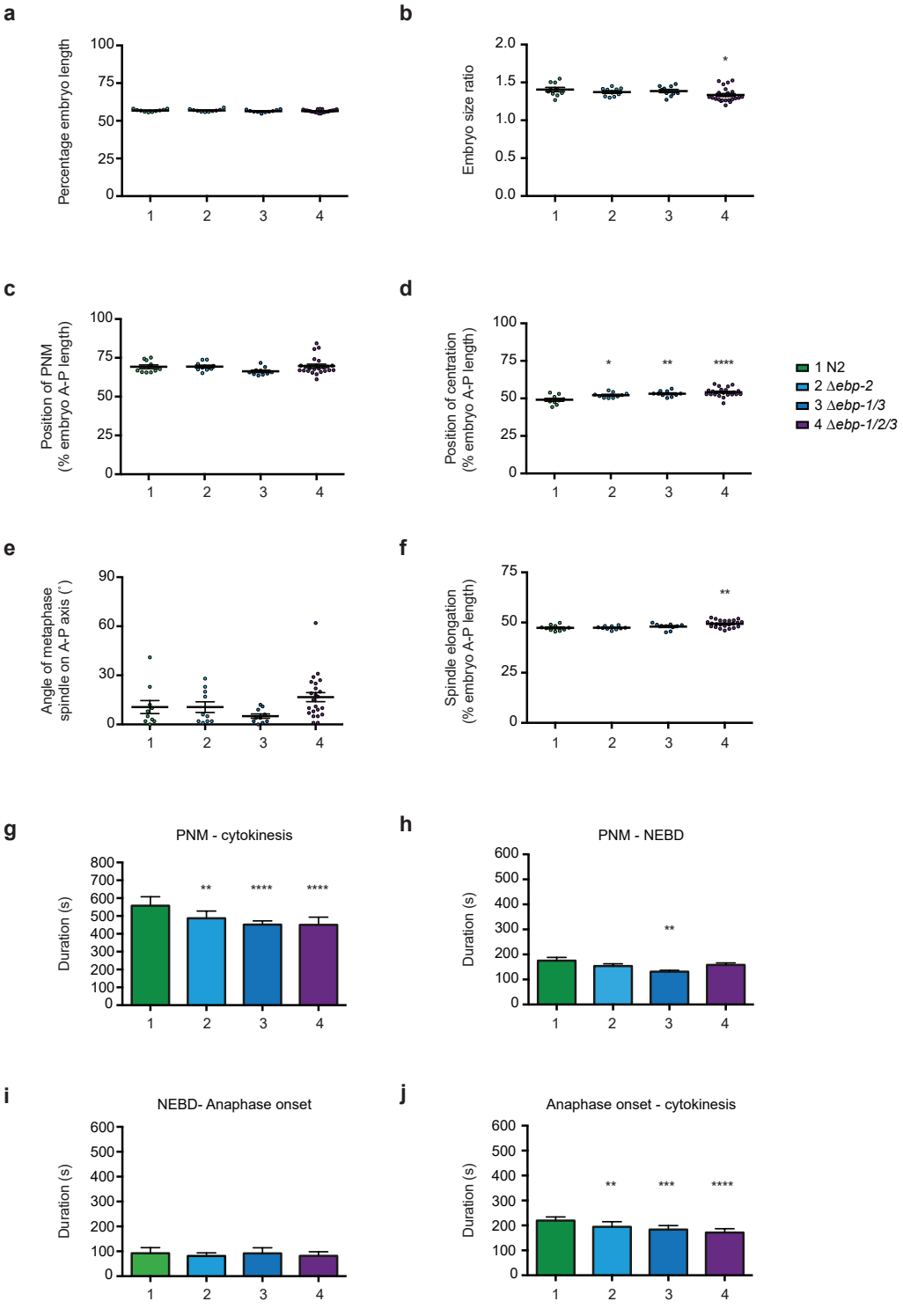
a
Percentage embryo length
100
75
50
25
0
1
2
3
4
b
Embryo size ratio
2.0
1.5
1.0
0.5
0.0
*
c
Position of PNM
(% embryo A-P length)
d
Position of centration
(% embryo A-P length)
*
**
****
1 N2
2 Δebp-2
3 Δebp-1/3
4 Δebp-1/2/3
e
Angle of metaphase
spindle on A-P axis (°)
90
60
30
0
f
Spindle elongation
(% embryo A-P length)
**
g
PNM - cytokinesis
Duration (s)
800
700
600
500
400
300
200
100
0
**
****
****
h
PNM - NEBD
Duration (s)
600
500
400
300
200
100
0
**
i
NEBD- Anaphase onset
Duration (s)
j
Anaphase onset - cytokinesis
Duration (s)
**
***
****

Figure S3. **Characterization of key mitotic events and their timing in Δ*ebp* mutant embryos.** Quantification of key mitotic events from DIC time-lapse movies of N2 (green), Δ*ebp-2* (light blue), Δ*ebp-1/3* (dark blue) and Δ*ebp-1/2/3* (purple) embryos during the first division. Asymmetry (**a**), position of pronuclear meeting (PNM, (**c**)) and centration (**d**) and spindle elongation (**f**) are plotted as a percentage of total embryo length, embryo size (**b**) as the ratio of embryo length over embryo height, and metaphase spindle angle as the angle relative to the embryo A-P axis. Errors are mean (N≥10) + SEM, unpaired Welch Student's *t*-test (**a**-**d** and **f**) or Mann-Whitney U-test (**e**); * P < 0.05, ** P < 0.01, **** P < 0.0001 compared to wt, no indication means no significant difference from wt.
(**g**-**j**) Quantification of duration of mitotic events from DIC time-lapse movies of N2 (green), Δ*ebp-2* (light blue), Δ*ebp-1/3* (dark blue) and Δ*ebp-1/2/3* (purple) embryos during the first division. Duration in seconds, errors are mean (N≥9) + SEM. unpaired Welch Student's *t*-test; * P < 0.05, ** P < 0.01, *** P < 0.001, **** P < 0.0001 compared to wt, no indication means no significant difference from wt.

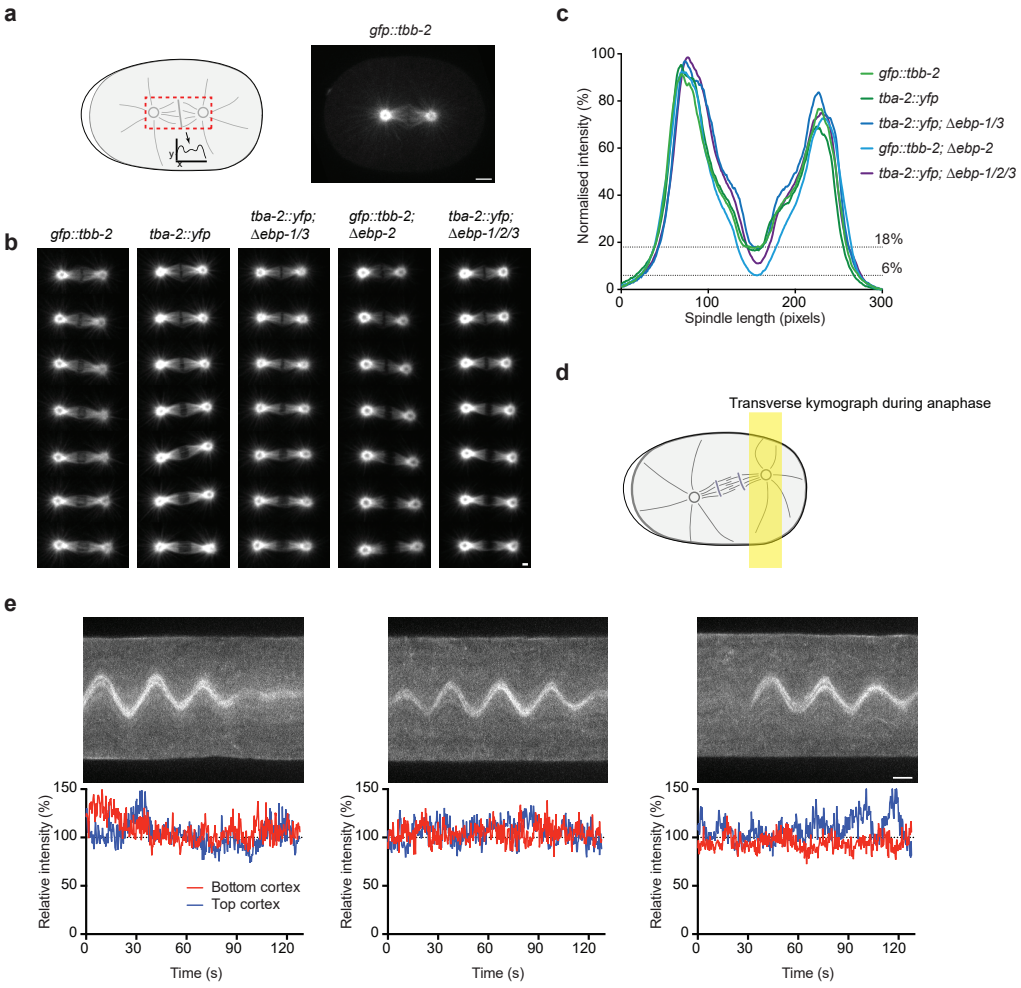
a
gfp::tbb-2
b
gfp::tbb-2
tba-2::yfp
tba-2::yfp; Δebp-1/3
gfp::tbb-2; Δebp-2
tba-2::yfp; Δebp-1/2/3
c
Normalised intensity (%)
Spindle length (pixels)
gfp::tbb-2
tba-2::yfp
tba-2::yfp; Δebp-1/3
gfp::tbb-2; Δebp-2
tba-2::yfp; Δebp-1/2/3
18%
6%
d
Transverse kymograph during anaphase
e
Relative intensity (%)
Bottom cortex
Top cortex
Time (s)

Figure S4. **EBP-2 is required for proper spindle midzone establishment, and cortical dynein patches follow oscillatory spindle movements.** (**a**) Schematic representation (left) of approach to measure MT (right) density along the mitotic spindle. (**b**) Montages of representative SDCLM movies of one-cell embryos expressing either GFP::TBB-2 or TBA-2::YFP (MTs), in different wt or Δ*ebp* mutant backgrounds as indicated in each image. Montages are generated from seven consecutive frames from time-lapse movies acquired at a rate of 1 frame per 5 seconds, all acquired with the same laser power and exposure time of 500 ms. Scale bar, 1 µm. (**c**) Quantification of MT abundance along the horizontal axis of the spindle in different genetic backgrounds during early anaphase as indicated in the graph, represented as average (N=7) intensity relative to the maximum value of all data sets. Spindle length in pixels. (**d**) Schematic representation of *C. elegans* embryo during anaphase spindle pole rocking, indicating where kymographs are positioned in the embryo. (**e**) Representative kymographs of eGFP::DHC-1 localization at the posterior pole and cortex during anaphase spindle rocking. Graphs show relative cortical eGFP::DHC-1 intensity, as quantified by generating linescans of both upper and lower cortex intensities and subsequent normalization over adjacent cytoplasmic values. Scale bar, 5 µm.

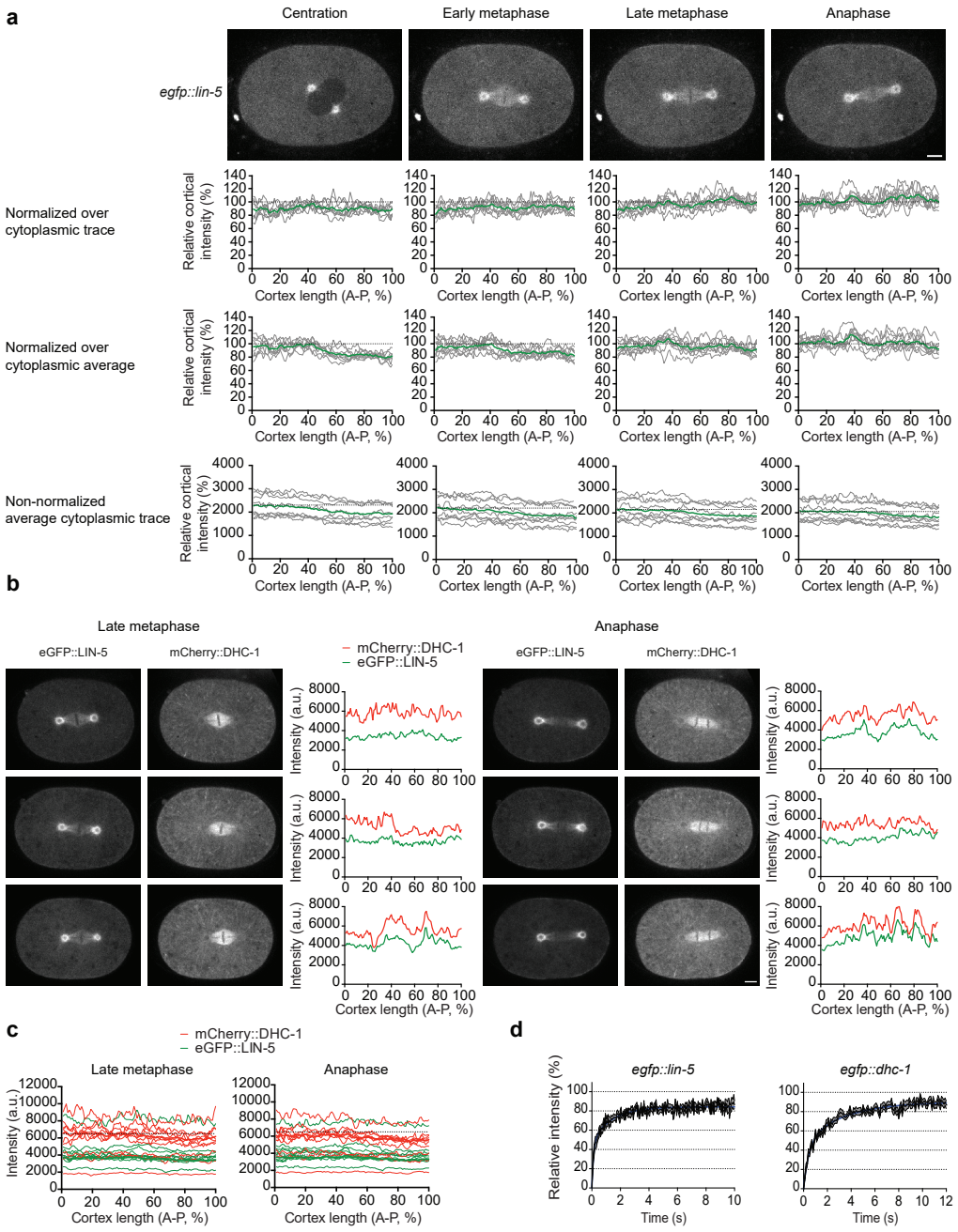

Figure S5. **Extended analysis of cortical LIN-5 and dynein localization during mitosis.** (a) Quantification of cortical eGFP::LIN-5 during centration, early metaphase, late metaphase and anaphase as shown in representative images in upper panels. Cortical intensity values are normalized over either cytoplasmic traces from below the cortex (first row of graphs) or over a single average cytoplasmic value (second row). Dotted lines at Y=100% indicate a 1:1 cortex to cytoplasm ratio. Non-normalized cytoplasmic intensities

indicating a gradient of eGFP::LIN-5 during all mitotic stages are also shown (third row). Scale bar, 5 µm. (**b**) Individual non-normalized cortical traces of embryos expressing eGFP::LIN-5 and mCherry::DHC-1 during late metaphase and anaphase. Three representative embryos from the dataset used to quantify cortical enrichment and the cross-correlation index in **figure 5c** are shown in both stages. Scale bar, 5 µm. (**c**) Quantification of cortical eGFP::LIN-5 and mCherry::DHC-1 during late metaphase and anaphase as shown in representative images in (**b**). Non-normalized cytoplasmic intensities are plotted as individual (thin) and average (thick) plots. (**d**) Quantification of cytoplasmic eGFP::LIN-5 and eGFP::DHC-1 FRAP. Curves are expressed as mean + SEM; *egfp::lin-5* (N=7), *egfp::dhc-1* (N=30).

Strain	Genotype
N2	*Wild type*
SV893	*dhc-1(or195ts) I; unc-119(ed3) III; ruIs57[unc-119(+) pie-1-GFP-α-tubulin]*
SV1589	*he244 [egfp::lin-5] II*
SV1598	*he248[dhc-1::mcherry] I*
SV1619	*he250[mcherry::dhc-1] I*
SV1635	*he244 [egfp::lin-5] II; he250[mcherry::dhc-1] I*
EU828	*dhc-1(or195ts) I*
TH65	*ddIs15 [unc-119(+) + C47B2.3(genomic)::YFP]]*
AZ224	*RuIs57[Ppie-1::gfp::tbb-2] V*
SV1702	*RuIs57[Ppie-1::gfp::tbb-2] V; he250[mcherry::dhc-1] I*
SV1703	*he258[Peft-3::ph::egfp::lov::tbb-2-3'UTR] IV; he250[mcherry::dhc-1] I*
SV1803	*he264[egfp::dhc-1] I*
SV1840	*ojIs5[pie-1::GFP::dnc-1 + unc-119(+)]; he250[mcherry::dhc-1]* I
SV1841	*ojIs57[Ppie-1::gfp::dnc-2 unc-119(+)]; he250[mcherry::dhc-1] I*
SV1857	*abcIs3[Ppie-1::ebp-2::gfp; unc-119(+)]; he250[mcherry::dhc-1] I*
SV1868	*he278[Δebp-2] II*
SV1872	*he279[Δebp-1, ΔY59A8B.25, Δebp-3]*
SV1873	*he278[Δebp-2]; he263[egfp::dhc-1] V*
SV1874	*he278[Δebp-2] II; RuIs57[Ppie-1::gfp::tbb-2] V*
SV1877	*he278[Δebp-2] II; he279[Δebp-1, ΔY59A8B.25, Δebp-3] V*
SV1878	*he279[Δebp-1, ΔY59A8B.25, Δebp-3] V; he263[egfp::dhc-1] I*
SV1879	*he279[Δebp-1, ΔY59A8B.25, Δebp-3] V; ddIs15 [[unc-119(+) + C47B2.3(genomic)::YFP]]*
SV1900	*unc-119(+) + C47B2.3(genomic)::YFP; he278[Δebp-2] II; he279[Δebp-1, ΔY59A8B.25, Δebp-3] V*
SV1956	*dhc-1(or195ts) I; unc-119(ed3) III; he278[Δebp-2]*

Supplementary table 1. **List of *C. elegans* strains used in this study.** This table shows a summary of the *C. elegans* strains including their corresponding genotypes as used in this study.

	eGFP::LIN-5			eGFP::DHC-1		
	Cortex anterior	Cortex posterior	Cytoplasm	Cortex anterior	Cortex posterior	Cytoplasm
N	28	22	7	19	19	15
One component fit						
Plateau (%)	89,31	83,74	81,98	87,61	75,71	85,21
95% CI	88,82 to 89,80	83,33 to 84,15	81,35 to 82,61	87,04 to 88,18	75,28 to 76,14	84,12 to 86,29
Half-life (s)	1,94	1,75	0,32	3,86	3,19	0,86
95% CI	1,88 to 1,20	1,70 to 1,80	0,230 to 0,34	3,768 to 3,966	3,11 to 3,28	0,80 to 0,92
Degrees of freedom	518	518	1357	599	599	119
R square	0,93	0,94	0,51	0,96	0,95	0,92
Two components fit						
Plateau (%)	94,49	86,73	84,27	94,69	80,89	90,02
95% CI	94,09 to 94,89	86,45 to 87,01	83,40 to 85,15	94,31 to 95,08	80,63 to 81,15	87,90 to 92,13
Percent fast (%)	46,36	42,6	57,51	28,56	33,86	51,81
Slow half-life (s)	4,73	3,58	0,99	7,11	6,25	2,26
95% CI	4,53 to 4,94	3,44 to 3,74	0,82 to 1,24	6,96 to 7,28	6,12 to 6,39	1,77 to 3,13
Fast half-life (s)	0,53	0,43	0,086	0,55	0,59	0,31
95% CI	0,50 to 0,57	0,40 to 0,47	0,066 to 0,12	0,52 to 0,59	0,56 to 0,62	0,24 to 0,43
Degrees of freedom	516	516	1355	597	597	117
R square	0,9937	0,9913	0,57	0,9973	0,9974	0,9656
Individual one-component fit	Slow phase	Slow phase		Slow phase	Slow phase	
Average plateau (%)	99,07	91,99	82,15	94,46	82,09	84,75
95% CI	90,97 to 107,2	82,79 to 101,2	76,60 to 87,69	88,13 to 100,8	73,83 to 90,35	79,84 to 89,75
Average half-life (s)	5,06	5,54	0,34	6,64	6,05	0,51
95% CI	3,38 to 6,73	2,41 to 8,67	0,19 to 0,49	5,62 to 7,66	4,79 to 7,33	0,25 to 0,78

	eGFP::DHC-1; Δ*ebp-2*		**eGFP::DHC-1; Δ*ebp-2* + *par-2* RNAi**		**eGFP::DHC-1; Δ*ebp-2* + *par-3* RNAi**	
	Cortex anterior	Cortex posterior	Cortex anterior	Cortex posterior	Cortex anterior	Cortex posterior
	35	35	24	24	21	21
	94,66	85,21	90,06	95,4	88,4	84,95
	93,95 to 95,36	84,60 to 85,82	89,52 to 90,60	94,73 to 96,07	87,68 to 89,12	84,19 to 85,71
	4,47	4,036	3,97	4,08	4,75	4,87
	4,35 to 4,59	3,929 to 4,149	3,89 to 4,07	3,98 to 4,20	4,62 to 4,89	4,73 to 5,02
	599	599	599	599	599	599
	0,96	0,95	0,96	0,95	0,95	0,95
	110,8	93,74	95,54	104,5	100,5	100,7
	109,6 to 112,0	93,35 to 94,14	95,31 to 95,77	104,2 to 104,9	99,93 to 101,0	99,94 to 101,6
	31,33	28,28	23,49	27,63	25,73	27,11
	10,92	7,86	6,37	7,75	9,61	11,39
	10,47 to 11,41	7,71 to 8,03	6,29 to 6,45	7,62 to 7,89	9,41 to 9,82	11,08 to 11,72
	0,94	0,5	0,37	0,5	0,58	0,66
	0,90 to 0,1	0,48 to 0,53	0,35 to 0,39	0,48 to 0,53	0,55 to 0,61	0,64 to 0,70
	597	597	597	597	597	597
	0,9971	0,9978	0,9986	0,9984	0,9983	0,998
	Slow phase	Slow phase	Slow phase	Slow phase	Slow phase	Slow phase
	116,3	96,88	101,3	113,8	101,3	98,49
	105,3 to 127,2	90,77 to 103,0	90,18 to 112,4	99,85 to 127,8	90,96 to 111,6	88,39 to 108,6
	11,02	8,28	7,71	9,32	8,67	9,38
	8,68 to 13,36	7,20 to 9,36	5,77 to 9,66	7,15 to 11,49	6,95 to 10,38	7,42 to 11,34

Supplementary table 2. Parameters from eGFP::LIN-5 and eGFP::DHC-1 FRAP data nonlinear regression curve fits. This table shows the parameters acquired from nonlinear regression curve fitting of the FRAP data described in **figure 6d**, **e**, **f**, **g**, and **h**. Genotypes are indicated above columns, parameter types and their respective units of measurement are indicated to the left for each row. Parameters from one- and two-component fits on average curves, and from fits on non-averaged individual curves are shown. The subcellular location that was analyzed and its corresponding N-value is indicated in the top of each column.

Allele	Application	Name
he248[*dhc-1::mcherry*] I	Repair template	oRS001
		oRS004
		oRS005
		oRS006
		oRS007
		oRS008
		oRS009
	gRNA	oRS002
		oRS003
	Sequencing	oRS026
		oRS027
		oRS028
		oVP327
he250[*mcherry::dhc-1*] I	Repair template	oRS116
&		oRS117
he264[*egfp::dhc-1*] I		oVP317
		oVP318
		oVP319
		oVP320
		oVP321
		oVP322
		oVP323
		oVP324
	gRNA	oVP315
		oVP316
	Sequencing	oRS043
		oRS048
		oLF032
		oVP325
he279[Δ*ebp-1*, Δ*Y59A8B.25*, Δ*ebp-3*] V	gRNA	oRS135
		oRS136
		oRS137
		oRS138
		oRS191
		oRS192
		oRS193
		oRS194
	Sequencing	oRS147
		oRS149
		oRS171
		oRS176
		oRS179
		oRS184
		oRS283
		oRS203
		oRS204
		oRS205

Sequence 5'-3'
CGACTCTTCTTGACCGCTGA
GCCAGTGAATTGTAATACGACTCACTATAGGGCGAATTGGGTACCCAACCTGCTTCGTTCTCTGTCA
TGGACATTCCCCCACCGCCGAGGGTGGAGTTAGCAACCAATGCAACTCCTCGTTG
TTGGTTGCTAACTCCACCCTCGGCGGTGGGGGAATGTCCAAGGGAGAGGAGGA
GAGAAAATAAATTACAATAAAGGAACGGAGACGATTACTTGTAGAGCTCGTCCATTCCTC
TAATCGTCTCCGTTCCTTTATTGTAATTTATTTTCTC
TAAAGGGAACAAAAGCTGGAGCTCCACCGCGGTGGCGGCCGCCAACAGACGTGGAATTCATCCCT
/5PHOS/AATTAGACGATTAGAGAGTTGAGT
/5PHOS/AAACACTCAACTCTCTAATCGTCT
CTTCAACGATTCTGACAACTCCAC
CTGCCGAGCCGAAAAGAAAC
CCAACTTTGGCGGCTAACAAATG
CATGAACTCCTTGATGATGGCC
CAAATTCTAAACGTTAACTATTAAATTCAATTTTCAGGTAATGTCCAAGGGAGAGGAGCT
TTGGATAATGCTACTTTCATTCCCACTATCCATTCCCCCACCGCCCTTGTAGAGCTCGTCCATTCCG
GCCAGTGAATTGTAATACGACTCACTATAGGGCGAATTGGGTACCGACTGCTTCAATGTGTTCCAGATG
TACCTGAAAATTGAATTTAATAGTTAACGTTTAGAATTTGC
CAAATTCTAAACGTTAACTATTAAATTCAATTTTCAGGTAATGTCCAAGGGAGAGGAGGA
TACTTTCATTCCCACTATCCATTCCCCCACCGCCCTTGTAGAGCTCGTCCATTCCTC
TACAAGGGCGGTGGGGGAATGGATAGTGGGAATGAAAGTAGCATTATCCAACCACCAAATCTTAAGACTGCCGCAGAAGG
CCTTCTGCGGCAGTCTTAAGATTTGGTGGTTGGATAATGCTACTTTCATTCCCACTATCCATTCCCCCACCGCCCTTGTA
GCATTATCCAACCACCAAATCTTAAGACTGCCGCAGAAGGAGATGTTAAAGAGTATATTGTGC
TAAAGGGAACAAAAGCTGGAGCTCCACCGCGGTGGCGGCCGCGTATGCAATGTCCACCTGCTCA
/5PHOS/AATTGCTGCGGTTTTTAAGTTTGG
/5PHOS/AAACCCAAACTTAAAAACCGCAGC
GGTCTTCATAGCGCTTGAAAGC
TCTTCCACGAGATCTCCGAGATC
GAAGAGCTCCTCTCCCTTGG
GAGGAACGGCGTATAAAGTGTCA
TCTTACTCCTCAAACCTAAAACAA
AAACTTGTTTTAGGTTTGAGGAGT
TCTTGTTAAATAGTTTAGAATTCTT
AAACAAGAATTCTAAACTATTTAAC
TCTTAGCCCATTGTTTTAGGTTTG
AAACCAAACCTAAAACAATGGGCT
TCTTGCCGCCATTTGCCTCGTCTTC
AAACGAAGACGAGGCAAATGGCGGC
TTCAGTTTTCCGGGAAACCGG
AGTGGAAAAGAAGAAGCGGCG
ACTTTTCCTCGTCCCTCGTG
AGCAGACCCAAGCATCTAACC
CGGCCAATTTGGTGCAGTTATTG
TGACATCGGAGCCTCGTTAC
GAATTTGCCGTTTGCCGAGC
GCAGTGAGAACGAAAATCGCGA
GGAAATCGGTGAACTGCAACAC
CAGGAATCACTTTCTCGACACCC

Allele	Application	Name
he278[Δ*ebp-2*] II	gRNA	oRS139
		oRS140
		oRS141
		oRS142
		oRS195
		oRS195
		oRS196
		oRS197
	Sequencing	oRS150
		oRS151
		oRS152
		oRS181
		oRS182
		oRS188
he258[*Peft-3::ph::egfp::lov::tbb-2-3'UTR*] IV	Repair template	oRS074
		oRS075
		oRS076
		oRS077
		oLF082
		oLF138
		oLF139
		oLF146
	gRNA	oRS131
		oLF087
	Sequencing	oRS22
		oRS067
		oRS070
		oLF035

	Sequence 5'-3'
	TCTTGTTTCAGAAACCGAGGCAAAA
	AAACTTTTGCCTCGGTTTCTGAAAC
	TCTTGCAGGCAAATCTGGACGATA
	AAACTATCGTCCAGATTTGCCTGC
	TCTTGCTCGTCGTTTTCAGAAACCG
	AAACCGGTTTCTGAAAACGACGAGC
	TCTTACGGGGATAGGATAAGCAAT
	AAACATTGCTTATCCTATCCCCGT
	TTCAGATTTCCAGCCCGAACG
	GAAGTTCTTCGCTTGCAGATGG
	TGGAGTCGGCTTGTTTCAGAG
	TGAAGAAGGCCAAGTTCCAGG
	AATGAGACCGGCGTACATCC
	GCGGCAGTTGGTTAGTCTATCTC
	TCCTGGAGCCCGTGCATTTTTGAGCAAAGTGTTTCCCAACTGA
	AAACACTTTGCTCAAAAATGCACGGGCTCCAGGATGAC
	TTGGACATTCCCCCACCGCCCTTCTGCCGCTGGTCCATG
	GGCAGAAGGGCGGTGGGGGAATGTCCAAGGGAGAGGAGCT
	AACAGTTTTGTCTTCCGACAGATGTGAGACGGAAAAATGGCCAAAATTCGAGATTTTGACTAAAATCAGTG
	CAATAAAAGACCAAAGGTGCGTTTGGACGCAAGTACACGATTG
	TCGTGTACTTGCGTCCAAACGCACCTTTGGTCTTTTATTGTCAACT
	AAATAGCAGGAAAATAAGAAATTTGGCCGTGTGTCACTAGTTGAGACTTTTTTCTTGGCGGC
	/5PHOS/TCTTAGCTCAATCGTGTACTTGCG
	/5PHOS/AAACCGCAAGTACACGATTGAGCT
	ACGGAGAACTTGTGTCCGTTGA
	GACTACTGTAGTGAGTACAGTAGGGC
	CCCCAAAACAAGTTGGAGGC
	ACATGGTCCTCAAGGAGTTCG

Supplementary table 3. **List of primers used in this study.** This table shows a summary of the primers used in this study. Primers are grouped by the CRISPR/Cas9-assisted genome engineering alleles that they were used for, and further subdivided based on their application (repair template or gRNA vector construction and sequencing).

Chapter 4

Optogenetic dissection of mitotic spindle positioning in vivo

Lars-Eric Fielmich[1,◊], **Ruben Schmidt[1,2,◊]**, Daniel J. Dickinson[3,4], Bob Goldstein[3], Anna Akhmanova[2] and Sander van den Heuvel[1]*

◊ These authors contributed equally to this publication

1 Developmental Biology, Department of Biology, Faculty of Sciences, Utrecht University, Padualaan 8, 3584 CH, Utrecht, The Netherlands.

2 Cell Biology, Department of Biology, Faculty of Sciences, Utrecht University, Padualaan 8, 3584 CH, Utrecht, The Netherlands.

3 Department of Biology and Lineberger Comprehensive Cancer Center, University of North Carolina at Chapel Hill, Chapel Hill, NC, 27599, USA

4 Current address: Department of Molecular Biosciences, University of Texas at Austin, Austin, TX, USA

* Corresponding author. Email: s.j.l.vandenheuvel@uu.nl; tel: +31302533573

The manuscript in this chapter was adapted from:
Fielmich, L.-E., **Schmidt, R.**, Dickinson, D.J., Goldstein, B., Akhmanova, A. and van den Heuvel, S. (2018). Optogenetic dissection of mitotic spindle positioning in vivo. eLife 7, 1–31.

Abstract

The position of the mitotic spindle determines the plane of cell cleavage, and thereby daughter cell location, size, and content. Spindle positioning is driven by dynein-mediated pulling forces exerted on astral microtubules, which requires an evolutionarily conserved complex of Gα·GDP, GPR-1/2P$^{Pins/LGN}$, and LIN-5$^{Mud/NuMA}$ proteins. To examine individual functions of the complex components, we developed a genetic strategy for light-controlled localization of endogenous proteins in *C. elegans* embryos. By replacing Gα and GPR-1/2 with a light-inducible membrane anchor, we demonstrate that Gα·GDP, Gα·GTP, and GPR-1/2 are not required for pulling-force generation. In the absence of Gα and GPR-1/2, cortical recruitment of LIN-5, but not dynein itself, induced high pulling forces. The light-controlled localization of LIN-5 overruled normal cell-cycle and polarity regulation and provided experimental control over the spindle and cell-cleavage plane. Our results define Gα·GDP–GPR-1/2$^{Pins/LGN}$ as a regulatable membrane anchor, and LIN-5$^{Mud/NuMA}$ as a potent activator of dynein-dependent spindle-positioning forces.

Introduction

Animal cells control the position of the spindle to determine the plane of cell cleavage. Regulated spindle positioning is therefore critical for asymmetric cell division and tissue formation (Pietro et al., 2016). Early work in *C. elegans* demonstrated that cortical pulling forces position the spindle through a protein complex that consists of a heterotrimeric G protein alpha subunit, GOA-1^{Gαo} or GPA-16^{Gαi} (together referred to as Gα), a TPR-GoLoco domain protein GPR-1/2, and the coiled-coil protein LIN-5 (Colombo et al., 2003; Gotta and Ahringer, 2001; Gotta et al., 2003; Grill et al., 2001; Lorson et al., 2000; Miller and Rand, 2000; Srinivasan et al., 2003). This complex, and the closely related *Drosophila* $Gα_{i/o}$–Pins–Mud and mammalian $Gα_{i/o}$–LGN–NuMA protein complexes, recruit the microtubule motor dynein to the cell cortex (Bellaïche et al., 2001; Bowman et al., 2006; Du and Macara, 2004; Du et al., 2001; Izumi et al., 2004; Nguyen-Ngoc et al., 2007; Schaefer et al., 2001; Zheng et al., 2010; Zhu et al., 2011) (**Figure 1a**). While regulation at the level of individual components has been described, it remains unclear whether these proteins only form a physical anchor for dynein, or whether individual subunits contribute additional functions in spindle positioning.

As a potential additional function, force generation may require a dynein adaptor that activates dynein motility. Such an adaptor is necessary for the processive movement of mammalian cytoplasmic dynein during cargo transport along microtubules (Reck-Peterson et al., 2018). This process differs substantially from microtubule-dependent cortical pulling, in which force is generated by dynein in association with shrinking microtubules (Laan et al., 2012). Without adaptor, surface-anchored yeast dynein in contact with depolymerizing microtubules generates pulling forces *in vitro* (Laan et al., 2012). However, yeast dynein

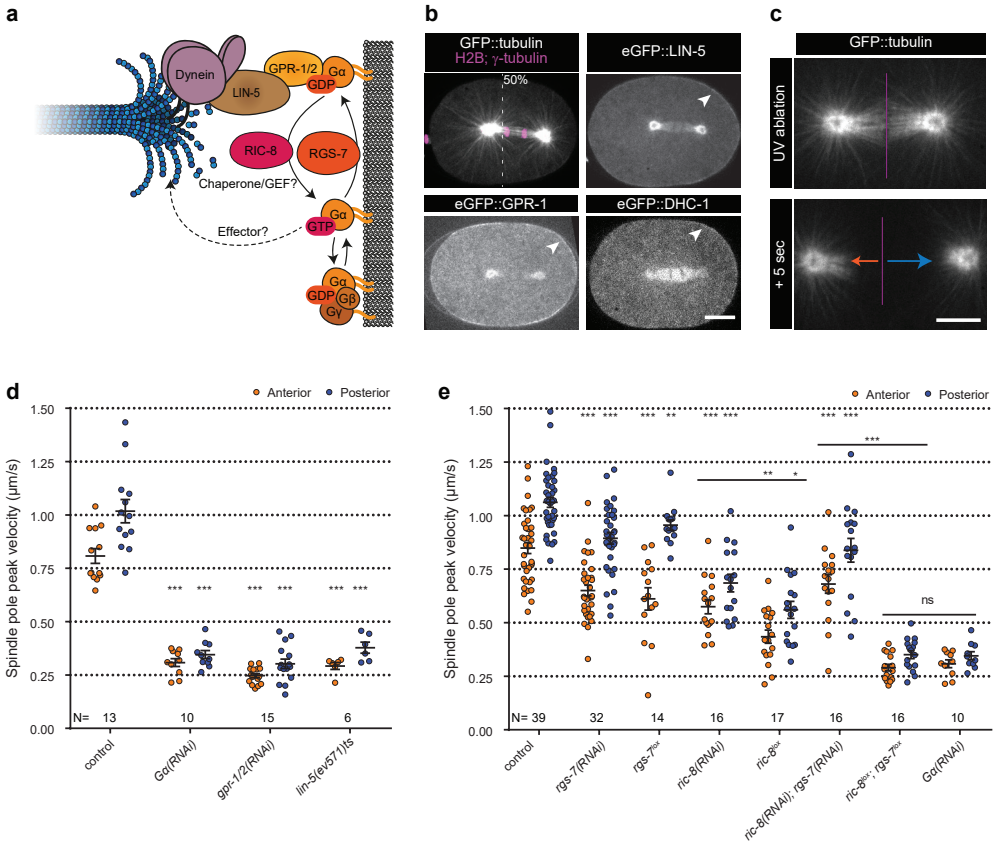

Figure 1. **Gα regulation by RIC-8 and RGS-7 is essential for cortical pulling force generation.** (**a**) Cartoon model representing mechanisms and functions discussed in the text. Gα·GDP–GPR-1/2–LIN-5–dynein anchors dynamic microtubule plus-ends and generates cortical pulling forces on the mitotic spindle. Gα·GDP can assemble a Gαβγ or Gα–GPR-1/2–LIN-5 trimer. The Gα·GDP/GTP nucleotide state is regulated by the GAP RGS-7. For RIC-8, functions as Gα GEF and chaperone are reported. Gα·GTP could promote spindle positioning through unknown downstream effectors. (**b**) Spinning disk confocal images of anaphase spindle positioning away from the cell center (white triangle) in the *C. elegans* zygote. The upper left panel shows the spindle with labeled tubulin and DNA. Other panels: endogenous GPR-1, LIN-5, and dynein (DHC-1) fused to eGFP are present in the cytoplasm, at the cortex (arrowheads), and spindle structures. Scale bar: 10 µm. (**c**) Spinning disk confocal images of the mitotic spindle (marked by GFP::tubulin). Upon UV-laser ablation of the spindle midzone (violet line), spindle poles separate with velocities that represent the respective net force acting on each pole (arrows). Scale bar: 5 µm. (**d**) Spindle pole peak velocities after midzone ablation. Control is *gfp::tubulin* strain. Other conditions: inactivation of Gα, GPR-1/2, and LIN-5. Error bars: s.e.m. Welch's Student's t-test; *** $P < 0.001$. (**e**) Spindle severing experiments in embryos where RIC-8 and RGS-7 were depleted by RNAi or induced tissue specific Cre-lox-mediated knockout of the endogenous gene (lox). Control is *gfp::tubulin* strain, see **figure 1-figure supplement 1** for knockout method and additional controls. Error bars: s.e.m. Welch's Student's t-test and Mann Whitney U test; * $P < 0.05$, ** $P < 0.01$, *** $P < 0.001$. See **supplementary table 1** for detailed genotypes. Anterior is to the left in all microscopy images.

moves processively on its own (Reck-Peterson et al., 2006). Hence, it remains unknown whether cortical pulling force generation in animal cells depends just on anchoring of dynein, or whether this requires an additional dynein activator.

The role of $G\alpha_{i/o}$ subunits in pulling force generation has also remained ambiguous (**Figure 1a**). Membrane-attached Gα·GDP associates with GoLoco motifs present in the homologous GPR-1/2, Pins, and LGN proteins (Kimple et al., 2002; Schaefer et al., 2001). This preference for the GDP-bound 'inactive' Gα state explains why RGS-7, a putative GTPase activating protein (GAP), promotes spindle positioning (Hess et al., 2004). However, the role of another conserved regulator of Gα signaling, RIC-8, remains poorly understood (Afshar et al., 2004; Miller and Rand, 2000; Tall et al., 2003). RIC-8 was shown to act as a guanine nucleotide exchange factor (GEF) in vitro, while it may function in vivo as a Gα chaperone or as both a GEF and chaperone (Afshar et al., 2004, 2005; David et al., 2005; Gabay et al., 2011; Hampoelz et al., 2005; Tall et al., 2003; Wang et al., 2005). In addition to RIC-8, G-protein coupled receptors and $G\alpha_o$·GTP signaling contribute to spindle positioning in *Drosophila* neuroblasts and sensory organ precursor cells (Katanaev et al., 2005; Schaefer et al., 2001; Yoshiura et al., 2012). Therefore, it has been proposed that the Gα·GTP-binding and hydrolysis cycle forms a critical step in cortical pulling force generation (Afshar et al., 2004; Srinivasan et al., 2003; Yoshiura et al., 2012). However, it is difficult to distinguish whether $G\alpha_o$·GTP contributes to force generation, or more indirectly relays cell-cell signaling to the spindle.

Here, we describe an optogenetic strategy for the systematic examination of individual contributions of cortical pulling force components in vivo. We use the *C. elegans* one-cell embryo (P0), which undergoes reproducible spindle positioning and asymmetric cell division in the absence of cell-cell signaling (**Video 1**) (Rose and Gönczy, 2014). As an initial hurdle, modifying endogenous genes with tunable light-controlled interacting protein tags (TULIPs) induced strong germline silencing. We developed a strategy to promote expression of foreign sequences in the *C. elegans* germline, which is based in part on a new codon usage adaptation method (GLO, GermLine Optimized). This allowed the light-controlled localization of endogenous proteins through ePDZ–LOV domain interactions in the early *C. elegans* embryo. Our results show that Gα·GDP and GPR-1/2 can be replaced with a light-inducible membrane anchor, while LIN-5 is required as activator of dynein-dependent cortical pulling force generation. Local light-controlled LIN-5 recruitment enabled us to manipulate the spindle position and orientation, and thereby the outcome of cell division in the early embryo.

Results

Germline-specific gene knockout reveals that RIC-8 and RGS-7 cooperate in positive Gα regulation and cortical pulling force generation

We set out to systematically investigate the individual roles of the proteins involved in cortical pulling force generation. Our previous studies and CRISPR/Cas9-assisted endogenous tagging demonstrated that cytoplasmic dynein and the Gα–GPR-1/2–LIN-5 complex overlap and function together in pulling force generation at the cell cortex of *C. elegans* early blastomeres (**Figure 1b**) (Portegijs et al., 2016; Schmidt et al., 2017; van der Voet et al., 2009). As a read-out for pulling forces, we measured spindle pole peak velocities after UV-laser ablation of the spindle midzone (Grill et al., 2001) (**Figure 1c** and **video 2**). Interfering with Gα, GPR-1/2, or LIN-5 function abolished significant force generation, as previously reported (**Figure 1d**). RNA interference (RNAi) of *ric-8* or *rgs-7* by dsRNA injection resulted in partial loss of pulling forces (**Figure 1e**). Double *ric-8(RNAi); rgs-7(RNAi)* did not further decrease pulling forces as might be expected when RIC-8 and RGS-7 both promote a critical GTPase cycle (Hess et al., 2004; Srinivasan et al., 2003). However, RNAi of *ric-8* and *rgs-7* is known to cause incomplete gene inactivation, which could also explain the limited defects. To circumvent this caveat, we set out to generate germline-inducible knock-out alleles, as *ric-8* and *rgs-7* null mutants produce no or very few viable progeny (Hess et al., 2004; Reynolds et al., 2005). To this end, we inserted *lox* sites in the endogenous *ric-8* and *rgs-7* loci by CRISPR/Cas9-assisted recombineering (**Figure 1-figure supplement 1**), and expressed the CRE recombinase specifically in the germline (**Figure 1-figure supplement 1**). Compared to the control without CRE activity, knockout embryos showed reduced spindle pole peak velocities *(ric-8^{lox}*: anterior -50% and posterior -48%; *rgs-7^{lox}*: anterior -29% and posterior -11%), similar to or more defective than the corresponding RNAi embryos (**Figure 1e** and **Figure 1-figure supplement 2**). Importantly, the double knock-out of *ric-8^{lox}; rgs-7^{lox}* showed much reduced spindle pole movements (anterior -68% and posterior -67%), thereby resembling *Gα(RNAi)* (**Figure 1e**). This indicates that RIC-8 and RGS-7 act independently, or partly redundant, as positive regulators of Gα.

Germline-optimized codon adaptation promotes germline expression of transgenes

To gain further insight into the individual functions of cortical pulling force regulators, we sought to obtain spatiotemporal control of protein localization. To this end, we explored implementing the ePDZ–LOV system, which makes use of exposure to blue light to control protein heterodimerization (Harterink et al., 2016; Strickland et al., 2012). As introduction of *epdz*, *lov*, and *cre* sequences induced strong germline silencing responses, we developed a computational approach to design protein-coding sequences that are resistant to silencing in the germline. Our design algorithm assembles a coding sequence

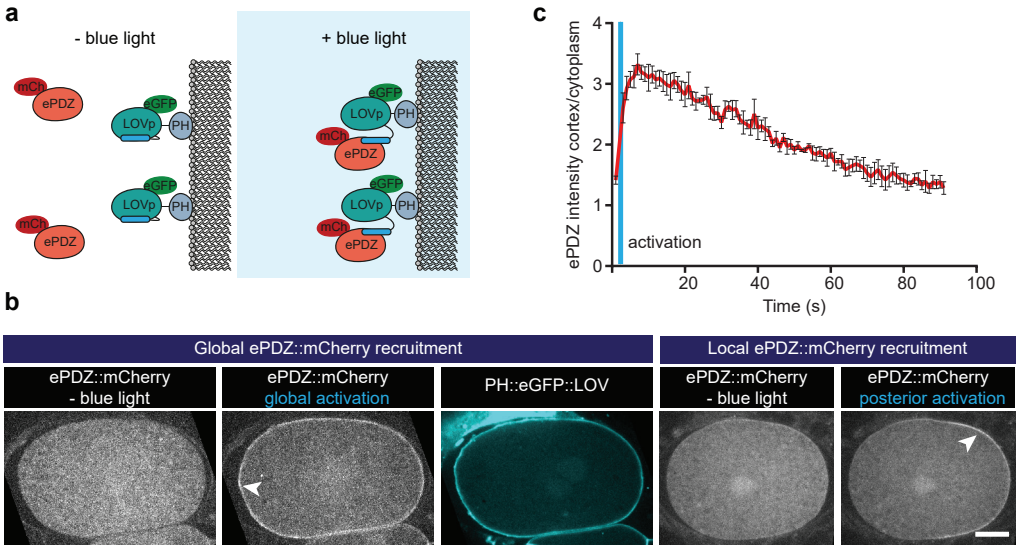

Figure 2. **Optimized ePDZ–LOV enables light-inducible control of endogenous protein localization in the *C. elegans* one-cell embryo.** (**a**) Cartoon model illustrating the proof of concept wherein cytosolic ePDZ::mCherry is cortically recruited to membrane PH::LOV upon activation with blue light. Blue fields indicate conditions in which both ePDZ- and LOV components are present, and an ePDZ–LOV interaction is induced with blue light. (**b**) Spinning disk confocal images showing light-controlled localization of proteins in the *C. elegans* zygote (arrowheads). See materials & methods for the local activation procedure. Also see **videos 3-5**. Scale bar: 10 µm. Anterior is to the left in all microscopy images. (**c**) Quantification of cortical ePDZ::mCherry enrichment measured over time after a 1 second pulse activation (blue vertical line). Error bars: s.e.m. $t^1/_2$ calculated with single component non-linear regression.

for any desired polypeptide from a list of 12-nucleotide words found in native germline-expressed genes (**Figure 2-figure supplement 1**). We hypothesized that transgenes designed in this way would mimic native genes and thereby evade the germline silencing machinery. Indeed, using this approach, we could obtain robust expression of several foreign transgenes that were otherwise silenced (**Figure 2-figure supplement 2**). Although most of these transgenes were stably expressed for many generations, two out of 16 distinct constructs tested showed evidence of gradual silencing when passaging strains in culture (**Figure 2-figure supplement 3**). Therefore, as a further buffer against silencing, we combined our germline-optimized exons with poly-AT-cluster rich intron sequences, which were recently demonstrated to protect against germline silencing (Frøkjær-jensen et al., 2016; Zhang et al., 2018). This combined approach resulted in stable germline expression of eight out of eight transgenes and enabled implementation of the ePDZ–LOV system for use in the *C. elegans* early embryo.

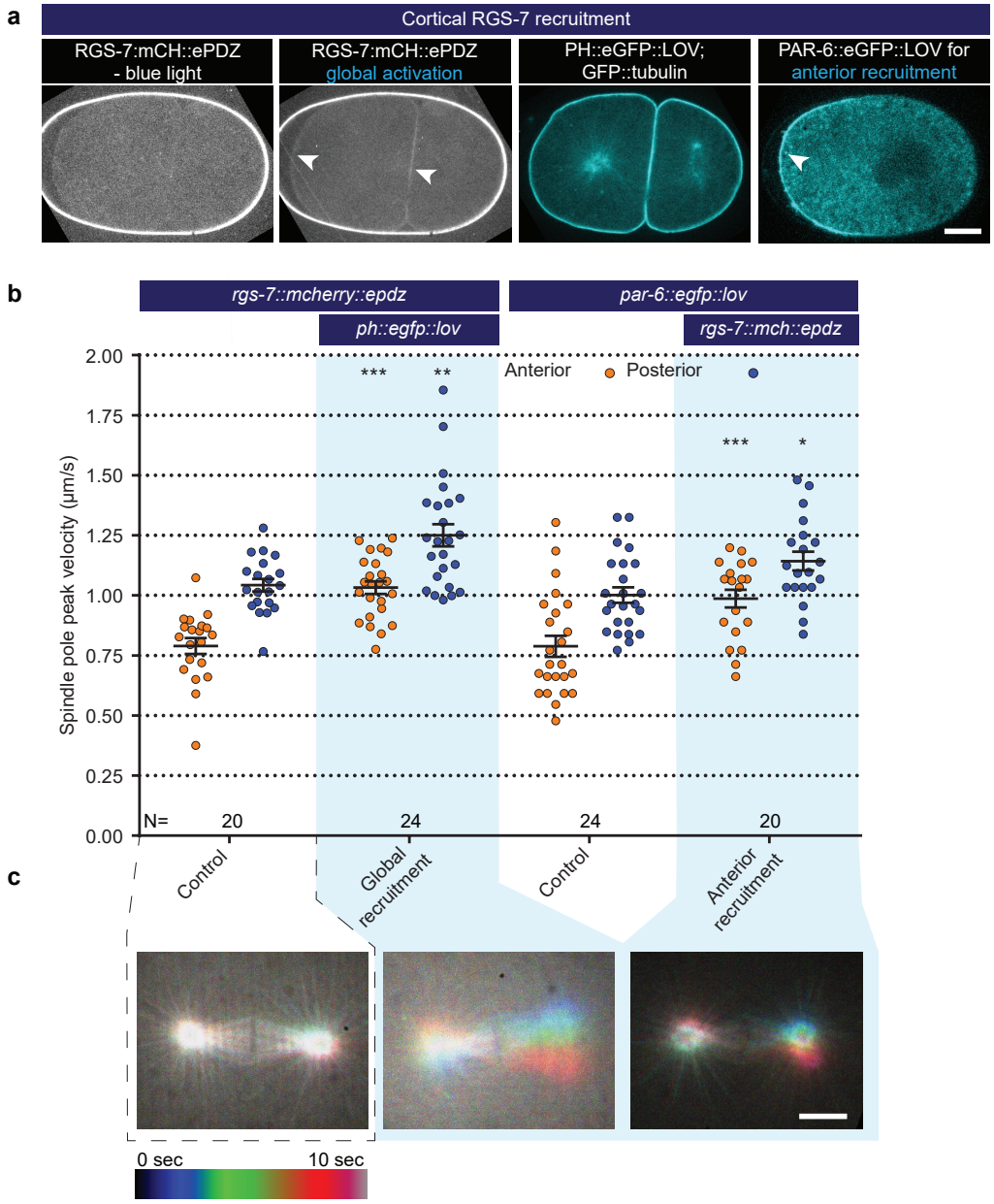

Figure 3. **Light-controlled localization of endogenous Gα regulator RGS-7 in the *C. elegans* embryo.** (**a**) Light-controlled localization of endogenous RGS-7 to membrane PH::LOV (arrowheads, note that the eggshell shows strong autofluorescence in the red channel). Most right panel: anterior localization of PAR-6::eGFP::LOV. Scale bar: 10 µm. (**b**) Spindle severing experiments after light-induced cortical localization of RGS-7 (blue fields). Controls are *rgs-7::mcherry::epdz* and *par-6::egfp::lov* strains. Experimental conditions: combination with *ph::egfp::lov* and *rgs-7::mcherry::epdz*. Blue fields indicate conditions in which both ePDZ- and LOV components are present, and an ePDZ–LOV interaction is induced with blue light. Blue light activation was global and continuous. Error bars: s.e.m. Welch's Student's *t-test*;

* $P < 0.05$, ** $P < 0.01$, *** $P < 0.001$. (**c**) Maximum projections of spindle movements for 10 seconds using a temporal color coding scheme to visualize spindle movement. A stationary spindle produces a white maximum projection, whereas a mobile spindle leaves a colored trace. Scale bar: 5 µm.

An optimed ePDZ-LOV system enables subcellular control of protein localization in the *C. elegans* early embryo

To characterize the ePDZ–LOV system, we created a strain with a membrane-bound LOV2 domain, expressed as a pleckstrin-homology domain (PH)–eGFP protein fusion (PH::LOV), together with cytosolic ePDZ::mCherry (**Figure 2a**). Illumination with a blue (491 nm) laser rapidly induced recruitment of ePDZ::mCherry to PH::LOV, and allowed both global and local cortical enrichment in one-cell embryos (**Figure 2b** and **videos 3-5**). Because GFP is also excited with blue light, experiments that involve GFP imaging imply global and continuous induction of the ePDZ–LOV interaction. To test the reversibility of the ePDZ–LOV interaction, we followed ePDZ::mCherry membrane localization after a global activation pulse, and found dissociation kinetics similar to those reported by others (Hallett et al., 2016) (t ½=42 s; **Figure 2c** and **video 6**). Thus, we conclude that the ePDZ–LOV system is suitable for controlled protein localization in the early *C. elegans* embryo.

Next, we examined whether membrane recruitment of RGS-7 and RIC-8 promotes pulling forces. This could provide insight into the in vivo relevance of the Gα·GDP/GTP cycle and indicate whether RIC-8 is more likely to contribute as a chaperone or as a GEF. Regulation of the Gα·GDP/GTP cycle normally takes place at the cell membrane, while chaperoning of Gα folding and trafficking is expected to occur in the cytosol and at endomembranes (Gabay et al., 2011). We created strains expressing endogenous RIC-8 and RGS-7 as ePDZ::mCherry protein fusions. When combined with PH::LOV, this resulted in light-inducible membrane recruitment of RIC-8 and RGS-7 (**Figure 3a**, **4a**, and **video 7**). Global cortical enrichment of RGS-7 enhanced spindle pole movements (anterior +25% and posterior +20%) (**Figure 3b**) and spindle oscillations (**Figure 3c**). The RGS-7::ePDZ signal was too subtle to reliably control its local recruitment. As an alternative strategy, we fused eGFP::LOV to endogenous PAR-6, which localizes to the anterior cortex of the zygote (**Figure 3a**). Following global light exposure, recruitment of RGS-7::ePDZ to PAR-6::LOV enhanced the peak velocities of both spindle poles, but most significantly the movement of the anterior pole (anterior +25% and posterior +14%; **Figure 3b**, **c**). Thus, cortical recruitment of RGS-7 acutely increases pulling forces, in agreement with its proposed function as a GAP that promotes Gα·GDP–GPR-1/2 interaction. In contrast, cortical enrichment of RIC-8 did not significantly enhance pulling forces (**Figure 4b**). Thus, in agreement with the *ric-8^{lox}; rgs-7^{lox}* synergistic phenotype, our optogenetic localization experiments support a model in which RIC-8 and RGS-7 promote Gα function at different levels. While RGS-7 probably functions as a GAP, our data are in line with RIC-8 acting in vivo as a Gα chaperone, rather than a GEF, thus indirectly promoting force generation.

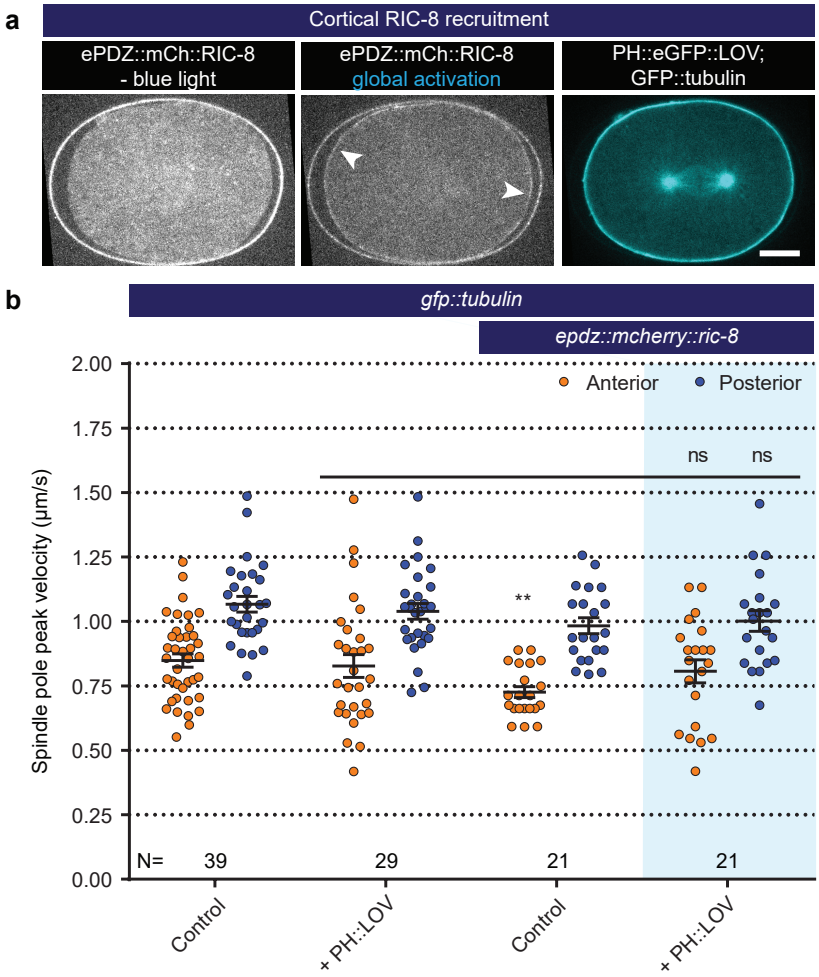

Figure 4. **Light-controlled localization of the endogenous Gα regulator RIC-8 in the *C. elegans* embryo.** (**a**) Light-controlled localization of endogenous RIC-8 to membrane PH::eGFP::LOV (arrowheads, note that the eggshell shows strong autofluorescence in the red channel). Scale bar: 10 µm. (**b**) Spindle severing experiments after light-induced cortical localization of RIC-8 (blue fields). Controls are *gfp::tubulin* and *epdz::mcherry::ric-8* strains. Experimental conditions: combination with *ph::egfp::lov*. Blue fields indicate conditions in which both ePDZ- and LOV components are present, and an ePDZ–LOV interaction is induced with blue light. Error bars: s.e.m. Welch's Student's t-test; ns $P > 0.05$. See **supplementary table 1** for detailed genotypes. Anterior is to the left in all microscopy images.

Membrane anchoring of GPR-1$^{Pins/LGN}$ in the absence of Gα reconstructs a cortical pulling force generator

To directly address whether Gα·GTP might contribute to spindle positioning and if Gα·GDP serves merely as a membrane anchor, we aimed to reconstruct a cortical force generator in the absence of Gα (**Figure 5a**). We obtained optogenetic control over the membrane

localization of GPR-1 by combining endogenously labeled *epdz::mcherry::gpr-1* (ePDZ::GPR-1) with knockout of *gpr-2*, expression of PH::LOV and Gα RNAi (**Figure 5b**, **c**, and **video 8**, **9**). Live imaging and immunohistochemistry confirmed light-induced cortical recruitment of ePDZ::GPR-1 and consequently LIN-5 (**Figure 5b** and **figure 5-figure supplement 1**). Spindle movements appeared reduced following the tagging of *gpr-1* and knockout of *gpr-2* (anterior -40% and posterior -26%) (**Figure 5-figure supplement 2**). However, light-induced ePDZ::GPR-1 recruitment increased spindle pole movements (anterior +56% and posterior +10%) (**Figure 5d**, **f**). Moreover, membrane-localized ePDZ::GPR-1 sustained force generation in the absence of Gα (anterior +195% and posterior +232%), indicating that Gα is dispensable for cortical pulling force generation. Recruitment of ePDZ::GPR-1 restored spindle pole movements to a similar degree in *Gα(RNAi)* and *Gα(RNAi); ric-8(RNAi)* embryos (**Figure 5d**). Thus, cortical pulling forces can be generated when the Gα membrane anchor function is replaced by PH::LOV, and most likely in the absence of $G\alpha_{i/o}$·GTP. We conclude that Gα functions as a membrane anchor and that Gα·GTP does not perform an essential function in pulling force generation.

Light-controlled heterodimerization exhibits a certain level of dark state activity (Hallett et al., 2016). We performed spindle severing experiments in the absence of blue light to confirm the light-specificity of recruitment. Replacement of *gfp::tubulin* with an *mcherry::tubulin* transgene allowed for tracking of the spindle in the absence of blue light and consequently LOV activation. We observed that the scattering of UV-light (355 nm) during midzone ablation also uncages the LOV domain. Nevertheless, the presence of blue light resulted in substantially elevated spindle pulling forces when compared to dark state experiments (anterior +33% and posterior +35%) (**Figure 5e**). We conclude that the observed spindle pole movements are light-dependent and the specific result of inducible cortical recruitment of GPR-1.

Considering that spindle poles moved in three dimensions after recruitment of GPR-1, measuring peak velocities after midzone severing by tracking the poles in two dimensions likely underestimates the resulting pulling forces. Therefore, we used an additional read-out of cortical pulling forces. Cortical pulling events cause inward movements of the plasma membrane, which are visible by spinning disk-confocal fluorescence microscopy as extended invaginations of the plasma membrane (Redemann et al., 2010) (**Figure 5g** and **video 10**, **11**). These membrane invaginations occur in wild type embryos, depend on microtubules and cortical force generator components, and correlate with the distribution of pulling force generators (Redemann et al., 2010). Therefore, these membrane invaginations most likely reveal the presence and distribution of active individual force generators.

Using spinning disk confocal microscopy, we quantified membrane invaginations by counting the number of transient cortical PH::GFP dots in the sub-cortical plane. Control PH::GFP embryos showed on average 138 membrane invaginations during anaphase in

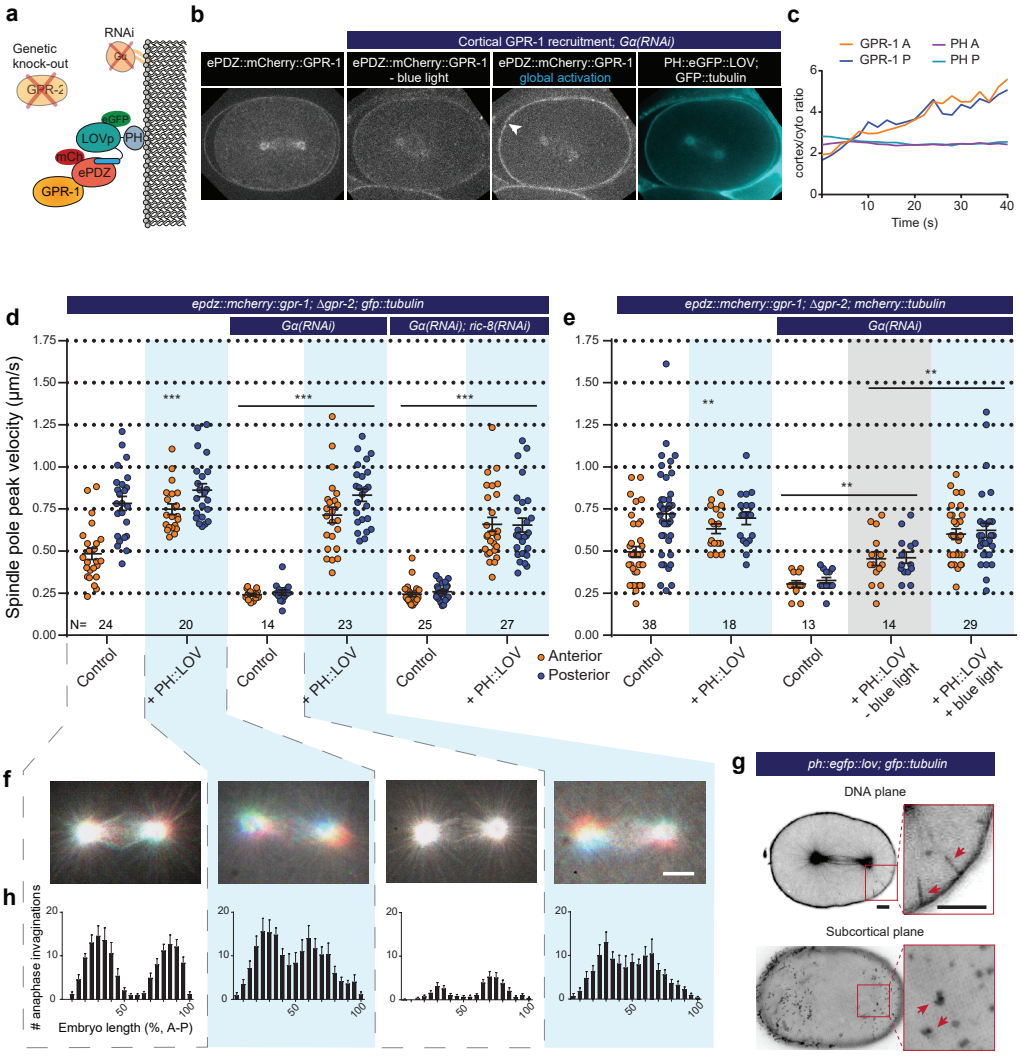

an area covering approximately $^{1}/_{3}$ of the cell surface (**Figure 5g**). When plotted along the anterior-posterior axis, the distribution of these invaginations reflected the three described cortical domains: anterior, posterior, and a posterior lateral region at ±60% embryo length (Rose and Gönczy, 2014) (**Figure 5h-**left). The posterior lateral band region localizes the LET-99 DEP-domain protein, which antagonizes the localization of GPR-1/2 and thereby pulling force generation (Krueger et al., 2010; Tsou et al., 2003). This explains the absence of invaginations around 60% embryo length (**Figure 5h-**left).

Cortical GPR-1 recruitment resulted in a total number of 174 (+25% compared to *ph::lov* control) invaginations in the presence, and 122 invaginations (+249% compared to *Gα(RNAi)* embryos) in the absence of Gα (**Figure 5** and **figure 5-figure supplement 3**).

Figure 5. **Light-inducible GPR-1 recruitment to the cortex rescues pulling force generation in the absence of** Gα. (**a**) Cartoon model illustrating the experiment that localizes GPR-1 directly to the membrane, bypassing the wild type membrane anchor Gα which is inactivated by RNAi. (**b**) Spinning disk confocal images of light-controlled cortical GPR-1 recruitment independent of the wild type anchor Gα (arrowheads; note the autofluorescent eggshell in the mCherry channel). Scale bar: 10 µm. (**c**) Quantification of cortical GPR-1 recruitment during continuous activation of the ePDZ–LOV interaction, represented as the ratio of cortical/cytoplasmic signal. Also see **video 8**, **9**. (**d**) Spindle severing experiments in combination with cortical recruitment of endogenous GPR-1. Control is the *epdz::mch::gpr-1; Δgpr-2; gfp::tubulin* strain. Experimental conditions: combinations with *ph::egfp::lov*, *Gα(RNAi)*, and *Gα(RNAi); ric-8(RNAi)*. Blue fields indicate conditions in which both ePDZ- and LOV components are present, and an ePDZ–LOV interaction is induced with blue light. Blue light activation was global and continuous. Error bars: s.e.m. Welch's Student's *t-test* and Mann Whitney U test; ** $P < 0.01$, *** $P < 0.001$. (**e**) Spindle severing experiments in combination with cortical recruitment of endogenous GPR-1. Control is the *epdz::mch::gpr-1; Δgpr-2; mcherry::tubulin* strain. Experimental conditions: combinations with *ph::egfp::lov*, *Gα(RNAi)*, and the absence of blue light (grey field). Blue fields indicate conditions in which an ePDZ- and LOV component are present, and an ePDZ–LOV interaction is induced using blue light. Blue light activation was global and continuous. Error bars: s.e.m. Welch's Student's *t-test* and Mann Whitney U test; ** $P < 0.01$, *** $P < 0.001$. (**f**) Maximum projections of spindle movements for 10 seconds using a temporal color coding scheme to visualize spindle movement as in **figure 3c**. (**g**) Plasma membrane invaginations resulting from cortical pulling forces are visible as lines in the DNA plane and dots in the subcortical plane (red arrows). Larger structures are membrane ruffles, which are distinct from the more dynamic invaginations, as can be seen in **video 11**. Scale bar: 5 µm. (**h**) Distribution of anaphase membrane invaginations plotted along anterior-posterior embryo length. Conditions were the same as for the connected experiments in d and f, except for the control, which was the *ph::egfp::lov; gfp::tubulin* strain and not *epdz::mch::gpr-1; Δgpr-2*. Scale bar: 5 µm. Blue fields indicate conditions in which ePDZ and LOV components are present, and an ePDZ–LOV interaction is induced using blue light. See **supplementary table 1** for detailed genotypes. Anterior is to the left in all microscopy images.

Thus, in agreement with our observations in spindle severing assays, GPR-1 recruitment to the membrane induces cortical pulling forces, even in the apparent absence of Gα proteins. The lack of invaginations around 60% embryo length was no longer detected when ePDZ::GPR-1 was recruited to PH::LOV. In agreement, the characteristic dip in cortical GPR-1 localization (e.g.: **figure 1b**) was no longer detected after ectopic GPR-1 recruitment (**Figure 5b**). Thus, as expected, LET-99 does not antagonize the cortical recruitment of ePDZ::GPR-1 by PH::LOV, in contrast to the Gα·GDP-mediated localization of endogenous GPR-1/2. The pattern of invaginations still showed two peaks and a mild dip at 50% embryo length (**Figure 5h**). The remaining peak numbers of invaginations likely represent the cortical regions closest to the spindle poles, as these sites contact the highest numbers of astral microtubules. Taken together, Gα is not essential for force generation, but the characteristic distribution of force generating events is likely regulated in part at the Gα protein or Gα–GPR-1/2 protein interaction level.

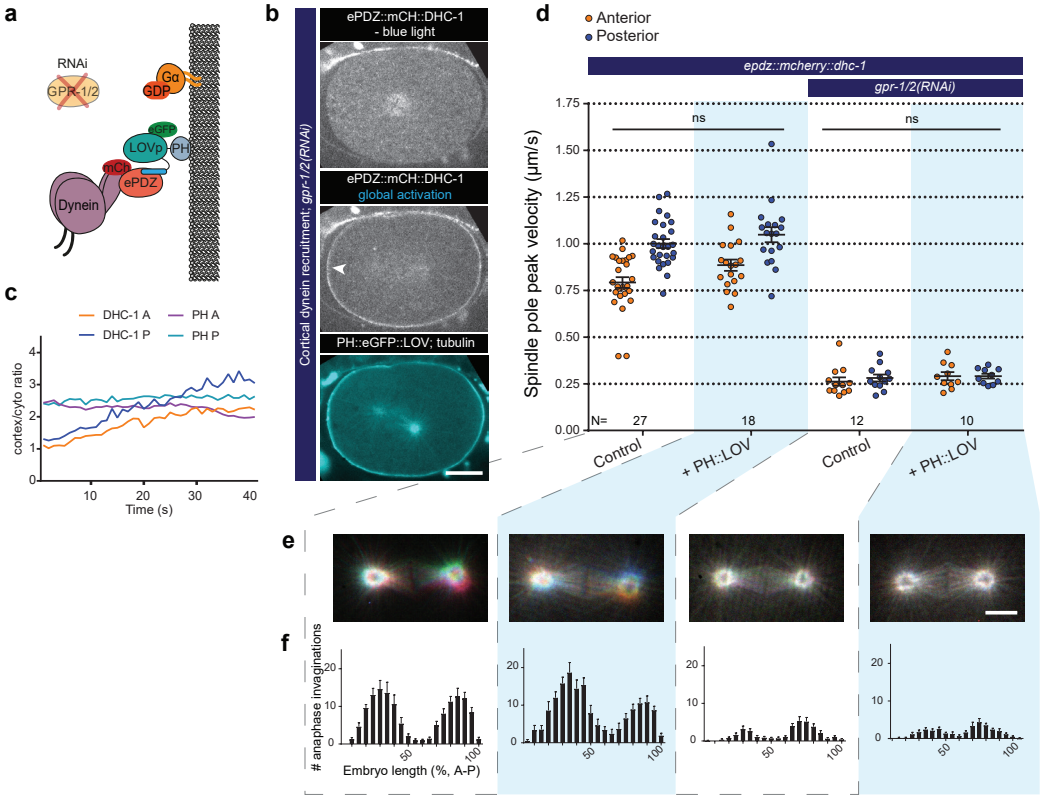

Figure 6. **Direct cortical anchoring of dynein (DHC-1) is insufficient for cortical pulling force generation.** (**a**) Cartoon model illustrating the experiment where dynein is recruited directly to the cortex. The wild type force generator complex is inactivated by RNAi. (**b**) Spinning disk confocal images showing light-controlled recruitment of dynein to the cortex (arrowheads, note the autofluorescent eggshell in the mCherry channel). Scale bar: 10 µm. (**c**) Quantification of cortical dynein recruitment during continuous activation of PH::LOV with blue light. (**d**) Spindle severing experiments with cortical dynein recruitment. Control is the *epdz::mch::dhc-1; gfp::tubulin* strain. Experimental conditions: combination of *ph::egfp::lov* and *gpr-1/2(RNAi)*. Blue light activation was global and continuous. Error bars: s.e.m. Welch's Student's t-test and Mann Whitney U test; ns $P > 0.05$. (**e**) Maximum projections of spindle movements for 10 seconds using a temporal color coding scheme to visualize spindle movement as in **figure 3c**. Scale bar: 5 µm. (**f**) Distribution of anaphase membrane invaginations plotted along anterior-posterior embryo length. Conditions were the same as for the connected experiments in d and e, except for the control, which was the *ph::egfp::lov; gfp::tubulin* strain and not *epdz::mch::dhc-1*. Blue fields indicate conditions in which both ePDZ and LOV components are present, and an ePDZ–LOV interaction is induced with blue light. See **supplementary table 1** for detailed genotypes. Anterior is to the left in all microscopy images.

Direct cortical anchoring of dynein is insufficient for cortical pulling force generation

The Gα–GPR-1/2–LIN-5 complex has been suggested to function as a dynein anchor (Kotak et al., 2012; Pietro et al., 2016). Our optogenetic approach allows replacing the entire complex by PH::LOV, and examining whether the complex strictly acts as an anchor,

or whether individual components have additional functions (**Figure 6a**). To directly recruit dynein to the cortex, we generated an *epdz::mcherry* knock-in allele of *dhc-1* (dynein heavy chain). While homozygous *epdz::mcherry::dhc-1* (ePDZ::DHC-1) was viable, its combination with *ph::egfp::lov* was lethal. This effect was also observed for an ePDZ::GFP fusion of DHC-1 in the presence of PH::LOV, but not in the absence of PH::LOV or for mCherry::DHC-1 without the ePDZ domain. Therefore, we attributed the lethality to ePDZ–LOV dark state interactions that disturb essential dynein functions. We circumvented this effect by using *epdz::mcherry::dhc-1* in combination with a wild-type allele (*epdz::mcherry::dhc-1/+*) to control dynein localization (**Figure 6b**, **c** and **video 12**, **13**). We found that induced ePDZ::DHC-1 cortical recruitment in the presence of the wild type complex slightly (but not significantly) increased spindle pole movements (anterior +10% and posterior +5%, 162 membrane invaginations: +17%; **figure 6d-f**). In addition, cortical recruitment of ePDZ::DHC-1 slightly increased the nearly absent spindle pole movements in *lin-5(RNAi)* embryos (**Figure 6-figure supplement 2**). Notably, however, cortical ePDZ::DHC-1 recruitment in the absence of a wild type complex (*Gα(RNAi), gpr-1/2(RNAi)* or *lin-5(RNAi)* embryos) did not result in substantial pulling force generation, spindle movements, or membrane invaginations (**Figure 6d-f** and **figure 6-figure supplement 1**). Because direct cortical dynein anchoring does not support force generation, it is likely that the LIN-5 complex performs essential functions beyond providing a structural dynein anchor.

Cortical LIN-5$^{MuD/NuMA}$ is essential and sufficient for dynein-dependent pulling force generation

In vitro reconstitution studies established that homodimerizing adapters containing extended coiled-coil domains are critical for dynein activity (McKenney et al., 2014; Schlager et al., 2014). LIN-5 and its homologs NuMA and Mud are predicted to contain a long coiled-coil domain, to homodimerize, and to interact with dynein (Kotak et al., 2012; Lorson et al., 2000; Merdes et al., 1996). To investigate if LIN-5 can activate dynein-dependent force generation, we recruited endogenous LIN-5 to the cortex (**Figure 7a-c** and **video 14**, **15**). Spindle severing experiments and invagination counting revealed that cortical LIN-5 recruitment greatly increased spindle pulling forces in otherwise wild type embryos (anterior +131% and posterior +68%, 557 invaginations: +303%) (**Figure 7d**, **e** and **figure 7-figure supplement 1**). *gpr-1/2*(*RNAi)* embryos also showed strong dynein-dependent forces after cortical recruitment of LIN-5 (anterior +183% and posterior +244%, 429 invaginations: +1488%). In fact, cortical LIN-5 recruitment generated extreme premature pulling forces (**Video 16**) that could result in separation of centrosomes and their associated pronuclei even before formation of a bipolar spindle (**Video 17**). Therefore, embryos were kept in the absence of blue light until mitotic metaphase. Subsequent blue light exposure induced cortical LIN-5 recruitment within seconds, and the spindles showed excessive movements in all three dimensions well before cortical LIN-5

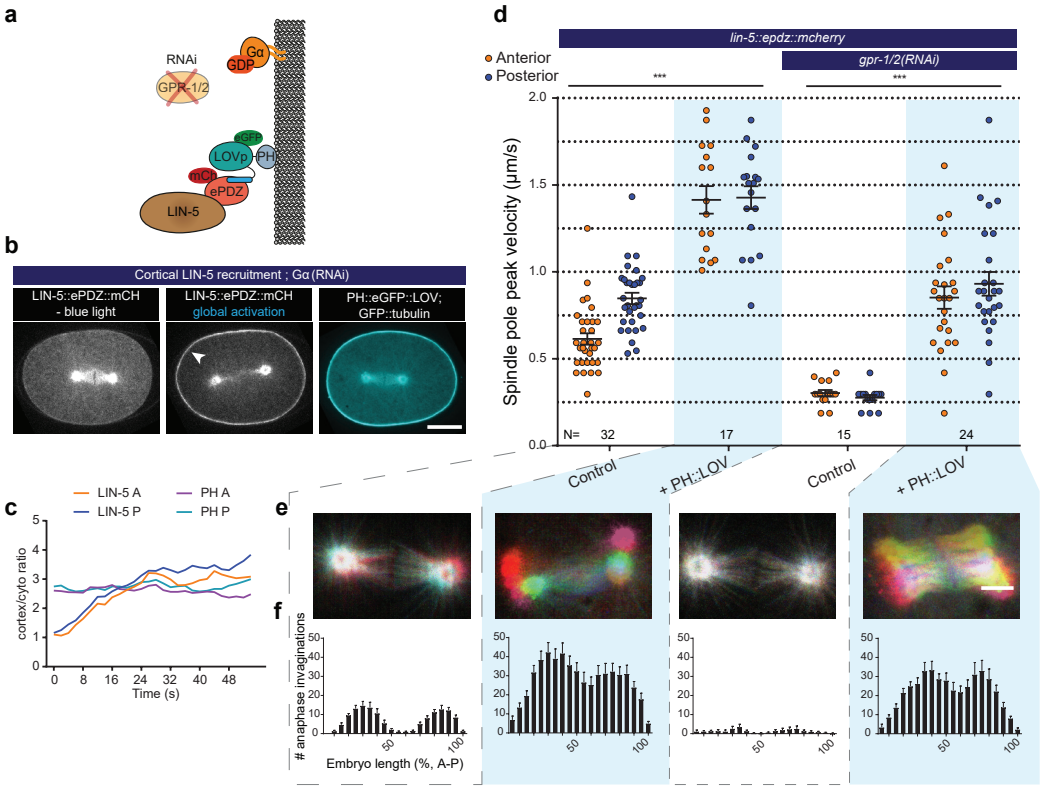

Figure 7. **LIN-5 is a strong and essential activator of dynein-dependent cortical pulling forces.** (**a**) Cartoon model illustrating the experiments in which LIN-5 is recruited to the cortex independently of the wild type Gα–GPR-1/2 anchor. (**b**) Spinning disk confocal images showing light-controlled recruitment of endogenous LIN-5 in the absence of Gα (arrow head). See also **video 14**, **15**. (**c**) Cortical LIN-5 recruitment during continuous activation of the ePDZ–LOV interaction, represented as the ratio of cortical/cytoplasmic signal. Scale bar: 10 µm. (**d**) Spindle severing experiments in combination with cortical recruitment of endogenous LIN-5. Control is the *lin-5::epdz::mcherry; gfp::tubulin* strain. Experimental conditions: combinations with *ph::egfp::lov* and *gpr-1/2(RNAi)*. Error bars: s.e.m. Welch's Student's t-test and Mann Whitney U test; *** $P < 0.001$. (**e**) Maximum projections of spindle movements for 10 seconds using a temporal color coding scheme to visualize spindle movement as in **figure 3c**. Scale bar: 5 µm. (**f**) Anaphase membrane invaginations plotted along anterior-posterior embryo length. Conditions were the same as for the connected experiments in d and e, except for the control, which was the *ph::egfp::lov; gfp::tubulin* strain and not *lin-5::epdz::mch*. Blue fields indicate conditions in which ePDZ and LOV components are present, and an ePDZ–LOV interaction is induced using blue light. See **supplementary table 1** for detailed genotypes. Anterior is to the left in all microscopy images.

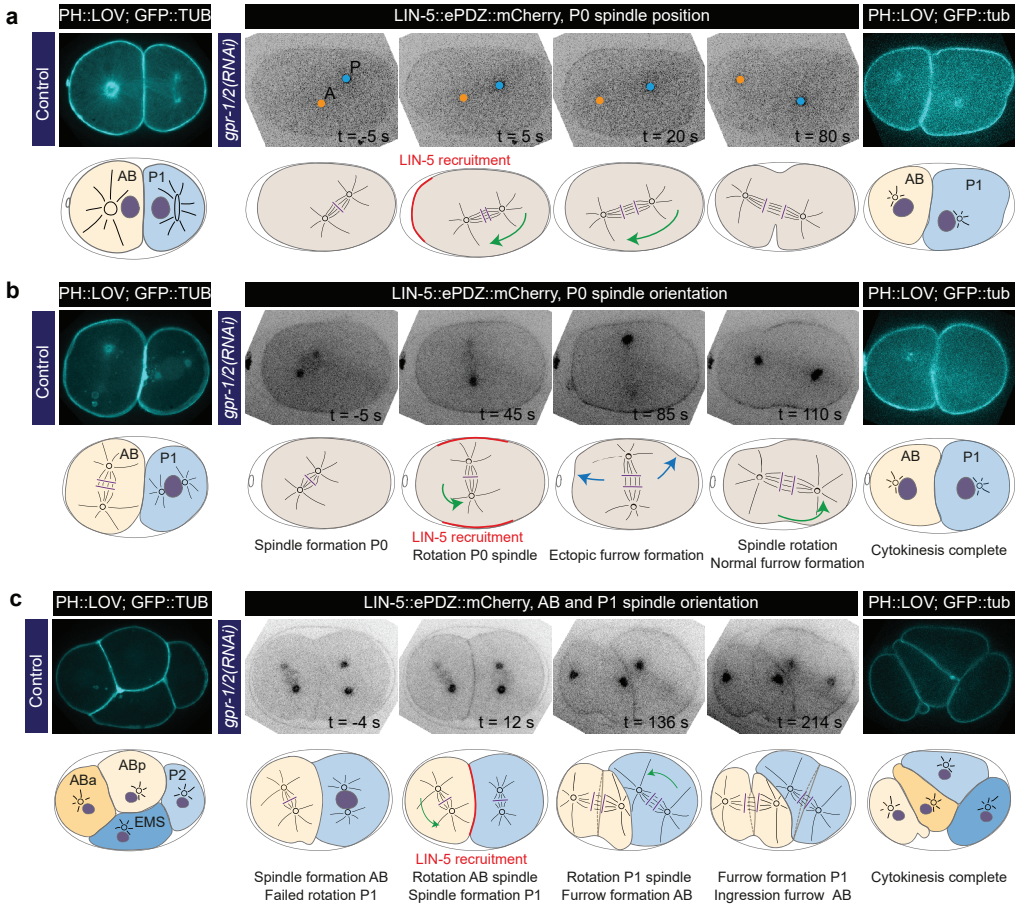

Figure 8. **Experimentally induced spindle positioning by controlled localization of endogenous LIN-5.** (**a**) Selected time points of **video 18** showing induced anterior displacement of the P0 spindle upon local cortical recruitment of LIN-5. Images are annotated with centrosome positions shown as circles (orange, anterior pole; blue, posterior pole). (**b**) Selected time points of **video 19** showing induced transverse P0 spindle orientation upon local cortical recruitment of LIN-5. Blue arrows, ectopic furrowing. (**c**) Selected time points of **video 20** showing induced AB and P1 spindle rotation upon local cortical recruitment of LIN-5. In **a**, **b**, and **c** panels 1-4 show LIN-5::ePDZ::mCherry fluorescence, panel 5 shows PH::LOV and GFP::tubulin. Cartoons accompanying images illustrate key events. Red, local LIN-5 recruitment. Green arrows, spindle movements. leftmost panels show control two- and four-cell embryos labeled with PH::eGFP::LOV and GFP::Tubulin. See Materials & Methods for the local activation procedure. See **supplementary table 1** for detailed genotypes. Anterior is to the left in all microscopy images.

reached peak levels (**Figure 7c**, **e**, **video 14**, **15**). Therefore, the number of membrane invaginations in anaphase probably reflects the pulling forces more accurately than the average peak velocities of the poles (**Figure 7f** and **figure 7-figure supplement 1**). These results identify LIN-5 as a strong activator of dynein in the generation of cortical pulling forces.

We observed similarly high pulling forces upon cortical LIN-5 recruitment in *gpr-1/2(RNAi)* and *Gα(RNAi)* embryos (**Figure 7-figure supplement 1**). Thus, neither Gα nor GPR-1/2 are required for force generation, and this particular context did not reveal a positive contribution of Gα·GTP either. In immunofluorescence staining experiments, we observed that cortical recruitment of LIN-5 localized dynein to the cortex (**Figure 7-figure supplement 2**). Notably, the reverse was also seen: we detected LIN-5 at the cortex following the direct recruitment of ePDZ::DHC-1 to PH::LOV, even after knockdown of *gpr-1/2* by RNAi (**Figure 6-figure supplement 2**, top). The p150(Glued) dynactin subunit DNC-1 was also present at the cell cortex of such embryos, which indicates that at least some PH::LOV-localized dynein complexes contain the dynactin cofactor (**Figure 6-figure supplement 2**, lower panels). DNC-1^{p150} colocalized with PH::LOV membrane-recruited dynein even in *lin-5(RNAi)* embryos. Thus, the cortical localization of dynein through a direct PH::LOV interaction leads to co-recruitment of LIN-5 and dynactin, but not to significant force generation. It is possible that these complexes adapt an inactive conformation or lack specific subunits of the dynein-dynactin motor complex. In contrast, dynein anchored at the cell cortex through the LIN-5 intermediate generated strong pulling forces. Together, these data indicate that association with membrane-attached LIN-5 is essential for dynein to generate cortical pulling forces.

Local LIN-5$^{Mud/NuMA}$ recruitment provides experimental control over spindle and cell cleavage plane positioning

Next, we examined whether we could deploy cortical LIN-5 to manipulate spindle positioning and the outcome of cell division by local illumination with blue light. In the normal P0 cell, the spindle is displaced towards the posterior and cell cleavage creates a larger anterior blastomere (AB) and a smaller posterior blastomere (P1). Local recruitment of LIN-5 to the anterior cortex from metaphase onwards caused the P0 spindle to position anteriorly, which inverted the AB:P1 size asymmetry after cell division (**Figure 8a** and **video 18**). In addition, recruiting LIN-5 laterally induced a completely perpendicular spindle position (**Figure 8b** and **video 19)**. While this triggered some furrowing at the anterior and posterior cell poles, the spindle switched back to an anterior-posterior orientation during cytokinesis, possibly resulting from geometric constraints. We therefore switched to two-cell embryos with the relatively round AB and P1 blastomeres. In two-cell *gpr-1/2(RNAi)* embryos, the spindle fails to rotate in P1, resulting in a transverse spindle orientation in both blastomeres (Srinivasan et al., 2003). Importantly, local recruitment of LIN-5 to the membranes between AB and P1 promoted anterior-posterior spindle

orientations in both blastomeres of *gpr-1/2(RNAi)* embryos (**Figure 8c** and **video 20**, **21**). These spindles maintained their anterior-posterior orientation throughout mitosis and induced cleavage furrows that reproducibly followed the spindle position. These experiments underline the determining role of LIN-5-dependent cortical pulling in spindle orientation and cell cleavage plane determination.

Discussion

Recent advances in CRISPR/Cas9-mediated genome engineering and optogenetics hold far-reaching potential for cell and developmental biology (Johnson and Toettcher, 2018; Waaijers and Boxem, 2014). We combined these strategies to systematically control the localization of endogenous proteins in the *C. elegans* early embryo by light-induced ePDZ–LOV heterodimerization, to determine their individual contributions in spindle positioning. This demonstrated that LIN-5, but not Gα, RIC-8 and GPR-1/2, is intrinsically required for dynein-dependent pulling force generation. Based on our quantitative analyses, we propose that Gα–GPR-1/2 provides a regulatable membrane anchor, while membrane-bound LIN-5 acts as an obligate adapter and activator of cytoplasmic dynein at the cell cortex.

Our observations fit with and expand on those from studies in which the LIN-5-related Mud and NuMA proteins where tethered to the cortex. In two earlier studies, this resulted in the conclusion that the NuMA complex acts as a dynein anchor, but substitution of components or Gα protein removal was not tested (Kotak et al., 2012; Ségalen et al., 2010). However, a very recent study of HeLa cells followed an optogenetic strategy similar to ours, and also observed that a membrane anchor cannot replace the entire Gα–LGN–NuMA complex (Okumura et al., 2018). As in *C. elegans* embryos, a CAAX membrane anchor could substitute for Gα–LGN in Hela cells, while dynein needed to be anchored through NuMA in order to generate spindle positioning forces (Okumura et al., 2018). Thus, observations in two different systems indicate that dynein activation at microtubule plus ends requires the LIN-5/NuMA adaptor protein, similar to the requirement for an activating dynein adaptor in cargo transport (McKenney et al., 2014; Schlager et al., 2014; Zhang et al., 2017).

It is tempting to speculate that activation by LIN-5^{NuMA} specifically promotes dynein function in generating membrane associated pulling forces. In the cytoplasm, dynein adopts an inactive conformation and does not show processive movement in the absence of an activating adaptor (Reck-Peterson et al., 2018). Adaptor proteins such as BicD2 and Hook3 interact with specific cargo as well as with the dynein tail regions and the universal activating complex dynactin (McKenney et al., 2014; Schlager et al., 2014; Zhang et al., 2017). Thereby, these adaptors promote the formation of stable and active dynein-dynactin-adaptor complexes. Recent stuctural analyses revealed that the coiled-coil regions of the adaptors extend in between dynein and dynactin, with multiple adaptor-

specific interaction sites, and with several adaptors promoting the recruitment of two dynein complexes in parallel (Grotjahn et al., 2018; Sladewski et al., 2018; Urnavicius et al., 2018).

Although structural studies have focused on factors promoting minus-end directed transport, it is likely that dynein-dependent cortical pulling forces also involve an activating adaptor. As such, LIN-5^{NuMA} could promote the assembly of stable dynein–dynactin-complexes and release dynein autoinhibition. It is remarkable, however, that direct recruitment of dynein to the cortex did not result in cortical pulling forces, despite the co-recruitment of LIN-5 and the dynactin subunit DNC-1^{p150}. At present, we do not know whether this reflects individual dynein–LIN-5 and dynein–dynactin interactions, or the formation of stable dynein–dynactin–LIN-5 complexes. The lack of pulling forces, despite co-recruitment of LIN-5^{NuMA} and DNC-1^{p150} together with dynein, may indicate that the complex needs to be anchored through LIN-5 in order to achieve a specific conformation and facilitate microtubule end-on pulling forces. Such a requirement could prevent inappropriate activation of dynein–dynactin–LIN-5^{NuMA} complexes in the cytoplasm. In the optogenetic experiments in HeLa cells, dynein also localized p150 at the membrane, however in contrast to our findings, NuMA was not observed to be co-recruited in this study (Okumura et al., 2018). While the reason for this discrepancy is currently unknown, it might be related to the remarkably different kinetics of the two systems. Using the TULIP system, we observed membrane localization of ePDZ-tagged endogenous proteins within seconds, whereas in the iLID experiments in HeLa cells accumulation took place over multiple minutes. It is possible that in the longer time frame, cytoplasmic dynein complexes are recruited to the cortex with adaptors other than NuMA.

Since only LIN-5 is strictly required for cortical pulling force generation, the question arises why a tripartite dynein anchor is conserved from worm to man. In yeast, dynein is localized by the single-component cortical anchor Num1, a coiled-coil domain protein with a PH-domain for membrane localization (Ananthanarayanan, 2016). Our ectopic ePDZ–LOV heterodimerization experiments show that membrane-tethered LIN-5 could suffice as a dynein anchor and activator, and that local regulation is needed to rotate and displace the spindle. Conceivably, the trimeric dynein anchor/adaptor evolved in metazoans to augment context-specific regulation and reduce stochastic activation of spindle pulling forces.

Which factors may normally control the Gα–GPR-1/2 membrane anchor? The LET-99 protein was previously reported to restrict the localization of GPR-1/2 in a posterior-lateral band region of the one-cell embryo, thereby contributing to higher net pulling forces in the posterior direction (Tsou et al., 2002, 2003). Our observation that direct membrane recruitment of GPR-1 overcomes this regulation is in agreement with LET-99 normally antagonizing Gα·GDP–GPR-1/2 interaction. Another level of Gα–GPR-1/2 regulation that remains incompletely understood is the contribution of RIC-8 in spindle positioning. The *ric-8* gene was discovered through “resistant to inhibitors of cholinesterase 8” mutants in

C. elegans, which are defective in $G\alpha_q$-stimulated neurotransmitter release (Miller et al., 2000). The discovery that *ric-8* acts also with GOA-1 in spindle positioning indicated a general role for RIC-8 in Gα regulation (Miller and Rand, 2000). Indeed, two different general functions have been reported. Based on in vitro experiments, mammalian RIC-8A acts as a non-receptor GEF, which surprisingly does not activate Gαβγ trimers, but shows higher affinity for free Gα·GDP and the Gα·GDP–LGN–NuMA complex (Tall and Gilman, 2005; Tall et al., 2003). In contrast, experiments in *Drosophila* and mouse embryonic stem cells demonstrated a chaperone function required for the cortical localization of Gα subunits (David et al., 2005; Gabay et al., 2011; Hampoelz et al., 2005; Wang et al., 2005). Only the *Drosophila* $G\alpha_i$ protein forms a complex with Pins–Mud (Schaefer et al., 2001), and *Drosophila* $G\alpha_i$, but not $G\alpha_o$, depends on RIC-8 for its cortical localization (David et al., 2005). Seemingly unifying these independently described RIC-8 functions, *C. elegans* RIC-8 was shown to exhibit both GEF and chaperone activity, depending on the Gα subunit (Afshar et al., 2004, 2005).

The *C. elegans* GOA-1 and GPA-16 Gα proteins act in a substantially redundant manner in spindle positioning, but diverge in other ways. GPA-16 is closest to the $G\alpha_i$ class, has been implicated only in spindle positioning, and depends on RIC-8 for its cortical localization (Afshar et al., 2005; Bergmann et al., 2003; Gotta and Ahringer, 2001). Thus, both *C. elegans* and *Drosophila* RIC-8 appears to act as a chaperone for $G\alpha_i$ to promote spindle positioning. Also similar to *Drosophila,* the $G\alpha_o$ GOA-1 subunit does not require RIC-8 for its membrane localization (David et al., 2005; Afshar et al., 2005). Instead, RIC-8 was reported to act as a GEF for GOA-1 (Afshar et al., 2004), and is usually considered to act as a GEF for $G\alpha_q$ and $G\alpha_o$ in neurotransmitter release. However, the contribution of a $G\alpha_o$ GEF in spindle positioning would mean that either Gα·GTP or Gα·GDP/GTP cycling promotes spindle pulling forces. Both of these possibilities seem unlikely in light of the results described here. The fact that Gα can be replaced with a PH–membrane anchor dismisses a general requirement for Gα·GTP in pulling force generation. Moreover, RIC-8 functioning in a Gα·GDP/GTP cycle is not supported by our knockout and membrane localization studies. Therefore, there is reason to question whether RIC-8 really functions as a GEF. The strongest support for such a function has come from in vitro experiments, in which RIC-8 showed rather inefficient GEF activity towards Gα·GDP (Kant et al., 2016; Thomas et al., 2008). It appears conceivable that incubation of Gα with a chaperone that affects its folding causes nucleotide dissociation. If correct, the membrane localized GOA-1 in *ric-8* mutants would reflect an incompletely functional form.

Despite the observed replaceability of Gα with a general membrane anchor, Gα·GTP has been reported to affect the spindle orientation in specific tissues (Katanaev et al., 2005; Schaefer et al., 2001; Yoshiura et al., 2012). In *Drosophila* neuroblasts and sensory organ precursor cells, canonical G-protein signaling is used to align cellular polarity with tissue polarity (Katanaev et al., 2005; Yoshiura et al., 2012). As such, Gα·GTP may indirectly contribute to spindle positioning. In addition, one of the *Drosophila* Pins GoLoco

domains was found to preferentially interact with $G\alpha_o$·GTP, thereby linking the spindle positioning machinery with canonical G-protein signaling (Kopein and Katanaev, 2009; Yoshiura et al., 2012). Thus, while not needed for the generation of dynein-dependent cortical pulling forces, further studies will need to reveal to what extent Gα·GTP contributes to spindle positioning in a tissue or developmental context specific manner.

For our in vivo dissection of spindle positioning, we developed and applied methods for germline-specific gene knockout, tagging of endogenous proteins, reliable expression of foreign sequences in the germline, and light-inducible protein heterodimerization. These methods further expand the molecular biology toolbox for in vivo studies and can be broadly applied to other biological processes. Of particular interest is the acquired possibility to experimentally control the position of the spindle, for instance for future studies aimed at deciphering how the spindle determines the plane of cell cleavage, and whether specific cell-cell contacts affect cell fate.

Materials and Methods

Key resources table

Reagent type (species) or resource	Designation	Source or reference	Identifiers	Additional information
strain, strain background (*Caenorhabditis elegans*)	All strains derived from N2	CGC		
Antibody	mouse polyclonal anti-LIN-5	Lorson et al. J Cell Bio, 2000		
Antibody	mouse monoclonal anti-FLAG M2	Sigma-Aldrich	Cat. No. F1804	
Antibody	rabbit polyclonal anti-DHC-1	Gonczy et al, J Cell Bio, 1999		
software, algorithm	GLO (germline optimized) sequence optimization algorithm	this study		accessible via http://104.131.81.59/

C. elegans strains and maintenance

The names and associated genotypes of *C. elegans* strains used in this study are included in **supplementary table 1**. Animals were maintained at either 15 or 20˚C as described previously (Brenner, 1974). Strains expressing both ePDZ and LOV protein motifs were regarded as light-sensitive and thus cultured in the dark, and transferred while using red light only. Animals were kept on plates that contained nematode growth medium (NGM) that had been seeded with OP50 *Escherichia coli* bacteria.

Molecular cloning

DNA vector-based repair templates to be used for CRISPR/Cas9-mediated genome editing were designed in A plasmid Editor (M. Wayne Davis) to include 500-1500 bp homology arms. These and all other sequences used were generated starting from either purified *C. elegans* genomic DNA or pre-existing vectors via PCR amplification using Q5 Hot Start High-Fidelity DNA Polymerase (New England Biolabs). A list of all cloning, repair template and genotyping primers (Integrated DNA technologies) and DNA templates used has been included in **supplementary table 2**. PCR fragments were gel purified (Qiagen), their concentrations measured using a BioPhotometer D30 (Eppendorf) and then ligated into pBSK by Gibson assembly (New England Biolabs). gRNA vectors were generated by annealing of antisense oligonucleotide pairs and subsequent ligation into BbsI-linearized pJJR50 or BsaI-linearized pMB70 using T4 ligase (New England Biolabs). All DNA vectors used for genome editing were transformed into DH5α competent cells and subsequently purified by midiprep (Qiagen).

Design of germline-optimized coding sequences

Custom Perl scripts were written to design germline-optimized coding sequences according to the algorithm described in the legend of **figure 2-figure supplement 1**. After designing each coding sequence, we inserted either 1) normal synthetic introns with the sequence gtaagttt(n36)ttttcag, where n36 is a 36 bp random DNA sequence with 30% GC content; or 2) PATC introns (Frøkjær-jensen et al., 2016). Our design algorithm is accessible via a web interface at http://104.131.81.59/, and the source code can be found at https://github.com/dannyhmg/germline. Germline-optimized sequences were synthesized as gBlocks (Integrated DNA Technologies) and single-copy transgenes were generated using standard methods (Frøkjær-Jensen et al., 2012). Please refer to **supplementary table 2** for detailed sequence features of each transgene.

Design of inducible germline-specific gene knockout

loxP and *loxN* sequences were integrated in the endogenous loci of essential genes (see CRISPR/Cas9-mediated genome editing section for details). For the FLP recombinase, the hyperactive FLP G5D variant (Schwartz and Jorgensen, 2016) was used (pMLS262, Addgene #73718). For germline-specific expression, we used a long version of the *pie-1*

promoter including enhancer sequences (pAZ132, a kind gift from A. A. Hyman). To initiate the recombination cascade, the germline-specific FLP expression vector was injected in P0 mothers with the following protocol to favor germline expression (Personal communication Oliver Hobert, Worm Breeders Gazette, February 21, 2013); linearized FLP construct (2 ng/µl), PvuII digested *E. coli* genomic DNA (150 ng/µl), co-injection marker *Pmyo-2::tdtomato* (2 ng/µl). Transgenic F1 animals were singled and allowed to lay eggs for at least 24 hrs. From F1 with 100% embryonic lethal broods (*ric-8* and *rgs-7* are essential for embryogenesis), early embryos were isolated and used for spindle severing experiments.

CRISPR/Cas9-mediated genome editing

Either the wild type N2 or SV1818 (*pha-1*(*e2123*ts) 4x outcrossed) *C. elegans* genetic background was used for the generation of CRISPR/Cas9 alleles. Injection mixes with a total volume of 50 µl were prepared in MilliQ H_2O and contained a combination of 50 ng/µl *Peft-3:cas9* (Addgene ID #46168 (Friedland et al., 2013) or 60 ng/µl pJW1285 (Addgene ID #61252 (Dickinson et al., 2013)), 50-100 ng/µl *u6::sgRNA* (targeting genomic sequences listed in **supplementary table 2**), 50 ng/µl of (PAGE-purified oligonucleotide) repair template and 2.5 ng/µl of the co-injection pharyngeal marker *Pmyo-2::tdtomato*. Injection mixes were spun down in a microcentrifuge (Eppendorf) for at least 10 minutes at 13,000 RPM prior to use. Young adult hermaphrodites were injected in the germline using an inverted micro-injection setup (Eppendorf). After injection, animals were singled and grown at 15 or 20˚C. F1 animals were then picked to a total of at least 96, and grown with two or three animals per plate for 7-8 days at 20˚C until freshly starved. Half a plate containing F2 and F3 animals was then washed off with M9 medium supplemented with 0.05% Tween-20, and subsequently lysed to extract genomic DNA. Some knock-ins were obtained using co-CRISPR selection: rescue of *pha-1*(*e2123*ts) (Ward, 2014), generation of visible *unc-22* (Kim et al., 2014) or *dpy-10* (Paix et al., 2015) phenotypes, or integration of an self-excisable cassette carrying a visible marker (Dickinson et al., 2015). Genotyping was carried out by PCR amplification with OneTaq polymerase (New England Biolabs) of genome sequences using primers annealing in the inserted sequence and a genomic region not included in the repair template. Confirmed alleles were subsequently sequenced (Macrogen Europe).

Spinning disk microscopy

Prior to live imaging, embryos were dissected from adult hermaphrodites onto coverslips (Menzel-Gläser) in 0.8x egg salts buffer (94 mM NaCl, 32 mM KCl, 2.7 mM CaCl2, 2.7 mM MgCl2, 4 mM HEPES, pH 7.5; (Tagawa et al., 2001)) or M9, and mounted on 4% agarose pads. Spinning disk imaging of embryos was performed using a Nikon Eclipse Tı with Perfect Focus System, Yokogawa CSU-X1-A1 spinning disk confocal head, Plan Apo VC 60x N.A. 1.40 oil and S Fluor 100x N.A. 0.5-1.3 (at 1.3, used for UV-laser photo-ablation)

objectives, Photometrics Evolve 512 EMCCD camera, DV2 two-channel beam-splitter for simultaneous dual-color imaging, Vortran Stradus 405 nm (100 mW), Cobolt Calypso 491 nm (100 mW), Cobolt Jive 561 nm (100 mW), Vortran Stradus 642 nm (110 mW) and Teem Photonics 355 nm Q-switched pulsed lasers controlled with the ILas system (Roper Scientific France/ PICT-IBiSA, Institut Curie, used for photo-ablation), ET-GFP (49002), ET-mCherry (49008), ET-GFPmCherry (49022) and ET-Cy5 (49006) filters, ASI motorized stage MS-2000-XYZ with Piezo Top Plate, and Sutter LB10-3 filter wheel. The microscope was operated using MetaMorph 7.7 software and situated in a temperature-controlled room (20˚C). The temperature of the stage and objective was controlled at 25˚C with a Tokai Hit INUBG2E-ZILCS Stage Top Incubator during experiments. Images were acquired in either streaming mode with 250 or 500 ms exposure, or time-lapse mode with 250, 500 or 1500 ms exposure and 2 or 5 second intervals. Laser power and exposure times were kept constant within experiments. For the quantification of membrane invaginations embryos were imaged by 250 ms exposure stream acquisition starting in the DNA plane at anaphase onset, as judged by GFP::Tubulin signal. During anaphase, the spinning disk imaging plane was moved as close to the membrane as possible while keeping the cytosol discernable from the membrane signal. Acquisitions were terminated at early telophase, as judged by the PH::eGFP::LOV signal. For experiments involving balanced *epdz::mcherry::dhc-1/+*, each animal was confirmed to be positive for *epdz::mcherry::dhc-1* by fluorescence before the experiment. Images acquired by spinning disk microscopy were rotated, cropped, annotated, provided with scale bars, and processed further by linear adjustment of brightness and contrast using ImageJ and FIJI. Fluorophores used in this study include (e)GFP, mCherry, Alexa 488, Alexa 568 and Atto 647N.

RNA-mediated interference (RNAi)

For immunohistochemistry experiments L4 hermaphrodites were grown on RNAi plates seeded with HT115 *Escherichia coli* bacteria strains generating double-stranded RNA (dsRNA) targeting genes of interest (*goa-1, gpa-16, gpr-1*) for 48 hours at 15˚C prior to fixation (Timmons and Fire, 1998). For all other gene knock-down experiments, young adult hermaphrodites were injected with dsRNA targeting genes of interest (*goa-1, gpa-16, gpr-1, ric-8, rgs-7*) and grown for 48 hours at 15˚C (Fire et al., 1998) prior to experiments. To generate dsRNA, coding regions of genes of interest were PCR amplified using Q5 Hot Start High-Fidelity DNA Polymerase (New England Biolabs). These PCR products were used as templates for *in vitro* dsRNA synthesis (MEGAscript T7 transcription kit, ThermoFisher Scientific). dsRNA was diluted 5x in DEPC H_2O prior to micro-injection. ORF clones from the Vidal and Ahringer RNAi libraries were used (Kamath et al., 2003; Rual et al., 2004).

Spindle severing assays

Mitotic spindle severing was performed in essence as described (Grill et al., 2001; Portegijs et al., 2016). One-cell embryos expressing GFP- or mCherry-labeled tubulin were imaged during mitosis using the spinning disk microscope setup described above, equipped with a Teem Photonics 355 nm Q-switched pulsed laser controlled with the ILas system (Roper Scientific France/ PICT-IBiSA, Institut Curie). At anaphase onset, as judged by spindle morphology and mobility, spindles were severed as shown in **figure 1c** and **video 2**. Centrosome displacement was recorded by 500 ms exposure streaming acquisition, and peak velocities were subsequently extrapolated using the FIJI TrackMate plugin.

Dark state experiments and local recruitment of ePDZ-tagged proteins to membrane LOV

Dark state experiments were performed on the spinning disk setup described above. For local photoactivation of LOV2 in *C. elegans* embryos, light was applied in a region of variable size depending on each individual experiment using a 491 nm laser controlled with the ILas system (Roper Scientific France/PICT-IBiSA, Institut Curie). Due to high sensitivity of LOV2 to blue light and variations in laser power, embryos of strain SV2061 (expressing diffuse ePDZ::mCherry and PH::eGFP::LOV) were used to calibrate the amount of laser power required for local activation of LOV2 prior to experiments. During both global and local photoactivation assays and dark state spindle severing experiments embryos were kept away from blue light as much as practically feasible. To this end, aluminum foil was used to cover the microscope setup, and optical filters were inserted in the light path to remove LOV2-activating wavelengths from the transmitted light used to locate embryos on slides. Prior to experimental use of embryos, unintended premature cortical recruitment of ePDZ-mCherry or ePDZ-mCherry-LIN-5 was assessed by observation of mCherry localization patterns.

Antibodies and immunocytochemistry

For immunostaining of *C. elegans* embryos, embryos were dissected from adults in 10 µl MilliQ H_2O on slides coated with poly-L-lysine. Samples were then freeze-cracked and fixed in methanol for 5 min. at -20˚C and subsequently in acetone for 5 min. at -20˚C. Embryos were then rehydrated in phosphate buffered saline + 0.05% Tween-20 (PBST), blocked for 1 hour at 4˚C in PBST + 1% bovine serum albumin and 1% goat serum (Sigma-Aldrich), and then incubated at room temperature with primary antibodies for 1 hour and then with secondary antibodies for 45 min., both in blocking solution, with four 10 minute washes in PBST following each antibody mix. Finally, embryos were embedded in ProLong Gold Antifade with DAPI. Primary antibodies used were mouse anti-LIN-5 [1:10, (Lorson et al., 2000)], mouse anti-FLAG M2 (Sigma-Aldrich) and rabbit anti-DHC-1 (1:100 (Gönczy et al., 1999); a kind gift from P. Gönczy). Secondary antibodies used were goat

anti-rabbit Alexa 488, goat anti-rabbit Alexa 568, goat anti-mouse Alexa 488, goat anti-mouse Alexa 568 (Invitrogen) and goat anti-mouse Atto 647N (Sigma-Aldrich), all at 1:500 dilution in blocking solution. Imaging of immunolabeled embryos was performed on the spinning disk setup described above.

Data analysis: membrane invaginations and fluorescence intensity measurements

All quantitative spinning disk image analyses were performed in either ImageJ or FIJI. For quantification of membrane invaginations, movies were limited to the 200 frames (50 seconds) preceding the onset of telophase. Images were then cropped to include the outer limits of the PH::eGFP signal. Transient cortical dots were tracked manually using the MTrackJ ImageJ plugin. Larger, more static structures result from membrane ruffles, which are distinct from the more dynamic invaginations, as can be seen in **video 11**. To yield the distribution of invaginations on the length axis of the visible embryo cortex, recorded x coordinates were incremented into groups of 5% embryo length each. To quantify the cortical recruitment and dynamics of ePDZ::mCherry, ePDZ::mCherry::GPR-1, LIN-5::ePDZ::mCherry and ePDZ::mCherry::DHC-1 by PH::eGFP::LOV, multiple 20 px wide linescans were drawn perpendicular to the membrane per analyzed embryo. An intensity profile was plotted per linescan at each acquired time point, from each of which an average of the maximum 3 pixel values was extracted to yield the peak intensity values at the membrane. Each intensity measurement was first corrected for background noise with a value measured outside of the embryo in a 50x50 px region of interest, and cortex to cytoplasm intensity ratios were calculated using average cytoplasmic intensity measurements in a 50x50 or 29x23 px region of interest at all timepoints analyzed. Fluorescence intensity measurements as measure for *Cre(FLPon)* activation (**Figure 1-figure supplement 2c**) were taken as total embryo average intensity minus background signal using ImageJ measurement tool. The half time of ePDZ-LOV interaction after a pulse activation was inferred from a non-linear, single component regression. All numerical data processing and graph generation was performed using Excel 2011 (Microsoft) and Prism 7 (GraphPad software, inc.).

Statistical analysis

All data were shown as means with SEM. Statistical significance as determined using two-tailed unpaired Student's t-tests, Mann-Whitney U tests and the Wilcoxon matched-pairs signed rank test. Correlation coefficients between two data sets were calculated using Pearson *r* correlation tests or Spearman rank correlation tests. Data sets were assessed for their fit to a Gaussian distribution using the D'Agostino-Pearson omnibus K2 normality test prior to application of appropriate statistical test. A p-value of <0.05 was considered significant. *, P<0.05; **, P<0.01; ***, P<0.001; ****, P<0.0001. All statistical analyses were performed in Prism 7 (GraphPad software, inc.).

Code availability
Our design algorithm is accessible via a web interface at http://104.131.81.59/, and the source code can be found at https://github.com/dannyhmg/germline.

Data availability
The data that support the findings of this study are included in the supplementary information.

Acknowledgements

We thank S. Jonis, Y. Onderwater, H. Pires, P. van Bergeijk, P. Gönczy, Ahna Skop, and M. Harterink for reagents and L. Kapitein for technical advice. We also thank all the members of the van den Heuvel, Akhmanova, Goldstein, Boxem, and Kapitein groups for helpful discussion and general support. We further thank A. Thomas for critically reading the manuscript. We acknowledge Wormbase and the Biology Imaging Center at the Faculty of Sciences, Department of Biology, Utrecht University. Some strains were provided by the Caenorhabditis Genetics Center (CGC), which is funded by NIH Office of Research Infrastructure Programs (P40OD010440).

Competing interests statement

Anna Akhmanova is a deputy editor of eLife Magazine. There are no further conflicting interests.

Video legends

Embryos are oriented with their anterior to the left in all movies.
All movies were made using spinning disk confocal microscopy.

Video 1. Movie montage of mitosis in a one-cell *C. elegans* embryo expressing GFP::Tubulin (greyscale, microtubules), mCherry::TBG-1 (magenta, centrosomes) and mCherry::HIS-48 (magenta, DNA). Images, which are single planes, were made as a time-lapse with one acquisition per 2 seconds and played back at 10 frames per second, with time point 0 being the final frame before the initiation of pronuclear meeting. Movie corresponds to the upper left panel in **figure 1b**.

Video 2. Movie montage of a mitotic spindle severing assay in a one-cell *C. elegans* embryo expressing GFP::Tubulin (greyscale, microtubules). The spindle is severed at the onset of anaphase using a pulsed UV laser (not visible), after which centrosomes are separated with speeds proportional to the net forces acting on them. Images, which are

single planes, were made as a streaming acquisition with 0.5 seconds of exposure and played back at 10 frames per second, with time point 0 between late metaphase and anaphase initiation. Movie corresponds to **figure 1c**.

Video 3. Movie montage of a mitotic one-cell *C. elegans* embryo expressing diffuse cytosolic ePDZ::mCherry (greyscale, left; red, right) without PH::eGFP::LOV (green background, right). The movie shows diffuse localization of ePDZ::mCherry in presence of global and continual blue light exposure but in absence of a cortical LOV anchor. Images, which are single planes, were made as a time-lapse with one acquisition per 2 seconds for both 568 nm and 491 nm illumination and played back at 10 frames per second, with time point 0 starting at metaphase. The acquisition in the 568 nm channel at time point 0 shows localization of ePDZ::mCherry in complete absence of blue light, as embryos were kept in the dark before image acquisition. Movie corresponds to no main Figure, and serves as a control for **video 4**.

Video 4. Movie montage of a mitotic one-cell *C. elegans* embryo expressing diffuse cytosolic ePDZ::mCherry (greyscale, left; red, right) and the membrane anchor PH::eGFP::LOV (green, right). The movie shows relocalization of diffuse ePDZ::mCherry to the cortex by global and continual activation of cortical LOV using blue light. Images, which are single planes, were made as a time-lapse with one acquisition per 2 seconds for both 568 nm and 491 nm illumination and played back at 10 frames per second, with time point 0 starting at late prophase. The acquisition in the 568 nm channel at time point 0 shows localization of ePDZ::mCherry in complete absence of blue light, as embryos were kept in the dark before image acquisition. Movie corresponds to the upper panels in **figure 2b**.

Video 5. Movie montage of a mitotic one-cell *C. elegans* embryo expressing diffuse cytosolic ePDZ::mCherry (inverted greyscale) and the membrane anchor PH::eGFP::LOV (not shown). The movie shows relocalization of diffuse ePDZ::mCherry to the posterior cortex by local activation of cortical LOV using low-intensity blue light. Activation of the ePDZ–LOV2 interaction is induced at the posterior cortex using local illumination with a 491 nm laser. The embryo was otherwise shielded from blue light before and during the experiment. Images, which are single planes, were made as a streaming acquisition with 0.5 seconds of exposure and played back at 10 frames per second, with time point 0 corresponding to late prophase. Movie corresponds to the lower panels in **figure 2b**.

Video 6. Movie montage of a four-cell *C. elegans* embryo expressing diffuse cytosolic ePDZ::mCherry (greyscale) and the membrane anchor PH::eGFP::LOV (not shown). The movie shows relocalization of diffuse ePDZ::mCherry to the cortex by activation of cortical LOV using a single pulse of blue light, and subsequent return to the dark state in absence

of blue light. Images, which are single planes, were made as a time-lapse with one acquisition per 2 seconds played back at 10 frames per second, where time point 0 is the last acquisition before a single 1 second global pulse of 491 nm light. The acquisition at time point 0 shows localization of ePDZ::mCherry in complete absence of blue light, as the embryo was kept in the dark before and after global induction of the LOV–ePDZ interaction. Movie corresponds to **figure 2c**.

Video 7. Movie montage of a mitotic one-cell *C. elegans* embryo expressing endogenously labeled ePDZ::mCherry::RIC-8 (greyscale, left; red, right), the membrane anchor PH::eGFP::LOV and GFP::Tubulin (both green, right). The movie shows relocalization ePDZ::mCherry::RIC-8 to the cortex by global and continual activation of cortical LOV using blue light. Images, which are single planes, were made as a time-lapse with one acquisition per 2 seconds for both 568 nm and 491 nm illumination and played back at 10 frames per second, with time point 0 starting at late prophase. The acquisition in the 568 nm channel at time point 0 shows localization of ePDZ::mCherry::RIC-8 in complete absence of blue light, as embryos were kept in the dark before image acquisition. Movie corresponds to **figure 3c**.

Video 8. Movie montage of a mitotic one-cell *C. elegans* embryo expressing endogenously labeled ePDZ::mCherry::GPR-1 (greyscale, left; red, right) in a Δ*gpr-2* genetic background, the membrane anchor PH::eGFP::LOV and GFP::Tubulin (both green, right). The movie shows relocalization of ePDZ::mCherry::GPR-1 to the cortex by global and continual activation of cortical LOV using blue light. Images, which are single planes, were made as a time-lapse with one acquisition per 2 seconds for both 568 nm and 491 nm illumination and played back at 10 frames per second, with time point 0 corresponding with early metaphase. The acquisition in the 568 nm channel at time point 0 shows localization of ePDZ::mCherry::GPR-1 in complete absence of blue light, as embryos were kept in the dark before image acquisition. Movie serves as a control to **video 9**.

Video 9. Movie montage of a mitotic one-cell *C. elegans* embryo treated with Gα RNAi expressing endogenously labeled ePDZ::mCherry::GPR-1 (greyscale, left; red, right) in a Δ*gpr-2* genetic background, the membrane anchor PH::eGFP::LOV and GFP::Tubulin (both green, right). The movie shows relocalization of ePDZ::mCherry::GPR-1 to the cortex by global and continual activation of cortical LOV using blue light. Images, which are single planes, were made as a time-lapse with one acquisition per 2 seconds for both 568 nm and 491 nm illumination and played back at 10 frames per second, with time point 0 corresponding with early metaphase. The acquisition in the 568 nm channel at time point 0 shows localization of ePDZ::mCherry::GPR-1 in complete absence of blue light, as embryos were kept in the dark before image acquisition. Movie corresponds to **figure 5b**.

Video 10. Movie montage of a mitotic one-cell *C. elegans* embryo expressing GFP::Tubulin (greyscale, microtubules) and PH::eGFP::LOV (greyscale, membrane). Invaginations (black arrows) are visible at the embryo membrane most pronouncedly in the posterior during late metaphase and anaphase. Images, which are single planes, were made as a streaming acquisition with 0.5 seconds of exposure and played back at 10 frames per second, with time point 0 between late metaphase and anaphase initiation. Movie corresponds to **figure 5g**.

Video 11. Movie montage of the subcortical area of a mitotic one-cell *C. elegans* embryo expressing GFP::Tubulin (inverted greyscale, microtubules), PH::eGFP::LOV (inverted greyscale, membrane). Invaginations are visible as dots protruding inwards from the embryo membrane during late metaphase and anaphase. Images, which are single planes, were made as a streaming acquisition with 0.25 seconds of exposure and played back at 10 frames per second, with time point 0 corresponding with anaphase, 50 seconds before telophase initiation. Movie corresponds to **figure 5g**.

Video 12. Movie montage of a mitotic one-cell *C. elegans* embryo expressing endogenously labeled ePDZ::mCherry::DHC-1 (greyscale, left; red, right), the membrane anchor PH::eGFP::LOV and GFP::Tubulin (both green, right). The movie shows relocalization of ePDZ::mCherry::DHC-1 to the cortex by global and continual activation of cortical LOV using blue light. Images, which are single planes, were made as a time-lapse with one acquisition per 2 seconds for both 568 nm and 491 nm illumination and played back at 10 frames per second, with time point 0 corresponding with early metaphase. The acquisition in the 568 nm channel at time point 0 shows localization of ePDZ::mCherry::GPR-1 in complete absence of blue light, as embryos were kept in the dark before image acquisition. Movie serves as a control to **video 13**.

Video 13. Movie montage of a mitotic one-cell *C. elegans* embryo treated with *gpr-1/2* RNAi expressing endogenously labeled ePDZ::mCherry::DHC-1 (greyscale, left; red, right), the membrane anchor PH::eGFP::LOV and GFP::Tubulin (both green, right). The movie shows relocalization of ePDZ::mCherry::DHC-1 to the cortex by global and continual activation of cortical LOV using blue light. Images, which are single planes, were made as a time-lapse with one acquisition per 2 seconds for both 568 nm and 491 nm illumination and played back at 10 frames per second, with time point 0 corresponding with early metaphase. The acquisition in the 568 nm channel at time point 0 shows localization of ePDZ::mCherry::DHC-1 in complete absence of blue light, as embryos were kept in the dark before image acquisition. Movie corresponds to **figure 6b**.

Video 14. Movie montage of a mitotic one-cell *C. elegans* embryo expressing endogenously labeled LIN-5::ePDZ::mCherry (greyscale, left; red, right) and the

membrane anchor PH::eGFP::LOV and GFP::Tubulin (both green, right). The movie shows relocalization of LIN-5::ePDZ::mCherry to the cortex by global and continual activation of cortical LOV using blue light. Images, which are single planes, were made as a time-lapse with one acquisition per 2 seconds for both 568 nm and 491 nm illumination and played back at 10 frames per second, with time point 0 corresponding with metaphase. The acquisition in the 568 nm channel at time point 0 shows localization of LIN-5::ePDZ::mCherry in complete absence of blue light, as embryos were kept in the dark before image acquisition. Movie serves as a control to **video 15**.

Video 15. Movie montage of a mitotic one-cell *C. elegans* embryo treated with Gα RNAi expressing endogenously labeled LIN-5::ePDZ::mCherry (greyscale, left; red, right), the membrane anchor PH::eGFP::LOV and GFP::Tubulin (both green, right). The movie shows relocalization of LIN-5::ePDZ::mCherry to the cortex by global and continual activation of cortical LOV using blue light. Images, which are single planes, were made as a time-lapse with one acquisition per 2 seconds for both 568 nm and 491 nm illumination and played back at 10 frames per second, with time point 0 corresponding with metaphase. The acquisition in the 568 nm channel at time point 0 shows localization of LIN-5::ePDZ::mCherry in complete absence of blue light, as embryos were kept in the dark before image acquisition. Movie corresponds to **figure 7b**
.

Video 16. Movie montage of a mitotic one-cell *C. elegans* embryo treated with *gpr-1/2* RNAi expressing endogenously labeled LIN-5::ePDZ::mCherry (not shown), the membrane anchor PH::eGFP::LOV and GFP::Tubulin (both inverted greyscale). The movie shows excessive rocking of centrosomes with associated pronuclei prior to mitotic spindle assembly. Images, which are single planes, were made as a streaming acquisition with 0.5 seconds of exposure and played back at 20 frames per second, with time point 0 corresponding with late prophase. Movie corresponds to no figure, but is discussed in the text.

Video 17. Movie montage of a mitotic one-cell *C. elegans* embryo expressing endogenously labeled LIN-5::ePDZ::mCherry (not shown) and the membrane anchor PH::eGFP::LOV (inverted greyscale). The movie shows separation of centrosomes and associated pronuclei in prophase upon global and continuous activation of LOV with blue light. Images, which are single planes, were made as a streaming acquisition with 0.5 seconds of exposure and played back at 10 frames per second, with time point 0 corresponding with prophase. Movie corresponds to no figure, but is discussed in the text.

Video 18 Movie montage of a mitotic one-cell *C. elegans* embryo treated with *gpr-1/2* RNAi expressing endogenously labeled LIN-5::ePDZ::mCherry (inverted greyscale) and the membrane anchor PH::eGFP::LOV (not shown). The movie shows anterior

displacement of the spindle and subsequent inverted asymmetric division resulting in a small anterior and large posterior blastomere after local recruitment of LIN-5::ePDZ::mCherry to the anterior cortex. Images, which are single planes, were made as a time-lapse with one acquisition per 5 seconds and played back at 5 frames per second, with time point 0 corresponding with metaphase. Movie corresponds to **figure 8a**.

Video 19. Movie montage of a mitotic one-cell *C. elegans* embryo treated with *gpr-1/2* RNAi expressing endogenously labeled LIN-5::ePDZ::mCherry (inverted greyscale) and the membrane anchor PH::eGFP::LOV (not shown). The movie shows artificial transverse positioning of the metaphase mitotic spindle and its subsequent correction to an anterior-posterior position in late anaphase after local recruitment of LIN-5::ePDZ::mCherry to the opposing equatorial cortexes. Images, which are averages of groups of 2 subsequent frames, were made as a time-lapse with one acquisition per 2 seconds and played back at 5 frames per second, with time point 0 corresponding with metaphase. Movie corresponds to **figure 8b**.

Video 20. Movie montage of a mitotic two-cell *C. elegans* embryo treated with *gpr-1/2* RNAi expressing endogenously labeled LIN-5::ePDZ::mCherry (inverted greyscale) and the membrane anchor PH::eGFP::LOV (not shown). The movie shows artificial rotation of transverse aligned AB and P1 spindles to an anterior-posterior position, and concurrent reorientation of the cleavage planes after local recruitment of LIN-5::ePDZ::mCherry to the central region where AB and P1 cortexes touch. Images, which are averages of groups of 2 subsequent frames, were made as a streaming acquisition with 0.5 seconds of exposure and played back at 10 frames per second, with time point 0 corresponding with metaphase in the AB blastomere. Movie corresponds to **figure 8c**.

Video 21. Movie montage of a mitotic two-cell *C. elegans* embryo treated with *gpr-1/2* RNAi expressing endogenously labeled LIN-5::ePDZ::mCherry (inverted greyscale) and the membrane anchor PH::eGFP::LOV (not shown). The movie shows artificial rotation of transverse aligned AB and P1 spindles to an anterior-posterior position, and concurrent reorientation of the cleavage planes after local recruitment of LIN-5::ePDZ::mCherry to the central region where AB and P1 cortexes touch. Images, which are averages of groups of 2 subsequent frames, were made as a streaming acquisition with 0.5 seconds of exposure and played back at 20 frames per second, with time point 0 corresponding with metaphase in the AB blastomere. Movie corresponds to **figure 8c**.

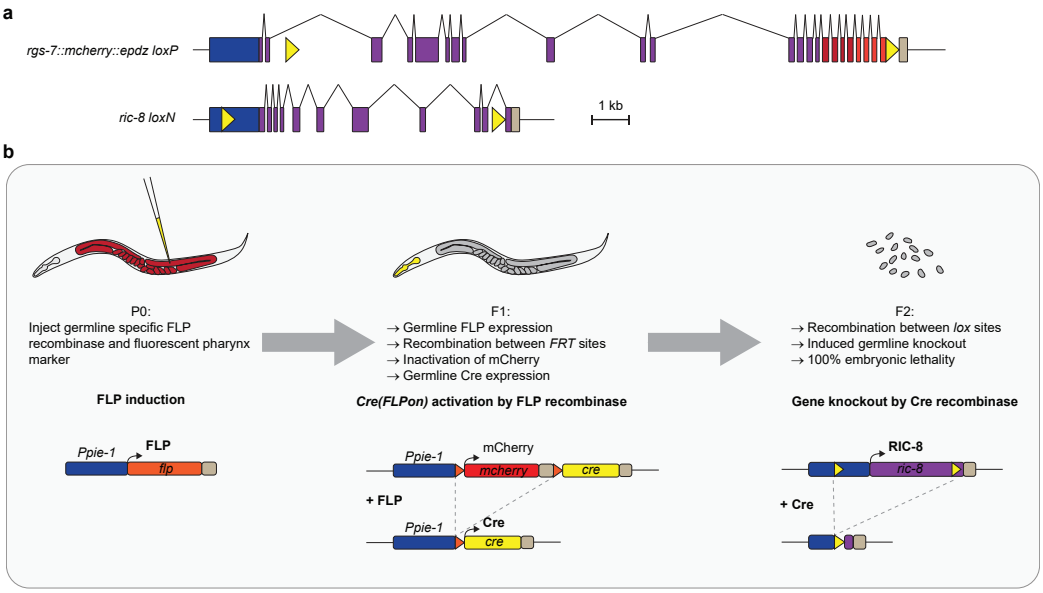

Figure 1-figure supplement 1. **Method of inducible knockout of essential genes in the *C. elegans* germline.** (**a**) Position of *lox* sites (yellow triangles) in *rgs-7* and *ric-8* loci with promoter (blue), coding sequence (purple), 3' UTR (khaki), mcherry (red), and epdz (orange). We paid attention not to disturb annotated genetic elements or to create splice donor/acceptor consensus sites. Scale bar: 1 kb. (**b**) Flow chart of the inducible tissue-specific knock-out procedure. The system depends on successive expression of two recombinases: FLP and Cre. This bipartite nature allows for both spatial and temporal control. For spatial control, we chose the long *Ppie-1* germline-specific promoter including enhancer, which is active in every region of the germline during all developmental stages (Merritt et al., 2008). Temporal control depends on injection of the *Ppie-1::flp* construct (including a fluorescent co-injection marker) in P0 germlines. Transgenic F1 express germline FLP, which recombines between two *FRT sites* (orange triangles). As a result, the integrated tissue-specific *Cre(FLPon)* construct switches expression from *mcherry* to *cre*. *mcherry* and *cre* sequences were germline-optimized for reliable germline expression (see **figure 2-figure supplement 1-3**). For the *Cre(FLPon)* construct, we chose the *cep-1* 3' UTR because it contains a strong poly-adenylation signal consensus (aataaa) and permits expression in every region and developmental stage of the germline (Merritt et al., 2008). The induced, tissue-specific Cre recombines between *lox* sites (yellow triangles), generating a knockout and 100% embryonic lethal F2 generation. The two-step knockout creates a delay that results in germline Cre activity only in the F1 germline. P0 germline Cre activity generates knockout F1 animals but does not deplete maternal protein product. See **supplementary table 1** for detailed genotypes.

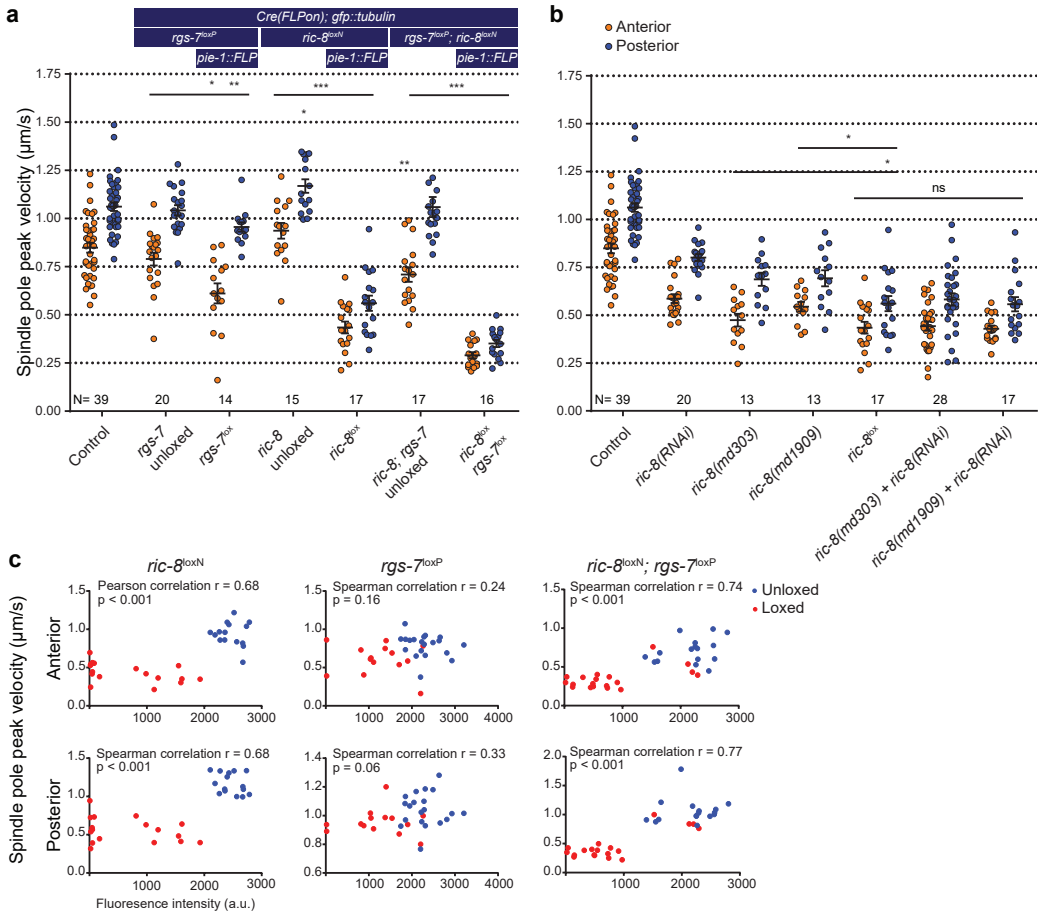

Figure 1-figure supplement 2. **Inducible knockout of essential genes in the *C. elegans* germline.** (**a**) Spindle severing experiments of the induced *rgs-7^{lox}* and *ric-8^{lox}* knockout alleles compared to embryos in which FLP and the consequent recombination cascade were not induced. Control is the *gfp::tubulin* strain. Error bars: s.e.m. Welch's Student's t-test and Mann Whitney U test; * $P < 0.05$, ** $P < 0.01$, *** $P < 0.001$. (**b**) Spindle severing experiments to compare the induced *ric-8*P^{lox}P knockout phenotype with feeding RNAi, two *ric-8* partial loss of function alleles, and mutants + RNAi. Control is the *gfp::tubulin* strain. Error bars: s.e.m. Welch's Student's t-test and Mann Whitney U test; ns $P < 0.05$, * $P < 0.05$. (**c**) Scatter plots showing a correlation between loss of *mcherry* expression (Cre activation) and reduced spindle pole peak velocities for *ric-8^{loxN}*, *rgs-7^{loxP}*, and *ric-8^{loxN}; rgs-7^{loxP}* embryos. Embryos were isolated from transgenic F1 (loxed), and control animals that were not injected with the FLP construct (unloxed) embryos. Clearly, some of the *ric-8^{loxN}; rgs-7^{loxP}* loxed cluster with the unloxed. These were discarded as outliers from further analyses. Data points were from the same experiment as in a. See **supplementary table 1** for detailed genotypes.

b

Fluorescent Protein	Codon Adaptation Index	Germline Optimization Score
mTagBFP2 (CAI=1)	0.96	146
mTagBFP2 (GLO)	0.52	531
mTurquoise2 (CAI=1)	0.88	305
mTurquoise2 (GLO)	0.57	728
GFP (from Fire kit)	0.30	76
GFP (CAI=1)	0.96	329
GFP (GLO)	0.57	704
mNeonGreen (CAI=1)	1.00	134
mNeonGreen (GLO)	0.46	481
mScarlet-I (CAI=1)	1.00	341
mScarlet-I (GLO)	0.57	822
mKate2 (CAI=1)	0.97	129
mKate2 (GLO)	0.54	672
HaloTag (CAI=1)	0.93	180
HaloTag (GLO)	0.55	621

Figure 2-figure supplement 1. **Method of germline-optimization of coding sequences confers resistance to silencing.** (**a**) Strategy for designing germline-optimized coding sequences. We used an RNAseq dataset from one-cell embryos (Gerstein et al., 2014; Hillier et al., 2008) as a proxy for germline-expressed mRNAs, because one-cell embryos are not transcriptionally active and thus their entire mRNA content should be derived from the maternal germline. We made a list of all 12-nucleotide coding words and assigned each word a score that is the sum of the RPKM expression values of the germline mRNAs in which that word appears. Thus, words that appear frequently, or in highly-expressed germline genes, will have high scores. Although the germline silencing machinery is presumably blind to reading frame, we only considered in-frame 12mers so that our design algorithm would implicitly account for codon usage. Finally, we developed an algorithm to assemble any desired coding sequence from our list of coding 12mers. The algorithm is as follows: 1) Based on the desired amino acid sequence, assemble a list of all 12mers that could appear in the coding sequence, and sort these words by score; 2) Assemble a draft coding sequence by plugging in one word at a time, beginning with the highest-scoring possible word and continuing until the sequence is complete; 3) Compute a score for the entire draft sequence by averaging the scores of each word it contains; 4) Refine the sequence by randomly choosing one word at a time, changing it to a different word, and checking whether the overall sequence score improves. Repeat step (4) until no further improvements are found after a certain number of iterations, which is chosen based on the sequence length such that each residue has a 99% chance of being tested at least once. The random optimization in step (4) is necessary because step (2) favors the highest-scoring words without considering context. Choosing a high-scoring word at one position constrains the subsequent choice of words that overlap the high-scoring word. In some cases, a higher overall score results from choosing two moderately- scoring words, rather than a high- and a low-scoring word, when the two words overlap. Random optimization ensures that these

cases are found and maximizes the overall score of the designed sequence. (**b**) Images of germline fluorescence in animals carrying either codon-optimized (Redemann et al., 2011) or germline-optimized mNeonGreen::AraD transgenes. AraD is a tetrameric bacterial protein used as a control for single-molecule fluorescence photobleacing experiments (Dickinson et al., 2017). See **supplementary table 1** for detailed genotypes.

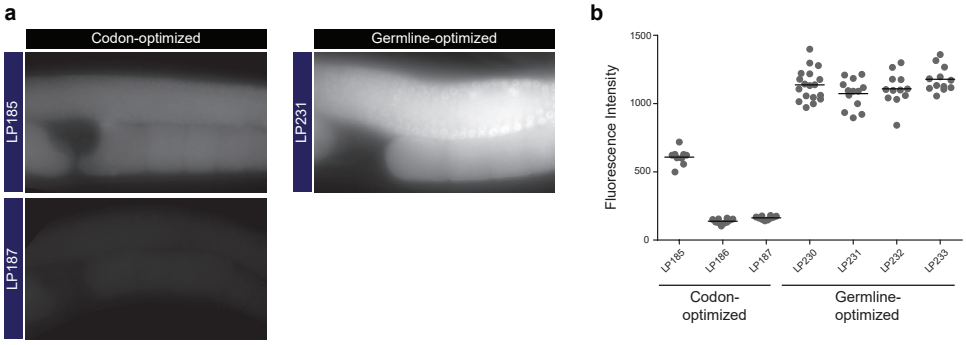

Figure 2-figure supplement 2. **Germline-optimization of coding sequences confers resistance to silencing.** (**a**) Measurements of fluorescence intensity in the germlines of strains carrying either codon-optimized or germline-optimized mNeonGreen::AraD transgenes. Each data point represents one animal. The high expression of the germline-optimized transgenes was stable for >20 generations. (**b**) Images of germline fluorescence in animals carrying GFP::CDK-1 transgenes made with either non-optimized or germline-optimized GFP. *gfp::cdk-1* was tested because this transgene is especially prone to silencing (Lee et al., 2012). A non-transgenic (N2) animal is shown as an example of autofluorescence. We consistently observed expression of germline-optimized GFP::CDK-1 shortly after transgene isolation, although this expression was gradually lost over ~10 generations when we cultured these strains without selecting fluorescent animals at each passage. See **supplementary table 1** for detailed genotypes.

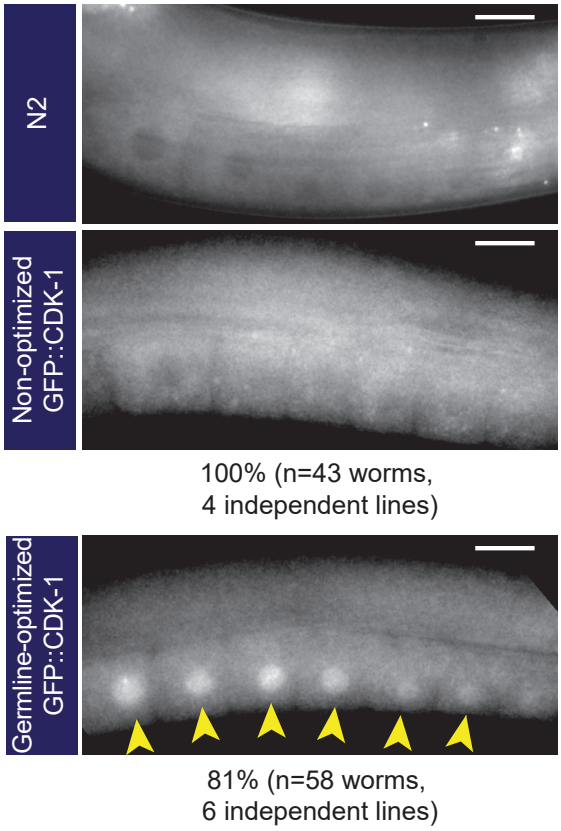

Figure 2-figure supplement 3. **Germline-optimized fluorescent protein tags.** Results of applying our germline optimization algorithm to a selected set of fluorescent protein tags. Codon adaptation index (Redemann et al., 2011) and our germline optimization score are shown for coding sequences designed to maximize optimal codon usage (CAI=1 indicates that sequence was designed to have a codon adaptation index as close as possible to 1.00) or to maximize the germline optimization score (GLO, GermLine Optimized). Germline optimization significantly increases the germline optimization score as expected, at the cost of a moderate reduction in codon adaptation index. Despite the lower codon adaptation index, germline-optimized transgenes were most often expressed at higher levels than their codon-optimized counterparts (see above and our unpublished observations). Constructs containing the listed germline-optimized fluorescent protein sequences will be deposited at Addgene. See **supplementary table 1** for detailed genotypes.

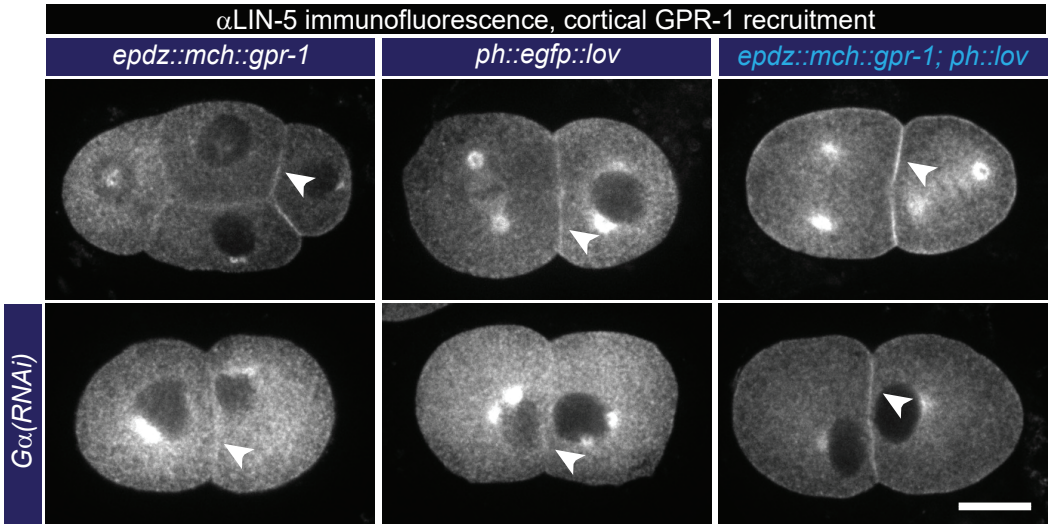

Figure 5-figure supplement 1. **Cortical GPR-1 recruitment subsequently recruits LIN-5 to the cortex.** Immunofluorescent staining of LIN-5 in early embryos. Controls are the *epdz::mch::gpr-1* and *ph::egfp::lov* strains. Experimental condition is the combination of the two controls (GPR-1 recruitment to membrane LOV) in otherwise wildtype embryos or *Gα(RNAi)* embryos. Arrowheads indicate cortical LIN-5. Scale bar: 10 μm. Images are maximum projections of 9 imaging planes with 0.25 μm spacing. See **supplementary table 1** for detailed genotypes. Anterior is to the left in all microscopy images.

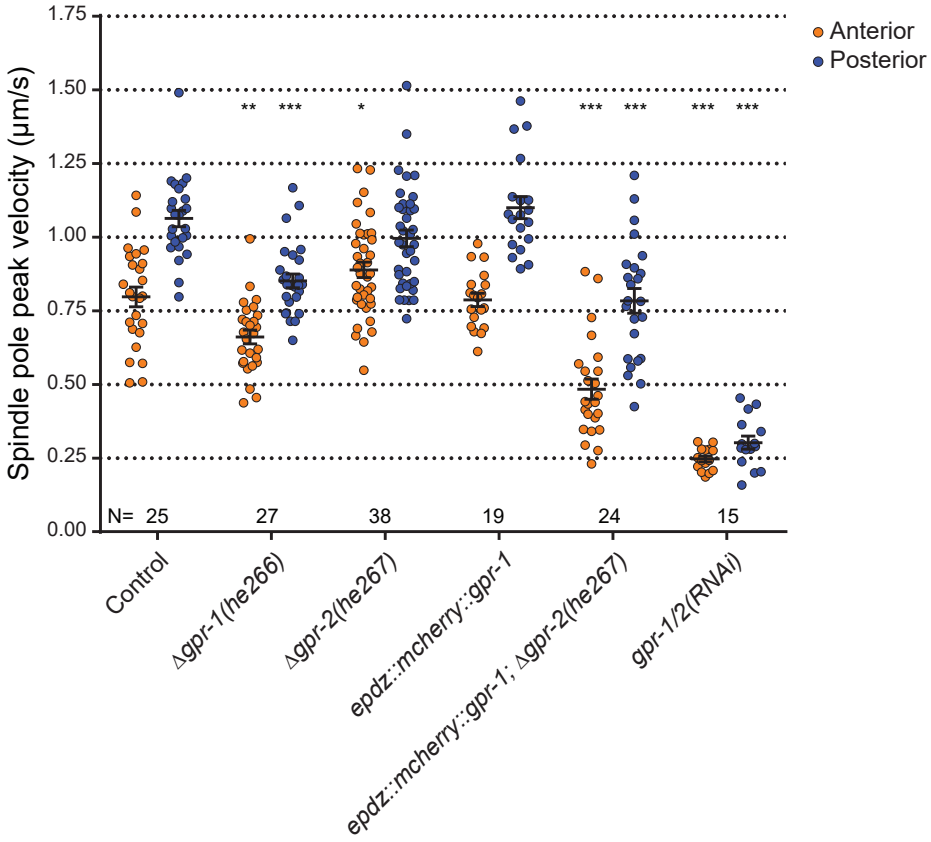

Figure 5-figure supplement 2. Spindle severing experiments of CRISPR/Cas9-mediated *gpr-1* and *gpr-2* knockout alleles, and tagged *gpr-1*. *egfp::tubulin* (control) and *gpr-1/2(RNAi)* are wildtype and *gpr-1/2* loss of function controls. Error bars: s.e.m. Welch's Student's *t-test* and Mann Whitney U test; * $P < 0.05$, ** $P < 0.01$, *** $P < 0.001$. See **supplementary table 1** for detailed genotypes.

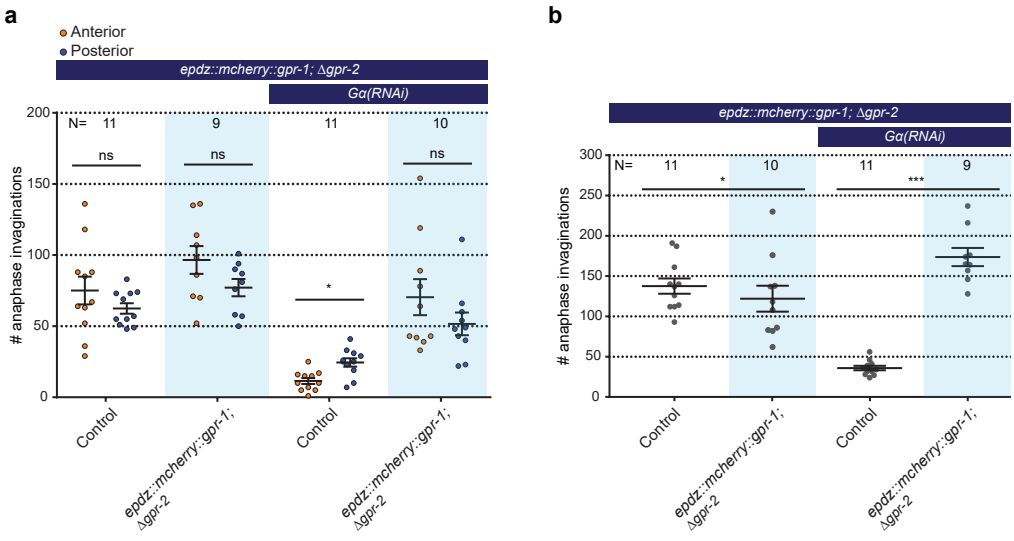

Figure 5-figure supplement 3. **Cortical GPR-1 recruitment increases cortical pulling forces and the number of plasmamembrane invaginations.** (**a**) Number of membrane invaginations, anterior and posterior compared for indicated genotypes. Control is *gfp::tubulin; ph::egfp::lov* strain. Error bars: s.e.m. Paired, two-tailed Student's *t-test*; ns $P > 0.05$, * $P < 0.05$. (**b**) Total number of membrane invaginations for the indicated genotypes. Control is *gfp::tubulin; ph::egfp::lov* strain. Error bars: s.e.m. Welch's Student's t-test; * $P < 0.05$, *** $P < 0.001$. Blue fields indicate conditions in which an ePDZ- and LOV component are present, and an ePDZ–LOV interaction is induced using blue light. See **supplementary table 1** for detailed genotypes. Anterior is to the left in all microscopy images.

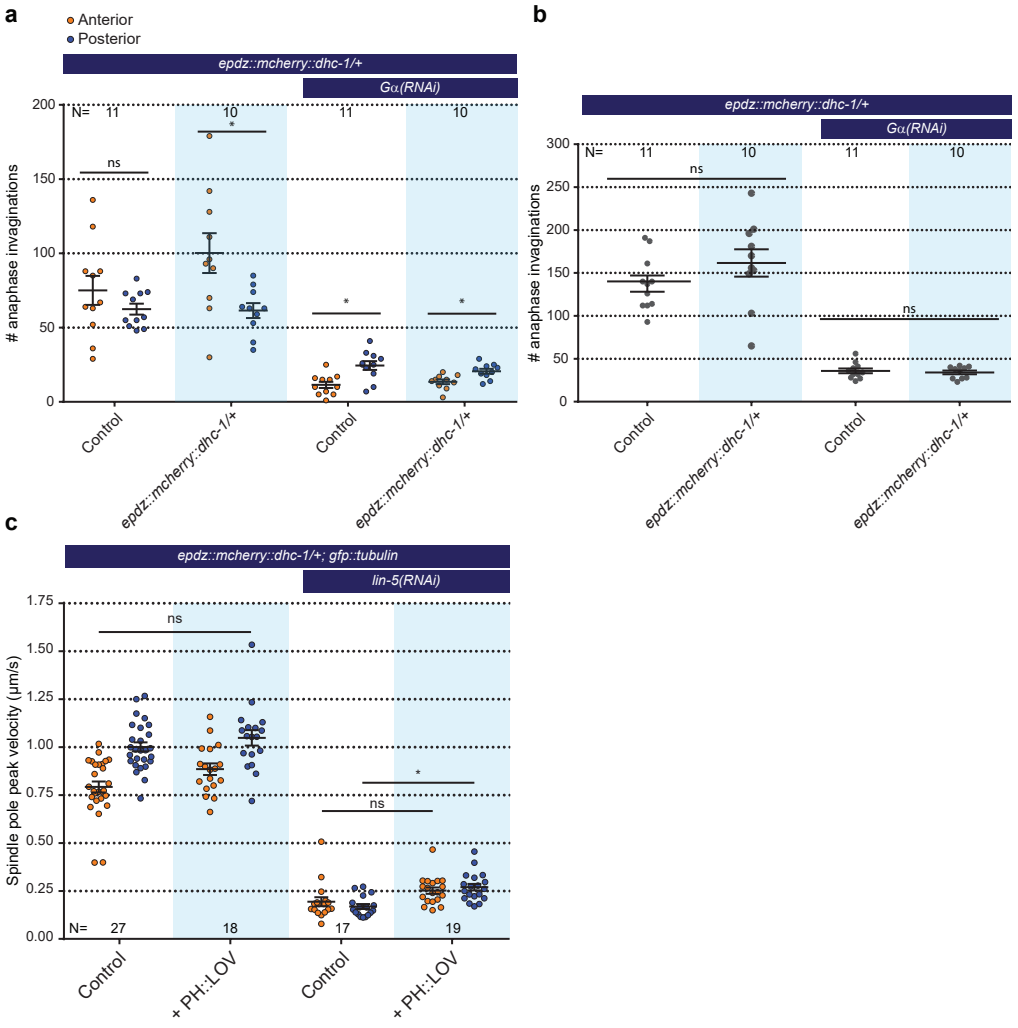

Figure 6-figure supplement 1. **Cortical dynein (DHC-1) recruitment does not enhance cortical pulling force generation.** (**a**) Number of membrane invaginations, anterior and posterior compared for indicated genotypes. Control is the *gfp::tubulin; ph::egfp::lov* strain. Error bars: s.e.m. Paired, two-tailed Student's t-test; ns $P > 0.05$, * $P < 0.05$. (**b**) Total number of membrane invaginations for the indicated genotypes. Control is the *gfp::tubulin; ph::egfp::lov* strain. Error bars: s.e.m. Welch's Student's t-test; ns $P > 0.05$. (**c**) Spindle severing experiments with cortical dynein recruitment. Control is the *epdz::mch::dhc-1; gfp::tubulin* strain. Experimental conditions: combination of *ph::egfp::lov* and *lin-5(RNAi)*. Error bars: s.e.m. Welch's Student's t-test and Mann Whitney U test; ns $P > 0.05$, * $P < 0.05$. Blue fields indicate conditions in which an ePDZ- and LOV component are present, and an ePDZ–LOV interaction is induced using blue light. See **supplementary table 1** for detailed genotypes.

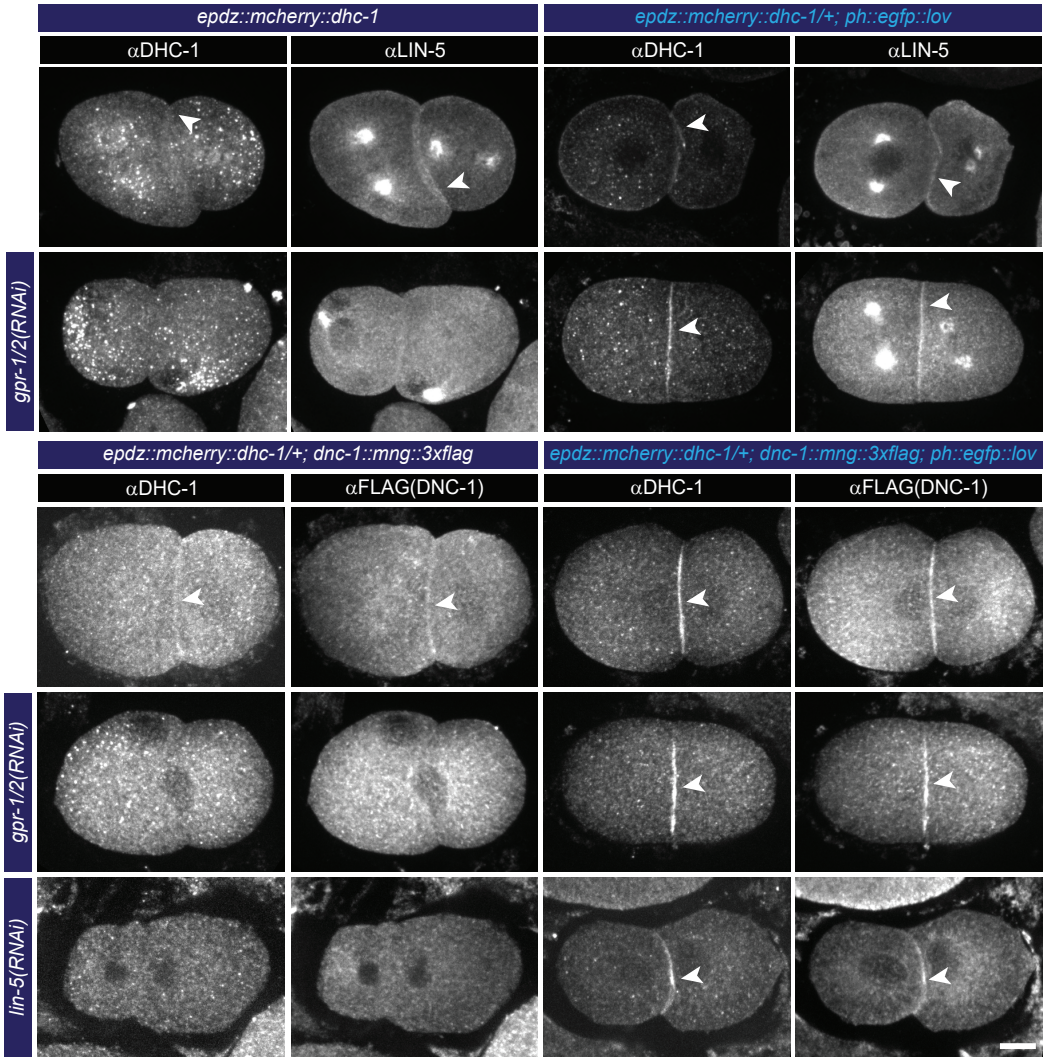

Figure 6-figure supplement 2. **Cortical dynein (DHC-1) recruitment localizes LIN-5.** Immunofluorescent staining of DHC-1, LIN-5 and DNC-1 (dynactin) in early embryos. Control is *epdz::mch::dhc-1/+* strain. Experimental condition is cortical dynein recruitment in *gpr-1/2(RNAi)* or otherwise wildtype embryos. Arrowheads indicate cortical staining. Scale bar: 10 μm. Images are maximum projections of 9 imaging planes with 0.25 μm spacing. Blue light activation was global and continuous. Anterior is to the left in all microscopy images.

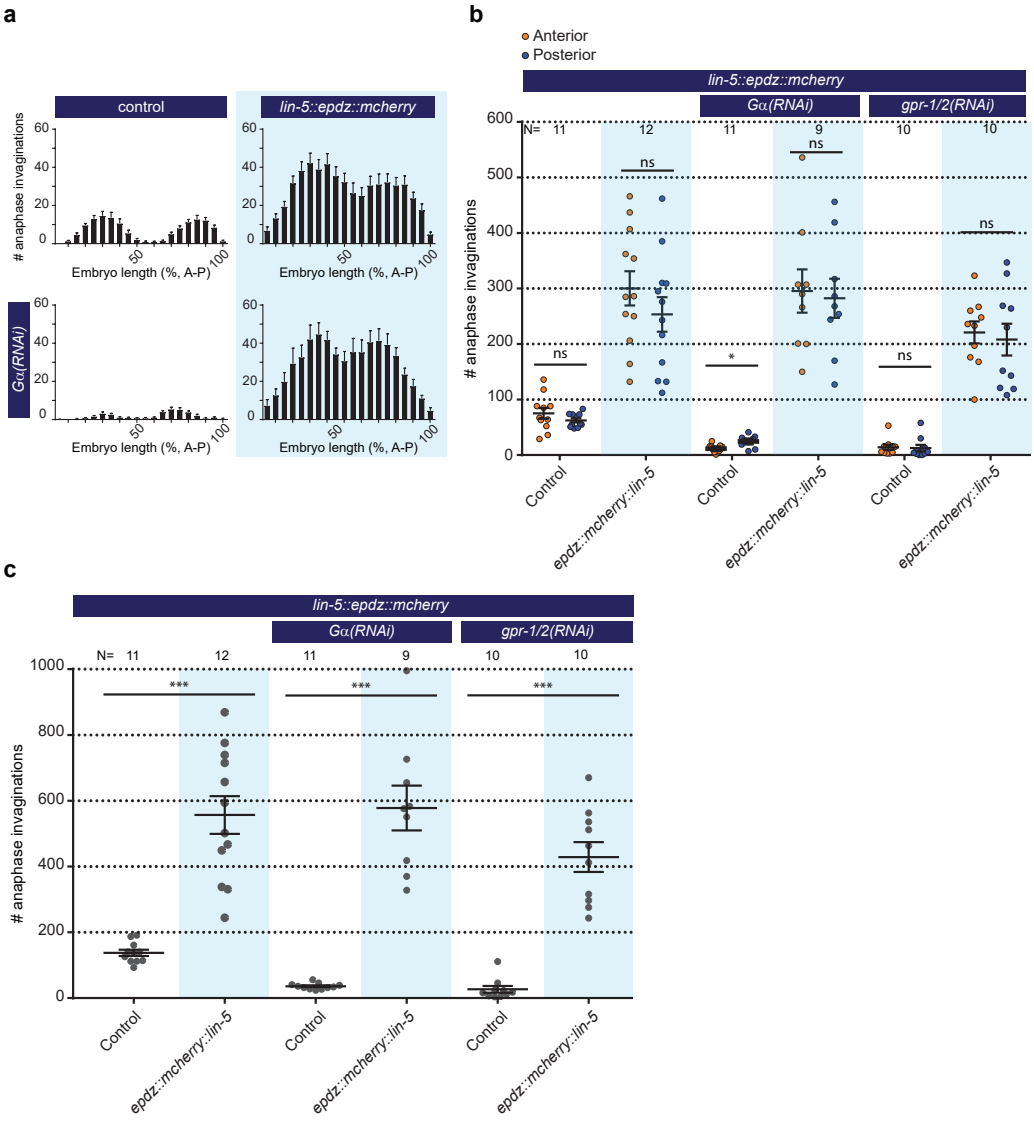

Figure 7-figure supplement 1**. Cortical LIN-5 recruitment strongly increases cortical pulling force generation.** (**a**) Distribution of membrane invaginations along the one-cell embryo anterior-posterior axis. Control is the *ph::egfp::lov; gfp::tubulin* strain with and without *Gα* RNAi. Experimental condition is the combination of control with *lin-5::epdz::mch* for cortical LIN-5 recruitment. (**b**) Number of membrane invaginations, anterior and posterior compared for indicated genotypes. Control is the *gfp::tubulin; ph::egfp::lov* strain. Error bars: s.e.m. Paired, two-tailed Student's t-test; ns $P > 0.05$, * $P < 0.05$. (**c**) Total number of membrane invaginations for the indicated genotypes. Control is the *gfp::tubulin; ph::egfp::lov* strain. Error bars: s.e.m. Welch's Student's *t-test*; *** $P < 0.001$. Blue fields indicate conditions in which an ePDZ- and LOV component are present, and an ePDZ–LOV interaction is induced using blue light. Blue light activation was global and continuous. See **supplementary table 1** for detailed genotypes. Anterior is to the left in all microscopy images.

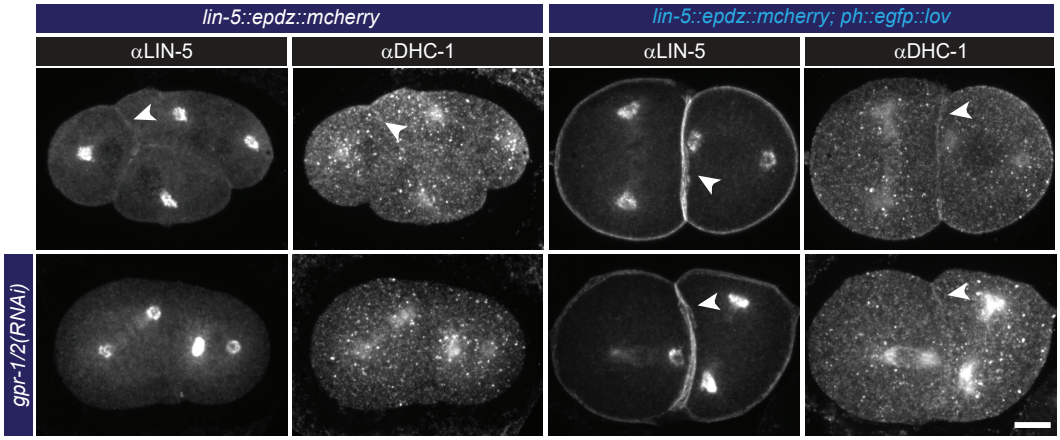

Figure 7-figure supplement 2. **Cortical LIN-5 recruitment localizes dynein (DHC-1)**. Immunofluorescent staining of LIN-5 and DHC-1 in early embryos. Control is *lin-5::epdz::mch* strain. Experimental condition is cortical LIN-5 recruitment in *gpr-1/2(RNAi*) or otherwise wildtype embryos. Arrowheads indicate cortical staining. Scale bar: 10 μm. Images are maximum projections of 9 imaging planes with 0.25 μm spacing. Blue light activation was global and continuous. See **supplementary table 1** for detailed genotypes

Supplementary table 1: Genotypes of *C. elegans* used in this study, listed per figure

Figure	Strain	Genotype	Source
1b	SA250	*tjIs54(Ppie-1::gfp::tbb-2 + Ppie-1::2xmcherry::tbg-1 + unc-119(+));* *Tjls57(Ppie-1::mcherry::his-48 + unc-119(+))*	CGC
	SV1589	*lin-5(he244[co-egfp::lin-5]) II*	Portegijs et al., 2016
	SV1569	*gpr-1(he238[co-fkbp::co-egfp::gpr-1]) III*	Portegijs et al., 2016
	SV1803	*dhc-1(he263[egfp::dhc-1]) I*	Schmidt et al., 2017
1c	AZ244	*unc-119(ed3) III; ruIs57[Ppie-1::gfp::tbb-2 + unc119(+)] V*	CGC
1d	AZ244	*unc-119(ed3) III; ruIs57[Ppie-1::gfp::tbb-2 + unc119(+)] V*	CGC
	SV1485	*lin-5(ev571ts) II; ruIs57[Ppie-1::gfp::tbb-2 + unc119(+)] V*	
1e	AZ244	*unc-119(ed3) III; ruIs57[Ppie-1::gfp::tbb-2 + unc119(+)] V*	CGC
	SV2035	*ttTi5605(he312[Ppie-1(long)::frt::glo-mcherry::cep-1(3'UTR)::frt::egl-13nls::glo-cre::cep-1 (3'UTR)]) II; ric-8(he280[loxN -741/loxN 4624]) IV; ruIs57[Ppie-1::gfp::tbb-2 + unc119(+)] V; Ppie-1::sv40nls::flp(G5D)::egl-13nls::tbb-2(3'UTR) + Pmyo-2::tdtomato + E. coli DNA c/w PvuII Ex*	
	SV2087	*ttTi5605(he312[Ppie-1(long)::frt::glo-mcherry::cep-1(3'UTR)::frt::egl-13nls::glo-cre::cep-1 (3'UTR)]) II; ruIs57[Ppie-1::gfp::tbb-2 + unc119(+)] V; rgs-7(he300[loxP in intron 2 + -CT co-mcherry::co-epdz::tev::loxP::3xflag]) X; Ppie-1::sv40nls::flp(G5D)::egl-13nls::tbb-2(3'UTR) + Pmyo-2::tdtomato + E. coli DNA c/w PvuII Ex*	
	SV2088	*ttTi5605(he312[Ppie-1(long)::frt::glo-mcherry::cep-1(3'UTR)::frt::egl-13nls::glo-cre::cep-1 (3'UTR)]) II; ric-8(he280[loxN -741/loxN 4624]) IV; ruIs57[Ppie-1::gfp::tbb-2 + unc119(+)] V; rgs-7(he300[loxP in intron 2 + -CT co-mCherry::co-epdz::tev::loxP::3xflag]) X; Ppie-1::sv40nls::flp(G5D)::egl-13nls::tbb-2(3'UTR) + Pmyo-2::tdtomato + E. coli DNA c/w PvuII Ex*	
2b	SV2061	*ttTi5605(he314[Ppie-1::glo-epdz::mcherry(smu-1)::tbb-2(3'UTR)]) II;* *cxTi10816(he259[Peft-3::ph::co-egfp::co-lov::tbb-2(3'UTR)]) IV*	
3a	SV2076	*cxTi10816(he259[Peft-3::ph::co-egfp::co-lov::tbb-2(3'UTR)]) IV;* *ruIs57[Ppie-1::gfp::tbb-2 + unc119(+)] V; rgs-7(he290[rgs-7::co-mcherry::co-epdz]) X*	
	SV2062	*par-6(he322[par-6::gfp(smu-1 introns)::glo-lov] I*	
3b	SV2074	*ruIs57[Ppie-1::gfp::tbb-2 + unc119(+)] V; rgs-7(he290[rgs-7::co-mcherry::co-epdz]) X*	
	SV2076	*CxTi 10816(he259[Peft-3::PH::eGFP::LOV::tbb-2]) IV; ruIs57[Ppie-1::Tub::GFP] V;* *rgs-7(he290[rgs-7::co-mCherry::co-ePDZ]) X*	
	SV2109	*par-6(he322[par-6::gfp(smu-1 introns)::glo-lov]) I; ruIs57[Ppie-1::Tub::GFP] V*	
	SV2143	*par-6(he322[par-6::gfp(smu-1 introns)::glo-lov]) I; ruIs57[Ppie-1::gfp::tbb-2 + unc119(+)] V;* *rgs-7(he290[rgs-7::co-mcherry::co-epdz]) X*	
3c	SV2074	*ruIs57[Ppie-1::gfp::tbb-2 + unc119(+)] V; rgs-7(he290[rgs-7::co-mcherry::co-epdz]) X*	
	SV2076	*CxTi 10816(he259[Peft-3::PH::eGFP::LOV::tbb-2]) IV; ruIs57[Ppie-1::Tub::GFP] V;* *rgs-7(he290[rgs-7::co-mCherry::co-ePDZ]) X*	
	SV2143	*par-6(he322[par-6::gfp(smu-1 introns)::glo-lov] I; ruIs57[Ppie-1::gfp::tbb-2 + unc119(+)] V;* *rgs-7(he290[rgs-7::co-mcherry::co-epdz]) X*	
4a	SV2147	*ric-8(he339[glo-epdz::mcherry(smu-1 introns)::ric-8]) IV;* *cxTi10816(he259[Peft-3::ph::co-egfp::co-lov::tbb-2(3'UTR)]) IV;* *ruIs57[Ppie-1::gfp::tbb-2 + unc119(+)] V*	
4b	AZ244	*unc-119(ed3) III; ruIs57[Ppie-1::gfp::tbb-2 + unc119(+)] V*	CGC
	SV2085	*cxTi10816(he259[Peft-3::ph::co-egfp::co-lov::tbb-2(3'UTR)]) IV;* *ruIs57[Ppie-1::gfp::tbb-2 + unc119(+)] V*	
	SV2146	*ric-8(he339[glo-epdz::mcherry(smu-1 introns)::ric-8]) IV;* *ruIs57[Ppie-1::gfp::tbb-2 + unc119(+)] V*	

Figure	Strain	Genotype	Source
	SV2147	*ric-8(he339[glo-epdz::mcherry(smu-1 introns)::ric-8]) IV; cxTi10816(he259[Peft-3::ph::co-egfp::co-lov::tbb-2(3'UTR)]) IV; ruls57[Ppie-1::gfp::tbb-2 + unc119(+)] V*	
5b	SV2043	*gpr-1(he301[glo-epdz::mcherry(smu-1 introns)::gpr-1]), gpr-2(he311[Δ7 - 1212]) III; cxTi10816(he259[Peft-3::ph::co-egfp::co-lov::tbb-2(3'UTR)]) IV*	
5c	SV2043	*gpr-1(he301[glo-epdz::mcherry(smu-1 introns)::gpr-1]), gpr-2(he311[Δ7 - 1212]) III; cxTi10816(he259[Peft-3::ph::co-egfp::co-lov::tbb-2(3'UTR)]) IV*	
5d	SV2038	*gpr-1(he301[glo-epdz::mcherry(smu-1 introns)::gpr-1]), gpr-2(he311[Δ7 - 1212]) III; ruls57[Ppie-1::gfp::tbb-2 + unc119(+)] V*	
	SV2059	*gpr-1(he301[glo-epdz::mcherry(smu-1 introns)::gpr-1]), gpr-2(he311[Δ7 - 1212]) III; cxTi10816(he259[Peft-3::ph::co-egfp::co-lov::tbb-2(3'UTR)]) IV; ruls57[Ppie-1::gfp::tbb-2 + unc119(+)] V*	
5e	SV2091	*weIs21[pJA138 (Ppie-1::mcherry::tubulin::pie-1 + unc-119(+)]; unc-119(ed3) III; gpr-1(he301[glo-epdz::mcherry(smu-1 introns)::gpr-1]), gpr-2(he311[Δ7 - 1212]) III*	
	SV2099	*weIs21(pJA138[Ppie-1::mcherry::tubulin::pie-1(3'UTR)]); gpr-1(he301[glo-epdz::mcherry(smu-1 introns)::gpr-1]), gpr-2(he311[Δ7-1212])III; cxTi10816(he259[Peft-3::ph::co-egfp::co-lov::tbb-2(3'UTR)]) IV*	
5f	SV2085	*cxTi10816(he259[Peft-3::ph::co-egfp::co-lov::tbb-2(3'UTR)]) IV; ruls57[Ppie-1::gfp::tbb-2 + unc119(+)] V*	
	SV2038	*gpr-1(he301[glo-epdz::mcherry(smu-1 introns)::gpr-1]), gpr-2(he311[Δ7 - 1212]) III; ruls57[Ppie-1::gfp::tbb-2 + unc119(+)] V*	
	SV2059	*gpr-1(he301[glo-epdz::mcherry(smu-1 introns)::gpr-1]), gpr-2(he311[Δ7 - 1212]) III; cxTi10816(he259[Peft-3::ph::co-egfp::co-lov::tbb-2(3'UTR)]) IV; ruls57[Ppie-1::gfp::tbb-2 + unc119(+)] V*	
5g	SV2085	*cxTi10816(he259[Peft-3::ph::co-egfp::co-lov::tbb-2(3'UTR)]) IV; ruls57[Ppie-1::gfp::tbb-2 + unc119(+)] V*	
5h	SV2085	*cxTi10816(he259[Peft-3::ph::co-egfp::co-lov::tbb-2(3'UTR)]) IV; ruls57[Ppie-1::gfp::tbb-2 + unc119(+)] V*	
	SV2059	*gpr-1(he301[glo-epdz::mcherry(smu-1 introns)::gpr-1]), gpr-2(he311[Δ7 - 1212]) III; cxTi10816(he259[Peft-3::ph::co-egfp::co-lov::tbb-2(3'UTR)]) IV; ruls57[Ppie-1::gfp::tbb-2 + unc119(+)] V*	
6b	SV2090	*dhc-1(he255[epdz::mcherry::dhc-1])/+ I; cxTi10816(he259[Peft-3::ph::co-egfp::co-lov::tbb-2(3'UTR)]) IV; ruls57[Ppie-1::gfp::tbb-2 + unc119(+)] V*	
6c	SV2090	*dhc-1(he255[epdz::mcherry::dhc-1])/+ I; cxTi10816(he259[Peft-3::ph::co-egfp::co-lov::tbb-2(3'UTR)]) IV; ruls57[Ppie-1::gfp::tbb-2 + unc119(+)] V*	
6d	SV2095	*dhc-1(he255[epdz::mcherry::dhc-1]) I; ruls57[Ppie-1::gfp::tbb-2 + unc119(+)] V*	
	SV2090	*dhc-1(he255[epdz::mcherry::dhc-1])/+ I; cxTi10816(he259[Peft-3::ph::co-egfp::co-lov::tbb-2(3'UTR)]) IV; ruls57[Ppie-1::gfp::tbb-2 + unc119(+)] V*	
6e	SV2095	*dhc-1(he255[epdz::mcherry::dhc-1]) I; ruls57[Ppie-1::gfp::tbb-2 + unc119(+)] V*	
	SV2090	*dhc-1(he255[epdz::mcherry::dhc-1])/+ I; cxTi10816(he259[Peft-3::ph::co-egfp::co-lov::tbb-2(3'UTR)]) IV; ruls57[Ppie-1::gfp::tbb-2 + unc119(+)] V*	
6f	SV2095	*dhc-1(he255[epdz::mcherry::dhc-1]) I; ruls57[Ppie-1::gfp::tbb-2 + unc119(+)] V*	
	SV2090	*dhc-1(he255[epdz::mcherry::dhc-1])/+ I; cxTi10816(he259[Peft-3::ph::co-egfp::co-lov::tbb-2(3'UTR)]) IV; ruls57[Ppie-1::gfp::tbb-2 + unc119(+)] V*	

Supplementary table 1: Genotypes of *C. elegans* used in this study, listed per figure (Continued)

Figure	Strain	Genotype	Source
7b	SV2121	*lin-5(he330[lin-5::glo-epdz::mcherry(smu-1 introns)]) II; cxTi10816(he259[Peft-3::ph::co-egfp::co-lov::tbb-2(3'UTR)]) IV; ruls57[Ppie-1::gfp::tbb-2 + unc119(+)] V*	
7c	SV2121	*lin-5(he330[lin-5::glo-epdz::mcherry(smu-1 introns)]) II; cxTi10816(he259[Peft-3::ph::co-egfp::co-lov::tbb-2(3'UTR)]) IV; ruls57[Ppie-1::gfp::tbb-2 + unc119(+)] V*	
7d	SV2120	*lin-5(he330[lin-5::glo-epdz::mcherry(smu-1 introns)]) II; ruls57[Ppie-1::gfp::tbb-2 + unc119(+)] V*	
	SV2121	*lin-5(he330[lin-5::glo-epdz::mcherry(smu-1 introns)]) II; cxTi10816(he259[Peft-3::ph::co-egfp::co-lov::tbb-2(3'UTR)]) IV; ruls57[Ppie-1::gfp::tbb-2 + unc119(+)] V*	
7e	SV2120	*lin-5(he330[lin-5::glo-epdz::mcherry(smu-1 introns)]) II; ruls57[Ppie-1::gfp::tbb-2 + unc119(+)] V*	
	SV2121	*lin-5(he330[lin-5::glo-epdz::mcherry(smu-1 introns)]) II; cxTi10816(he259[Peft-3::ph::co-egfp::co-lov::tbb-2(3'UTR)]) IV; ruls57[Ppie-1::gfp::tbb-2 + unc119(+)] V*	
7f	SV2085	*cxTi10816(he259[Peft-3::ph::co-egfp::co-lov::tbb-2(3'UTR)]) IV; ruls57[Ppie-1::gfp::tbb-2 + unc119(+)] V*	
	SV2120	*lin-5(he330[lin-5::glo-epdz::mcherry(smu-1 introns)]) II; ruls57[Ppie-1::gfp::tbb-2 + unc119(+)] V*	
	SV2121	*lin-5(he330[lin-5::glo-epdz::mcherry(smu-1 introns)]) II; cxTi10816(he259[Peft-3::ph::co-egfp::co-lov::tbb-2(3'UTR)]) IV; ruls57[Ppie-1::gfp::tbb-2 + unc119(+)] V*	
8a	SV2121	*lin-5(he330[lin-5::glo-epdz::mcherry(smu-1 introns)]) II; cxTi10816(he259[Peft-3::ph::co-egfp::co-lov::tbb-2(3'UTR)]) IV; ruls57[Ppie-1::gfp::tbb-2 + unc119(+)] V*	
8b	SV2121	*lin-5(he330[lin-5::glo-epdz::mcherry(smu-1 introns)]) II; cxTi10816(he259[Peft-3::ph::co-egfp::co-lov::tbb-2(3'UTR)]) IV; ruls57[Ppie-1::gfp::tbb-2 + unc119(+)] V*	
8c	SV2121	*lin-5(he330[lin-5::glo-epdz::mcherry(smu-1 introns)]) II; cxTi10816(he259[Peft-3::ph::co-egfp::co-lov::tbb-2(3'UTR)]) IV; ruls57[Ppie-1::gfp::tbb-2 + unc119(+)] V*	
Figure 1-figure suppl. 2a	AZ244	*unc-119(ed3) III; ruls57[Ppie-1::gfp::tbb-2 + unc119(+)] V*	CGC
	SV2087	*ttTi5605(he312[Ppie-1(long)::frt::glo-mcherry::cep-1(3'UTR)::frt::egl-13nls::glo-cre::cep-1 (3'UTR)]) II; ruls57[Ppie-1::gfp::tbb-2 + unc119(+)] V; rgs-7(he300[loxP in intron 2 + -CT co-mcherry::co-epdz::tev::loxP::3xflag]) X Ppie-1::sv40nls::flp(G5D)::egl-13nls::tbb-2(3'UTR) + Pmyo-2::tdtomato + E. coli DNA c/w PvuII Ex*	
	SV2035	*ttTi5605(he312[Ppie-1(long)::frt::glo-mcherry::cep-1(3'UTR)::frt::egl-13nls::glo-cre::cep-1 (3'UTR)]) II; ric-8(he280[loxN -741/loxN 4624]) IV; ruls57[Ppie-1::gfp::tbb-2 + unc119(+)] V; Ppie-1::sv40nls::flp(G5D)::egl-13nls::tbb-2(3'UTR) + Pmyo-2::tdtomato + E. coli DNA c/w PvuII Ex*	

Figure	Strain	Genotype	Source
	SV2088	*ttTi5605(he312[Ppie-1(long)::frt::glo-mcherry::cep-1(3'UTR)::frt::egl-13nls::glo-cre::cep-1 (3'UTR)]) II; ric-8(he280[loxN -741/loxN 4624]) IV; ruIs57[Ppie-1::gfp::tbb-2 + unc119(+)] V; rgs-7 (he300 [loxP in intron 2 + -CT co-mCherry::co-epdz::TEV::loxP::3xFlag]) X; Ppie-1::sv40nls::flp(G5D)::egl-13nls::tbb-2(3'UTR) + Pmyo-2::tdtomato + E. coli DNA c/w PvuII Ex*	
Figure 1-figure suppl. 2b	AZ244	*unc-119(ed3) III; ruIs57[Ppie-1::gfp::tbb-2 + unc119(+)] V*	CGC
	SV1460	*ric-8(md303) I; ruIs57[Ppie-1::gfp::tbb-2 + unc119(+)] V*	
Figure 2-figure suppl. 2a	LP185	*cpIs25[Pmex-5::mNeonGreen::AraD::2xStrep::tbb-2 3'UTR + unc-119(+)] II; unc-119(ed3) III*	
	LP186	*cpIs26[Pmex-5::mNeonGreen::AraD::2xStrep::tbb-2 3'UTR + unc-119(+)] II; unc-119(ed3) III*	
	LP187	*cpIs27[Pmex-5::mNeonGreen::AraD::2xStrep::tbb-2 3'UTR + unc-119(+)] II; unc-119(ed3) III*	
	LP230	*cpIs36[Pmex-5::mNeonGreen::3xFlag::AraD::tbb-2 3'UTR + unc-119(+)] II; unc-119(ed3) III*	
	LP231	*cpIs37[Pmex-5::mNeonGreen::3xFlag::AraD::tbb-2 3'UTR + unc-119(+)] II; unc-119(ed3) III*	
	LP232	*cpIs38[Pmex-5::mNeonGreen::3xFlag::AraD::tbb-2 3'UTR + unc-119(+)] II; unc-119(ed3) III*	
	LP233	*cpIs39[Pmex-5::mNeonGreen::3xFlag::AraD::tbb-2 3'UTR + unc-119(+)] II; unc-119(ed3) III*	
Figure 2-figure suppl. 2b	LP185	*cpIs25[Pmex-5::mNeonGreen::AraD::2xStrep::tbb-2 3'UTR + unc-119(+)] II; unc-119(ed3) III*	
	LP186	*cpIs26[Pmex-5::mNeonGreen::AraD::2xStrep::tbb-2 3'UTR + unc-119(+)] II; unc-119(ed3) III*	
	LP187	*cpIs27[Pmex-5::mNeonGreen::AraD::2xStrep::tbb-2 3'UTR + unc-119(+)] II; unc-119(ed3) III*	
	LP230	*cpIs36[Pmex-5::mNeonGreen::3xFlag::AraD::tbb-2 3'UTR + unc-119(+)] II; unc-119(ed3) III*	
	LP231	*cpIs37[Pmex-5::mNeonGreen::3xFlag::AraD::tbb-2 3'UTR + unc-119(+)] II; unc-119(ed3) III*	
	LP232	*cpIs38[Pmex-5::mNeonGreen::3xFlag::AraD::tbb-2 3'UTR + unc-119(+)] II; unc-119(ed3) III*	
	LP233	*cpIs39[Pmex-5::mNeonGreen::3xFlag::AraD::tbb-2 3'UTR + unc-119(+)] II; unc-119(ed3) III*	
Figure 2-figure suppl. 3	LP288	*cpSi22[Pcdk-1::gfp::cdk-1 + unc-119(+)] II; unc-119(ed3) III*	
	LP294	*cpSi28[Pcdk-1::gfp-GLO::cdk-1 + unc-119(+)] II; unc-119(ed3) III*	
Figure 5-figure suppl. 1	SV1972	*gpr-1(he301[glo-epdz::mcherry(smu-1 introns)::gpr-1]) III*	
	SV2085	*cxTi10816(he259[Peft-3::ph::co-egfp::co-lov::tbb-2(3'UTR)]) IV; ruIs57[Ppie-1::gfp::tbb-2 + unc119(+)] V*	
	SV1982	*gpr-1 (he301[glo-epdz::mcherry(smu-1 introns)::gpr-1]) III; cxTi10816(he259[Peft-3::ph::co-egfp::co-lov::tbb-2(3'UTR)]) IV*	
Figure 5-figure suppl. 2	AZ244	*unc-119(ed3) III; ruIs57[Ppie-1::gfp::tbb-2 + unc119(+)] V*	CGC
	SV1815	*gpr-1(he266[Δgpr-1 -443 to 2039]) III; ruIs57[Ppie-1::gfp::tbb-2 + unc119(+)] V*	
	SV1816	*gpr-2 (he267[Δgpr-2 368 to 1953]) III; ruIs57[Ppie-1::gfp::tbb-2 + unc119(+)] V*	
	SV2075	*gpr-1(he301[glo-epdz::mcherry(smu-1 introns)::gpr-1]) III; ruIs57[Ppie-1::gfp::tbb-2 + unc119(+)] V*	

Supplementary table 1: Genotypes of *C. elegans* used in this study, listed per figure (Continued)

Figure	Strain	Genotype	Source
	SV2038	*gpr-1(he301[glo-epdz::mcherry(smu-1 introns)::gpr-1]), gpr-2(he311[Δ7 - 1212]) III; ruIs57[Ppie-1::gfp::tbb-2 + unc119(+)] V*	
Figure 5-figure suppl. 3a	SV2085	*cxTi10816(he259[Peft-3::ph::co-egfp::co-lov::tbb-2(3'UTR)]) IV; ruIs57[Ppie-1::gfp::tbb-2 + unc119(+)] V*	
	SV2059	*gpr-1(he301[glo-epdz::mcherry(smu-1 introns)::gpr-1]), gpr-2(he311[Δ7 - 1212]) III; cxTi10816(he259[Peft-3::ph::co-egfp::co-lov::tbb-2(3'UTR)]) IV; ruIs57[Ppie-1::gfp::tbb-2 + unc119(+)] V*	
Figure 5-figure suppl. 3b	SV2085	*cxTi10816(he259[Peft-3::ph::co-egfp::co-lov::tbb-2(3'UTR)]) IV; ruIs57[Ppie-1::gfp::tbb-2 + unc119(+)] V*	
	SV2059	*gpr-1(he301[glo-epdz::mcherry(smu-1 introns)::gpr-1]), gpr-2(he311[Δ7 - 1212]) III; cxTi10816(he259[Peft-3::ph::co-egfp::co-lov::tbb-2(3'UTR)]) IV; ruIs57[Ppie-1::gfp::tbb-2 + unc119(+)] V*	
Figure 6-figure suppl. 1a	SV2085	*CxTi 10816(he259[Peft-3::PH::eGFP::LOV::tbb-2]) IV; ruIs57[Ppie-1::Tub::GFP] V*	
	SV2090	*dhc-1(he255[epdz::mcherry::dhc-1])/+ I; cxTi10816(he259[Peft-3::ph::co-egfp::co-lov::tbb-2(3'UTR)]) IV; ruIs57[Ppie-1::gfp::tbb-2 + unc119(+)] V*	
Figure 6-figure suppl. 1b	SV2085	*CxTi 10816(he259[Peft-3::PH::eGFP::LOV::tbb-2]) IV; ruIs57[Ppie-1::Tub::GFP] V*	
	SV2090	*dhc-1(he255[epdz::mcherry::dhc-1])/+ I; cxTi10816(he259[Peft-3::ph::co-egfp::co-lov::tbb-2(3'UTR)]) IV; ruIs57[Ppie-1::gfp::tbb-2 + unc119(+)] V*	
Figure 6-figure suppl. 1c	SV2095	*dhc-1(he255[epdz::mcherry::dhc-1]) I; ruIs57[Ppie-1::gfp::tbb-2 + unc119(+)] V*	
	SV2090	*dhc-1(he255[epdz::mcherry::dhc-1])/+ I; cxTi10816(he259[Peft-3::ph::co-egfp::co-lov::tbb-2(3'UTR)]) IV; ruIs57[Ppie-1::gfp::tbb-2 + unc119(+)] V*	
Figure 6-figure suppl. 2	SV1673	*dhc-1(he255[epdz::mcherry::dhc-1]) I*	
	SV2090	*dhc-1(he255[epdz::mcherry::dhc-1])/+ I; cxTi10816(he259[Peft-3::ph::co-egfp::co-lov::tbb-2(3'UTR)]) IV; ruIs57[Ppie-1::gfp::tbb-2 + unc119(+)] V*	
	SV2171	*dhc-1(he255[epdz::mcherry::dhc-1])/+ I; dnc-1(cp271[dnc::co-mng::3xFlag]) IV; ruIs57[Ppie-1::gfp::tbb-2 + unc119(+)] V*	
	SV2172	*dhc-1(he255[epdz::mcherry::dhc-1])/+ I; cxTi10816(he259[Peft-3::ph::co-egfp::co-lov::tbb-2(3'UTR)]) IV; dnc-1(cp271[dnc::co-mng::3xFlag]) IV; ruIs57[Ppie-1::gfp::tbb-2 + unc119(+)] V*	
	SV2120	*lin-5(he330[lin-5::glo-epdz::mcherry(smu-1 introns)]) II; ruIs57[Ppie-1::gfp::tbb-2 + unc119(+)] V*	
	SV2121	*lin-5(he330[lin-5::glo-epdz::mcherry(smu-1 introns)]) II; cxTi10816(he259[Peft-3::ph::co-egfp::co-lov::tbb-2(3'UTR)]) IV; ruIs57[Ppie-1::gfp::tbb-2 + unc119(+)] V*	

Figure	Strain	Genotype	Source
Figure 7-figure suppl. 1	SV2085	*cxTi10816(he259[Peft-3::ph::co-egfp::co-lov::tbb-2(3'UTR)]) IV; ruls57[Ppie-1::gfp::tbb-2 + unc119(+)] V*	
	SV2120	*lin-5(he330[lin-5::glo-epdz::mcherry(smu-1 introns)]) II; ruls57[Ppie-1::gfp::tbb-2 + unc119(+)] V*	
	SV2121	*lin-5(he330[lin-5::glo-epdz::mcherry(smu-1 introns)]) II; cxTi10816(he259[Peft-3::ph::co-egfp::co-lov::tbb-2(3'UTR)]) IV; ruls57[Ppie-1::gfp::tbb-2 + unc119(+)] V*	
Figure 7-figure suppl. 2	SV2085	*cxTi10816(he259[Peft-3::ph::co-egfp::co-lov::tbb-2(3'UTR)]) IV; ruls57[Ppie-1::gfp::tbb-2 + unc119(+)] V*	
	SV2120	*lin-5(he330[lin-5::glo-epdz::mcherry(smu-1 introns)]) II; ruls57[Ppie-1::gfp::tbb-2 + unc119(+)] V*	
	SV2121	*lin-5(he330[lin-5::glo-epdz::mcherry(smu-1 introns)]) II; cxTi10816(he259[Peft-3::ph::co-egfp::co-lov::tbb-2(3'UTR)]) IV; ruls57[Ppie-1::gfp::tbb-2 + unc119(+)] V*	

Supplementary table 2: DNA oligo's used in this study

Used for allele	Code	Name	Purpose	PCR template
CxTi10816(he258[Peft-3::ph::co-egfp::co-lov::tbb-2(3'UTR)]) IV	oRS074	GA Peft-3 PH R	clone pBSK HDR repair template	pVP019
	oRS075	GA PH Peft-3 F		pVP019
	oRS076	GA PH eGFP R		pLF035
	oRS077	GA eGFP PH F		pLF035
	oLF082	GA CxTi10816 fix F		pLF035
	oLF138	CxTi10816 eft-3 R		pLF035
	oLF139	Eft-3 CxTi10816 F		pLF035
	oLF146	Tbb-2 CxTi10816 R		pLF035
	oRS131	CxTi10816 gRNA_F	ligate in pJJR50	
			sgRNA vector	
	oLF087	CxTi10816 gRNA_R		
rgs-7(he290[rgs-7::co-mcherry::co-epdz]) X	oLF233	SEC mod mCh-ePDZ #1 F Bsu361	clone pBSK HDR repair template	pLF056
	oLF234	SEC mod mCh-ePDZ #2 R	modification of pDD082 (Addgene)	pLF056
	oLF284	GA rgs-7 UTR RH SEC F		genomic DNA
	oLF285	GA rgs-7 UTR RH SEC R		genomic DNA
	oLF282	GA rgs-7 LH SEC F		genomic DNA
	oLF289	GA rgs-7 LH SEC Rev wo linker		genomic DNA
ttTi5605(he314[Ppie-1::glo-epdz::mcherry(smu-1)::tbb-2(3'UTR)]) II	oLF504	GA Cx right ttTi5605 pBSK F	clone pBSK HDR repair template	genomic DNA
epdz::mcherry	oLF505	GA Cx right ttTi5605 xhoI cx left R		genomic DNA
	oLF506	GA Cx left ttTi5605 XhoI cx rigth F		genomic DNA
	oLF507	Ga Cx left ttTi5605 pBSK R		genomic DNA
	oLF508	GA pie-1 enhancer ttTI5605 F		pAZ123 (Addgene)
	oLF509	long pie-1p 700 R		pAZ123 (Addgene)
	oLF510	long pie-1p 652 F		pAZ123 (Addgene)
	oLF511	GA long pie-p xhoI ttTi5605 R		pAZ123 (Addgene)
	oRS316	GA tbb-2 UTR mcherry (smu-1) R		pRS096
	oRS317	GA mcherry (smu-1) tbb-2 UTR F		pRS053
	oRS318	GA ttTi5605 tbb-2 UTR R		pRS053
	oRS336	GA Ppie-1 long epdz GLO F v2		pRS096
gpr-1(he301[glo-epdz::mcherry(smu-1 introns)::gpr-1]) III	oLF 465	GA pGPR-1 glo-epdz R	clone pBSK HDR repair template	pLF063
	oLF 466	GA pGPR-1 pbsk F		pLF063
	oLF 467	GA GPR-1 mch(smu-1) F		pLF063
	oLF 468	GA GPR-1 pbsk R		pLF063
	oLF482	GLO ePDZ 1 F		pRS093
	oLF483	GA MCH SMU-1 gpr-1 R		pRS093
	oVP283	gpr-1 17 U6_gRNA_F	ligate in sgRNA vector	
	oVP284	gpr-1 17 U6_gRNA_R		

Sequence 5' to 3'
TCCTGGAGCCCGTGCATTTTTGAGCAAAGTGTTTCCCAACTGA
AAACACTTTGCTCAAAAATGCACGGGCTCCAGGATGAC
TTGGACATTCCCCCACCGCCCTTCTGCCGCTGGTCCATG
GGCAGAAGGGCGGTGGGGGAATGTCCAAGGGAGAGGAGCT
AACAGTTTTGTCTTCCGACAGATGTGAGACGGAAAAATGGCCAAAATTCGAGATTTTGACTAAAATCAGTG
CAATAAAAGACCAAAGGTGCGTTTGGACGCAAGTACACGATTG
TCGTGTACTTGCGTCCAAACGCACCTTTGGTCTTTTATTGTCAACT
AAATAGCAGGAAAATAAGAAATTTGGCCGTGTGTCACTAGTTGAGACTTTTTTCTTGGCGGC
/5PHOS/TCTTAGCTCAATCGTGTACTTGCG
/5PHOS/AAACCGCAAGTACACGATTGAGCT
CCTCAGGagcatcgATGTCCAAGGGAGAGGAGGA
ctttccggattgaaagtacagattctcTCAGGTACGGTAGTTGATGGAGA
CGACGACAAGCGTGATTACAAGGATGACGATGACAAGAGATGAgcaatcatattctcattttatgatcttttgt
atttcacacaggaaacagctatgaccatgttatcgatttcaacaaaaatgtcaccatgtcaatcgaa
cccagtcacgacgttgtaaaacgacggccagtcgccggcaTTGAAAAAGGAGTTTTCCGATGAGAAC
CTCCCTTGGACATCGATGCTCCTGAGGCTCCCGATGCTCCTGACGGTGATGATGACGTGG
ccATCgaattatcaactatgtataatAAAGTTGCGGTACCgaatcactacgtgcgggatcat
cgaaatgtcctcctCTCGAGgattccatgatggtagcaaactcac
accatcatggaatcCTCGAGaggaggacatttcgacaatgtcatataat
AAGGGAACAAAAGCTGGAGCTCCACCGCGGTGGCGGCCGCggagttggtccaatttcgtgg
cttgcacttaacgaagtgagtttgctaccatcatggaatcggaagtaaaatattgtaatattttccctaaatttcacttaaaaataa
CGGGAACATAAAATTCTGAGAATGCG
GCGCCAAAAACGTGGTGAAATA
atttttcaaacattatatgacattgtcgaaatgtcctcctCTCGAGCTGGAAAAGAAAATTTGATTTTTAATTGTTTGGG
aggattttgcatttatcTTACTTGTAAAGCTCATCCATTCCTCCG
TGGATGAGCTTTACAAGTAAgataaatgcaaaatcctttcaagcattcc
tttttcaaacattatatgacattgtcgaaatgtcctcctCtgagacttttttcttggcggc
TCCCAAACAATTAAAAATCAAATTTTCTTTTCCAGCaaaaATGCCAGAGCTCGGATTCTC
CTCCGACACCTCCGGAGATCGAGAATCCGAG CTCTGGCATtcgttttgcgaatgtggaaacttc
AAAACGACGGCCAGTGAATTGTAATACGACTCACTATAGGGCGAATTGGccagtttcatctcaagattctccatct
CACCGGAGGAATGGATGAGCTTTACAAGggaggcggtgggATGGATGTCTCCTACTATGACGGT
TAACCCTCACTAAAGGGAACAAAAGCTGGAGCTCCACCGCCGTAATAGGCGATGTGAACTGC
ATGCCAGAGCTCGGATTCTC
ACATCCATcccaccgcctccCTTGTAAAGCTCATCCATTCCTCCG
/5phos/aattATGGACGTCTCTTATTACGA
/5phos/aaacTCGTAATAAGAGACGTCCAT

Supplementary table 2: DNA oligo's used in this study (Continued)

Used for allele	Code	Name	Purpose	PCR template
gpr-2(he311[Δ7 - 1212]) III	oLF158	gpr-2 5'UTR 99 gRNA F	ligate in sgRNA vector	
	oLF159	gpr-2 5'UTR 99 gRNA R		
	oLF160	gpr-2 3'UTR 210 gRNA F		
	oLF161	gpr-2 3'UTR 210 gRNA R		
gpr-1(he266[Δ -443 - + 2039]) III	oLF154	gpr-1 5'UTR 62 gRNA F	ligate in sgRNA vector	
	oLF155	gpr-1 5'UTR 62 gRNA R		
	oLF156	gpr-1 3'UTR 293 gRNA F		
	oLF157	gpr-1 3'UTR 293 gRNA R		
gpr-2(he267[Δ 368 - 1953]) III	oLF158	gpr-2 5'UTR 99 gRNA F	ligate in sgRNA vector	
	oLF159	gpr-2 5'UTR 99 gRNA R		
	oLF160	gpr-2 3'UTR 210 gRNA F		
	oLF161	gpr-2 3'UTR 210 gRNA R		
lin-5(he330[lin-5::glo-epdz::mcherry(smu-1 introns)]) II	oRS382	pBSK lin-5 CDS F	clone pBSK HDR repair template	
	oRS383	ePDZ GLO lin-5 CDS R		
	oRS384	lin-5 CDS ePDZ GLO F		
	oRS385	lin-5 UTR mCh smu-1 R		
	oRS386	mCh smu-1 lin-5 UTR F		
	M13R	M13R		
	oRS428	lin-5 2681 R		
	oRS429	lin-5 2755 F		
	oRS430	lin-5 PAM disruption cloning fragment F		
	oRS431	lin-5 PAM disruption cloning fragment R		
ric-8(he339[glo-epdz::mcherry(smu-1 introns)::ric-8) IV	oRS448	ric-8 gRNA 0 F	ligate in sgRNA vector	
	oRS449	ric-8 gRNA 0 R		
	oRS450	ric-8 gRNA 20 F		
	oRS451	ric-8 gRNA 20 R		
	oRS452	ric-8 gRNA 21 F		
	oRS453	ric-8 gRNA 21 R		
	oLF569	GA PRIC-8 pbsk F	clone pBSK HDR repair template	Genomic DNA
	oRS454	oRS454 GA epdz glo ric-8p R		Genomic DNA
	oRS455	GA ric-8p epdz glo F		pRS121
	oRS456	GA ric-8 cds mch smu-1 R		pRS121
	oRS457	GA mch smu-1 ric-8 cds F		Genomic DNA
	oLF571	GA RIC-8 pbsk R		Genomic DNA
	oRS458	ric-8 check -993 F		
	oRS459	GA ric-8 F		

	Sequence 5' to 3'
	/5phos/tcttgcttttgaaatgacgttggg
	/5phos/aaaccccaacgtcatttcaaaagc
	/5phos/tcttaaacagacaaaaatttcacg
	/5phos/aaaccgtgaaatttttgtctgttt
	/5phos/tcttagcaaaaataaaagaaatag
	/5phos/aaacctatttcttttatttttgct
	/5phos/tcttgagccggattttgaaattcg
	/5phos/aaaccgaatttcaaaatccggctc
	/5phos/tcttgcttttgaaatgacgttggg
	/5phos/aaaccccaacgtcatttcaaaagc
	/5phos/tcttaaacagacaaaaatttcacg
	/5phos/aaaccgtgaaatttttgtctgttt
	GTGAATTGTAATACGACTCACTATAGGGCGAATTGGGCCGATAATGGACCAACAATTACC
	GACACCTCCGGAGATCGAGAATCCGAGCTCTGGCATCTGCTTTTTGCTCGAAAAAGCAGA
	TCGGGATTCGATTTTTTCTGCTTTTTCGAGCAAAAAGCAGATGCCAGAGCTCGGATTCTC
	aaaaagttatattacaatgtatgaaagtatattTTACTTGTAAAGCTCATCCATTCCTCC
	GGATGAGCTTTACAAGTAAaatatactttcatacattgtaatataacttttcacaacac
	CAGGAAACAGCTATGACCATG
	GATGGCGAATTCGTACTTCCAAC
	GATTCGATTTTTTCTGCTTTTTCGAGC
	GGAAGTACGAATTCGCCATCtGCAGACGAGGAGAATATCAAGAAGTCCAAGAAAAAGAAtCGTCGaGATTCGATTTTTTCTGCTTTTTCG
	CGAAAAAGCAGAAAAAATCGAATCtCGACGaTTCTTTTTCTTGGACTTCTTGATATTCTCCTCGTCTGCaGATGGCGAATTCGTACTTCC
	tcttGGAATGTAGTTCTTCAGACA
	aaacTGTCTGAAGAACTACATTCC
	tcttccATGTCTGAAGAACTACAT
	aaacATGTAGTTCTTCAGACATgg
	tcttGAAAATCGACGCAATCAGGT
	aaacACCTGATTGCGTCGATTTTC
	GCCAGTGAATTGTAATACGACTCACTATAGGGCGAATTGGccgcacgtgcatgttgttta
	ggaattgcctgaaaatcatgaaaaattaattatttac
	ctcgtaaataattaatttttcatgattttcaggcaattccATGCCAGAGCTCGGATTCTC
	TCaGAATGTAGTTCTTCAGACATcccaccgcctccCTTGTAAAGCTCATCCATTCCTCCG
	ACAAGggaggcggtgggATGTCTGAAGAACTACATTCtGACCTGATTGCGTCGATTTTCG
	TAACCCTCACTAAAGGGAACAAAAGCTGGAGCTCCACCGCATTGACGACGTTTTTCGGCG
	acgttcttccgaaagttcgagc
	GTCTGAAGAACTACATTCtGACCTGATTG

Supplementary table 2: DNA oligo's used in this study (Continued))

Used for allele	Code	Name	Purpose	PCR template
dhc-1(he255[co-epdz::co-mcherry::dhc-1]	oLF116	Pdhc-1 -1119 Acc65I F	clone pBSK HDR repair template)	pRS006
	oLF137	Pdhc-1 -28 HpaI R corr		pLF38
	oVP315	dhc-1 37 U6_gRNA_F	ligate in sgRNA vector	
	oVP316	dhc-1 37 U6_gRNA_R		
par-6(he322[par-6::gfp (smu-1 introns)::glo-lov] I		PAR-6_sgRNA_F	ligate in sgRNA vector	
		PAR-6_sgRNA_R		
		PAR-6_F2	clone SEC HDR	genomic DNA
			repair template	
		PAR-6_R2		
		PAR-6_F3		
		PAR-6_R3		
	oLF484	GFP smu-1 Bsu36I F		pRS101
	oLF485	glo-LOV Acc65I R		

	Sequence 5' to 3'
	aaaaGGTACCacgtggtgcttcgtgtataatttg
	aaaaGTTAACgtttagaatttgcaaaaagaacgaataaacgg
	/5phos/aattgctgcggtttttaagtttgg
	/5phos/aaacccaaacttaaaaaccgcagc
	tcttGACGCAAATGATTCGGACAG
	aaacCTGTCCGAATCATTTGCGTC
	acgttgtaaaacgacggccagtcgccggcactaggcgagcggaagttgaa
	gatgctcctgaggctcccgatgctccGTCCTCTCCACTATCACTGTCATTTGCGTCGTGCT
	CGTGATTACAAGGATGACGATGACAAGAGATGAaaaactcttttcagccatttttcc
	ggaaacagctatgaccatgttatcgatttccccgaaattatgtcatttctggga
	AAAAACCTCAGGAGCATCGTCCAAGGGAGAGGAGCTCT
	AAAAAGGTACCTGCGGCCGCTTAGACCCAAGTGTCGACGG

Chapter 5

Genetic and optogenetic dissection of cytokinetic furrowing in vivo

Ruben Schmidt, Amir Homavar[◊], Emilia Cadar[◊], Anna Akhmanova and Sander van den Heuvel

[◊] These authors contributed equally to this manuscript.

The manuscript in this chapter is in preparation.

Abstract

The mitotic spindle instructs the site of cell cleavage during the division of animal cells. How microtubules of the anaphase spindle direct the positioning of an actomyosin contractile ring, or cleavage furrow, remains poorly understood. In the early *C. elegans* embryo, microtubules from the spindle asters and midzone provide redundant furrow-inducing signals. The astral cytokinesis signal involves proteins with well-described functions in spindle positioning, Gα, GPR-1/2$^{Pins–LGN}$, and LET-99. However, the mechanisms by which these proteins promote cytokinesis are not known. In this study, we follow an optogenetic strategy to further dissect the factors that induce furrow formation in the one-cell *C. elegans* embryo. We created a new LOV-domain membrane anchor for light-inducible recruitment of endogenous ePDZ-tagged proteins, and show that the correct cortical distribution of LIN-5$^{Mud–NuMA}$ is critical for cytokinesis in the absence of a functional midzone. Further, we find that the DEP-domain protein LET-99 promotes furrow formation, at least in part independently of its antagonist LIN-5, which inhibits furrowing at the cortex. Our combined data support a model in which the cytokinetic furrow is positioned by three concerted mechanisms, including Gα–GPR-1/2–LIN-5 mediated astral relaxation, together with midzone- and LET-99-mediated equatorial stimulation of RHO-1^{RhoA} GTPase activity.

Introduction

The cell division cycle is concluded with cytokinesis, during which phase the cytoplasm of the mother cell is physically separated to form two daughter cells. Cytokinesis occurs after segregation of the genetic material and other cellular components to opposite poles, and involves a dramatic reorganization of the cell cortex. In animal cells, this process is driven by the cytokinetic furrow; a ring-like structure that forms on the cytoplasmic side of the cell membrane and constricts, until abscission eventually pinches off the daughter cells. The construction of a cytokinetic furrow is triggered by local activation of the conserved master regulator RhoA. This small GTPase is activated by the guanine nucleotide exchange factor (GEF) ECT-2$^{Pebble–Ect2}$ in conjunction with centralspindlin, a heterotetrameric complex of ZEN-4$^{Pavarotti–MKLP1}$ and CYK-4$^{RacGAP–MgcRacGAP}$. Active RhoA·GTP drives the assembly of the main furrow filaments actin, myosin II and septin as well as their concerted constriction (Reviewed in Green et al., 2012; Basant and Glotzer, 2018). The local activation of RhoA and actin remodeling at the cell cortex has long been known to be controlled by microtubules (MTs) of the mitotic spindle, which coordinates chromosome segregation with cleavage plane specification.

Classic micromanipulation experiments in sand dollar eggs and sea urchin embryos have shown that displacement of the mitotic spindle causes reformation of a cytokinetic furrow at a location that matches the new position of the spindle (Rappaport, 1961).

Signals from two distinct MT populations within the spindle have been implicated in specifying furrow positioning. On the one hand, the midzone of the anaphase spindle has been described to locally stimulate furrow contractility. This midzone region is formed in between the segregating chromosomes and harbors a stable array of antiparallel interdigitating MTs (Euteneuer McIntosh, 1980; Mastronarde et al., 1993; also referred to as central spindle). On the other hand, the bipolar MT arrays of opposing asters can induce a furrow capable of full ingression at their cortical midpoint, even when segregated chromosomes and a midzone are absent (Rappaport, 1961; Reviewed in Oegema and Mitchison, 1997). Diverging models have been proposed that describe how both populations of MTs may contribute to furrowing. However, an all-encompassing mechanism has yet to be established. Major complicating factors are differences between model organisms, cell types and geometries, and a high degree of redundancy between multiple pathways that contribute to cytokinesis.

A clear role in furrow stimulation has been described for the midzone. The structural integrity of the midzone is maintained by PRC1$^{SPD-1/Feo}$ and centralspindlin protein complexes that drive antiparallel MT bundling (Jiang et al., 1998; Mishima et al., 2002; Verbrugghe and White, 2004; Verni et al., 2004; Reviewed in White and Glotzer, 2012). In addition to midzone maintenance, centralspindlin also locally activates RhoA in multiple systems, through the activation and localization of Ect2^{RhoGEF} at the equatorial cortex (Yuce et al., 2005; Su et al., 2011). In contrast to the midzone, the mechanisms by which astral MTs regulate cytokinesis have remained unclear. Experiments in which the density and distribution of astral MTs was altered by drug treatment or UV ablation have provided evidence for an astral relaxation model. Such studies have indicated that astral MT repress RhoA and myosin II activity, thereby confining the zone of furrow formation to the equatorial cortex (Canman et al., 2000; Bement et al., 2005; Chen et al., 2008; Foe and von Dassow, 2008; Murthy et al., 2008; von Dassow et al., 2009; Su et al., 2014). Conversely, cortical contractility that results from local RhoA activation in cultured mammalian cells through light-inducible Ect2 is not suppressed by astral MTs (Wagner and Glotzer, 2016). Thus, whether astral MTs modulate cortical contractility through local regulation of RhoA activity, and/or through the inhibition of downstream effectors, requires further study.

In addition to an astral relaxation mechanism (Wolpert, 1960; White and Borisy, 1983), equatorial stimulation by astral MTs has also been observed in different cell types. Such a mechanism may result from the formation of stable midzone-like interdigitating MTs at the cortex (Canman et al., 2003; Inoue et al., 2004). However, the presence of antiparallel bundled MTs in between the asters does not appear to be required for furrow initiation in cultured mammalian cells (Savoian et al., 1999). Whether through astral relaxation or equatorial stimulation, a minimal degree of spindle pole separation has been proposed to be needed for aster-induced furrow initiation (Rappaport, 1969; Dechant and Glotzer, 2003; von Dassow et al., 2009; Lewellyn et al., 2010), although this is not observed in all

studies (Verbrugghe and White, 2007; Price and Rose, 2017). Anaphase astral MT have also been suggested to initially provide an equatorial stimulation followed by polar relaxation (Motegi et al., 2006). Thus, the molecular mechanisms by which astral microtubules control the positioning of a cleavage furrow remain far from clear.

The large *C. elegans* embryo has long been an attractive model for studies of spindle positioning and cytokinesis (Reviewed by Pintard and Bowerman, 2019). Even the first embryonic divisions require regulated spindle positioning for the control of daughter cell size and arrangement, as well as developmental fate. Experiments based on midzone severing with a UV laser in the one-cell embryo revealed that the spindle is positioned by cortical pulling forces that act on astral MTs (Grill et al., 2001). In response to PAR protein polarity, such pulling forces are higher in the posterior, which underlies a displacement of the spindle toward the posterior and the ensuing asymmetric cell division. The spindle positioning forces are mediated by a conserved cortical complex of Gα·GDP, GPR-1/2$^{Pins–LGN}$, and LIN-5$^{Mud–NuMA}$ proteins (Lorson et al., 2000; Miller and Rand, 2000; Gotta and Ahringer, 2001; Grill et al., 2001; Colombo et al., 2003;; Gotta et al., 2003; Srinivasan et al., 2003), which recruit the molecular motor dynein to pull on dynamic astral MT plus ends that grow toward the cortex (Nguyen-ngoc et al., 2007; van der Voet et al., 2011; Kotak et al., 2012; Schmidt et al., 2017; Fielmich et al., 2018; **Chapters 3**, **4**). The distribution of cortical pulling forces is modulated by the DEP domain protein LET-99, which becomes localized to a band-region in the mid-posterior cortex, and which counteracts cortical pulling forces (Tsou et al., 2002; Tsou et al., 2003; Park and Rose, 2008; Krueger et al., 2010).

Additional spindle severing experiments have shown that the midzone and asters deliver sequential furrow positioning signals that can be separated both spatiotemporally and genetically. An initial signal is provided by astral MTs, which is then refined by the midzone. Importantly, these signals are strongly redundant as either one will suffice to drive complete cytokinesis (Bringmann et al., 2005). Interestingly, the spindle positioning proteins Gα, GPR-1/2, and LET-99 have been proposed to contribute to the astral cytokinesis signal. This followed from the discovery that their removal, when combined with physical ablation or genetic disruption of the midzone, completely blocks cytokinesis. How these proteins may contribute a furrow-inducing signal remains puzzling, in particular because GPR-1/2 and LET-99 show opposing cortical distributions during metaphase and anaphase. GPR-1/2 localizes in particular to the polar cortices, while LET-99 initially forms a central cortical band in metaphase, which is controlled by antagonistic regulation from both anterior and posterior PAR proteins (Tsou et al., 2002; 2003b; Bringmann et al., 2007). In anaphase, LET-99 forms a mid-posterior band which matches the presumptive furrow, and is controlled by the position of the spindle. It remains unexplored whether LET-99 locally stimulates contractility (Bringmann et al., 2007; Werner et al., 2007; Price and Rose, 2017), whether Gα–GPR-1/2 mediates astral relaxation, possibly in combination with LIN-5–dynein, and how this relates to their role in spindle positioning.

Furthermore, recent studies have implicated other factors contributing to the astral cytokinesis signal, such as the scaffolding protein ANI-1^{Anillin} (Tse et al., 2011), the *C. elegans*-specific activator of ECT-2, NOP-1 (Tse et al., 2012), and cortical contractility regulating factors TPXL-1^{TPX2}–AIR-1$^{Aurora\ A}$ (Mangal et al., 2018). It remains currently unclear whether these factors function through a common mechanism or contribute different effects of astral MTs in regulating cortical contractility.

In this study, we describe a systematic analysis of the astral cytokinesis signal in the one-cell *C. elegans* embryo. First, we show that LIN-5 participates in the astral cytokinesis signal, in addition to the previously reported Gα, GPR-1/2$^{Pins–LGN}$, and LET-99 proteins (Bringmann et al., 2007). Next, we apply an optogenetic strategy to control the localization of endogenous proteins through a light-inducible ePDZ–LOV domain interaction. Hereto, we created a 3xPH::LOV membrane anchor that allows localized cortical protein recruitment, and use this to show that polar enrichment of LIN-5 contributes to cleavage furrow specification. We use a variety of independent ways to disrupt the midzone – through UV ablation, perturbing the SPD-1^{PRC1} midzone organizer, or preventing kinetochore formation through HCP-3^{CENP-A} depletion – which turn out to affect cytokinesis differently. When combined with interference of the astral signal, midzone ablation or *spd-1* mutation prevent successful cytokinesis, while *hcp-3* RNAi causes delayed and prolonged furrowing. This difference may be determined by the availability of the SPD-1^{PRC1} and/or CYK-4–ZEN-4 centralspindlin complexes, which organize the midzone but also appear to participate in the astral signal. We found that ZEN-4 localizes to the equatorial cortex before furrowing, dependent on the presence of LET-99. Moreover, we demonstrate that light-inducible cortical recruitment of CYK-4 induces cytokinesis and ectopic furrowing, dependent on the presence of the RhoGEF ECT-2. Our data support the model that LET-99 at the equatorial cortex promotes the localization of the centralspindlin component CYK-4$^{RacGAP/MgcRacGAP}$, which likely leads to local activation of the Ect2 RhoGEF.

Results

LIN-5 is required for cytokinesis in the absence of a functional midzone

We set out to examine whether LIN-5 participates in delivering the astral cytokinesis signal, as has been show for its complex components Gα and GPR-1/2, as well as their antagonist LET-99 (Bringmann et al., 2007) (**Figure 1a**). To this end, we disrupted the midzone through ablation with a focused UV laser during early anaphase (in essence as described earlier by Grill et al., 2001). We used time-lapse spinning disc confocal microscopy of embryos expressing GFP::TBB-2$^{\beta\text{-tubulin}}$ and PH::GFP to track movements of the spindle and cell membrane (Fielmich et al., 2018; **Chapter 4**). Control embryos with and without severed spindles successfully initiated and completed cytokinesis, as did embryos in which solely *gpr-1/2* or *lin-5* was depleted by injection of dsRNA. Conversely, cytokinesis failure resulted from the combination of spindle severing with depletion of *gpr-1/2* (N=9, 66%) or *lin-5* (N=21, 33%). Embryos often displayed cortical ingressions over a broad range of the cortex instead of forming a single furrow (**Figure 1b**, **c**). This indicates that cortical contractility was still induced but no longer properly spatially regulated. For all conditions, midzone ablation prolonged the duration of furrow ingression, even in embryos that completed cytokinesis (**Figure 1-figure supplement 1a**). This confirms that the midzone is important for the pace of constriction, as concluded in earlier studies (Bringmann et al., 2005; Basant et al., 2015). Previous work has implicated pole separation in the furrowing ability of midzone-defective embryos (Dechant and Glotzer, 2003). To examine such a correlation, we quantified the extent of pole separation in manipulated embryos. Spindle severing rescued the diminished pole separation resulting from depleting cortical pulling force components, and we found no correlation between successful cytokinesis and increased pole separation (**Figure 1-figure supplement 1b-d**). These data indicate that GPR-1/2 and LIN-5 contribute to aster-positioned cytokinesis independently of their role in spindle elongation. Imaging of embryos expressing a membrane marker revealed that RNAi of *gpr-1/2* or *lin-5* did not block cytokinesis, although furrowing defects were frequently observed. Membrane blebbing during cytokinesis occurred in both conditions (0%, N=29 for untreated controls; 60%, N=25 for *gpr-1/2(RNAi)*; 42,9%, N=49 for *lin-5(RNAi)*) (**Figure 1-figure supplement 2a**), and is associated with decreased cortical stability (Severson et al., 2002). Consistent with previous experiments (Bringmann et al., 2007), these data show that the full Gα–GPR-1/2–LIN-5 complex plays a role in regulating aster-mediated focusing of cortical contractility.

Depletion of LIN-5 rescues midzone rupture resulting from *spd-1* inactivation

Next, we wanted to investigate whether cortical LIN-5 could directly inhibit cortical contractility. If true, this would fit into an astral relaxation model that was previously proposed for aster-directed cytokinesis (Wolpert, 1960; White and Borisy, 1983), and also

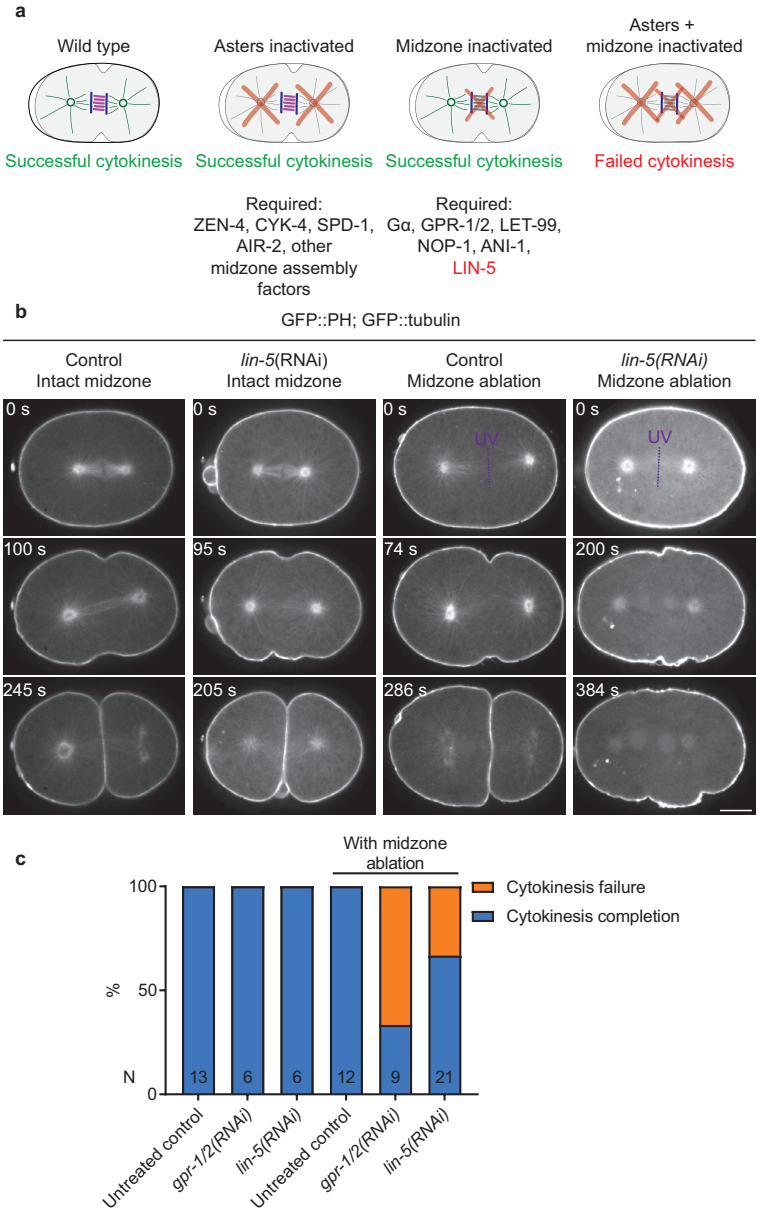

Figure 1. **GPR-1/2 and LIN-5 are required for proper aster-directed cytokinesis**. (**a**) Cartoon model representing the redundancy of aster- and midzone-derived cytokinesis signals and the proteins known to be required for each specific signal. (**b**) Spinning disk confocal microscopy images of one-cell embryos showing fluorescently labeled mitotic spindles (visualized by GFP::tubulin) and cell membranes (visualized by PH::GFP::LOV). Representative metaphase/early anaphase (top), late anaphase/telophase (middle) and late telophase (bottom) single frames are shown from time-lapse movies of control, *lin-5(RNAi)*, midzone UV ablated and *lin-5(RNAi)* + midzone UV ablated embryos. UV ablated regions are indicated in purple. (**c**) Quantification of percentage embryos that completed (blue) or failed (orange) cytokinesis in indicated conditions, either with or without midzone ablation. N values are indicated in graphs. Scale bar: 10 μm.

match the cortical distribution of LIN-5 during anaphase (Park and Rose, 2008; Schmidt et al., 2017; **Chapter 3**). As an alternative to this model, LIN-5 could be required together with Gα–GPR-1/2 to confine LET-99 to the equatorial cortex where it might stimulate local contractility (Bringmann et al., 2007; Werner et al., 2007; Price and Rose, 2017). We aimed to combine midzone inactivation with spatiotemporal control of cortical protein localization using the light-induced LOV–ePDZ system (Strickland et al., 2012). However, the 355 nm UV laser used for spindle severing experiments globally activates LOV. This precludes any combined spindle severing and local recruitment experiments. Thus, an alternative strategy for midzone disruption is required to allow for optimal use of the LOV–ePDZ system.

We decided to perturb midzone function genetically, making use of *spd-1* loss of function through either RNAi, or the previously described temperature sensitive *spd-1(oj5)* allele (O'Connell et al., 1998; Verbrugghe and White, 2004; Bringmann et al., 2007). SPD-1 is required together with centralspindlin to bundle antiparallel MTs in the midzone. Consistent with previous reports, disrupting the midzone by *spd-1(RNAi)* or *spd-1(oj5)* did not interfere with cytokinesis. A low incidence of late cytokinesis failure resulted from *spd-1; lin-5* double RNAi, while *spd-1(oj5); lin-5(RNAi)* embryos showed much stronger cytokinesis defects (**Figure 2a-c**). In agreement with a recent report, however, depletion of cortical pulling forces by RNAi of *gpr-1/2* or *lin-5* rescued the midzone rupturing that occurs when inactivating *spd-1* alone (**Figure 2-figure supplement 1**). Based on this latter observation, it is questionable whether the synergistic effect of *lin-5(RNAi)* and *spd-1(oj5)* really results from a combined loss of midzone and astral cytokinesis signals.

GPR-1/2, LIN-5 and LET-99 are required for the proper timing of furrow formation in the absence of a functional midzone

As an alternate approach to *spd-1* knockdown, we *targeted hcp-3* for midzone disruption. HCP-3 is a CENP-A-related core centromere component, which is required for kinetochore assembly and chromosome segregation. However, one-cell embryos that lack functional HCP-3 progress through the cell cycle with normal kinetics (Buchwitz et al., 1999; Oegema et al., 2001). We followed embryos expressing fluorescent TBG-1 and HIS-48 by time-lapse differential interference contrast (DIC) and widefield fluorescence microscopy, to follow centrosomes and DNA, respectively (Toya et al., 2010). Resembling control-treated embryos, *hcp-3(RNAi)* embryos successfully progressed through mitosis and completed cytokinesis (**Figure 3a**, **b** and **figure 3-figure supplement 1a**). The same was observed for *gpr-1/2(RNAi), lin-5(RNAi)* and *let-99(RNAi)* embryos, consistent with previous reports (Rose et al., 1998; Colombo et al., 2003; Lorson et al., 2000 Srinivasan et al., 2003). Surprisingly, embryos subject to double depletion of *gpr-1/2(RNAi); hcp-3(RNAi), lin-5(RNAi); hcp-3(RNAi)* or *let-99(RNAi); hcp-3(RNAi)* all completed cytokinesis also (**Figure 3c**, **figure 3-figure supplement 1a**). This occurred despite complete absence of a midzone, as determined by imaging of embryos expressing endogenously tagged

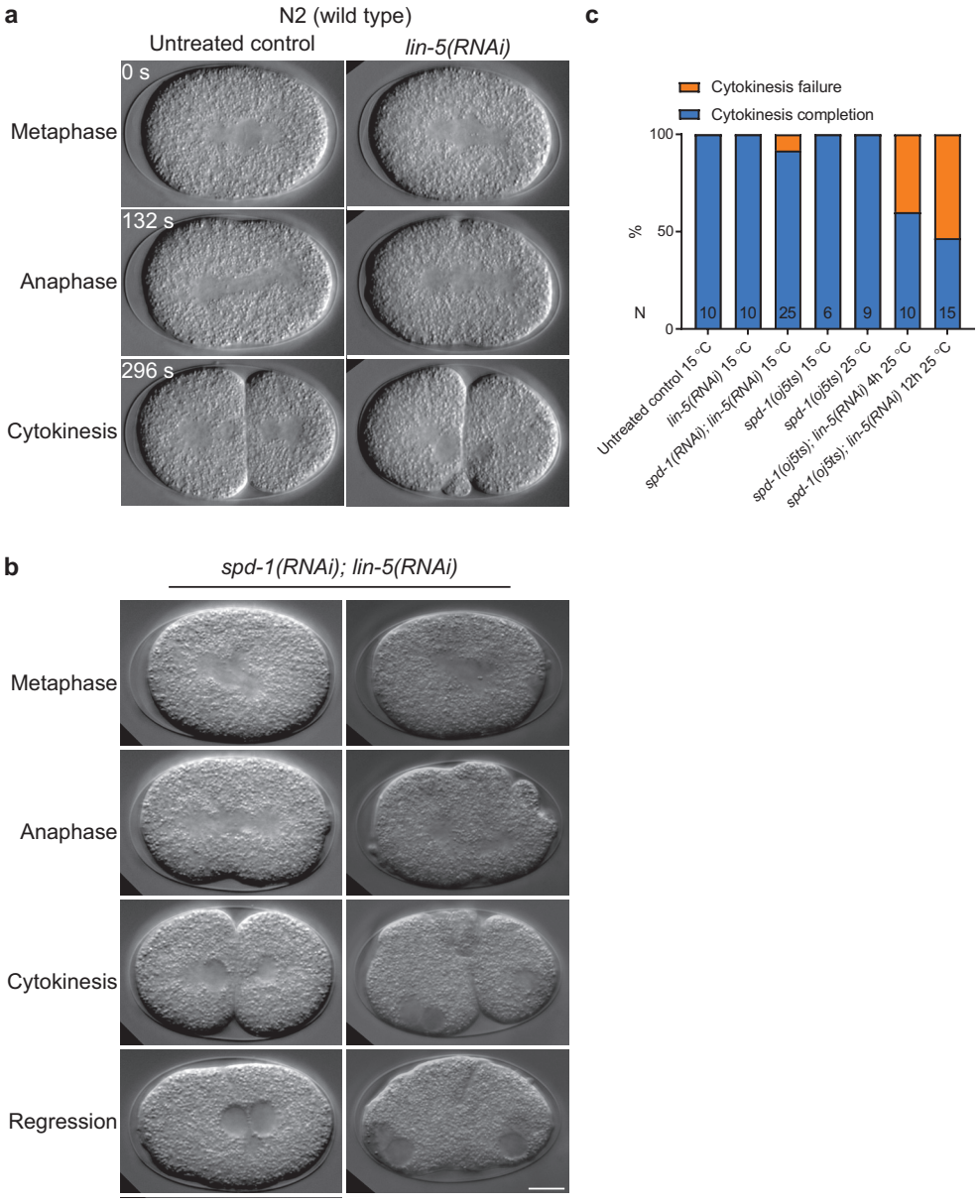

Figure 2. **Combined disruption of SPD-1 and LIN-5 results in late cytokinesis failure**. (**a**, **b**) DIC microscopy movies of N2 (wild type) embryos. Representative metaphase, anaphase, cytokinesis and regression single frames are shown from time-lapse movies of untreated control embryo and *lin-5(RNAi)* (**a**) or *spd-1(RNAi)*; *lin-5(RNAi)* (**b**) embryos. (**c**) Quantification of percentage embryos that fail cytokinesis in embryos of indicated genotypes dissected from parents shifted from 15°C to 25°C, either for 4h or 12h prior to imaging. Indicated is successful cytokinesis (blue), abscission failure in the first (orange) or first and second round of mitosis (red). N values are indicated in graph. Scale bar: 10 µm.

GFP::ZEN-4 (generated by the Galli lab, unpublished personal communication), or GFP::SPD-1 (**Figure 3-figure supplement 2**). Notably, when we combined endogenous *gfp::spd-1* with *let-99; hcp-3* double RNAi, proper furrow formation and cell division were blocked (N=7). The tagged endogenous SPD-1 protein appears functional, based on full viability of the *gfp::spd-1* strain and correct protein localization (Verbrugghe and White, 2004; Nahaboo et al., 2015), yet is probably somewhat compromised. This would indicate that embryos with reduced midzone and astral cytokinesis signals are very sensitive to SPD-1 function, which is possibly also reflected by the *spd-1(oj5)* sensitivity described above.

To better characterize the cytokinesis phenotypes, we quantified the interval between the start of anaphase spindle pole separation and appearance of the cytokinetic furrow. The *hcp-3(RNAi)* embryos that lack functional kinetochores were found to exhibit premature spindle pole separation, as observed in a previous study (Lewellyn et al., 2010). In addition, the spindle length at the start of furrowing was strongly increased in *hcp-3(RNAi)* embryos, compared to untreated controls (**Figure 3-figure supplement 3**). This effect compensated for the reduced pole separation following *gpr-1/2(RNAi), lin-5(RNAi)* or *let-99(RNAi)*, resulting in pole separation in double-depleted embryos that is close to normal (**Figure 3-figure supplement 3**). Furrow initiation was slightly delayed in *gpr-1/2(RNAi), lin-5(RNAi)* and *let-99(RNAi)* embryos. Interestingly, embryos subject to double depletion of *gpr-1/2(RNAi); hcp-3(RNAi), lin-5(RNAi); hcp-3(RNAi)*, or *let-99(RNAi); hcp-3(RNAi)* all showed a substantial delay in furrow initiation (**Figure 3d** and **figure 3-figure supplement 4**). In addition to furrow initiation, *let-99(RNAi); hcp-3(RNAi)* embryos also showed defective furrow ingression that was not present in any other condition (**Figure 3-figure supplement 2b**). This latter result indicates that LET-99 may have an additional function in promoting efficient furrow ingression. Collectively, these data show that cytokinesis can occur when the midzone as well as astral cytokinesis pathway components are absent. Yet, furrowing is strongly delayed when both pathways are compromised.

To assess whether the distribution of cortical furrowing components was affected in these embryos, we fluorescently tagged endogenous ANI-1. As GFP::ANI-1 appears functional, we followed the protein distribution during furrow initiation by live imaging of homozygous animals. Notably, cortical levels of GFP::ANI-1 became enhanced upon depletion of *gpr-1/2*. This effect was specific to the posterior cortex and extended to the equatorial region upon co-depletion of *hcp-3*. Interestingly, this effect was not observed upon depletion of *let-99* (**Figure 3-figure supplement 5**). Akin to the specific effect of *let-99* knockdown on the duration of furrow ingression, described above, this phenotypic difference between depletion of GPR-1/2 and LET-99 suggests that these proteins might contribute to cytokinesis via partly independent pathways.

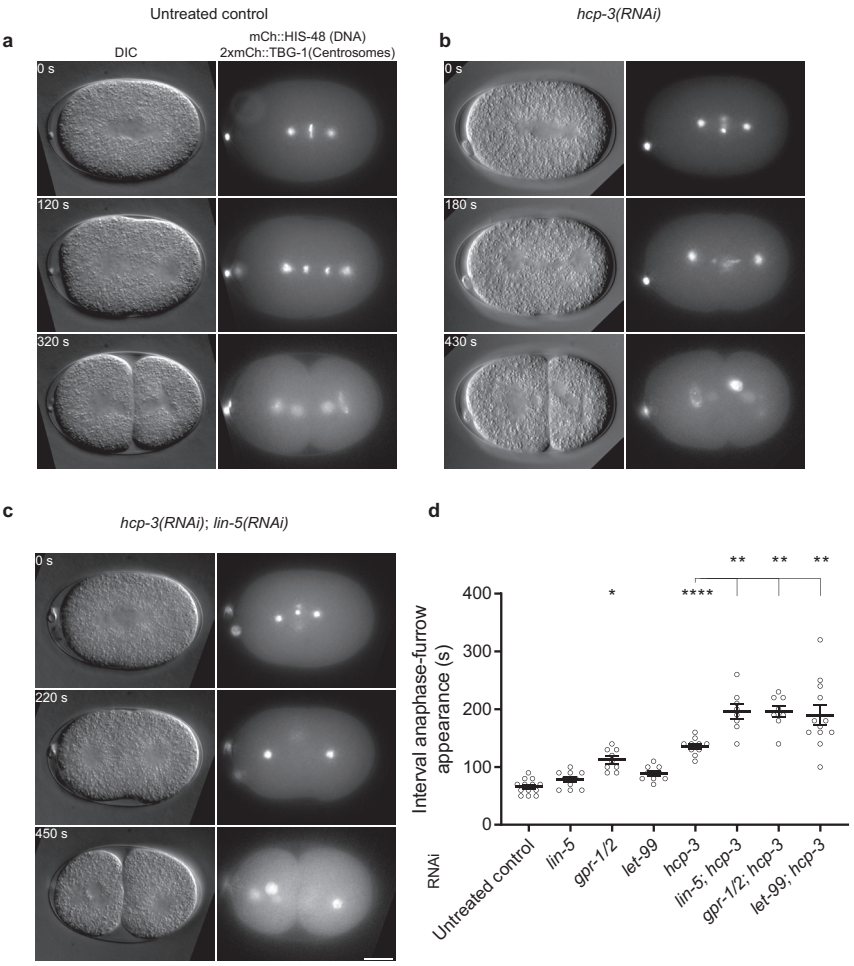

Figure 3. **GPR-1/2, LIN-5 and LET-99 are required for the proper timing of furrowing in the absence of a functional midzone.** DIC and widefield fluorescence microscopy movies of embryos showing fluorescently labeled DNA (visualized by mCherry::HIS-48) and centrosomes (visualized by 2xmCherry::TBG-1). Representative metaphase, late anaphase and cytokinesis single frames are shown from time-lapse movies of control (**a**), *hcp-3(RNAi)* (**b**) and *hcp-3(RNAi); lin-5(RNAi)* (**c**) embryos. (**d**) Quantification of the interval between anaphase spindle pole separation onset and furrow initiation for embryos of the indicated genotypes. One-way ANOVA. * P<0.05; ** P<0.01; **** P<0.0001. N=8-13. Scale bar: 10 μm.

Cortical LIN-5 locally inhibits cytokinetic furrowing

To further assess furrowing contributions of astral pathway components at the cell cortex, we applied light-inducible protein localization, based on the LOV–ePDZ protein heterodimerization system (Strickland et al., 2012; van Bergeijk et al., 2014; Harterink et al., 2016). We recently optimized this system for use in the *C. elegans* embryo, along with tagging of endogenous loci by CRISPR/Cas9-assisted recombineering (Fielmich et al., 2018; **Chapter 4**). Combining the cortical anchor PH::GFP::LOV (PH::LOV) with ePDZ-tagged proteins of interest allowed for rapid, reversible, and local protein accumulation at the cortex. We previously created endogenous *lin-5::epdz::mcherry* (LIN-5::ePDZ), which is homozygous viable and functional (Fielmich et al., 2018; **Chapter 4**). Exposure of embryos at anaphase onset to blue light (491 nm) recruited LIN-5::ePDZ globally to the PH::LOV anchor at the cortex (**Figure 4a**). This resulted in excessive spindle movements and did not disrupt cytokinesis (**Figure 4c**). In contrast, cortical LIN-5::ePDZ recruitment combined with *gpr-1/2, hcp-3* double RNAi resulted in frequent abscission failure (41,7%, N=12; **Figure 4b**, **c**), while pole separation remained at control levels (**Figure 4-figure supplement 1a**). Thus, in the absence of functional Gα–GPR-1/2–LIN-5 complexes, as a result of *gpr-1/2* RNAi, global LIN-5 localization to the cortex does not improve but further interferes with cytokinesis (**Figure 4-figure supplement 1b**). We observed an increased duration of furrow ingression upon global recruitment of LIN-5 in *hcp-3(RNAi)* embryos, as well as in *gpr-1/2(RNAi); hcp-3(RNAi)* and *let-99(RNAi); hcp-3(RNAi)* double-defective embryos (**Figure 4-figure supplement 1c**). This delay was similar to the effect of *lin-5* RNAi in *hcp-3(RNAi)* embryos, described above, and suggests that both the absence and the ectopic cortical localization of LIN-5 inhibit cytokinetic furrowing.

Possibly, a local minimum of Gα–GPR-1/2–LIN-5 at the equator contributes to efficient furrowing together with a stimulating signal from the midzone. We hypothesized that such a local minimum could either act through inhibition of contractility at the polar cortex, or by ensuring the proper localization of LET-99 to locally stimulate cytokinesis at the equator. Consistent with the first idea, global recruitment of LIN-5 combined with *let-99*; *hcp-3* double RNAi also resulted in abscission failure (25%, N=4; **Figure 4a**, **c**). Moreover, global LIN-5 recruitment in combination with midzone ablation resulted in a complete failure to divide (100%, N=11; **Figure 4-figure supplement 2a**, **b**). Excessive movement of the separated centrosomes in the Z-direction precluded the quantification of pole separation by spinning disc confocal fluorescence microscopy of these embryos. To be able to assess whether cortical LIN-5 modulates the distribution of furrow components, we genetically modified the PH::GFP::LOV anchor to a dark version by excising *gfp* through CRISPR/Cas9. This allowed for simultaneous global LIN-5::ePDZ recruitment and imaging of endogenous GFP::ANI-1 dynamics. Global recruitment of LIN-5 did not significantly alter the distribution or cortical levels of ANI-1. Interestingly, while *gpr-1/2* RNAi alleviates the posterior dip in cortical ANI-1, as described above, this effect was independent of global LIN-5::ePDZ recruitment (**Figure 4-figure supplement 3**). Collectively, these data suggest

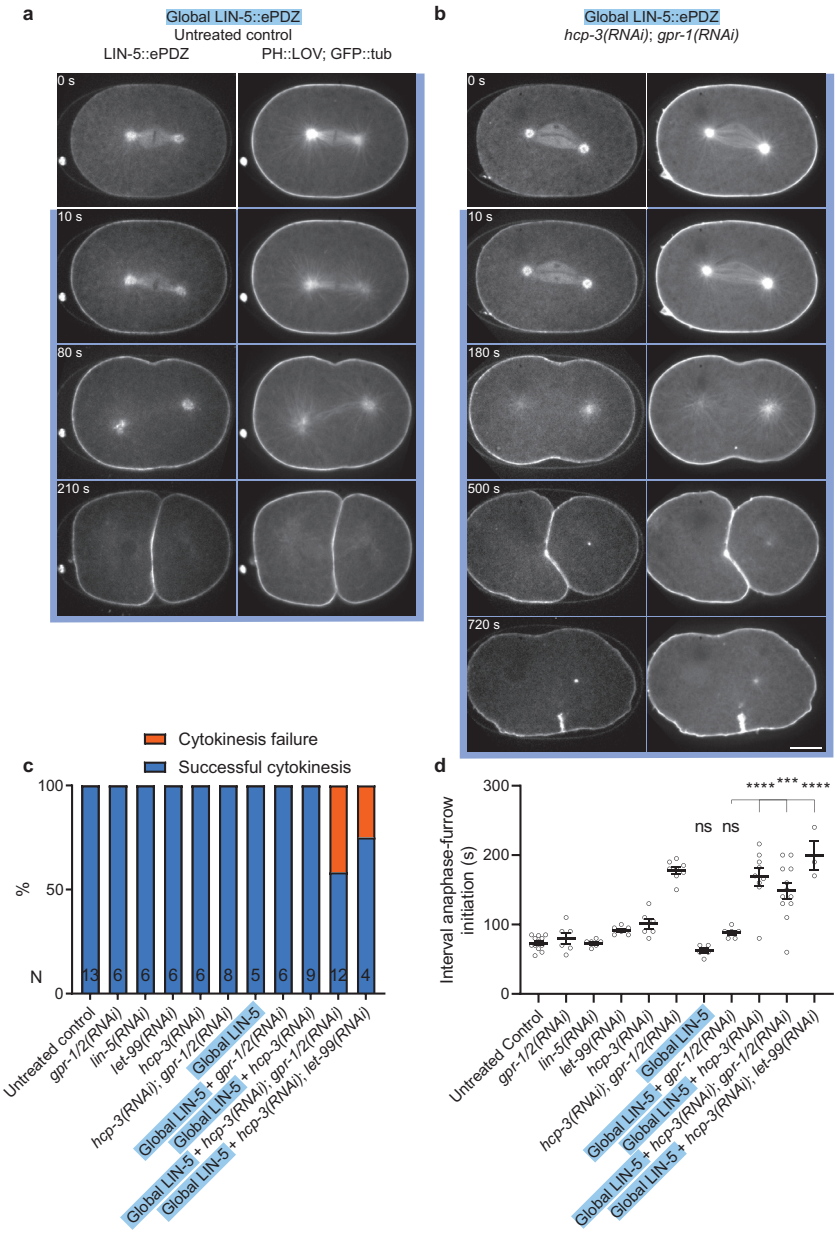

Figure 4. **Global cortical localization of LIN-5 inhibits cytokinetic furrowing**. Spinning disk confocal microscopy images of one-cell embryos showing fluorescently labeled endogenous LIN-5::ePDZ::mCherry, mitotic spindles (visualized by GFP::tubulin) and cell membranes (visualized by PH::GFP::LOV). Representative metaphase pre- and post-activation, late anaphase, cytokinesis and regression stage single frames are shown from time-lapse movies of control (**a**) and *hcp-3*(RNAi); *gpr-1/2(RNAi)* (**b**) embryos. Blue backgrounds indicate that embryos have been exposed to blue (491 nm) light at these timepoints. Quantifications of (**c**) percentage embryos that fail cytokinesis and (**d**) the interval between anaphase spindle pole separation onset and furrow initiation in embryos of indicated genotypes, with or without global recruitment of LIN-5 (indicated in blue). One-way ANOVA. *** P<0.001; **** P<0.0001. N=3-13. Scale bar: 10 µm.

that LIN-5 inhibits furrowing at the cortex through an as yet unknown mechanism, and that midzone ablation with a UV laser interferes with furrow stimulation more severely than genetic disruption.

Next, we sought to use the ePDZ–LOV system to recruit LIN-5 specifically to the equatorial cortex (**Figure 5a**). Hereto, we created endogenously tagged ePDZ-LET-99 and LIN-5-LOV (**Figure 5-figure supplement 1**), and generated a strain with the double homozygous tagged alleles. Exposure of such embryos to blue light resulted in a more uniform cortical distribution of both proteins (**Figure 5b**). We reasoned that redistribution of LIN-5 from the polar to equatorial cortex may be prevented by its normal anchor (Gα–GPR-1/2). Thus, we treated embryos with *gpr-1/2(RNAi)*, which broadened the distribution of cortical ePDZ::LET-99 but could reliably displace LIN-5::LOV to the equatorial region from the poles (**Figure 5-figure supplement 2a**). Equatorial recruitment of LIN-5 combined with *gpr-1/2(RNAi); hcp-3(RNAi)* resulted in recurrent cytokinesis failure (33.3%, N=9; **Figure 5c**), while combination of equatorial LIN-5 with *gpr-1/2(RNAi)* or *hcp-3(RNAi)* individually did not (**Figure 5d**). Of the three embryos that did not complete cytokinesis, one furrow regressed after failed abscission while the other two only generated a partially contracting furrow. Of note, the spindle pole separation defect caused by *gpr-1/2* RNAi was not fully rescued by *hcp-3* RNAi in this case (**Figure 5-figure supplement 2b**). Thus, a potential effect of reduced aster separation on cytokinesis of these embryos cannot be excluded. Collectively, these data further support the view that cortical LIN-5 locally inhibits cytokinetic furrowing.

If we assume that a bipolar distribution pattern of LIN-5 is required for aster-mediated cytokinesis, then reconstituting this cortical pattern should rescue the effect of LIN-5 depletion or dislocation. To test this, we wanted to recruit LIN-5::ePDZ locally to PH::LOV, specifically to the anterior and posterior poles, but not in the equatorial region. In previous local illumination experiments, we noticed a strong tendency of the PH::LOV anchor to diffuse laterally, which limits the extent of control over protein localization during longer timescales (Fielmich et al., 2018; **Chapter 4**). To improve the anchor, we added tandem PH domains in order to limit the rate of lateral membrane diffusion. This strategy was based on a recent report, in which clustered membrane interaction domains severely limited lateral diffusion of cortical proteins in HeLa cells (Van Geel et al., 2018). We compared PH::LOV to 3xPH::LOV in one-cell embryos expressing diffuse ePDZ::mCherry, and observed that the latter supports stable local recruitment to the cortex for noticeably longer time periods than the previous PH::LOV anchor (**Figure 6-figure supplement 1**). Using this optimized anchor and timed local illumination, LIN-5::ePDZ could be stably and reproducibly maintained at the poles from the start of anaphase until the initiation of cytokinesis in one-cell embryos (**Figure 6a**, **b**). Precise control of cortical LIN-5::ePDZ was feasible only when its normal Gα–GPR-1/2 cortical anchor was removed. In *gpr-1/2(RNAi)* embryos, polar recruitment of LIN-5::ePDZ in early anaphase resulted in significantly enhanced spindle pole separation (**Figure 6-figure supplement 2a**). Moreover, polar

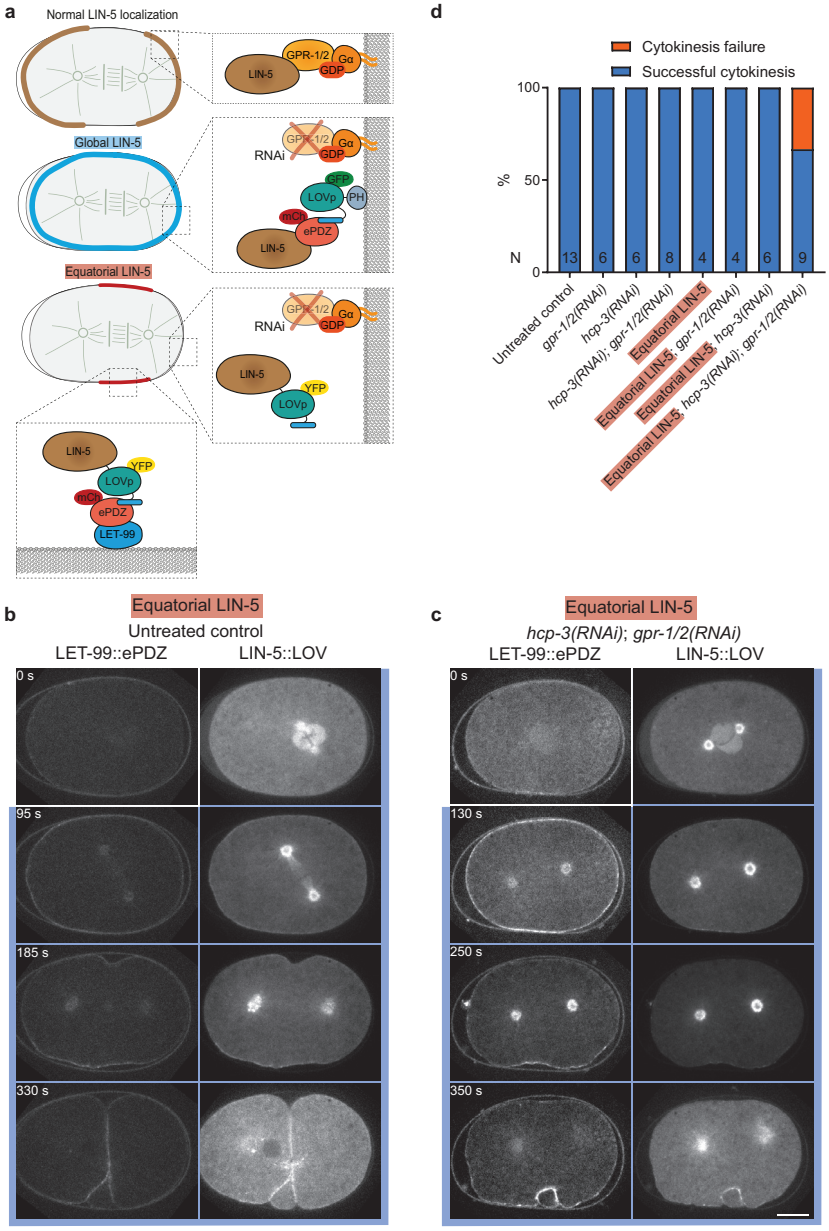

Figure 5. **Equatorial recruitment of LIN-5 inhibits cytokinetic furrowing**. (**a**) Cartoon model showing normal LIN-5 distribution and the strategies used for LIN-5 recruitment, either globally via PH::GFP::LOV, or equatorially via ePDZ::LET-99. (**b**, **c**) Spinning disk confocal microscopy images of one-cell embryos showing fluorescently labeled endogenous LIN-5::YFP::LOV and ePDZ::mCherry::LET-99. Representative metaphase before activation and post-activation, late anaphase and telophase single frames are shown from time-lapse movies of control (**b**) and *hcp-3*(RNAi); *gpr-1/2(RNAi)* (**c**) embryos. (**d**) The interval between anaphase spindle pole separation onset and furrow initiation in embryos of indicated genotypes, with or without global (indicated in blue) or equatorial (indicated in red) recruitment of LIN-5. N values are indicated in graph. Scale bar: 10 μm.

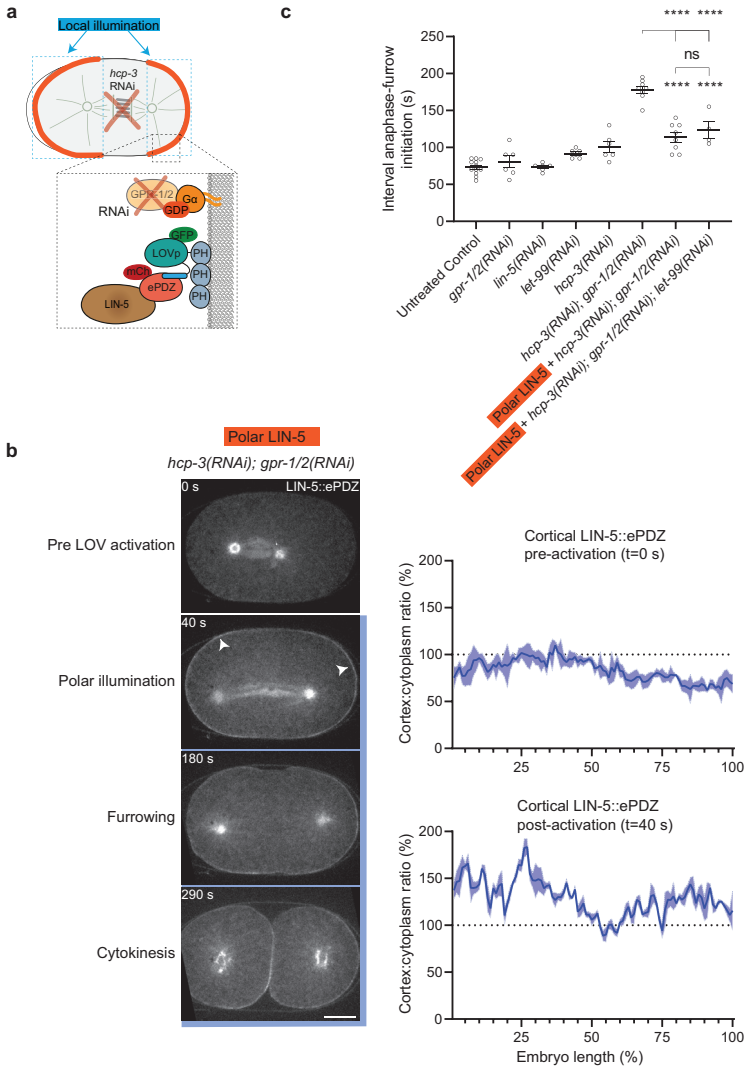

Figure 6. **Bipolar recruitment of LIN-5 rescues cytokinetic furrowing**. (**a**) Cartoon model showing the strategy used for polar LIN-5 recruitment through local activation of 3xPH::GFP::LOV. (**b**) Spinning disk confocal microscopy images of one-cell embryos showing fluorescently labeled endogenous LIN-5::ePDZ::mCherry. Representative metaphase before and after local activation, late anaphase and telophase single frames are shown from a time-lapse movie of an *hcp-3(RNAi)*; *gpr-1/2(RNAi)* embryo. Arrowheads indicate the presence of cortical LIN-5. Graphs show the cortical distribution of LIN-5 pre- (top) and post-local activation (bottom) in a single embryo, quantified as cortex:cytoplasm intensity ratio distributed over embryo length. (**c**) The interval between anaphase spindle pole separation onset and furrow initiation in embryos of indicated genotypes, with or without global (indicated in blue) or polar (indicated in orange) recruitment of LIN-5. One-way ANOVA. **** P<0.0001. N=4-12. Scale bar: 10 µm.

LIN-5::ePDZ recruitment accelerated cytokinesis in *gpr-1/2(RNAi); hcp-3(RNAi)* embryos (**Figure 6c**), and did not induce cytokinesis failure as opposed to global or equatorial recruitment of LIN-5 (**Figure 6-figure supplement 2b**). To determine whether LIN-5 inhibits contractility at the polar cortex or exerts its effect indirectly through maintaining proper equatorial localization of LET-99, we expanded polar LIN-5::ePDZ recruitment in *hcp-3(RNAi); gpr-1/2(RNAi)* embryos with *let-99* RNAi. This also rescued the delayed furrow induction of *hcp-3(RNAi); gpr-1/2(RNAi)* embryos and brings the timing of furrow initiation back to that of *hcp-3(RNAi)* alone (**Figure 6c**). Collectively, these results indicate that cell pole-enriched LIN-5 promotes cytokinesis, at least in part independently of equatorial LET-99 restriction, and likely participating in an astral relaxation pathway.

The mitotic cortical LET-99 band is positioned by PAR polarity and GPR-1/2–LIN-5

One of the questions arising from the above described observations is whether LET-99 contributes to the astral cytokinesis signal independently of the LIN-5 complex. Indeed, in a recent study, LET-99 was proposed to promote cytokinesis in both symmetrically and asymmetrically dividing blastomeres, and independently of its role in spindle positioning and Gα regulation (Price et al., 2017). To further explore the role of LET-99 in cytokinesis, we performed a detailed study of its endogenous localization pattern. Previous studies showed that LET-99 is positioned as a downstream target of PAR polarity regulators, and that LET-99 counteracts the localization of GPR-1/2–LIN-5 at the cortex (Tsou et al., 2002; Tsou et al., 2003; Bringmann et al., 2007; Park and Rose, 2007; our unpublished data). We created endogenously tagged *gfp::let-99,* which is homozygous viable and thus at least partly functional. Time-lapse confocal microscopy and quantification of cortical GFP::LET-99 from prometaphase until cytokinesis revealed that cortical enrichment of LET-99 first became apparent during prometaphase, with levels gradually increasing until they reached a maximum in late metaphase. Our observations of endogenous LET-99 differed from those previously reported (Bringmann et al., 2007). Specifically, we observed that the LET-99 band was set up slightly posterior, with a peak concentration at ~54% embryo length (instead of 50%) in metaphase, and did not shift position with the transition to anaphase. The LET-99 band did narrow in anaphase, which moved the peak further toward the posterior (**Figure 7-figure supplement 1a**). This focusing may be caused by increasing levels of Gα–GPR-1/2 complexes that counteract LET-99 localization during anaphase. Our RNAi experiments confirmed the requirement for PAR-2, PAR-3, and GPR-1/2 for the localization of LET-99 in a mid-posterior band pattern and expanded these requirements to include LIN-5. Interestingly, depletion of *gpr-1/2* or *lin-5* led to significantly increased total cortical LET-99 levels, and this effect was even stronger following the depletion of PAR-2 or PAR-3 (**Figure 7-figure supplement 1b-h**). Especially in these latter conditions the cortical band pattern of LET-99 disappeared, as instead global cortical enrichment of LET-99 was observed. Thus, anterior and posterior PAR polarity proteins as

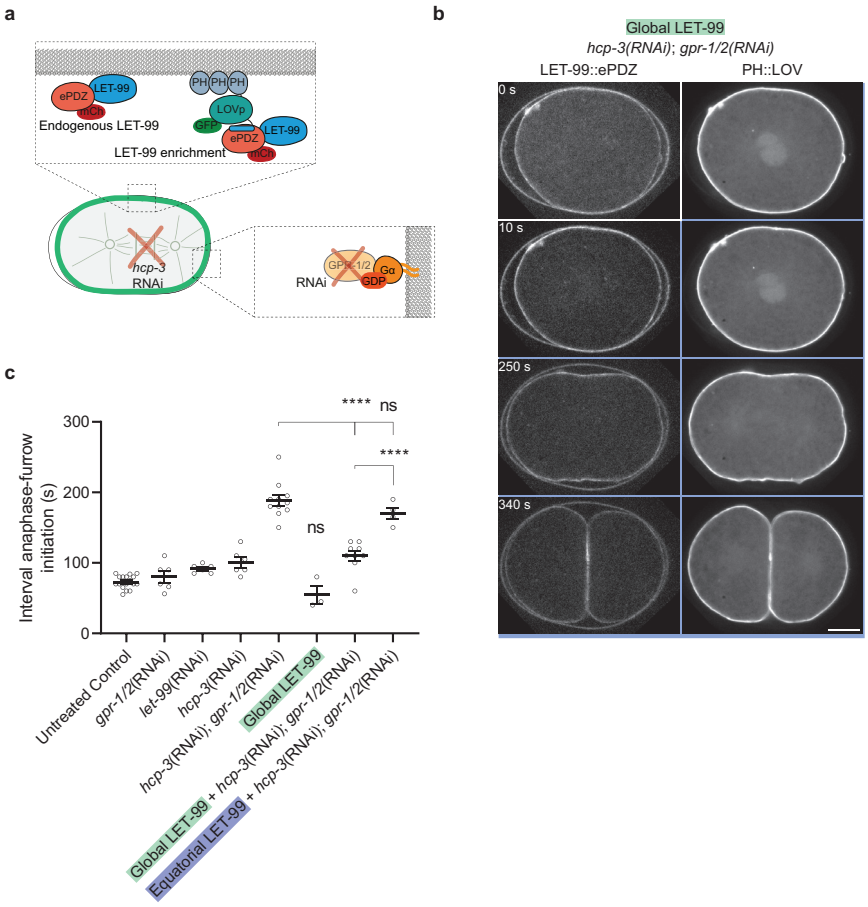

Figure 7. **Cortical recruitment of LET-99 stimulates cytokinesis**. (**a**) Cartoon model showing the strategy used for equatorial LET-99 recruitment through activation of 3xPH::GFP::LOV. (**b**) Spinning disk confocal microscopy images of one-cell embryos showing endogenous ePDZ::mCherry::LET-99 and 3xPH::GFP::LOV. Representative metaphase pre- and post- global activation, late anaphase and telophase single frames are shown from a time-lapse movie of a *hcp-3(RNAi)*; *gpr-1/2(RNAi)* embryo. (**c**) The interval between anaphase spindle pole separation onset and furrow initiation in embryos of indicated genotypes, with or without global (indicated in green) or equatorial (indicated in blue) recruitment of LET-99. One-way ANOVA. **** P<0.0001. N=4-17. Scale bar: 10 µm.

well as the GPR-1/2–LIN-5 pulling force regulators antagonize cortical LET-99 localization and promote its concentration in a posterior band.

Cortical LET-99 acutely promotes cytokinetic furrowing

To experimentally control the cortical distribution of LET-99, we generated endogenous *epdz::mcherry::let-99* (ePDZ::LET-99), which was homozygous viable but with a reduced

brood size. We combined ePDZ::LET-99 with the 3xPH::LOV anchor for light-inducible localization studies. Our attempts to locally enrich LET-99 by illumination of the equatorial cortex during mitosis were not successful. In contrast, global cortical enrichment of LET-99 was readily achieved (**Figure 7a**, **b**). Remarkably, this enrichment accelerated the initiation of cytokinetic furrowing in *hcp-3(RNAi); gpr-1/2(RNAi)* embryos and brought its timing back to *hcp-3(RNAi)* levels (**Figure 7c**). Out of 10 embryos analyzed one failed to complete cytokinesis, which may indicate that LET-99 interacts with a critical regulator of cytokinesis (**Figure 7-figure supplement 2**). These data strongly suggest that LET-99 stimulates furrowing at the cortex.

LET-99 has been reported to contribute to the proper distribution of cortical myosin in the one-cell embryo (Goulding et al., 2007; Werner et al., 2007; Price et al., 2017), but a direct link between LET-99 and stimulation of cortical contractility has not been established. By coincidence, we encountered a possible connection when tagging LET-99 at its C-terminus with YFP::LOV. While *let-99::yfp::lov* animals are homozygous viable, the cortical LET-99 localization was strongly reduced compared to normal, in particular in the one-cell embryo, and even when the linker between LET-99 and YFP::LOV expanded. Intriguingly, both LET-99::LOV fusions were detectable at the midzone region during anaphase (**Figure 7-figure supplement 3a**, **b**). This ectopic localization might reflect interaction with a protein partner that has affinity for LET-99, but in an unperturbed situation cannot compete with its membrane localization. Given the clear effect of LET-99 in stimulating cortical contractility, we hypothesized that the centralspindlin complex (which consists of ZEN-4 and CYK-4 in *C. elegans*) might be an interaction partner of LET-99.

LET-99 promotes the cortical enrichment of centralspindlin

To reveal the localization of centralspindlin in the early embryo, we decided to study ZEN-4 localization, making use of fluorescently tagged endogenous GFP::ZEN-4 (generated by the Galli lab, unpublished personal communication). GFP::ZEN-4 was mainly expressed in the germline of adult hermaphrodites. Confocal fluorescence microscopy of untreated control embryos expressing GFP::ZEN-4 showed clear concentration of the protein at the midzone, but did not reveal obvious cortical enrichment during mitosis in the one-cell embryo. These observations are consistent with previous studies of ectopic expression and immunohistochemical staining of ZEN-4 (Raich et al., 1998; Verbrugghe and White, 2004). However, by using total internal reflection fluorescence (TIRF) microscopy to specifically image fluorescent molecules near the embryo cortex, we observed dynamic speckles of GFP::ZEN-4 in late anaphase, which progressively concentrated in the equatorial cortex before furrowing initiates. To our knowledge, this is the first report of cortical ZEN-4 localization prior to furrow ingression. To explore whether LET-99 contributes to this cortical enrichment of centralspindlin, we treated embryos with *hcp-3*; *let-99* or *hcp-3; let-99* RNAi. Strikingly, quantification of the relative fluorescence signal revealed that *let-99(RNAi)* and especially

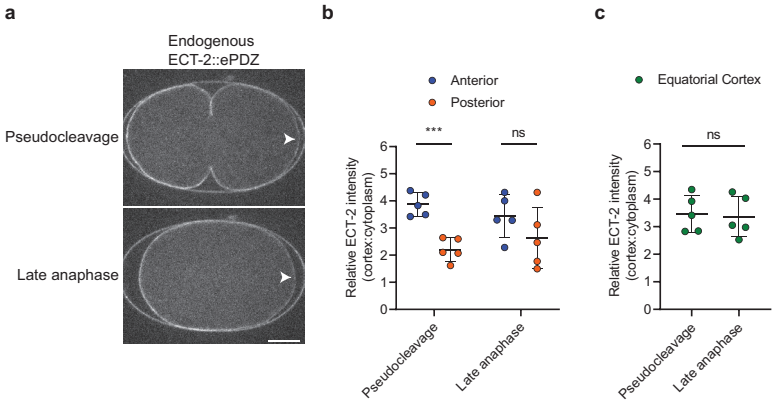

Figure 8. **The mitotic cortical localization pattern of ECT-2 does not predict its role in cytokinesis in the one-cell embryo**. (**a**) Spinning disk confocal microscopy images of a one-cell embryo showing fluorescently labelled endogenous ECT-2::ePDZ::mCherry during pseudocleavage and late anaphase. Red arrowheads indicate the previously reported posterior dip in ECT-2 localization. Quantification of relative cortical:cytoplasm ECT-2::ePDZ enrichment at the anterior (blue) and posterior (orange) poles (**b**) and equatorial (green) cortex (**c**) during pseudocleavage and late anaphase. Exact quantification method shown in **figure 8-figure supplement 1c**. Unpaired Welch's Student's *t* test. *** P<0.001. N=5 embryos. Scale bar: 10 µm.

hcp-3(RNAi); let-99(RNAi) embryos exhibited significantly reduced equatorial ZEN-4 enrichment in late anaphase (**Figure 7-figure supplement 3c**). Notably, some of the observed GFP::ZEN-4 speckles moved in a pattern that suggested interaction with MTs. This might indicate that *C. elegans* centralspindlin associates with cortical MTs in addition to midzone MTs in late anaphase. Based on the results above, we propose that LET-99 stimulates furrowing through promoting centralspindlin enrichment at the equatorial cortex. In accordance with this idea, DEP domains have been implicated in the cortical recruitment of diverse protein interactors (Consonni et al., 2014). Further investigations should reveal whether LET-99 interacts directly, or perhaps via yet unidentified binding partners, with centralspindlin.

The cortical distribution of the RhoGEF ECT-2 does not correlate with furrow placement in the one-cell embryo

Centralspindlin has been well-described to cooperate with the RhoGEF Ect2 in the induction of actomyosin ring contractility in various systems (Somers and Saint, 2003; Yuce et al., 2005; Chalamalasetty et al., 2006; Nishimura and Yonemura, 2006). The function and subcellular localization of *C. elegans* ECT-2 have been best defined during polarization of the fertilized egg. RNAi of *ect-2* interferes with cortical contractility and polarization, similar to depletion of its target GTPase RHO-1 (Jenkins et al., 2006; Motegi and Sugimoto, 2006). Based on transgene expression, GFP::ECT-2 and GFP::RHO-1

localize universally to the cell cortex before polarization of the one-cell embryo (Motegi and Sugimoto, 2006; Schmutz et al., 2007; Spiga et al., 2013). Polarization initiates when the mature paternal centrosomes approach the posterior cortex, which coincides with local exclusion of ECT-2. This depletion is thought to induce reorganization of the actomyosin cytoskeleton, which triggers the establishment of two mutually exclusive PAR protein domains (Motegi and Sugimoto, 2006). We wondered whether actomyosin contractile ring formation could also be driven by restricted cortical ECT-2 localization in *C. elegans*. Therefore, we tagged endogenous ECT-2 with ePDZ::mCherry, to be able to study the subcellular localization and function of ECT-2 in optogenetic experiments.

N-terminal tagging of endogenous ECT-2 with ePDZ::mCherry resulted in loss of function, as concluded from homozygous *epdz::mcherry::ect-2* animals not forming a functional germline and developing into sterile adults. Conversely, C-terminal tagging of ECT-2 with ePDZ::mCherry resulted in homozygous viable animals with normal brood size and embryonic viability (data not shown). Consistent with previous observations of *Ppie-1::gfp::ect-2* expression (Praitis et al., 2001; Motegi and Sugimoto 2006), the endogenous ECT-2::ePDZ fusion protein localized to the one-cell embryo cortex and became locally excluded from the posterior cortex at the time of polarity establishment. Surprisingly, this localization pattern persisted throughout mitosis (**Figure 8a**). As such, we found no apparent correlation between cytokinetic furrowing and the cortical organization of ECT-2 in the one-cell embryo. Attempts to modulate cortical ECT-2::ePDZ distribution through recruitment to PH::LOV did not noticeably affect ECT-2 cortical distribution or cortical contractility. Mitosis progressed as normal in the presence of blue light (N=5) and the cortical distribution of ECT-2::ePDZ was not quantifiably affected (**Figure 8-figure supplement 1**). Collectively, our observations of endogenously tagged ECT-2 do not support that local enrichment of ECT-2 determines furrow induction in *C. elegans*.

Global cortical CYK-4 recruitment stimulates contractility during pseudocleavage and mitosis

ECT-2 localizes to the cortex throughout the mitotic cell cycle in the *C. elegans* embryo while contractility is regulated in a spatiotemporal manner. As an alternative for regulation by localization, ECT-2 RhoGEF activity may be locally activated at the cortex. In mammalian cells, the centralspindlin complex stimulates both cortical recruitment and activation of ECT-2 (Yüce et al., 2005; Zhao and Fang, 2005). To examine an acute role of centralspindlin at the cortex, we attempted to endogenously tag ZEN-4 and CYK-4 with ePDZ::mCherry for optogenetic studies. While attempts to tag endogenous ZEN-4 with ePDZ were unsuccessful, we did obtain a homozygous viable strain carrying C-terminally tagged CYK-4::ePDZ::mCherry (CYK-4::ePDZ). Based on a reduced brood size and increase in embryonic lethality, the *cyk-4::epdz::mcherry* allele appears incompletely functional. In a subset of embryos, the midzone was ruptured during anaphase (**Figure 9-figure supplement 1**). CYK-4 normally interacts with both SPD-1 and ZEN-4,

which may be attenuated through the endogenous tagging, resulting in decreased MT bundling activity and midzone stability (Lee et al., 2015). Nevertheless, CYK-4::ePDZ was largely functional, and fluorescence microscopy of CYK-4::ePDZ embryos revealed a strong localization at the midzone and weakly at the ingressing furrow tip, as reported for germline-expressed transgenes (Verbrugghe and White, 2004).

Through combination with 3xPH::LOV and exposure to blue light, we globally recruited CYK-4::ePDZ to the cortex in one-cell embryos (**Figure 9a-c**). Cortical recruitment of CYK-4::ePDZ induced changes in several mitotic events, in particular furrowing behavior. The timing of furrow initiation was not significantly affected by global recruitment of CYK-4::ePDZ. However, complete cytokinetic furrow ingression occurred significantly faster than normal (**Figure 9-figure supplement 2c**, **d**). The combination of GFP::ZEN-4 with CYK-4::ePDZ did not appear viable, therefore we examined interaction between these centralspindlin components in genetic experiments. RNAi of *zen-4* results in defective furrowing (Raich et al., 1998), which was suppressed by cortical CYK-4::ePDZ recruitment, even though a full rescue of cytokinesis did not occur (**Figure 9-figure supplement 2e**). The maximum furrow ingression was significantly enhanced by global CYK-4::ePDZ recruitment in *zen-4(RNAi)* embryos, compared to *zen-4(RNAi)* alone (75,4 ± 16,11% vs. 56,5 ± 6,5%; N=5; **Figure 9-figure supplement 2f**). Depending on the stage of the cell cycle, these embryos showed ectopic cortical contractility after global CYK-4::ePDZ recruitment (**Figure 9-figure supplement 2a**). Thus, cortically localized CYK-4 promotes furrow ingression, even in the absence of *zen-4* function.

When CYK-4::ePDZ was recruited to the cortex after meeting of the pronuclei, excess contractility became apparent only upon completion of mitosis. Both the AB and P1 blastomeres initially formed extra furrows and cortical ruffles that eventually disappeared (N=5/5, **figure 9b**). It is interesting that global recruitment of CYK-4::ePDZ following pronuclear meeting only resulted in excess contractility after the completion of cytokinesis. Possibly, activating CYK-4 phosphorylation by Plk1 and a cessation of ECT-2 inhibition by Cyclin B/CDK-1 (Burkard et al., 2009; Wolfe et al., 2009; Yuce et al., 2005; Su et al., 2011; Leung and Glover, 2011) could be required for excess cortical CYK-4 to promote RhoA activity.

Remarkably, global recruitment of CYK-4 prior to the start of maternal pronucleus migration consistently resulted in premature cell division, through pseudocleavage turning into full cytokinesis, in the absence of a mitotic spindle or segregated DNA (N=5/5 embryos, **figure 9c**). In all cases, the maternal and paternal pronucleus were inherited by the anterior and posterior cell, respectively. An embryo that was followed after such premature cell division showed a second round of mitosis of the posterior – but not anterior – cell, thus resulting in a three-celled embryo (**Figure 9c**). Possibly, only the cell with inherited centrosomes retains the ability to divide in these embryos.

To examine dependence of ectopic contractility on ECT-2, we imaged F1 embryos 20 hours post *ect-2* dsRNA injection. Such partial ECT-2 depletion allowed embryos to

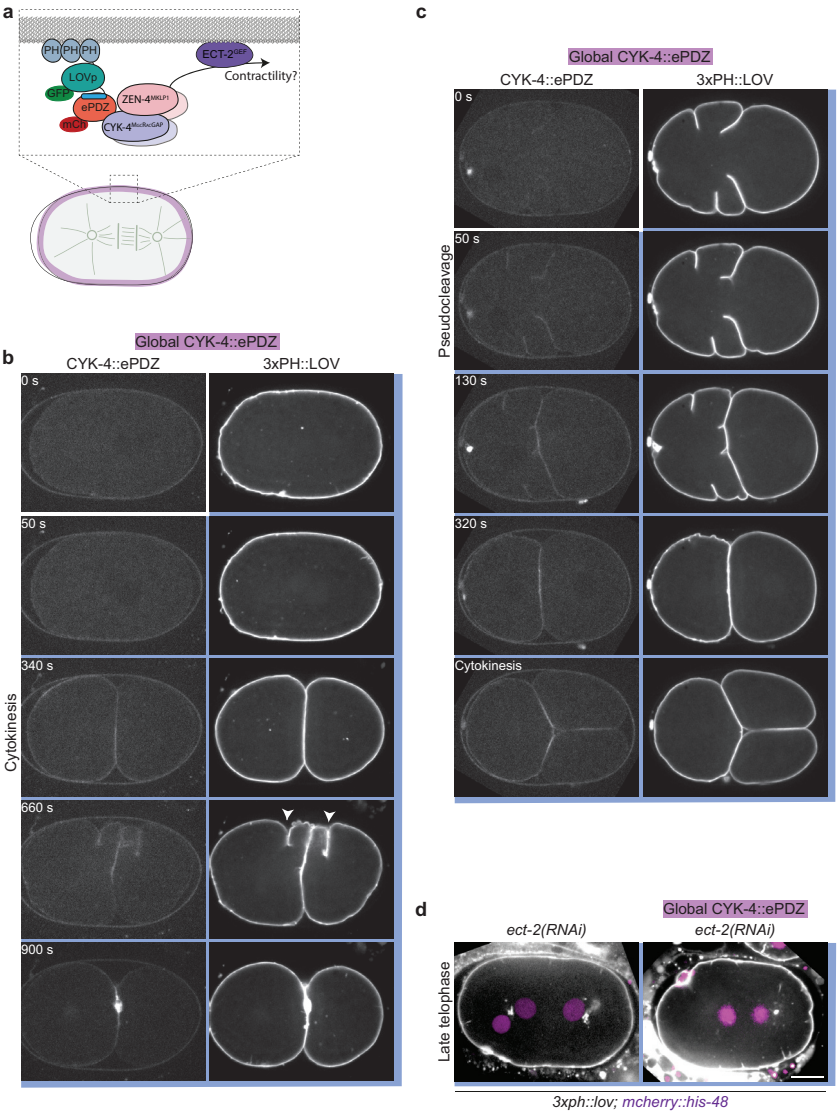

Figure 9. **Cortical CYK-4::ePDZ recruitment induces ectopic contractility**. (**a**) Cartoon model showing the strategy used for global CYK-4::ePDZ recruitment through activation of 3xPH::GFP::LOV. (**b**, **c**) Spinning disk confocal microscopy images of one-cell embryos showing fluorescently labeled endogenous CYK-4::ePDZ::mCherry and cell membranes (visualized by 3xPH::GFP::LOV). Representative pre- and post-activation and either post-cytokinesis (**b**) or post-complete pseudocleavage (**c**) single frames are shown from time-lapse movies. (**d**) Spinning disk confocal microscopy images of telophase one-cell embryos during late telophase, showing labeled membrane (3xPH::LOV, greyscale) and DNA (mCherry::HIS-48, magenta) with or without global CYK-4::ePDZ recruitment combined with *ect-2(RNAi)*. Blue backgrounds indicate that embryos have been exposed to blue (491 nm) light at these timepoints. Scale bar: 10 μm.

polarize and to asymmetrically position the spindle, while pseudocleavage and cytokinetic furrow formation were efficiently blocked (N=7). No ectopic contractility was observed when CYK-4::ePDZ was globally recruited to the cortex in *ect-2(RNAi)* embryos (N=3; **Figure 9d**). Thus, ectopic contractility as a result of CYK-4::ePDZ recruitment depends on ECT-2, which likely is a downstream effector. Collectively, these data show that cortical CYK-4 is capable of promoting contractility during pseudocleavage and late mitosis, probably through activation of ECT-2.

Discussion

The cytokinetic furrow is positioned by redundant signals from the spindle midzone and its two adjacent asters. In this study we have explored how the previously identified astral pathway components Gα–GPR-1/2–LIN-5 and their cortical antagonist LET-99 regulate furrowing in one-cell *C. elegans* embryos. By combining physical and genetic disruptions of the midzone with improved methods for optogenetic control of endogenous protein localization we showed that LIN-5 and LET-99 both contribute to efficient aster-directed furrowing. Our data revealed that the bipolar distribution of LIN-5 is required for properly timed furrow initiation in the absence of a functional midzone, and that LET-99 stimulates furrowing, probably through promoting cortical centralspindlin localization. These two antagonists mediate astral cytokinesis through partially independent pathways. In addition, we showed that cortical localization of CYK-4 promotes contractility during pseudocleavage and late mitosis and that this requires the RhoGEF ECT-2.

The role of Gα–GPR-1/2–LIN-5–dynein in modulating cortical contractility

Genetic requirements for the astral cytokinesis signal have been identified in *C. elegans*, but a molecular mechanism is yet to be uncovered. Our experiments revealed that cortical LIN-5 plays a critical role in inducing cytokinesis in the one-cell embryo. For one, LIN-5 could act through an astral relaxation mechanism during anaphase. Such a model was recently proposed to apply to the essential mitotic kinase AIR-1$^{\text{aurora A}}$. In conjunction with its activator TPXL-1$^{\text{TPX2}}$, AIR-1 triggers the clearance of ANI-1 and actin from the polar cortex during cytokinesis, which aids in the focusing of furrow components at the equator (Mangal et al., 2018). While no direct molecular link between contractility factors and AIR-1–TPXL-1 has been established, the authors speculated that activated AIR-1 might diffuse from astral MTs to the cortex where it facilitates clearance through the phosphorylation of specific targets. Contrary to AIR-1 and TPXL-1, Gα–GPR-1/2–LIN-5 localizes to the polar cortexes during anaphase, even though its enrichment is not uniform outside the equatorial region (Lorson et al., 2000; Miller and Rand, 2000; Gotta and Ahringer, 2001; Colombo et al., 2003; Gotta et al., 2003; Srinivasan et al., 2003; **Chapter 3**, **4**). Possibly, the connection between astral MTs and the cortex established by this force generator complex facilitates cortical clearance in an indirect manner. For example,

through promoting the cortical association of AIR-1–TPXL-1 or by enabling the initiation of dynein-mediated transport of contractility regulating factors along MTs. In support of such a model, depletion of the essential dynactin component p150^{Glued} in cultured *D. melanogaster* S2 cells results in the aberrant cortical localization of ZEN-4-related Pavarotti (Delcros et al., 2006). The dependency on ZEN-4 for ectopic furrowing in *gpr-1/2(RNAi)* embryos further reinforces this model (Verbrugghe and White, 2007). Alternatively, more downstream furrowing components such as NMY-2 could be selectively removed from the polar cortex through dynein-mediated transport, as was also suggested in a pre-print manuscript (Chapa-y-Lazo et al., 2018). This study showed that dynein is needed for the relaxation of polar cortexes during anaphase in one-cell *C. elegans* embryos. Transport of NMY-2 from the polar cortex toward the centrosome was shown to correlate to the initiation of cortical flows toward the equatorial cortex, which contribute to the properly timed construction of the contractile ring. In our current study, we did not explore the contribution of dynein to the regulation of cortical contractility through the LIN-5 complex. Further investigation will be required to reveal the workings of such an aster-directed clearance mechanism. In this light, follow-up experiments could assess the connection between dynein and NMY-2, and a possible activating role in this process for LIN-5.

The role of LET-99 in promoting cytokinetic furrowing

In addition to mediating astral relaxation, the LIN-5 complex could act through constraining the localization of LET-99 to the equatorial cortex. However, based on our observations, this model is less attractive, as polar recruitment of LIN-5::ePDZ rescues the delay in furrowing caused by *gpr-1/2; hcp-3* double knockdown even when LET-99 is depleted simultaneously. Nonetheless, we identified a positive contribution for LET-99 in the regulation of cytokinetic furrowing by globally recruiting the protein to the cortex via PH::LOV. Thus, it is conceivable that LET-99 and LIN-5 contribute to cytokinesis via different mechanisms. Interestingly, it was recently suggested that LET-99 stimulates furrowing in symmetrically and asymmetrically dividing blastomeres independently of its role in regulating spindle orientation and Gα (Price and Rose, 2017). In this study, the authors proposed that LET-99 functions in the astral pathway in parallel to ANI-1 and promotes the cortical enrichment of NMY-2 at the site of furrowing. The idea that LET-99 promotes contractility has been posed in earlier work as well; LET-99 regulates the distribution of NMY-2 in one-cell embryos with extremely posteriorly displaced and rotated spindles (Werner et al., 2007). Also, LET-99 was shown to be required for the distribution of cortical NMY-2 during nucleocentrosomal complex centration, a function which requires proper Gα function (Goulding et al., 2007). Whether the above are direct effects, however, remains to be experimentally tested. Finally, LET-99 has been hypothesized by Bringmann et al. to localize to the regions of highest cortical tension through a mechanosensory mechanism. Astral MTs contact the equatorial cortex at different incident angles compared

to the poles. The resulting lateral forces might generate cortical tension and lead to the local enrichment of LET-99, allowing it to promote furrowing locally (Bringmann et al., 2007).

Taking the above findings in consideration, the question remains of how exactly the LIN-5 complex and LET-99 are involved in delivering the astral cytokinesis signal (**Figure 10**). A weak interaction between ZEN-4 and LIN-5 was previously detected through affinity purification followed by mass spectrometry (AP-MS) of ectopically expressed GFP::ZEN-4 in *C. elegans* embryos (Galli et al., 2011b). Conceivably, LIN-5 could mediate the cortical clearance of centralspindlin through its interaction with ZEN-4. Such a mechanism could be comparable to what has recently been shown for TPXL-1–AIR-1 in *C. elegans* one-cell embryos (Mangal et al., 2018). Possibly, multiple parallel mechanisms could be involved in the clearance of cortical contractility-promoting factors during furrow specification. These mechanisms could include both an interaction between ZEN-4–LIN-5(–dynein), and the cortical clearance of NMY-2 via dynein-mediated transport described above (Chapa-y-Lazo et al., 2018). It is tempting to speculate that LET-99 and the centralspindlin complex interact during mitosis, as the cortical localization of both is promoted through *par-5* depletion (Wu et al., 2016; Basant et al., 2015). Interestingly, our largely functional endogenous LET-99::LOV tag does not appear to localize to the cortex, but instead localizes to the midzone during anaphase. Considering that C-terminal tagging of LET-99 might interrupt its cortical association, centralspindlin at the midzone might compete with the cortex for LET-99 binding. It is tempting to speculate that astral MTs modulate centralspindlin localization indirectly by fine-tuning the distribution of LET-99 at the cortex.

Separating spindle positioning and cytokinetic furrowing

How are the functions of the LIN-5 complex in spindle positioning and cytokinesis separated? Possibly, LIN-5 in metaphase and early anaphase determines spindle positioning, while the subsequent LIN-5 localization in late anaphase is dependent on the position of the spindle instead. Such a mechanism was previously proposed to separate the role of LET-99 during these subsequent phases. By physically manipulating embryos in such a way that the spindle became displaced in anaphase, the authors showed that cortical LET-99 in anaphase follows the localization of the spindle (Bringmann et al., 2007). Conversely, the metaphase LET-99 band could not be displaced using the same approach. Our detailed analysis of endogenous GFP::LET-99 localization in one-cell embryos revealed that the band pattern is set up gradually during prometaphase and metaphase, peaking at ~54% cortex length. This is in contrast with the above discussed study where the band was suggested to be set up at 50% embryo length, after which it displaces toward the posterior as the spindle displaces (Bringmann et al., 2007). Differences between these reports might result from varying experimental setups (widefield versus confocal microscopy), but are more likely to be caused by the use of

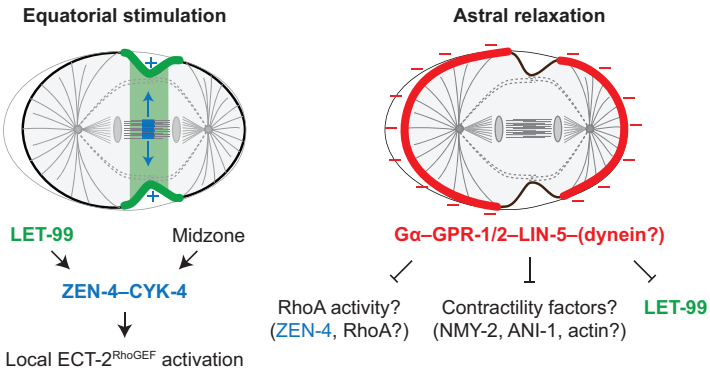

Figure 10. **Regulation of cytokinetic furrowing through the LIN-5 complex and its cortical antagonist LET-99**. Cartoon model depicting the models discussed in the text. Stimulation of contractility at the equatorial cortex occurs through local activation of ECT-2^{RhoGEF} by the centralspindlin complex (ZEN-4–CYK-4). Both the midzone and LET-99 stimulate the local cortical accumulation of centralspindlin during anaphase. A complex of Gα–GPR-1/2–LIN-5 inhibits cortical contractility outside of the equatorial region through a yet unknown mechanism, which might include dynein function. This pathway might involve direct or indirect inhibition of RhoA activity, downstream contractility factors and/or the distribution of LET-99.

ectopic expression as opposed to endogenous tagging. In addition, we did not observe a clear band pattern during nucleocentrosomal complex centration, as opposed to an earlier study in which LET-99 was visualized using immunohistochemistry (Tsou et al., 2002). This might be explained by the relatively low levels of endogenous expression of LET-99, which could affect the sensitivity of our assay, although we consider this option unlikely. As an alternative, low levels of equatorial LET-99 enrichment might not be observed during prophase due to eggshell autofluorescence. Interestingly, we generated two independent homozygous viable knock-ins for LET-99::LOV, which did not appear to localize to the cortex in one-cell embryos. Cortical localization was observed in subsequent developmental stages, which indicates that C-terminally tagged LET-99 retained a low but sufficient affinity for the cortex. Still, it is surprising that even without a clear band pattern of LET-99 one-cell embryos are capable of producing viable larvae.

In cultured mammalian cells, a gradient of Ran-GTP that originates at the chromosomes excludes NuMA from the equatorial region during metaphase, but not during anaphase. Interestingly, the exclusion of NuMA from the equatorial region during anaphase depends on centralspindlin components CYK4^{CYK-4} and MKLP1^{ZEN-4} instead. In cells depleted of centralspindlin, but not in those where Rock kinase was chemically inhibited, NuMA localized globally to the cortex. This result indicates that centralspindlin, but not successful cytokinesis signaling, modulates cortical NuMA localization (Kotak et al., 2014). However, NuMA can localize to the cortex during anaphase both via PIP/PIP$_2$ and 4.1G/R function (Kiyomitsu and Cheeseman, 2013; Kotak et al., 2014). Such interactions have not been reported for *C. elegans* embryos, in which GPR-1/2 and Gα appear exclusively required

for the cortical localization of LIN-5 during metaphase and anaphase (Srinivasan et al., 2003; Nguyen-Ngoc et al., 2007; Schmidt et al., 2017; **Chapter 3**). Possibly, LET-99 mediates the exclusion of the LIN-5 complex from the equator in conjunction with centralspindlin, which would be an interesting mechanism to explore in future studies.

A late rescue mechanism for cytokinesis?

The experiments presented in this study further emphasize the robustness of mitotic mechanisms in the *C. elegans* embryo. Depletion of HCP-3, an essential component of the centromere, results in a kinetochore null phenotype. In these embryos, both kinetochore formation and subsequent midzone formation were completely blocked, but the initial division proceeds with wild type kinetics. Such phenotypes were the basis for concluding that mitotic checkpoints are inactivated in the early divisions of the *C. elegans* embryo (Gonczy et al., 1999; Oegema et al., 2001), although later reports showed that mitosis involves a spindle checkpoint during these early stages (Encalada et al., 2005; Galli and Morgan, 2016). Even when components of the astral cytokinesis pathway were depleted simultaneously with the midzone, we did not observe a failure of embryos to divide. These results differ from those obtained in experiments in which the midzone was inactivated through physical ablation or disruption of *spd-1* function. A more dramatic cytokinesis phenotype was reported in earlier work, and resulted from UV laser-mediated ablation compared to that of *spd-1* depletion (Bringmann et al., 2007; Verbrugghe and White, 2007). These latter effects were proposed to result from partial inactivation of *spd-1* through RNAi, or the use of a partially penetrant temperature-sensitive allele. A later report showed that reducing cortical pulling forces rescues the compromised stability of the midzone that results from SPD-1 depletion (Lee et al., 2015). Accordingly, SPD-1 was shown to drive the elongation phase, but not the kinetochore-dependent initiation phase of midzone assembly (Maton et al., 2015), indicating that full disruption of the midzone requires inhibition of a more upstream component. In our experiments, physical disruption of the midzone also resulted in a stronger effect compared to genetic midzone disruption by *spd-1* or *hcp-3* knockdown. Interestingly, even though depletion of pulling forces (e.g. through *lin-5* RNAi) rescued the stability of the midzone, synergistic cytokinesis effects were observed. Such a result is surprising, as embryos with an intact midzone would be expected to complete cytokinesis regardless of whether the astral signal is disrupted, according to the redundant astral and midzone cytokinesis model (Bringmann et al., 2005; 2007). We observed only rare cytokinesis failure in *lin-5(RNAi)*; *spd-1(RNAi)* embryos, while cytokinesis often fails in *spd-1(oj5)*; *lin-5(RNAi)* embryos at the non-permissive temperature. Such different effects could result from inefficient depletion of proteins in double RNAi experiments, even though double loss-of-function is usually efficiently created by dsRNA injection (Portegijs et al., 2016; Schmidt et al., 2017; Fielmich et al., 2018; **Chapters 2-4**). Alternatively, the *spd-1(oj5)* allele might sensitize embryos for astral cytokinesis defects in addition to decreasing midzone stability. We favor this option

because, first, *spd-1(oj5)* specifically disrupts the interaction between SPD-1 and CYK-4, which is required for both the midzone and astral cytokinesis pathways. Importantly, abolishing this interaction does not perturb SPD-1 dimerization/oligomerization nor its MT binding and bundling (Lee et al., 2015). Second, our endogenous GFP::SPD-1 tag localizes not only to the midzone but also to astral MTs. Third, partial loss-of-function GFP::SPD-1 embryos display completely penetrant cytokinesis failure upon *hcp-3(RNAi); let-99(RNAi)*, as opposed to embryos in which SPD-1 is not tagged. The latter result indicates that in addition to stabilizing MTs in the spindle midzone, SPD-1 has additional cytokinesis-related functionality in the early embryo. Such a model would also explain why LET-99, Gα and GPR-1/2 were identified in an RNAi screen for astral cytokinesis pathway components where *spd-1(oj5)* was used to inactivate the midzone (Bringmann et al., 2007), even though their depletion probably rescued midzone destabilization in these embryos. We observed GFP::SPD-1-labeled MTs at the cortex in *hcp-3(RNAi); let-99(RNAi)* embryos in which cytokinesis was delayed. These cortical MTs appear in late M phase and may constitute a SPD-1-dependent late rescue mechanism in embryos in which both the astral and midzone signals have been disabled. The inactivation of CDK1 is required for increased MT stabilization, which drives the progression of anaphase and cytokinesis (Wheatley et al., 1997). Possibly, the stabilization of antiparallel MTs near the equatorial cortex could concentrate centralspindlin-induced RhoA activity, which allows embryos to complete cytokinesis. While we did not specifically explore whether these MTs were also positive for centralspindlin complexes, endogenous GFP::ZEN-4 occasionally showed MT-like localization patterns in our TIRF imaging experiments. This could indicate that also in *C. elegans*, centralspindlin can interact with astral MTs as was reported for *X. laevis* embryos, cultured *D. melanogaster* S2 cells and mammalian cells. In these systems, the MT-centralspindlin interaction is thought to involve an EB-interaction motif in Tumbleweed/RacGAP50C (Nishimura and Yonemura, 2006; Breznau et al., 2017; Verma et al., 2019). This motif does not appear conserved in the related CYK-4 protein, hence cortical MT localization would likely use a different mechanism in *C. elegans*. Finally, previous reports from other systems have underlined the importance of stabilization or bundling of non-midzone MTs in the induction of cytokinesis (Alsop et al., 2003; Canman et al., 2003; Inoue et al., 2004; Shannon et al., 2005; Verbrugghe et al., 2007). As such, the bundling of cortical MTs late in mitosis could allow embryos to complete cytokinesis even when both midzone and astral signaling pathways are defunct.

The role of cortical ECT-2 and centralspindlin in regulating contractility

ECT-2 is locally excluded from the future posterior cortex following centrosome proximity, which clearly correlates with the reorganization of the actomyosin network during polarization of the one-cell *C. elegans* embryo (Motegi and Sugimoto 2006). Contrary to this stage and to mitosis in other species studied to date, we found that the mitotic cortical

localization pattern of ECT-2 does not correlate with its role in cytokinetic furrowing. Interestingly, ECT-2::ePDZ was not readily recruited to 3xPH::LOV, which could indicate that the protein forms a relatively stable interaction with the cortex. Further analysis, for example through the execution of FRAP (fluorescent recovery after photobleaching) experiments, should reveal the cortical dynamics of ECT-2 in more detail. Considering the unexpected localization of ECT-2 during mitosis, we reasoned that cytokinesis in *C. elegans* embryos is likely to involve local activation of ECT-2 at the cortex. CYK-4 appears a good candidate for an ECT-2 activator, as its homologs are involved in relieving ECT2 of autoinhibition in other species (Burkard et al., 2009; Wolfe et al., 2009). Our global recruitment of CYK-4::ePDZ to the cortex in one-cell *C. elegans* embryos induced strong ectopic and ECT-2-dependent contractility. Recruitment of CYK-4::ePDZ prior to pronuclear meeting even resulted in full ingression and abscission of the pseudocleavage furrow. This led to a situation in which the anterior cell inherited the maternal, while the posterior cell inherited the paternal set of chromosomes. This is reminiscent of the non-mendelian inheritance of parental genomes through overexpression of GPR-1 (Besseling et al., 2016; Bringmann et al., 2011; Artiles et al., 2019). However, in our experiments the anterior cell inherits no centrosomes, and stops cell division. In addition to the completion of pseudocleavage, embryos specifically portrayed more rapid ingression of the P0 cytokinetic furrow, as well as prolonged cortical contractility following its completion. The apparent cell-cycle dependency of these effects suggests that cortical CYK-4::ePDZ is subject to additional regulation, for example through phosphorylation by Plk1 and inhibition of ECT-2 by Cyclin B/CDK1 (Kim et al., 2005; Burkard et al., 2009; Wolfe et al., 2009; Su et al., 2011). The generation of phospho-mutants for CYK-4::ePDZ and their recruitment to the cortex at different phases of the cell cycle could offer more insight in the regulation of contractility through CYK-4 and ECT-2. In our hands, global recruitment of CYK-4::ePDZ during mitosis does not result in the formation of ectopic furrows prior to the initiation of a normal furrow that ingressed with faster than normal kinetics. This would suggest that while cortical accumulation of CYK-4::ePDZ can boost the speed of furrow ingression, the activity of CYK-4::ePDZ that accumulates outside of the equatorial cortex is still efficiently suppressed, possibly through the inhibitory action of astral MTs. This is in contrast with observations from the optogenetic cortical recruitment of the truncated ECT-2 RhoGEF domain in cultured mammalian cells, which induced RhoA activation that was not restricted through the action of astral MTs (Wagner and Glotzer, 2016). In this context it would be interesting to follow the activation of RhoA through the use of a GFP-labeled RhoA biosensor (Tse et al., 2012) upon recruitment of CYK-4::ePDZ to the cortex in the presence and absence of astral MTs.

Our TIRF experiments were the first to show cortical localization of endogenous centralspindlin prior to furrow initiation in otherwise wild type one-cell embryos. Further analysis will be important to reveal what requirements have to be met for centralspindlin to translocate to the cortex to activate RhoA. Considering that the *C. elegans* P0 blastomere

is a relatively large cell, a signal passively diffusing from the midzone would be expected to take a long time to travel to the equatorial cortex, and to not be very precisely focused. Possibly, astral MTs help focus this midzone-derived signal, which could occur through the antagonism between LET-99 and the LIN-5 complex (**Figure 10**). We hypothesize that LIN-5–dynein could play a dual role in transporting centralspindlin off the cortex at the polar cortex, thus performing astral relaxation, while at the same time confining the localization of LET-99 which promotes the cortical focusing of centralspindlin. In turn, astral MTs modulate the cortical localization of both proteins in late anaphase. In this manner, the redundant signals from the midzone and asters are integrated to robustly position the cytokinetic furrow with respect to the position of the spindle.

Materials & methods

C. elegans strains and maintenance

The *C. elegans* strain names and their genotypes used in this study are found in **supplementary table 1**. Animals were grown on plates that contained nematode growth medium seeded with OP50 *Escherichia coli* bacteria at either 15, 20 or 25˚C as described elsewhere (Brenner, 1974). Strains that expressed either or both ePDZ and LOV fused to an endogenous gene were kept in the dark.

Molecular cloning

For CRISPR/Cas9-mediated genome editing, DNA repair templates were designed in A plasmid Editor (M. Wayne Davis) to include 500 bp homology arms. These and all other sequences used were generated starting from either purified *C. elegans* genomic DNA or pre-existing vectors via PCR amplification using Q5 Hot Start High-Fidelity DNA Polymerase (New England Biolabs). PCR fragments were gel purified (Qiagen), their concentrations measured using a BioPhotometer D30 (Eppendorf) and then ligated into pBSK by Gibson Assembly (New England Biolabs). gRNA vectors were generated by annealing of antisense oligonucleotide pairs and subsequent ligation into non-dephosphorylated BbsI-linearized pJJR50 or BsaI-linearized pMB70 using T4 ligase (New England Biolabs). The *yfp* coding sequence was germline-optimized using the algorithm described previously (Fielmich et al., 2018; **Chapter 4**) and then synthesized as a gBlock (Integrated DNA Technologies). All DNA vectors used for genome editing were transformed into DH5α competent cells and subsequently purified by midiprep (Qiagen). A list of DNA primers and vectors used for genetic manipulation in this study is available upon request.

CRISPR/Cas9-mediated genome editing

The wild type N2 *C. elegans* genetic background was used for the generation of CRISPR/Cas9 alleles. Injection mixes with a total volume of 50 µl were prepared in MilliQ H_2O and contained a combination of 50 ng/µl *Peft-3:cas9* (Addgene ID #46168 (Friedland

et al., 2013)regularly interspaced, short palindromic repeats (CRISPR or 60 ng/µl pJW1285 (Addgene ID #61252 (Dickinson et al., 2013)), 50 ng/µl *u6::sgRNA*, 50 ng/µl of DNA vector repair template and 2.5 ng/µl of the co-injection pharyngeal *Pmyo-2::tdtomato* marker. Injection mixes were spun down in a microcentrifuge (Eppendorf) for at least 10 minutes at 13,000 rpm prior to use. Young adult hermaphrodites were injected in the germline using an inverted micro-injection setup (Eppendorf). After injection, two animals per plate were grown at 15 or 20˚C. F1 animals were then picked to a total of at least 96, and grown with two animals per plate for at least 7-8 days at 20˚C until freshly starved. Half a plate containing F2 and F3 animals was then washed off with M9 medium supplemented with 0.05% Tween-20, and subsequently lysed to extract genomic DNA. The *gfp::let-99* knock-in was obtained using co-CRISPR selection through integration of a self-excisable cassette carrying a visible marker (Dickinson et al., 2015). Genotyping was carried out by PCR amplification with OneTaq polymerase (New England Biolabs) of genome sequences using primers annealing in the inserted sequence and a genomic region not included in the repair template. Confirmed alleles were subsequently sequenced (Macrogen Europe).

Spinning disk confocal and TIRF microscopy

Prior to live imaging, embryos were dissected from adult hermaphrodites onto coverslips (Menzel-Gläser) in 0.8x egg salts buffer (94 mM NaCl, 32 mM KCl, 2.7 mM CaCl2, 2.7 mM MgCl2, 4 mM HEPES, pH 7.5; (Tagawa et al., 2001) thereby establishing the animal's anterior-posterior (a-p or M9, and mounted on 4% agarose pads. Spinning disk imaging of embryos was performed using a Nikon Eclipse Ti with Perfect Focus System, Yokogawa CSU-X1-A1 spinning disk confocal head, Plan Apo VC 60x N.A. 1.40 oil and S Fluor 100x N.A. 0.5-1.3 (at 1.3, used for UV-laser photo-ablation) objectives, Photometrics Evolve 512 EMCCD camera, DV2 two-channel beam-splitter for simultaneous dual-color imaging, Vortran Stradus 405 nm (100 mW), Cobolt Calypso 491 nm (100 mW), Cobolt Jive 561 nm (100 mW), Vortran Stradus 642 nm (110 mW) and Teem Photonics 355 nm Q-switched pulsed lasers controlled with the ILas system (Roper Scientific France/ PICT-IBiSA, Institut Curie, used for photo-ablation), ET-GFP (49002), ET-mCherry (49008), ET-GFPmCherry (49022) and ET-Cy5 (49006) filters, ASI motorized stage MS-2000-XYZ with Piezo Top Plate, and Sutter LB10-3 filter wheel. The microscope was operated using MetaMorph 7.7 software and situated in a temperature-controlled room (20˚C). The temperature of the stage and objective was controlled at 25˚C with a Tokai Hit INUBG2E-ZILCS Stage Top Incubator during experiments.

TIRF imaging of embryos was performed on an Eclipse Ti with Perfect Focus System, an Apochromat TIRF 100× 1.49 NA oil objective (Nikon), an Evolve 512 electron-multiplying charge-coupled device camera, an Optosplit III beam-splitter (Andor Technology) for simultaneous dual-color imaging, 488-nm (150 mW) and Cobolt Jive 561-nm (100 mW) lasers, ET-GFP (49002), ET-mCherry (49008), and ET-GFPmCherry

(49022) filters, an ASI motorized stage MS-2000-XY System for Inverted Microscope Te/Ti 2000 (Nikon), and an LB10-3 filter wheel. Acquisition was controlled with MetaMorph 7.7 software (Molecular Devices), and the setup was situated in a temperature-controlled room at 20°C.

Images were acquired in either streaming mode with 250-500 ms exposure, or time-lapse mode with 1000 ms exposure and 2 or 5 second frame-to-frame intervals. Laser power and exposure times were kept constant within experiments.

Images acquired by fluorescence microscopy were rotated, cropped, annotated, provided with scale bars, and processed further by linear adjustment of brightness and contrast using ImageJ and Adobe Photoshop. Fluorophores used in this study include GFP, mCherry and YFP.

RNA-mediated interference (RNAi)

Young adult hermaphrodites were injected with dsRNA targeting genes of interest (*gpr-1, lin-5, let-99, hcp-3, spd-1, ect-2, zen-4, par-2, par-3*) and grown for 48 or 20 hours (*ect-2*) at 15˚C (Fire et al., 1998; Montgomery and Fire, 1998) prior to imaging experiments. To generate dsRNA, coding regions of genes of interest were PCR amplified using Q5 Hot Start High-Fidelity DNA Polymerase (New England Biolabs). These PCR products were used as templates for *in vitro* dsRNA synthesis (MEGAscript T7 transcription kit, ThermoFisher Scientific). dsRNA was diluted 5x in DEPC H_2O prior to micro-injection. Clones from the Vidal and Ahringer RNAi libraries were used (Kamath et al., 2003; Rual et al., 2004).

Midzone severing assays

Mitotic spindle severing was performed in essence as described (Grill et al., 2001; Portegijs et al., 2016; **Chapter 2**). One-cell embryos expressing GFP-labeled tubulin were imaged during mitosis using the spinning disk microscope setup described above, equipped with a Teem Photonics 355 nm Q-switched pulsed laser controlled with the ILas system (Roper Scientific France/ PICT-IBiSA, Institut Curie). At anaphase onset, as judged by spindle morphology and mobility, spindles were manually targeted and subsequently severed.

Local recruitment of ePDZ-tagged proteins to membrane LOV

For local photoactivation of LOV2 in *C. elegans* embryos, light was applied in a region of variable size and with frequencies depending on each individual experiment using a 491 nm laser controlled with the ILas system (Roper Scientific France/ PICT-IBiSA, Institut Curie). Due to high sensitivity of LOV2 to blue light and variations in laser power, embryos of strain SV2061 (expressing diffuse ePDZ::mCherry and PH::GFP::LOV) or SV2212 (expressing diffuse ePDZ::mCherry and 3xPH::GFP::LOV)) were used to calibrate the amount of laser power required for local activation of LOV2 prior to experiments. During

local photoactivation assays embryos were kept away from blue light as much as practically feasible. To this end, aluminum foil was used to cover the microscope setup, and optical filters were inserted in the light path to remove LOV2-activating wavelengths from the transmitted light used to locate embryos on slides. Prior to experimental use of embryos, premature cortical recruitment of ePDZ-mCherry-tagged proteins of interest was assessed by observation of mCherry localization patterns.

Data analysis

All quantitative spinning disk image analyses were performed in ImageJ. To quantify the local cortical recruitment of GFP::ANI-1 or LIN-5::ePDZ::mCherry, five linescans of 10 px wide were drawn from anterior to posterior along both the top and bottom cortices of one embryo. For the quantification of cortical ECT-2::ePDZ::mCherry, linescans were drawn perpendicular to cortical regions of interest. Plot profiles were generated and further data processing was performed as described in **figure 8-figure supplement 1c**. For the quantification of cortical GFP::LET-99, ten linescans of 10 px wide were drawn along each of the cortices as well as a matching linescan in the cytoplasm adjacent to the cortex for a total of five embryos per RNAi condition. For the quantification of GFP::ZEN-4 signal from TIRF images, regions of 50x50 px were measured within the equatorial and polar cortexes as described in **figure 7-figure supplement 3c**. After measurement, all pixel values from regions of interests were saved in Excel 2016 (Microsoft). An average sample background intensity was measured outside of the embryo in a 50x50 px region and this value was subtracted from all cortical and cytoplasmic measurements. The intensity values from each plot were averaged to 100 x bins to equalize their slight variances in lengths due to manual tracking. Subsequently, matching bins for cortical and cytoplasmic values were used to calculate the fold enrichment of cortex over cytoplasm intensities, or the fold enrichment of equatorial over polar intensities in the case of GFP::ZEN-4 TIRF measurements. The extent of furrow ingression or spindle elongation was measured manually in ImageJ based on DIC images or fluorescence signals from the spindle or cell membrane and expressed in either µm or a percentage of total embryo width or length. The timing of stereotypical events in the embryo (centrosome centration, metaphase plate assembly, chromosome segregation, spindle pole separation, furrow initiation and cytokinesis) and previously described RNAi phenotypes were judged by eye in ImageJ from both DIC and fluorescence signals. All further numerical data processing and graph generation was performed using Excel 2016 (Microsoft) and Prism 8 (GraphPad software, inc.).

Statistical analysis

All data were shown as the mean with SEM. Statistical significance as determined using two-tailed unpaired Student's t-tests, Mann-Whitney U tests and the Wilcoxon matched-pairs signed rank test. Correlation coefficients between two data sets were calculated

using Pearson *r* correlation tests or Spearman rank correlation tests. Data sets were assessed for their fit to a Gaussian distribution using the D'Agostino-Pearson omnibus K2 and Shapiro-Wilk normality test prior to application of appropriate statistical test. A p-value of <0.05 was considered significant. *, P<0.05; **, P<0.01; ***, P<0.001; ****, P<0.0001. ns or unlabeled, not significant. All statistical analyses were performed in Prism 8 (GraphPad software, inc.).

Acknowledgements

We thank V. Portegijs, M. Godfrey, J. Kroll, M. van Luyk and M. Harterink for sharing reagents and discussing experiments. We also thank all the members of the van den Heuvel, Akhmanova, Boxem, and Kapitein groups for helpful discussion and general support. We acknowledge Wormbase and the Biology Imaging Center at the Faculty of Sciences, Department of Biology, Utrecht University. Some strains were provided by the Caenorhabditis Genetics Center (CGC), which is funded by NIH Office of Research Infrastructure Programs (P40OD010440).

Author contribution

R.S. and S.v.d.H. designed the study and wrote the manuscript. R.S. carried out most experiments. A. H. imaged and quantified cortical distribution of GFP::LET-99 and generated the knock-in allele. E.C. imaged and quantified cortical distribution of GFP::ANI-1 and carried out light-controlled localization experiments of CYK-4 and ECT-2.

Competing interests

The authors declare no conflicts of interest.

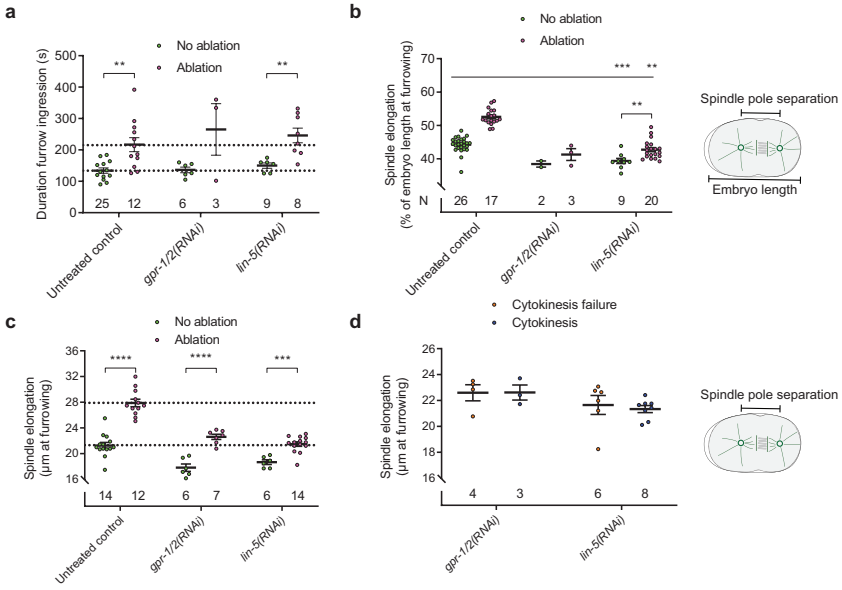

Figure 1-figure supplement 1. **Additional quantifications of data described in figure 1**. (**a**) Duration of furrow ingression (interval between furrow appearance and completion of ingression) for both embryos with (blue dots) and without midzone ablation (orange dots). Unpaired Welch's Student's *t* test. **, P<0.01. (**b**, **c**) Extent of spindle elongation (measured as % of total embryo length or in µm distance between centrosomes) at furrow initiation for both embryos with (blue dots) and without midzone ablation (orange dots). Only embryos that successfully initiated a furrow were analyzed. Unpaired Welch's Student's *t* test and Mann–Whitney *U* test (unequal variances). ** P<0.01; *** P<0.001; **** P<0.0001. (**d**) Extent of spindle elongation (measured as % of total embryo length or in µm distance between centrosomes) at furrow initiation for both embryos that completed (blue dots) and failed (orange dots) cytokinesis. Only embryos exposed to midzone UV ablation were analyzed. Unpaired Welch's Student's *t* test and Mann–Whitney *U* test (unequal variances). N values are indicated in graphs.

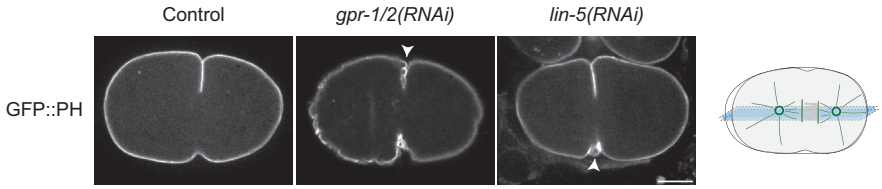

Figure 1-figure supplement 2. **Furrow integrity is perturbed by depletion of GPR-1/2 or LIN-5**. Spinning disk confocal microscopy images of one-cell embryos showing fluorescently labeled cell membranes (visualized by PH::GFP). Representative telophase maximum projections of 2 adjacent Z positions are shown from time-lapse movies of control, *gpr-1/2(RNAi)* and *lin-5(RNAi)* conditions. Arrowheads indicate cytoplasmic blebs that form at the site of cytokinetic furrow ingression. Scale bar: 10 µm.

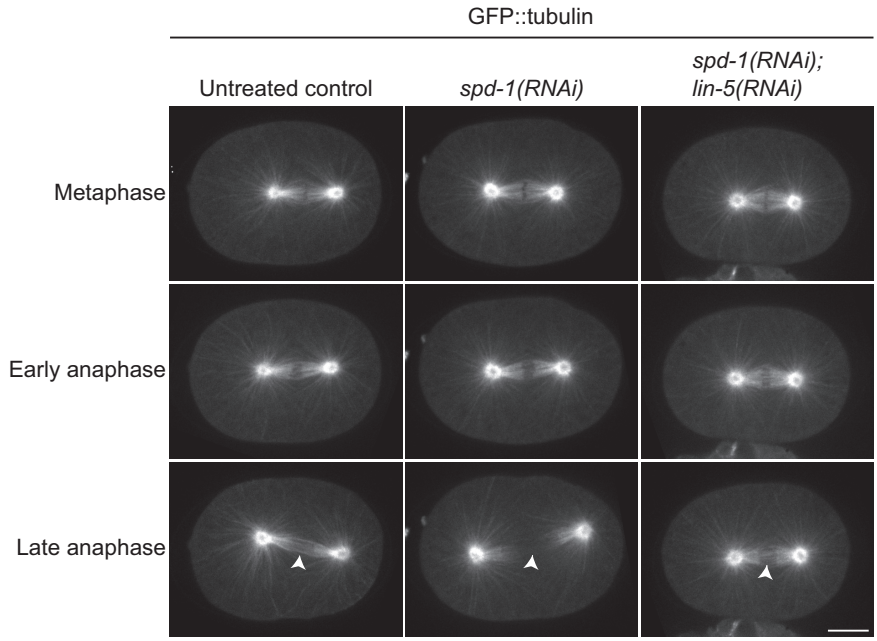

Figure 2-figure supplement 1. ***lin-5* RNAi rescues midzone integrity in *spd-1(RNAi)***. (**a**) Spinning disk confocal microscopy images of one-cell embryos showing fluorescently labeled mitotic spindles (visualized by GFP::tubulin). Representative metaphase, early anaphase and late anaphase frames are shown from time-lapse movies of control, *spd-1(RNAi)* and *spd-1(RNAi); lin-5(RNAi)* embryos. Arrowheads indicate either the presence or absence of midzone MTs. Scale bar: 10 μm

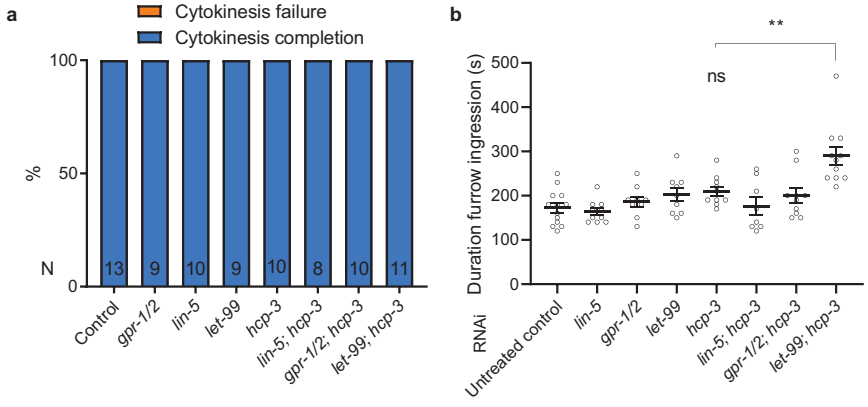

Figure 3-figure supplement 1. **Additional quantifications of embryos described in figure 3.**
(**a**) Quantification of percentage embryos that completed (blue) and failed (orange) cytokinesis in embryos of indicated genotypes. (**b**) Duration of furrow ingression (interval between furrow appearance and completion of ingression) for the conditions described in (**a**). One-way ANOVA. ** P<0.01. N=8-13.

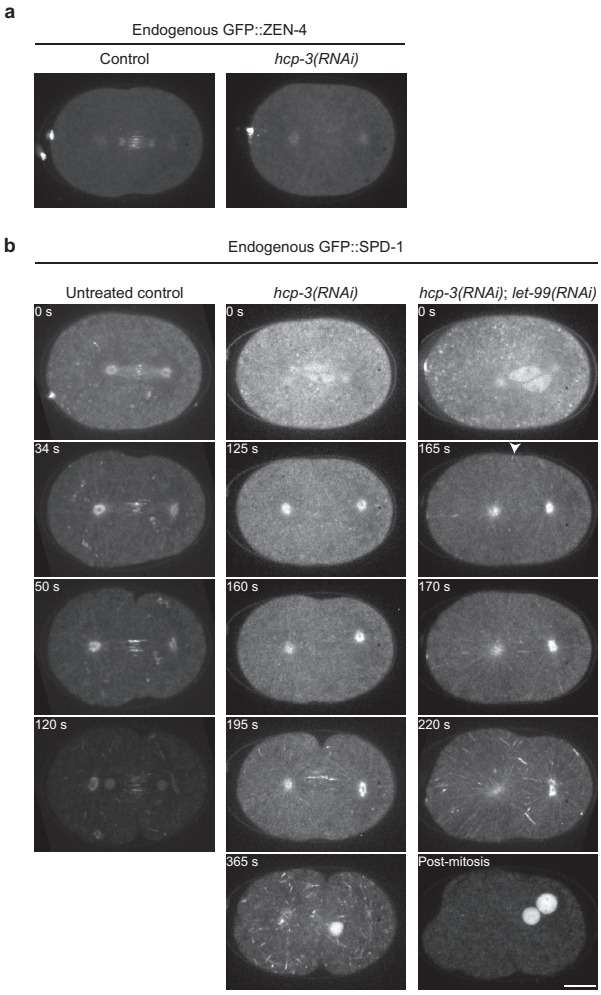

Figure 3-figure supplement 2. **Inactivation of *hcp-3* disrupts midzone formation.** Spinning disk confocal microscopy images of one-cell embryos showing endogenous GFP::ZEN-4 (**a**) and GFP::SPD-1 (**b**). Representative metaphase, late anaphase, cytokinesis and regression stage single frames are depicted from time-lapse movies of indicated conditions. Arrowhead indicates GFP::SPD-1-labeled MTs near the equatorial cortex. Scale bar: 10 μm.

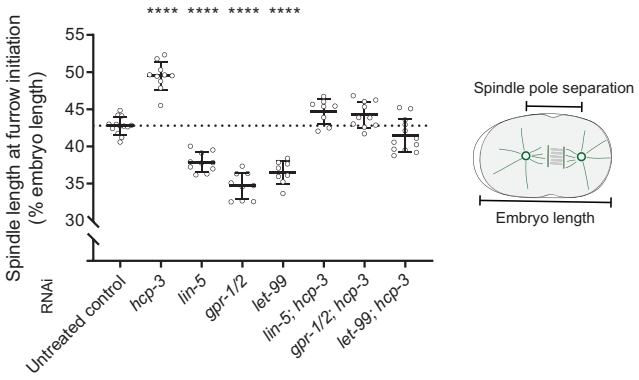

Figure 3-figure supplement 3. **Additional quantifications of embryos described in figure 3**. Extent of spindle elongation (measured as % of total embryo length) at furrow initiation in embryos of indicated genotypes. One-way ANOVA. **** P<0.0001. N=8-13.

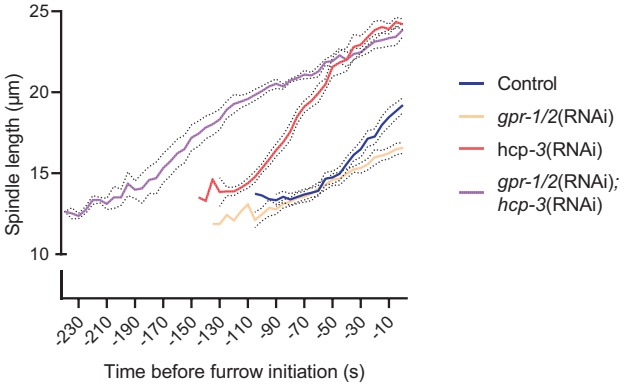

Figure 3-figure supplement 4. **Additional quantifications of embryos described in figure 3.** Spindle length is measured (in µm) over time (s) between metaphase and cytokinesis in embryos of indicated genotypes (N=4, mean (thick colored line) ± SEM (dotted lines)).

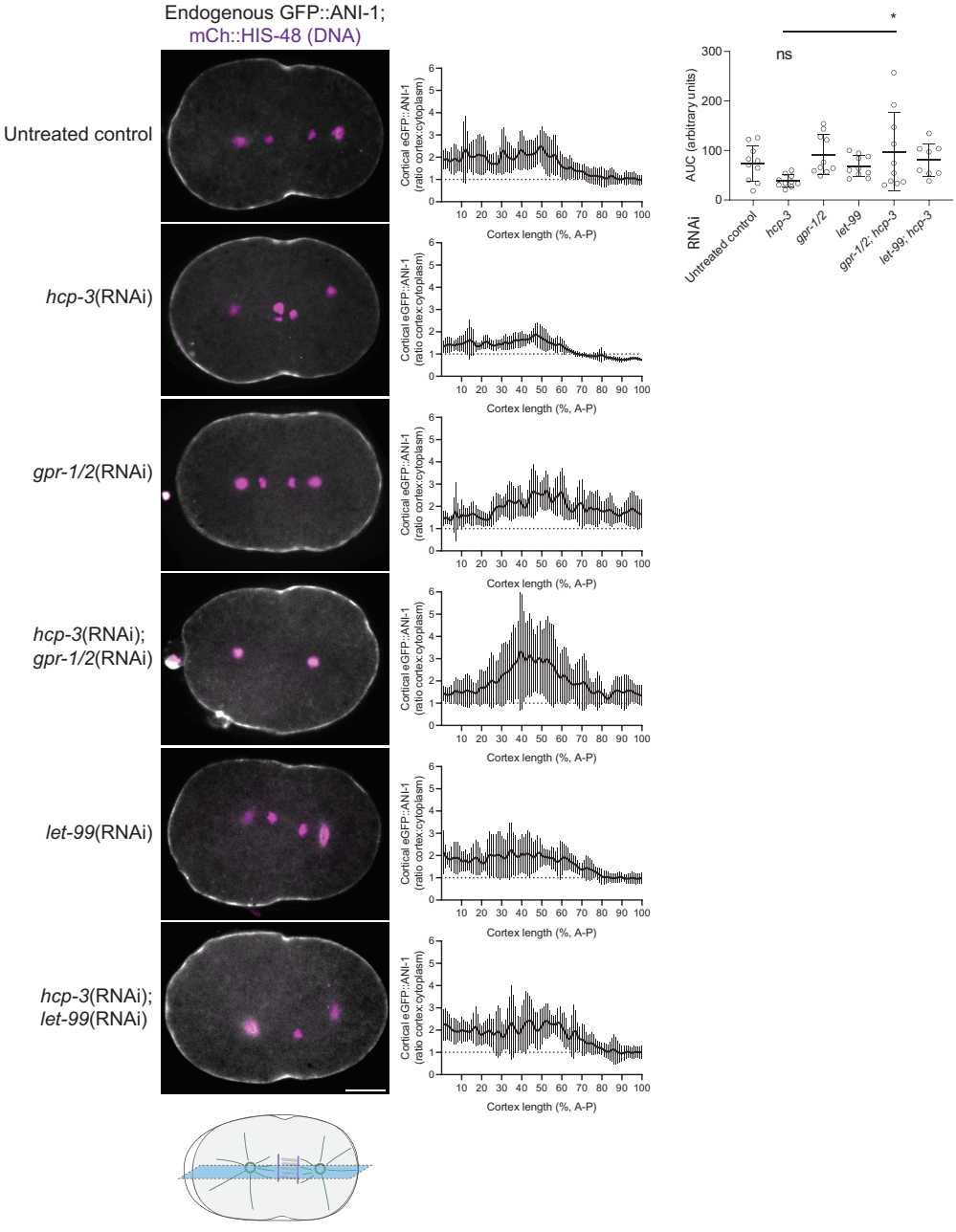

Figure 3-figure supplement 5. **Proper cortical distribution of ANI-1 depends on *gpr-1/2* and *let-99* function.** Spinning disk confocal microscopy images of telophase one-cell embryos showing endogenous GFP::ANI-1 localization and labeled DNA (mCherry::HIS-48, magenta), with or without *hcp-3(RNAi)*, *gpr-1/2(RNAi)* or *let-99(RNAi)* or combinations thereof. Graphs show quantifications of cortical enrichment ratios over cytoplasmic intensities (mean ± SD). N=5 embryos per condition, 2 averages of 5 cortical scans each (top and bottom) per embryo. Scale bar, 5 µm.

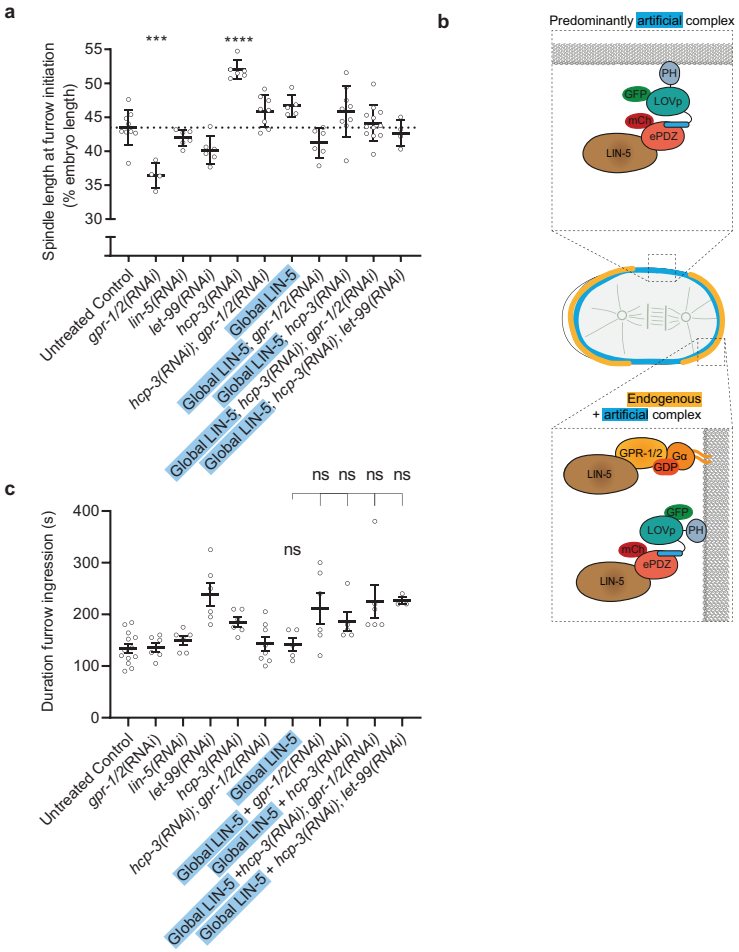

Figure 4-figure supplement 1. **Additional controls for experiments shown in figure 4.** Quantification of the (**a**) extent of spindle elongation (measured as % of total embryo length) at furrow initiation and (**c**) the interval between furrow initiation and cytokinesis completion in embryos of indicated genotypes, with or without global recruitment of LIN-5 (indicated in blue). One-way ANOVA. *** P<0.001; **** P<0.0001. N=3-12. (**b**) Cartoon model representing the distribution of endogenous and artificial light-recruited LIN-5 complexes.

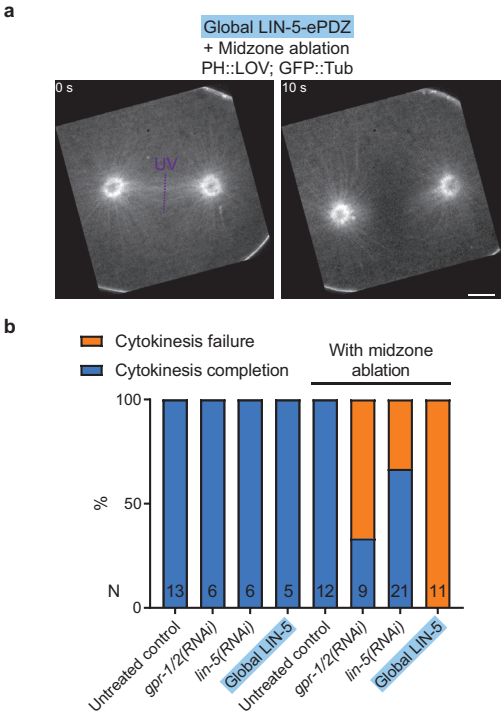

Figure 4-figure supplement 2. **Cortical recruitment of LIN-5 inhibits furrowing in midzone-ablated embryos**. (**a**) Spinning disk confocal microscopy images of one-cell embryos showing fluorescently labeled mitotic spindles (visualized by GFP::tubulin) and cell membranes (visualized by PH::GFP::LOV). Representative early anaphase pre- and post-midzone severing, late anaphase/telophase and late telophase single frames are shown from a time-lapse movie of a midzone UV ablated embryo with global cortical recruitment of LIN-5. UV ablated region is indicated in purple. (**b**) Quantification of percentage embryos that completed (blue) and failed (orange) cytokinesis in control, *gpr-1/2(RNAi)*, *lin-5(RNAi)* and global LIN-5 cortical recruitment conditions, either with or without midzone ablation. N values are indicated in graph. Scale bar: 5 μm.

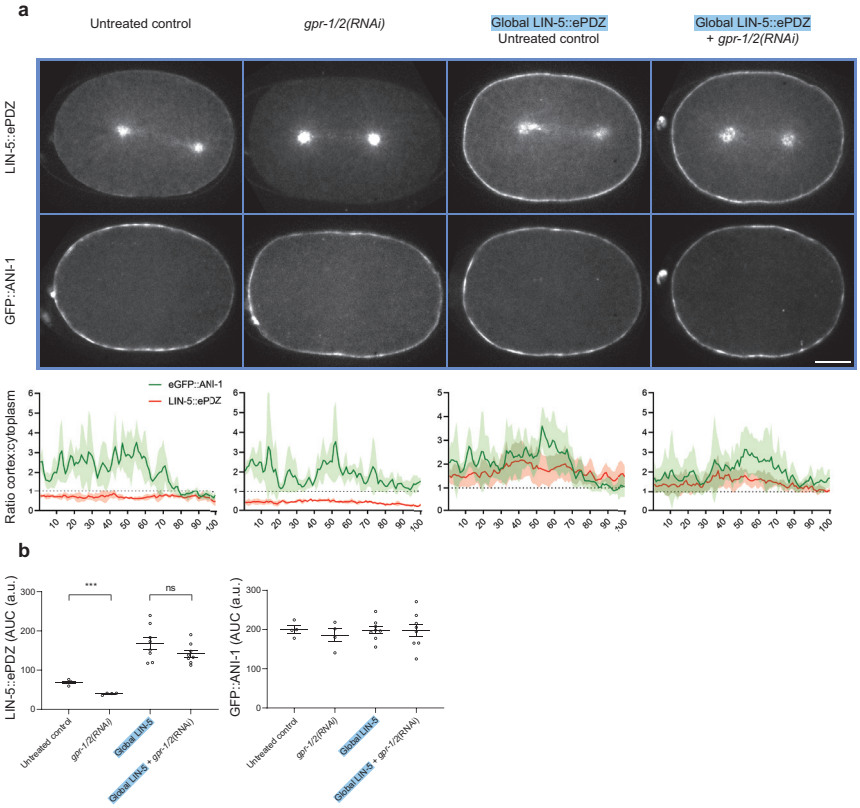

Figure 4-figure supplement 3. **Cortical recruitment of LIN-5 has no significant effect on endogenous ANI-1 distribution**. (**a**) Spinning disk confocal microscopy images of late anaphase one-cell embryos showing endogenous LIN-5::ePDZ and GFP::ANI-1 localization, with or without and *gpr-1/2(RNAi)*, and recruitment of LIN-5 through PH::LOV(dark). Graphs show quantifications of cortical enrichment ratios over cytoplasmic intensities for both proteins. (**b**) Quantifications of total area under the curve (AUC) for the conditions shown in (**a**). N=2-4 embryos, 2 cortical scans (top and bottom) per embryo. Unpaired Welch's Student's *t* test. *** P<0.001. Scale bar, 10 µm.

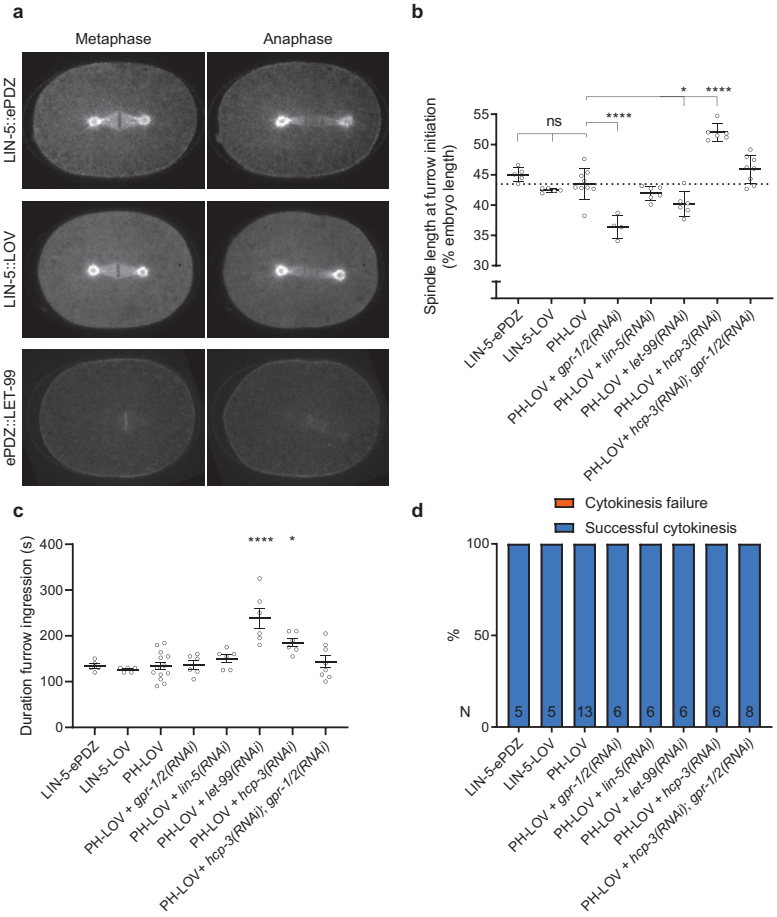

Figure 5-figure supplement 1. **Additional controls for experiments shown in figure 5**. (**a**) Spinning disk confocal microscopy images of one-cell embryos showing fluorescently labeled endogenous LIN-5::ePDZ::mCherry, LIN-5::YFP::LOV or ePDZ::LET-99 at metaphase and anaphase. Quantifications of (**b**) the interval between anaphase spindle pole separation onset and furrow initiation, (**c**) the interval between furrow initiation and cytokinesis completion, and (**d**) percentage embryos that fail (blue) or complete (orange) cytokinesis combined for embryos expressing endogenously tagged LIN-5::ePDZ::mCherry, LIN-5::YFP::LOV or ePDZ::LET-99, or PH::GFP::LOV combined with indicated RNAi conditions. One-way ANOVA. ** P<0.01; **** P<0.0001. N=5-12. Scale bar: 10 µm.

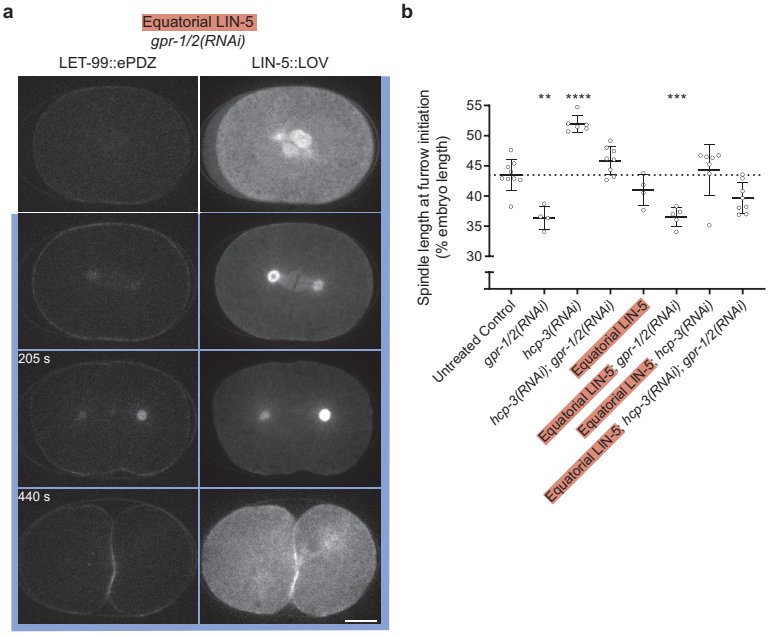

Figure 5-figure supplement 2. **Additional controls and quantifications of embryos described in figure 5.** Spinning disk confocal microscopy images of one-cell embryos showing fluorescently labeled endogenous LIN-5::YFP::LOV and ePDZ::mCherry::LET-99. Representative metaphase pre- and post-activation, late anaphase and telophase single frames are shown from time-lapse movies of *gpr-1/2(RNAi)* (**a**) embryos. (**b**) Quantification of the extent of spindle elongation (measured as % of total embryo length) at furrow initiation in embryos of indicated genotypes, with or without global (indicated in blue) or equatorial (indicated in red) recruitment of LIN-5. One-way ANOVA. ** P<0.01; *** P<0.001; **** P<0.0001. N=4-9. Scale bar: 10 µm.

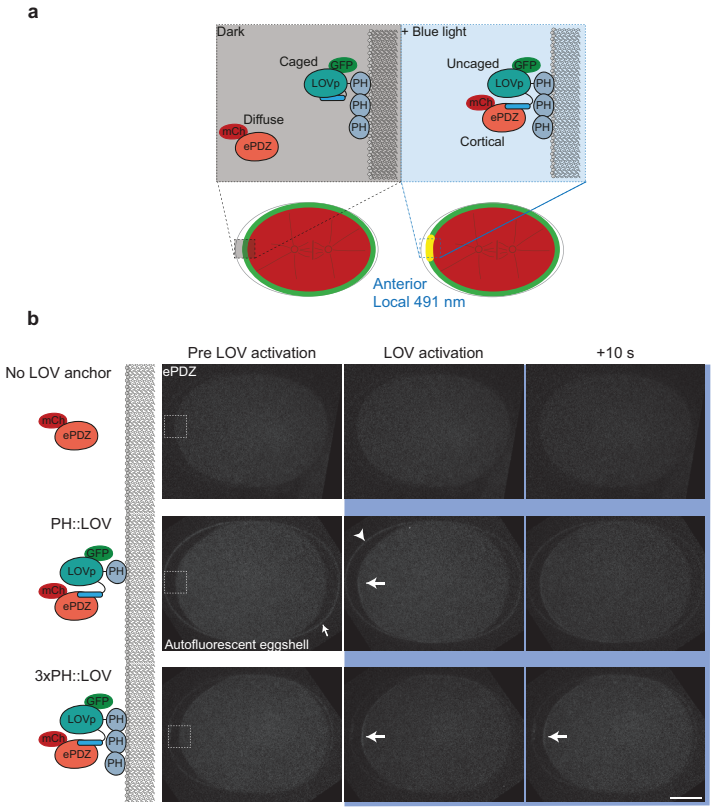

Figure 6-figure supplement 1. **Proof of principle for the improved LOV anchor used in figure 6**.
(**a**) Cartoon model showing the strategy used for the proof of principle of 3xPH::GFP::LOV. (**b**) Spinning disk confocal microscopy images of one-cell embryos showing fluorescently labeled ePDZ::mCherry co-expressed without LOV anchor, or with either PH::GFP::LOV or 3xPH::GFP::LOV. Constant laser exposure is used in all three conditions to locally illuminate the anterior cortex (indicated with a white dotted square) during metaphase, to circumvent overlap with the auto fluorescent eggshell (arrowhead). Arrows indicate the presence of cortical ePDZ::mCherry. Pre- and post-activation, and 10 seconds post activation acquisitions are shown. Scale bar: 10 μm.

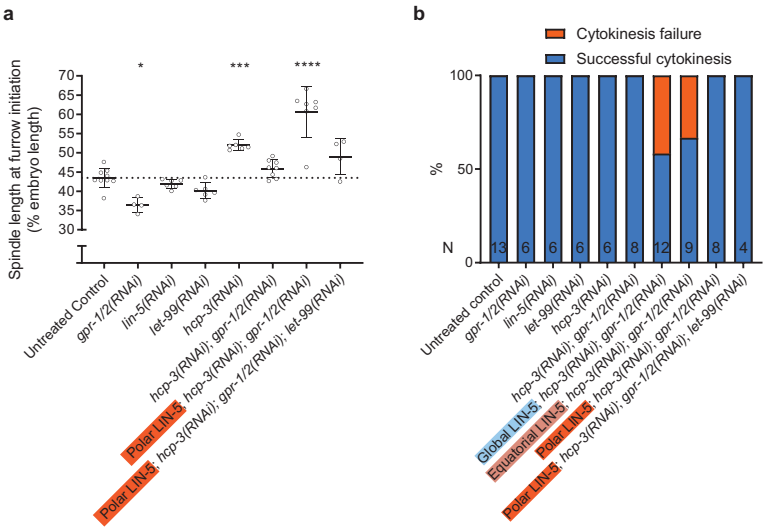

Figure 6-figure supplement 2. **Additional quantifications for experiments shown in figure 6**.
(**a**) Quantification of the extent of spindle elongation (measured as % of total embryo length) at furrow initiation in embryos of indicated genotypes, with or without polar (indicated in orange) recruitment of LIN-5. One-way ANOVA. * P<0.05; *** P<0.001; **** P<0.0001. N=4-12. (**b**) Quantification of percentage embryos that completed (blue) and failed (orange) cytokinesis in conditions described as in (**a**), with or without global (indicated in blue), equatorial (indicated in red) or polar (indicated in orange) recruitment of LIN-5. N values are indicated in graph.

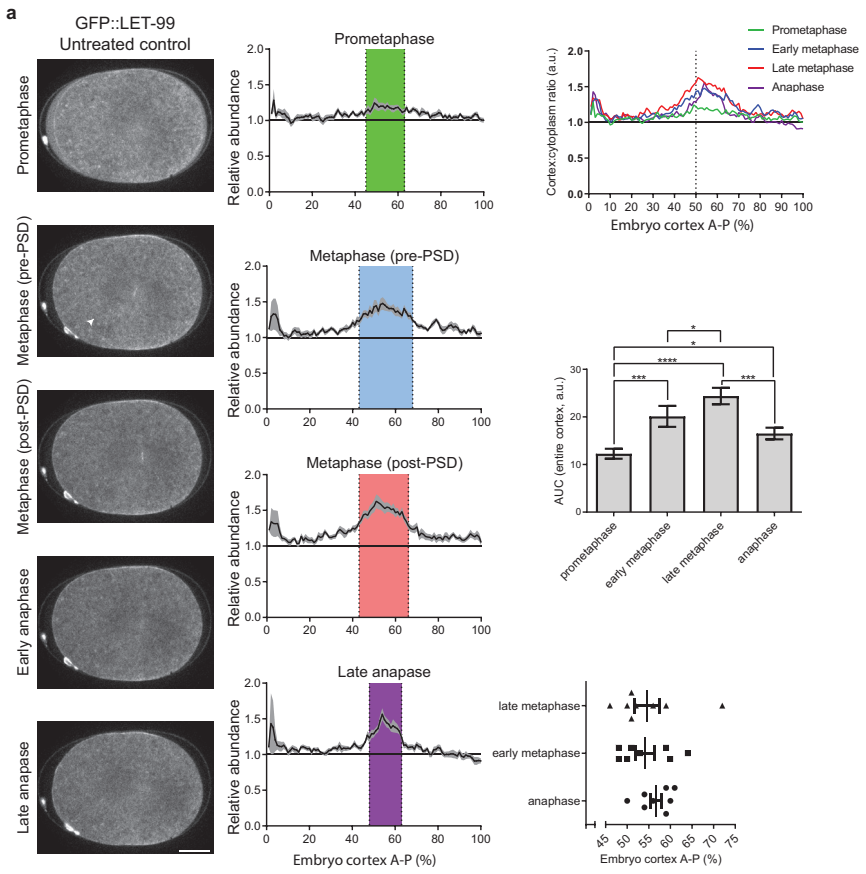

Figure 7-figure supplement 1. **Quantification of cortical distribution of endogenous LET-99**. (**a**) Spinning disk confocal microscopy images of a one-cell embryo showing fluorescently labeled endogenous GFP::LET-99 at different mitotic phases. Graphs indicate relative cortical:cytoplasm fluorescence intensity ratios plotted against percentage cortex length, as well as area under the curve (between y=1.0 and curves), and peak fluorescence localizations at early (pre-posterior spindle displacement (PSD)) and late metaphase and anaphase. Dotted vertical line indicates 50% cortex length, continuous horizontal line indicates 1:1 cortex:cytoplasm ratio. All values above this line are considered as cortical enrichment. Regions of higher variation are a result of interference by polar bodies that carry a strong fluorescent signal (arrowhead).
(Figure continued on next page)

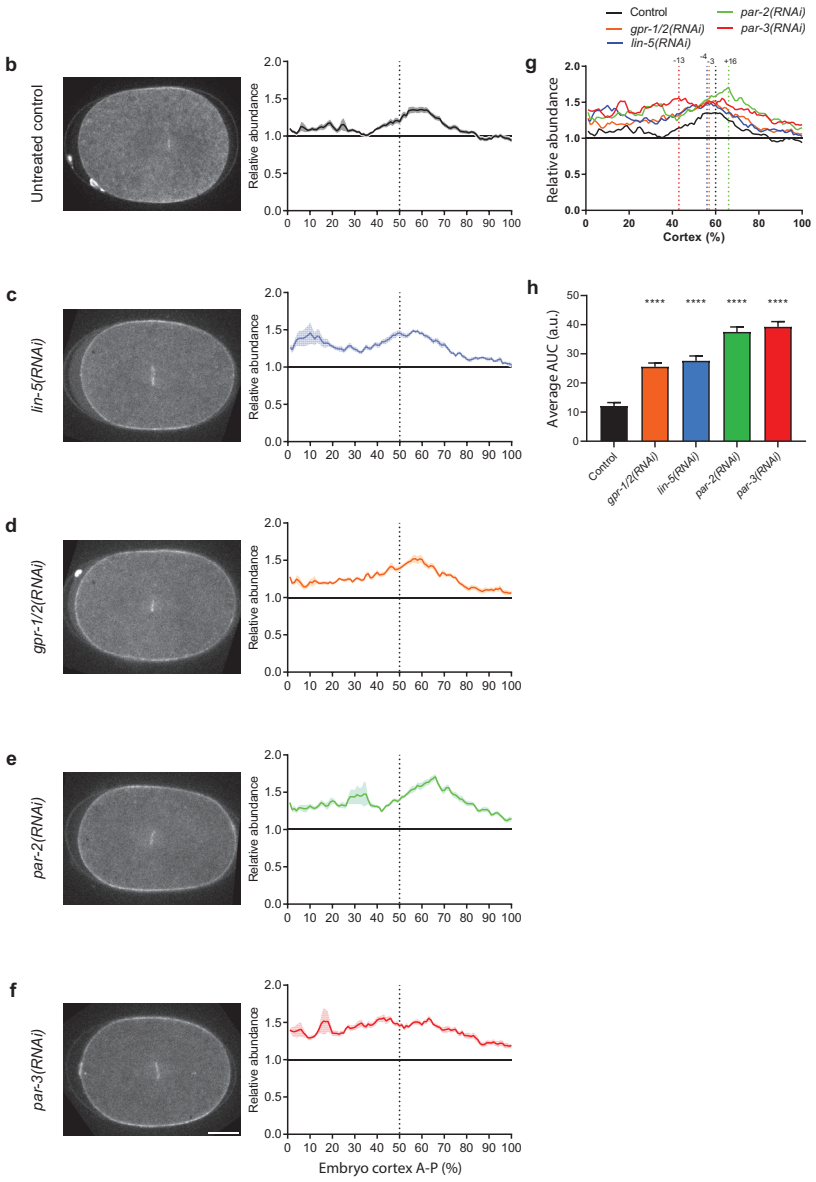
b
Untreated control
c
lin-5(RNAi)
d
gpr-1/2(RNAi)
e
par-2(RNAi)
f
par-3(RNAi)
Relative abundance
Embryo cortex A-P (%)
g
Control
gpr-1/2(RNAi)
lin-5(RNAi)
par-2(RNAi)
par-3(RNAi)
-13
-4
-3
+16
Cortex (%)
h
Average AUC (a.u.)
****
Control
gpr-1/2(RNAi)
lin-5(RNAi)
par-2(RNAi)
par-3(RNAi)

Figure 7-figure supplement 1 (Continued). **Quantification of cortical distribution of endogenous LET-99**. (**b-f**) Spinning disk confocal microscopy images of one-cell embryos showing fluorescently labeled endogenous GFP::LET-99 at late metaphase (the last recorded frame prior to anaphase initiation, as judged by LET-99 localization to DNA) in either control (**b**), *lin-5(RNAi)* (**c**), *gpr-1/2(RNAi)* (**d**), *par-2(RNAi)* (**e**) or *par-3(RNAi)* (**f**) conditions. Graphs show the cortical distribution of LET-99 quantified as cortex:cytoplasm intensity ratio (average ± SEM) distributed over cortex length. (**g**) Combined average traces (without error margins, for clarity) for the conditions described in (**b-f**). Dotted vertical lines indicate peaks, associated numbers indicate the shift of these peaks in % cortex length compared to the control (black) peak. (**h**) Total area under the curve (auc), between horizontal 1:1 cortex:cytoplasm threshold (see (**f**)) and average curves calculated for each condition and used as a read-out for total cortical enrichment. N=5 embryos per condition, n=10 cortical traces per cortex. One-way ANOVA. * P<0.05; *** P<0.001; **** P<0.0001. Scale bar: 10 µm.

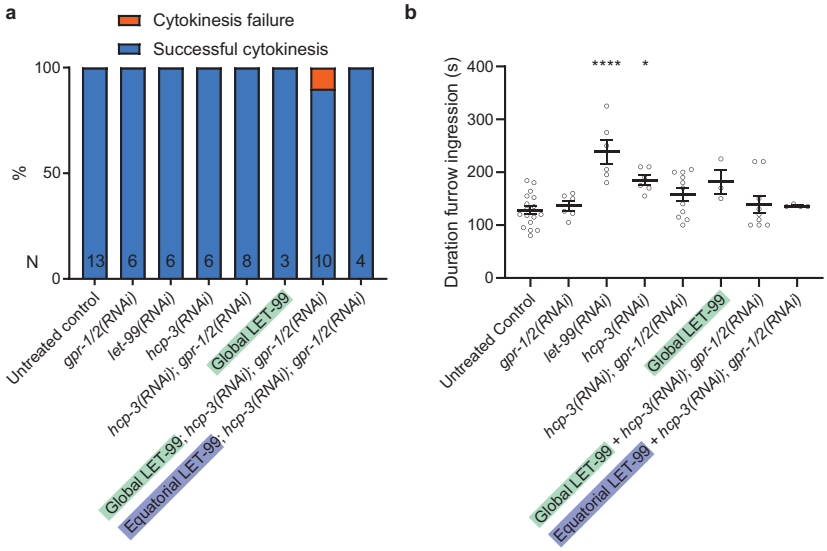

Figure 7-figure supplement 2. **Artificial global cortical LET-99 stimulates cytokinesis**. (**a**) Quantification of percentage embryos that completed (blue) and failed (orange) cytokinesis in control, *gpr-1/2(RNAi)*, *let-99(RNAi)*, *hcp-3(RNAi)*, *hcp-3(RNAi); gpr-1/2(RNAi)* embryos, with or without global (indicated in green) or equatorial (indicated in blue) recruitment of LET-99. Quantifications of the interval between (**b**) furrow initiation and cytokinesis completion for control, *hcp-3(RNAi), gpr-1/2(RNAi)*, *let-99(RNAi)*, *hcp-3(RNAi); gpr-1/2(RNAi)* embryos, with or without cortical recruitment of LET-99. One-way ANOVA. * P<0.05; **** P<0.0001. N values are indicated on graph (**a**), equal for (**b**). Scale bar: 10 µm.

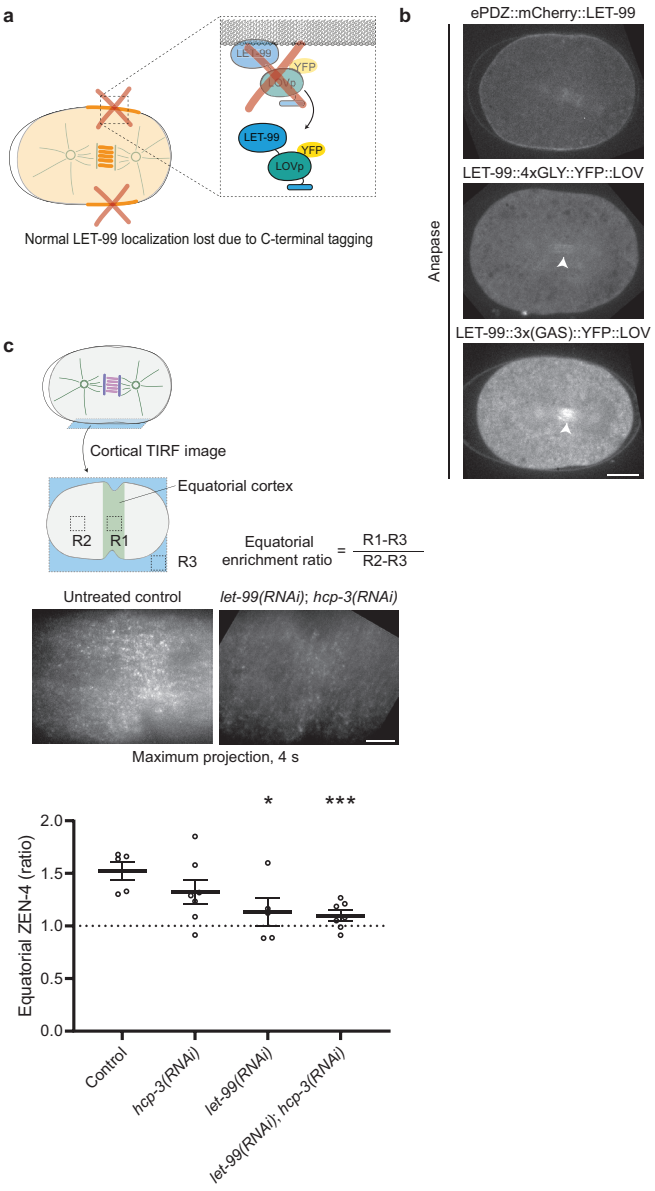

Figure 7-figure supplement 3. **Depletion of LET-99 disrupts normal anaphase cortical ZEN-4 distribution**. (**a**) Cartoon model showing the strategy used for LET-99::YFP::LOV tagging and its effect on localization of the protein. (**b**) Spinning disk confocal microscopy images of one-cell embryo showing fluorescently labelled endogenous ePDZ::mCherry::LET-99, LET-99::4xGLY::YFP::LOV and LET-99::GASGASGAS::YFP::LOV. Arrowheads indicate midzone localization of LET-99. Scale bar: 10 μm. (**c**) Cartoon showing the strategy used for imaging and quantification of equatorial GFP::ZEN-4 fluorescence. Images show embryos as imaged by TIRF microscopy during furrow initiation, both for control and *hcp-3(RNAi)*; *let-99(RNAi)* conditions. Quantification shows equatorial enrichment of GFP::ZEN-4 at furrow initiation for control, *hcp-3(RNAi)*, *let-99(RNAi)* and *hcp-3(RNAi)*; *let-99(RNAi)* conditions. Unpaired Welch's Student's *t* test. * P<0.05; *** P<0.001. N=5-7 embryos per condition. Scale bar: 5 μm.

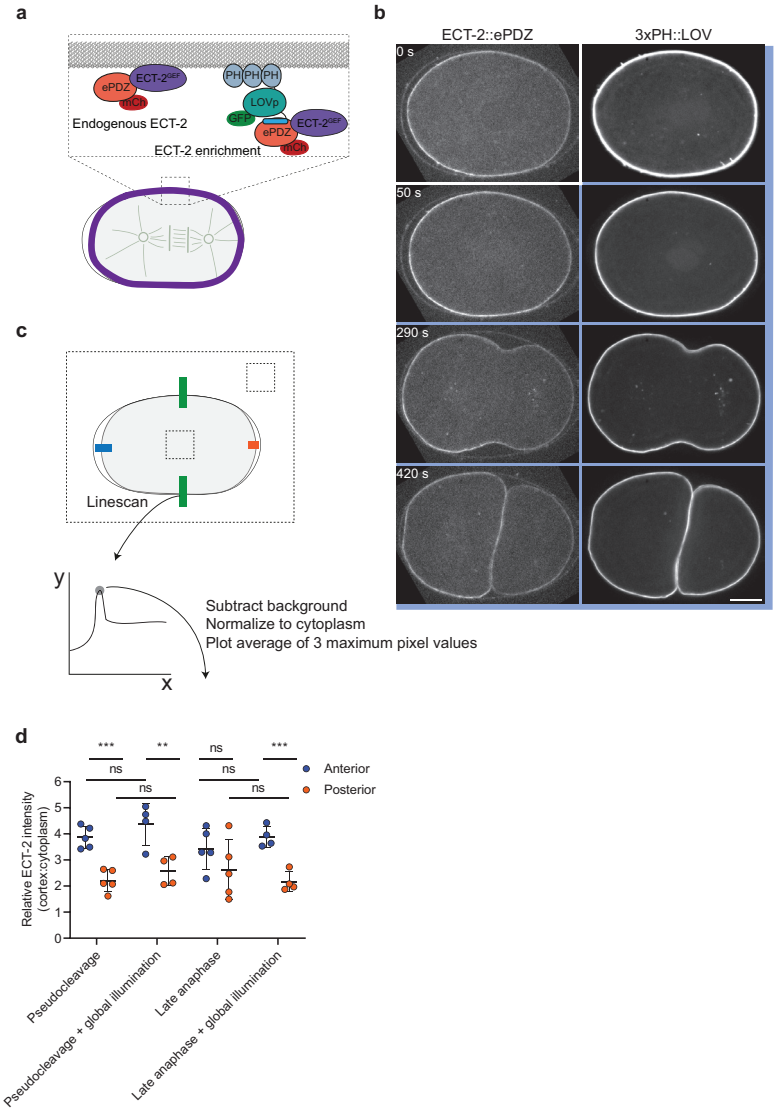

Figure 8-figure supplement 1. **Endogenous cortical ECT-2::ePDZ is not readily translocated to 3xPH::LOV.** (**a**) Cartoon model showing the strategy used for global ECT-2::ePDZ recruitment through activation of 3xPH::GFP::LOV. (**b**) Spinning disk confocal microscopy images of one-cell embryos showing fluorescently labeled endogenous ECT-2::ePDZ::mCherry and cell membranes (visualized by 3xPH::GFP::LOV). Representative pre- and post-activation and cytokinesis single frames are shown from a time-lapse movie of a single embryo. Blue backgrounds indicate that embryos have been exposed to blue (491 nm) light at these timepoints. (**c**) Cartoon model showing the quantification method used for measuring relative cortical ECT-2::ePDZ enrichment. Perpendicular line-scans are drawn over cortical regions of interest and used to generate intensity profiles. Three maximum pixel values are taken from each profile and averaged after background subtraction and normalization to an average cytoplasmic value. (**d**) Quantification of relative cortical:cytoplasm ECT-2::ePDZ enrichment at the anterior (blue) and posterior (orange) poles during pseudocleavage and late anaphase with and without global illumination with blue (491 nm) light. Unpaired Welch's Student's *t* test. *** P<0.001. N=5 embryos. Scale bar: 10 µm.

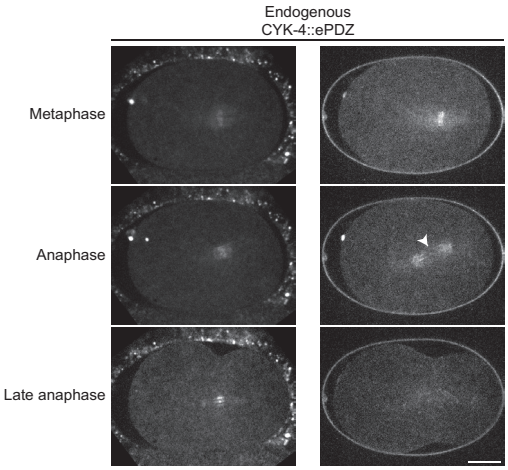

Figure 9-figure supplement 1. **Endogenous tagging of CYK-4::ePDZ results in occasional midzone instability**. (**a**) Spinning disk confocal microscopy images of one-cell embryos showing fluorescently labelled endogenous CYK-4::ePDZ::mCherry during metaphase, anaphase and telophase. The red arrowhead indicates midzone rupture during anaphase. Scale bar: 10 µm.

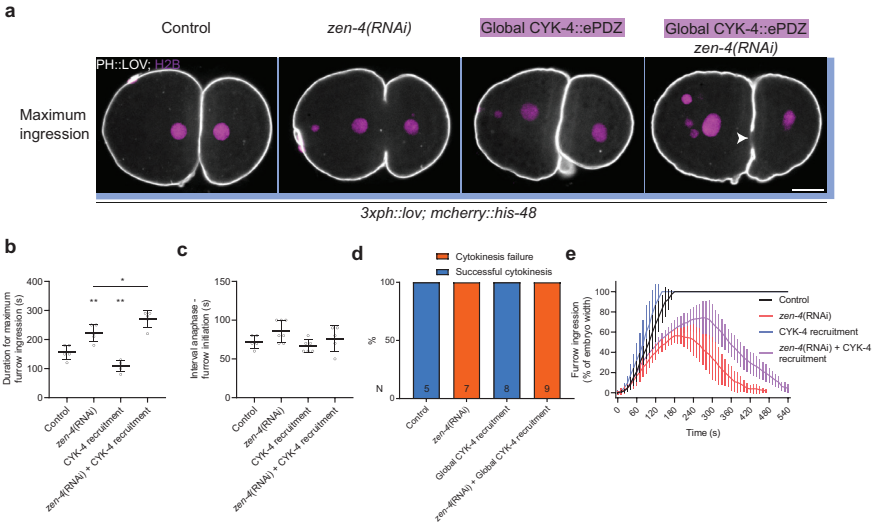

Figure 9-figure supplement 2. **Artificial global cortical CYK-4::ePDZ recruitment partially rescues the furrowing defect resulting from *zen-4* inactivation.** Spinning disk confocal microscopy images of telophase one-cell embryos at the point of maximal furrow ingression, showing labeled membrane (3xPH::LOV, greyscale) and DNA (mCherry::HIS-48, magenta) with or without *zen-4(RNAi)* and global CYK-4::ePDZ recruitment. Quantifications of the interval between anaphase start and maximal furrow ingression (**b**), interval between anaphase start and furrow initiation (**c**), rate of cytokinesis success (**d**) and furrow ingression over time as a percentage of total embryo width (**e**) for the different conditions shown in (**a**). Unpaired Welch's Student's *t* test. * P<0.05; ** P<0.01. N=5 embryos per condition. Scale bar: 10 µm.

Chapter 6

Summary and general discussion

Ruben Schmidt and Sander van den Heuvel

The mitotic spindle determines the outcome of cell division in animals. Proper positioning of the spindle is crucial for coordinating chromosome segregation with cleavage plane specification. The placement of the mitotic spindle downstream of cell polarity drives the generation of unequal daughters through cell division, which is of vital importance to proper animal development. In the preceding experimental chapters, we have explored some of the diverse molecular mechanisms that regulate spindle and cleavage plane positioning in the early *C. elegans* embryo. In this final chapter, we will begin with a brief summary of the findings presented in this thesis. Thereafter these results will be discussed in the broader context of contemporary research and experimental developments.

In **chapter 2**, we followed up on earlier studies originating from our lab that focused on spindle positioning in the one-cell *C. elegans* embryo. We revealed that phosphorylation of LIN-5 by different kinases modulates its interaction with the binding partners GPR-1/2 and the essential dynein motor complex. These post-translational modifications turned out to be crucial for the precise spatiotemporal control of spindle positioning in early embryos. In **chapter 3**, we assessed the dynamics of endogenous dynein complexes. Here, we found that two cortical populations of dynein drive robust spindle positioning in the one-cell embryo. One population binds to the growing MT plus end via the +TIP EBP-2. The other population of dynein is tethered to the cortex via the LIN-5 complex. The cortical LIN-5-bound population of dynein shows asymmetric dynamics, which are driven by polarity complexes that define the anterior-posterior symmetry axis of the embryo. In **chapter 4**, we used recent technological developments to reconstitute cortical force generator complexes with different molecular compositions. Such experiments allowed us to reveal that LIN-5 is a potent activator of dynein-dependent spindle pulling forces. Conversely, while Gα–GPR-1/2 turned out not to be essential for the generation of pulling forces, these components are indispensable for the proper distribution of pulling forces along the anterior-posterior axis of the embryo. Local recruitment of LIN-5 to the cortex allowed us to experimentally control the displacement and orientation of the mitotic spindle. Such experiments could prove to be a valuable tool for future research concerning mitotic spindle and cleavage plane positioning. Finally, in **chapter 5** we explored the role of the LIN-5 complex and its cortical antagonist LET-99 in driving aster-dependent cytokinetic furrowing. We compared various methods for midzone disruption and simultaneously controlled the cortical distribution of proteins of interest with improved light-inducible tools. In doing so, we found that the LIN-5 complex inhibits contractility at the polar cortex. We also observed that LET-99 stimulates furrowing at the equator, at least in part independently of LIN-5, and possibly in conjunction with cortical centralspindlin. Interestingly, light-controlled localization of the centralspindlin component CYK-4 at the cortex leads to ectopic contractility during pseudocleavage and late mitosis in the early embryo.

In addition to the improved understanding of biological processes, this research is of general importance in the greater context of research that uses *C. elegans* as a model

system, because all experimental chapters provide both new and improved methods for the detailed study of diverse molecular processes. We have extensively applied CRISPR/Cas9-mediated genome editing to study the functionality of endogenous proteins. Excitingly, we also managed to adapt the light-inducible LOV–ePDZ system to the *C. elegans* germline, which allows us to precisely control the subcellular localization of proteins of interest. In the remainder of this chapter, we will further summarize and discuss the results presented in this thesis and place our findings in the greater context of the scientific questions that remain unanswered.

Translating cell polarity to asymmetric spindle positioning through phosphorylation of LIN-5

Depending on the developmental stage and cellular context, asymmetric cell division relies on intrinsic regulation through cell polarity factors or extracellular signaling cascades. The blastomeres in the early *C. elegans* embryo are separated from their surroundings by an impermeable eggshell. This barrier prevents any instructive signals from the environment that could steer the division process from reaching the embryo proper. The eggshell has formed by the time meiosis progresses to anaphase II and is further modified during the initial embryonic divisions (reviewed in Stein and Golden, 2015). Fertilization occurs as the oocyte passes through the spermatheca, which triggers the development of most layers of the eggshell. The point of sperm entry determines which of the two poles of the axially naïve oocyte will constitute its posterior end (Goldstein and Hird, 1996). The eggshell forms soon after delivery of this cue, and the events after this point in development are likely to depend on intrinsic regulation and cell-cell contacts within the context of the embryo.

As we have discussed in the introductory chapter of this thesis, a conserved network of PAR proteins sets up and maintains the anterior-posterior symmetry axis in the one-cell embryo. Prior to division of the P0 blastomere, the mitotic spindle is displaced towards the posterior to result in the formation of a smaller posterior and a larger anterior daughter blastomere, which have different developmental fates. A conserved cortical complex of Gα–GPR-1/2–LIN-5–dynein is essential for generating the forces that position the spindle. Early experiments revealed that these proteins act downstream of cell polarity to exert asymmetric pulling forces (Grill et al., 2001). Following the discovery and characterization of these essential components by our lab and others, different factors were shown to contribute to the translation of cell polarity to physical displacement of the spindle. For example, our lab revealed that the C-terminus of LIN-5 is directly phosphorylated by the anterior PAR protein PKC-3^{aPKC}. This modification results in the inhibition of anterior-directed pulling forces and a posterior displacement of the spindle (Galli et al., 2011a). However, substitution of the cluster of residues in LIN-5 that is targeted by PKC-3 with non-phosphorylatable amino acids does not prevent the spindle from being asymmetrically positioned in late mitosis. Thus, additional levels of regulation are involved in the

asymmetric distribution of cortical pulling forces. Besides the above-mentioned cluster, LIN-5 is heavily phosphorylated on other residues. We characterized which of these residues contribute to essential cell division functions of LIN-5 in **chapter 2**. Out of 25 in vivo phosphorylated amino acids that we analyzed, four such phosphosites appear essential for in vivo LIN-5 function. Two residues in the C-terminus were targeted sequentially by GSK3 and CK1 phosphorylation, and were found to mediate LIN-5–GPR-1/2 binding. However, we did not find evidence for dynamic regulation of this interaction during development. Furthermore, replaceability of these residues with negatively charged phosphorylated residues indicated that not phosphorylation per se, but instead charge is likely to mediate the interaction between LIN-5 and GPR-1/2. The other two essential residues we studied are located in the N-terminus of LIN-5 and are phosphorylated by Cyclin B/CDK-1. Interestingly, this modification proved vital for the proper cortical recruitment of dynein. Our data indicate that sequential phosphorylation and dephosphorylation of these LIN-5 residues could be crucial for the proper cell cycle-dependent regulation of cortical dynein. While we are yet to identify a phosphatase that targets LIN-5, it will be interesting to assess what other interactors mediate this aspect of the LIN-5–dynein interaction. In mammalian cells, NuMA^{LIN-5} requires removal of Cyclin B/CDK-1-dependent phosphorylation at residue T2055 in order to localize to the cortex together with dynein (Kotak et al., 2013). In this case, phosphorylation is actively counteracted by the phosphatase PPP2CA. Thus, it is possible that multiple Cyclin B/CDK-1-mediated phosphorylated residues contribute to the cortical localization of dynein in mitosis.

Cortical distribution of the endogenous force generator complex

When we recruited endogenous LIN-5 to the cortex through light-inducible protein-protein heterodimerization, we observed abnormally strong movements of the mitotic spindle, and even the nucleocentrosomal complex prior to spindle assembly (**Chapter 4**). These results suggest that the cortical localization of LIN-5–dynein is sufficient for the induction of pulling forces on astral MTs, as dynein was efficiently co-recruited with LIN-5. Based on these findings, it is likely that cortical LIN-5–dynein can generate pulling forces regardless of its PKC-3, GSK-3/CK1 or Cyclin B/CDK-1-regulated phosphorylation state and cell cycle progression. Thus, we propose that one of the main methods for the cell to modulate and distribute the intensity of cortical pulling forces is through precisely tuned cortical levels of the dynein activator LIN-5. Whether such regulation requires dynamic phosphorylation of LIN-5 at different residues remains to be assessed. It would be interesting to recruit the different LIN-5 phosphomutants presented in **chapter 2** to the cortex, with the methods described in **chapter 4**. Such experiments might reveal whether different phosphorylation states of LIN-5 contribute to the cortical recruitment, and activation of dynein.

It is intriguing that LIN-5 acts as a potent activator of dynein regardless of *Gα* and *gpr*-1/2 function. If Gα–GPR-1/2 function is not necessary for the generation of pulling

forces, then how has a trimeric membrane anchor for dynein evolved? When we globally recruit GPR-1 to the cortex, forces become symmetrically distributed. This indicates that in a wild type situation, a level of asymmetry is introduced at the level of Gα–GPR-1/2. How could these proteins be regulated asymmetrically? Previous description of the GAP RGS-7 and GEF RIC-8 suggests that efficient force generation is promoted by 1) a cycle of GTP hydrolysis that 'recycles' the force generator complex (Tall and Gilman, 2005), 2) Gα·GTP downstream signaling (Afshar et al., 2004), and/or 3) chaperone function of RIC-8 for the biosynthesis, plasma membrane targeting or stability of Gα (David et al., 2005; Hampoelz et al., 2005; Wang et al., 2005; Nagai et al., 2010; Gabay et al., 2011). In our hands, cortical targeting of RIC-8 did not result in an acute effect on spindle movements. This observation suggests that the generation of Gα·GTP is unlikely to be essential for force generation. Instead, it indicates that RIC-8 is more likely to function as a chaperone for Gα, at least in the isolated one-cell *C. elegans* embryo. Conversely, the cortical recruitment of RGS-7 promotes spindle movements, which further underlines the function of Gα·GDP as an anchor for GPR-1/2–LIN-5–dynein. It remains puzzling that we did not find any direct effect of cortical RIC-8 recruitment, as RIC-8 has been shown to promote force generation in the one-cell embryo (Afshar et al., 2004). However, our experiments were executed in the context of a one-cell embryo where no cell-cell communication occurs. Possibly, the cortical stimulation of Gα·GTP generation could serve a role in spindle orientation during later stages of development. This is conceivable, as a body of work on RIC-8 function originates from multicellular contexts such as *D. melanogaster* SOP cells or neuroblasts, where G-protein coupled receptor signaling regulates spindle orientation (Katanaev et al., 2005). Following early immunostaining and transgene overexpression experiments (Afshar et al., 2004; Hess et al., 2004), our efforts to endogenously tag RIC-8 and RGS-7 with genetically-encoded fluorophores were the first to our knowledge. Interestingly, we did not observe obvious asymmetries in the localization of either protein during spindle positioning in the one-cell embryo. Expression levels of these proteins are extremely low, especially for RGS-7, which complicates the quantitative analysis of their subcellular localization patterns. Thus, with the current data we have to conclude that asymmetries in the regulation of Gα–GPR-1/2 are not likely to arise through cortical RGS-7 or RIC-8 in a wild type situation, even though this is difficult to relate to their loss-of-function phenotypes. While local recruitment of RGS-7 through an intrinsically asymmetrically localized PAR-6::LOV anchor yields an asymmetric increase in spindle movements (**Chapter 4**), tagging of RGS-7 with a brighter fluorophore than mCherry or enhancement of the signal via immunostaining could reveal its detailed localization pattern.

To date, the question of how PAR protein asymmetry is mechanistically translated to the modulation of molecular interactions and force generation remains incompletely answered. Conceivably, asymmetric localization of force generators could result in asymmetric spindle positioning (Grill et al., 2003). The exact distribution of force generator complex

components has been under debate ever since their initial discovery. Immunostainings for GOA-1 and GPA-16 revealed global and seemingly non-polarized distribution patterns (Miller and Rand, 2000; Gotta et al., 2001; Afshar 2005; Park and Rose, 2008). Similar experiments revealed that GPR-1/2 might be asymmetrically distributed during initial spindle displacement (Colombo et al., 2003; Gotta et al., 2003; Tsou et al., 2003b; Park and Rose, 2008; Panbianco et al., 2008; Krueger et al., 2010). One mechanism contributing to the translation of PAR polarity could act through PIP_2 synthesis by PPK-1. The PPK-1 enzyme localizes to the posterior cortex downstream of PAR polarity. This localization requires the casein kinase CSNK-1, and it promotes the cortical localization of GPR-1/2 and LIN-5. However, experiments within our group do not support that GPR-1/2 is asymmetrically distributed during metaphase spindle displacement (Srinivasan et al., 2003). Regardless of whether GPR-1/2 is distributed in an asymmetric fashion, its localization pattern does not appear to translate directly to the distribution of the dynein activator LIN-5 (Lorson et al., 2000; Srinivasan et al., 2003; Galli et al., 2011a; b).

Immunostaining experiments by Park and Rose revealed that both GPR-1/2 and LIN-5 are enriched at the anterior cortex during prophase, when the nucleocentrosomal complex migrates from the posterior to the cell center (Park and Rose, 2008). Experiments in our group revealed a similar pattern of anterior cortical enrichment during (pro)metaphase (Galli et al., 2011a). Even during late metaphase spindle migration, only one out of three embryos were shown to harbor posteriorly enriched absolute levels of LIN-5 (Park and Rose, 2008). Quantifications of cortical LIN-5 enrichment during this stage are complicated by the anterior enrichment of the cytoplasmic pool of LIN-5. Calculating ratios of LIN-5 at the cortex over adjacent cytoplasmic values revealed posterior cortical enrichment in most late metaphase embryos (Park and Rose, 2008). However, whether such local differences in cortex to cytoplasm relationships could be sensed by the cell to position the spindle asymmetrically remains unclear. Perhaps cortical LIN-5 competes for dynein binding with the cytoplasmic pool? If this were true, then the symmetry in absolute cortical LIN-5 levels during metaphase and early anaphase would not be likely to contribute to asymmetric pulling force generation. Contrary to the situation during prophase and metaphase, the cortical distributions of GPR-1/2 and LIN-5 show a clear enrichment at the posterior cortex during late anaphase (Park and Rose, 2008).

Considering that most of the quantifications discussed above were performed on immunostained embryos, we decided to quantify the distribution of LIN-5 and dynein using endogenous tagging strategies. While we managed to tag GPR-1 endogenously with GFP (**Chapter 2**), expression levels are particularly low, which precludes the quantification of cortical protein enrichment in one-cell embryos. For LIN-5 and dynein, which are expressed at more readily quantifiable levels, we found that there was no significant enrichment of either during metaphase (**Chapter 3**). As previously reported by Park and Rose, cytoplasmic LIN-5 is enriched in the anterior during prophase and metaphase. Our detailed analysis of endogenous LIN-5 distribution revealed that this cytoplasmic gradient

does not depend on GPR-1/2 (our unpublished results). Furthermore, significant cortical enrichment of LIN-5 in the posterior only becomes apparent during late anaphase, following the posterior migration of the spindle. Endogenous dynein complexes followed a similar localization pattern, as both its mCherry- and GFP-fusions enriched in the cytoplasm prior to late anaphase. Dynein levels at the cortex do not become detectably enriched at the cortex during metaphase, and thus do not correlate with asymmetric spindle positioning. We observed LIN-5-dependent patches of cortical dynein during anaphase, and their appearance is inversely correlated with the proximity of the oscillating spindle poles. In cultured mammalian cells the cortical association of dynein–dynactin with its anchor NuMA–LGN is controlled by spindle pole-localized Plk1 (Kiyomitsu and Cheeseman, 2012). Possibly, a similar mechanism could regulate the cortical localization of dynein in the *C. elegans* embryo. However, this would be specific to anaphase, when the oscillations of mainly the posterior spindle pole close the gap between the cortex and spindle. During metaphase, we managed to reproducibly cross-correlate the cortical localization of fluorescently labeled endogenous LIN-5 and DHC-1 (**Chapter 3**). Collectively, our analysis of endogenously tagged protein localization revealed for the first time that cortical dynein in the one-cell embryo depends on LIN-5, but we found no correlation between cortical protein distribution and asymmetric spindle displacement.

Regardless of the conclusions drawn from the above-discussed analyses, asymmetric cortical protein enrichment that remains below our detection limit could contribute to spindle displacement. Using TIRF microscopy, we visualized both endogenous LIN-5 and dynein during metaphase. This approach also revealed no obvious asymmetric localization patterns. However, FRAP analysis revealed that the cortical population of dynein displays PAR-dependent differences in stable fractions between the anterior and posterior. A more stable fraction of cortical dynein was observed in the posterior. Such differences could be constituted by varying cortical retention times between the anterior and posterior LIN-5–dynein complexes. Possibly, this PAR-dependent stable fraction of LIN-5–dynein drives asymmetric spindle migration. Interestingly, we did not detect significant asymmetries in the stable fraction of LIN-5, although the relevant dynein-bound subpopulation of LIN-5 might have been obscured in the total population during these experiments (Schmidt et al., 2017; **Chapter 3**). Based on these data, we conclude that factors other than differences in cortical protein levels are likely to drive asymmetric spindle positioning. Such regulation could occur through dynamic phosphorylation of LIN-5 (**Chapter 2**), but this remains to be experimentally tested. In addition to asymmetrically regulating the force generator complex itself, MT dynamics at the cortex could also be locally modulated. For example, the tumor suppressor APR-1^{APC} was recently shown to become enriched at the anterior cell cortex, where it locally stabilizes astral MTs downstream of PAR polarity (Labbe et al., 2003; Sugioka et al., 2018).

The interaction of dynamic MT plus ends with the cell cortex

During spindle positioning, dynamic astral MTs grow to the cortex where they are captured by force generator complexes. In **chapter 3**, we explored the role of proteins associated with dynamic plus ends in one-cell *C. elegans* embryos. The EB proteins are master regulators of the MT +TIP network. EBs directly recognize the growing plus end, and recruit a variety of other proteins that modulate MT growth dynamics. Proper maintenance of the +TIP is important for the modulation of the MT network, and its connection to diverse cellular structures (Akhmanova and Steinmetz, 2015). Thus, one might expect that EBs are vital for viability across the animal kingdom. However, simultaneous knockout of all EB isoforms had not been achieved in vivo. The *C. elegans* genome harbors three putative EB homologs; *ebp-1*, *-2* and *-3*. We were surprised to find that animals carrying triple homozygous knockout alleles for these genes were fully viable. In addition, we observed no defects in one-cell embryos, with the exception of a SPD-1^{PRC1}-like loss-of-function phenotype in which the spindle midzone ruptured during anaphase (**Chapter 3**). This effect could result from slightly diminished MT growth or stability. Nevertheless, the effect is not strong enough to disrupt normal spindle assembly and positioning. A simultaneous study reported similar results using cultured mammalian cells. The authors also used CRISPR/Cas9 to knockout EB2, EB3 and the C-terminus of EB1, which contains essential dimerization and protein-protein interaction motifs (Yang et al., 2017). Stable cell lines lacking EB1/2/3 could be generated, and further analysis revealed effects on Golgi morphology, cell migration, formation of focal adhesions and cell polarity. However, consistent with our analysis of early *C. elegans* embryos, only mild effects in cell division and MT polymerization emerge in these mutants. Interestingly, while HeLa cells could be stably maintained as triple knockouts, no triple mutant retinal pigment epithelium (RPE1) or HT1080 fibrosarcoma cells could be obtained for yet unknown reasons. In addition, acute knockout of EB1 and EB3 in HeLa cells resulted in strongly synergistic effects on spindle morphology compared to depletion of either protein alone (McKinley and Cheeseman., 2017). Such contrasting results might indicate that the presence of mutations in the background of these cell lines contributes to their adaptability to loss of EB function. However, in the case of the triple EB knockout in *C. elegans*, such selection is not likely, because of careful backcrossing, as well as the robustness of cell divisions and their coordination required to constitute an entire animal, in contrast to individual cultured immortal cells.

In **chapter 3**, we also found that dynein associates with the growing MT plus end during mitosis in *C. elegans* embryos, as it does in other species of animals (Vaughan et al., 1999; Han et al., 2001; Lenz et al., 2006; Kobayashi and Murayama, 2009). Localization to the MT plus end depended on the function of *ebp-2*, but not *ebp-1/3*. Strikingly, the contribution of dynein plus end tracking to mitosis only became apparent when dynein function was partly disrupted in a conditional mutant. Thus, we conclude that plus end tracking of dynein is likely to act as a backup mechanism to ensure robust spindle

positioning. Importantly, the mechanism by which dynein plus end tracking contributes to force generation is unlikely to act through the delivery of dynein to the cortex. In *Saccharomyces cerevisiae* (budding yeast), dynein is actively transported to the MT plus end by the kinesin Kip2. In cooperation with EB1 and CLIP-170 homologs, Kip2 maintains the plus end localization of dynein as it attempts to move towards the minus end (Roberts et al., 2014). Dynein is actively off-loaded during mitosis in budding yeast cells, after which it associates with its cortical anchor Num1 to position a spindle-like MT array (Markus and Lee, 2011). This mechanism is different from the mode of dynein plus end-tracking observed in animals, where the motor protein is transiently concentrated at the growing MT plus end. This transient association reflects the interaction dynamics of EB proteins with the growing plus end. The relatively weak intermolecular associations of EB proteins with the plus end allow for a very dynamic and readily remodified +TIP network (Akhmanova and Steinmetz, 2015). Thus, we propose that transient enrichment of dynein at MT plus ends contributes to efficient force generation by increasing the local concentration of cytoplasmic dynein molecules at the MT–cortex interface. This concentration could promote the formation of complete Gα–GPR-1/2–LIN-5–dynein complexes. In our model, dynein is effectively recruited to the cortex from the cytoplasm by LIN-5. Such a model has been proposed to work for *D. melanogaster* RhoGEF2, which concentrates at MT plus ends, and initiates cortical remodeling through the stimulation of actomyosin contractility (Rogers et al., 2004). A similar mechanism might function in *C. elegans* one-cell embryos, where the local concentration of dynein stimulates the formation of active force generators during mitosis.

The asymmetrical distribution of force generation events

In addition to LIN-5 and dynein, we analyzed the cortical distribution of the Gα–GPR-1/2 antagonist LET-99. Previous studies have reported on LET-99 localization based on immunostainings and ectopic transgene expression. Contrary to a study by Bringmann et al., we observed that the endogenous LET-99 band is assembled at ~54% instead of ~50% cortex length (A-P) during prometaphase. The LET-99 band was proposed to shift toward the posterior during the transition from metaphase to anaphase, thereby following the position of the spindle (Bringmann et al., 2007). Consistent with this study, we found that the peak of cortical LET-99 intensity shifts toward the posterior due to narrowing of the band at late anaphase (**Chapter 5**). By quantifying the distribution of membrane invaginations (Redemann et al., 2010) during posterior spindle migration, we confirmed that LET-99 locally inhibits cortical pulling forces. We found that the suppression of force generation events in a band in the mid-posterior requires *let-99* function (**Appendix 1**) (Fielmich et al., 2018). These results match those of centrosome fragmentation assays, and spindle bisection experiments (Grill et al., 2003; Krueger et al., 2010). The localization of LET-99 at the cortex reciprocates that of GPR-1/2 (Bringmann et al., 2007), and LIN-5 (**Chapter 5**) during mitosis. Interestingly, global cortical recruitment of either endogenous

GPR-1 or LIN-5 overrules the mid-posterior suppression of pulling forces (**Chapter 5**). These observations suggest that LET-99 locally expels GPR-1/2–LIN-5 complexes from the cortex to mediate the proper distribution of force generation. As a result, force generation events become more concentrated at the posterior end of the embryo, which could contribute to posterior spindle migration.

An important footnote to the results discussed above is the difference between normal cortical protein enrichment compared to the levels recruited through LOV–ePDZ. Immunostainings (Park and Rose, 2008) and live imaging of endogenous proteins (**Chapters 3**, **4**) clearly demonstrated that cortical levels of GPR-1/2, LIN-5, and dynein do not extend more than a factor of ~x1.6 over cytoplasmic levels in otherwise unperturbed one-cell embryos. In contrast, ePDZ-tagged proteins of interest become enriched 2-6x over cytoplasmic values following the global activation of LOV. Such ratios could be slightly overestimated, considering that cortical recruitment has a clear diminishing effect on the concentration of cytoplasmic protein, which leads to higher measured cortex to cytoplasm enrichment. Regardless, the global activation of LOV clearly results in stronger enrichment of cortical proteins of interest than occur in a wild type situation. Considering that the use of the iLID system results in similar cortex to cytoplasm ratios of ~4x for NuMA and 2-3x for dynein, the effect does not seem to depend on which light-inducible system is applied (Guntas et al., 2015; Okumura et al., 2018). Thus, the recruitment of GPR-1 and LIN-5 could simply overrule local regulation by LET-99 through excess levels of cortical protein. The slight cortical enrichment of endogenous LET-99 over cytoplasmic levels might not be able to counteract such cortical enrichment of GPR-1 and LIN-5 (**Chapter 5**). In future experiments, non-continuous illumination of embryos could be attempted in order to recruit levels of proteins of interest that more closely resemble those found in wild type situations. Local illumination experiments (**Chapters 4**, **5**) clearly demonstrated that the LOV–ePDZ system is sensitive enough to allow for the cortical recruitment of reduced levels of protein. Alternatively, global and continuous LOV activation could be combined with lower expression levels of the PH::LOV anchor used in our studies.

How are force generation events asymmetrically distributed to allow for posterior migration of the spindle? In our quantifications of membrane invaginations during spindle displacement, we observed no significant enrichment of force generation events in the posterior pole of the embryo (**Appendix 1**). Thus, we reason that LET-99 function concentrates active force generators in a smaller area of the posterior cortex. This focusing through the inhibition of mid-posterior lateral pulling forces could deliver a more directed net pulling force toward the posterior. In addition, we observed that invaginations persist for significantly longer periods of time, and physically extend further into the cytoplasm in the posterior region of the cortex (**Appendix 2**). These differences between anterior and posterior invaginations are likely to depend on cortical rigidity, as the duration and length of invaginations becomes equally distributed upon partial *nmy-2(RNAi)*. These results suggest that, in addition to being asymmetrically distributed along the cortex, force

generation events also differ in per-event force delivery (Redemann et al., 2010; Afshar et al., 2010; Berends et al., 2013; Kozlowski et al., 2007). However, such a model is in contrast with measurements and modeling performed by Grill et al., who concluded that the number of force generators is asymmetrically enriched while per-event force delivery is constant (Grill et al., 2003). Possibly, multiple force generators could interact with a single MT simultaneously, which delivers a higher net force per event while the force delivered per complex remains constant.

It will be interesting to further explore exactly how force generation events are regulated in an asymmetrical manner. Correlation of the number of membrane invaginations with the number of EBP-2 comets suggest that the amount of MT plus ends that reach the cortex vastly exceeds the amount of force generation events during spindle migration. Thus, there is likely to be strong selectivity in the emergence of force generation events, as not every MT that reaches the cortex initiates a pulling force. We found no evidence for asymmetry in the growth rate of MTs between the anterior and posterior half of the embryo. In addition, previous work demonstrated that there is no asymmetry in the amount of MT plus ends that reach the cortex during spindle positioning (Kozlowski et al., 2007). Thus, chance is likely to occur at the interface of the MT with the cortex during the assembly of an active force generator-MT complex.

How much force is required to displace the spindle?

In addition to the above-discussed question of asymmetry, how cortical complexes manage to generate the proper amount of pulling forces required to displace the spindle remains elusive. In a recent study by Okumura et al., NuMA, DHC, and dynactin were recruited to the cortex using optogenetics in cultured mammalian cells (Okumura et al., 2018). These experiments suggested that clusters of active force generator complexes collectively pull on astral MTs. The authors observed that cortical NuMA forms punctate foci that overlap with LGN and dynein, and that this clustering is required to initiate spindle movements. Clustering requires a 10 aa C-terminal clustering domain that is conserved in vertebrate NuMA. Whether LIN-5 harbors a functionally similar domain remains to be explored. Okumura et al. proposed a model in which cortical clusters of multiple Gα–LGN–NuMA–dynein–dynactin complexes capture and pull on astral MTs to position the spindle. Earlier in vitro work demonstrated that NuMA spontaneously forms clusters of 10-12 dimers that self-assemble into a ring-like structure (Harborth et al., 1999). Using the long (~200 nm) extension of NuMA, and the association with dynein–dynactin, such clusters might efficiently capture dynamic astral MTs. However, evidence other than in vitro NuMA multimerization, and a requirement for the NuMA C-terminal clustering domain to induce spindle migration is currently missing to fully support this model (Okumura et al., 2018). Considering that dynein has a stall force of ~5 pN, and depolymerizing MTs generate up to 30-65 pN in vitro, it will be interesting to further explore such a clustering model (Grishchuk et al., 2005; Laan et al., 2012b; Roberts et al., 2013).

In the *C. elegans* embryo, cortical force generators are estimated to interact with astral MTs for about one second or less (Kozlowski et al., 2007). Multiple simultaneous protein-protein interactions might be required for such prolonged interaction with a depolymerizing MT. Mammalian NuMA readily forms homodimers in vitro (Harborth et al., 1999), which suggests that a single force generator complex could include multiple LGN proteins due to the 1:1 stoichiometry of LGN–NuMA (Culurgioni et al., 2011; Zhu et al., 2011). LGN harbors four GoLoco motifs, each of which can associate with a single Gα·GDP (Jia et al., 2012). For *C. elegans* GPR-1/2, in contrast, a single GoLoco domain has been described (Colombo et al., 2003; Kimple et al., 2008). Two or more cortical dynein molecules might interact with the plus end of a single depolymerizing MT (Laan et al., 2012b). Moreover, the direct interaction of NuMA with MTs was shown to be important for proper spindle orientation in mammals (Okumura et al., 2018; Seldin et al., 2016). Thus, dynein might not be the only molecule in the force generator complex to associate with depolymerizing MTs. Collectively, it is likely that depending on the species, cortical force generators might consist of higher-order protein complexes that efficiently capture and hold on to dynamic astral MTs. The multimerization of such complexes might be regulated in a spatiotemporal manner through phosphorylation, for example of LIN-5 (**Chapter 2**).

Despite our extensive attempts to visualize the formation of endogenous LIN-5–dynein complexes using simultaneous dual-color TIRF microscopy, we did not manage to visualize such events. As an alternative, we attempted to visualize endogenous dynein complexes at the tip of membrane invaginations in the one-cell *C. elegans* embryo. However, the number of dynein molecules at the MT-cortex interface likely remained below our detection limit (**Chapter 3**). Further analysis, for example through the visualization of active force generator complexes by cryo-EM, would aid to deliver further insight on this matter (Bai et al., 2015). Cryo-EM experiments have revealed the conformational states and intermolecular interactions of dynein in other cellular contexts in great detail (Imai et al., 2015; Urnavicius et al., 2015; Zhang et al., 2017; Can et al., 2019).

Activating dynein at the cortex

Dynein has been firmly established as a major player in the positioning of the mitotic spindle in animal cells. Yet, its mode of activation at the cortex has remained elusive. A recent study made use of the dynein gliding and motor ATPase activity inhibitor ciliobrevin D to show that dynein activity is required for the generation of spindle pulling forces (Firestone et al., 2012; Okumura et al., 2018). Cytoplasmic dynein requires an adaptor to efficiently link the complex to both dynactin and its cargo. This coupling is key for its specificity and activation in the context of diverse cellular functions (Raaijmakers et al., 2013). In our studies, light-induced recruitment of endogenous dynein directly to the cortex in mitotic one-cell *C. elegans* embryos does not result in enhanced spindle movements (**Chapter 4**). This was surprising, considering that recruitment through LOV–ePDZ enriched cortical dynein levels up to three times over cytoplasmic levels. Given the low,

almost undetectable levels of endogenous cortical dynein in untreated one-cell mitotic embryos (**Chapter 3**), we expected cortical enrichment of dynein to result in a more dramatic effect. These results clearly suggest that cortical dynein either needs to be activated in addition to being recruited to the cortex, and/or that a specific conformation at the cortex is vital for its ability to generate MT pulling forces.

Direct cortical recruitment of dynein at the cortex in one-cell embryos co-recruits both LIN-5 and the dynactin component DNC-1^{p150glued} (**Chapter 4**). These observations are surprising, given that no spindle movements are induced as a result. Association with dynactin increases the processivity of dynein (King et al., 2000). Yet, co-immunoprecipitation experiments showed very little coprecipitation for dynein and dynactin (Splinter et al., 2012). Their coprecipitation is strongly enhanced by the presence of an activating adaptor like the N-terminus of BICD2. Dynein processivity is drastically promoted by the presence of both dynactin and the BICD2 N-terminus in vitro (McKenney et al., 2014; Schlager et al., 2014a; b). Different dynein adaptors have been shown to perform dual roles in the regulation of dynein activity. Adaptors both stabilize the interaction of dynein–dynactin (Splinter et al., 2012; Hoogenraad and Akhmanova, 2016), and link its core machinery to specific cellular cargo (McKenney et al., 2014; Schlager et al., 2014a; b; Olenick et al., 2016; Schroeder and Vale, 2016; Zhang et al., 2017; Reviewed by Reck-Peterson et al., 2018). At least eight such activating adaptors have been shown to increase dynein processivity in vitro. While no obvious common sequence motifs have been identified, all these adaptors contain a coiled coil domain of at least 200 residues. In addition, these adaptors contain both a binding site for the dynein light intermediate chain (Gama et al., 2017), and a protein that provides a link with cellular cargo (e.g., endosomes or peroxisomes). Cryo-EM has revealed the detailed molecular structures of dynein–adaptor–dynactin complexes, in which the coiled coil of the activating adaptor runs along the actin-like filament of dynactin. Interestingly, multiple activating adaptors have even been shown to recruit two dyneins simultaneously (Grotjahn et al., 2018; Urnavicius et al., 2018). Such interactions could provide one more amplification step in the context of cortical pulling force generation, as discussed above.

Most importantly, NuMA was proposed to be one of the dynein-activating adaptors (Reck-Peterson et al., 2018). This prediction is based on the co-immunoprecipitation of NuMA with dynein–dynactin, and the observation that this motor complex transports NuMA along spindle MTs, which is required for spindle pole formation (Merdes et al., 2000; Radulescu and Cleveland, 2010; Hueschen et al., 2019). Importantly, NuMA contains a long coiled coil domain as is typical for the other activating adaptors identified to date, as well as a Hook domain (Reck-Peterson et al., 2018). Hook is a dynein activator in the context of Golgi and endosome transport, which binds directly to the dynein light intermediate chain and is implicated in the stabilization of dynein–dynactin (Kramer and Phistry, 1999; Bielska et al., 2014; Zhang et al., 2014; Schroeder and Vale 2016). Furthermore, the dynactin subunit Arp1 (actin related protein 1) co-immunoprecipitates

with other dynactin components, as well as the N-terminal calponin homology domain of NuMA (Merdes et al., 2000). Thus, it is tempting to suggest that NuMA performs the essential adaptor function that connects dynein to dynactin at the cortex during mitotic spindle positioning. However, if this were true, then why did we not observe an enhancement of spindle movements upon direct cortical recruitment of dynein, together with LIN-5 and dynactin? The co-recruitment of the dynactin subunit DNC-1^{p150glued} is independent of *lin-5* function (Fielmich et al., 2018; **Chapter 5**). In a similar optogenetic approach in HeLa cells, Okumura et al. observed that direct cortical recruitment of dynein with associated dynactin does not induce spindle movements (Okumura et al., 2018). However, such observations could be explained by the noticeable absence of cortical NuMA in these experiments. Thus, in cultured mammalian cells the generation of cortical pulling forces might require NuMA as an adaptor. In *C. elegans*, however, both LIN-5 and dynactin were co-recruited with dynein (Fielmich et al., 2018; **Chapter 5**). Possibly, other essential subunits of the dynactin complex might not be present at the cortex in these experiments. Alternatively, the assembled complexes could take on an inactive conformation. This would be conceivable given the large conformational changes involved in dynein MT binding and stepping cycles (Zhang et al., 2017).

Based on these collective results, we favor the model in which dynein–dynactin has to be recruited through LIN-5 in order to initiate spindle pulling forces. It would be interesting to assess whether dynein can be activated at the cortex through other adaptors. The overexpression of BICD-1 was previously applied to induce dynein-dependent mitochondrial transport in *C. elegans* dendrites (Harterink et al., 2016). In this context, the N-terminus of BICD-1 was used as a dynein activator as the full-length protein is autoinhibited (Hoogenraad et al., 2001; 2003). Whether a similar type of dynein activation occurs during spindle pulling remains unclear, because dynein–MT association occurs in an end-on fashion at the cortex, which is likely mechanically different from its mode of transport along the MT lattice. While we attempted to achieve light-controlled cortical recruitment of BICD-1 in the early embryo, even slight ectopic expression of ePDZ-tagged BICD-1N in the *C. elegans* germline causes strong dominant effects. Thus, it would be interesting to explore the possible similarities between dynein activating adaptors with alternate approaches. For example, this might be achieved through the use of temperature-sensitive promotors (Bacaj and Shaham, 2007; Tursun et al., 2011), or the injection of protein to circumvent the negative effects caused by constitutive germline expression.

The regulation of cortical contractility through the GPR-1/2–LIN-5 complex

In **chapter 5**, we explored the role of the antagonistic relationship between the cortical LIN-5 complex and LET-99 in the context of cleavage plane specification in the one-cell *C. elegans* embryo. Disruption of *gpr-1/2* function in embryos without a functional midzone results in delayed furrow initiation, and an abnormally broad distribution of the cytokinetic

ring component ANI-1^{anillin}. This result is reminiscent of the cortical ANI-1 distribution observed by Mangal et al. upon perturbation of AIR-1$^{Aurora\ A}$–TPXL-1^{TPX2} (Mangal et al., 2018). Depletion of *gpr-1/2* function enhances the cortical enrichment of ANI-1 specifically at the posterior cortex. ANI-1 is normally cleared from the polar cortices following anaphase onset (Mangal et al., 2018). These observations suggest that the GPR-1/2–LIN-5 complex could be directly or indirectly involved in regulating the distribution of cortical furrowing components. Interestingly, an active cortical clearance mechanism that involves AIR-1–TPXL-1 has been described to be specific for the anterior pole of the cell cortex. However, AIR-1 and TPXL-1 are not asymmetrically distributed in the embryo during anaphase (Mangal et al., 2018). It would be interesting to explore whether there is cross-talk, or possibly redundancy, between the regulation of cortical contractility through AIR-1–TPXL-1 and GPR-1/2–LIN-5 in the one-cell embryo. For example, the anterior clearance of excess cortical ANI-1 and actin, resulting from simultaneous disruption of *rga-3/4* and *nmy-2*, depends on *tpxl-1* function (Mangal et al., 2018). Depletion of *gpr-1/2* or *lin-5* in *rga-3/4*; *nmy-2* embryos could reveal whether the LIN-5 complex has a similar function at the anterior and/or posterior cell cortex. Alternatively, local recruitment of endogenous GPR-1 or LIN-5 (**Chapter 4**) to the cortex could reveal whether cortical localization of GPR-1/2–LIN-5 acutely affects this clearance mechanism. To this end, we have developed a dark version of the stable 3xPH::LOV anchor by genetically excising *GFP* using CRISPR/Cas9 (data not shown).

Mammalian NuMA is phosphorylated by Aurora A during mitosis, which regulates cortical NuMA localization and spindle orientation in cultured cells (Kettenbach et al., 2011; Gallini et al., 2016). Aurora A is a main regulator of centrosome maturation, MT dynamics, as well as spindle assembly and orientation (Schumacher et al., 1998; Hannak et al., 2001; Srayko et al., 2005). Thus, it is a challenge to separate the possible direct and indirect effects of Aurora A on spindle positioning, and/or the regulation of cortical contractility. Further complicating the issue, several regulations may jointly control both processes. A complex of the phosphatase PPH-6 and its interactor SAPS-1 stimulates cortical contractility by promoting cortical NMY-2 during anaphase in the one-cell *C. elegans* embryo (Afshar et al., 2010). PPH-6–SAPS-1 also promotes spindle pulling forces by stimulating the cortical localization of GPR-1/2–LIN-5. Furthermore, PP6^{PPH-6} inhibits the activation of TPX2-bound Aurora A in cultured cells (Zeng et al., 2010). PPH-6–SAPS-1 inhibits the cortical localization of AIR-1$^{Aurora\ A}$ in the one-cell *C. elegans* embryo in a similar fashion (Kotak et al., 2016). Cortical contractility is attenuated following excess cortical localization of AIR-1, resulting from disruption of *saps-1* function. Small molecule-mediated inhibition of AIR-1 leads to excessive spindle movements, possibly through increased cortical LIN-5–dynein localization (Kotak et al., 2016).

The interplay between the abovementioned observations seems counterintuitive. PPH6–SAPS-1 promotes spindle movements through promoting the cortical enrichment of GPR-1/2–LIN-5 complexes, possibly by inhibiting cortical localization of AIR-1, which itself

negatively regulates spindle movements through inhibition of cortical GPR-1/2–LIN-5. This would argue against AIR-1–TPXL-1 and GPR-1/2–LIN-5 cooperating in cortical clearance of contractility factors. Conversely, chemical inactivation of Aurora A in cultured mammalian cells results in attenuation of cortical NuMA–dynein levels during metaphase, while LGN is seemingly unaffected. Concomitantly, phosphorylated NuMA accumulates at the spindle poles (Kotak et al., 2016; Gallini et al., 2016). These contradictory observations might constitute differences in the mechanisms that control spindle positioning in the *C. elegans* embryo and mammalian cells. Possibly, regulation of the centrosomal versus the cortical pool of GPR-1/2–LIN-5 by AIR-1 contributes to a cortical clearance mechanism. GPR-1/2–LIN-5 and AIR-1–TPXL-1 could each perform a dual role in spindle positioning/elongation and polar clearance of furrow components. Furthermore, simultaneous but not individual disruption of *tpxl-1* and *gpr-1/2* results in the dramatic emergence of ectopic cytokinetic furrows (Lewellyn et al., 2010). Such observations would argue for redundant functions between the GPR-1/2–LIN-5 and AIR-1–TPXL-1 pathways. It will be interesting to further explore the role of both AIR-1–TPXL-1 and LIN-5/LET-99 in the regulation of cortical contractility. Especially separating the roles of these proteins in spindle assembly, positioning and elongation versus their effects on contractility will be a challenge for further research.

Local activation of RhoA through the concerted effects of spindle MTs

How is RhoA locally activated to stimulate the formation of a focused cytokinetic furrow? To further explore this mechanism, we endogenously labeled the core components involved in RhoA activation during cytokinesis in the *C. elegans* embryo (**Chapter 5**). Consistent with previous reports, we observed that the centralspindlin components ZEN-4 and CYK-4 enrich at the spindle midzone during anaphase, and the ingressing furrow tip during telophase in one-cell embryos (Kaitna et al., 2000; Gruneberg et al., 2002; Mishima et al., 2004; Verbrugge and White, 2004). Using TIRF microscopy, we managed to observe speckles of endogenous ZEN-4 at the equatorial cortex prior to furrow initiation in late anaphase for the first time. This observation points to a role of cortical centralspindlin in stimulating local furrowing in unperturbed *C. elegans* embryos. In contrast, the endogenous RhoGEF ECT-2 displays constitutive cortical localization in the one-cell embryo. Consistent with an earlier study that employed ectopic germline expression of a *gfp::ect-2* transgene, we observed that cortical ECT-2 levels became diminished at the posterior pole during polarization of the embryo (Motegi and Sugimoto, 2006). Interestingly, this local depletion persisted throughout mitosis, and we measured no enrichment of ECT-2 at the equator during cytokinesis. In addition, we did not observe localization of ECT-2 to the midzone during anaphase. Ect2 readily localizes to the midzone in mammalian cells, although this localization is not required for midzone assembly and cytokinesis (Somers and Saint, 2003; Chalamalasetty et al., 2006; Nishimura and Yonemura, 2006). Most notably, the absence of equatorial enrichment of

ECT-2 in one-cell embryos was surprising, considering that Ect2 is recruited to the equatorial cortex in a cell-cycle-dependent manner in mammalian cells (Su et al., 2011). This cortical localization requires both the Ect2 C-terminus, which contains a PH domain, and the N-terminal BRCT domains that interact with Cyk4^{CYK-4}. Collectively, these interactions lead to local activation of Ect2 at the cortex (Somers and Saint, 2003; Saito et al., 2004; Kim et al., 2005; Yuce et al., 2005; Chalamalasetty et al., 2006; Nishimura and Yonemura, 2006). Activation of Ect2 requires the Plk1-dependent phosphorylation of Cyk4 (Burkard et al., 2009; Wolfe et al., 2009; Zhao et al., 2005). The Ect2 C-terminus harbors a conserved polybasic cluster, which mediates Ect2 membrane binding even in the absence of its PH domain. This cluster contains a consensus Cdk1 phosphorylation motif, and Cdk1 accordingly inhibits the membrane association of Ect2. However, the polybasic cluster is not conserved in *C. elegans* ECT-2 (Su et al., 2011). Ect2 is autoinhibited through the interaction of its phosphobinding N-terminal BRCT, and the C-terminal PH and RhoGEF DH domains (Kim et al., 2005). Conceivably, the priming phosphorylation by Plk1 allows for Ect2 to bind Cyk4. This interaction relieves autoinhibition of Ect2 together with its release from CDK-1-mediated autoinhibition, and leads to the cortical localization of Ect2–Cyk4. Thus, mammalian Ect2 is activated by a dual mechanism during anaphase. Importantly, this model could help to explain why ECT-2 is constitutively membrane-associated throughout the cell cycle in the *C. elegans* embryo. The absence of a C-terminal polybasic cluster and CDK1 targeting motif in ECT-2 is likely to allow its constant association with the cell membrane. Thus, local activation of ECT-2, and with that RhoA, might instead require the local cortical recruitment of centralspindlin. This model is further supported by the observation that cortical recruitment of CYK-4 induces ECT-2-dependent contractility in the one-cell *C. elegans* embryo (**Chapter 5**). How the local exclusion of ECT-2 from the posterior cortex during polarization is achieved remains an open question. However, given the current data, it is unlikely that the role of ECT-2 in regulating cytokinesis involves a similar mechanism.

The exact contributions of CYK-4, and especially its GAP domain, to cytokinesis have only recently started to unfold. Interestingly, Prc1 facilitates phosphorylation of Cyk4 by Plk1 (Wolfe et al., 2009). This interaction might help to explain the additive effects of *spd-1* disruption that we observed in **chapter 5**. In addition, the existence of an active feedback mechanism between centralspindlin and activated RhoA might contribute to proper ingression of the cytokinetic furrow. Active RhoA could be a target for binding by the CYK-4 GAP domain, which would help to further enhance local contractility during furrow ingression (Lewellyn et al., 2010; Zhang et al., 2015). In this manner, attenuated cortical enrichment of centralspindlin due to a disruption of *let-99* function could result in incomplete furrow ingression. This idea is further supported by the observation that inactivation of *zen-4* or *cyk-4* during the late phases of cytokinesis results in failure to complete cytokinesis in the one-cell embryo (Severson et al. 2000; Davies et al. 2014).

Ultimately, how can the roles of centralspindlin, LET-99 and the LIN-5 complex be

integrated into a coherent model for cytokinesis in the *C. elegans* one-cell embryo? Based on the current data, we propose that the LIN-5 complex and LET-99 modulate the cortical localization of centralspindlin to focus contractility at the equatorial cortex. Because of the large size of the *C. elegans* one-cell embryo, a midzone-based diffusion mechanism might not result in very focused equatorial accumulation of centralspindlin. Specific tracking of equatorial MT plus ends allows centralspindlin to precisely localize at the site of furrow formation in *X. laevis* embryos and *D. melanogaster* S2 cells (Vale et al., 2009; Breznau et al., 2017; Verma and Maresca, 2019). However, we did not observe such localization for endogenous ZEN-4 nor CYK-4, which is in accordance with weak conservation of the CYK4 SxIP motif (Breznau et al., 2017). Thus, in *C. elegans* embryos, the reciprocal localization of LET-99 and the LIN-5 complex may communicate the position of the spindle to locally activate RhoA. We propose that both the midzone and astral cytokinesis signals convene at the local recruitment of centralspindlin and the subsequent activation of ECT-2. This model is supported by the observation that in sea urchin or sand dollar embryos, Cyk4 and Ect2 localize to aster-induced furrows (Su and von Dassow, 2014). It will be interesting to further explore the role of astral MTs in modulating contractility. For example, do astral MTs modulate the contractility induced by artificial targeting of CYK-4 to the cortex? Optogenetically localized ECT-2 in cultured mammalian cells induces contractility in both interphase and mitosis regardless of the presence of astral MTs (Wagner and Glotzer, 2016). In contrast, inactivation of *par-5*, or specifically blocking the regulation of ZEN-4 by PAR-5, results in ectopic furrowing at cortical sites that are not contacted by astral MTs (Basant et al., 2015). These observations indicate that the ectopic accumulation of centralspindlin, or the result of its downstream signaling, can be modulated by astral MTs in *C. elegans*. Careful comparison between model organisms will be needed to reveal the common mechanisms of cytokinesis regulation that apply broadly to the animal kingdom.

Improved tools for studying cellular and developmental processes

In addition to the increased understanding of the biological mechanisms at work during cell division, the experiments presented in this thesis include important new research tools. First and foremost, the use of CRISPR/Cas9 has been of vital importance for almost every experiment presented in this thesis. We almost exclusively used endogenous tagging strategies to study the functions of genes of interest. In **chapter 2**, we presented a novel balancing strategy that allows for the study of endogenous loss-of-function alleles in an otherwise unperturbed, in vivo setting. Furthermore, our studies of endogenously tagged protein localization have played a central role in increasing our understanding of how these proteins contribute to proper cell division. CRISPR/Cas9 allows us to modify the genetic code at nearly any desired position in the genome. However, the integration of non-optimized exogenous sequences might nonetheless result in severely altered expression levels. For example, in preparation of the experiments presented in **chapter 4**,

we observed that the use of somatic codon-optimization (Redemann et al., 2011) resulted in full germline silencing of the essential *lin-5* gene following endogenous integration of *epdz::mcherry::lin-5*. Germline silencing has long been a notorious roadblock in *C. elegans* research focusing on the germline or early embryonic development (Merritt and Seydoux, 2010). As a workaround, we studied the dominant codon usage of germline-expressed genes to develop a novel, germline-specific codon optimization index algorithm. Such optimization proved essential of our optogenetic manipulation strategies, in conjunction with the use of introns that incorporate periodic A_n/T_n-clusters (PATCs; Frokjaer-Jensen et al., 2016). This strategy allowed us to control the spatiotemporal distribution of proteins of interest in the early embryo, which we extensively applied to study both spindle positioning and cytokinesis in **chapters 4 and 5**. The LOV–ePDZ system has previously been applied by others to control protein localization in vitro (Strickland et al., 2012; van Bergeijk et al., 2015; Wagner and Glotzer, 2016), and in vivo (Harterink et al., 2016; Johnson et al., 2017). However, we were the first to control the localization of endogenous proteins in the early *C. elegans* embryo. Both *epdz* and *lov* domains can be expressed genetically, without the need for an exogenous cofactor. Interaction dynamics are rapid and reversible and can be locally controlled. Thus, LOV–ePDZ presents a number of clear advantages over other protein heterodimerization strategies, such as the rapamycin-induced FKBP–FRB system (Rivera et al., 1996).

Light-controlled protein localization experiments are rapidly becoming part of the already extensive toolkit used to study in vivo processes. Accordingly, other light-inducible systems have been developed in addition to LOV–ePDZ to meet the needs of different experimental setups. For example, iLIDs (improved light inducible dimers; Guntas et al., 2015) offer an alternative to the LOV–ePDZ system. iLIDs are also based on uncaging of the *Avena sativa* (common oat) light-oxygen-voltage 2 (LOV2) domain. Contrary to LOV–ePDZ, iLID applies the interaction of a bacterial SsrA peptide conjugated to LOV to interact with SsrB in the presence of blue light. Conveniently, re-engineering of the iLID system has brought about variants with different binding affinities to suit different types of experiments (Zimmerman et al., 2016). iLIDs allow for N-terminal conjugation of LOV–SsrA, contrary to the LOV–ePDZ system in which the LOV peptide has to be present at the C-terminus (Hallett et al., 2016). In addition, the iLID system does not make use of a PDZ domain, the inclusion of which might lead to unwarranted cross-talk with endogenous proteins (Guntas et al., 2015). In a study comparable to the work presented in **chapter 4**, iLIDs were used to control the cortical localization of NuMA, dynein, and dynactin subunits in mammalian cells. Interestingly, recruitment of these proteins to the cortex requires minutes of illumination, while the activation of iLIDs was reported to occur within seconds (Guntas et al., 2015; Okumura et al., 2018). Activation of the LOV–ePDZ system in the one-cell *C. elegans* embryo is significantly more rapid (**Chapter 4**). It will be interesting to further explore such differences in dynamics across experimental systems. As an alternative approach, systems that are not based on LOV have been applied to control

subcellular protein localization. For example, *Arabidopsis thaliana* Cry2–CIB1 associates rapidly in the presence of blue light, but dissociates on a ~10-minute timescale and is prone to clustering (Kennedy et al., 2010; Bugaj et al., 2013). In addition, *A. thaliana* PhyB/PIF dimerizes by exposure to red light, and can be actively dissociated by exposure to far-red light. However, its activation requires a cofactor that is not endogenously expressed in animal cells (Levskaya et al., 2009). In summary, we conclude that LOV–ePDZ is currently the most suitable protein heterodimerization system for use in the *C. elegans* one-cell embryo.

Concluding remarks

Light-controlled protein heterodimerization systems offer great potential for both in vitro and in vivo studies. Various applications have been developed in addition to those used and discussed in this thesis. These include, but are certainly not limited to the spatiotemporal control of cell polarization (Strickland et al., 2012), subcellular transport (van Bergeijk et al., 2015; Ballister et al., 2015), gene expression and epigenetics (Kim et al., 2019; Konermann et al., 2013), protein dissociation (Wang et al., 2016), MT dynamics (van Haren et al., 2018), cytoskeletal cross-linking (Adikes et al., 2018), integrin-matrix interactions (Baaske et al., 2019), and knock-sideways experiments (Milas et al., 2018). Despite such extensive successes, further optimization of the available light-inducible systems will be required to apply these tools in different experimental systems (Johnson and Toettcher, 2018). In our initial experiments, a combination of rapid lateral diffusion and light scattering severely limited the accuracy of local protein recruitment (**Chapter 4**). However, optimization of the PH::LOV anchor by addition of tandem membrane interaction domains greatly improved the precision of such experiments (van Geel et al., 2018; **Chapter 5**). In addition, we have developed ‘dark’ versions of this LOV anchor through genetic excision of *gfp*. This modified anchor allows for the simultaneous recruitment of a red fluorophore-tagged endogenous protein while simultaneously observing the distribution of a green fluorophore-tagged protein of interest (**Chapter 5**). Such tools should prove to be helpful for further research not only in the early *C. elegans* embryo, but also in somatic tissues of the worm, and by extrapolation, other model organisms.

The work presented in this thesis was performed in the context of the ERC synergy MODELCELL project. This goal of this project is to further our understanding of how the living cell is organized, with a strong emphasis on the dynamic cytoskeleton. The in vitro reconstitution of biological processes with the use of minimal components will be essential to further develop our understanding of the core machineries that drive cellular dynamics. To come to such understanding, the integration of in vitro and in vivo data from biological, chemical and physical perspectives is vital. All experiments in this thesis were performed with a ‘top-down’ rationale; we start with a functional single cell that is the basis for the development of a living organism. The inner workings of these cells can be studied through the perturbation or alteration of endogenous gene expression, protein function,

and localization combined with high resolution microscopy and careful quantitative analysis. Simultaneously, efforts have been made to reconstitute these processes with minimal components in vitro using a 'bottom-up' approach (Vleugel et al., 2016). For example, studying the dynamics of reconstituted spindle-like structures within emulsion droplets complements our in vivo studies of spindle positioning. Ultimately, such efforts might even be applied to reconstitute a functional cell, which is the aim of initiatives such as the Building a Synthetic Cell (BaSyC) consortium (Exterkate and Driessen, 2019). The collection of high-quality data from in vivo systems will be essential in achieving such goals. The quantitative description of endogenous protein function and dynamics require their efficient manipulation in the context of the living cell. With the combined developments of CRISPR/Cas9 genome editing, optimized germline knockout and light-controlled protein heterodimerization systems, we have come one step closer to achieving such fundamental efforts.

Appendix 1. **LET-99 inhibits cortical pulling forces in a mid-posterior band during early anaphase spindle migration in the one-cell *C. elegans* embryo**. One-cell embryos expressing the PH::GFP::LOV membrane marker were followed during a 10 second time interval starting from the initiation of anaphase. GFP fluorescence was continuously recorded in a subcortical plane of the embryo by spinning disc confocal microscopy with an exposure time of 250 ms. The total number of membrane invaginations that occurred at the anterior (0-49% embryo length) and posterior (50-100% embryo length) cortices during the acquisition is plotted for untreated control (**a**) and *nmy-2(RNAi)* embryos (**b**). Partial RNAi of *nmy-2* was performed by feeding of L4 hermaphrodites for 24 hours. This treatment allowed one-cell embryos to polarize and asymmetrically position the mitotic spindle, while simultaneously weakening cortical rigidity through perturbation of the actomyosin network. Microscopy recording of one-cell embryos and the quantification of the cortical distribution of force generation events through counting of membrane invaginations were performed as described in the materials and methods section of **chapter 4**. Spinning disc confocal microscopy images of untreated control (**c**) and *let-99(RNAi)* embryos (**d**) are shown. RNAi of *let-99* was performed by dsRNA injection of young adult hermaphrodites 48 hours prior to imaging experiments. Graphs indicate the cortical distribution of membrane invaginations for both conditions, shown as means + SEM. Statistics performed by unpaired Welch's Student's *t* tests. ns, not significant. N=5-7 embryos per condition. Scale bar: 5 µm.

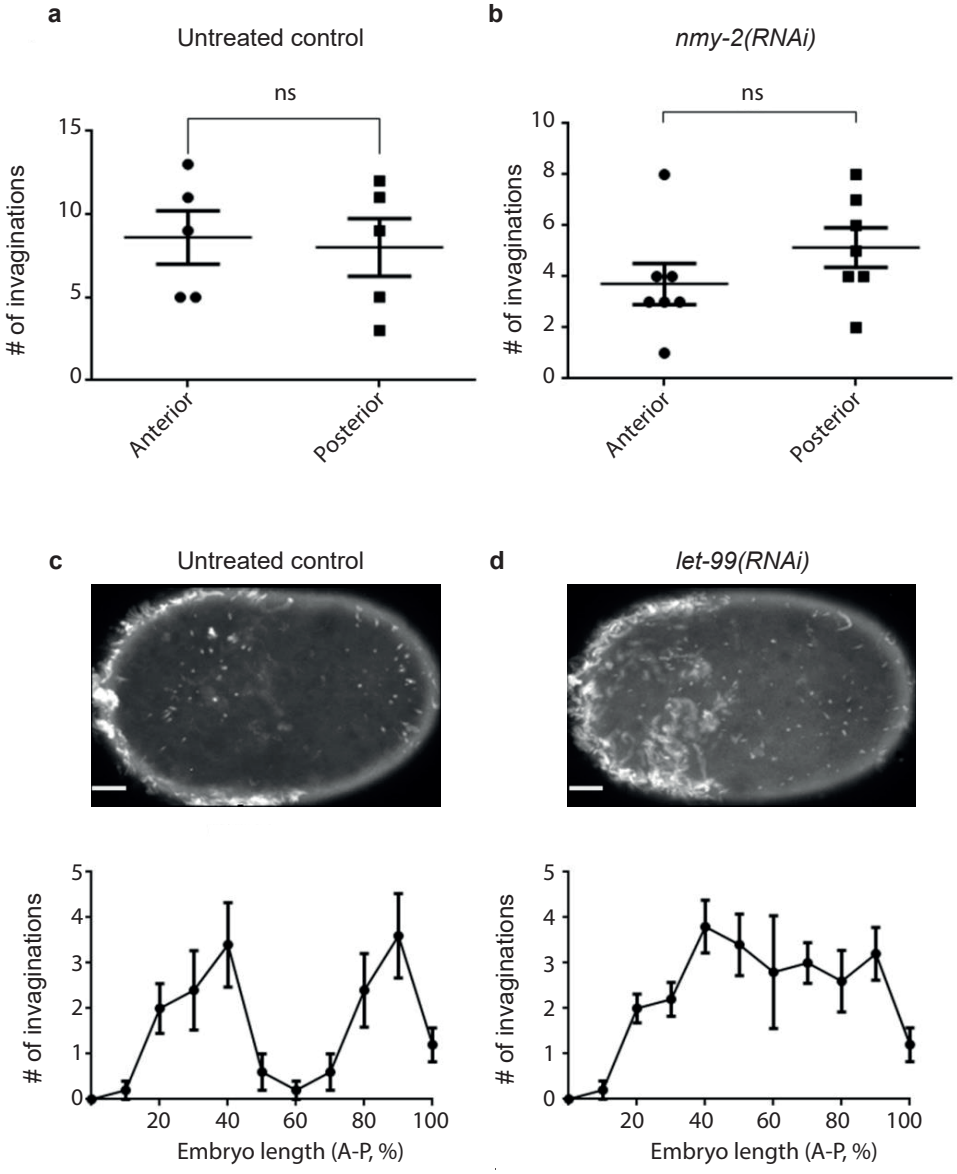
a
Untreated control
ns
# of invaginations
15
10
5
0
Anterior
Posterior
b
nmy-2(RNAi)
ns
# of invaginations
10
8
6
4
2
0
Anterior
Posterior
c
Untreated control
# of invaginations
5
4
3
2
1
0
20
40
60
80
100
Embryo length (A-P, %)
d
let-99(RNAi)
# of invaginations
5
4
3
2
1
0
20
40
60
80
100
Embryo length (A-P, %)

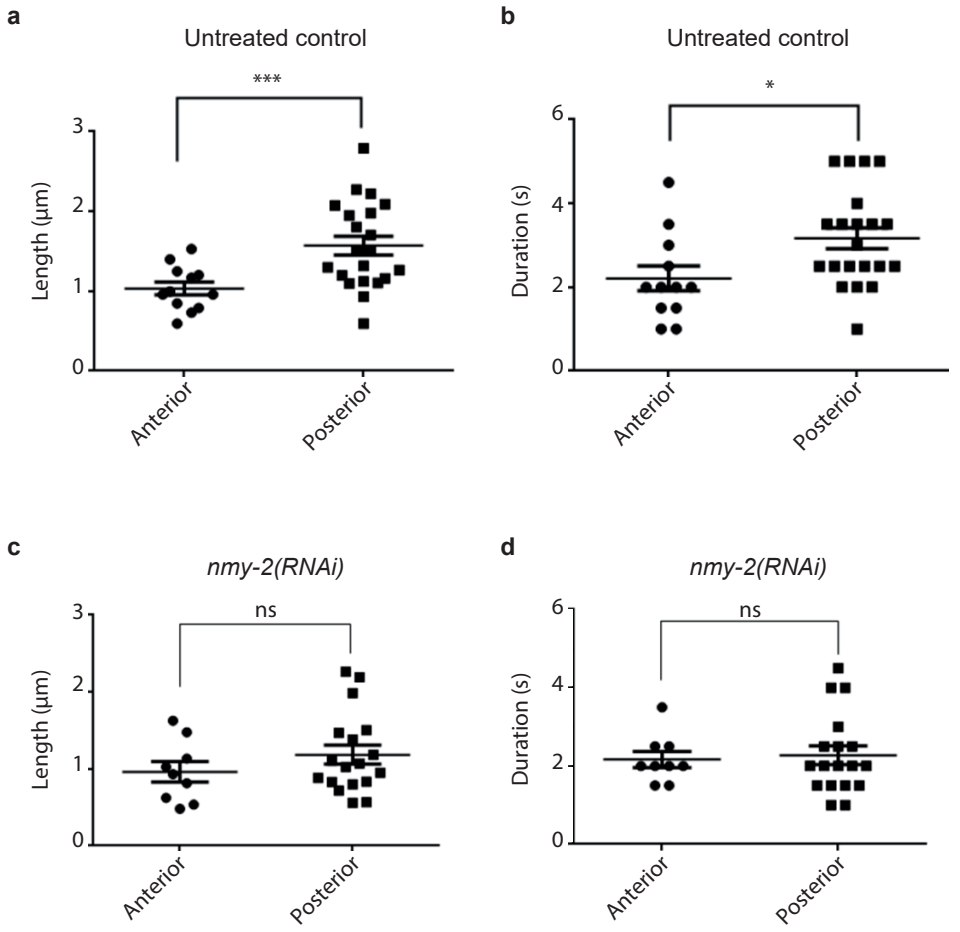

Appendix 2. **The asymmetric distribution of membrane invagination length and duration depend on the cortical actomyosin cytoskeleton in the one-cell** *C. elegans* embryo. One-cell embryos expressing the PH::GFP::LOV membrane marker were followed during a 20 second time interval starting from the initiation of anaphase. GFP fluorescence was continuously recorded in the DNA plane of the embryo by spinning disc confocal microscopy with an exposure time of 250 ms. The duration of invaginations in seconds was determined by multiplication of the number of frames on which a single invagination was observed with the exposure time of the acquisition. This protocol was repeated for every invagination occurring in the anterior (0-49% embryo length) and posterior (50-100% embryo length) regions of five embryos. Length was measured in µm during maximal extension of each invagination. Invagination length (**a**, **c**) and duration (**b**, **d**) are plotted for untreated control (**a**, **b**) and *nmy-2(RNAi)* embryos (**c**, **d**) as means + SEM. Partial RNAi of *nmy-2* was performed by feeding of L4 hermaphrodites for 24 hours. This treatment allowed one-cell embryos to polarize and asymmetrically position the mitotic spindle, while simultaneously weakening cortical rigidity through perturbation of the actomyosin network. Microscopy recording of one-cell embryos was performed as described in the materials and methods section of **chapter 4**. Statistics performed by unpaired Welch's Student's *t* tests. ns, not significant; * P<0.05; *** P<0.001. N=5 embryos per condition.

Appendix

Reference list

Adams, R.R., Tavares, A.A.M., Salzberg, A., Bellen, H.J. and Glover, D.M. (1998). Pavarotti encodes a kinesin-like protein required to organize the central spindle and contractile ring for cytokinesis. Genes Dev. 12, 1483–1494.

Adikes, R.C., Hallett, R.A., Saway, B.F., Kuhlman, B. and Slep, K.C. (2018). Control of microtubule dynamics using an optogenetic microtubule plus end-F-actin cross-linker. J. Cell Biol. 217, 779–793.

Adriaans, I.E., Basant, A., Ponsioen, B., Glotzer, M. and Lens, S.M.A. (2019). PLK1 plays dual roles in centralspindlin regulation during cytokinesis. J. Cell Biol. 218, 1250–1264.

Afshar, K., Willard, F.S., Colombo, K., Johnston, C.A., Mccudden, C.R., Siderovski, D.P., Go, P., Hill, C. and Carolina, N. (2004). RIC-8 Is Required for GPR-1/2-Dependent Gα Function during Asymmetric Division of *C. elegans* Embryos. Cell 119, 219–230.

Afshar, K., Willard, F.S., Colombo, K., Siderovski, D.P. and Gönczy, P. (2005). Cortical localization of the Gα protein GPA-16 requires RIC-8 function during *C. elegans* asymmetric cell division. Development 132, 4449–4459.

Afshar, K., Werner, M.E., Tse, Y.C., Glotzer, M. and Gönczy, P. (2010). Regulation of cortical contractility and spindle positioning by the protein phosphatase 6 PPH-6 in one-cell stage *C. elegans* embryos. Development 137, 237–247.

Aist, J.R., Bayles, C.J., Tao, W. and Berns, M.W. (1991). Direct experimental evidence for the existence, structural basis and function of astral forces during anaphase B in vivo. J. Cell Sci. 100, 279–288.

Akhmanova, A. and Steinmetz, M.O. (2015). Control of microtubule organization and dynamics: two ends in the limelight. Nat. Rev. Mol. Cell Biol. 16, 711–726.

Akhmanova, A. and Steinmetz, M.O. (2019). Microtubule minus-end regulation at a glance. J. Cell Sci. 132, 1–7.

Alberts, B., Johnson, A., Lewis, J., Raff, M., Roberts, K., Walter, P. (2008). Molecular biology of the cell (New York, NY: Garland Science).

Albertson, D.G., Sulston, J.E. and White, J.G. (1978). Cell cycling and DNA replication in a mutant blocked in cell division in the nematode *Caenorhabditis elegans*. Dev. Biol. 63, 165–178.

Alsop, G.B. and Zhang, D. (2003). Microtubules are the only structural constituent of the spindle apparatus required for induction of cell cleavage. J. Cell Biol. 162, 383–390.

Ananthanarayanan, V., M. Schattat, S.K. Vogel, A. Krull, N. Pavin and I.M. Tolić-Nørrelykke (2013). Dynein motion switches from diffusive to directed upon cortical anchoring. Cell 153, 1526-1536.

Ananthanarayanan, V. (2016). Activation of the motor protein upon attachment: Anchors weigh in on cytoplasmic dynein regulation. BioEssays 38, 514–525.

Arnal, I. and Wade, R.H. (1995). How does taxol stabilize microtubules? Curr. Biol. 5, 900–908.

Arribere, J.A., Bell, R.T., Fu, B.X.H., Artiles, K.L., Hartman, P.S. and Fire, A.Z. (2014). Efficient marker-free recovery of custom genetic modifications with CRISPR/Cas9 in *Caenorhabditis elegans*. Genetics 198, 837–846.

Artiles, K.L., Fire, A.Z. and Frøkjær-Jensen, C. (2019). Assessment and Maintenance of Unigametic Germline Inheritance for *C. elegans*. Dev. Cell 48, 827-839.

Aumeier, C., Schaedel, L., Gaillard, J., John, K., Blanchoin, L. and Théry, M. (2016). Self-repair promotes microtubule rescue. Nat. Cell Biol. 18, 1054–1064.

Baaske, J., Mühlhäuser, W.W.D., Yousefi, O.S., Zanner, S., Radziwill, G., Hörner, M., Schamel, W.W.A. and Weber, W. (2019). Optogenetic control of integrin-matrix interaction. Commun. Biol. 2, 1–8.

Bacaj, T. and Shaham, S. (2007). Temporal control of cell-specific transgene expression in *Caenorhabditis elegans*. Genetics 176, 2651–2655.

Bai, X.-C., McMullan, G. and Scheres, S.H.W. (2015). How cryo-EM is revolutionizing structural biology. Trends Biochem. Sci. 40, 49–57.

Baines, A.J., Lu, H.C. and Bennett, P.M. (2014). The Protein 4.1 family: Hub proteins in animals for organizing membrane proteins. Biochim. Biophys. Acta. 1838, 605–619.

Ballister, E.R., Ayloo, S., Chenoweth, D.M., Lampson, M.A. and Holzbaur, E.L.F. (2015). Optogenetic control of organelle transport using a photocaged chemical inducer of dimerization. Curr. Biol. 25, R407–R408.

Ban, R., Irino, Y., Fukami, K. and Tanaka, H. (2004). Human Mitotic Spindle-associated Protein PRC1 Inhibits MgcRacGAP Activity toward Cdc42 during the Metaphase. J. Biol. Chem. 279, 16394–16402.

Ban, R., Matsuzaki, H., Akashi, T., Sakashita, G., Taniguchi, H., Park, S.Y., Tanaka, H., Furukawa, K. and Urano., T. (2009). Mitotic regulation of the stability of microtubule plus-end tracking protein EB3 by ubiquitin ligase SIAH-1 and aurora mitotic kinases. J. Biol. Chem. 284, 28367–28381.

Baruni, J.K., Munro, E.M. and von Dassow, G. (2008). Cytokinetic furrowing in toroidal, binucleate and anucleate cells in *C. elegans* embryos. J. Cell Sci. 121, 306–316.

Basant, A. and Glotzer, M. (2017). A GAP that Divides. F1000Research 6, 1–10.

Basant, A. and Glotzer, M. (2018). Spatiotemporal Regulation of RhoA during Cytokinesis. Curr. Biol. 28, R570–R580.

Basant, A., Lekomtsev, S., Tse, Y.C., Zhang, D., Longhini, K.M., Petronczki, M. and Glotzer, M. (2015). Aurora B kinase promotes cytokinesis by inducing centralspindlin oligomers that associate with the plasma membrane. Dev. Cell 33, 204–215.

Bastos, R.N., Penate, X., Bates, M., Hammond, D. and Barr, F. A. (2012). CYK4 inhibits Rac1-dependent PAK1 and ARHGEF7 effector pathways during cytokinesis. J. Cell Biol. 198, 865–880.

Bei, Y., Hogan, J., Berkowitz, L. a., Soto, M., Rocheleau, C.E., Pang, K.M., Collins, J., Mello, C.C. (2002). SRC-1 and Wnt signaling act together to specify endoderm and to control cleavage orientation in early *C. elegans* embryos. Dev. Cell 3, 113–125.

Bellaïche, Y., Radovic, A., Woods, D.F., Hough, C.D., Parmentier, M.L., O'Kane, C.J., Bryant, P.J. and Schweisguth, F. (2001). The Partner of Inscuteable/Discs-large complex is required to establish planar polarity during asymmetric cell division in *Drosophila*. Cell 106, 355–366.

Bement, W.M., Benink, H. a and von Dassow, G. (2005). A microtubule-dependent zone of active RhoA during cleavage plane specification. J. Cell Biol. 170, 91–101.

Bement, W.M., Miller, A.L. and Von Dassow, G. (2006). Rho GTPase activity zones and transient contractile arrays. BioEssays 28, 983–993.

Bement, W.M., Leda, M., Moe, A.M., Kita, A.M., Larson, M.E., Golding, A.E., Pfeuti, C., Su, K.C., Miller, A.L., Goryachev, A.B. and von Dassow, G. (2015). Activator-inhibitor coupling between Rho signalling and actin assembly makes the cell cortex an excitable medium. Nat. Cell Biol. 17, 1471–1483.

Bendris, N., Lemmers, B. and Blanchard, J.M. (2015). Cell cycle, cytoskeleton dynamics and beyond: the many functions of cyclins and CDK inhibitors. Cell Cycle 14, 1786–1798.

Benink, H.A. and Bement, W.M. (2005). Concentric zones of active RhoA and Cdc42 around single cell wounds. J. Cell Biol. 168, 429–439.

Berends, C.W.H., Muñoz, J., Portegijs, V., Schmidt, R., Grigoriev, I., Boxem, M., Akhmanova, A., Heck, A.J.R. and van den Heuvel, S. (2013). F-actin asymmetry and the ER-associated TCC-1 protein contribute to stereotypic spindle movements in the *C. elegans* embryo. Mol. Biol. Cell 1–31.

Van Bergeijk, P., Adrian, M., Hoogenraad, C.C. and Kapitein, L.C. (2015). Optogenetic control of organelle transport and positioning. Nature 518, 111–114.

Bergmann, D.C., Lee, M., Robertson, B., Meng-Fu, B., Rose, L.S. and Wood, W.B. (2003). Embryonic handedness choice in *C. elegans* involves the Gα protein GPA-16. Development 130, 5731–5740.

Berlin, V., Styles, C.A. and Fink, G.R. (1990). BIK1, a protein required for microtubule function during mating and mitosis in *Saccharomyces cerevisiae*, colocalizes with tubulin. J. Cell Biol. 111, 2573–2586.

Bergstralh, D.T., Dawney, N.S. and St Johnston, D. (2017). Spindle orientation: A question of complex positioning. Dev. 144, 1137–1145.

Berrueta, L., Tirnauer, J.S., Schuyler, S.C., Pellman, D. and Bierer, B.E. (1999). The APC-associated protein EB1 associates with components of the dynactin complex and cytoplasmic dynein intermediate chain. Curr. Biol. 9, 425–428.

Besseling, J. and Bringmann, H. (2016). Engineered non-Mendelian inheritance of entire parental genomes in *C. elegans*. Nat. Biotechnol. 34, 982–986.

Bieling, P., Telley, I.A. and Surrey, T. (2010). A minimal midzone protein module controls formation and length of antiparallel microtubule overlaps. Cell 142, 420–432.

Bielska, E., Schuster, M., Roger, Y., Berepiki, A., Soanes, D.M., Talbot, N.J. and Steinberg, G. (2014). Hook is an adapter that coordinates kinesin-3 and dynein cargo attachment on early endosomes. J. Cell Biol. 204, 989–1007.

Bisgrove, S.R., Lee, Y.-R. J., Liu, B., Peters, N.T. and Kropf, D.L. (2008). The microtubule plus-end binding protein EB1 functions in root responses to touch and gravity signals in Arabidopsis. Plant Cell. 20, 396–410.

Bowman, S.K., Neumüller, R.A., Novatchkova, M., Du, Q. and Knoblich, J.A. (2006). The *Drosophila* NuMA Homolog Mud regulates spindle orientation in asymmetric cell division. Dev. Cell 10, 731–742.

Boxem, M., Srinivasan, D.G., van den Heuvel, S. (1999). The *Caenorhabditis elegans* gene *ncc-1* encodes a *cdc2*-related kinase required for M phase in meiotic and mitotic cell divisions, but not for S phase. Dev. Camb. Engl. 126, 2227–39.

Boxem, M., Maliga, Z., Klitgord, N., Li, N., Lemmens, I., Mana, M., de Lichtervelde, L., Mul, J.D., van de Peut, D., Devos, M., Simonis, N., Yildirim, M. a, Cokol, M., Kao, H.-L., de Smet, A.-S., Wang, H., Schlaitz, A.-L., Hao, T., Milstein, S., Fan, C., Tipsword, M., Drew, K., Galli, M., Rhrissorrakrai, K., Drechsel, D., Koller, D., Roth, F.P., Iakoucheva, L.M., Dunker, a K., Bonneau, R., Gunsalus, K.C., Hill, D.E., Piano, F., Tavernier, J., van den Heuvel, S., Hyman, A. a, Vidal, M. (2008). A protein domain-based interactome network for *C. elegans* early embryogenesis. Cell 134, 534–45.

Boyd, L., Quo, S., Levitan, D., Stinchcomb, D.T. and Kemphues, K.J. (1996). PAR-2 is asymmetrically distributed and promotes association of P granules and PAR-1 with the cortex in *C. elegans* embryos. Development 122, 3075–3084.

Brennan, I.M., Peters, U., Kapoor, T.M. and Straight, A.F. (2007). Polo-like kinase controls vertebrate spindle elongation and cytokinesis. PLoS One 2, 1–8.

Brenner, S. (1974). The genetics of *Caenorhabditis elegans*. Genetics 77, 71–94.
Breznau, E.B., Murt, M., Blasius, T.L., Verhey, K.J. and Miller, A.L. (2017). The MgcRacGAP SxIP motif tethers Centralspindlin to microtubule plus ends in *Xenopus laevis*. J. Cell Sci. 130, 1809–1821.
Bringmann, H. and Hyman, A.A. (2005). A cytokinesis furrow is positioned by two consecutive signals. Nature 436, 731–734.
Bringmann, H., Cowan, C.R., Kong, J. and Hyman, A. a (2007). LET-99, GOA-1/GPA-16 and GPR-1/2 are required for aster-positioned cytokinesis. Curr. Biol. 17, 185–191.
Buchwitz, B.J., Ahmad, K., Moore, L.L., Roth, M.B. and Henikoff, S. (1999). A histone-H3-like protein in *C. elegans* A class of porous. Nature 401, 547–548.
Budnar, S., Husain, K.B., Gomez, G.A., Naghibosadat, M., Varma, A., Verma, S., Hamilton, N.A., Morris, R.G. and Yap, A.S. (2019). Anillin Promotes Cell Contractility by Cyclic Resetting of RhoA Residence Kinetics. Dev. Cell 49, 894-906.
Bugaj, L.J., Choksi, A.T., Mesuda, C.K., Kane, R.S. and Schaffer, D. V. (2013). Optogenetic protein clustering and signaling activation in mammalian cells. Nat. Methods 10, 249–252.
Burakov, A., Nadezhdina, E., Slepchenko, B. and Rodionov, V. (2003). Centrosome positioning in interphase cells. J. Cell Biol. 162, 963–969.
Burkard, M.E., Randall, C.L., Larochelle, S., Zhang, C., Shokat, K.M., Fisher, R.P. and Jallepalli, P. V. (2007). Chemical genetics reveals the requirement for Polo-like kinase 1 activity in positioning RhoA and triggering cytokinesis in human cells. Proc. Natl. Acad. Sci. U.S.A. 104, 4383–4388.
Burkard, M.E., Maciejowski, J., Rodriguez-Bravo, V., Repka, M., Lowery, D.M., Clauser, K.R., Zhang, C., Shokat, K.M., Carr, S.A., Yaffe, M.B. and Jallepalli, P.V. (2009). Plk1 self-organization and priming phosphorylation of HsCYK-4 at the spindle midzone regulate the onset of division in human cells. PLoS Biol. 7, 1-16.
Can, S., Lacey, S., Gur, M., Carter, A.P. and Yildiz, A. (2019). Directionality of dynein is controlled by the angle and length of its stalk. Nature 566, 407–410.
Canman, J., Lewellyn, L., Laband, K., Smerdon, S.J., Desai, A., Bowerman, B. and Oegema, K. (2008). Inhibition of Rac by the GAP Activity of Centralspindlin Is Essential for Cytokinesis. Science 322, 1543–1546.
Canman, J.C., Hoffman, D.B. and Salmon, E.D. (2000). The role of pre- and post-anaphase microtubules in the cytokinesis phase of the cell cycle. Curr. Biol. 10, 611–614.
Canman, J.C., Cameron, L.A., Maddox, P.S., Fang, G., Kapoor, T.M. and Salmon, E.D. (2003). Determining the position of the cell division plane. 424, 1074–1078.
Cao, L.G. and Wang, Y.L. (1996). Signals from the spindle midzone are required for the stimulation of cytokinesis in cultured epithelial cells. Mol. Biol. Cell 7, 225–232.
Carazo-Salas, R.E., Guarguaglini, G., Gruss, O.J., Segref, A., Karsenti, E. and Mattaj, L.W. (1999). Generation of GTP-bound ran by RCC1 is required for chromatin-induced mitotic spindle formation. Nature 400, 178–181.
Carazo-Salas, R.E., Gruss, O.J., Mattaj, I.W. and Karsenti, E. (2001). Ran-GTP coordinates regulation of microtubule nucleation and dynamics during mitotic-spindle assembly. Nat. Cell Biol. 3, 228–234.
Carminati, J.L. and Stearns, T. (1997). Microtubules orient the mitotic spindle in yeast through dynein- dependent interactions with the cell cortex. J. Cell Biol. 138, 629–641.
Carvalho, A., Olson, S.K., Gutierrez, E., Zhang, K., Noble, L.B., Zanin, E., Desai, A., Groisman, A. and Oegema, K. (2011). Acute drug treatment in the early *C. elegans* embryo. PLoS One. 6, e24656.
Caussinus, E. and Gonzalez, C. (2005). Induction of tumor growth by altered stem-cell asymmetric division in *Drosophila melanogaster*. Nat. Genet. 37, 1125–1129.
Chalamalasetty, R.B., Hümmer, S., Nigg, E.A. and Silljé, H.H.W. (2006). Influence of human Ect2 depletion and overexpression on cleavage furrow formation and abscission. J. Cell Sci. 119, 3008–3019.
Chapa-y-Lazo, B., Hamanaka, M., Wray, A., K, B.M. and Mishima, M. (2018). Polar relaxation by dynein-mediated removal of cortical myosin II. bioRxiv.
Chen, C., Fenk, L. a, de Bono, M. (2013). Efficient genome editing in *Caenorhabditis elegans* by CRISPR-targeted homologous recombination. Nucleic Acids Res. 41, e193.
Chen, B., Sun, Y., Niu, J., Jarugumilli, G.K. and Wu, X. (2018). Protein lipidation in cell signaling and diseases: function, regulation and therapeutic opportunities. Cell Chem. Biol. 25, 817–831.
Chen, D., Wilkinson, C.R.M., Watt, S., Penkett, C.J., Toone, W.M., Jones, N. and Bähler, J. (2008a). mDia2 induces the actin scaffold for the contractile ring and stabilizes its position during cytokinesis in NIH 3T3 cells. Mol. Biol. Cell 19, 308–317.
Chen, W., Foss, M., Tseng, K.-F. and Zhang, D. (2008b). Redundant mechanisms recruit actin into the contractile ring in silkworm spermatocytes. PLoS Biol. 6, e209.
Cho, C., Reck-Peterson, S.L. and Vale, R.D. (2008). Regulatory ATPase sites of cytoplasmic dynein affect processivity and force generation. J. Biol. Chem. 283, 25839–25845.
Cockell, M.M., Baumer, K. and Gönczy, P. (2004). *lis-1* is required for dynein-dependent cell division processes in *C. elegans* embryos. J. Cell Sci. 117, 4571–4582.

Colombo, K., Grill, S.W., Kimple, R.J., Willard, F.S., Siderovski, D.P. and Gönczy, P. (2003). Translation of polarity cues into asymmetric spindle positioning in *Caenorhabditis elegans* embryos. Science 300, 1957–1961.
Conduit, P.T., Wainman, A. and Raff, J.W. (2015). Centrosome function and assembly in animal cells. Nat. Rev. Mol. Cell Biol. 16, 611–624.
Cong, L., Ran, F.A., Cox, D., Lin, S., Barretto, R., Habib, N., Hsu, P.D., Wu, X., Jiang, W., Marraffini, L. A. and Zhang, F. (2013). Multiplex genome engineering using CRISPR/Cas systems. Science 339, 819–823.
Consonni, S. V., Maurice, M.M. and Bos, J.L. (2014). DEP domains: Structurally similar but functionally different. Nat. Rev. Mol. Cell Biol. 15, 357–362.
Cortes, D.B., Dawes, A., Liu, J., Nickaeen, M., Strychalski, W. and Maddox, A.S. (2018). Unite to divide – How models and biological experimentation have come together to reveal mechanisms of cytokinesis. J. Cell Sci. 131, 1-10.
Couwenbergs, C., Labbé, J.C., Goulding, M., Marty, T., Bowerman, B. and Gotta, M. (2007). Heterotrimeric G protein signaling functions with dynein to promote spindle positioning in *C. elegans*. J. Cell Biol. 179, 15–22.
Cowan, C.R. and Cowan, A.A. (2004). Centrosomes direct cell polarity independently of microtubule assembly in *C. elegans* embryos. Nature 431, 92–96.
Crowder, M.E., Flynn, J.R., McNally, K.P., Cortes, D.B., Price, K.L., Kuehnert, P. A., Panzica, M.T. andaya, A., Leary, J. A., McNally, F.J. (2015). Dynactin-dependent cortical dynein and spherical spindle shape correlate temporally with meiotic spindle rotation in *Caenorhabditis elegans*. Mol. Biol. Cell 26, 3030–3046.
Culurgioni, S., Alfieri, A., Pendolino, V., Laddomada, F. and Mapelli, M. (2011). Inscuteable and NuMA proteins bind competitively to Leu-Gly-Asn repeat-enriched protein (LGN) during asymmetric cell divisions. Pnas 108, 20998–21003.
D'Avino, P.P., Savoian, M.S. and Glover, D.M. (2004). Mutations in sticky lead to defective organization of the contractile ring during cytokinesis and are enhanced by Rho and suppressed by Rac. J. Cell Biol. 166, 61–71.
D'Avino, P.P., Takeda, T., Capalbo, L., Zhang, W., Lilley, K.S., Laue, E.D. and Glover, D.M. (2008). Interaction between Anillin and RacGAP50C connects the actomyosin contractile ring with spindle microtubules at the cell division site. J. Cell Sci. 121, 1151–1158.
Dammermann, A., Müller-Reichert, T., Pelletier, L., Habermann, B., Desai, A. and Oegema, K. (2004). Centriole assembly requires both centriolar and pericentriolar material proteins. Dev. Cell 7, 815–829.
von Dassow, G., Verbrugghe, K.J.C., Miller, A.L., Sider, J.R. and Bement, W.M. (2009). Action at a distance during cytokinesis. J. Cell Biol. 187, 831–845.
David, A.F., Roudot, P., Legant, W.R., Betzig, E., Danuser, G. and Gerlich, D.W. (2019). Augmin accumulation on long-lived microtubules drives amplification and kinetochore-directed growth. J. Cell Biol. 218, 2150–2168.
David, N.B., Martin, C.A., Segalen, M., Rosenfeld, F., Schweisguth, F. and Bellaïche, Y. (2005). *Drosophila* Ric-8 regulates Gαi cortical localization to promote Gαi-dependent planar orientation of the mitotic spindle during asymmetric cell division. Nat. Cell Biol. 7, 1083–1090.
Davies, T., Jordan, S.N., Chand, V., Sees, J.A., Laband, K., Carvalho, A.X., Shirasu-Hiza, M., Kovar, D.R., Dumont, J. and Canman, J.C. (2014). High-Resolution Temporal Analysis Reveals a Functional Timeline for the Molecular Regulation of Cytokinesis. Dev. Cell 30, 209–223.
Davies, T., Kodera, N., Kaminski Schierle, G.S., Rees, E., Erdelyi, M., Kaminski, C.F. ando, T. and Mishima, M. (2015). CYK4 promotes antiparallel microtubule bundling by optimizing MKLP1 neck conformation. PLoS Biol. 13, 1–26.
Dechant, R. and Glotzer, M. (2003). Centrosome separation and central spindle assembly act in redundant pathways that regulate microtubule density and trigger cleavage furrow formation. Dev. Cell 4, 333–344.
Delcros, J.G., Prigent, C. and Giet, R. (2006). Dynactin targets Pavarotti-KLP to the central spindle during anaphase and facilatates cytokinesis in *Drosophila* S2 cells. J. Cell Sci. 119, 4431–4441.
Desai, A., Verma, S., Mitchison, T.J. and Walczak, C.E. (1999). Kin I kinesins are microtubule-destabilizing enzymes. Cell 96, 69–78.
Devore, J.J., Conrad, G.W. and Rappaport, R. (1989). A model for astral stimulation of cytokinesis in animal cells. J. Cell Biol. 109, 2225–2232.
Diakowski, W., Grzybek, M. and Sikorski, A.F. (2006). Protein 4.1, a component of the erythrocyte membrane skeleton and its related homologue proteins forming the protein 4.1/FERM superfamily. Folia Histochem. Cytobiol. 44, 231–248.
Dickinson, D.J., Ward, J.D., Reiner, D.J. and Goldstein, B. (2013). Engineering the *Caenorhabditis elegans* genome using Cas9-triggered homologous recombination. Nat. Methods 10, 1028–1034.
Dickinson, D.J. and Goldstein, B. (2016). CRISPR-based methods for *Caenorhabditis elegans* genome engineering. Genetics 202, 885–901.
Dickinson, D.J., Schwager, F., Pintard, L., Gotta, M. and Goldstein, B. (2017). A Single-Cell Biochemistry Approach Reveals PAR Complex Dynamics during Cell Polarization. Dev. Cell 42, 416–434.
Dickinson, D.J., Pani, A.M., Heppert, J.K., Higgins, C.D. and Goldstein, B. (2015). Streamlined genome engineering with a self-excising drug selection cassette. Genetics 200, 1035–1049.

Dogterom, M., Kerssemakers, J.W.J., Romet-Lemonne, G. and Janson, M.E. (2005). Force generation by dynamic microtubules. Curr. Opin. Cell Biol. 17, 67–74.
Douglas, M.E., Davies, T., Joseph, N. and Mishima, M. (2010). Aurora B and 14-3-3 coordinately regulate clustering of centralspindlin during cytokinesis. Curr. Biol. 20, 927–933.
Draviam, V.M., Shapiro, I., Aldridge, B. and Sorger, P.K. (2006). Misorientation and reduced stretching of aligned sister kinetochores promote chromosome missegregation in EB1- or APC-depleted cells. EMBO J. 25, 2814–27.
Du, Q., Stukenberg, P.T. and Macara, I.G. (2001). A mammalian Partner of inscuteable binds NuMA and regulates mitotic spindle organization. Nat. Cell Biol. 3, 1069–1075.
Du, Q. and Macara, I.G. (2004). Mammalian Pins is a conformational switch that links NuMA to heterotrimeric G proteins. Cell 119, 503–516.
Duellberg, C., Trokter, M., Jha, R., Sen, I., Steinmetz, M. O. and Surrey, T. (2014). Reconstitution of a hierarchical +TIP interaction network controlling microtubule end tracking of dynein. Nat. Cell Biol. 16.
Ellefson, M.L. and McNally, F.J. (2011). CDK-1 inhibits meiotic spindle shortening and dynein-dependent spindle rotation in *C. elegans*. J. Cell Biol. 193, 1229–1244.
Errico, A., Deshmukh, K., Tanaka, Y., Pozniakovsky, A. and Hunt, T. (2010). Identification of substrates for cyclin dependent kinases. Adv. Enzyme Regul. 50, 375–399.
Espiritu, E.B., Krueger, L.E., Ye, A. and Rose, L.S. (2012). CLASPs function redundantly to regulate astral microtubules in the *C. elegans* embryo. Dev. Biol. 368, 242–254.
Etemad-Moghadam, B., Guo, S. and Kemphues, K.J. (1995). Asymmetrically distributed PAR-3 protein contributes to cell polarity and spindle alignment in early *C. elegans* embryos. Cell 83, 743–752.
Euteneuer, U. and Richard Mcintosh, J. (1980). Polarity of midbody and phragmoplast microtubules. J. Cell Biol. 87, 509–515.
Exterkate, M. and Driessen, A.J.M. (2019). Synthetic Minimal Cell: Self-Reproduction of the Boundary Layer. ACS Omega 4, 5293–5303.
Faulkner, N.E., Dujardin, D.L., Tai, C.Y., Vaughan, K.T., O'connell, C.B., Wang, Y.L. and Vallee, R.B. (2000). A role for the lissencephaly gene Lis1 in mitosis and cytoplasmic dynein function. Nat. Cell Biol. 2, 784–791.
Fededa, J.P., Esk, C., Mierzwa, B., Stanyte, R., Yuan, S., Zheng, H., Ebnet, K., Yan, W., Knoblich, J.A. and Gerlich, D.W. (2016). MicroRNA-34/449 controls mitotic spindle orientation during mammalian cortex development. EMBO J. 35, 2386–2398.
Ferreira, J.G., Pereira, A.J., Akhmanova, A. and Maiato, H. (2013). Aurora B spatially regulates EB3 phosphorylation to coordinate daughter cell adhesion with cytokinesis. J. Cell Biol. 201, 709–724.
Fielmich, L-E., Schmidt, R., Dickinson, D.J., Goldstein, B., Akhmanova, A. and van den Heuvel, S. (2018). Optogenetic dissection of mitotic spindle positioning in vivo. Elife 7, 1–31.
Fire, A., Xu, S., Montgomery, M.K., Kostas, S.A., Driver, S.E. and Mello, C.C. (1998). Potent and specific genetic interference by double-stranded RNA in *Caenorhabditis elegans*. Nature 391, 806–811.
Firestone, A.J., Weinger, J.S., Maldonado, M., Barlan, K., Langston, L.D., O'Donnell, M., Gelfand, V.I., Kapoor, T.M. and Chen, J.K. (2012). Small-molecule inhibitors of the AAA+ ATPase motor cytoplasmic dynein. Nature 484, 125–129.
Fisk Green, R., Lorson, M., Walhout, A.J.M., Vidal, M., van den Heuvel, S. (2004). Identification of critical domains and putative partners for the *Caenorhabditis elegans* spindle component LIN-5. Mol. Genet. Genomics MGG 271, 532–44.
Foe, V.E. and von Dassow, G. (2008). Stable and dynamic microtubules coordinately shape the myosin activation zone during cytokinetic furrow formation. J. Cell Biol. 183, 457–470.
Franck, A.D., Powers, A.F., Gestaut, D.R., Gonen, T., Davis, T.N. and Asbury, C.L. (2007). Tension applied through the Dam1 complex promotes microtubule elongation providing a direct mechanism for length control in mitosis. Nat. Cell Biol. 9, 832–837.
Frémont, S. and Echard, A. (2018). Membrane Traffic in the Late Steps of Cytokinesis. Curr. Biol. 28, R458–R470.
Frenette, P., Haines, E., Loloyan, M., Kinal, M., Pakarian, P. and Piekny, A. (2012). An anillin-Ect2 complex stabilizes central spindle microtubules at the cortex during cytokinesis. PLoS One 7, e34888.
Friedland, A.E., Tzur, Y.B., Esvelt, K.M., Colaiácovo, M.P., Church, G.M. and Calarco, J.A. (2013). Heritable genome editing in *C. elegans* via a CRISPR-Cas9 system. Nat. Methods 10, 741–743.
Frøkjær-Jensen, C., Davis, M.W., Ailion, M. and Jorgensen, E.M. (2012). Improved Mos1-mediated transgenesis in *C. elegans*. Nat. Methods 9, 117–118.
Frøkjær-Jensen, C., Jain, N., Hansen, L., Davis, M.W., Li, Y., Zhao, D., Rebora, K., Millet, J.R.R.M., Liu, X., Kim, S.K., Dupuy, S.K., Jorgensen, E.M. and Fire, A.Z. (2016). An abundant class of non-coding DNA can prevent stochastic gene silencing in the *C. elegans* germline. Cell 166, 343–357.
Gabay, M., Pinter, M.E., Wright, F.A., Chan, P.Y., Murphy, A.J., Valenzuela, D.M., Yancopoulos, G.D. and Tall, G.G. (2011). Ric-8 proteins are molecular chaperones that direct nascent G protein α subunit membrane association. Sci. Signal. 4, 1–14.

Gaillard, J., Neumann, E., van Damme, D., Stoppin-Mellet, V., Ebel, C., Barbier, E., Geelen, D. and Vantard, M. (2008). Two microtubule-associated proteins of arabidopsis MAP65s promote antiparallel microtubule bundling. Mol. Biol. Cell 19, 4523–4544.
Galli, M., Bodor, D., Etemad, B., Muñoz, J., Heck, A. and van den Heuvel, S. (2011b). LIN-5 is required for the aster-derived cytokinesis signal. In Determination of the cell cleavage plane by the LIN-5 complex, 86-100.
Galli, M. and van den Heuvel, S. (2008). Determination of the cleavage plane in early *C. elegans* embryos. Annu. Rev. Genet. 42, 389–411.
Galli, M., Muñoz, J., Portegijs, V., Boxem, M., Grill, S.W., Heck, A.J.R. and van den Heuvel, S. (2011). aPKC phosphorylates NuMA-related LIN-5 to position the mitotic spindle during asymmetric division. Nat. Cell Biol. 13, 1132–1138.
Gallini, S., Carminati, M., De Mattia, F., Pirovano, L., Martini, E., Oldani, A., Asteriti, I.A., Guarguaglini, G. and Mapelli, M. (2016). NuMA phosphorylation by aurora-a orchestrates spindle orientation. Curr. Biol. 26, 458–469.
Gama, J.B., Pereira, C., Simões, P.A., Celestino, R., Reis, R.M., Barbosa, D.J., Pires, H.R., Carvalho, C., Amorim, J., Carvalho, A.X., Cheerambathur, D.K. and Gassmann, R. (2017). Molecular mechanism of dynein recruitment to kinetochores by the Rod-Zw10-Zwilch complex and Spindly. J. Cell Biol. 216, 943–960.
Garzon-Coral, C., Fantana, H.A. and Howard, J. (2016). A force-generating machinery maintains the spindle at the cell center during mitosis. Science 352, 1124–1127.
Gassmann, R., Essex, A., Hu, J.-S., Maddox, P.S., Motegi, F., Sugimoto, A., O'Rourke, S.M., Bowerman, B., McLeod, I., Yates, J.R., Oegema, K., Cheeseman, I.M. and Desai, A. (2008). A new mechanism controlling kinetochore-microtubule interactions revealed by comparison of two dynein-targeting components: SPDL-1 and the Rod/Zwilch/Zw10 complex. Genes Dev. 22, 2385–99.
Van Geel, O., Hartsuiker, R. and Gadella, T.W.J. (2018). Increasing spatial resolution of photoregulated GTPases through immobilized peripheral membrane proteins. Small GTPases, 1–10.
Gehmlich, K., Haren, L., Merdes, A. (2004). Cyclin B degradation leads to NuMA release from dynein/dynactin and from spindle poles. EMBO Rep. 5, 97–103.
Gennerich, A., Carter, A.P., Reck-Peterson, S.L. and Vale, R.D. (2007). Force-induced bidirectional stepping of cytoplasmic dynein. Cell 131, 952–965.
Gerstein, M.B., Rozowsky, J., Yan, K.K., Wang, D., Cheng, C., Brown, J.B., Davis, C.A., Hillier, L., Sisu, C., Li, J.J., et al. (2014). Comparative analysis of the transcriptome across distant species. Nature 512, 445–448.
Giet, R. and Glover, D.M. (2001). *Drosophila* aurora B kinase is required for histone H3 phosphorylation and condensin recruitment during chromosome condensation and to organize the central spindle during cytokinesis. J. Cell Biol. 152, 669–681.
Goldstein, B. and Hird, S.N. (1996). Specification of the anteroposterior axis in *Caenorhabditis elegans*. Development 122, 1467–1474.
Goldstein, B. and Macara, I.G. (2007). The PAR proteins: fundamental players in animal cell polarization. Dev. Cell 13, 609–622.
Goldstein, A.Y.N., Jan, Y.N. and Luo, L. (2005). Function and regulation of Tumbleweed (RacGAP50C) in neuroblast proliferation and neuronal morphogenesis. Proc. Natl. Acad. Sci. U.S.A. 102, 3834–3839.
Gönczy, P., Pichler, S., Kirkham, M. and Hyman, A.A. (1999). Cytoplasmic dynein is required for distinct aspects of MTOC positioning, including centrosome separation, in the one cell stage *Caenorhabditis elegans* embryo. J. Cell Biol. 147, 135–150.
Gönczy, P., Echeverri, C., Oegema, K., Coulson, A, Jones, S.J., Copley, R.R., Duperon, J., Oegema, J., Brehm, M., Cassin, E., Hannak, E., Kirkham, M., Pichler, S., Flohrs, K., Goessen, A., Leidel, S., Alleaume, A.-M., Martin, C., Özlü, N., Bork, P. and Hyman, A.A. (2000). Functional genomic analysis of cell division in *C. elegans* using RNAi of genes on chromosome III. Nature 408, 331–336.
Gönczy, P. (2008). Mechanisms of asymmetric cell division: flies and worms pave the way. Nat. Rev. Mol. Cell Biol. 9, 355–66.
Goode, B.L. and Eck, M.J. (2007). Mechanism and Function of Formins in the Control of Actin Assembly. Annu. Rev. Biochem. 76, 593–627.
Gotta, M. and Ahringer, J. (2001). Distinct roles for Galpha and Gbetagamma in regulating spindle position and orientation in *Caenorhabditis elegans* embryos. Nat. Cell Biol. 3, 297–300.
Gotta, M., Dong, Y., Peterson, Y.K., Lanier, S.M. and Ahringer, J. (2003). Asymmetrically Distributed *C. elegans* Homologs of AGS3 / PINS Control Spindle Position in the Early Embryo. Curr. Biol. 13, 1029–1037.
Goulding, M.B., Canman, J.C., Senning, E.N., Marcus, A.H. and Bowerman, B. (2007). Control of nuclear centration in the *C. elegans* zygote by receptor-independent Galpha signaling and myosin II. J. Cell Biol. 178, 1177–1191.
Green, R.A., Wollman, R. and Kaplan, K.B. (2005). APC and EB1 function together in mitosis to regulate spindle dynamics and chromosome alignment. Mol. Biol. Cell. 16, 4609–4622.
Green, R. A, Paluch, E. and Oegema, K. (2012). Cytokinesis in animal cells. Annu. Rev. Cell Dev. Biol. 28, 29–58.
Gregory, S.L., Ebrahimi, S., Milverton, J., Jones, W.M., Bejsovec, A. and Saint, R. (2008). Cell division requires a direct link between microtubule-bound RacGAP and Anillin in the contractile ring. Curr. Biol. 18, 25–29.

Grill, S.W. and Hyman, A.A. (2005). Spindle positioning by cortical pulling forces. Dev. Cell 8, 461–465.
Grill, S.W., Gönczy, P., Stelzer, E.H. and Hyman, A.A. (2001). Polarity controls forces governing asymmetric spindle positioning in the *Caenorhabditis elegans* embryo. Nature 409, 630–633.
Grill, S.W., Howard, J., Schäffer, E., Stelzer, E.H.K. and Hyman, A. a (2003). The distribution of active force generators controls mitotic spindle position. Science 301, 518–521.
Grishchuk, E.L., Molodtsov, M.I., Ataullakhanov, F.I. and McIntosh, J.R. (2005). Force production by disassembling microtubules. Nature 438, 384–388.
Grotjahn, D.A., Chowdhury, S., Xu, Y., McKenney, R.J., Schroer, T.A. and Lander, G.C. (2018). Cryo-electron tomography reveals that dynactin recruits a team of dyneins for processive motility. Nat. Struct. Mol. Biol. 25, 203–207.
Gruneberg, U., Glotzer, M., Gartner, A. and Nigg, E.A. (2002). The CeCDC-14 phosphatase is required for cytokinesis in the *Caenorhabditis elegans* embryo. J. Cell Biol. 158, 901–914.
Guilgur, L.G., Prudêncio, P., Ferreira, T., Pimenta-Marques, A.R. and Martinho, R.G. (2012). *Drosophila* aPKC is required for mitotic spindle orientation during symmetric division of epithelial cells. Development 139, 503–513.
Guntas, G., Hallett, R.A., Zimmerman, S.P., Williams, T., Yumerefendi, H., Bear, J.E. and Kuhlman, B. (2015). Engineering an improved light-induced dimer (iLID) for controlling the localization and activity of signaling proteins. Proc. Natl. Acad. Sci. U.S.A. 112, 112–117.
Guse, A., Mishima, M. and Glotzer, M. (2005). Phosphorylation of ZEN-4/MKLP1 by aurora B regulates completion of cytokinesis. Curr. Biol. 15, 778–786.
Gusnowski, E.M. and Srayko, M. (2011). Visualization of dynein-dependent microtubule gliding at the cell cortex: implications for spindle positioning. J. Cell Biol. 194, 377–386.
Hallett, R.A., Zimmerman, S.P., Yumerefendi, H., Bear, J.E. and Kuhlman, B. (2016). Correlating in Vitro and in Vivo Activities of Light-Inducible Dimers: A Cellular Optogenetics Guide. ACS Synth. Biol. 5, 53–64.
Hamaguchi, M.S. and Hiramoto, Y. (1986). Analysis of the role of astral rays in pronuclear migration in sand dollar eggs by the coldemid-UV method. Dev. Growth Differ. 28, 143–156.
Hamill, D.R., Severson, A.F., Carter, J.C. and Bowerman, B. (2002). Centrosome maturation and mitotic spindle assembly in *C. elegans* require SPD-5, a protein with multiple coiled-coil domains. Dev. Cell 3, 673–684.
Hampoelz, B., Hoeller, O., Bowman, S.K., Dunican, D. and Knoblich, J.A. (2005). *Drosophila* Ric-8 is essential for plasma-membrane localization of heterotrimeric G proteins. Nat. Cell Biol. 7, 1099–1105.
Han, G., Liu, B., Zhang, J., Zuo, W., Morris, N.R. and Xiang, X. (2001). The aspergillus cytoplasmic dynein heavy chain and nudf localize to microtubule ends and affect microtubule dynamics. Curr. Biol. 11, 719–724.
Hannabuss, J., Lera-Ramirez, M., Cade, N.I., Fourniol, F.J., Nédélec, F. and Surrey, T. (2019). Self-organization of minimal anaphase spindle midzone bundles. Curr. Biol. 29, 2120-2130.
Hannak, E., Kirkham, M., Hyman, A.A. and Oegema, K. (2001). Aurora-A kinase is required for centrosome maturation in *Caenorhabditis elegans*. J. Cell Biol. 155, 1109–1116.
Hao, Y., Du, Q., Chen, X., Zheng, Z., Balsbaugh, J.L., Maitra, S., Shabanowitz, J., Hunt, D.F. and Macara, I.G. (2010). Par3 controls epithelial spindle orientation by aPKC-mediated phosphorylation of apical Pins. Curr. Biol. 20, 1809–1818.
Harashima, H., Dissmeyer, N. and Schnittger, A. (2013). Cell cycle control across the eukaryotic kingdom. Trends Cell Biol. 23, 345–356.
Harborth, J., Wang, J., Gueth-Hallonet, C., Weber, K. and Osborn, M. (1999). Self assembly of NuMA: multiarm oligomers as structural units of a nuclear lattice. EMBO J. 18, 1689–1700.
Van Haren, J., Charafeddine, R.A., Ettinger, A., Wang, H., Hahn, K.M. and Wittmann, T. (2018). Local control of intracellular microtubule dynamics by EB1 photodissociation. Nat. Cell Biol. 20, 252–261.
Harterink, M., Van Bergeijk, P., Allier, C., De Haan, B., Van Den Heuvel, S., Hoogenraad, C.C. and Kapitein, L.C. (2016). Light-controlled intracellular transport in *Caenorhabditis elegans*. Curr. Biol. 26, R153–R154.
Hauf, S., Cole, R.W., LaTerra, S., Zimmer, C., Schnapp, G., Walter, R., Heckel, A., Van Meel, J., Rieder, C.L. and Peters, J.M. (2003). The small molecule Hesperadin reveals a role for Aurora B in correcting kinetochore-microtubule attachment and in maintaining the spindle assembly checkpoint. J. Cell Biol. 161, 281–294.
Hehnly, H., Canton, D., Bucko, P., Langeberg, L.K., Ogier, L., Gelman, I., Fernando Santana, L., Wordeman, L. and Scott, J.D. (2015). A mitotic kinase scaffold depleted in testicular seminomas impacts spindle orientation in germ line stem cells. Elife 4, 1–22.
Hendricks, A.G., Lazarus, J.E., Perlson, E., Gardner, M.K., Odde, D.J., Goldman, Y.E. and Holzbaur, E.L.F. (2012). Dynein tethers and stabilizes dynamic microtubule plus ends. Curr. Biol. 22, 632–637.
Hess, H. a, Röper, J.-C., Grill, S.W. and Koelle, M.R. (2004). RGS-7 completes a receptor-independent heterotrimeric G protein cycle to asymmetrically regulate mitotic spindle positioning in *C. elegans*. Cell 119, 209–218.
Hilger, D., Masureel, M. and Kobilka, B.K. (2018). Structure and dynamics of GPCR signaling complexes. Nat. Struct. Mol. Biol. 25, 4–12.

Hill, D.P. and Strome, S. (1988). An analysis of the role of microfilaments in the establishment and maintenance of asymmetry in *Caenorhabditis elegans* zygotes. Dev. Biol. 125, 75–84.
Hillier, L., Reinke, V., Green, P., Hirst, M., Marra, M.A. and Waterston, R.H. (2008). Massively parallel sequencing of the polyadenylated transcriptome of Celegans. Genome Res. 657–666.
Hirokawa, N., Noda, Y., Tanaka, Y. and Niwa, S. (2009). Kinesin superfamily motor proteins and intracellular transport. Nat. Rev. Mol. Cell Biol. 10, 682–696.
Holt, L.J., Tuch, B.B., Villen, J., Johnson, A.D., Gygi, S.P., Morgan, D.O. (2009). Global Analysis of Cdk1 Substrate Phosphorylation Sites Provides Insights into Evolution. Science 325, 1682–1686.
Holy, T.E., Dogterom, M., Yurke, B. and Leibler, S. (1997). Assembly and positioning of microtubule asters in microfabricated chambers. Proc. Natl. Acad. Sci. U.S.A. 94, 6228–6231.
Honnappa, S., Okhrimenko, O., Jaussi, R., Jawhari, H., Jelesarov, I., Winkler, F.K. and Steinmetz, M.O. (2006). Key interaction modes of dynamic +TIP networks. Mol. Cell. 23, 663–671.
Hoogenraad, C.C. and Akhmanova, A. (2016). Bicaudal D family of motor adaptors: linking dynein motility to cargo binding. Trends Cell Biol. 26, 327–340.
Hoogenraad, C.C., Akhmanova, A., Howell, S.A., Dortland, B.R., De Zeeuw, C.I., Willemsen, R., Visser, P., Grosveld, F. and Galjart, N. (2001). Mammalian golgi-associated Bicaudal-D2 functions in the dynein-dynactin pathway by interacting with these complexes. EMBO J. 20, 4041–4054.
Hoogenraad, C.C., Wulf, P., Schiefermeier, N., Stepanova, T., Galjart, N., Small, J.V., Grosveld, F., De Zeeuw, C.I. and Akhmanova, A. (2003). Bicaudal D induces selective dynein-mediated microtubule minus end-directed transport. EMBO J. 22, 6004–6015.
Horvitz, H.R. and Sulston, J.E. (1980). Isolation and genetic characterization of cell-lineage mutants of the nematode *Caenorhabditis elegans*. Genetics 98, 435–454.
Howard, J. (2006). Elastic and damping forces generated by confined arrays of dynamic microtubules. Phys. Biol. 3, 54–66.
Hu, C.-K., Coughlin, M., Field, C.M. and Mitchison, T.J. (2011). KIF4 regulates midzone length during cytokinesis. Curr. Biol. 21, 815–824.
Hueschen, C.L., Galstyan, V., Amouzgar, M., Phillips, R. and Dumont, S. (2019). Microtubule end-clustering maintains a steady-state spindle shape. Curr. Biol. 29, 700-708.
Hutterer, A., Glotzer, M. and Mishima, M. (2009). Clustering of centralspindlin is essential for its accumulation to the central spindle and the midbody. Curr. Biol. 19, 2043–2049.
Imai, H., Shima, T., Sutoh, K., Walker, M.L., Knight, P.J., Kon, T. and Burgess, S.A. (2015). Direct observation shows superposition and large scale flexibility within cytoplasmic dynein motors moving along microtubules. Nat. Commun. 6, 1–11.
Inoue, Y.H., Savoian, M.S., Suzuki, T., Máthé, E., Yamamoto, M.-T. and Glover, D.M. (2004). Mutations in orbit/mast reveal that the central spindle is comprised of two microtubule populations, those that initiate cleavage and those that propagate furrow ingression. J. Cell Biol. 166, 49–60.
Ishikawa, T. (2016). Axoneme structure from motile cilia. Cold Spring Harb. Perspect. Biol. 9.
Izumi, Y., Ohta, N., Itoh-Furuya, A., Fuse, N. and Matsuzaki, F. (2004). Differential functions of G protein and Baz-aPKC signaling pathways in *Drosophila* neuroblast asymmetric division. J. Cell Biol. 164, 729–738.
Izumi, Y., Ohta, N., Hisata, K., Raabe, T. and Matsuzaki, F. (2006). *Drosophila* Pins-binding protein Mud regulates spindle-polarity coupling and centrosome organization. Nat. Cell Biol. 8, 2–9.
Janson, M.E., De Dood, M.E. and Dogterom, M. (2003). Dynamic instability of microtubules is regulated by force. J. Cell Biol. 161, 1029–1034.
Janson, M.E., Loughlin, R., Loïodice, I., Fu, C., Brunner, D., Nédélec, F.J. and Tran, P.T. (2007). Crosslinkers and motors organize dynamic microtubules to form stable bipolar arrays in fission yeast. Cell 128, 357–368.
Jantsch-plunger, V., Gönczy, P., Romano, A., Schnabel, H., Hamill, D., Schnabel, R., Hyman, A.A. and Glotzer, M. (2000). CYK-4: a Rho family GTPase activating protein (GAP) required for central spindle formation and cytokinesis. 149, 1391–1404.
Jia, M., Li, J., Zhu, J., Wen, W., Zhang, M. and Wang, W. (2012). Crystal structures of the scaffolding protein LGN reveal the general mechanism by which GoLoco binding motifs inhibit the release of GDP from Gαi. J. Biol. Chem. 287, 36766–36776.
Jiang, W., Jimenez, G., Wells, N.J., Hope, T.J., Wahl, G.M., Hunter, T. and Fukunaga, R. (1998). PRC1: A human mitotic spindle-associated CDK substrate protein required for cytokinesis. Mol. Cell 2, 877–885.
John, C.M., Hite, R.K., Weirich, C.S., Fitzgerald, D.J., Jawhari, H., Faty, M., Schläpfer, D., Kroschewski, R., Winkler, F.K., Walz, T., Barral, Y. and Steinmetz, M.O. (2007). The *Caenorhabditis elegans* septin complex is nonpolar. EMBO J. 26, 3296–3307.
Johnson, H.E. and Toettcher, J.E. (2018). Illuminating developmental biology with cellular optogenetics. Curr. Opin. Biotechnol. 52, 42–48.
Johnson, H.E., Goyal, Y., Pannucci, N.L., Schüpbach, T., Shvartsman, S.Y. and Toettcher, J.E. (2017). The spatiotemporal limits of developmental Erk signaling. Dev. Cell 40, 185–192.

Jongsma, M.L.M., Berlin, I. and Neefjes, J. (2015). On the move: Organelle dynamics during mitosis. Trends Cell Biol. 25, 112–124.
Julian, M., Tollon, Y., Lajoie-Mazenc, I., Moisand, A., Mazarguil, H., Puget, A. and Wright, M. (1993). γ-tubulin participates in the formation of the midbody during cytokinesis in mammalian cells. J. Cell Sci. 105, 145–156.
Kaitna, S., Mendoza, M., Jantsch-Plunger, V. and Glotzer, M. (2000). Incenp and an Aurora-like kinase form a complex essential for chromosome segregation and efficient completion of cytokinesis. Curr. Biol. 10, 1172–1181.
Kamath, R.S., Fraser, A.G., Dong, Y., Poulin, G., Durbin, R., Gotta, M., Kanapin, A., Le Bot, N., Moreno, S., Sohrmann, M., Welchman, D.P., Zipperlen, P. and Ahringer, J. (2003). Systematic functional analysis of the *Caenorhabditis elegans* genome using RNAi. Nature 421, 231–237.
Kant, R., Zeng, B., Thomas, C.J., Bothner, B. and Sprang, S.R. (2016). Ric-8A, a G protein chaperone with nucleotide exchange activity induces long-range secondary structure changes in Gα. Elife 5, 1–20.
Kardon, J.R. and Vale, R.D. (2009). Regulators of the cytoplasmic dynein motor. Nat. Rev. Mol. Cell Biol. 10, 854–865.
Katanaev, V.L., Ponzielli, R., Sémériva, M. and Tomlinson, A. (2005). Trimeric G protein-dependent frizzled signaling in *Drosophila*. Cell 120, 111–122.
Kemp, C.A., Kopish, K.R., Zipperlen, P., Ahringer, J. and O'Connell, K.F. (2004). Centrosome maturation and duplication in *C. elegans* require the coiled-coil protein SPD-2. Dev. Cell 6, 511–523.
Kemphues, K. (2000). PARsing embryonic polarity. Cell 101, 345–348.
Kemphues, K.J., Priess, J., Cheng, N.S. and Morton, D. (1988). Identification of Genes Required for Cytoplasmic Localization in C-Elegans. J. Cell. Biochem. 52, 311-320.
Kennedy, M.J., Hughes, R.M., Peteya, L.A., Schwartz, J.W., Ehlers, M.D. and Tucker, C.L. (2010). Rapid blue-light-mediated induction of protein interactions in living cells. Nat. Methods 7, 973–975.
Kettenbach, A.N., Schweppe, D.K., Faherty, B.K., Pechenick, D., Pletnev, A.A. and Gerber, S.A. (2011). Quantitative phosphoproteomics identifies substrates and functional modules of Aurora and Polo-like kinase activities in mitotic cells. Sci. Signal. 4, 1-16.
Kim, H., Ishidate, T., Ghanta, K.S., Seth, M., Conte, D., Shirayama, M. and Mello, C.C. (2014). A Co-CRISPR strategy for efficient genome editing in *Caenorhabditis elegans*. Genetics 197, 1069–1080.
Kim, J.E., Billadeau, D.D. and Chen, J. (2005). The tandem BRCT domains of Ect2 are required for both negative and positive regulation of Ect2 in cytokinesis. J. Biol. Chem. 280, 5733–5739.
Kim, J.H., Rege, M., Valeri, J., Dunagin, M.C., Metzger, A., Titus, K.R., Gilgenast, T.G., Gong, W., Beagan, J.A., Raj, A. and Philips-Cremins, J.E. (2019). LADL: light-activated dynamic looping for endogenous gene expression control. Nat. Methods 16, 633–639.
Kimble, J. and Hirsh, D. (1979). The postembryonic cell lineages of the hermaphrodite and male gonads in *Caenorhabditis elegans*. Dev. Biol. 70, 396–417.
Kimple, R.J., Kimple, M.E., Betts, L., Sondek, J., Siderovski, D.P. (2002). Structural determinants for GoLoco-induced inhibition of nucleotide release by Galpha subunits. Nature 416, 878–81.
Kimple, A., Yasgar, A., Hughes, M., Jadhav, A., Willard, F., Muller, R., Austin, C., Inglese, J., Ibeanu, G., Siderovski, D. and Simeonov, A. (2008). A high throughput fluorescence polarization assay for inhibitors of the GoLoco motif/G-alpha interaction. Comb. Chem. High Throughput Screen. 11, 396–409.
Kimple, R.J., De Vries, L., Tronchère, H., Behe, C.I., Morris, R.A., Farquhar, M.G. and Siderovski, D.P. (2001). RGS12 and RGS14 GoLoco motifs are gαi interaction sites with guanine nucleotide dissociation inhibitor activity. J. Biol. Chem. 276, 29275–29281.
Kimura, A. and Onami, S. (2007). Local cortical pulling-force repression switches centrosomal centration and posterior displacement in *C. elegans*. J. Cell Biol. 179, 1347–1354.
Kimura, K. and Kimura, A. (2011). Intracellular organelles mediate cytoplasmic pulling force for centrosome centration in the *Caenorhabditis elegans* early embryo. PNAS 108, 137–142.
King, S.J. and Schroer, T.A. (2000). Dynactin increases the processivity of the cytoplasmic dynein motor. Nat. Cell Biol. 2, 20–24.
Kirschner, M. and Mitchison, T. (1986). Beyond self-assembly: From microtubules to morphogenesis. Cell. 45:329–342.
Kiyomitsu, T. and Cheeseman, I.M. (2012). Chromosome-and spindle-pole-derived signals generate an intrinsic code for spindle position and orientation. Nat. Cell Biol. 14, 311–317.
Kiyomitsu, T. and Cheeseman, I.M. (2013). Cortical dynein and asymmetric membrane elongation coordinately position the spindle in anaphase. Cell 154, 391–402.
Klinkert, K., Levernier, N., Gross, P., Gentili, C., Tobel, L. Von, Pierron, M., Busso, C., Herrman, S., Grill, S.W., Kruse, K. and Gönczy, P. (2019). Aurora A depletion reveals centrosome-independent polarization mechanism in *Caenorhabditis elegans*. Elife 8, 1–31.
Knoblich, J. a (2010). Asymmetric cell division: recent developments and their implications for tumour biology. Nat. Rev. Mol. Cell Biol. 11, 849–860.

Knoblich, J.A. (2008). Mechanisms of asymmetric stem cell division. Cell 132, 583–597.
Kobayashi, T. and Murayama, T. (2009). Cell cycle-dependent microtubule-based dynamic transport of cytoplasmic dynein in mammalian cells. PLoS One 4, e7827.
Komarova, Y., de Groot, C.O., Grigoriev, I., Gouveia, S.M., Munteanu, E.L., Schober, J.M., Honnappa, S., Buey, R.M., Hoogenraad, C.C., Dogterom, M., Borisy, G.G., Steinmetz, M.O. and Akhmanova, A. (2009). Mammalian end binding proteins control persistent microtubule growth. J. Cell Biol. 184, 691–706.
Konermann, S., Brigham, M.D., Trevino, A.E., Hsu, P.D., Heidenreich, M., Cong, L., Platt, R.J., Scott, D.A., Church, G.M. and Zhang, F. (2013). Optical control of mammalian endogenous transcription and epigenetic states. Nature 500, 472–476.
Koonce, M.P. (1999). Dynein motor regulation stabilizes interphase microtubule arrays and determines centrosome position. EMBO J. 18, 6786–6792.
Kopein, D. and Katanaev, V.L. (2009). *Drosophila* GoLoco-protein Pins is a target of Gαo-mediated G protein–coupled receptor signaling. Mol. Biol. Cell. 20, 3865–3877.
Kotak, S. (2019). Mechanisms of spindle positioning: Lessons from worms and mammalian cells. Biomolecules 9, 1-15.
Kotak, S., Busso, C. and Gönczy, P. (2012). Cortical dynein is critical for proper spindle positioning in human cells. J. Cell Biol. 199, 97–110.
Kotak, S., Busso, C. and Gönczy, P. (2013). NuMA phosphorylation by CDK1 couples mitotic progression with cortical dynein function. EMBO J. 32, 2517–2529.
Kotak, S., Busso, C. and Gönczy, P. (2014). NuMA interacts with phosphoinositides and links the mitotic spindle with the plasma membrane. EMBO J. 33, 1815–1830.
Kotak, S., Afshar, K., Busso, C. and Gönczy, P. (2016). Aurora A kinase regulates proper spindle positioning in *C. elegans* and in human cells. J. Cell Sci. 129, 3015–3025.
Kotýnková, K., Su, K.C., West, S.C. and Petronczki, M. (2016). Plasma membrane association but not midzone recruitment of RhoGEF ECT2 is essential for cytokinesis. Cell Rep. 17, 2672–2686.
Kozlowski, C., Srayko, M. and Nedelec, F. (2007). Cortical microtubule contacts position the spindle in *C. elegans* embryos. Cell 129, 499–510.
Krämer, H. and Phistry, M. (1999). Genetic analysis of hook, a gene required for endocytic trafficking in *Drosophila*. Genetics 151, 675–684.
Krueger, L.E., Wu, J.C., Tsou, M.F.B. and Rose, L.S. (2010). LET-99 inhibits lateral posterior pulling forces during asymmetric spindle elongation in *C. elegans* embryos. J. Cell Biol. 189, 481–495.
Kurasawa, Y., Earnshaw, W.C., Mochizuki, Y., Dohmae, N. and Todokoro, K. (2004). Essential roles of KIF4 and its binding partner PRC1 in organized central spindle midzone formation. EMBO J. 23, 3237–3248.
Kushnirov, V. V. (2000). Rapid and reliable protein extraction from yeast. Yeast 16, 857–860.
Laan, L., Roth, S. and Dogterom, M. (2012a). End-on microtubule-dynein interactions and pulling-based positioning of microtubule organizing centers. Cell Cycle 11, 3750–3757.
Laan, L., Pavin, N., Husson, J., Romet-Lemonne, G., Van Duijn, M., López, M.P., Vale, R.D., Jülicher, F., Reck-Peterson, S.L. and Dogterom, M. (2012b). Cortical dynein controls microtubule dynamics to generate pulling forces that position microtubule asters. Cell 148, 502–514.
Labbé, J., Maddox, P.S., Salmon, E.D., Goldstein, B., Hill, C. and Carolina, N. (2003). PAR proteins regulate microtubule dynamics at the cell cortex in *C. elegans*. The University of North Carolina at Chapel Hill. 13, 707–714.
Labbé, J.C., McCarthy, E.K. and Goldstein, B. (2004). The forces that position a mitotic spindle asymmetrically are tethered until after the time of spindle assembly. J. Cell Biol. 167, 245–256.
Lansbergen, G., Komarova, Y., Modesti, M., Wyman, C., Hoogenraad, C.C., Goodson, H.V., Lemaitre, R.P., Drechsel, D.N., van Munster, E., Gadella, T.W.J., Grosveld, F., Galjart, N., Borisy, G.G. and Akhmanova, A. (2004). Conformational changes in CLIP-170 regulate its binding to microtubules and dynactin localization. J. Cell Biol. 166, 1003–1014.
Lechler, T. and Fuchs, E. (2005). Asymmetric cell divisions promote stratification and differentiation of mammalian skin. Nature 437, 275–280.
Lee, W.L., Oberle, J.R. and Cooper, J.A. (2003). The role of the lissencephaly protein Pac1 during nuclear migration in budding yeast. J. Cell Biol. 160, 355–364.
Lee, H.-C., Gu, W., Shirayama, M., Youngman, E., Conte, D. and Mello, C.C. (2012). *C. elegans* piRNAs mediate the genome-wide surveillance of germline transcripts. Cell 150, 78–87.
Lee, K.Y., Esmaeili, B., Zealley, B. and Mishima, M. (2015). Direct interaction between centralspindlin and PRC1 reinforces mechanical resilience of the central spindle. Nat. Commun. 6, 1–10.
Lekomtsev, S., Su, K.-C., Pye, V.E., Blight, K., Sundaramoorthy, S., Takaki, T., Collinson, L.M., Cherepanov, P., Divecha, N. and Petronczki, M. (2012). Centralspindlin links the mitotic spindle to the plasma membrane during cytokinesis. Nature 492, 276–279.

Lenz, J.H., Schuchardt, I., Straube, A. and Steinberg, G. (2006). A dynein loading zone for retrograde endosome motility at microtubule plus-ends. EMBO J. 25, 2275–2286.
Leslie, R.J. and Pickett Heaps, J.D. (1983). Ultraviolet microbeam irradiations of mitotic diatoms: Investigation of spindle elongation. J. Cell Biol. 96, 548–561.
Leung, C.C.Y. and Glover, J.N.M. (2011). BRCT domains: Easy as one, two, three. Cell Cycle 10, 2461–2470.
Levskaya, A., Weiner, O.D., Lim, W.A. and Voigt, C.A. (2009). Spatiotemporal control of cell signalling using a light-switchable protein interaction. Nature 461, 997–1001.
Lewellyn, L., Dumont, J., Desai, A. and Oegema, K. (2010). Analyzing the Effects of Delaying Aster Separation on Furrow Formation during Cytokinesis in the *Caenorhabditis elegans* Embryo. Mol. Biol. Cell 21, 50–62.
Lewellyn, L., Carvalho, A., Desai, A., Maddox, A.S. and Oegema, K. (2011). The chromosomal passenger complex and centralspindlin independently contribute to contractile ring assembly. J. Cell Biol. 193, 155–169.
Loïodice, I., Staub, J., Setty, T.G., Nguyen, N.-P.T., Paoletti, A. and Tran, T. (2005). Ase1p organizes antiparallel microtubule arrays during interphase and mitosis in fission yeast. Mol. Biol. Cell 16, 1745–1768.
Lombillo, V.A., Stewart, R.J. and Mc Intosh, J.R. (1995). Minus-end-directed motion of kinesin–coated microspheres driven by microtubule depolymerization. Nature 373, 161–164.
Loria, A., Longhini, K.M. and Glotzer, M. (2012). The RhoGAP domain of CYK-4 has an essential role in RhoA activation. Curr. Biol. 22, 213–219.
Lorson, M.A., Horvitz, H.R. and van den Heuvel, S. (2000). LIN-5 is a novel component of the spindle apparatus required for chromosome segregation and cleavage plane specification in *Caenorhabditis elegans*. J. Cell Biol. 148, 73–86.
Maddox, A.S., Habermann, B., Desai, A. and Oegema, K. (2005). Distinct roles for two *C. elegans* anillins in the gonad and early embryo. Development 132, 2837–2848.
Maddox, A.S., Lewellyn, L., Desai, A. and Oegema, K. (2007). Anillin and the septins promote asymmetric ingression of the cytokinetic furrow. Dev. Cell 12, 827–835.
Maiato, H., Fairley, E.A.L., Rieder, C.L., Swedlow, J.R., Sunkel, C.E. and Earnshaw, W.C. (2003). Human CLASP1 is an outer kinetochore component that regulates spindle microtubule dynamics. Cell 113, 891–904.
Mali, P., Yang, L., Esvelt, K.M., Aach, J., Guell, M., DiCarlo, J.E., Norville, J.E. and Church, G.M. (2013). RNA-guided human genome engineering via Cas9. Science 339, 823–826.
Mallik, R., Carter, B.C., Lex, S.A., King, S.J. and Gross, S.P. (2004). Cytoplasmic dynein functions as a gear in response to load. Nature 427, 649–652.
Mangal, S., Sacher, J., Kim, T., Osório, D.S., Motegi, F., Carvalho, A.X., Oegema, K. and Zanin, E. (2018). TPXL-1 activates Aurora A to clear contractile ring components from the polar cortex during cytokinesis. J. Cell Biol. 217, 837–848.
Markus, S.M. and Lee, W.L. (2011). Regulated offloading of cytoplasmic dynein from microtubule plus ends to the cortex. Dev. Cell 20, 639–651.
Mastronarde, D.N., McDonald, K.L., Ding, R. and McIntosh, J.R. (1993). Interpolar spindle microtubules in PTK cells. J. Cell Biol. 123, 1475–1489.
Maton, G., Edwards, F., Lacroix, B., Stefanutti, M., Laband, K., Lieury, T., Kim, T., Espeut, J., Canman, J.C. and Dumont, J. (2015). Kinetochore components are required for central spindle assembly. Nat. Cell Biol. 17, 697–705.
Matsumura, F., Yamakita, Y. and Yamashiro, S. (2011). Myosin light chain kinases and phosphatase in mitosis and cytokinesis. Arch. Biochem. Biophys. 510, 76–82.
Maurer, S.P., Fourniol, F.J., Bohner, G., Moores, C.A. and Surrey, T. (2012). EBs recognize a nucleotide-dependent structural cap at growing microtubule ends. Cell. 149, 371–382.
Maurer, S.P., Cade, N.I., Bohner, G., Gustafsson, Boutant, N.E. and Surrey, T. (2014). EB1 accelerates two conformational transitions important for microtubule maturation and dynamics. Curr. Biol. 24, 372–384.
McCarthy Campbell, E.K., Werts, A.D., Goldstein, B. (2009). A cell cycle timer for asymmetric spindle positioning. PLoS Biol. 7, e1000088.
McCudden, C.R., Hains, M.D., Kimple, R.J., Siderovski, D.P. and Willard, F.S. (2005). G-protein signaling: back to the future. Cell. Mol. Life Sci. 62, 551–577.
McIntosh, J.R., Volkov, V., Ataullakhanov, F.I. and Grishchuk, E.L. (2010). Tubulin depolymerization may be an ancient biological motor. J. Cell Sci. 123, 3425–3434.
McKenney, R.J., Huynh, W., Tanenbaum, M.E., Bhabha, G. and Vale, R.D. (2014). Activation of cytoplasmic dynein motility by dynactin-cargo adapter complexes. Science 345, 337–341.
McKinley, K.L. and Cheeseman, I.M. (2017). Large-scale analysis of CRISPR/Cas9 cell-cycle knockouts reveals the diversity of p53-dependent responses to cell-cycle defects. Dev. Cell 40, 405-420.
McNally, F.J. (2013). Mechanisms of spindle positioning. J. Cell Biol. 200, 131–40.
Merdes, A., Ramyar, K., Vechio, J.D. and Cleveland, D.W. (1996). A complex of NuMA and cytoplasmic dynein is essential for mitotic spindle assembly. Cell 87, 447–458.

Merdes, A., Heald, R., Samejima, K., Earnshaw, W.C. and Cleveland, D.W. (2000). Formation of spindle poles by dynein/dynactin-dependent transport of NuMA. J. Cell Biol. 149, 851–861.
Merritt, C., Rasoloson, D., Ko, D. and Seydoux, G. (2008). 3′ UTRs are the primary regulators of gene expression in the *C. elegans* germline. Curr. Biol. 18, 1476–1482.
Merritt, C. and Seydoux, G. (2010). Transgenic solutions for the germline. *WormBook*, ed. The *C. elegans* Research Community, Wormbook.
Mierzwa, B. and Gerlich, D.W. (2014). Cytokinetic abscission: molecular mechanisms and temporal control. Dev. Cell 31, 525–538.
Milas, A., Jagrić, M., Martinčić, J. and Tolić, I.M. (2018). Optogenetic reversible knocksideways, laser ablation and photoactivation on the mitotic spindle in human cells. Methods Cell Biol. 145, 191–215.
Miller, K.G., Alfonso, A., Nguyen, M., Crowell, J.A., Johnson, C.D. and Rand, J.B. (1996). A genetic selection for *Caenorhabditis elegans* synaptic transmission mutants. Proc. Natl. Acad. Sci. U.S.A. 93, 12593–12598.
Miller, A.L. and Bement, W.M. (2009). Regulation of cytokinesis by Rho GTPase flux. Nat. Cell Biol. 11, 71–77.
Miller, K.G. and Rand, J.B. (2000). A role for RIC-8 (synembryn) and GOA-1 ($G_o\alpha$) in regulating a subset of centrosome movements during early embryogenesis in *Caenorhabditis elegans*. Genetics 156, 1649–1660.
Miller, K.G., Emerson, M.D., McManus, J.R. and Rand, J.B. (2000). RIC-8 (Synembryn): a novel conserved protein that is required for $G_q\alpha$ signaling in the *C. elegans* nervous system. Neuron 27, 289–299.
Minc, N., Burgess, D. and Chang, F. (2011). Influence of cell geometry on division-plane positioning. Cell 144, 414–426.
Mishima, M., Kaitna, S. and Glotzer, M. (2002). Central spindle assembly and cytokinesis require a kinesin-like protein/RhoGAP complex with microtubule bundling activity. Dev. Cell 2, 41–54.
Mishima, M., Pavicic, V., Grüneberg, U., Nigg, E.A. and Glotzer, M. (2004). Cell cycle regulation of central spindle assembly. Nature 430, 908–913.
Mollinari, C., Kleman, J., Saoudi, Y., Jablonski, S.A., Perard, J., Yen, T.J. and Margolis, R.L. (2005). Ablation of PRC1 by small interfering RNA demonstrates that cytokinetic abscission requires a central spindle bundle in mammalian cells, whereas completion of furrowing does not. 16, 1043–1055.
Montesano, R., Schaller, G. and Orci, L. (1991). Induction of epithelial tubular morphogenesis in vitro by fibroblast-derived soluble factors. Cell 66, 697–711.
Montgomery, M.K., Xu, S. and Fire, A. (1998). RNA as a target of double-stranded RNA-mediated genetic interference in *Caenorhabditis elegans*. Proc. Natl. Acad. Sci. U.S.A. 95, 15502–15507.
Morin, X. and Bellaïche, Y. (2011). Mitotic Spindle Orientation in Asymmetric and Symmetric Cell Divisions during Animal Development. Dev. Cell 21, 102–119.
Motegi, F. and Seydoux, G. (2007). Revisiting the role of microtubules in *C. elegans* polarity. J. Cell Biol. 179, 367–369.
Motegi, F. and Seydoux, G. (2013). The PAR network: redundancy and robustness in a symmetry-breaking system. Philos. Trans. R. Soc. B Biol. Sci. 368, 1-11.
Motegi, F. and Sugimoto, A. (2006). Sequential functioning of the ECT-2 RhoGEF, RHO-1 and CDC-42 establishes cell polarity in *Caenorhabditis elegans* embryos. Nat. Cell Biol. 8, 978–985.
Motegi, F., Velarde, N. V., Piano, F. and Sugimoto, A. (2006). Two phases of astral microtubule activity during cytokinesis in *C. elegans* embryos. Dev. Cell 10, 509–520.
Munro, E., Nance, J. and Priess, J.R. (2004). Cortical flows powered by asymmetrical contraction transport PAR proteins to establish and maintain anterior-posterior polarity in the early *C. elegans* embryo. Dev. Cell 7, 413–424.
Murthy, K. and Wadsworth, P. (2008). Dual role for microtubules in regulating cortical contractility during cytokinesis. J. Cell Sci. 121, 2350–2359.
Musacchio, A. and Desai, A. (2017). A molecular view of kinetochore assembly and function. Biology, 6, 1-47.
Nagai, Y., Nishimura, A., Tago, K., Mizuno, N. and Itoh, H. (2010). Ric-8B stabilizes the α subunit of stimulatory G protein by inhibiting its ubiquitination. J. Biol. Chem. 285, 11114–11120.
Nahaboo, W., Zouak, M., Askjaer, P. and Delattre, M. (2015). Chromatids segregate without centrosomes during *Caenorhabditis elegans* mitosis in a Ran- and CLASP-dependent manner. Mol. Biol. Cell 26, 2020–2029.
Natochin, M., Gasimov, K.G. and Artemyev, N.O. (2001). Inhibition of GDP/GTP exchange on Gα subunits by proteins containing G-protein regulatory motifs. Biochemistry 40, 5322–5328.
Neef, R., Gruneberg, U., Kopajtich, R., Li, X., Nigg, E.A., Sillje, H. and Barr, F.A. (2007). Choice of Plk1 docking partners during mitosis and cytokinesis is controlled by the activation state of Cdk1. Nat. Cell Biol. 9, 436–444.
Nguyen-Ngoc, T., Afshar, K. and Gönczy, P. (2007). Coupling of cortical dynein and Gα proteins mediates spindle positioning in *Caenorhabditis elegans*. Nat. Cell Biol. 9, 1294–1302.
Nguyen, P. A., Groen, A. C., Loose, M., Ishihara, K., Wuhr, M., Field, C.M. and Mitchison, T.J. (2014). Spatial organization of cytokinesis signaling reconstituted in a cell-free system. Science 346, 244–247.
Nguyen, T.Q., Sawa, H., Okano, H. and White, J.G. (2000). The *C. elegans* septin genes, unc-59 and unc-61, are required for normal postembryonic cytokineses and morphogenesis but have no essential function in embryogenesis. J. Cell Sci. 113, 3825–3837.

Nicholas, M.P., Höök, P., Brenner, S., Wynne, C.L., Vallee, R.B. and Gennerich, A. (2015). Control of cytoplasmic dynein force production and processivity by its C-terminal domain. Nat. Commun. 6, 1–8.
Niehrs, C. and Shen, J. (2010). Regulation of Lrp6 phosphorylation. Cell. Mol. Life Sci. 67, 2551–2562.
Niiya, F., Xie, X., Lee, K.S., Inoue, H. and Miki, T. (2005). Inhibition of cyclin-dependent kinase 1 induces cytokinesis without chromosome segregation in an ECT2 and MgcRacGAP-dependent manner. J. Biol. Chem. 280, 36502–36509.
Nishimura, Y. and Yonemura, S. (2006). Centralspindlin regulates ECT2 and RhoA accumulation at the equatorial cortex during cytokinesis. J. Cell Sci. 119, 104–114.
Nislow, C., Sellitto, C., Kuriyama, R. and McIntosh, J.R. (1990). A monoclonal antibody to a mitotic microtubule-associated protein blocks mitotic progression. J. Cell Biol. 111, 511–522.
Nislow, C., Lombillo, V.A., Kuriyama, R. and McIntosh, J.R. (1992). A plus-end-directed motor enzyme that moves antiparallel microtubules in vitro localizes to the interzone of mitotic spindles. Nature 359, 543–547.
Noatynska, A., Gotta, M. and Meraldi, P. (2012). Mitotic spindle (DIS)orientation and DISease: cause or consequence? J. Cell Biol. 199, 1025–1035.
O'Connell, K.F., Leys, C.M. and White, J. G. (1998) A genetic screen for temperature-sensitive cell-division mutants of *Caenorhabditis elegans*. Genetics 149, 1303-1321.
O'Connell, K.F., Maxwell, K.N. and White, J.G. (2000). The spd-2 gene is required for polarization of the anteroposterior axis and formation of the sperm asters in the *Caenorhabditis elegans* zygote. Dev. Biol. 222, 55–70.
O'Rourke, S.M., Dorfman, M.D., Carter, J.C. and Bowerman, B. (2007). Dynein modifiers in *C. elegans*: light chains suppress conditional heavy chain mutants. PLoS Genet. 3, e128.
O'Rourke, S.M., Christensen, S.N. and Bowerman, B. (2010). *Caenorhabditis elegans* EFA-6 limits microtubule growth at the cell cortex. Nat. Cell Biol. 12, 1235–1241.
Odronitz, F. and Kollmar, M. (2007). Drawing the tree of eukaryotic life based on the analysis of 2,269 manually annotated myosins from 328 species. Genome Biol. 8, 1–23.
Oegema, K. and Mitchison, T.J. (1997). Rappaport rules : cleavage furrow induction in animal cells. 94, 4817–4820.
Oegema, K., Desai, A., Rybina, S., Kirkham, M. and Hyman, A.A. (2001). Functional analysis of kinetochore assembly in *Caenorhabditis elegans*. J. Cell Biol. 153, 1209–1225.
Okumura, M., Natsume, T., Kanemaki, M.T. and Kiyomitsu, T. (2018). Dynein–dynactin–NuMA clusters generate cortical spindle-pulling forces as a multiarm ensemble. Elife 7, 1–24.
Olenick, M.A., Tokito, M., Boczkowska, M., Dominguez, R. and Holzbaur, E.L.F. (2016). Hook adaptors induce unidirectional processive motility by enhancing the Dynein-Dynactin interaction. J. Biol. Chem. 291, 18239–18251.
Olsen, J. V, Vermeulen, M., Santamaria, A., Kumar, C., Martin, L., Jensen, L.J., Gnad, F., Cox, J., Jensen, T.S., Nigg, E.A., Brunak, S., Mann, M. (2010). Quantitative Phosphoproteomics Reveals Widespread Full Phosphorylation Site Occupancy During Mitosis. Sci. Signal. 3, 1–16.
van Oostende Triplet, C., Jaramillo Garcia, M., Haji Bik, H., Beaudet, D. and Piekny, A. (2014). Anillin interacts with microtubules and is part of the astral pathway that defines cortical domains. J. Cell Sci. 127, 3699–3710.
Ouellet, J. and Barral, Y. (2012). Organelle segregation during mitosis: lessons from asymmetrically dividing cells. J. Cell Biol. 196, 305–313.
Paix, A., Folkmann, A., Rasoloson, D., Seydoux, G. (2015). High efficiency, homology-directed genome editing in *Caenorhabditis elegans* using CRISPR-Cas9 ribonucleoprotein complexes. Genetics 201, 47–54.
Panbianco, C., Weinkove, D., Zanin, E., Jones, D., Divecha, N., Gotta, M. and Ahringer, J. (2008). A casein kinase 1 and PAR proteins regulate asymmetry of a PIP2 synthesis enzyme for asymmetric spindle positioning. Dev. Cell 15, 198–208.
Park, D.H. and Rose, L.S. (2008). Dynamic localization of LIN-5 and GPR-1/2 to cortical force generation domains during spindle positioning. Dev. Biol. 315, 42–54.
Pavicic-kaltenbrunner, V., Mishima, M. and Glotzer, M. (2007). Cooperative assembly of CYK-4/MgcRacGAP and ZEN-4/MKLP1 to form the centralspindlin complex. Mol. Biol. Cell. 18, 4992–5003.
Pavin, N. and Tolić, I.M. (2016). Self-organization and forces in the mitotic spindle. Annu. Rev. Biophys. 45, 279–298.
Pecreaux, J., Röper, J.-C., Kruse, K., Jülicher, F., Hyman, A. a, Grill, S.W. and Howard, J. (2006). Spindle oscillations during asymmetric cell division require a threshold number of active cortical force generators. Curr. Biol. 16, 2111–2122.
Petronczki, M., Lénárt, P. and Peters, J.M. (2008). Polo on the rise-from mitotic entry to cytokinesis with Plk1. Dev. Cell 14, 646–659.
Petry, S., Groen, A.C., Ishihara, K., Mitchison, T.J. and Vale, R.D. (2013). Branching microtubule nucleation in *Xenopus* egg extracts mediated by augmin and TPX2. Cell 152, 768–777.
Phair, R., Gorski, S. and Misteli, T. (2003). Measurement of dynamic protein binding to chromatin in vivo, using photobleaching microscopy. Methods Enzymol. 375, 393–414.

Piekny, A.J. and Maddox, A.S. (2010). The myriad roles of Anillin during cytokinesis. Semin. Cell Dev. Biol. 21, 881–891.
di Pietro, F., Echard, A. and Morin, X. (2016). Regulation of mitotic spindle orientation: an integrated view. EMBO Rep. 17, 1106–1130.
Pines, J. (2011). Cubism and the cell cycle: The many faces of the APC/C. Nat. Rev. Mol. Cell Biol. 12, 427–438.
Pinkse, M.W.H., Mohammed, S., Gouw, J.W., Van Breukelen, B., Vos, H.R., Heck, A.J.R. (2008). Highly robust, automated and sensitive online TiO2-based phosphoproteomics applied to study endogenous phosphorylation in *Drosophila* melanogaster. J. Proteome Res. 7, 687–697.
Pintard, L. and Bowerman, B. (2019). Mitotic cell division in *Caenorhabditis elegans*. Wormbook, 35-73.
Plowman, G.D., Sudarsanam, S., Bingham, J., Whyte, D., Hunter, T. (1999). The protein kinases of *Caenorhabditis elegans*: a model for signal transduction in multicellular organisms. Proc. Natl. Acad. Sci. U.S.A. 96, 13603–13610.
Pollard, T.D. (2017). Nine unanswered questions about cytokinesis. J. Cell Biol. 216, 3007–3016.
Portegijs, V., Fielmich, L-E., Galli, M., Schmidt, R., Muñoz, J., van Mourik, T., Akhmanova, A., Heck, A.J.R., Boxem, M. and van den Heuvel, S. (2016). Multisite phosphorylation of NuMA-related LIN-5 controls mitotic spindle positioning in *C. elegans*. PLoS Genet. 12, 1–32.
Poser, I., Sarov, M., Hutchins, J.R.A., Hériché, J.-K., Toyoda, Y., Pozniakovsky, A., Weigl, D., Nitzsche, A., Hegemann, B., Bird, A.W., Pelletier, L., Kittler, R., Hua, S., Naumann, R., Augsburg, M., M.M. Sykora, Hofemeister, H., Zhang, Y., Nasmyth, K., White, K.P., Dietzel, S., Mechtler, K., Durbin, R., Stewart, A.F., Peters, J.-M., Buchholz, F. and Hyman, A. (2008). BAC TransgeneOmics: a high-throughput method for exploration of protein function in mammals. Nat. Methods. 5, 409–415.
Potapova, T.A., Daum, J.R., Pittman, B.D., Hudson, J.R., Jones, T.N., Satinover, D.L., Stukenberg, P.T. and Gorbsky, G.J. (2006). The reversibility of mitotic exit in vertebrate cells. Nature 440, 954–958.
Powers, J., Bossinger, O., Rose, D., Strome, S. and Saxton, W. (1998). A nematode kinesin required for cleavage furrow advancement. Curr. Biol. 8, 1133–1136.
Praitis, V., Casey, E., Collar, D. and Austin, J. (2001). Creation of low-copy integrated transgenic lines in *Caenorhabditis elegans*. Genetics 157, 1217–1226.
Price, K.L. and Rose, L.S. (2017). LET-99 functions in the astral furrowing pathway, where it is required for myosin enrichment in the contractile ring. Mol. Biol. Cell 28, 2360–2373.
Prokopenko, S.N., Brumby, A., O'Keefe, L., Prior, L., He, Y., Saint, R. and Bellen, H.J. (1999). A putative exchange factor for Rho1 GTPase is required for initiation of cytokinesis in *Drosophila*. Genes Dev. 13, 2301–2314.
Prosser, S.L. and Pelletier, L. (2017). Mitotic spindle assembly in animal cells: A fine balancing act. Nat. Rev. Mol. Cell Biol. 18, 187–201.
Quyn, A.J., Appleton, P.L., Carey, F.A., Steele, R.J.C., Barker, N., Clevers, H., Ridgway, R.A., Sansom, O.J. and Näthke, I.S. (2010). Spindle orientation bias in gut epithelial stem cell compartments is lost in precancerous tissue. Cell Stem Cell 6, 175–181.
Raaijmakers, J. a, Tanenbaum, M.E. and Medema, R.H. (2013). Systematic dissection of dynein regulators in mitosis. J. Cell Biol. 201, 201–215.
Radulescu, A.E. and Cleveland, D.W. (2010). NuMA after 30 years: the matrix revisited. Trends Cell Biol. 20, 214–222.
Raich, W.B., Moran, A.N., Rothman, J.H. and Hardin, J. (1998). Cytokinesis and midzone microtubule organization in *Caenorhabditis elegans* require the kinesin-like protein ZEN-4. Mol. Biol. Cell 9, 2037–2049.
Rappaport, R. (1961). Experiments concerning the cleavage stimulus in sand dollar eggs. J Exp Zool 148, 81–89.
Rappaport, R. (1969). Aster-equatorial surface relations and furrow establishment. J Exp Zool1 171, 59–68.
Rappaport, R. (1986). Establishment of the mechanism of cytokinesis in animal cells. Int. Rev. Cytol. 105, 245–281.
Rappaport, R. (1996). Cytokinesis in animal cells (Cambridge University Press).
Reck-Peterson, S.L., Yildiz, A., Carter, A.P., Gennerich, A., Zhang, N. and Vale, R.D. (2006). Single-molecule analysis of dynein processivity and stepping behavior. Cell 126, 335–348.
Reck-Peterson, S.L., Redwine, W.B., Vale, R.D. and Carter, A.P. (2018). The cytoplasmic dynein transport machinery and its many cargoes. Nat. Rev. Mol. Cell Biol. 19, 382–398.
Redemann, S., Pecreaux, J., Goehring, N.W., Khairy, K., Stelzer, E.H.K., Hyman, A.A. and Howard, J. (2010). Membrane invaginations reveal cortical sites that pull on mitotic spindles in one-cell *C. elegans* embryos. PLoS One 5, e12301.
Redemann, S., Schloissnig, S., Ernst, S., Pozniakowsky, A., Ayloo, S., Hyman, A.A. and Bringmann, H. (2011). Codon adaptation-based control of protein expression in *C. elegans*. Nat. Methods 8, 250–252.
Redemann, S., Baumgart, J., Lindow, N., Shelley, M., Nazockdast, E., Kratz, A., Prohaska, S., Brugués, J., Fürthauer, S. and Müller-Reichert, T. (2017). *C. elegans* chromosomes connect to centrosomes by anchoring into the spindle network. Nat. Commun. 8, 1–13.
Redwine, W.B., DeSantis, M.E., Hollyer, I., Htet, Z.M., Tran, P.T., Swanson, S.K., Florens, L., Washburn, M.P. and Reck-Peterson, S.L. (2017). The human cytoplasmic dynein interactome reveals novel activators of motility. Elife 6, 1–27.

Reymann, A.C., Staniscia, F., Erzberger, A., Salbreux, G. and Grill, S.W. (2016). Cortical flow aligns actin filaments to form a furrow. Elife 5, 1-25.
Reynolds, N.K., Schade, M.A. and Miller, K.G. (2005). Convergent, RIC-8-dependent Gα signaling pathways in the *Caenorhabditis elegans* synaptic signaling network. Genetics 169, 651–670.
Riche, S., Zouak, M., Argoul, F., Arneodo, A., Pecreaux, J. and Delattre, M. (2013). Evolutionary comparisons reveal a positional switch for spindle pole oscillations in *Caenorhabditis* embryos. J. Cell Biol. 201, 653–662.
Rieder, C.L., Khodjakov, A., Paliulis, L. V., Fortier, T.M., Cole, R.W. and Sluder, G. (1997). Mitosis in vertebrate somatic cells with two spindles: Implications for the metaphase/anaphase transition checkpoint and cleavage. Proc. Natl. Acad. Sci. U.S.A. 94, 5107–5112.
Rivera, V.M., Clackson, T., Natesan, S., Pollock, R., Amara, J.F., Keenan, T., Magari, S.R., Phillips, T., Courage, N.L., Cerasoli, F., Holt, D.A. and Gilman, M. (1996). A humanized system for pharmacologic control of gene expression. Nat. Med. 2, 1028–1032.
Roberts, A.J. (2018). Emerging mechanisms of dynein transport in the cytoplasm versus the cilium. Biochem. Soc. Trans. 46, 967–982.
Roberts, A.J., Kon, T., Knight, P.J., Sutoh, K. and Burgess, S.A. (2013). Functions and mechanics of dynein motor proteins. Nat. Rev. Mol. Cell Biol. 14, 713–726.
Roberts, A.J., Goodman, B.S. and Reck-Peterson, S.L. (2014). Reconstitution of dynein transport to the microtubule plus end by kinesin. Elife 3, e02641.
Rogers, S.L., Wiedermann, U., Häcker, U., Turck, C. and Vale, R.D. (2004). *Drosophila* RhoGEF2 associates with microtubule plus ends in an EB1-dependent manner. Curr. Biol. 14, 1827–1833.
Rose, L.S. and Kemphues, K. (1998). The *let-99* gene is required for proper spindle orientation during cleavage of the *C. elegans* embryo. Development 125, 1337–1346.
Rose, L.S., Lamb, M.L., Hird, S.N. and Kemphues, K.J. (1995). Pseudocleavage is dispensable for polarity and development in *C. elegans* embryos. 479–489.
Rose, L. and Gönczy, P. (2014). Polarity establishment, asymmetric division and segregation of fate determinants in early *C. elegans* embryos. *WormBook*, ed. The *C. elegans* Research Community, Wormbook.
Rual, J.F., Ceron, J., Koreth, J., Hao, T., Nicot, A.S., Hirozane-Kishikawa, T., Vandenhaute, J., Orkin, S.H., Hill, D.E., van den Heuvel, S. and Vidal, M. (2004). Toward improving *Caenorhabditis elegans* phenome mapping with an ORFeome-based RNAi library. Genome Res. 14, 2162–2168.
Ruchaud, S., Carmena, M. and Earnshaw, W.C. (2007). Chromosomal passengers: conducting cell division. Nat. Rev. Mol. Cell Biol. 8, 798–812.
Saito, S., Liu, X.F., Kamijo, K., Raziuddin, R., Tatsumoto, T., Okamoto, I., Chen, X., Lee, C.C., Lorenzi, M. V., Ohara, N. and Miki, T. (2004). Deregulation and mislocalization of the cytokinesis regulator ECT2 activate the Rho signaling pathways leading to malignant transformation. J. Biol. Chem. 279, 7169–7179.
Salic, A., Lee, E., Mayer, L. and Kirschner, M.W. (2000). Control of beta-catenin stability: reconstitution of the cytoplasmic steps of the wnt pathway in *Xenopus* egg extracts. Mol. Cell 5, 523–532.
Sallé, J., Xie, J., Ershov, D., Lacassin, M., Dmitrieff, S. and Minc, N. (2018). Asymmetric division through a reduction of microtubule centering forces. J. Cell Biol. 218, 771–782.
Savoian, M.S., Earnshaw, W.C., Khodjakov, A. and Rieder, C.L. (1999). Cleavage furrows formed between centrosomes lacking an intervening spindle and chromosomes contain microtubule bundles, INCENP and CHO1 but not CENP-E. Mol. Biol. Cell 10, 297–311.
Schaedel, L., John, K., Gaillard, J., Nachury, M. V., Blanchoin, L. and Thery, M. (2015). Microtubules self-repair in response to mechanical stress. Nat. Mater. 14, 1156–1163.
Schaefer, M., Shevchenko, A., Shevchenko, A. and Knoblich, J.A. (2000). A protein complex containing inscuteable and the Gα-binding protein pins orients asymmetric cell divisions in *Drosophila*. Curr. Biol. 10, 353–362.
Schaefer, M., Petronczki, M., Dorner, D., Forte, M. and Knoblich, J.A. (2001). Heterotrimeric G proteins direct two modes of asymmetric cell division in the *Drosophila* nervous system. Cell 107, 183–194.
Schlager, M.A., Hoang, H.T., Urnavicius, L., Bullock, S.L. and Carter, A.P. (2014a). In vitro reconstitution of a highly processive recombinant human dynein complex. EMBO J. 33, 1855–1868.
Schlager, M.A., Serra-Marques, A., Grigoriev, I., Gumy, L., Esteves da Silva, M., Wulf, P.S., Akhmanova, A. and Hoogenraad, C.C. (2014b). Bicaudal D Family adaptor proteins control the velocity of dynein-based movements. Cell Rep. 8, 1248–1256.
Schmidt, D.J., Rose, D.J., Saxton, W.M. and Strome, S. (2005). Functional analysis of cytoplasmic dynein heavy chain in *Caenorhabditis elegans* with fast-acting temperature-sensitive mutations. Mol. Biol. Cell 16, 1200–1212.
Schmidt, R., Fielmich, L-E., Grigoriev, I., Katrukha, E.A., Akhmanova, A. and van den Heuvel, S. (2017). Two populations of cytoplasmic dynein contribute to spindle positioning in *C. elegans* embryos. J. Cell Biol. 216, 2777–2793.
Schmutz, C. (2007). Characterization of the RhoGAP proteins RGA-3 and RGA-4 and the centrosomal protein SAS-5 in the early *Caenorhabditis elegans* embryo.

Schonegg, S., Constantinescu, A.T., Hoege, C. and Hyman, A.A. (2007). The Rho GTPase-activating proteins RGA-3 and RGA-4 are required to set the initial size of PAR domains in *Caenorhabditis elegans* one-cell embryos. Proc. Natl. Acad. Sci. U.S.A. 104, 14976–14981.
Schroeder, C.M. and Vale, R.D. (2016). Assembly and activation of dynein-dynactin by the cargo adaptor protein Hook3. J. Cell Biol. 214, 309–318.
Schroer, T.A. (2004). Dynactin. Annu. Rev. Cell Dev. Biol 20, 759–779.
Schumacher, J.M., Ashcroft, N., Donovan, P.J. and Golden, A. (1998). A highly conserved centrosomal kinase, AIR-1, is required for accurate cell cycle progression and segregation of developmental factors in *Caenorhabditis elegans* embryos. Development 125, 4391–4402.
Schwartz, M.L. and Jorgensen, E.M. (2016). SapTrap, a Toolkit for High-Throughput CRISPR/Cas9 Gene Modification in *Caenorhabditis elegans*. Genetics 202, 1277–1288.
Ségalen, M., Johnston, C.A., Martin, C.A., Dumortier, J.G., Prehoda, K.E., David, N.B., Doe, C.Q. and Bellaïche, Y. (2010). The Fz-Dsh planar cell polarity pathway induces oriented cell division via Mud/NuMA in *Drosophila* and zebrafish. Dev. Cell 19, 740–752.
Seldin, L., Poulson, N.D., Foote, H.P. and Lechler, T. (2013). NuMA localization, stability and function in spindle orientation involve 4.1 and Cdk1 interactions. Mol. Biol. Cell 24, 3651–3662.
Seldin, L., Muroyama, A. and Lechler, T. (2016). NuMA-microtubule interactions are critical for spindle orientation and the morphogenesis of diverse epidermal structures. Elife 5, 1–18.
Sendoel, A., Maida, S., Zheng, X., Teo, Y., Stergiou, L., Rossi, C.A., Subasic, D., Pinto, S.M., Kinchen, J.M., Shi, M., Boettcher, S., Meyer, J.N., Manz, M.G., Bano, D. and Hengartner, M.O. (2014). DEPDC1/LET-99 participates in an evolutionarily conserved pathway for anti-tubulin drug-induced apoptosis. Nat. Cell Biol. 16, 812–820.
Severson, A.F. and Bowerman, B. (2003). Myosin and the PAR proteins polarize microfilament-dependent forces that shape and position mitotic spindles in *Caenorhabditis elegans*. J. Cell Biol. 161, 21–26.
Severson, A.F., Hamill, D.R., Carter, J.C., Schumacher, J. and Bowerman, B. (2000). The Aurora-related kinase AIR-2 recruits ZEN-4/CeMKLP1 to the mitotic spindle at metaphase and is required for cytokinesis. Curr. Biol. 10, 1162–1171.
Severson, A.F., Baillie, D.L. and Bowerman, B. (2002). A formin homology protein and a profilin are required for cytokinesis and Arp2/3-independent assembly of cortical microfilaments in *C. elegans*. Curr. Biol. 12, 2066–2075.
Shannon, K.B., Canman, J.C., Moree, C. Ben, Tirnauer, J.S. and Salmon, E.D. (2005). Taxol-stabilized Microtubules Can Position the Cytokinetic Furrow in Mammalian Cells. Mol. Biol. Cell 16, 4423–4436.
Sheeman, B., Carvalho, P., Sagot, I., Geiser, J., Kho, D., Hoyt, M.A. and Pellman, D. (2003). Determinants of *S. cerevisiae* dynein localization and activation: implications for the mechanism of spindle positioning. Curr. Biol. 13, 364–372.
Siddiqui, S.S. (2002). Metazoan motor models: kinesin superfamily in *C. elegans*. Traffic 3, 20–28.
Siller, K.H. and Doe, C.Q. (2009). Spindle orientation during asymmetric cell division. Nat. Cell Biol. 11, 365–374.
De Simone, A., Nédélec, F. and Gönczy, P. (2016). Dynein transmits polarized actomyosin cortical flows to promote centrosome separation. Cell Rep. 14, 2250–2262.
Skop, A.R. and White, J.G. (1998). The dynactin complex is required for cleavage plane specification in early *Caenorhabditis elegans* embryos. Curr. Biol. 8, 1110–1116.
Sladewski, T.E., Billington, N., Ali, M.Y., Bookwalter, C.S., Lu, H., Krementsova, E.B., Schroer, T.A. and Trybus, K.M. (2018). Recruitment of two dyneins to an mRNA- dependent Bicaudal D transport complex. eLife 7, e36306.
Slep, K.C. and Vale, R.D. (2007). Structural basis of microtubule plus end tracking by XMAP215, CLIP-170 and EB1. Mol. Cell. 27, 976–991.
Somers, W. and Saint, R. (2003). A RhoGEF and Rho family GTPase-activating protein complex links the contractile ring to cortical microtubules at the onset of cytokinesis. Dev. Cell 4, 29–39.
Somma, M.P., Fasulo, B., Cenci, G., Cunadari, E. and Gatti, M. (2002). Molecular dissection of cytokinesis by RNA interference in *Drosophila* cultured cells. Mol. Biol. Cell 13, 2448–2460.
Sönnichsen, B., Koski, L.B., Walsh, A., Marschall, P., Neumann, B., Brehm, M., Alleaume, A.-M., Artelt, J., Bettencourt, P., Cassin, E., Hewitson, M., Holz, C., Khan, M., Lazik, S., Martin, C., Nitzsche, B., Ruer, M., Stamford, J., Winzi, M., Heinkel, R., Röder, M., Finell, J., Häntsch, H., Jones, S.J.M., Jones, M., Piano, F., Gunsalus, K.C., Oegema, K., Gönczy, P., Coulson, A., Hyman, A.A. and Echeverri, C.J. (2005). Full-genome RNAi profiling of early embryogenesis in *Caenorhabditis elegans*. Nature 434, 462–469.
Spiga, F.M., Prouteau, M. and Gotta, M. (2013). The TAO kinase KIN-18 regulates contractility and establishment of polarity in the *C. elegans* embryo. Dev. Biol. 373, 26–38.
Splinter, D., Razafsky, D.S., Schlager, M.A., Serra-Marques, A., Grigoriev, I., Demmers, J., Keijzer, N., Jiang, K., Poser, I., Hyman, A.A., Hoogenraad, C.C., King, S.J. and Akhmanova, A. (2012). BICD2, dynactin and LIS1 cooperate in regulating dynein recruitment to cellular structures. Mol. Biol. Cell 23, 4226–4241.
Srayko, M., Kaya, A., Stamford, J. and Hyman, A.A. (2005). Identification and characterization of factors required for microtubule growth and nucleation in the early *C. elegans* embryo. Dev. Cell 9, 223–236.

Srinivasan, D.G., Fisk, R.M., Xu, H. and Van den Heuvel, S. (2003). A complex of LIN-5 and GPR proteins regulates G protein signaling and spindle function in *C. elegans*. Genes Dev. 17, 1225–1239.
Stein, K.K. and Golden, A. (2015). The *C. elegans* eggshell. *WormBook*, ed. The *C. elegans* Research Community, Wormbook.
Straight, A.F., Field, C.M. and Mitchison, T.J. (2005). Anillin binds nonmuscle myosin II and regulates the contractile ring. Mol. Biol. Cell 16, 193–201.
Strickland, D., Lin, Y., Wagner, E., Hope, C.M., Zayner, J., Antoniou, C., Sosnick, T.R., Weiss, E.L. and Glotzer, M. (2012). TULIPs: tunable, light-controlled interacting protein tags for cell biology. Nat. Methods 9, 379–384.
Su, K.-C., Bement, W.M., Petronczki, M. and von Dassow, G. (2014). An astral simulacrum of the central spindle accounts for normal, spindle-less and anucleate cytokinesis in echinoderm embryos. Mol. Biol. Cell 25, 4049–4062.
Su, K.C., Takaki, T. and Petronczki, M. (2011). Targeting of the RhoGEF Ect2 to the equatorial membrane controls cleavage furrow formation during cytokinesis. Dev. Cell 21, 1104–1115.
Sugioka, K., Fielmich, L.-E., Mizumoto, K., Bowerman, B., Van Den Heuvel, S., Kimura, A. and Sawa, H. (2018). Tumor suppressor APC is an attenuator of spindle-pulling forces during *C. elegans* asymmetric cell division. Proc. Natl. Acad. Sci. U.S.A. 115, 954–963.
Sulston, J. E., Horvitz, H.R. (1977). Post-embryonic cell lineages of the Nematode, *Caenorhabditis elegans*. Dev. Biol. 56, 110–156.
Sulston, J.E. and Horvitz, H.R. (1981). Abnormal cell lineages in mutants of the nematode *Caenorhabditis elegans*. Dev. Biol. 82, 41–55.
Sulston, J.E., Schierenberg, E., White, J.G. and Thomson, J.N. (1983). The embryonic cell lineage of the nematode *Caenorhabditis elegans*. Dev. Biol. 100, 64–119.
Suzuki, K., Sako, K., Akiyama, K., Isoda, M., Senoo, C., Nakajo, N., Sagata, N. (2015). Identification of non-Ser/Thr-Pro consensus motifs for Cdk1 and their roles in mitotic regulation of C2H2 zinc finger proteins and Ect2. Sci. Rep. 5, 7929.
Tagawa, A., Rappleye, C.A. and Aroian, R. V (2001). *pod-2*, along with *pod-1*, defines a new class of genes required for polarity in the early *Caenorhabditis elegans* embryo. Dev. Biol. 233, 412–424.
Takeshita, H. and Sawa, H. (2005). Asymmetric cortical and nuclear localizations of WRM-1/beta-catenin during asymmetric cell division in *C. elegans*. Genes Dev. 19, 1743–8.
Tall, G.G. and Gilman, A.G. (2005). Resistance to inhibitors of cholinesterase 8A catalyzes release of Gαi-GTP and nuclear mitotic apparatus protein (NuMA) from NuMA/LGN/Gαi-GDP complexes. Proc. Natl. Acad. Sci. U.S.A. 102, 16584–16589.
Tall, G.G., Krumins, A.M. and Gilman, A.G. (2003). Mammalian Ric-8A (synembryn) is a heterotrimeric Gα protein guanine nucleotide exchange factor. J. Biol. Chem. 278, 8356–8362.
Tame, M.A., Raaijmakers, J.A., van den Broek, B., Lindqvist, A., Jalink, K. and Medema, R.H. (2014). Astral microtubules control redistribution of dynein at the cell cortex to facilitate spindle positioning. Cell Cycle 13, 1162–1170.
Tame, M.A., Raaijmakers, J.A., Afanasyev, P. and Medema, R.H. (2016). Chromosome misalignments induce spindle-positioning defects. EMBO Rep. 17, 317–325.
Tamura, N., Simon, J.E., Nayak, A., Shenoy, R., Hiroi, N., Boilot, V., Funahashi, A. and Draviam, V.M. (2015). A proteomic study of mitotic phase-specific interactors of EB1 reveals a role for SXIP-mediated protein interactions in anaphase onset. Biol. Open. 4, 155–69.
Tatsumoto, T., Xie, X., Blumenthal, R., Okamoto, I. and Miki, T. (1999). Human ECT2 is an exchange factor for Rho GTPases, phosphorylated in G2/M phases and involved in cytokinesis. Cell 147, 921–927.
Tcherkezian, J. and Lamarche-Vane, N. (2007). Current knowledge of the large RhoGAP family of proteins. Biol. Cell 99, 67–86.
Teichmann, E. (1903). Über die Beziehung zwischen Astrosphären und Furchen: Experimentelle Untersuchungen am Seeigelei. Wilhelm Roux Arch. Entwickl. Mech. Org. 243–327.
Terasawa, M., Toya, M., Motegi, F., Mana, M., Nakamura, K. and Sugimoto, A. (2010). *Caenorhabditis elegans* ortholog of the p24/p22 subunit, DNC-3, is essential for the formation of the dynactin complex by bridging DNC-1/p150Glued and DNC-2/dynamitin. Genes to Cells 15, 1145–1157.
Théry, M., Racine, V., Pépin, A., Piel, M., Chen, Y., Sibarita, J.B. and Bornens, M. (2005). The extracellular matrix guides the orientation of the cell division axis. Nat. Cell Biol. 7, 947–953.
Thomas, C.J., Tall, G.G., Adhikari, A. and Sprang, S.R. (2008). Ric-8A catalyzes guanine nucleotide exchange on G alphai1 bound to the GPR/GoLoco exchange inhibitor AGS3. J. Biol. Chem. 283, 23150–23160.
Timmons, L. and Fire, A. (1998). Specific interference by ingested dsRNA. Nature 395, 854.
Toba, S., Watanabe, T.M., Yamaguchi-Okimoto, L., Toyoshima, Y.Y. and Higuchi, H. (2006). Overlapping hand-over-hand mechanism of single molecular motility of cytoplasmic dynein. Proc. Natl. Acad. Sci. U.S.A. 103, 5741–5745.
Toya, M. and Takeichi, M. (2016). Organization of non-centrosomal microtubules in epithelial cells. Cell Struct. Funct. 41, 127–135.

Toya, M., Iida, Y. and Sugimoto, A. (2010). Imaging of mitotic spindle dynamics in *Caenorhabditis elegans* embryos. Meth. Cell Biol. 97, 359-372.
Toyoshima, F. and Nishida, E. (2007). Integrin-mediated adhesion orients the spindle parallel to the substratum in an EB1- and myosin X-dependent manner. EMBO J. 26, 1487–1498.
Tran, P.T., Marsh, L., Doye, V., Inoué, S. and Chang, F. (2001). A mechanism for nuclear positioning in fission yeast based on microtubule pushing. J. Cell Biol. 153, 397–411.
Tsai, M.C. and Ahringer, J. (2007). Microtubules are involved in anterior-posterior axis formation in *C. elegans* embryos. J. Cell Biol. 179, 397–402.
Tse, Y.C., Piekny, A. and Glotzer, M. (2011). Anillin promotes astral microtubule-directed cortical myosin polarization. Mol. Biol. Cell 22, 3165–3175.
Tse, Y.C., Werner, M., Longhini, K.M., Labbe, J.C., Goldstein, B. and Glotzer, M. (2012). RhoA activation during polarization and cytokinesis of the early *Caenorhabditis elegans* embryo is differentially dependent on NOP-1 and CYK-4. Mol. Biol. Cell 23, 4020–4031.
Tsou, M.-F.B., Hayashi, A., DeBella, L.R., McGrath, G. and Rose, L.S. (2002). LET-99 determines spindle position and is asymmetrically enriched in response to PAR polarity cues in *C. elegans* embryos. Development 129, 4469–4481.
Tsou, M.F.B., Ku, W., Hayashi, A. and Rose, L.S. (2003a). PAR-dependent and geometry-dependent mechanisms of spindle positioning. J. Cell Biol. 160, 845–855.
Tsou, M.F.B., Hayashi, A. and Rose, L.S. (2003b). LET-99 opposes Gα/GPR signaling to generate asymmetry for spindle positioning in response to PAR and MES-1/SRC-1 signaling. Development 130, 5717–5730.
Tursun, B., Patel, T., Kratsios, P. and Hobert, O. (2011). Direct conversion of *C. elegans* germ cells into specific neuron types. Science 331, 304–308.
Urnavicius, L., Zhang, K., Diamant, A.G., Motz, C., Schlager, M.A., Yu, M., Patel, N.A., Robinson, C. V. and Carter, A.P. (2015). The structure of the dynactin complex and its interaction with dynein. Science 347, 1441–1446.
Urnavicius, L., Lau, C.K., Elshenawy, M.M., Morales-Rios, E., Motz, C., Yildiz, A. and Carter, A.P. (2018). Cryo-EM shows how dynactin recruits two dyneins for faster movement. Nature 554, 202–206.
Valfort, A.C., Launay, C., Sémon, M. and Delattre, M. (2018). Evolution of mitotic spindle behavior during the first asymmetric embryonic division of nematodes. PLoS Biol. 1, 1-23.
Vaughan, K.T., Hughes, S.H., Echeverri, C.J., Faulkner, N.F. and Vallee, R.B. (1999). Co-localization of dynactin and cytoplasmic dynein with CLIP-170 at microtubule distal ends. J. Cell Sci. 112, 1437–1447.
Vaughan, P.S., Miura, P., Henderson, M., Byrne, B. and Vaughan, K.T. (2002). A role for regulated binding of p150(Glued) to microtubule plus ends in organelle transport. J. Cell Biol. 158, 305–319.
Vemu, A., Szczesna, E., Zehr, E.A., Spector, J.O., Grigorieff, N., Deaconescu, A.M. and Roll-Mecak, A. (2018). Severing enzymes amplify microtubule arrays through lattice GTP-tubulin incorporation. Science 361, 1-12.
Verbrugghe, K.J.C. and White, J.G. (2004). SPD-1 is required for the formation of the spindle midzone but is not essential for the completion of cytokinesis in *C. elegans* embryos. Curr. Biol. 14, 1755–1760.
Verbrugghe, K.J.C. and White, J.G. (2007). Cortical centralspindlin and Gα have parallel roles in furrow initiation in early *C. elegans* embryos. J. Cell Sci. 120, 1772–1778.
Verde, F., Dogterom, M., Stelzer, E., Karsenti, E. and Leibler, S. (1992). Control of microtubule dynamics and length by cyclin A- and cyclin B-dependent kinases in *Xenopus* egg extracts. J. Cell Biol. 118, 1097–1108.
Verma, V. and Maresca, T.J. (2019). Microtubule plus-ends act as physical signaling hubs to activate RhoA during cytokinesis. Elife 8, 1–34.
Vernì, F., Somma, M.P., Kristin, C.G., Bonaccorsi, S., Belloni, G., Goldberg, M.L. and Gatti, M. (2004). Feo, the *Drosophila* homolog of PRC1, is required for central-spindle formation and cytokinesis. Curr. Biol. 14, 1569–1575.
Vidal, M., Brachmann, R.K., Fattaey, A., Harlow, E., Boeke, J.D. (1996a). Reverse two-hybrid and one-hybrid systems to detect dissociation of protein-protein and DNA-protein interactions. Proc. Natl. Acad. Sci. U.S.A. 93, 10315–10320.
Vidal, M., Braun, P., Chen, E., Boeke, J.D., Harlow, E. (1996b). Genetic characterization of a mammalian protein-protein interaction domain by using a yeast reverse two-hybrid system. Proc. Natl. Acad. Sci. U.S.A. 93, 10321–10326.
Vleugel, M., Kok, M. and Dogterom, M. (2016). Understanding force-generating microtubule systems through in vitro reconstitution. Cell Adhes. Migr. 10, 475–494.
van der Voet, M., Berends, C.W.H., Perreault, A., Nguyen-Ngoc, T., Gönczy, P., Vidal, M., Boxem, M. and van den Heuvel, S. (2009). NuMA-related LIN-5, ASPM-1, calmodulin and dynein promote meiotic spindle rotation independently of cortical LIN-5/GPR/Gα. Nat. Cell Biol. 11, 269–277.
de Vries, L., Fischer, T., Tronchère, H., Brothers, G.M., Strockbine, B., Siderovski, D.P. and Farquhar, M.G. (2000). Activator of G protein signaling 3 is a guanine dissociation inhibitor for gα subunits. Proc. Natl. Acad. Sci. U.S.A. 97, 14364–14369.
Waaijers, S., Portegijs, V., Kerver, J., Lemmens, B.B.L.G., Tijsterman, M., van den Heuvel, S. and Boxem, M. (2013). CRISPR/Cas9-targeted mutagenesis in *Caenorhabditis elegans*. Genetics 195, 1187–1191.

Waaijers, S., Boxem, M. (2014). Engineering the *Caenorhabditis elegans* genome with CRISPR/Cas9. Methods 68, 381-388.
Wagner, E. and Glotzer, M. (2016). Local RhoA activation induces cytokinetic furrows independent of spindle position and cell cycle stage. J. Cell Biol. 213, 641–649.
Wallenfang, M.R. and Seydoux, G. (2000). Polarization of the anterior-posterior axis of *C. elegans* is a microtubule-directed process. Nature 408, 89–92.
Wang, Y.L. (2001). The mechanism of cytokinesis: reconsideration and reconciliation. Cell Struct. Funct. 26, 633–638.
Wang, H., Ng, K.H., Qian, H., Siderovski, D.P., Chia, W. and Yu, F. (2005). Ric-8 controls *Drosophila* neural progenitor asymmetric division by regulating heterotrimeric G proteins. Nat. Cell Biol. 7, 1091–1098.
Wang, H., Vilela, M., Winkler, A., Tarnawski, M., Schlichting, I., Yumerefendi, H., Kuhlman, B., Liu, R., Danuser, G. and Hahn, K.M. (2016). LOVTRAP: an optogenetic system for photoinduced protein dissociation. Nat. Methods 13, 755–758.
Ward, J.D. (2015). Rapid and precise engineering of the *Caenorhabditis elegans* genome with lethal mutation co-conversion and inactivation of NHEJ repair. Genetics 199, 363–377.
Werner, M., Munro, E. and Glotzer, M. (2007). Astral signals spatially bias cortical myosin recruitment to break symmetry and promote cytokinesis. Curr. Biol. 17, 1286–1297.
Wheatley, S.P., Hinchcliffe, E.H., Glotzer, M., Hyman, A.A., Sluder, G. and Wang, Y.L. (1997). CDK1 inactivation regulates anaphase spindle dynamics and cytokinesis in vivo. J. Cell Biol. 138, 385–393.
White, E.A. and Glotzer, M. (2012). Centralspindlin: at the heart of cytokinesis. Cytoskeleton 69, 882–892.
White, J.G. and Borisy, G.G. (1983). On the mechanisms of cytokinesis in animal cells. J. Theor. Biol. 101, 289–316.
Wilde, A., Lizarraga, S.B., Zhang, L., Wiese, C., Gliksman, N.R., Walczak, C.E. and Zheng, Y. (2001). Ran stimulates spindle assembly by altering microtubule dynamics and the balance of motor activities. Nat. Cell Biol. 3, 221–227.
Wildwater, M., Sander, N., de Vreede, G., van den Heuvel, S. (2011). Cell shape and Wnt signaling redundantly control the division axis of *C. elegans* epithelial stem cells. Dev. Camb. Engl. 138, 4375–4385.
Wilson, E.B. (1928). The cell in development and heredity (New York, NY).
Wolf, F., Sigl, R. and Geley, S. (2007). '… The End of the Beginning': Cdk1 Thresholds and Exit from Mitosis. Cell Cycle 6, 1407–1410.
Wolfe, B.A., Takaki, T., Petronczki, M. and Glotzer, M. (2009). Polo-like kinase 1 directs assembly of the HsCyk-4 RhoGAP/Ect2 RhoGEF complex to initiate cleavage furrow formation. PLoS Biol. 7, e1000110.
Wolpert, L., Smith, J., Jessel, T., Lawrence, P., Robertson, E., Meyerowitz, E. (2007). Principles of development (Oxford University Press).
Wolpert, L. (1960). The mechanics and mechanism of cleavage. Int. Rev. Cytol. 10, 163–216.
Wong, H.C., Mao, J., Nguyen, J.T., Srinivas, S., Zhang, W., Liu, B., Li, L., Wu, D. and Zheng, J. (2000). Structural basis of the recognition of the dishevelled DEP domain in the Wnt signaling pathway. Nat. Struct. Biol. 7, 1178–1184.
Woodard, G.E., Huang, N.-N., Cho, H., Miki, T., Tall, G.G. and Kehrl, J.H. (2010). Ric-8A and Giα recruit LGN, NuMA and dynein to the cell cortex to help orient the mitotic spindle. Mol. Cell. Biol. 30, 3519–3530.
Wu, G., Huang, H., Garcia Abreu, J. and He, X. (2009). Inhibition of GSK3 phosphorylation of beta-catenin via phosphorylated PPPSPXS motifs of Wnt coreceptor LRP6. PloS One 4, e4926.
Wu, J.C., Espiritu, E.B. and Rose, L.S. (2016). The 14-3-3 protein PAR-5 regulates the asymmetric localization of the LET-99 spindle positioning protein. Dev. Biol. 412, 288–297.
Yamada, T., Hikida, M. and Kurosaki, T. (2006). Regulation of cytokinesis by mgcRacGAP in B lymphocytes is independent of GAP activity. Exp. Cell Res. 312, 3517–3525.
Xia, P., Wang, Z., Liu, X., Wu, B., Wang, J., Ward, T., Zhang, L. and Ding, X. (2012). EB1 acetylation by P300/CBP-associated factor (PCAF) ensures accurate kinetochore–microtubule interactions in mitosis. PNAS 109, 16564-16569.
Yang, C., Wu, J., de Heus, C., Grigoriev, I., Liv, N., Yao, Y., Smal, I., Meijering, E., Klumperman, J., Qi, R.Z. and Akhmanova, A. (2017). EB1 and EB3 regulate microtubule minus end organization and Golgi morphology. J. Cell Biol. 216, 3179–3198.
Yoshiura, S., Ohta, N. and Matsuzaki, F. (2012). Tre1 GPCR signaling orients stem cell divisions in the *Drosophila* central nervous system. Dev. Cell 22, 79–91.
Yüce, O., Piekny, A. and Glotzer, M. (2005). An ECT2-centralspindlin complex regulates the localization and function of RhoA. J. Cell Biol. 170, 571–582.
Zadran, S., Standley, S., Wong, K., Otiniano, E., Amighi, A. and Baudry, M. (2012). Fluorescence resonance energy transfer (FRET)-based biosensors: visualizing cellular dynamics and bioenergetics. Appl. Microbiol. Biotechnol. 96, 895–902.
Zanic, M., Widlund, P.O., Hyman, A.A. and Howard, J. (2013). Synergy between XMAP215 and EB1 increases microtubule growth rates to physiological levels. Nat. Cell Biol. 15, 1–8.

Zavortink, M., Contreras, N., Addy, T., Bejsovec, A. and Saint, R. (2005). Tum/RacGAP50C provides a critical link between anaphase microtubules and the assembly of the contractile ring in *Drosophila melanogaster*. J. Cell Sci. 118, 5381–5392.
Zeng, X., Tamai, K., Doble, B., Li, S., Huang, H., Habas, R., Okamura, H., Woodgett, J. and He, X. (2005). A dual-kinase mechanism for Wnt co-receptor phosphorylation and activation. Nature 438, 873–7.
Zeng, K., Bastos, R.N., Barr, F.A. and Gruneberg, U. (2010). Protein phosphatase 6 regulates mitotic spindle formation by controlling the T-loop phosphorylation state of Aurora A bound to its activator TPX2. J. Cell Biol. 191, 1315–1332.
Zhang, D. and Glotzer, M. (2015). The RhoGAP activity of CYK-4/MgcRacGAP functions non-canonically by promoting RhoA activation during cytokinesis. Elife 4, 1–25.
Zhang, J., Qiu, R., Arst, H.N., Peñalva, M.A. and Xiang, X. (2014). HookA is a novel dynein-early endosome linker critical for cargo movement in vivo. J. Cell Biol. 204, 1009–1026.
Zhang, L., Ward, J.D., Cheng, Z. and Dernburg, A.F. (2015a). The auxin-inducible degradation (AID) system enables versatile conditional protein depletion in *C. elegans*. Development. 142, 4374–4384.
Zhang, R., Alushin, G.M., Brown, A. and Nogales, E. (2015b). Mechanistic origin of microtubule dynamic instability and its modulation by EB proteins. Cell. 162, 849–859.
Zhang, K., Foster, H.E., Rondelet, A., Lacey, S.E., Bahi-Buisson, N., Bird, A.W. and Carter, A.P. (2017). Cryo-EM reveals how human cytoplasmic dynein is auto-inhibited and activated. Cell 169, 1303-1314.
Zhang, D., Tu, S., Stubna, M., Wu, W., Huang, W., Weng, Z. and Lee, H. (2018). The piRNA targeting rules and the resistance to piRNA silencing in endogenous genes. Science 592, 587–592.
Zhao, W.M. and Fang, G. (2005). MgcRacGAP controls the assembly of the contractile ring and the initiation of cytokinesis. Proc. Natl. Acad. Sci. U.S.A. 102, 13158–13163.
Zhao, P., Teng, X., Tantirimudalige, S.N., Nishikawa, M., Wohland, T., Toyama, Y. and Motegi, F. (2019). Aurora-A breaks symmetry in contractile actomyosin networks independently of Its role in centrosome maturation. Dev. Cell 48, 631-645.
Zheng, Z., Zhu, H., Wan, Q., Liu, J., Xiao, Z., Siderovski, D.P. and Du, Q. (2010). LGN regulates mitotic spindle orientation during epithelial morphogenesis. J. Cell Biol. 189, 275–288.
Zheng, Z., Wan, Q., Meixiong, G. and Du, Q. (2014). Cell cycle-regulated membrane binding of NuMA contributes to efficient anaphase chromosome separation. Mol. Biol. Cell 25, 606–619.
Zhou, M. and Wang, Y.-L. (2008). Distinct pathways for the early recruitment of myosin II and actin to the cytokinetic furrow. Mol. Biol. Cell 19, 318-326.
Zhu, C. and Jiang, W. (2005). Cell cycle-dependent translocation of PRC1 on the spindle by Kif4 is essential for midzone formation and cytokinesis. Proc. Natl. Acad. Sci. U.S.A. 102, 343–348.
Zhu, C., Lau, E., Schwarzenbacher, R., Bossy-Wetzel, E. and Jiang, W. (2008). Spatiotemporal control of spindle midzone formation by PRC1 in human cells. PNAS 103, 6196–6201.
Zhu, J., Wen, W., Zheng, Z., Shang, Y., Wei, Z., Xiao, Z., Pan, Z., Du, Q., Wang, W. and Zhang, M. (2011). LGN/mInsc and LGN/NuMA complex structures suggest distinct functions in asymmetric cell division for the Par3/mInsc/LGN and Gαi/LGN/NuMA pathways. Mol. Cell 43, 418–431.
Zimmerman, S.P., Hallett, R.A., Bourke, A.M., Bear, J.E., Kennedy, M.J. and Kuhlman, B. (2016). Tuning the binding affinities and reversion kinetics of a light inducible dimer allows control of transmembrane protein localization. Biochemistry 55, 5264–5271.
Zimniak, T., Stengl, K., Mechtler, K. and Westermann, S. (2009). Phosphoregulation of the budding yeast EB1 homologue Bim1p by Aurora/Ipl1p. J. Cell Biol. 186, 379–391.
Zonies, S., Motegi, F., Hao, Y. and Seydoux, G. (2010). Symmetry breaking and polarization of the *C. elegans* zygote by the polarity protein PAR-2. Development 137, 1669–1677.
Zwaal, R.R., Ahringer, J., Van Luenen, H.G.A.M., Rushforth, A. anderson, P. and Plasterk, R.H.A. (1996). G proteins are required for spatial orientation of early cell cleavages in *C. elegans* embryos. Cell 86, 619–629.

Nederlandse samenvatting

Introductie: de cel

Biologie is de natuurwetenschap waarin we bestuderen hoe het leven op aarde functioneert. Dit leven is eindeloos complex en bestaat uit miljoenen soorten van onder andere bacteriën, schimmels, planten en dieren. Afgezien van hun overdonderende diversiteit zijn er ook veel overeenkomsten tussen deze soorten te vinden. Al het leven bestaat namelijk uit cellen. Dit zijn de basiseenheden waaruit ieder organisme is opgebouwd. Zij het een ééncellige zoals een bacterie of sommige schimmels, of de mens met ongeveer 37,2 triljoen (37.200.000.000.000.000.000) cellen, we bestaan allemaal uit grofweg dezelfde bouwstenen.

Een cel kan in het lichaam verschillende functies vervullen. Zo geeft bijvoorbeeld een neuron informatie door, slaan vetcellen energie op, transporteren rode bloedcellen zuurstof en nemen darmcellen selectief voedingstoffen op. Maar net zoals de verschillende soorten organismen bestaan uit vergelijkbare cellen, bestaan ook deze verschillende cellen uit veelal dezelfde onderdelen. Iedere cel in ons lichaam wordt omsloten door een membraan dat bestaat uit een dunne laag vetzuren. Daarbinnen zijn ruimtes afgebakend waarin chemische processen plaatsvinden. Deze ruimtes worden ook wel organellen genoemd. Ook heeft bijna iedere cel een kern waarin DNA, het genetisch materiaal, wordt opgeslagen. Dit DNA bevat de genen die de blauwdruk vormen van eiwitten die in de cel worden geproduceerd. Deze eiwitten zijn de werkpaarden van de cel en ze vervullen ieder hun eigen functie; zo zal het ene eiwit het andere transporteren naar een specifieke plek binnen de cel, terwijl een ander eiwit de cel laat bewegen of wordt uitgescheiden om zo te communiceren omliggende cellen. Zo zijn er nog vele andere functies op te noemen. Afhankelijk van welke genen in een cel ‘aan’ en ‘uit’ worden gezet zal een andere set eiwitten geproduceerd worden. Uiteindelijk bepaalt dit wat voor type cel er gevormd wordt.

Celdeling en differentiatie

Alle cellen in het menselijk lichaam zijn uiteindelijk afkomstig van één moedercel: een eicel waarin bij de bevruchting het DNA van de vader en moeder worden gecombineerd. Deze enkele cel deelt zich na de bevruchting in twee dochtercellen. Dit proces wordt vele malen herhaald om uiteindelijk tot de hierboven genoemde 37,2 triljoen te komen. Cellen moeten niet alleen heel vaak delen; ze zullen ook onderling moeten bepalen welke cel welke functie gaat vervullen om zo een functionerend organisme te vormen. Uiteindelijk stoppen de meeste cellen met delen en ontwikkelen ze zich verder tot een specifiek celtype, zoals bijvoorbeeld de eerdergenoemde neuronen, vet-, darm- en bloedcellen. Dit proces van ontwikkeling noemen we differentiatie. Hoe celdeling en differentiatie met elkaar gecoördineerd worden om uiteindelijk een werkend organisme te vormen is waar we binnen de ontwikkelingsbiologie in geïnteresseerd zijn.

Ons onderzoek binnen deze stroming is van groot belang. Dit omdat bijvoorbeeld de ziekte kanker, om maar één van vele voorbeelden te noemen, zich ontwikkelt middels ontregelde celdeling. Om dit soort ziekten te kunnen bestrijden is het essentieel om passende geneesmiddelen te ontwikkelen. Hierbij kun je denken aan medicijnen die celdelingen remmen, of die specifiek cellen aanvallen wanneer ze zich ontwikkelen tot een kankercel. Maar hiervoor moeten we wel een goed idee hebben van hoe een cel precies werkt en wat hierin mis kan gaan. Zodoende is de fundamentele wetenschap van groot belang; we proberen in zoveel mogelijk detail te begrijpen wat er in een cel gebeurt zodat we onze natuur een handje kunnen helpen wanneer daar vanuit de maatschappij vraag naar is.

Het *Caenorhabditis elegans* embryo als modelsysteem

In dit proefschrift gebruiken we voornamelijk het ééncellig embryo van een nematode (rondworm) om onderzoek te doen naar celdelingen. Deze nematode, in wetenschappelijke termen aangeduid als *Caenorhabditis elegans* (in het vervolg verkort tot *C. elegans*), is een klassiek modelorganisme binnen de ontwikkelingsbiologie en genetica. Het diertje wordt namelijk al meer dan 40 jaar gebruikt om onderzoek mee te doen. Naast *C. elegans* zijn er veel andere welbekende modelorganismen zoals het fruitvliegje (*Drosophila melanogaster*), de klauwkikker (*Xenopus laevis*), de zebravis (*Danio rerio*) en de huismuis (*Mus musculus*). Deze organismen worden gebruikt om wetenschappelijk onderzoek te verrichten dat niet uitgevoerd mag worden op menselijke embryo's, om duidelijke ethische redenen. Gelukkig zijn van de processen die zich afspelen in de cellen van *C. elegans* en de andere hierboven genoemde voorbeelden sterk vergelijkbaar met wat zich in onze eigen cellen afspeelt. Dit is dan ook de reden dat we door proeven te doen met meerdere modelorganismen veel kunnen leren over hoe de menselijke cel in mekaar steekt.

Een volwassen *C. elegans* wormpje bestaat uit enkel 959 cellen en is maar 1 mm lang. Dus net groot genoeg om met het blote oog te kunnen zien op een petrischaal (**Figuur 1a**, **b**). De wormpjes zijn hermafrodiet; dit wil zeggen dat ze zowel mannelijke als vrouwelijke voortplantingsorganen hebben en zichzelf kunnen bevruchten. Binnen de

Figuur 1. **Celdeling in het ééncellig *C. elegans* embryo.** In dit figuur zoomen we met stappen in op de componenten die in dit proefschrift bestudeerd worden; van een petrischaal met daarop groeiende wormpjes van zo'n 1 mm lang die net met het blote oog zichtbaar zijn (**a**, **b**) tot het ééncellige embryo met dimensies van 50x30 micrometer (**c**). Door de mitotische spoel te verplaatsen van het midden (rode stippellijn) naar de achterkant van de cel (blauwe stippellijn) wordt de eerste celdeling asymmetrisch (**d**). Een schematische weergave laat zien waar de PAR eiwitten (rood en groen) zich bevinden aan de cortex van de cel en hoe dit overeenkomt met de voor- en achterkant van het embryo. De mitotische spoel (blauw) is verbonden met het DNA (paars) en zal voor het delen de chromosomen scheiden (**e**). Als we nog verder inzoomen laat een schematische weergave zien hoe de eiwitten Gα, GPR-1/2, LIN-5 en dynein elkaar aan de celmembraan verbinden en tegelijkertijd trekkracht uitoefenen op een microtubulus van de mitotische spoel (**f**). Foto in (**b**) gemaakt door Victoria Garcia Castiglioni.

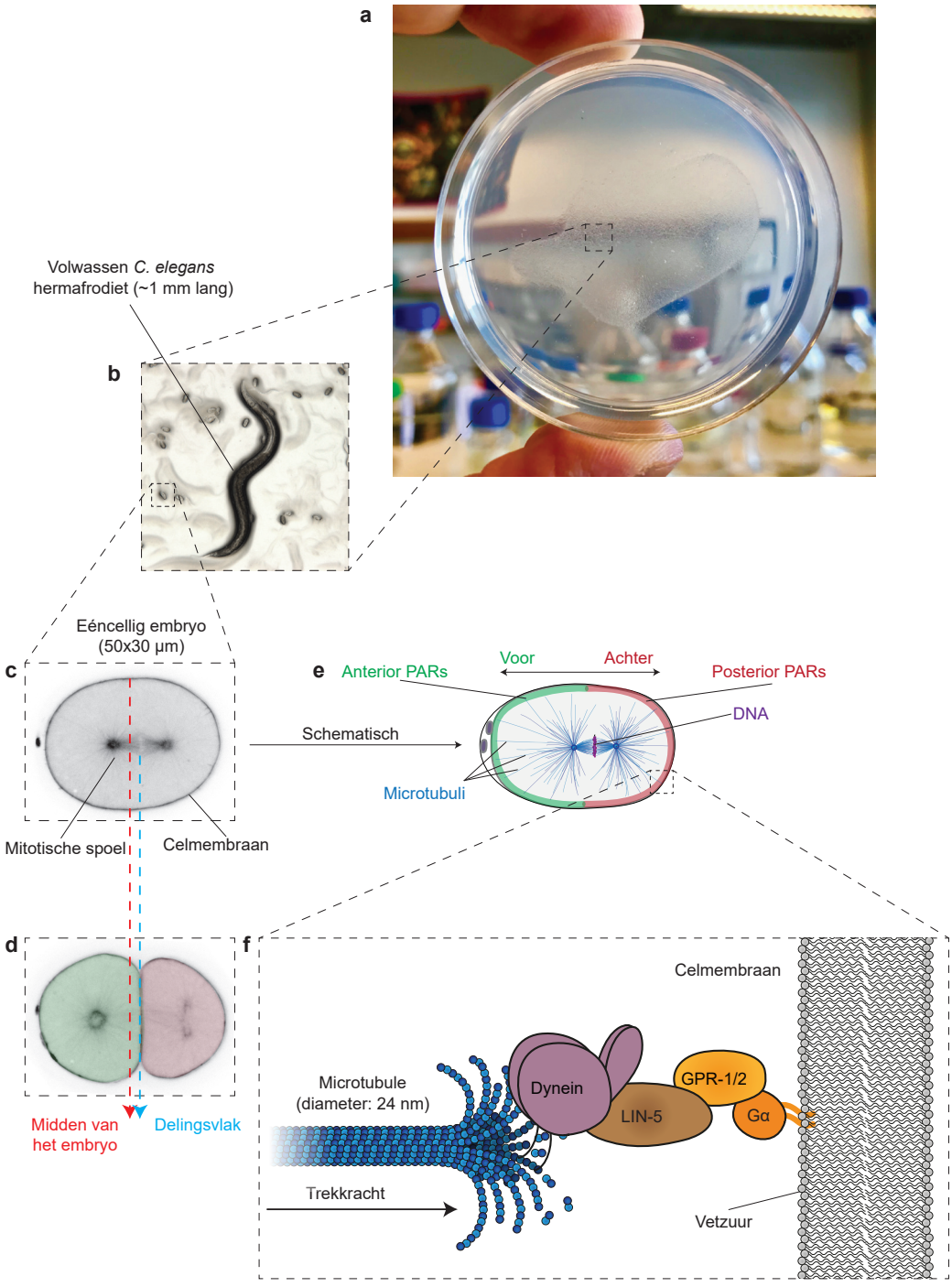
a
Volwassen C. elegans
hermafrodiet (~1 mm lang)
b
Eéncellig embryo
(50x30 µm)
c
Mitotische spoel
Celmembraan
Schematisch
e
Anterior PARs
Voor
Achter
Posterior PARs
DNA
Microtubuli
d
Midden van
het embryo
Delingsvlak
f
Celmembraan
Microtubule
(diameter: 24 nm)
Dynein
LIN-5
GPR-1/2
Gα
Trekkracht
Vetzuur

tijdspanne van een week kan één wormpje zich niet alleen van een bevruchte eicel ontwikkelen tot een volwassen diertje, maar dan ook nog eens zo'n 300 nakomelingen voortbrengen. Dit is één van de vele redenen waarom *C. elegans* een aantrekkelijk modelorganisme is om te gebruiken voor onderzoek. Daarnaast zijn de wormpjes ook grotendeels doorzichtig, wat het mogelijk maakt om veel van diens cellen zonder dissectie te kunnen bestuderen met de microscoop. Verder zijn er doorheen de jaren veel wetenschappelijke technieken ontwikkeld om de worm genetisch aan te passen. Dit is van essentieel belang om de functies van bepaalde genen en de eiwitten die zij produceren te kunnen bestuderen.

Het embryo van *C. elegans* bestaat uit een relatief grote ovale cel van zo'n 50x30 micrometer (een micrometer is een miljoenste deel van een meter). Hierdoor is het embryo zeer goed in beeld te brengen met hedendaagse microscopen (**Figuur 1c**). De eerste celdeling die plaatsvindt in het embryo is asymmetrisch. Dat wil zeggen dat de twee dochtercellen die hierbij gevormd worden niet gelijk zijn qua afmetingen en/of chemische samenstelling (**Figuur 1d**). Eén dochtercel is namelijk groter dan de ander en vormt in opeenvolgende celdelingen de basis voor andere weefsels. Veel van de celdelingen die plaatsvinden in het vroege *C. elegans* embryo zijn asymmetrisch, zo worden veel van de verschillende celtypen die aanwezig zijn in de volwassen worm al vroeg vastgelegd. Dit is ook een van de grote voordelen van *C. elegans* als modelsysteem; van iedere cel in het lichaam van de worm is bekend waar en wanneer deze gevormd wordt. Dit maakt het een gebruiksvriendelijk organisme om afwijkingen in te ontdekken, bijvoorbeeld ten gevolge van genetische variatie. De asymmetrische deling van het ééncellig embryo komt tot stand als gevolg van celpolariteit. Dit betekent dat in de cel onderscheid gemaakt kan worden tussen de symmetrieassen voor, achter, links, rechts, boven en onder. In het ééncellig stadium bestaat er alleen nog een onderscheid tussen voor en achter, of anterieur en posterior in wetenschappelijke termen. De overige symmetrieassen komen in latere stadia van de ontwikkeling tot stand. Het onderscheid tussen voor en achter wordt in het ééncellig embryo gemaakt door verschillende eiwitten die zich aan de tegenovergestelde zijden van de cel bevinden (**Figuur 1e**, schematisch). Deze eiwitten zijn sterk behouden gebleven doorheen miljoenen jaren evolutie; ze vervullen namelijk een vergelijkbare functie in de cellen van andere soorten, waaronder die van de mens. Ze zijn echter voor het eerst gevonden en bestudeerd in *C. elegans*, waarna ze benoemd werden tot de zogeheten PAR-eiwitten. Deze naam is ontleend aan het fenotype (het zichtbare effect van een genetische eigenschap) dat we observeren wanneer deze eiwitten niet functioneel zijn. PAR staat namelijk voor 'partitioning defective'; embryo's waarin PAR-eiwitten niet functioneel zijn kunnen niet goed polariseren en dus niet bepalen wat de voor- en achterkant van het embryo is. Als gevolg vormt het embryo een ongedefinieerde hoop cellen zonder duidelijke organisatie en komt er geen levend wormpje tot stand. Veel genen en eiwitten in *C. elegans* zijn op dezelfde manier benoemd; op basis van het fenotype dat ontstaat wanneer hun functie verstoord wordt.

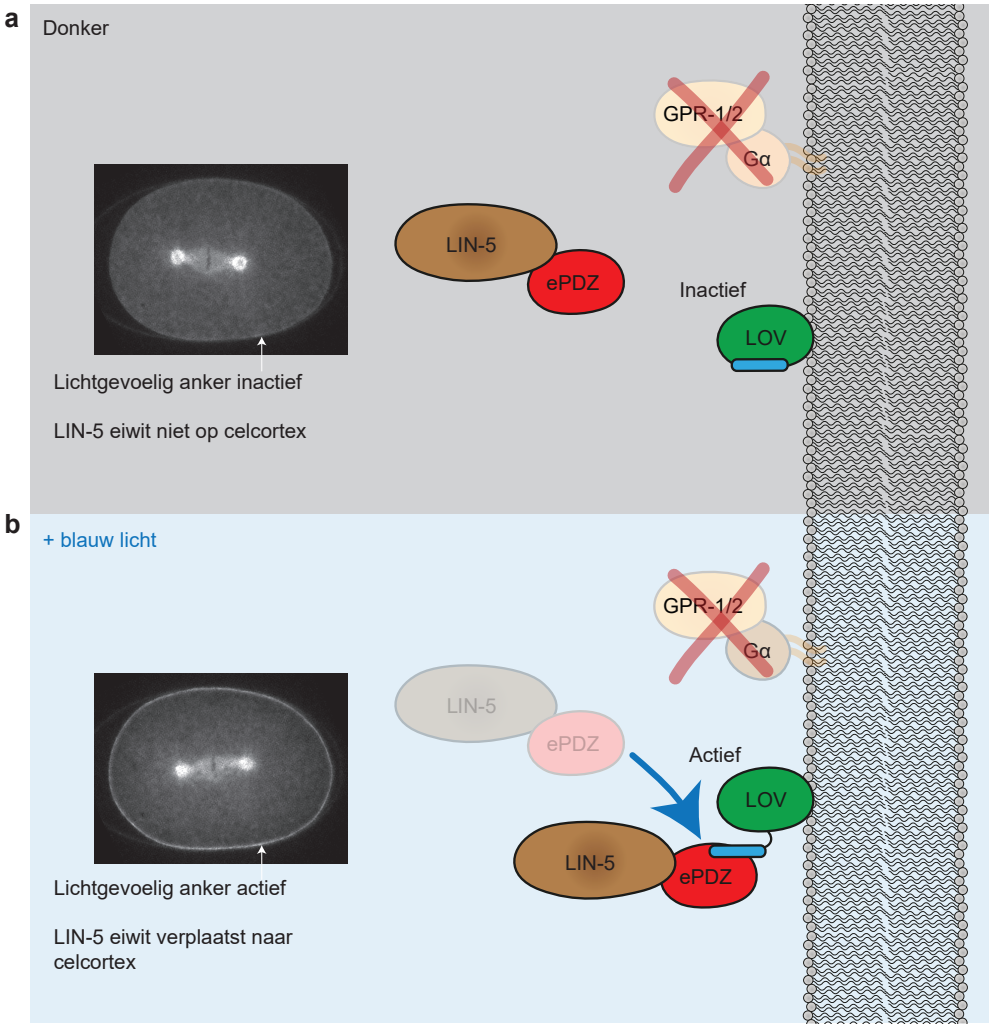

Figuur 2. **Verplaatsing van het eiwit LIN-5 binnen de cel met licht.** Twee afbeeldingen van hetzelfde ééncellig embryo in het donker (**a**) en na blootstelling aan blauw licht (**b**) laten de verplaatsing van LIN-5 naar de cortex van de cel zien. Een schematische weergave (rechts) illustreert hoe het LOV eiwit actief wordt in aanwezigheid van blauw licht en vervolgens het ePDZ eiwit naar de cortex van de cel brengt. LIN-5 bevindt zich in het donker niet meer aan de celmembraan, omdat het anker bestaande uit Gα en GPR-1/2 met een genetische truc is uitgeschakeld.

Van celpolariteit tot asymmetrische deling

Nu komen we tot de vraag waar wij als onderzoeksgroep in geïnteresseerd zijn: hoe wordt celpolariteit vertaald naar een asymmetrische celdeling? Om hier op in te gaan moeten we eerst in detail kijken naar wat er precies gebeurt tijdens de celdeling. Voorafgaand aan het delen wordt al het DNA in de cel gedupliceerd. Het wordt vervolgens evenredig verdeeld

over de twee dochtercellen zodat beide eenzelfde kopie van het DNA erven. Het scheiden van het DNA wordt gedreven door de mitotische spoel, of 'mitotic spindle' in het Engels. Dit is een zeer complexe structuur die bestaat uit minuscule flexibele buisjes, de microtubuli (enkelvoud microtubulus). De doorsnede van zo'n buisje is ongeveer 24 nanometer (een miljardste deel van een meter) **(figuur 1f**). Deze microtubuli zijn opgebouwd uit eiwitten en ze kunnen zeer snel opgebouwd en afgebroken worden; we zeggen ook wel dat ze sterke dynamische instabiliteit vertonen. Voorafgaand aan de celdeling wordt het DNA, bestaande uit meerdere chromosomen, in het midden van de cel verzameld en wordt het vastgegrepen door microtubuli van de twee tegenover elkaar liggende kanten van de cel (F**iguur 1e**; DNA in paars, microtubuli in blauw). De microtubuli trekken dan de chromosomen fysiek uit elkaar, waardoor het zich verplaatst van het midden van de cel en evenredig verdeelt over de twee toekomstige dochtercellen.

Naast het verdelen van het DNA heeft de mitotische spoel ook andere belangrijke functies tijdens de celdeling. Zo bepaalt haar positie ook waar de cel zich precies in tweeën deelt. Het klievingsvlak van de cel richt zich namelijk altijd precies door het midden van de mitotische spoel. Op deze manier kan een gepolariseerde cel asymmetrisch delen. Verplaatst de mitotische spoel namelijk van het midden meer naar de voor- of achterkant van de cel, dan worden bij de asymmetrische deling een grotere en een kleinere dochtercel gevormd. Op deze manier deelt het ééncellig *C. elegans* embryo asymmetrisch; voor het delen verplaatst de mitotische spoel zich namelijk een beetje richting de achterkant, of posterieur, van de cel (**Figuur 1c**, **d**; vergelijk rode en blauwe stippellijn). Daarnaast worden afhankelijk van celpolariteit ook andere eiwitten ongelijk verdeeld over de twee dochtercellen, waardoor hun verdere ontwikkeling van elkaar afwijkt. Dit type deling noemen we een intrinsiek asymmetrische deling, omdat het ééncellig embryo zich ongelijk deelt zonder invloed van omliggende cellen. Er bestaan ook symmetrische delingen waarbij de twee dochtercellen in grootte en inhoud gelijk zijn. Ten slotte zijn er ook extrinsiek asymmetrische delingen, waarbij twee gelijke dochtercellen andere signalen van de cellulaire omgeving ontvangen waardoor hun ontwikkeling op verschillende wijze gestuurd wordt.

Hoe wordt de mitotische spoel gepositioneerd?

Tijdens het positioneren van de mitotische spoel in het ééncellig *C. elegans* embryo worden er trekkrachten van de celcortex, de regio aan de binnenkant van het cel omsluitende membraan, op de spoel uitgeoefend. Deze trekkrachten worden opgewekt door samenwerking van een groep eiwitten bestaande uit Gα, GPR-1/2, en LIN-5. Zij vormen een complex aan de cortex van de cel door aan elkaar te binden terwijl Gα zich aan de membraan bevestigt (**Figuur 1f**). Dit complex functioneert als een anker voor dynein, een zogenaamd motoreiwit. Dynein kan door met twee moleculaire stengeltjes (soms ook wel aangeduid als 'pootjes') achtereenvolgens aan microtubuli te binden een stappende beweging maken. Op deze manier gebruikt dynein de microtubuli als een

moleculaire snelweg waarover het zichzelf en andere componenten van de cel transporteert. Dit is een zeer belangrijke proces binnen het functioneren van de cel, omdat veel eiwitten en organellen niet vanuit zichzelf op de juiste plek terecht kunnen komen; ze moeten daarvoor actief getransporteerd worden. Dynein is dan ook een essentieel en multifunctioneel eiwit. Naast transport zorgt het namelijk ook voor het positioneren van de mitotische spoel. Door via LIN-5 aan de celcortex bevestigd te worden en tegelijkertijd aan microtubuli te binden trekt dynein aan de mitotische spoel (**Figuur 1f**). Eerdere experimenten waarbij de mitotische spoel met een laser doormidden werd gesneden hebben uitgewezen dat de mitotische spoel door asymmetrische trekkrachten wordt gepositioneerd. De krachten die aan de achterkant van de cel worden opgewekt zijn namelijk hoger dan die aan de voorkant. Zo verplaatst de mitotische spoel zich naar de achterkant van de cel en kan deze asymmetrisch delen.

In dit proefschrift onderzoeken we hoe deze asymmetrische trekkrachten worden opgewekt. Er moet namelijk communicatie zijn tussen de eiwitten die de celpolariteit in stand houden en de eiwitten die trekkrachten opwekken. Eerder onderzoek heeft uitgewezen dat de eerste deling van het embryo symmetrisch in plaats van asymmetrisch wordt wanneer de PAR-eiwitten of het eiwitcomplex gevormd door Gα, GPR-1/2, en LIN-5 niet functioneert. Zij zorgen dus samen voor het correct verplaatsen van de mitotische spoel. Eén van de manieren waarop deze eiwitten met elkaar kunnen communiceren is door middel van eiwitmodificaties. Sommige eiwitten kunnen bijvoorbeeld LIN-5 van een extra moleculaire groep, een fosfaat, voorzien. Dit proces noemen we fosforylatie. Dit verandert de gedragingen van het eiwit en kan er bijvoorbeeld voor zorgen dat de interactie met andere eiwitten verandert.

De fosforylering van LIN-5

In hoofdstuk 2 bestuderen we de fosforylatie van het eiwit LIN-5. Voorgaand onderzoek dat verricht werd in ons lab heeft laten zien dat één van de essentiële polariteitseiwitten LIN-5 fosforyleert. Dit gebeurt alleen aan de voorkant van de cel en zorgt ervoor dat specifiek daar trekkrachten worden verlaagd. Dit is één van de manieren waarop LIN-5 wordt gereguleerd tijdens het positioneren van de mitotische spoel. Maar er zijn nog vele andere plekken op het LIN-5 eiwit die gefosforyleerd worden. In dit hoofdstuk gebruiken we een revolutionaire nieuwe techniek, CRISPR/Cas9, om het lin-5 gen (de namen van genen worden in tegenstelling tot eiwitten aangeduid met kleine cursieve letters) dat de blauwdruk is voor het LIN-5 eiwit op verschillende manieren aan te passen. Door fosforylatie van LIN-5 te blokkeren of juist na te bootsen en vervolgens de gedragingen van de mitotische spoel te bestuderen komen we meer te weten over de regulatie van LIN-5. Zo identificeren we bijvoorbeeld een deel van het eiwit dat gefosforyleerd wordt door de zogeheten kinase eiwitten GSK3 en CK1 en benodigd is voor de interactie van LIN-5 met GPR-1/2. Ook vinden we gefosforyleerde onderdelen van LIN-5 die belangrijk zijn voor de interactie met het motoreiwit dynein. Daarnaast presenteren we in dit

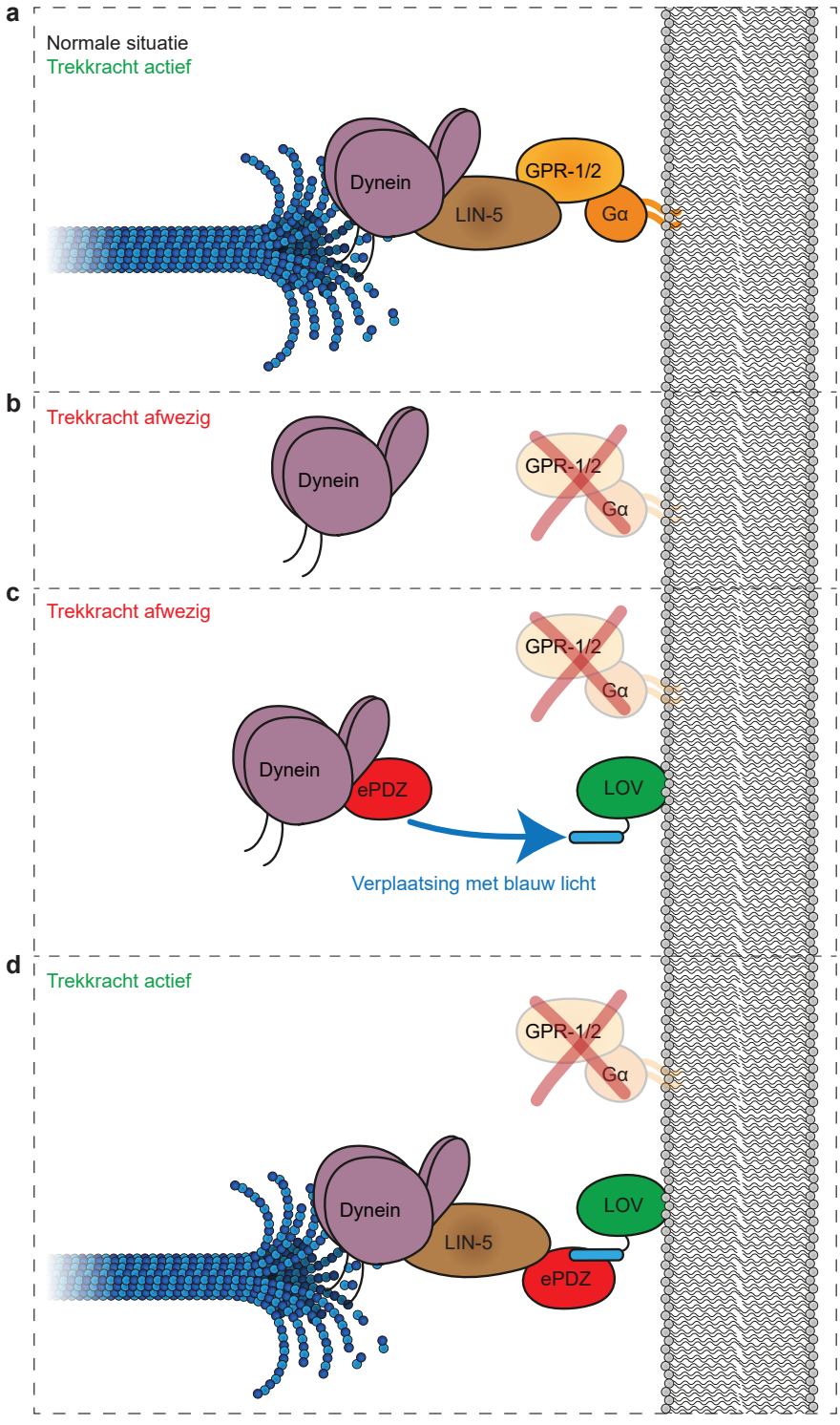
a
Normale situatie
Trekkracht actief
Dynein
LIN-5
GPR-1/2
Gα
b
Trekkracht afwezig
Dynein
GPR-1/2
Gα
c
Trekkracht afwezig
GPR-1/2
Gα
Dynein
ePDZ
LOV
Verplaatsing met blauw licht
d
Trekkracht actief
GPR-1/2
Gα
Dynein
LIN-5
LOV
ePDZ

Figuur 3. **Dynein moet via LIN-5 aan de celmembraan verankerd worden om trekkrachten op te kunnen wekken.** Dit zijn schematische weergaven van een paar proeven uit hoofdstuk 4. In een normale situatie wordt dynein naar de celmembraan gebracht via het anker bestaande uit de eiwitten Gα, GPR-1/2 en LIN-5. Zo kan het aan de microtubuli van de mitotische spoel trekken (**a**). Wanneer het anker wordt verstoord raken deze trekkrachten verloren omdat dynein niet langer op de celmembraan geplaatst wordt (**b**). Wanneer we met het lichtgevoelige LOV anker dynein naar de celmembraan verplaatsen worden nog steeds geen trekkrachten opgewekt (**c**). Dynein alleen is dus niet genoeg voor het genereren van trekkrachten. Wanneer dynein via LIN-5 naar de celmembraan wordt getransporteerd (**d**) kunnen trekkrachten worden opgewekt, zelfs wanneer de normaal zo essentiële onderdelen van het anker, Gα en GPR-1/2, niet functioneren.

hoofdstuk ook een nieuwe methode die gebruikt kan worden om met essentiële genen te werken, welke vaak moeilijk te analyseren zijn omdat ze in niet-functionele vorm de voortplanting van de worm blokkeren. Zo dragen we niet alleen bij aan de kennis over specifiek het functioneren van het eiwitcomplex van Gα, GPR-1/2, LIN-5 en dynein, maar optimaliseren we ook het gebruik van een recente techniek die veel bij kan dragen aan hoe toekomstig onderzoek wordt uitgevoerd.

De dynamiek van dynein

In hoofdstuk 3 onderzoeken we hoe het motoreiwit dynein betrokken is bij mitotische spoel positionering. Een belangrijk aspect van hoe eiwitten functioneren is waar het zich in de cel bevindt en wat voor dynamiek, of beweging, ze vertonen. Eerdere onderzoeken hebben niet goed kunnen laten zien hoe het dynein eiwit zich door de cel heen beweegt in het ééncellig *C. elegans* embryo. In dit hoofdstuk gebruiken we wederom CRISPR/Cas9 om dynein direct te voorzien van een moleculaire groep die groen of rood licht kan afgeven. Zo kunnen we door middel van fluorescentie microscopie het dynein eiwit volgen in het embryo in zowel ruimte en tijd (**Hoofdstuk 3**, **figuur 1d**). Op deze manier ontdekken we voor het eerst dat dynein in *C. elegans* de snelgroeiende eindjes van microtubuli volgt. Microtubuli groeien voornamelijk aan hun zogeheten ‘plus eind’ vanuit de mitotische spoel naar de celcortex. Er zijn veel eiwitten bekend die de groeisnelheid en stabiliteit van microtubuli beïnvloeden door aan het plus eind te binden. Deze eiwitten zijn belangrijk om de groeidynamiek van microtubuli nauw te reguleren. Microtubuli groeien namelijk niet altijd met dezelfde snelheid en stabiliteit of naar dezelfde plek in de cel; het netwerk van microtubuli wordt constant gemoduleerd om bepaalde processen mogelijk te maken. Dit is vooral goed zichtbaar in verschillende stadia van de celcyclus, of de elkaar opvolgende fasen van celgroei en celdeling die een cel doormaakt. Tijdens interfase wanneer de cel onder andere groeit, heeft het netwerk van microtubuli een compleet andere organisatie vergeleken met de fase waarin celdeling plaatsvindt.

Aan het plus eind van microtubuli bindt een dicht netwerk bestaande uit veel verschillende eiwitten. De ‘end binding proteins’, ook wel EB-eiwitten, worden gezien als de basis waaruit dit netwerk is opgebouwd. De EB-eiwitten binden vanuit zichzelf aan het groeiende plus eind van microtubuli. Vervolgens rekruteren zij andere eiwitten die niet direct aan het groeiende eind van de microtubule kunnen binden. Door één van de

EB-eiwitten in het *C. elegans* embryo uit te schakelen konden we ervoor zorgen dat dynein niet langer op het groeiende plus eind van de microtubuli terecht komt. Interessant genoeg had dit geen tot weinig effect op hoe de mitotische spoel gepositioneerd wordt en hoe de cel deelt. Vervolgens schakelden we alle drie de EB-eiwitten die bekend zijn in *C. elegans* uit. Ook dit leek, tot onze grote verbazing, relatief weinig effect te hebben. Pas wanneer we de functie van dynein deels verstoorden in afwezigheid van een EB-eiwit, zagen we dat de trekkrachten die op de mitotische spoel uitgeoefend worden afnamen. Dit is interessant omdat het laat zien hoe robuust dit systeem werkelijk is; zelfs wanneer we een belangrijke schakel in het netwerk verstoren kunnen essentiële processen nog steeds plaatsvinden. Er is namelijk een tweede populatie van dynein die aan de cortex bindt via LIN-5, zoals hierboven beschreven. We kijken naar de dynamiek die deze populatie vertoont met een techniek genaamd FRAP (fluorescence recovery after photobleaching). Kortgezegd bleken we hiervoor lokaal een aantal dynein moleculen zodat ze geen licht meer uitstralen, en observeren we vervolgens hoe dit 'zwarte gat' wordt opgevuld door andere, nog wel fluorescente, moleculen uit de directe omgeving (**Hoofdstuk 3**, **figuur 6d**). Met welke snelheid en volledigheid dit gebeurt geeft een beeld van hoe dynamisch het bestudeerde eiwit is in de cel. Door dit te doen vonden we dat dynein verschillende mate van dynamiek vertoont aan de voor- en achterkant van de cel, en dit was afhankelijk van de functie van de hierboven beschreven PAR-polariteitseiwitten. Door dynein eiwitten van een fluorescente groep te voorzien hebben we dus gevonden dat er twee populaties van dynein bestaan; één aan het groeiende plus eind van microtubuli en één aan de celcortex. Het belang van de populatie aan het plus eind werd pas duidelijk bij gedeeltelijke verstoring van het dynein eiwit, wat aangeeft dat het als een 'back-up' kan worden gebruikt. Zo zou het systeem bijvoorbeeld nog steeds kunnen functioneren wanneer er genetische mutaties ontstaan, waardoor anders celdelingen verstoord zouden worden.

Het sturen van de mitotische spoel met licht

In hoofdstuk 4 gaan we pas echt experimenteel aan de slag. Het anker van dynein aan de celcortex bestaat uit drie eiwitten; Gα, GPR-1/2, en LIN-5 (**Figuur 1f**). Als de functie van deze eiwitten puur is om dynein naar de celcortex te brengen, zijn hier dan wel drie verschillende eiwitten voor nodig? Hebben zij individuele functies naast het bepalen van de lokalisatie van dynein binnen de cel, of vervullen ze samen één en dezelfde functie? Een klassieke methode om de functie van een eiwit te bestuderen is om het weg te halen of te muteren zodat het niet-functioneel wordt, om vervolgens te observeren wat voor effect dit heeft op processen in de cel. Voor Gα, GPR-1/2, en LIN-5 levert dit echter een probleem op. Als één van deze eiwitten niet functioneert, wordt de mitotische spoel niet langer correct gepositioneerd omdat dynein niet naar de celcortex gebracht wordt. Het bestuderen van hun individuele functies wordt hierdoor bemoeilijkt. In hoofdstuk 4 gebruiken we een experimentele omweg om alsnog de individuele functies van

Gα, GPR-1/2, en LIN-5 te kunnen bestuderen. Naast het verbinden van een fluorescent molecuul aan eiwitten kunnen ze namelijk ook op andere manieren worden aangepast. Door ze te verbinden met een relatief klein 'ePDZ' eiwit kunnen we een eiwit van interesse binnen de cel naar een andere plek sturen met licht. Dit is een relatief nieuwe techniek die niet eerder in het *C. elegans* embryo werd toegepast, ook al hebben meerdere labs dit in de afgelopen jaren geprobeerd. Om technische redenen was dit een lastig proces waar we jaren in hebben geïnvesteerd voordat het werkte. Onze modificaties van *C. elegans* genen kunnen er namelijk voor zorgen dat deze niet langer door de cel als eigen wordt beschouwd. Dit kan ertoe leiden dat een gen uitgeschakeld wordt, wat het onmogelijk maakt om de proef die we voor ogen hebben uit te voeren. Als omweg hebben we de genetische code van deze modificaties zo aangepast dat de modificaties meer lijken op genen die normaal in het embryo geactiveerd zijn en dus door de cel als eigen worden herkend. Op deze manier konden we ePDZ koppelen aan GPR-1/2, LIN-5 of dynein en de eiwitten zo met licht naar een bepaalde plek in de cel sturen. Hiervoor is ook een tweede eiwitcomponent nodig, genaamd 'LOV'. ePDZ en LOV binden aan elkaar, maar enkel in de aanwezigheid van blauw licht. Door LOV bijvoorbeeld aan de membraan te koppelen kan een eiwit waar een ePDZ modificatie aan zit naar het membraan verplaatst worden met licht (**Figuur 2**). Dit hebben we voor GPR-1/2, LIN-5 en dynein apart gedaan, terwijl we de andere onderdelen van het anker verstoorden.

Om een voorbeeld te noemen: we kunnen met dit systeem dynein naar de cortex brengen en tegelijkertijd Gα, GPR-1/2 en/of LIN-5 verstoren. Op deze manier wordt de lokalisatie van dynein aan de celcortex puur afhankelijk van de ePDZ-LOV interactie in aanwezigheid van blauw licht. Op deze manier kwamen we erachter dat enkel LIN-5 en dynein samen aan de celcortex genoeg zijn om trekkrachten op te wekken die de mitotische spoel verplaatsen. Gα en GPR-1/2 lijken dus niet essentieel voor het genereren van trekkrachten. Echter, we zien dat de plaatsing van de mitotische spoel dan wel symmetrisch wordt in plaats van asymmetrisch zoals in een normale situatie gebeurt. Het lijkt er dus op dat Gα en GPR-1/2 niet nodig zijn om aan microtubuli te trekken, maar dat ze er wel voor zorgen dat trekkrachten op een ongelijke manier verdeeld worden over de voor- en achterkant van het embryo. Daarnaast vonden we ook dat het anker een belangrijke rol vervult bij het activeren van de dynein motor. Als we namelijk dynein direct naar de celcortex brengen in afwezigheid van LIN-5 dan worden er geen trekkrachten uitgeoefend op de mitotische spoel (**Figuur 3**). Dit laat zien dat LIN-5 een essentiële activator is van dynein; enkel lokalisatie van dynein aan de cortex is niet genoeg om aan microtubuli te trekken. De rol van LIN-5 als activator van dynein kan goed benut worden voor onderzoek naar hoe de positie van de mitotische spoel bepaalt waar het delingsvlak van de cel gevormd wordt. We zijn namelijk in staat om LIN-5 lokaal naar de celcortex te brengen en zo ook lokaal dynein-afhankelijke trekkrachten te activeren. Zo kunnen we de positie van de mitotische spoel experimenteel veranderen. We slaagden er bijvoorbeeld in om deze in plaats van richting de achterkant, zoals in een normaal embryo gebeurt, juist

naar de voorkant te verplaatsen. Zo werd de uitkomst van celdeling precies omgekeerd; in plaats van een grote cel aan de voorkant en een kleine cel aan de achterkant, vormde er een kleine cel aan de voorkant en een grote cel aan de achterkant van het embryo. Ook konden we in tweecellige embryo's de mitotische spoel laten draaien onder een hoek van 90 graden, wat ertoe leidt dat de richting waarin cellen delen verandert (**Hoofdstuk 4**, **figuur 8**). Dit soort technieken kunnen in het vervolg van groot belang zijn voor verschillende typen onderzoek.

Van de mitotische spoel tot het klievingsvlak

Ten slotte gebruiken we vergelijkbare experimenten om de fysieke deling van het embryo te bestuderen in hoofdstuk 5. Naast het positioneren van de mitotische spoel moet namelijk ook deze diens vervolgens de plek aanwijzen waar de cel in tweeën klieft. Het delingsvlak positioneert zich namelijk haaks op het midden van de mitotische spoel. Twee onderdelen van de spoel zijn belangrijk voor het instrueren van het klievingsvlak; de asters en de centrale spoel (**Hoofdstuk 1**, **figuur 5a**). Deze onderdelen van de mitotische spoel leveren beide signalen aan de celcortex die het samentrekken van de celmembraan stimuleren, zodat de cel op het juiste punt in tweeën kan klieven. GPR-1/2 en LET-99 zijn twee eiwitten die hierbij betrokken zijn, en wij vinden dat ook LIN-5 in dit proces een rol speelt. Door de lokalisatie van LIN-5 en LET-99 aan de celcortex te veranderen met de lichtgevoelige techniek beschreven in hoofdstuk 4, laten we zien dat de verdeling van deze eiwitten belangrijk is voor het positioneren van het klievingsvlak. Om dit te bewerkstelligen optimaliseren we het membraangebonden LOV-anker om zo nog preciezer de lokalisatie van ePDZ-gebonden eiwitten te kunnen bepalen.

Al met al voegt dit proefschrift belangrijke nieuwe vindingen toe in de context van het positioneren van zowel de mitotische spoel als het klievingsvlak in *C. elegans* embryo's. Omdat veel van de eiwitten die betrokken zijn bij deze processen geconserveerd zijn in andere dieren zoals het fruitvliegje, kikkers, muizen en de mens geeft het werk dat hier besproken wordt belangrijke nieuwe inzichten die breed toe te passen zijn op het dierenrijk. Door een combinatie van nieuwe technieken voor genetische manipulatie, microscopie en het besturen van eiwitten met behulp van licht toe te passen en te optimaliseren dragen we niet alleen bij aan bestaande kennis, maar openen we ook deuren voor vervolgonderzoek. Duidelijk is dat Gα, GPR-1/2, LIN-5 en dynein allen zeer belangrijk zijn voor het correct reguleren van celdelingen in het vroege embryo, en dat meerdere niveaus van regulatie aangrijpen op deze eiwitten om zo een robuust systeem te creëren.

Curriculum vitae (English)

Ruben Schmidt was born as the son of Peter Schmidt and Lynde Tak on June 24th 1989 in Rotterdam, the Netherlands. In 2007 he finished his pre-university education (profile nature and health with Latin) at the Melanchthon Schiebroek high school in Rotterdam. After starting his bachelor in architecture at the technical university of Delft in 2007, he transitioned to the bachelor biology at Utrecht University in 2008. He completed his bachelor studies in 2011 with the research thesis entitled “The regulatory role of insulin-like peptides and growth factors on fish spermatogenesis. Identification and characterization of igf3 and insl3 transcripts in the Atlantic salmon testis”. This thesis completed an internship supervised by dr. Jan Bogerd and dr. Rüdiger Schulz in the reproductive biology group at Utrecht University. This work was part of the initial honors program of the biology bachelor program which was coordinated by dr. Fred Wiegant en dr. Ton Peeters. As part of this program, he contributed to the book entitled “Biologie in de 21ste eeuw” (biology in the 21st century) which was published in 2011 (de Graaff publishers). This book discussed diverse recent interesting developments in the field of biology and their implications for contemporary society. This publication was written by students, for students. The book was first used as teaching material in the the bachelor program of 2010-2011 at Utrecht University.

In 2011 Ruben started his master Molecular and Cellular Life Sciences at the Graduate School of Life Sciences at Utrecht University, which he completed in 2013. This master included two internships at Utrecht University. The major internship took place under supervision of dr. Jan Bogerd and dr. Rüdiger Schulz and concerned the subject “Isolation, pharmacological characterization and phylogenetic analysis of four Atlantic salmon (*Salmo salar*) gonadotropin-releasing hormone receptors”. The minor research internship took place under supervision of Vincent Portegijs and prof. dr. Sander van den Heuvel at the developmental biology research group, and was entitled “Studying the role of cortical LIN-5 during asymmetric force generation in the early *C. elegans* embryo by using artificial protein heterodimerization”. During both internships Ruben contributed to experiments that would be published in diverse scientific reports. He concluded his master with a thesis entitled “Ubiquitin & Wnt: the diverse roles of ubiquitin in canonical Wnt signaling”, which was supervised by dr. Rik Korswagen at the Hubrecht institute in Utrecht.

In 2014 Ruben started his PhD at Utrecht University in the labs of prof.dr. Sander van den Heuvel (developmental biology) and prof.dr. Anna Akhmanova (cell biology). During his PhD he studied the mechanisms of cell division in the early embryo of the nematode *Caenorhabditis elegans*, using recent developments such as those in genetic manipulation strategies and fluorescence microscopy. The findings of his research are compiled in this PhD thesis entitled “Genetic and optogenetic analysis of cell cleavage plane positioning”, and will be publicly defended on the 29th of January 2020 in the academy building of Utrecht University. During his time as a PhD student Ruben published multiple articles in

prestigious scientific journals. He also presented the results discussed herein at different international science meetings. In addition, during this time he contributed to university teaching by giving lectures for bachelor courses and supervising multiple master students in the lab. After his PhD Ruben will continue as a research assistant in the group of dr. Mike Boxem at Utrecht University. Here, he will support laboratory work such as microscopy and genetic experiments.

Curriculum vitae (Nederlands)

Ruben Schmidt werd geboren op 24 juni 1989 te Rotterdam als zoon van Peter Schmidt en Lynde Tak. In 2007 behaalde hij zijn gymnasiumdiploma (profiel Natuur en Gezondheid met Latijn) aan het Melanchthon Schiebroek te Rotterdam. Na in 2007 met de bachelor Bouwkunde aan de Technische Universiteit Delft te beginnen stapte hij in 2008 over op de bachelor Biologie aan de Universiteit Utrecht. Hier behaalde hij in 2011 zijn bachelordiploma met een onderzoeksscriptie getiteld “The regulatory role of insulin-like peptides and growth factors on fish spermatogenesis. Identification and characterization of igf3 and insl3 transcripts in the Atlantic salmon testis”. Deze scriptie sloot een stage af die werd begeleid door dr. Jan Bogerd en dr. Rüdiger Schulz binnen de groep reproductieve biologie aan de Universiteit Utrecht. Dit werk maakte deel uit van het eerste honoursprogramma binnen de bachelor biologie welke werd gecoördineerd door dr. Fred Wiegant en dr. Ton Peeters. Binnen het honoursprogramma werd onder andere een boek getiteld “Biologie in de 21ste eeuw” geschreven en gepubliceerd (de Graaff, 2011). In dit boek werden interessante vraagstukken binnen de hedendaagse biologie in de context van grote maatschappelijke problemen besproken door studenten, voor studenten. In studiejaar 2010-2011 werd het boek voor het eerst gebruikt als lesmateriaal binnen de bachelor biologie aan de Universiteit Utrecht.

In 2011 begon Ruben aan de master Molecular and Cellular Life Sciences binnen de Graduate School of Life Sciences aan de Universiteit Utrecht, waarvoor hij zijn diploma behaalde in 2013. Als onderdeel van deze master volgde hij twee onderzoeksstages aan de Universiteit Utrecht. Het major onderzoeksproject vond plaats onder leiding van dr. Jan Bogerd en dr. Rüdiger Schulz, met als onderwerp “Isolation, pharmacological characterization and phylogenetic analysis of four Atlantic salmon (*Salmo salar*) gonadotropin-releasing hormone receptors”. Het minor onderzoeksproject vond daarna plaats onder leiding van Vincent Portegijs en prof. dr. Sander van den Heuvel binnen de onderzoeksgroep ontwikkelingsbiologie, met als onderwerp “Studying the role of cortical LIN-5 during asymmetric force generation in the early *C. elegans* embryo by using artificial protein heterodimerization”. Gedurende beide onderzoeksstages leverde Ruben bijdragen aan werk dat gepubliceerd zou worden in diverse wetenschappelijke publicaties. Hij sloot zijn master af met een scriptie getiteld “Ubiquitin & Wnt: the diverse roles of ubiquitin in

canonical Wnt signaling" onder leiding van dr. Rik Korswagen aan het Hubrecht instituut te Utrecht.

In 2014 begon Ruben als promovendus aan de Universiteit Utrecht met een gedeelde aanstelling in de groepen van prof.dr. Sander van den Heuvel (ontwikkelingsbiologie) en prof.dr. Anna Akhmanova (celbiologie). Hier bestudeerde hij de mechanismen van celdeling in het vroege embryo van de nematode *Caenorhabditis elegans*, gebruikmakend van onder andere recente ontwikkelingen in de genetische manipulatie en fluorescentiemicroscopie. De bevindingen van zijn onderzoek zijn gebundeld in dit proefschrift getiteld "Genetic and optogenetic analysis of cell cleavage plane positioning" (Nederlandse titel: "Genetische en optogenetische analyse van de regulatie van asymmetrische celdeling") en worden publiekelijk verdedigd op 29 januari 2020 in het academiegebouw van de universiteit te Utrecht. Binnen zijn promotietraject publiceerde Ruben meerdere artikelen in prestigieuze wetenschappelijke tijdschriften. De resultaten die hierin werden besproken presenteerde hij ook op meerdere wetenschappelijke congressen binnen en buiten Nederland. Daarnaast leverde hij tijdens zijn promotietraject bijdragen aan bachelorcursussen in de vorm van hoorcolleges en begeleidde hij meerdere masterstudenten op het laboratorium. Als vervolg op zijn promotieonderzoek begint Ruben als onderzoeksmedewerker in de groep van dr. Mike Boxem aan de Universiteit Utrecht, waar hij ondersteuning zal leveren bij onder andere microscopie genetische experimenten op het laboratorium.

List of publications

Journal articles

Fielmich, L-E.◊, **Schmidt, R.** ◊, Dickinson, D.J., Goldstein, B., Akhmanova, A. and van den Heuvel, S. (2018). Optogenetic dissection of mitotic spindle positioning in vivo. eLife 7, 1-31.

Schmidt, R., Fielmich, L-E., Grigoriev, I., Katrukha, E.A., Akhmanova, A. and van den Heuvel, S. (2017). Two populations of cytoplasmic dynein contribute to spindle positioning in *C. elegans* embryos. J. Cell Biol. 216, 2777-2793.

Portegijs, V., Fielmich, L-E., Galli, M., **Schmidt, R.**, Muñoz, J., van Mourik, T., Akhmanova, A., Heck, A.J.R., Boxem, M. and van den Heuvel, S. (2016). Multisite phosphorylation of NuMA-related LIN-5 controls mitotic spindle positioning in *C. elegans*. PLoS Genet. 12, 1-32.

Berends, C.W.H., Muñoz, J., Portegijs, V., **Schmidt, R.**, Grigoriev, I., Boxem, M., Akhmanova, A., Heck, A.J.R. and van den Heuvel, S. (2013). F-actin asymmetry and the ER-associated TCC-1 protein contribute to stereotypic spindle movements in the *C. elegans* embryo. Mol. Biol. Cell 1-31.

Morais, R.D.V.S, Nóbrega, R.H., Gómez-González, N.E., **Schmidt, R.**, Bogerd, J., França, L.R. and Schulz, R.W (2013). Thyroid hormone stimulates the proliferation of Sertoli cells and single type A spermatogonia in adult zebrafish (*Danio rerio*) Testis. Endocrinology 154, 4365-4376.

Chen, S.X., Almeida, F.F., Andersson, E., Taranger, G.L., **Schmidt, R.,** Schulz, R.W. and Bogerd, J. (2012). Cloning, pharmacological characterization and expression analysis of Atlantic cod (*Gadus morhua*, L.) nuclear progesterone receptor. Gen Comp Endocrinol; 179, 71-77.

◊ These authors contributed equally to this publication

Books

Daggers, T., Verbiest, S., Kruit, R., **Schmidt, R.**, Cramwinckel, M., Jacobs, I., Bruens, L., Mol, C., Wiegant, F., Liddell, C., Kamp, S., Nuijten, R., Vermunt, D. and Verheugt, M. Biologie in de 21ste eeuw. Uitgeverij de Graaff, 2011. ISBN 978-90-77024-60-7

Oral presentations

Optogenetic control of spindle positioning
Ruben Schmidt, Lars-Eric Fielmich, Daniel J Dickinson, Bob Goldstein, Anna Akhmanova and Sander van den Heuvel
C. elegans development, cell biology and gene expression, EMBO workshop
13-17 June 2018, World Trade Center Barcelona, Spain

Optogenetic control of spindle positioning in vivo
Ruben Schmidt, Lars-Eric Fielmich, Daniel J Dickinson, Bob Goldstein, Anna Akhmanova and Sander van den Heuvel
DutchBioPhysics conference
1-2 October 2018, NH Koningshof Veldhoven, the Netherlands

Optogenetic control of spindle positioning in vivo
Ruben Schmidt, Lars-Eric Fielmich, Daniel J Dickinson, Bob Goldstein, Anna Akhmanova and Sander van den Heuvel
Chemistry As Innovating Science (CHAINS) conference
3-5 December 2018, NH Koningshof Veldhoven, the Netherlands

Optogenetic control of spindle positioning in vivo
Ruben Schmidt, Lars-Eric Fielmich, Daniel J Dickinson, Bob Goldstein, Anna Akhmanova and Sander van den Heuvel
Science for Life conference
19 November 2018, Jaarbeurs, Utrecht, the Netherlands

Acknowledgements (Dankwoord)

So, there it is; my thesis. Over five years of work condensed into book format. I say condensed, but as you might have noticed, the whole thing turned out a bit long. Nevertheless, I certainly hope you enjoyed reading about my work as a PhD candidate. I would lie if I said that these years were without challenge – something anyone following this career path can likely attest to. Yet, overall, this has been an extremely gratifying experience that has changed me a lot as a person. But enough about me. Here, I want to acknowledge the wonderful people that I have had the pleasure of being surrounded with during my studies. It goes without saying that I could not have realized any of this without your contributions. Be it at work, in my personal life, or both.

First of all, my promoter, Sander. Thank you so much for supporting and supervising me all these years. Your door was always open for new results and ideas, and I really appreciate your highly contagious scientific enthusiasm. Whenever an experiment yielded exciting results, I could not wait to share the news, even though I knew I would leave your office with double the amount of work ahead. Your input and the environment you created have allowed me to develop as a scientist, which is something I am very grateful for. Naturally, this also goes for Anna, my co-promoter. Anna, even though most of my time was spent in Sander's lab, having you as a supervisor has been indispensable for my studies. I really respect your approach to science and, even though it took a little getting used to, your direct and unfiltered way of supervising. I definitely will not be confusing kinetochores and kinetochore microtubules again any time soon! Frequenting the Synergy meetings together was very helpful for broadening my scientific horizons. Sander and Anna, thanks again, without your efforts I definitely could not have hoped to come this far. Then, my fellow spindle enthusiast - Lars! I could not have hoped for a better and ultimately more smooth and rewarding cooperation than we had together. Our casual and often three hour long meetings with Sander were incredibly enjoyable and stimulating, and your enthusiasm and inventiveness are things I can only admire. Thanks for everything and best of luck in the future. Vincent, who could deny your contribution to all of this? We met back in the long-gone days of our wild manes through a joint fascination for singing that goes "OÉH!" (met veel galm, uiteraard). Without our personal connection and a fun internship, I definitely would not have started this PhD, let alone finish it. Thanks for the great times in the lab, the support, the tergend flauwe humor, introducing me to the oh so sweet Gutenberg coffee, the hundreds of new bands to check out, and frankly, a very long list of good things. Next, my students. Amir, when we first met, I was positive that you would be a great addition to our embryo group. You definitely did not disappoint, which is something that this thesis can attest to; your thorough analyses have been included in two chapters. It is great that I got to see you grow into a PhD candidate yourself, even though you have left the embryo group behind! Merel, your relatively short internship was really intense. Your enthusiasm and energy are unparalleled, and I definitely needed that cup of

coffee in the morning to keep up with your tempo (thanks for reminding me frequently). Emilia, your experiments have made very important contributions to chapter 5. Even though I was writing my thesis for a large portion of your internship, you managed to do very complicated experiments independently. Many thanks to all three of you for picking me as your supervisor. You have definitely taught me a lot, and I am excited to see what the future will bring for you.

My thanks also go out to others who have directly contributed to the work bundled in this thesis; Eugene and Ilya, all of these chapters have relied heavily on your combined knowledge of microscopy and image analysis. Thank you for being the sturdy foundation of our beautiful imaging facility. Martin, Petra, without your pioneering work Lars and I would never have succeeded, and neither would we have had to spend so many hours in barely lit rooms! To our remote cooperators: Daniel Dickinson, Bob Goldstein, Christian Frokjær-Jensen and Andrew Fire, thank you for helping us to get a grip on that dreaded germline silencing. A special thanks to the members of the reading and doctoral committee for taking the time to thoroughly assess my thesis!

Now I'd like to mention the people who made life in and around the lab a joy for me, and who contributed so much through daily support and discussions. I am very grateful to have spent time together with you in and outside of the lab, be it at one of our BBQs, game nights, parties, conferences, or even at some of my concerts. Mike, I am glad to have been welcomed to your lab even before finishing my PhD. Thank you for the trust you have in me as a research assistant. May the future bring great things - as long as they are not all yeast two-hybrids! Adri, you are an amazing teacher and I am very fortunate to have followed your courses as a student. A special thanks for your invaluable input, advice, and for your contributions to my scientific writing skills. Inge, you are mostly teaching now, but I am happy to have had the pleasure of wrestling with the Biosorter together during my early PhD! Sannneeeee (in falsetto, obviously)! Not only are you a great partner in crime in the lab, but even willing to sell merch during my shows. What else should I wish for in a colleague? Thanks for all the great laughs, the chillings (dikke shout-out naar onze boy Daniel!), and the frequent Iron Maiden karaoke sessions. It really means a lot that you will be one of my paranymphs. João (aka J, J-man, J-J, Bob), 'sup! We started our master internships and PhDs around the same time, and now we are defending our theses only two weeks apart. I am sure you will do an amazing job as the *C. elegans* specialist surrounded by plants. A special thanks for all your selfless effort in evaluating CRISPR strategies and the good times outside work. Victoria, my relentlessly fast-speaking neighbor in both the lab and office. Thanks for always being up for good conversation – your general enthusiasm is a great motivator for me. Seeing all the work you are putting into your projects I am sure you will have an amazing thesis together in no time. Vamos! Molly, it is so sad to see you leave already, but I am glad that you will still be here for my defense. Best wishes back home together with Raam. Helena, our office is not the same without your laugh. Thanks for brightening up many of my days. Amalia, with

your arrival the lab became so much livelier. We just started our first joint project, and who knows, we might even be discussing things in Dutch along the way? Janine, thanks for the good times in the office, best of luck with the last steps in your PhD and have fun exploring the world! Suzanne, sharing the office with you was great fun, and I am really happy to see that you have found fresh motivation to tackle a postdoc. En ja, je voelt 'm al aankomen heuj: yéah, let's go! Thijs, you left the lab quite a while back, but I'm still recovering from some of your worst (or ... best?) jokes. Iets met een poolcafé … Man, man, man. Ben, the great new positive personality in the group! I am sure you will make an amazing teacher for the next generations of biologists to come. Great taste in pants, by the way. Jason, thank you for the good times in the office and I am excited to try some more of that tasty beer you brew. Tessa, as a quite recent (re-)addition to the lab you are fitting right in – it is so good to have another colleague with great taste in music! Aniek, your 'Rotterdamse tirades' really were something to behold. Hope you enjoy your new postdoc, and thanks for thinking of me when you see musical job offers! Jorian - the new ERM-guy - great job following up on João's work. Surely you will do very well in the remainder of your PhD. Jana, enjoy retirement and see you around in Lunetten. I guess will worry about the yeast plates in your stead! Selma and Suzan, we only overlapped during my early PhD, but thanks for helping me on my way. Suzan, by the time you read this you'll have returned to the Kruyt - welcome back!

Also, a big thanks to all those in the cell biology department I've had the pleasure of meeting and working with: Amol, Ankit, Boris, Peter Jan, Chao, York, Benjamin, Dieudonnée, Chiung-Yi, Dipti, Fangrui, Yuije, Liu, Helma, Ivar, Marina, Philipp, Laura, Maud, Max, Bas, Sam, Roderick, Jarno, Wilco, and the list goes on. A special thanks to Kai, Shasha and Jingchao for helping me find my way around the Akhmanova lab. Lukas and Casper, thank you for all the useful input and technical advice along the way. Rüdiger, I am glad to have spent so much of my time in your lab as both a Bachelor and Master student. Jan, thank you for all the effort you put into supervising me, for teaching me the ins and outs of cloning, the virtue of starting the workday early, and for giving me the opportunity to contribute to my first publications. Also, a great thank you to Roberto, Michelle, Kristine, Clara, Kimberley, Rafael Nóbrega and of course Rafael Kuradomi (yes, I will visit Brazil one day). Moving outside of the Kruyt - Rik, thank you for assessing not only my Master's, but also my PhD thesis! Also, a word of thanks to all those in the Hubrecht: Matilde, Lorenzo, Euclides, Annabel, Marco, Erik, Christa, Lotte, and Sanne. Sasha, thank you for the input and of course for organizing great pizza-fueled meetings!

I will continue with some words in Dutch towards my friends and family. Het zal voor niemand die mij een beetje kent een verrassing zijn dat een groot deel van mijn sociaal leven zich afspeelt in muzikale kringen. Zodoende zijn er een aantal medemuzikanten en muziekliefhebbers die in dit dankwoord niet mogen ontbreken. Jelle en Matthias, jullie leren kennen was voor mij een absoluut hoogtepunt van mijn migratie naar het kunstzinnige Utrecht. Onze filmavonden, epische tochten door Zeeland, happy hour in de

Booth, ik heb zo veel goede herinneringen. Jelle, wanneer gaat dat black metal museum nou officieel open? Matt, alleen een ferme “OEH!” dekt de lading. Zonder jullie was ik nooit in contact gekomen met de helden waarmee ik doorheen de jaren het podium heb mogen delen: Pascal, Wessel, David, Michiel, Steven, Leon C., Leon v. R., Yuri, Martijn, Mitch, Dennis, Jan, Wouter, het is me een waar genoegen om tijd met jullie door te brengen, hoe lastig dat soms ook te combineren was met een leven als promovendus. Gied, ik had me geen betere docent cello kunnen wensen. Ik verheug me nog altijd op iedere les. Ook mijn dank aan verdere samenwerkingen, o.a. met Christian en zijn vierkante bananen, de danskuikens van Laster, de volkshelden van Grafjammer, het helaas ter ziele Soulecy, thuisbasis dB’s en de onverslagen topatleten die we allemaal kennen als de Utrecht Feminists. Kris en Toon, boefjes, we moeten de Matrix-crew nieuw leven inblazen. Patricia, die mok is eng geniaal. Hak, maat, ik ben blij je gekend te hebben. Rust zacht.

Uiteraard kan mijn geweldige familie niet ontbreken in dit dankwoord. Opa en oma Tak, oma Schmidt, Coen en Martine, Roos en Vera, Mieke en Ben, Hans en Anita, allemaal bedankt voor de steun en interesse doorheen de jaren. Aan mijn ouders, Peter en Lynde, wat kan ik zeggen. Bedankt voor alles. Jullie onvoorwaardelijke steun betekent enorm veel voor me. Ik hoop dat jullie trots zullen zijn om dit proefschrift in handen te hebben, want hier hebben jullie heel veel aan bijgedragen. Lynde, bedankt dat je altijd voor me klaarstaat, een meer zorgzame moeder had ik mij niet durven wensen. Ik vraag me alleen af of die eerste pannenkoekplantjes van je wel zo’n goed idee waren. Mijn huiskamer begint zo langzamerhand wel erg groen te worden. Peet, wat heb je een werk in de vormgeving van dit proefschrift gestoken. Als we maar geen dikgedrukte komma over het hoofd hebben gezien! Om te zien of je aan het eind van de rit nog scherp bent zal ik hier nog éénmaal *lin-5* verstoppen, die kan natuurlijk niet van de regel afvallen. Ongelofelijk bedankt voor je grenzeloze inzet en enthousiasme, zo’n prachtig boekwerk had ik nooit in mijn eentje in elkaar kunnen draaien. Jade, mijn zusje, wat ben je gegroeid de afgelopen jaren. Figuurlijk dan. Ik ben heel trots dat je op 29 januari naast me staat als één van mijn paranimfen. Geen zorgen, de commissie stelt je vast geen al te lastige vragen!

Laetitia, iets meer dan een jaar geleden had ik niet gedacht iemand te ontmoeten waarmee ik zo op dezelfde golflengte zou zitten. Op de kortste dag van het jaar brengt Archspire mensen samen; duidelijk een traditie om in ere te houden. Ik ben benieuwd hoe ver je door dit boekwerk heen komt met je kersverse kennis van de moleculaire biologie ;). Je maakt me hartstikke gelukkig, bedankt voor een geniaal jaar en op naar een mooie toekomst!

Cheers,
Ruben